KIMBERLITES, MEGACRYSTS AND RELATED XENOCRYSTS FROM SOUTHERN AND CENTRAL AFRICA: GEOCHEMISTRY AND PETROLOGY

By

BULIBA NKERE

Thesis presented for the degree of Doctor of Philosophy (PhD) in Geology
Department of Geological Sciences
University of Cape Town
November 2018

Supervisor: Associate Professor **Philip Janney**

I know the meaning of plagiarism and declare that all of the work in the thesis, save for that which is properly acknowledged, is my own

Buliba Nkere Signed by candidate

November 2018

ACKNOWLEDGMENTS

This doctoral thesis was funded by a National Research Foundation (NRF) Innovation doctoral scholarship (2016 – 2018) and NRF Innovation masters scholarship (2015). The field work to the Kasai region in the DRC was funded by a Society of Economic Geologists (SEG) fellowship (2015). Additional funding was generously provided by the UCT Kimberlite Research Group (2015 – 2017) and my supervisor's research funds. I also gratefully acknowledge the financial support from the CCFS at Macquarie University for the dating work on the Tshibwe kimberlite (2017).

I would like to thank my supervisor, Professor Phil Janney, for the great opportunity he gave by taking me as one of his students and introduction to the mantle research. His supervision, guidance, patience, unmatched support, constructive comments, scientific rigor and encouragements were very critical in the successful completion of this academic journey. I would like to acknowledge the technical support received from Christel Tinguely, Jonathan van Rooyen, Dr Petrous Le Roux, Kerryn Gray, Fayrooza Rawoot, Dave Wilson, Sarah Gaines, Dr Rosana Murphy and Dr Montgarri Catisllo-Oliver.

I would like to thank my parents for their dedication and sacrifices since primary school. They did everything so I could get a better education. I also thank Françoise Kwinja who have been by my side since undergrad. To my best friend, Cyrille Fogno and his support during my stay in Lubumbashi in 2015 while I was en route to Kasai. To my supportive friends and colleagues (Tity Kalegamire, Zigabe Amuli, Basoshi Theophile, Aime Kitima, Eric Byumanine, Nomsa Maripa, Julieth Gudo, Michael Krichner, Arielle Mulunge, Jacky Cornille, Martha Kamkuemah, Rabbin Kabuende, Agnes Odri, Manapo Tebello), I am grateful for your devotion during all these years. I would like to thank my early mentors (Dr. Damien Delvaux and Prof Sarah Stamps) and their support.

I would like to dedicate this thesis to my former lecturers and professors at department of Geology at UOB (university of Bukavu), where I did my undergraduate (Tity Kalegamire, Severin Ongezo, Severin Muyisa, Espoir Mugisho, Basimike Joseph, Prof Charles Nzolang, Prof Muhigwa Bahananga and Prof Kapajika Badibanga, Prof François Lubala from University of Lubumbashi)

Abstract

Kimberlites, megacrysts and related xenocrysts from twelve localities in central and southern Africa have been investigated with particular emphasis on megacryst petrogenesis, the evolution of the subcontinental lithospheric mantle (SCLM) beneath the northeastern Kasai Craton, and the petrogenesis and sources of central African kimberlites. The geochemistry of southern and central African megacryst suites is generally consistent with their derivation from protokimberlitic magmas by a combined fractional crystallization-assimilation process. Through the comparison of the geochemistry of Group 1 and Group 2 kimberlite megacrysts, evidence is provided for a genetic link between megacrysts and their host kimberlites. Major element, trace element and Sr isotope similarities of Group 1 and Group 2 kimberlites and their respective megacrysts strongly suggest a close genetic relationship.

The geochemistry and single mineral thermobarometry of peridotitic clinopyroxene xenocrysts suggests that the SCLM is cooler and more depleted beneath Tshibwe compared to that below Mbuji-Mayi, and this is consistent with the finding from this work that the age of Tshibwe is 84 Ma, approximately 14 Myr older than Mbuji-Mayi. A metasomatic event in this region between 84 and 70 Ma is the simplest explanation for the differences in geochemistry and geothermal gradient inferred for the SCLM sampled by the two kimberlites. The Tshibwe and Mbuji-Mayi kimberlites belong to two clusters that together constitute the Mbuji-Mayi kimberlite field in the northeastern Kasai craton, and this field, possibly combined with the kimberlites of the Kabinda field further to the east in the DRC was formed by a pulse of kimberlite magmatism, from roughly 85 to 70 Ma, that formed a lineament with a roughly east-west orientation. The apparently similar age and orientation of these kimberlites suggests that they were emplaced along an east-west oriented zone of lithospheric weakness in the northeastern Kasai craton, tentatively termed the "Kasai corridor". This may connect with the "Lucapa corridor", a linear zone of concentrated kimberlite magmatism with a northeast-southwest orientation cutting across much of Angola.

The whole-rock composition of central African kimberlites is fairly similar to southern African kimberlites except for having generally lower MREE/HREE ratios, lower overall concentrations of incompatible elements and isotopic compositions ranging from those typical of southern African Group 1 kimberlites to extreme DUPAL signatures with high $^{207}Pb/^{204}Pb_i$ and $^{208}Pb/^{204}Pb_i$ for moderate $^{206}Pb/^{204}Pb_i$ values. Published data for Sr and Pb isotope compositions

of southern and southwestern African peridotite xenoliths indicate that this DUPAL signature most likely does not originate from the lithospheric mantle, but rather is present in the underlying convecting mantle, as appears to be the case for the source for Brazilian kimberlites with similar extreme DUPAL isotope signatures. Data from this study, therefore, require a greater lateral distribution for the extreme DUPAL signatures than has been previously recognised, extending from southwestern Africa to the far southern Mid-Atlantic Ridge to Brazil. The prior, exclusive attribution of this signature, to the "African large low shear velocity province" may be premature.

Thesis summary

Kimberlites, megacrysts and related xenocrysts from twelve localities situated in central and southern Africa have been investigated with particular emphases on megacryst petrogenesis, the evolution of the SCLM beneath the northwestern portion of the Kasai Craton and the petrogenesis and sources of central African kimberlites.

Clinopyroxene and garnet megacrysts from four Cambrian to mid-Cretaceous kimberlites of Group 1 and Group 2 affinities located on the Archaean Kaapvaal and Zimbabwe cratons of southern Africa, have been investigated to better understand megacryst petrogenesis. Additionally, clinopyroxene and ilmenite megacrysts from the late Cretaceous Tshibwe and Mbuji-Mayi kimberlites (located on the Kasai Craton in central Africa) have also been investigated. The geochemistry of southern and central African megacryst suites is generally consistent with their derivation from protokimberlitic magmas by a combined fractional crystallization-assimilation process. Percolation of megacryst parental magmas through fertile metasomatised lithospheric mantle causes assimilation that results in deflection of initial, fractionation-dominated, compositional trends towards higher Cr# and Mg# values with increasing Ca# (i.e., decreasing crystallization temperature) as well as an increase in LREE/HREE and other diagnostic incompatible element ratios and $^{87}Sr/^{86}Sr$ in clinopyroxene megacrysts. In contrast, percolation through infertile metasomatised lithospheric mantle results in the absence of the above deflection and the continuous decrease of Cr# and Mg# with increasing Ca#, as well as a lack of (or weak) increase in LREE/HREE and other diagnostic trace element ratios and $^{87}Sr/^{86}Sr$ in clinopyroxene megacrysts. In the two clinopyroxene megacryst suites investigated that contain both Cr-poor and Cr-rich varieties, there is a continuous compositional variation between them. This fact, and the

nature of their major and trace element variations, supports the notion that the Cr-poor and Cr-rich megacryst varieties are genetically related by the degree of assimilation of metasomatised lithospheric mantle that occurred during fractional crystallization. Pyroxene thermometry suggest that Cr-poor megacrysts crystallized earlier, at higher temperatures, and Cr-rich megacrysts in the same suite crystallized later (after significant lithospheric assimilation), at lower temperatures. A genetic relationship between megacrysts and their host kimberlites is supported by the similarity of their isotope compositions (especially $^{87}Sr/^{86}Sr$), as well as diagnostic trace element ratios. Through the comparison of the geochemistry of megacrysts from Group 1 and Group 2 kimberlites, further evidence has been provided for a genetic link between megacrysts and their host kimberlite. Similarities in major and trace element contents, trace element ratios and Sr isotope compositions between, respectively, Group 1 kimberlites and their megacrysts and Group 2 kimberlites and their megacrysts strongly suggest a close genetic relationship.

In order to put constraints on the evolution of the SCLM beneath the northeastern portion of the Kasai craton, clinopyroxene and garnet xenocrysts, obtained from heavy mineral concentrates from the Tshibwe and Mbuji-Mayi kimberlites, have been investigated. The presence of abundant peridotitic and eclogitic garnets as well as peridotitic clinopyroxenes, suggest that that the lithospheric mantle beneath the Kasai craton is composed of garnet lherzolite and eclogite. Pyroxenites are also likely present. Temperature and pressure estimates and geochemical data for peridotitic clinopyroxene can be used to construct a compositional and thermal profile beneath Tshibwe and Mbuji-Mayi to depths as great as 220 km. On the basis of the abundance and composition of peridotitic clinopyroxene (Sc/V ratios, REE and other incompatible element variations) and the abundance, paragenesis and trace element compositions of garnet, the SCLM beneath Tshibwe appears to be characterised by a lherzolitic lithology that is more garnet-poor, incompatible element-depleted and cooler than the SCLM beneath Mbuji-Mayi, which appears to have been warmer and extensively metasomatised. U-Pb isotopic analysis of groundmass perovskite from the Tshibwe kimberlite samples yielded an age of 84 ± 9.5 Ma, which is in agreement with stratigraphic and other circumstantial geological evidence. The cooler and more depleted SCLM beneath Tshibwe inferred from clinopyroxene thermobarometry and geochemistry is consistent with the fact that Tshibwe is approximately 14 Myr older than Mbuji-Mayi. A metasomatic event in the region between 84 and 70 Ma is the simplest explanation for the differences in geochemistry and thermal gradient of the SCLM inferred for the SCLM at the two

kimberlites from clinopyroxene compositions. The composition of Mbuji-Mayi and Tshibwe peridotitic garnets are consistent with this hypothesis.

The age of the Tshibwe kimberlite appears to have coincided with a change in the direction and velocity of African plate motion. The northeastern Kasai craton appears to have been affected by a pulse of kimberlite magmatism, from roughly 85 to 70 Ma, that was responsible for the Mbuji Mayi kimberlite field (including the Tshibwe cluster) and possibly the kimberlites of the Kabinda field further to the east in the DRC, all of which are in clusters with a roughly east-west orientation. Their apparently similar age and orientation suggests that they were emplaced along an east-west oriented zone of lithospheric weakness in the northeastern Kasai craton, tentatively termed the "Kasai corridor". This may correlate with the recently identified central Kasai shear zone (Jelsma et al., 2016) and may link up with a major kimberlitic lineament to the west, running northeast-southwest through Angola, termed the "Lucapa corridor" (Reis, 1972).

The geochemistry of whole-rock kimberlite samples from seven central African localities, situated on and off the Kasai craton, have been investigated here. The composition of central African kimberlites is fairly similar to southern African kimberlites except for lower MREE/HREE ratios, lower overall concentrations of incompatible elements and isotopic signatures ranging from depleted mantle to extreme DUPAL, with high $^{87}Sr/^{86}Sr_i$ (which may be partly due to alteration) and high $^{207}Pb/^{204}Pb_i$ and $^{208}Pb/^{204}Pb_i$ for moderate $^{206}Pb/^{204}Pb_i$ values. Trace element modeling suggest that the source regions of Group 1 kimberlites in central Africa had a lower proportion of residual garnet than the sources of similar magmas in southern Africa, but residual phlogopite was likely present. The radiogenic isotope character of central African kimberlites ranges from compositions typical of southern African kimberlites (the Kundelungu kimberlites) to extreme-DUPAL type mantle signatures at (Camatue) and depleted mantle components (Mbuji-Mayi and Kundelungu) have been identified.

An asthenospheric origin of the extreme DUPAL anomaly is favoured based on the lack of evidence for such signatures in southern African mantle xenoliths (Class and le Roex, 2005; 2011). A similar situation exists in the Minas Gerais region of Brazil, where kimberlites exhibit extreme DUPAL isotopic compositions (e.g., Bizzi et al., 1995) but there is no evidence from the geochemistry of peridotite xenoliths for such extreme DUPAL signatures in the Brazilian SCLM (Rivalenti et al., 2000; Carlson et al., 2007). The new central African kimberlite dataset presented in this study is not consistent with the hypothesis that mantle sources are homogeneous and that

protokimberlitic magmas are generated from this single depleted mantle source, as previously suggested by Griffin et al., (2014). The similarity between Camatue and Minas Gerais kimberlites, in terms of isotopic composition and inferred mid-Cretaceous emplacement age, adds further support to the hypothesis that these signatures (extreme DUPAL) have a deep origin in the convecting mantle, as this is the simplest way to explain the presence of a strong DUPAL signature extending from southwestern Africa, to the southern Mid-Atlantic Ridge, to eastern South America, over a distance of many thousands of kilometers, from the mid-Cretaceous to the present. This appears to require a greater lateral distribution for the extreme DUPAL signature than previously recognised. The exclusive attribution of this signature, as made by Class and le Roex (2011) to the "African large low shear velocity province" (LLSVP; Garnero et al., 2008), may be premature.

Table of Contents

INTRODUCTION

Just as seismology is an important tool to image the Earth's interior, so too are the chemical and isotopic compositions of kimberlites and their xenoliths, which originate at great depths within the upper mantle. Kimberlites entrain mantle xenoliths and xenocrysts, as well as crustal xenoliths, during their ascent. The petrology and geochemistry of these rocks and minerals have contributed significantly to our understanding of the evolution of the continental crust and lithospheric mantle. Kimberlites have been subdivided into two distinct varieties based on petrographic, chemical and radiogenic isotope affinities (Smith, 1983; Becker and le Roex, 2006; Kjarsgaard et al., 2009). Group I kimberlites have isotopic compositions similar to ocean island basalts and have been associated with sublithospheric (i.e convecting mantle) sources (le Roex et al., 2003; Tappe et al., 2013; Griffin et al., 2014). Group 2 kimberlites have more radiogenic Sr isotope and unradiogenic Nd isotope compositions and have been associated with ancient (metasomatised or enriched) subcontinental lithospheric mantle sources (Becker and Le Roex, 2006; Giuliani et al., 2015). A third minor group, transitional kimberlites, has also been recognized and has isotopic and petrographic characteristics intermediate between Group 1 and Group 2 kimberlites (Skinner et al., 1994; Becker et al., 2007). Kimberlites are found both on Archean cratons and Proterozoic mobile belts. Large numbers of diamondiferous kimberlites have been emplaced within the Kaapvaal and Zimbabwe cratons and have been, and continue to be, mined. These kimberlites and their recovered xenoliths and xenocrysts have been studied extensively. However, numerous kimberlites also exist in other regions of Africa, (e.g., Angola, Sierra Leone, Democratic Republic of Congo e.g., Tappe et al., 2018), but have been much less studied. This thesis attempts to help remedy this situation by providing new descriptions and data for kimberlites, megacrysts and xenocrysts from central Africa, as well as for megacrysts from some of the lesser-studied megacryst suites from the Kaapvaal and Zimbabwe cratons.

A. Objectives

The main objectives of this project are:

- To better understand the petrogenesis of kimberlite megacrysts from southern and central Africa, their relationship to their host kimberlites, and the differences in petrological

evolution and source character between megacrysts from Group1 and Group 2 kimberlites ;

- To use kimberlites and megacrysts to investigate the nature of melt-rock interactions in the lithospheric mantle;
- To place constraints on the composition, thermal structure and evolution of the lithospheric mantle beneath the northeastern portion of the Kasai craton;
- To place constraints on the petrogenesis and origin of central African kimberlites with particular attention on the evolution of mantle sources, geochemistry of source regions and geodynamic implications;
- To determine the emplacement age of the Tshibwe kimberlite in the DRC

B. Hypotheses and Topical questions

B.1. Megacryst petrogenesis

Controversy surrounds the origin and significance of kimberlite megacrysts. The nature of the magma that is parental to the megacrysts remains under debate and, by extension, the relationship between the megacryst minerals and their host kimberlites. One school of thought proposes that megacrysts are genetically related to the host kimberlite (i.e., a near-cognate origin) based on the similarity of Sr, Nd and Hf isotope ratios between kimberlites and megacrysts from each kimberlite group (e.g., Jones, 1987; Nowell et al., 2004). A second school of thought favors the hypothesis that megacrysts have no genetic relationship to their host kimberlite (i.e., a non-cognate origin) mainly on the basis of mismatches in (1) incompatible element compositions between southern African kimberlites and melts calculated to be in equilibrium with their megacryst suites, and (2) Pb isotope compositions between certain kimberlites and associated megacrysts (Davies et al., 2001; Merry and le Roex, 2007). This thesis will focus on developing a robust petrogenetic model to reconcile the major, trace element and isotopic compositions of kimberlites and their megacrysts in light of these topical questions: What is the relationship (if any) between megacrysts and their host kimberlites? What constraints can be placed on the nature of megacryst parent magmas and the lithospheric mantle wallrocks with which these magma interact? What are the similarities and differences in the chemical and isotopic systematics of megacrysts from Group 1 and Group 2 kimberlites? What are the differences (and similarities) in

the extent of melt-wallrock interaction in megacryst suites from kimberlites from southern and central Africa?

B.2. Mantle sources, origins and petrogenesis of central African kimberlites

The origin of kimberlites also remains a long-standing controversy. Their major element compositions require that kimberlites are generated by partial melting of carbonated peridotite. However, it is debated whether this occurs by melting within the convecting mantle, either within the ambient asthenosphere or with the involvement of a mantle plume (Tappe et al., 2011), and/or by melting within metasomatised continental lithospheric mantle. Metasomatism (enrichment in chemical elements by interactions with fluids or liquids) appropriate to explain the incompatible element and isotopic characteristics of kimberlites could have been caused by melts from mantle plumes (Group I) or subduction-related fluids/calc-alkaline melts (Group 2; le Roex et al., 2003; Becker & le Roex 2006). Regardless of their ultimate origins, the textural and geochemical characteristics of kimberlites requires that they have assimilated metasomatised, previously melt-depleted lithospheric mantle during ascent (Mitchell, 2008; Russell et al., 2012).

The quest to understand the origins and age-distance-compositional patterns of kimberlites remain major research goals. There has been a large amount of research conducted to better constrain the age, petrogenesis and sources of kimberlites, particularly in southern Africa, North America and northern Eurasia, through radiometric dating and geochemical analysis. Even so, a large proportion of kimberlites in southern Africa remain geochemically uncharacterised and undated, and kimberlites in other parts of Africa remain largely unstudied. There are very few published studies on the whole-rock major element, trace element and radiogenic isotope compositions of central African kimberlites (e.g., Demaiffe & Fieremans, 1982; Weis & Demaiffe, 1985; Egorov et al., 2007).

This thesis focuses on the whole rock geochemistry (major elements, trace elements and Sr, Nd and Pb isotopes) of the Camatue, Tshibwe and Kundelungu kimberlites of central Africa with the following questions in mind: What are the compositional similarities and differences between central and southern African Group 1 kimberlites? Do these kimberlites originate from the asthenosphere or the lithosphere? Do all central African kimberlites have similar mantle sources? What is the age of the previously undated Tshibwe kimberlite?

B.3. Thermal-chemical evolution of the northeastern Kasai lithospheric mantle

The precise thickness and structure of cratonic lithosphere is still debated (Griffin et al., 2009). Xenocrystic garnet brought up from the mantle by kimberlites carry large amounts of information on the subcontinental lithospheric mantle (SCLM; Ryan et al., 1996; Griffin et al., 2003). Its major and trace element compositions provide useful constraints on equilibration temperatures, pressures and geothermal gradients in the lithosphere at the time of kimberlite emplacment, as well as information on the fertility of, and nature of metasomatism within, the SCLM. Therefore, xenocrystic garnets from kimberlite heavy mineral concentrates can provide information on the thermal and chemical structure of the lithosphere up to depths of 250 km (Griffin, 1998; 2002). Mantle chemical tomography (hereafter simply termed "chemical tomography") is a term coined by Griffin et al. (2003) to describe the technique of using chemical data and depths (converted from pressures obtained from thermobarometry) for a population of mantle xenocrysts from a given locality, to depict how the composition of the lithospheric mantle changes with depth. This technique has some advantages over conventional xenolith studies because, for example, the number of available garnet grains from a given kimberlite locality typically exceeds the number of investigated mantle xenoliths by a factor of more than 100. Similar techniques have been developed using other mantle minerals, most notably clinopyroxene (e.g., Nimis, 1998; Nimis and Taylor, 2000). Such xenocryst-based techniques are particularly important and applicable in the case of central African kimberlites because of the difficulty (for reasons both logistical and climatic) in obtaining peridotite xenoliths samples for study.

The results of chemical tomography studies show that, in the southwestern part of the Kaapvaal craton, the SCLM is thicker, cooler and less metasomatised, whereas, in the northeastern Kaapvaal, the SCLM was strongly metasomatised (enrichment in chemical elements) and refertilised (addition of modal clinopyroxene and garnet) by the Bushveld event to produce more iron-rich mantle than in other regions (Griffin et al., 2003; Kobussen et al., 2008, 2009). Relatively few chemical tomography investigations have been performed for kimberlites from the Zimbabwe craton (Griffin et al., 2003; Begg et al., 2009), and even fewer such studies for kimberlites on the Kasai craton. The one published study (Batumike et al., 2009) suggests that the subcontinental mantle lithosphere beneath the northeastern part of the Kasai craton is composed largely of fertile

peridotite, with a lithosphere–asthenosphere boundary depth of 205 km. To increase the data set of xenocryst compositions and to infer the thermal and chemical state of the Kasai cratonic mantle, the composition of xenocrysts from the Mbuji-Mayi and Tshibwe kimberlites (northeastern Kasai craton) are investigated in this thesis. The following questions will be addressed: What constraints can xenocryst studies, based on garnet and clinopyroxene, provide on the composition of the subcontinental lithospheric mantle beneath the Kasai craton? What is the thermal structure beneath this region? How can chemical tomography results for kimberlites emplaced millions of years apart be used to infer the evolution of the composition and thermal state of the SCLM beneath this region through the Late Cretaceous?

CHAPTER 1. GEOCHEMISTRY OF SOUTHERN AFRICAN KIMBERLITE MEGACRYSTS: COMPARISON BETWEEN THOSE FROM GROUPS 1 AND 2 AND RELATIONSHIP TO HOST KIMBERLITE

1.1. INTRODUCTION

Megacrysts are large (≥ 10 mm) single crystals and crystal intergrowths found in kimberlites and other mafic/ultramafic alkaline volcanic rocks. They are distinguished from xenocrysts by the fact that, generally, they are out of chemical equlibrium with lithospheric peridotite. Megacrysts may consist of olivine, ortho- and clinopyroxene, garnet, ilmenite, and, more rarely, phlogopite and zircon (Harte and Gurney, 1981). They are typically unzoned (Gurney et al., 1979). They are often referred to as the "discrete nodule suite" (Nixon and Boyd, 1973b) to distinguish them from polymineralic xenoliths such as peridotites and eclogites. Eggler et al (1979) defined two distinct types of megacryst populations on the basis of compositon, in some cases with both occurring in the same kimberlite. These are (1) the Cr-poor megacryst suite, which are poor in Cr and Mg and rich in Fe and Ti relative to peridotite minerals, and (2) the Cr-rich megacryst suite, which have Mg- and Cr-rich and Fe- and Ti-poor compositions closer to those of peridotitic minerals. Common phases in the Cr-poor suite are magnesian ilmenite, titaniferous pyrope, subcalcic clinopyroxene, relatively Fe-rich enstatite and olivine. Phlogopite, zircon and pyroxene-garnet and pyroxene-ilmenite intergrowths also occur but tend to be rarer than the other megacryst types (Mitchell, 1986). The Cr-rich suite consists of pyrope, diopside, enstatite, olivine, ilmenite and spinel (Eggler et al, 1979). Additionally, there are differences in the minerals constituting the megacryst suites in Group 1 and 2 kimberlites, with the Cr-poor suite in Group 2 kimberlites being far less common overall than in southern African Group 1 kimberlites (Schulze, 1987) and, when present, nearly always being limited to cpx and/or garnet (Bell et al., 1995).

Most megacrysts are rounded to subangular in shape with smooth surfaces and also grooves, striations and pits that were developed during emplacement of kimberlites. Some megacrysts have shattered, with parting planes or exsolution lamellae producing angular fragments. Megacryst tend to be chemically homogeneous with occasional small mineral inclusions present, including silicates, oxides, carbonates and sulphides (Eggler et al, 1979;

Andersen et al., 1987). Some megacrysts (olivine and ilmenite) may also form polycrystalline aggregates (Schulze, 1984).

Among those mantle petrologists, who argue for a magmatic origin for kimberlite megacrysts, there is a general agreement that they form by fractional crystallization of a silicate melt at great depth, with temperatures ranging from 1400° C to ≈1000° C and pressures of 5 ± 1 GPa in the deep lithosphere, probably near the lithosphere-asthenosphere boundary (LAB; e.g., Harte & Gurney, 1981). In addition to being found in kimberlites, megacrysts can also be found in mafic alkaline rocks such as minettes, alnöites, nephelinites, basanites and alkaline basalts (Dawson, 1980; Mitchell, 1986). However, the mineral assemblage is different from what is typically found in kimberlites. In these alkaline rocks, there are Al-rich augite and enstatite, Ti-rich amphibole (kaersutite) and/or phlogopite, and anorthoclase feldspar in addition to, rarely, pyrope and spinel (Schulze, 1987). They can be genetically related to their host magmas in nearly all cases. The alnöites of Malaita (Solomon Islands, SW Pacific Ocean), on the margin of the Ontong Java plateau, and the Thumb minette (on the Colorado Plateau, western North America) are interesting exceptions because they contain megacryst suites including pyroxene, garnet and ilmenite, which are quite similar to those found in kimberlites (Schulze, 1987; Pearson et al, 2003).

Many studies have been carried out on the origin of kimberlite megacrysts with a particular focus on the nature of their relationship with their host kimberlites and peridotite mantle wallrocks (Nixon and Boyd, 1979b; Burgess and Harte, 1998, 2004; Hops et al. 1992; Bell and Moore, 2004; Moore & Belousova, 2005; Kopylova et al. 2009; Bussweiller et al., 2018). However, controversies remain regarding the origin of the megacrysts and, by extension, the precise relationship between the megacrysts and their host kimberlites. One school of thought proposes a direct genetic (i.e., cognate) relationship between megacrysts and proto-kimberlite magmas (e.g., Hops et al., 1992; Nowell et al., 2004; Janney and Bell, 2017). In this hypothesis, megacrysts (especially the Cr-poor variety) crystallize from deeply derived carbonated silicate melts percolating upward through the lower SCLM (e.g., Bell and Moore, 2004). The protokimberlite magmas undergo an extensive process of melt-rock interaction with the SCLM, which results in them being out of chemical equilibrium with early crystallized Cr-poor megacrysts, but the kimberlites and megacrysts retain a close isotopic similarity (e.g., Jones et al., 1987; Nowell et al., 2004).

A second school of thoughts favors a non-cognate origin in which the megacrysts have no genetic relationship to the host kimberlite. This hypothesis is based on two observations (1) the fact that the major and trace element compositions of kimberlite do not agree with that of the inferred composition of the magma from which the megacrysts (especially the Cr-poor suite) must have crystallized (e.g., Harte and Gurney, 1981; Merry and le Roex, 2007), calculated using standard (i.e., basaltic) partition coefficients; and (2) the distinct Pb isotopic composition of megacrysts and their host kimberlites in the only published study to report the Pb isotope composition of megacrysts (Davies et al., 2001). However, these interpretations may not sufficiently incorporate complications of kimberlite petrogenesis, particularly the fact that the presence of significant carbonate dissolved in melt has a marked effect on mineral-melt trace element partition coefficients (e.g., Keshav et al., 2005; Dasgupta et al., 2009), or the extensive assimilation of metasomatised, Mg- and Cr-rich peridotite by kimberlites en route to the surface (e.g., Russell et al., 2012). Also, more recent evidence suggests that the Pb isotope results of Davies et al. (2001) may have been affected by blank problems, and that the differences between the Pb isotope compositions of the kimberlites and megacrysts studied may be far smaller than initially reported (Janney and Bell, 2014).

Another major controversy related to megacrysts formation is whether they originated from magmatic or metasomatic processes. Contributions invoking magmatic models, propose that megacrysts are fractional crystallization products of protokimberlitic melts (Nixon and Boyd, 1973b; Gurney et al., 1979; Harte and Gurney, 1981; Jones, 1987) undergoing extensive lithospheric assimilation in a down-temperature evolution (Hops et al., 1992; Bell and Moore, 2004; Nowell et al., 2004). Contributions invoking metasomatic models, propose that megacrysts are metasomatic minerals formed due to reaction of kimberlitic fluid with the surrounding mantle in an up-temperature evolution (Rawlinson and Dawson, 1979; Boyd et al., 1984; Doyle et al., 2004; Burgess and Harte, 2004; Moore and Belousova, 2005; Pivin et al., 2009; Kopylova et al., 2009; Arndt et al., 2010; Cordier et al., 2015; Howarth and Taylor, 2016; Kargin et al., 2017).

This chapter will focus on developing a petrogenetic model to reconcile the major, trace element and isotopic compositions of megacrysts and host kimberlites through the detailed analysis of major and trace element and Sr isotopic data from megacryst suites from four southern African kimberlites, specifically two Group 1 kimberlites (Colossus and Orapa) and two Group 2 kimberlites (Kalkput and Bellsbank) located on the Archean Kaapvaal-Zimbabwe craton.

The following questions will be addressed:

(1) What constraints can be placed on the nature of megacryst parent magma or metasomatic fluids and the lithospheric mantle wallrocks with which these liquids interacted?
(2) What are the similarities and differences in the chemical and isotopic systematics of megacrysts from Group 1 and Group 2 kimberlites?
(3) What is the relationship between Cr-poor and Cr-rich megacryst suites?
(4) What constraints can be placed on temperature during megacryst formation?
(5) What are the major differences and similarities in the nature and extent of melt-wallrock interactions between southern Africa and other cratonic regions worldwide revealed by megacryst geochemistry, and what are their implications for the process(es) of megacryst petrogenesis?

The overall objective of this work is to obtain a better understanding of the relationship between megacrysts and their host kimberlites.

1.2. GEOLOGICAL SETTING

The Kaapvaal craton covers a surface of approximately 1.2 million square kilometers and consists predominantly of granitoids with older tonalitic gneisses (3.6-3.7 Ga) and narrow early Archean greenstone belts (3.0-3.5 Ga; Armstrong et al., 1990; De Wit et al., 1992; Kröner and Tegtmeyer, 1994). The Kaapvaal craton formed and stabilized between 3.7 and 2.6 billion years ago (de Wit et al., 1992). The Kaapvaal craton is comprised of an eastern domain with age of ca. 3.5 Ga and a western domain mostly younger than 3.2 Ga (Anhaeusser, 1990).

The Kaapvaal craton is bounded to the south, southwest and southeast by the Namaqua – Natal Proterozoic mobile belt (ca. 1.1– 1.9 Ga; Eglington, 2006). To the north of the Kaapvaal craton is the Zimbabwe craton and the two are attached by means of the by the Limpopo Belt, a late Archean orogenic belt. The Limpopo Belt, sandwiched between the two cratons, is a collisional terrane generally considered to have formed when the Kaapvaal and Zimbabwe cratons were consolidated in Late Archean time (van Reenen et al., 1992).

To the north of the Limpopo Belt, the Zimbabwe craton contains a 3.5–2.8 Ga TTG (tonalite-trondhjemite-granodiorite) complex, unconformably overlain by the 2.8–2.7 Ga Bulawayan Supergroup (komatiites, flood basalts, and sediments) and overprinted by ca. 2.6 Ga granitoids (Blenkinsop et al., 1997). The Great Dyke and its satellites were emplaced at 2.57 Ga (Oberthür et al., 2002). During Proterozoic time, the Zimbabwe craton remained uplifted, and no sedimentary basins formed (Dirks and Jelsma, 2002). Around 2.6 Ga, the stabilization of the Zimbabwe craton was associated with the emplacement of large volumes of granites belonging to the Chilemanzi suite (Wilson et al.,1995; Jelsma et al, 1996). The formation of the Zimbabwe craton is considered to have occurred in 2 distincts episodes: the first (3.8 to 3.2 Ga), which involved the formation of the early cratonic nucleus, and a second episode (3.0 to 2.6 Ga), which involved magma genesis and formation of mature continental crust (Horstwood et al., 1999; Gore et al, 2009).

Recent seismic studies suggest a stratification of Kaapvaal craton mantle, indicated by the presence of an apparent boundary separating depleted and metasomatised lithospheric layers (Sodoudi et al., 2013), which is supported by chemical tomography from garnet xenocryst studies (e.g., Kobussen et al., 2008; 2009). The following sections describe the age and setting of the different kimberlites studied:

1.2.1. COLOSSUS

Colossus is a Group 1 kimberlite located in the central part of Zimbabwe, 50 km north of Bulawayo city. This kimberlite is located on the Archean Zimbabwe craton and is part of the Wessels kimberlite field (Phillips et al., 1999). The age of emplacement of the Colossus kimberlite is 532.5 Ma (Phillips et al., 1999). The Formona granite (2.6 Ga) forms the country rock surrounding the kimberlite. The mineral chemistry of Colossus olivine megacrysts and their textural relationship to the surrounding kimberlite has been investigated by Moore (2012) and Moore and Costin (2016), and a limited set of garnet megacryst data from Colossus was previously reported by Bell and Moore (2004).

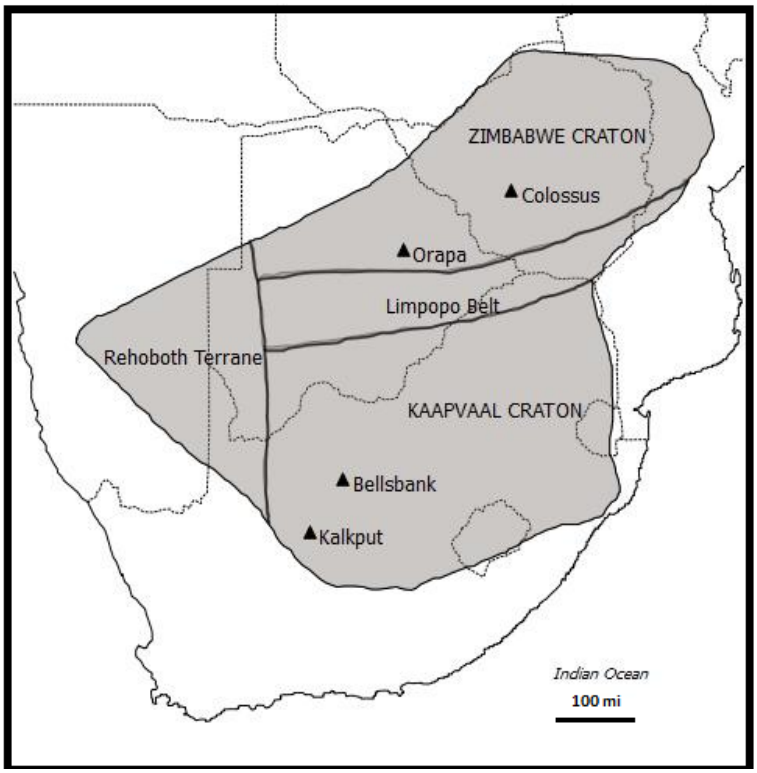

Figure 1.1: Locations of the studied southern African kimberlites, and the inferred boundaries of Archaean cratons and neighboring mobile belt terranes. Modified after Merry and le Roex, (2007).

1.2.2. ORAPA

The Orapa kimberlite (also termed pipe AK1; Shee and Gurney, 1979) is located 240 km west of Francistown in the western part of Botswana's Central District. There are 54 kimberlites in the Orapa cluster. Orapa is a Group 1 kimberlite and has an emplacement age of 92.1 Ma (Davis, 1977). Orapa penetrates through Archean granite-gneiss basement (of the Paleoproterozoic Magondi mobile belt, Stowe et al. 1984). Recent studies indicate that the underlying mantle lithosphere is Archean age and is a western extension of the Zimbabwe craton (Stiefenhofer, 1993; Carlson et al., 1999). The major element mineral chemistry of the Orapa megacrysts has been addressed previously to an extent by Shee (1978), Shee and Gurney (1979) and Tollo (1982) who analysed a wide range of xenolith and megacryst types from Orapa. Orapa has also yielded a suite of eclogite xenoliths, described by Viljoen et al. (1996) and Aulbach et al., (2017).

1.2.3. BELLSBANK

The Bellsbank kimberlite is located in the Northern Cape Province of South Africa, near Barkly West (34 km from Kimberley) and it has an age of 120 Ma (Smith, 1983), which is similar

to that of most Group 2 kimberlites in the western Kaapvaal craton (Smith et al., 1985). The Bellsbank kimberlite comprises a series of en echelon dykes that have intruded through the Archean basement overlain by dolomite of the Campbell-Rand series along two main fissure systems that strike NE-SW and are several kilometers long and several kilometers apart (Boctor and Boyd, 1982). Meyer and McCallister (1984) studied unusual two-pyroxene megacryst intergrowths from Bellsbank among other localities. Eclogite xenoliths from this locality have also been studied previously (Taylor and Neal, 1989; Neal et al., 1990).

1.2.4. KALKPUT

The Kalkput kimberlite is located in the Northen Cape, near Prieska (roughly 200 km southeast of Upington). It is a Group 2 kimberlite and located on the southwestern edge on the Kaapvaal craton. The emplacement age is 119 Ma (Smith et al, 1994). The Prieska district represents an area that is populated with an unusually high density of distinct Group 1 and Group 2 kimberlites. There are roughly 130 known kimberlite localities in the neighborhood of Prieska (Smith et al., 1994; Mitchell, 2013). Some clinopyroxene megacrysts data have been previously reported by Debruin (1999). Those data include major elements but no trace element data Kalkput clinopyroxene megacrysts.

1.3. SAMPLES AND ANALYTICAL METHODS

Clinopyroxene and garnet megacrysts from four southern African kimberlites (Kalkput, Bellsbank, Orapa and Colossus) were selected for analysis. These came primarily from coarse heavy mineral concentrates archived in the J.J. Gurney Upper Mantle Research Collection at the Unversity of Cape Town. Kalkput clinopyroxene megacrysts came from specimens collected by D. R. Bell. Minerals selected for analysis were between 5 and 20 mm in their largest dimension, with most being between 5 and 10 mm. However, these often had broken surfaces indicating that they represent fragments of originally larger grains. These mineral grains were broken into fragments and 2 fragments from each mineral were mounted in high-purity epoxy for in situ analysis by electron microprobe and laser ablation ICP-MS. A subset of clinopyroxenes were then selected for in situ Sr isotope measurements by LA-MC-ICPMS.

Electron Probe Microanalysis (EPMA)

Before mounting, each grain was carefully handpicked under the microscope in order to avoid grains that were altered or had inclusions. The major element compositions of individual mineral grains were determined using a JEOL JXA-8100 electron microprobe in the Department of Geological Sciences at the University of Cape Town. Data were acquired with an accelerating voltage of 15 kV and beam current of 40 nA. For each grain, 2 spots were analysed. Therefore, the data reported here for each megacrysts are averages of 4 spots. All electron microprobe measurement sessions included analysis of an in-house clinopyroxene, garnet or ilmenite mineral standard (from JJG-1424, a Thaba Putsoa garnet websterite or Monastery IL-52 ilmenite megacryst) at the beginning and once again roughly every 20 measurements. If the standard value deviated from the accepted value by more than 5-10 relative percent for any of the elements present at significant levels (e.g., SiO_2, Al_2O_3 , FeO, MgO or CaO for clinopyroxene), that element was re-calibrated. Precision was better than 2 % relative for concentrations above 0.5 wt.% and detection limits were as follow: SiO_2, NiO = 0.006 wt.%; Al_2O_3, Cr_2O_3, MgO, Na_2O = 0.04 wt.%; FeO, MnO = 0.07 wt.%; CaO = 0.03 wt.%; K_2O, TiO_2 = 0.02 wt.%. There was no evidence of zoning within individual mineral. A subset of the megacrysts were selected for trace element measurements on the basis of their major element compositions so as to represent (as much as possible) the full range of magmatic evolution and major element variation within each megacryst suite. Details with regard to standard values and analytical precision for the microprobe are given in appendix (Table 39 and 40; pages 303 – 304).

Laser Ablation Inductively Coupled Plasma-Mass Spectrometry (LA-ICP-MS)

Trace element data were acquired using a Thermo X-Series 2 quadrupole ICP-MS coupled to a 213 nm frequency-quintupled Nd-YAG New Wave UP213 laser ablation system. A typical analysis consisted of three replicates of 100 readings each, with each reading representing one sweep of the mass range. Helium was used as the ablation gas, and was mixed with argon prior to entering the plasma. The counting time for each sample was typically 140 seconds. Every hour a gas blank analysis was performed with the carrier gases flowing, but without the laser firing, to establish the background. The NIST 610 and 612 doped glass standards were used for calibration and were re-acquired after every 10 measurements. Measured concentrations were corrected by

use of a normalisation factor obtained by ratioing the intensities measured on ^{44}Ca (cpx) or ^{30}Si (garnet) to the value for that element determined by electron microprobe. Typical detection limits range from 10-20 ppb for REE, Ba, Rb, Th, U, Nb, Ta, Pb, Sr, Zr, Hf, 100 ppb for Sc, and 2 ppm for Ni. The typical precision and accuracy for a LA-ICP-MS analysis range from 1 to 10%. Details with regard to standard values and accuracy for laser ablation ICPMS are given in appendix (Table 41 and 42; pages 304 – 305).

Laser Ablation Multicollector Inductively Coupled Plasma-Mass Spectrometry (LA-MC-ICPMS)

In situ Sr isotope measurements were performed by LA-MC-ICP-MS at UCT using a Nu Plasma HR multicolletor ICP-MS instrument and a New Wave UP213 laser ablation system. All isotopes of Sr were measured, as was ^{85}Rb for correction of isobaric overlap of ^{87}Rb on ^{87}Sr. Hand-picked clinopyroxene grains were mounted in high purity epoxy discs and polished. Helium was used as a carrier gas which was mixed with Ar via a y-connector, before injection into the plasma. For Sr isotope analysis the area to be used for a 750µm line scan was first cleaned by rapid laser ablation (50µm/sec translation, 250µm spot, 20Hz repetition rate, ~0.65J/cm^2 energy density), and then sampled for 150 seconds (5µm/sec translation, 200µm spot, 20Hz repetition rate, ~5.8J/cm^2 energy density).

The general in situ Sr isotope analysis technique used in this study has been described by Copeland (2008), but in this study we used an in-house clinopyroxene laser standard, JJG1424. The Sr isotope composition of JJG1424 was characterized by solution MC-ICP-MS analysis, with the analysis of three separate 50 mg hand-picked aliquots of clinopyroxene yielding an average $^{87}Sr/^{86}Sr = 0.70495 \pm 0.00003$ (external $2s_{measured}$). This in-house clinopyroxene standard was analyzed by laser ablation at the start and end of each analytical session, i.e. between sample changes, to assess the instrument setup. Repeated in situ analysis by LA-MC-ICP-MS of this clinopyroxene standard over a period of 6 months gave average $^{87}Sr/^{86}Sr = 0.70482 \pm 0.00030$ (2s, n=143) and during the course of this study $^{87}Sr/^{86}Sr = 0.70496 \pm 0.00010$ (2s, n=18), in good agreement with the results from standard solution analysis. The intensity of the Sr isotope signal (total Sr voltage 1.4-2.5V) was blank corrected by subtraction of an initial 30 second on-peak background measurement of the gas blank. Instrumental mass fractionation was corrected using the exponential law and a value of $^{86}Sr/^{88}Sr = 0.1194$, whereas the interference by ^{87}Rb was

subtracted from the measured signal intensity of mass 87 by monitoring mass 85 and applying a $^{87}Rb/^{85}Rb$ value of 0.385706. Based on solution experiments this correction is robust when the ^{85}Rb signal is less than 0.3% of the total Sr signal and the analyses reported in Table 38 (Appendix) all had a ^{85}Rb signal smaller than this value, most with ^{85}Rb«0.1%.

1.4. RESULTS - GROUP 1 KIMBERLITE MEGACRYSTS

1.4.1. CLINOPYROXENE MEGACRYSTS FROM GROUP 1 KIMBERLITES

A. Major element systematics

Due to the pyroxene solvus (Lindsley, 1983), the Ca-number of pyroxene is a function of its crystallization temperature, with Ca# increasing in clinopyroxene with decreasing temperature (see section 1.7.1). Major element compositions of Colossus and Orapa clinopyroxene megacrysts are given in Tables 1 and 2 in the Appendix. Colossus clinopyroxenes display a restricted range of Ca# (29 – 36), while Orapa clinopyroxenes exhibit a wide range of Ca# variation (30 – 49, Fig. 1.2).

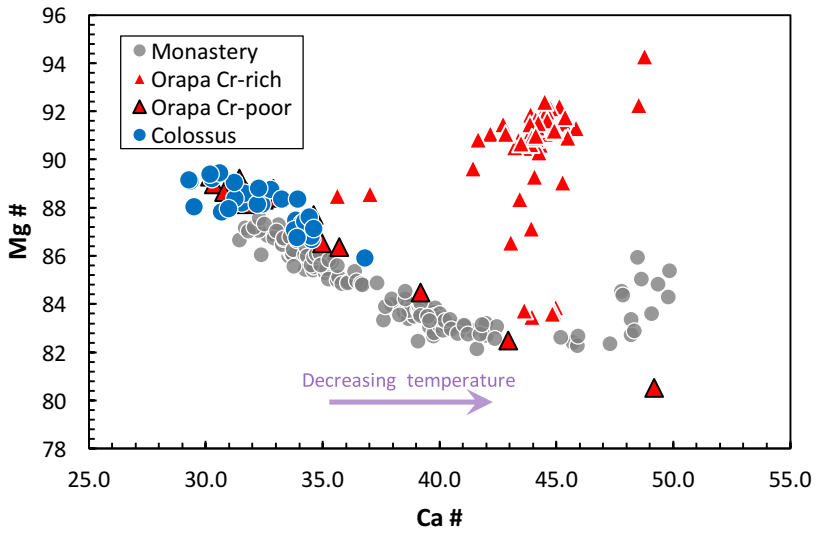

Figure 1.2: Ca # (100*Ca/(Ca +Mg) in atomic units) versus Mg # (100*Mg/(Mg + Fe) in atomic units) plot showing Orapa and Colossus clinopyroxene megacryst data. Monastery cpx megacrysts (Group 1) data are shown for comparison (compilation of data for Monastery cpx is from the UCT Kimberlite Research Group database and includes data from Jakob et al., 1977; 1979 and Moore, 1986, as well as unpublished data).

Mg# and Cr# in both Colossus and Orapa cpx megacrysts initially decrease with increasing Ca#,

as both Mg and Cr are being removed from the magma by the crystallization of clinopyroxene and possibly co-existing phases. In Orapa, however, there is a bifurcation early on (at a Ca# value of about 35) and, at higher Ca# values, one population of Orapa cpx continues to decrease in Mg# and Cr# but another, larger population tends to show an increase in these values, although with a considerable spread that increases with increasing Ca#. The two populations are most clearly distinct in plots of Ca# versus Cr# (Fig. 1.3)

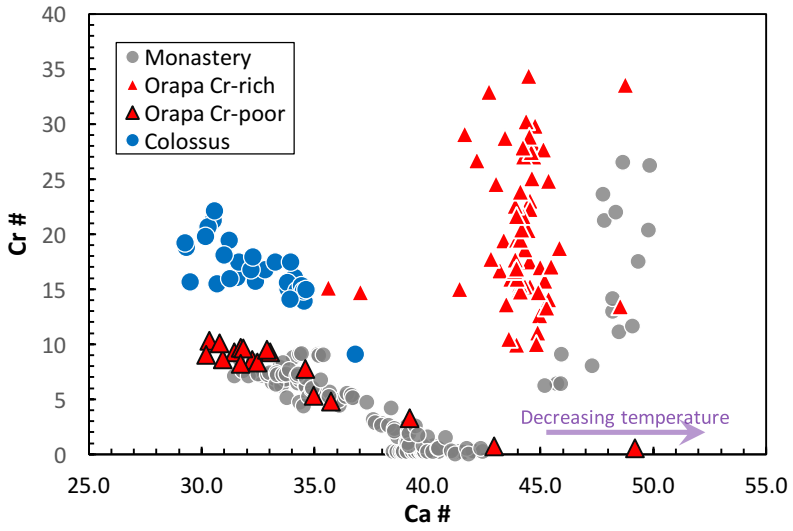

Figure 1.3: Ca# versus Cr # (100*Cr/(Cr + Al) in atomic units) plot showing Orapa and Colossus cpx megacryst data.. Monastery cpx megacrysts (Group 1) data are shown for comparison (compilations from UCT Kimberlite Research Group database).

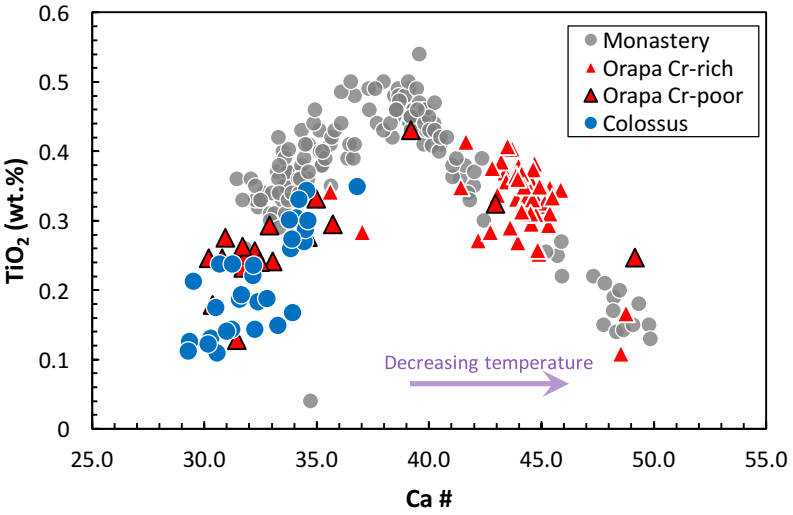

Figure 1.4: Plot of wt.% TiO_2 versus Ca # showing Orapa and Colossus cpx data. Note the sudden decrease in TiO_2 content beginning at about a Ca# value of 40, possibly indicating the onset of ilmenite crystallization.

In contrast, the TiO_2 content in both suites (Colossus and Orapa) initially increases, presumably due to the incompatibility of Ti in the crystallizing assemblage. At Ca# values greater than about 40 (exhibited only by Orapa, since the Colossus data do not extend to Ca# values greater than 37), this trend changes abruptly and TiO_2 contents begin to decline with decreasing crystallization temperature. A plausible explanation is that the decrease in TiO_2 is caused by the onset of ilmenite crystallization, which would effectively remove Ti from the magma (Fig. 1.4). The Cr-rich and Cr-poor clinopyroxene populations of Orapa megacrysts are not distinguishable, and both show the initial increase and later decrease in TiO_2 content. The vast majority of the Orapa Cr-rich and Colossus cpx megacrysts plot in the garnet peridotite field of Nimis (1998) in a plot of Al_2O_3 versus Cr_2O_3 (Fig. 1.5).

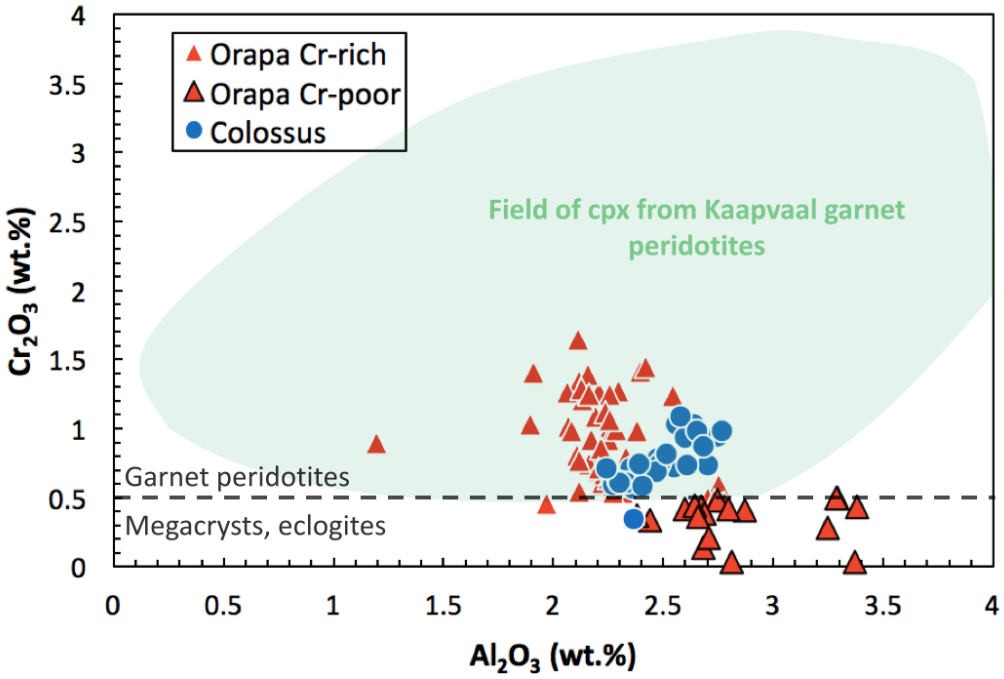

Figure 1.5: Plot of wt.% Al_2O_3 versus wt.% Cr_2O_3 (wt.%) showing Orapa and Colossus cpx megacryst data, along with data for Kaapvaal peridotitic clinopyroxene (Moore and Lock, 2001; Grégoire et al., 2003 and unpublished compilation of D.R. Bell) and the garnet peridotite and megacryst fields of Nimis (1998). The Cr-poor Orapa population falls within the megacryst field, whereas most Cr-rich Orapa megacrysts fall within the peridotitic field. Despite this, the Cr-rich Orapa megacrysts form a curvilinear trend with Orapa Cr-poor megacrysts.

B. Trace element systematics

Trace element data are given in Tables 8 and 9 in the Appendix. Colossus cpx megacrysts display nearly uniform trace element patterns, with moderate enrichment of light rare earth elements (LREE) relative to heavy rare earth elements (HREE; with $(Nd/Yb)_N$ ranging from 5.7 to 10.4), negative Pb and Zr-Hf anomalies relative to elements of similar incompatibility, and general depletion of the most highly incompatible elements (Rb, Ba, Th, U, Nb, Ta) relative to moderately and mildly incompatible elements (Fig. 1.6). The trace element concentrations in Colossus cpx megacrysts are relatively uniform. There is a small increase in LREE relative to HREE (e.g., in Nd/Yb ratio; Fig. 1.7) with increasing Ca#.

Orapa Cr-poor cpx megacrysts show similar REE and primitive mantle-normalised incompatible element patterns to the Colossus Cr-poor cpx megacrysts, although with slightly higher and more variable $(Nd/Yb)_N$ ratios (6.3 to 12.4). They show similar negative anomalies in Pb and Zr-Hf and depletions in the most highly incompatible elements, although with a pronounced negative Ba anomaly that is not seen at Colossus (Fig. 1.6d). The Cr-rich Orapa megacrysts show more variable, but generally greater, LREE enrichment ($(Nd/Yb)_N$ = 9.9 to 33.6) along with highly variable Zr-Hf anomalies (ranging from negative to positive) and highly variable contents of the most highly incompatible elements, ranging from significant depletions similar to the Cr-poor megacrysts to relative undepleted compositions (Fig. 1.6d). Orapa Cr-poor cpx show no systematic change in $(Nd/Yb)_N$ ratios with Ca#, but the Cr-rich megacrysts show an increase in variability in $(Nd/Yb)_N$, toward higher values, with increasing Ca# (Fig. 1.7), displaying similar behavior to that seen in plots of Ca# versus Mg# and Cr#.

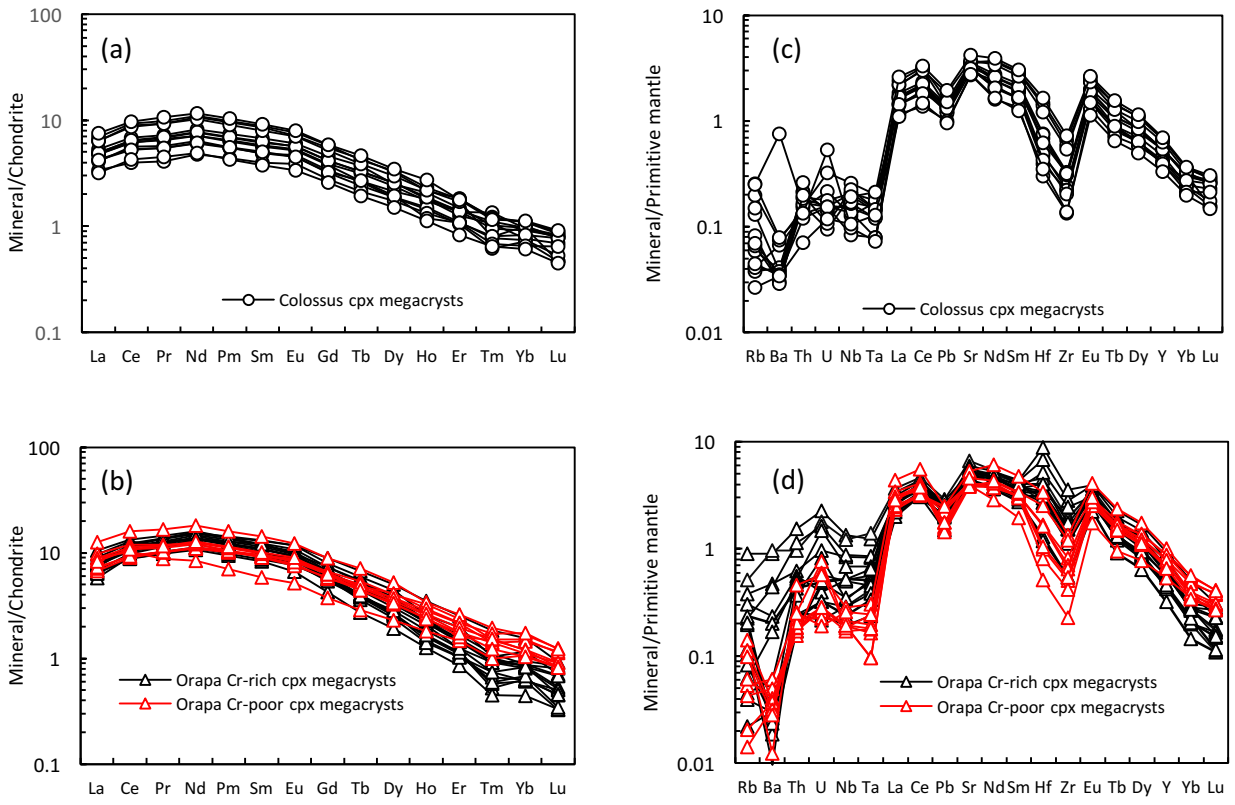

Figure 1.6: Chondrite-normalised REE patterns (a and b) and primitive mantle-normalised incompatible element patterns (c and d) of Colossus and Orapa cpx megacrysts. Note the nearly uniform patterns of the Cr-poor megacrysts from both localities compared to the more variable compositions for the Cr-rich Orapa megacrysts. Normalizing values from McDonough and Sun (1995).

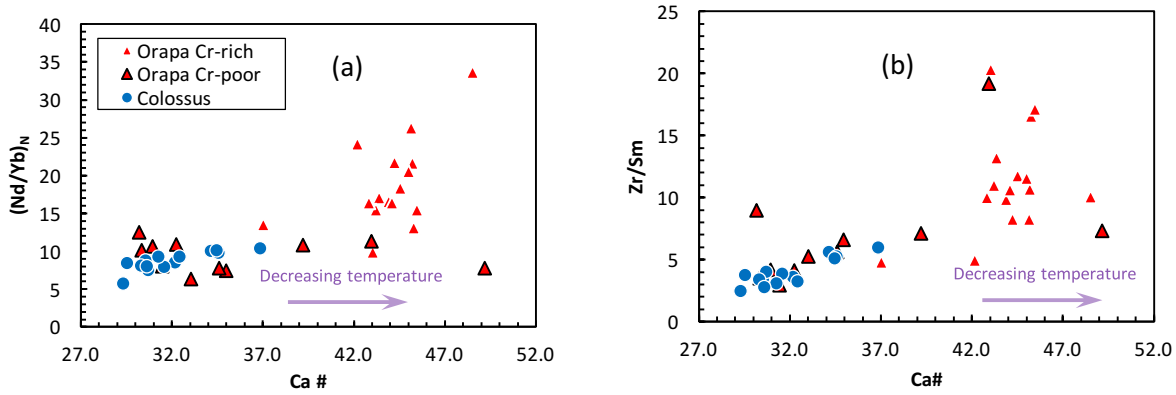

Figure 1.7: Ca # versus $(Nd/Yb)_N$ (a) and versus Zr/Sm (b) showing data for Orapa and Colossus cpx megacrysts. Note the strong increase in LREE relative to HREE with decreasing temperature displayed by the Orapa Cr-rich megacrysts. In contrast, no increase in LREE is seen in Orapa Cr-poor megacrysts. Normalizing values are from McDonough and Sun (1995).

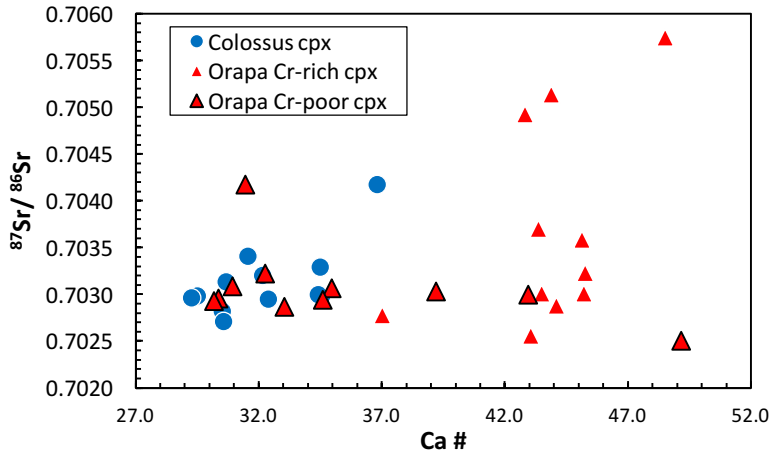

Figure 1.8: Ca # versus measured $^{87}Sr/^{86}Sr$ for Orapa and Colossus cpx megacrysts. Note the general increase in $^{87}Sr/^{86}Sr$ with increasing Ca# at Colossus and in the Orapa Cr-rich megacryst suite. Analytical uncertainties of ±0.0002

C. Sr isotope systematics

Colossus cpx megacrysts have measured $^{87}Sr/^{86}Sr$ ranging between 0.7021 and 0.7042, overlapping with, but extending to lower values than, the range for Group I kimberlites (e.g., Smith, 1983). Although the correlation between measured Sr isotope ratios and Ca# is not strong, there is a clear increase in $^{87}Sr/^{86}Sr$ with increasing Ca#. Data are given in Table 15 of the Appendix.

Orapa cpx megacrysts have a measured $^{87}Sr/^{86}Sr$ range that is similar to that of Colossus (0.7028 – 0.7057 and 0.7029 – 0.7042 for Orapa Cr-rich and Cr-poor cpx megacrysts respectively), also falling within the range of Group 1 kimberlites. Orapa Cr-rich megacrysts appear to show a broad increase in the variability of measured Sr isotope ratios, toward higher values with increasing Ca# (very similar to the pattern displayed by Ca# vs. $(Nd/Yb)_N$) and they also extend to higher $^{87}Sr/^{86}Sr$ values than the Orapa Cr-poor megacrysts. These latter megacrysts show a relatively constant $^{87}Sr/^{86}Sr$ value of ≈0.703, with one grain having a lower and one grain having a significantly higher value (Fig. 1.8).

1.4.2. GARNET MEGACRYSTS FROM GROUP 1 KIMBERLITES

Data are given in Tables 5 and 6 of the Appendix. The Orapa and Colossus garnet megacrysts plot in the G1 field of Grütter et al. (2004) and the two groups of Orapa garnets define two distinct trends on the plots in Figure 1.9. The low-Cr Orapa garnet megacrysts display a coherent trend in Figure 1.9, characterized by a strong positive correlation of Cr_2O_3 and CaO contents and these garnets extend to far lower MgO contents than either Orapa high-Cr or Colossus garnet megacrysts (Fig. 1.9). A second trend is exhibited by the Orapa high-Cr garnet megacrysts, with a weak positive correlation of CaO and Cr_2O_3, having a significantly steeper slope than that for the low-Cr megacrysts. The high-Cr Orapa megacrysts define a data envelope with an increasing variability of Cr_2O_3 contents as Mg# values increase above about 75.

The Colossus garnet megacryst data overlie the middle of the Orapa high-Cr garnet megacryst trend in Figure 1.9a, but show little correlation of CaO and Cr_2O_3 values. They display a clear positive correlation between Mg# and Cr_2O_3 contents that overlies the data field for the Orapa high-Cr megacryst data, which could be explained as a simple fractional crystallization trend.

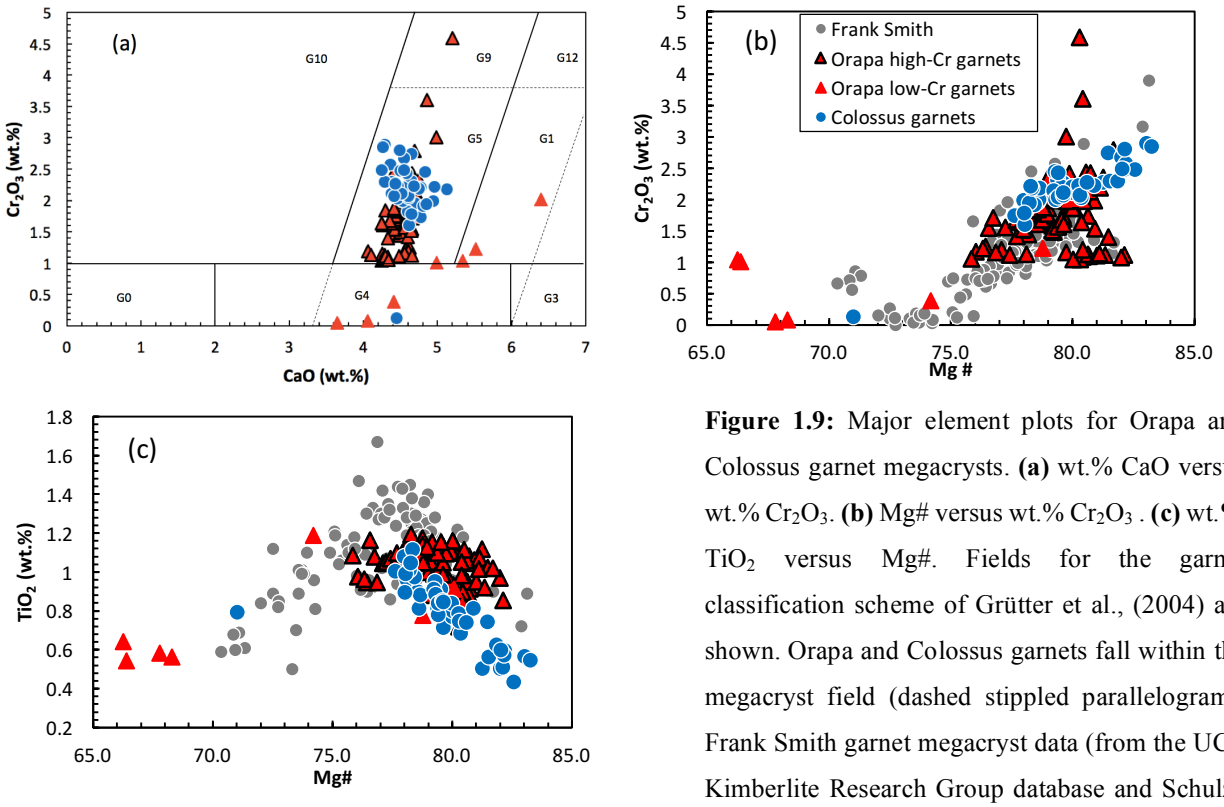

Figure 1.9: Major element plots for Orapa and Colossus garnet megacrysts. **(a)** wt.% CaO versus wt.% Cr_2O_3. **(b)** Mg# versus wt.% Cr_2O_3 . **(c)** wt.% TiO_2 versus Mg#. Fields for the garnet classification scheme of Grütter et al., (2004) are shown. Orapa and Colossus garnets fall within the megacryst field (dashed stippled parallelogram). Frank Smith garnet megacryst data (from the UCT Kimberlite Research Group database and Schulze et al., 2000) are shown for comparison.

The Orapa and Colossus garnet megacrysts examined show similar patterns in the plot of Mg# versus TiO_2 content (Fig. 1.9c). At Mg# values above about 75, there are strong (e.g., Colossus) to weak (e.g., Orapa high-Cr) negative correlations between Mg# and TiO_2. At Mg# values below 74, the relationship changes and TiO_2 content shows an apparent positive relationship with Mg#, where it decreases with decreasing Mg#. However, it must be noted that this positive correlation is only exihibited by the low-Cr megacryst data from Orapa, with one of the megacrysts from Colossus plotting in the midst of this second trend (there are no Orapa high-Cr megacryst data with Mg# of less than 75).

Trace element data are given in Tables 12 and 13 of the Appendix. Orapa and Colossus garnet megacrysts display REE patterns typical of mantle garnet (Fig. 1.10). Orapa and Colossus garnet megacrysts are enriched in Hf, Zr and HREE relative to the LREE, Sr, Nb, Ta, Th, U and Rb. Orapa low-Cr garnets are particularly highly enriched in Hf, Zr and HREE compared to their high-Cr counterparts (Fig. 1.10). All three garnet megacryst groups (Orapa high-Cr, Orapa low-Cr and Colossus) display positive correlations between chondrite-normalised Ce/Yb ratio and Mg#.

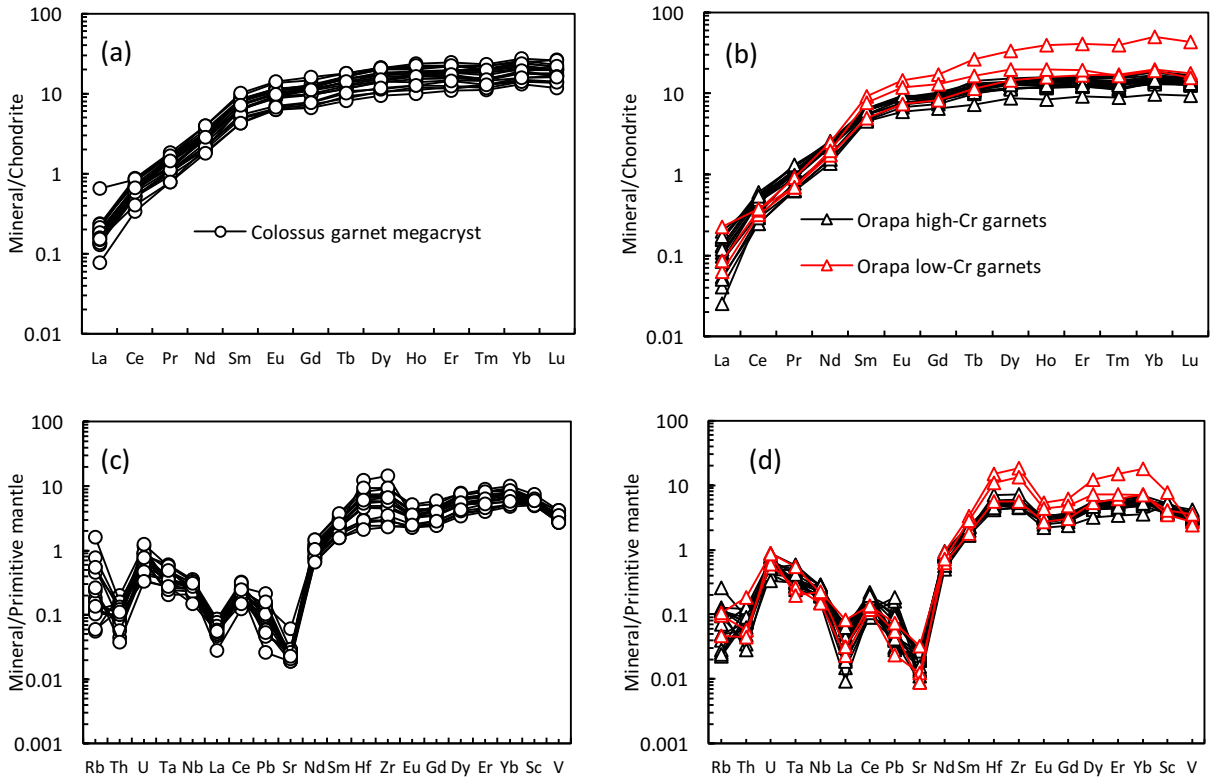

Figure 1.10: (a, b) Chondrite normalized REE patterns of Colossus and Orapa garnet megacrysts. (b,c) Primitive mantle normalized trace element patterns of Colossus and Orapa garnet megacrysts. Normalizing values are from McDonough and Sun (1995).

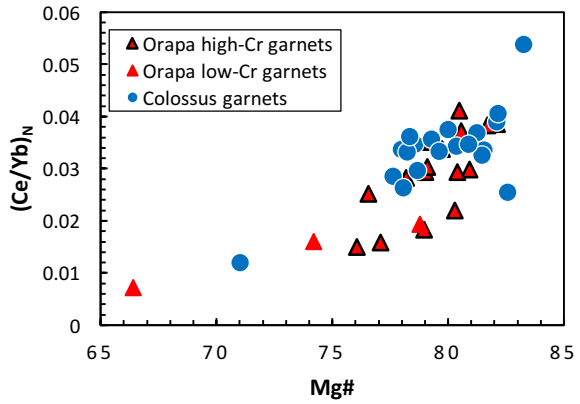

Figure 1.11: Plot of Mg # versus $(Ce/Yb)_N$ in Orapa and Colossus garnet megacryts. There is a steady decrease of $(Ce/Yb)_N$ with decreasing Mg# throughout the crystallization, this suggests that a process other than fractional crystallization is controlling the $(Ce/Yb)_N$ ratios.

1.5. RESULTS - GROUP 2 KIMBERLITE MEGACRYSTS

1.5.1. CLINOPYROXENE MEGACRYSTS FROM GROUP 2 KIMBERLITES

A. Major element systematics

Data are given in Tables 3, 4 and 44 of the Appendix. Kalkput clinopyroxene megacrysts display trends of decreasing Mg# and Cr# with increasing Ca# (Fig. 1.12). The Kalkput megacrysts (with highest Ca#) display low Mg# (74 – 60) and Cr# values near 0 (Fig. 1.13). However, there appears to be no correlation of Al content with Ca# (Fig. 1.15). Moreover, TiO_2 contents rise continuously with increasing Ca# (Fig. 1.14).

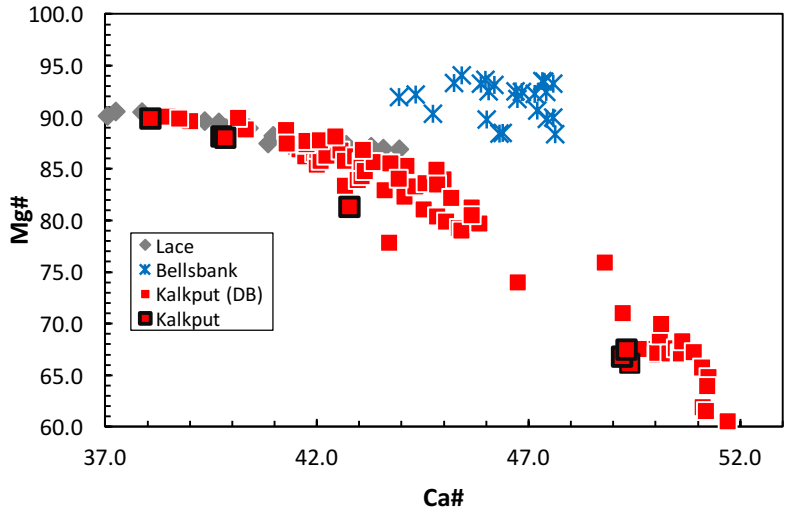

Figure 1.12: Plot of Ca # versus Mg # for clinopyroxene megacrysts from Kalkput and Bellsbank Group 2 kimberlites. Kalkput cpx megacrysts display the typical Cr-poor trend of decreasing Mg# with increasing Ca#. Bellsbank megacrysts show a restricted range of Ca-number and Mg-number with no clear trend. Kalkput (DB) data are unpublished data of Deon DeBruin. Data for clinopyroxene megacrysts from Lace (also a group 2 kimberlite) are unpublished data of D.R. Bell and D.J. Schulze.

Bellsbank cpx megacrysts are characterized by a restricted range of Ca, Mg and Ti contents. However, they do show large variations in Cr_2O_3 and Al_2O_3 (Fig.1.15). The Bellsbank cpx span a narrow range of Ca# (44-48) and have significantly higher Cr# values than all Kalkput megacrysts, as well as Mg# values that are higher at a given Ca# than those from Kalkput. The Bellsbank cpx megacrysts do not show typical megacryst fractional crystallization trends.

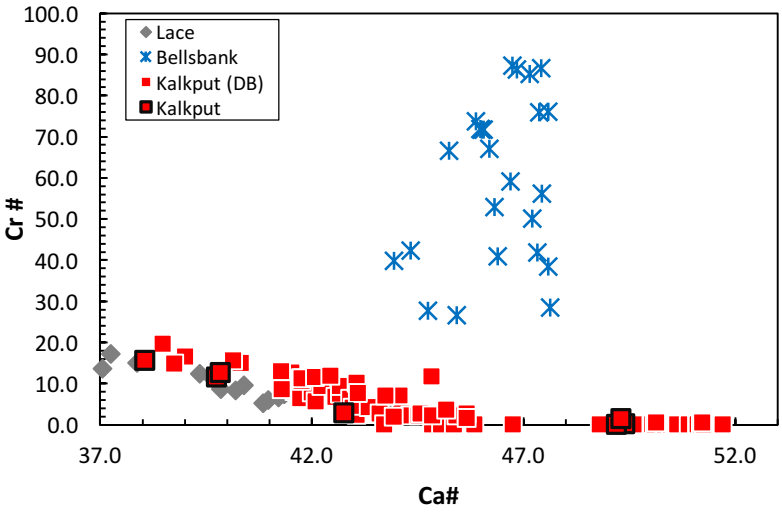

Figure 1.13: Plot of Ca # versus Cr # showing data for Bellsbank and Kalkput Group 2 cpx megacrysts. Kalkput cpx megacrysts show the typical Cr-poor megacryst trend of decreasing Cr content with increasing Ca# values. In contrast, Bellsbank megacrysts show an unsually wide range of Cr_2O_3 variation over a limited range of Ca#.

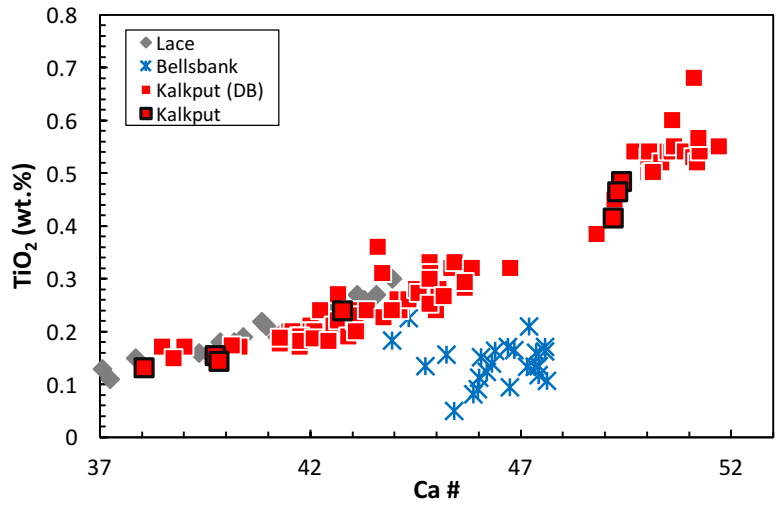

Figure 1.14: Plot of Ca# versus wt.% TiO_2 for Kalkput and Bellsbank cpx megacrysts. Unlike the Group 1 kimberlite cpx megacryst data, TiO_2 contents increase continuously with Ca# at Kalkput. Bellsbank megacrysts show a restricted range of Ti content.

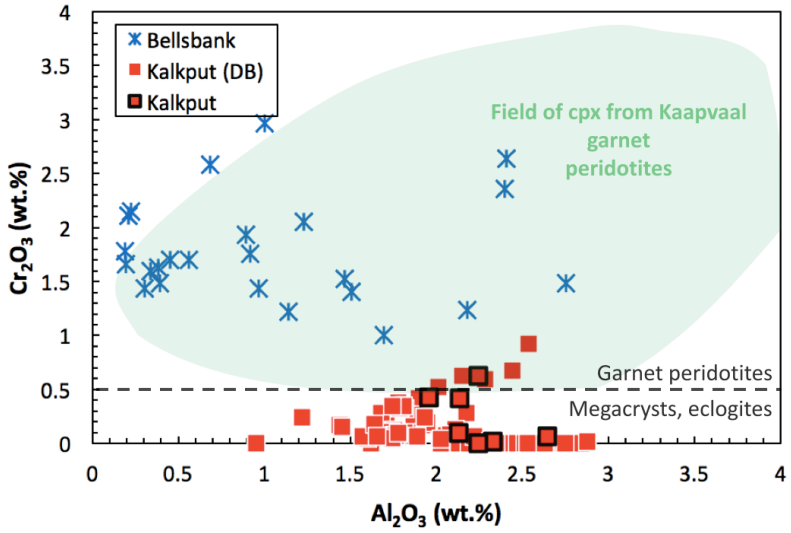

Figure 1.15: Plot of wt. Al_2O_3 versus wt.% Cr_2O_3 for Bellsbank and Kalkput cpx megacrysts. The fields for garnet peridotites and megacrysts & eclogites are from Nimis (1998). The Kaapvaal garnet peridotite field is from Grégoire et al., (2003) and unpublished data compilations of DR Bell. Most Kalkput cpx megacrysts plot in the megacryst field. In contrast, Bellsbank megacrysts plot entirely in the garnet peridotite field and exhibit a wide range of Al_2O_3 at relatively high Cr_2O_3 values.

B. Trace element systematics

Data are given in Tables 10 and 11 of the Appendix. Kalkput cpx megacrysts display nearly uniform trace element patterns with variable Hf-Zr abundances that range from strongly depleted to enriched relative to elements of similar incompatibility. Chondrite-normalised patterns show a moderate enrichment in LREE relative to HREE (e.g., with $(Nd/Yb)_N$ ranging from 13.5 to 16.4). On a plot of Ti/Eu versus chondrite-normalised La/Yb ratios, Kalkput cpx megacrysts plot in the silicate melt metasomatism field of Coltorti et al. (1999; Fig. 1.17) There is no systematic change of LREE/HREE ratios with Ca#, although there is a positive, strongly curved relationship between Ca# and Zr/Sm

Bellsbank cpx megacrysts show trace element patterns with a large degree of variability in LREE enrichment, extending to highly LREE-enriched (and HREE-depleted) compositions (e.g., $(Nd/Yb)_N$ = 17.6 to 167, Fig. 1.16) and range from undepleted to fairly strongly depleted in the other highly incompatible elements (e.g., Rb, Ba, Th, U, Nb; Fig. 1.16) relative to moderately and mildly incompatible elements. In contrast to kalkput, Bellsbank cpx megacrysts have relatively low Ti/Eu and high $(La/Yb)_N$ values consistent with carbonatite metasomatism (e.g., Rudnick et

al., 1993; Fig. 1.17). Also, unlike Kalkput, the Bellsbank cpx megacrysts do not show a clear trend in a plot of Ca# versus Zr/Sm ratio, although the variability in Zr/Sm ratios does increase as Cr# increases.

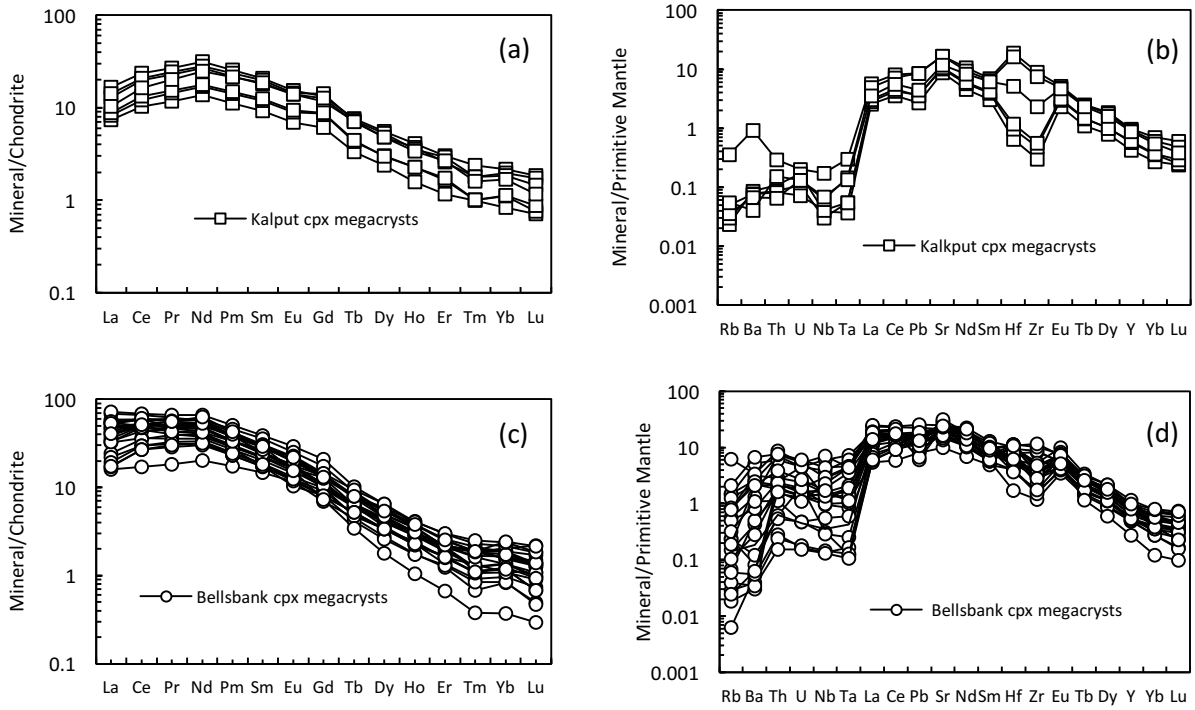

Figure 1.16: (a) Chondrite-normalised REE plot of Kalkput cpx megacrysts. **(b)** Primitive mantle-normalised trace element plot of Kalkput cpx megacrysts. **(c)** Chondrite-normalised REE plot of Bellsbank cpx megacrysts **(d)** Primitive mantle-normalised trace element plot of Bellsbank cpx megacrysts. Normalising values are from McDonough and Sun (1995). Note the greater LREE enrichment in the Bellsbank cpx as well as the large variations (from relatively undepleted to strongly depleted) in the most highly incomparible elements in panel (d).

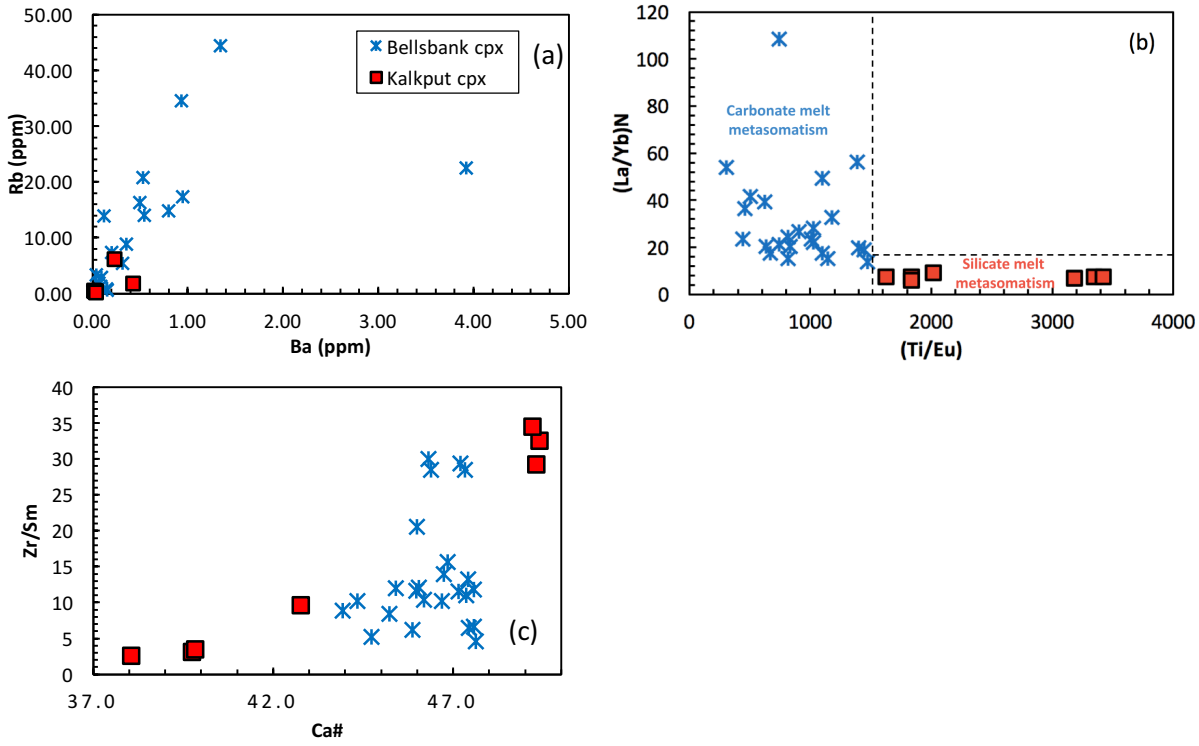

Figure 1.17: Variation of selected trace elements in Bellsbank and Kalkput cpx megacrysts. **(a)** Ba versus Rb. **(b)** Ti/Eu versus $(La/Yb)_N$. Carbonatite and silicate melt metasomatism fields are from Coltorti et al. (1999). (c) Ca# versus Zr/Sm ratio. Note the low Rb and Ba contents in Kalkput cpx versus the large variation of those elements in Bellsbank cpx megacrysts. In panel (b), the Bellsbank cpx largely plot in the carbonatite melt metasomatism field whereas the Kalkput cpx plot in the silicate melt metasomatism field. Normalising values from McDonough and Sun (1995).

C. Sr isotope systematics

Data are given in Table 16 of the Appendix. Kalkput cpx megacrysts display a very restricted range of measured $^{87}Sr/^{86}Sr$ ratios (0.7071 – 0.7076), that falls in the range of Group 2 kimberlites (e.g., Smith, 1983, Coe et al., 2008). There is no significant change in Sr isotope composition with Ca# or any other chemical parameter (Fig. 1.18). Bellsbank cpx megacrysts, in contrast, display a large variation of measured $^{87}Sr/^{86}Sr$ ratios (0.7076 – 0.7172), which overlaps with the range of Group 2 kimberlites, but extends to slightly higher values. It is noteworthy that the variability in $^{87}Sr/^{86}Sr$ of Bellsbank megacrysts increases dramatically with increasing Ca#, such that megacrysts with Ca# values of ≈46 display a range of 0.7076 to 0.7095, whereas those with Ca# values of 47-48 span a range from 0.7078 to 0.7172.

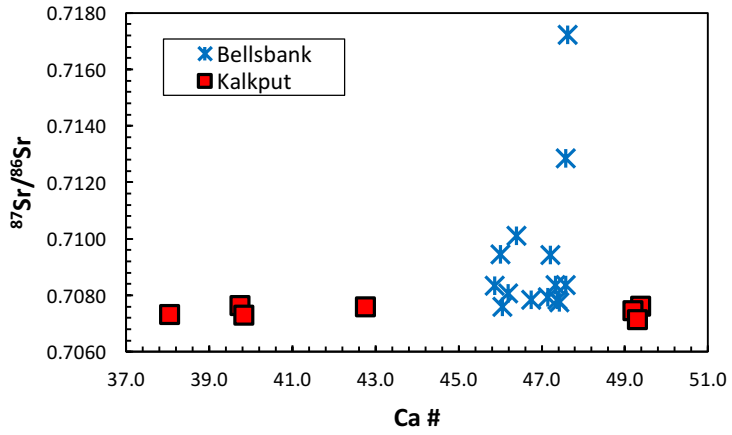

Figure 1.18: Plot of Ca # versus measured $^{87}Sr/^{86}Sr$ of Bellsbank and Kalkput cpx megacrysts. At Kalkput, cpx megacrysts define a very restricted range of Sr isotope composition. In contrast, at Bellsbank, cpx megacrysts display a large degree of measured Sr isotope variation.

1.5.2. GARNET MEGACRYSTS FROM GROUP 2 KIMBERLITES

Data are given in Table 7 of the Appendix. Of the two group 2 kimberlite megacryst suites investigated here, garnet megacrysts have been recovered only from Bellsbank. De Bruin (1999) noted that while garnet xenocryts had been recovered from Kalkput, these appeared to be entirely peridotitic rather than megacrystic in origin. On a plot of wt.% CaO versus wt.% Cr_2O_3 (Fig. 1.19a), the Bellsbank garnets fall in the G1 field of Grütter et al. (2004; Fig. 1.19). The Bellsbank garnets span a wide range in Cr_2O_3 (0.1 - 3.1 wt.%) and Mg# (69 - 85) and have relatively low TiO_2 contents (0.1 to 0.5 wt.%). For purposes of comparison, data for garnet megacrysts from the Lace and Star Group 2 kimberlites (Free State, South Africa) are shown on Figure 1.19. The Lace suite has very similar major element systematics in its clinopyroxene megacrysts to those from Kalkput. Lace and Star garnet megacrysts are similar to those from Bellsbank in having wide ranges of Cr_2O_3 contents and Mg# values. However, they are unlike garnets from Bellsbank in that Cr_2O_3 values show strong positive and negative correlations with Mg# (Fig 1.19c) and wt.% Al_2O_3 (Fig. 1.19d), as well as weak correlations between Mg# and TiO_2 (Fig. 1.19b), whereas Bellsbank garnet megacrysts show extremely weak correlations or none at all on these plots.

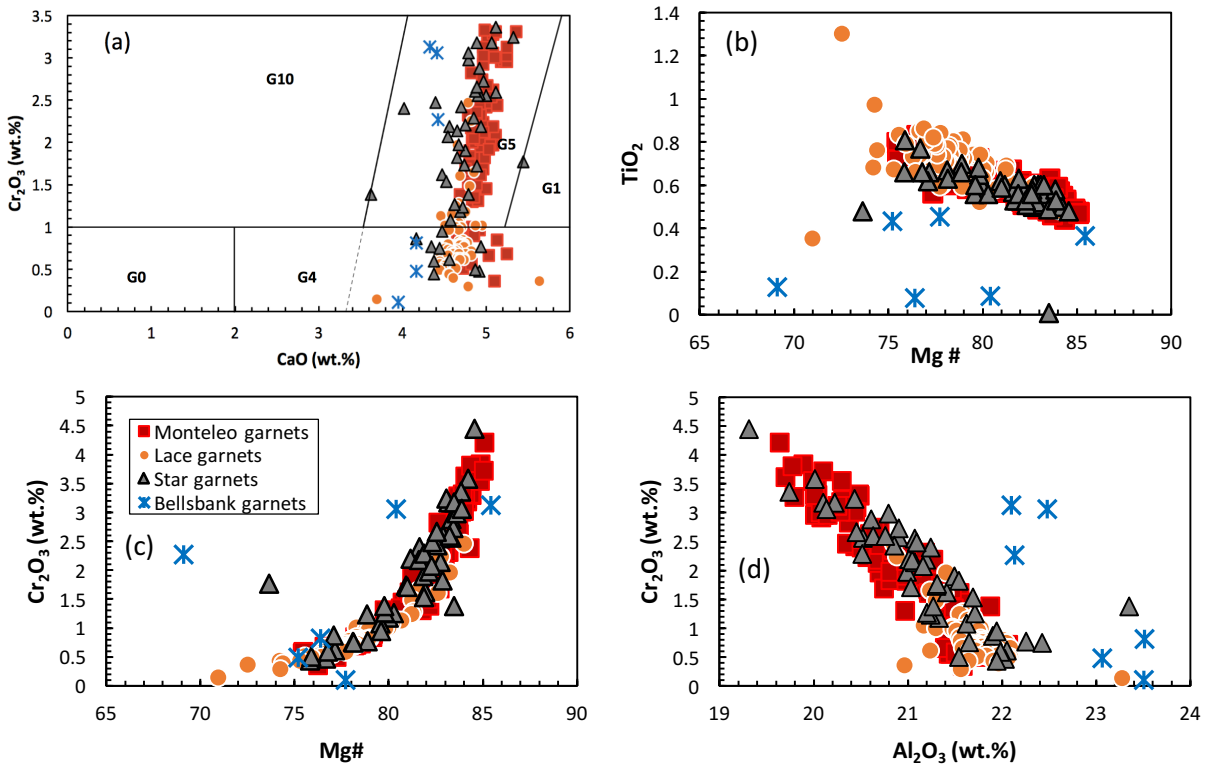

Figure 1.19: Variation of selected major elements in garnet megacrysts from the Bellsbank and, for comparison, the Lace and Star Group 2 kimberlites. Lace and Star data are from D.R. Bell (2010, unpublished data) and Hill (1989). Monteleo garnet megacryts data are from Perritt et al., (2015) **(a)** Plot of wt.% CaO versus wt. Cr_2O_3. **(b)** Plot of Mg# versus wt.% TiO_2. **(c)** Plot of Mg# versus wt.% Cr_2O_3. (d) Plot of wt.% Al_2O_3 versus wt.% Cr_2O_3.

Trace element data of Bellsbank garnets are given in Table 14 of the Appendix. Bellsbank garnets show trace element patterns characterized by strong positive U anomalies, depletions in Ba, Sr and the LREE and enrichments in the HREE, Sc and V (Fig. 1.20). Patterns tend to be less uniform than for the garnet megacrysts from Group 1 kimberlites.

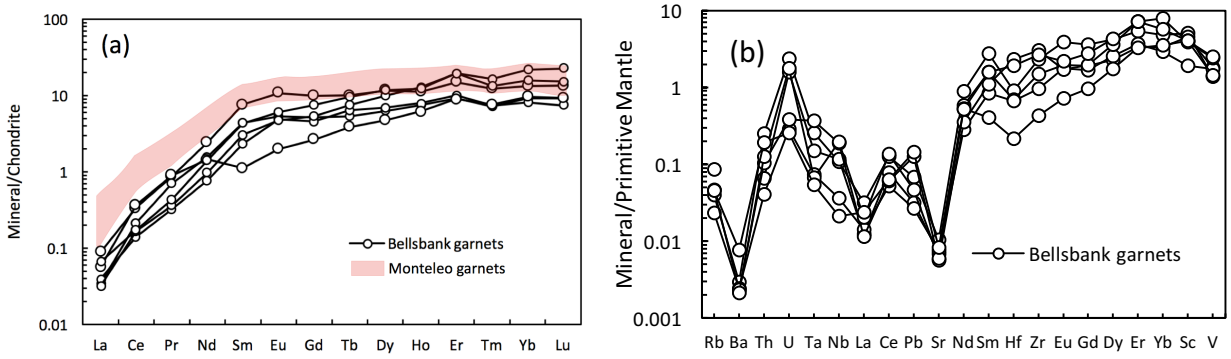

Figure 1.20: (a) Chondrite-normalised REE patterns of Bellsbank garnet. (b) Primitive-mantle-normalized trace element patterns of Bellsbank garnet. Monteleo garnets data are from Perrit et al., (2015). The latter data are not shown in panel b due to the lack of several elements such as U, Th, Rb, Ba in the dataset of Perrit et al., (2015). Normalizing values from McDonough and Sun (1995).

1.6. THERMOBAROMETRY

Using the thermobarometer of Nimis and Taylor (2000), P-T conditions of clinopyroxene megacrysts investigated in this study have been calculated. Most Group 1 clinopyroxene megacrysts used for PT calculations met the requirements (equilibrium with garnet and possibly orthopyroxene) set by Nimis and Taylor (2000) and Nimis et al., (2009). First, all clinopyroxenes used for these calculations have HREE depleted patterns, interpreted by several authors to be the evidence of equilibration in the presence of garnets (Nimis et al., 2009). In addition, Orthopyroxene and garnet megacrysts have been reported at kimberlite localities investigated in this chapter (Shee and Gurney, 1979; Hildebrand, 1993; Moore and Costin, 2016). The Nimis and Taylor (2000) thermobarometer has been used previously to infer the pressures and temperatures of megacryst formation (Kargin et al., 2017; Bussweiller et al., 2018).

Data obtained are given in Tables 45 and 46 of the Appendix. The thermobarometry results indicate that the Cr-poor megacrysts in this study crystallized at higher temperatures than Cr-rich cpx megacrysts (Fig. 1.20). However, many Group 2 clinopyroxene megacrysts display pressure values exceeding 6.5 GPa (possibly deeper than the base of the Kaapvaal lithosphere), especially those at such high pressures and low temperatures are suspicious. It's possible that the assumptions of the Nimis and Taylor thermobarometer (e.g., coexistence with garnet and opx) were not met in those cases (Group 2 clinopyroxene megacrysts). It is noteworthy to mention that the much larger spread in pressure values for Group 2 cpx megacrysts may indicate a problem with the thermobarometry, especially the assumption of coexistence with garnet (Fig. 1.21). The high

temperatures at moderate pressures for the Group 1 Cr-poor megacrysts overlaps temperature and pressure values for many sheared, high-temperature peridotites (e.g., N. Lesotho, Jagersfontein, Gibeon).

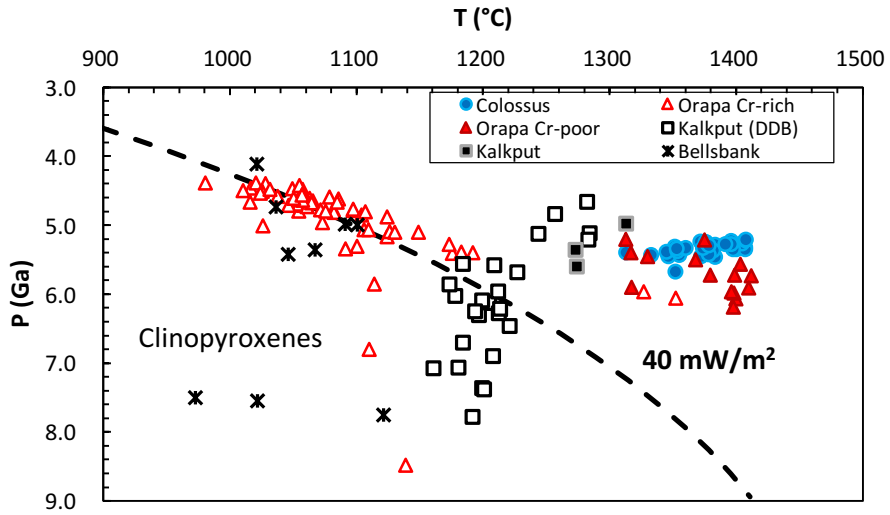

Figure 1.21: T (°C) versus P (GPa) plot of southern African clinopyroxene megacrysts, using the thermobarometer of Nimis and Taylor (2000). Note the higher crystallization temperatures of Group 1 Cr-poor cpx megacrysts relative to Group 2 Cr-poor cpx megacrysts. The dash curve represents the conductive 40 mW/m^2 geotherm of Pollack and Chapman (1977).

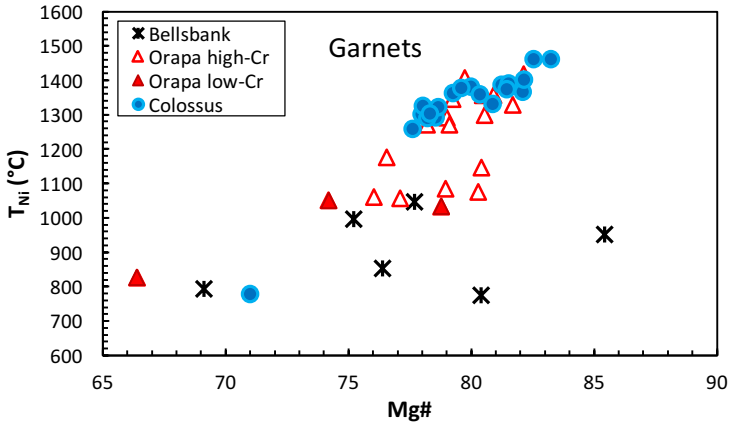

Figure 1.22: Mg# versus T(°C) plot of southern African garnet megacrysts, using the Ni-in-garnet thermometer (Ni value in olivine = 2900 ppm) of Ryan et al., (1996). Note the lack of correlation displayed by Bellsbank garnets.

Using the Ni-in-garnet thermometer of Ryan et al. (1996), crystallization temperatures of garnet megacrysts investigated in this study have been calculated. Garnet must be in equilibrium

with olivine in order to use this thermometer (Griffin et al., 1989; Ryan et al., 1996). This condition is likely met since olivine megacrysts have been reported at Colossus and Orapa. The Ni-in-garnet thermometer of Canil (1999) gives temperatures that are roughly 50°C higher than those obtained with the one of Ryan et al., (1996), but otherwise the variation in sample values is very similar. Data obtained are given in Table 47 of the Appendix. Garnet thermometry shows an overall positive correlation of temperature and Mg# in Orapa and Colossus garnet megacrysts. By contrast, Bellsbank garnets do not exhibit such a correlation (Fig. 1.22).

1.7. PETROGENESIS OF THE MEGACRYSTS

1.7.1. CA# FUNCTION OF CRYSTALLIZATION TEMPERATURE

Ca# in clinopyroxene only varies as a function of temperature if clinopyroxene is in equilibrium with orthopyroxene. This appears to be the case for the southern African megacrysts investigated in this thesis: (1) Orthopyroxene megacrysts have been described at Orapa (Shee and Gurney, 1979) and Colossus (Hildebrand, 1993; Moore and Costin, 2016). Also, orthopyroxene megacrysts are relatively common in southern African kimberlite megacryst suites generally (Nixon and Boyd, 1973b; Gurney et al., 1979; Mitchell, 1987; De Bruin, 2005). (2) The relative importance of orthopyroxene in megacryst mineral assemblages has likely been underestimated due to its preferential dissolution by kimberlite magmas. Such a process has been proposed to explain the relative lack of xenocrystic orthopyroxene, compared to other minerals such as olivine and garnet, in kimberlites (Mitchell, 2008; Russell et al., 2012; Pilbeam et al., 2013).

The following pieces of evidence from the literature support the validity of using Ca# of clinopyroxene megacrysts as a proxy of crystallization temperature: (1) All Cr-rich clinopyroxene megacrysts investigated in the literature (Eggler et al., 1979; Pivin, 2012; Kargin et al., 2017; Bussweiller et al., 2018), including those of Kopylova et al., (2009) display significantly lower temperatures of equilibration than Cr-poor megacrysts (Gurney et al., 1979; Eggler et al., 1979). This observation is consistent with temperatures of equilibration inferred from Ca# of clinopyroxene megacrysts, as most Cr-rich clinopyroxenes have significantly higher Ca# (which translates to low temperatures of equilibration) than Cr-poor clinopyroxene megacrysts (Fig. 1.21). (2) Gurney et al., (1979) presented thermobarometry data of megacrysts from Monastery using

different set of geothermometers on silicate-orthopyroxene and orthopyroxene-ilmenite intergrowths. They did find good agreement between equilibration temperatures obtained and those inferred from Ca# of clinopyroxenes. (3) Eggler et al., (1979) presented thermobarometry data of Cr-poor and Cr-rich megacrysts from the State Line kimberlites. Using different sets of geothermometers on orthopyroxene-clinopyroxene and orthopyroxene-ilmenite intergrowths, there is a good agreement between calculated temperatures and Ca# of clinopyroxenes. Equilibration temperatures of Cr-poor orthopyroxenes are higher than those obtained on Cr-rich orthopyroxenes, as predicted by the Ca# of clinopyroxenes. To date, there is no study that has challenged the results presented by either Eggler et al.,(1979) or Eggler et al., (1979).

1.7.2. MEGACRYST FORMATION MODELS

It has been recognised for the past 40 years that kimberlite megacrysts are physically and chemically distinct from peridotitic minerals due to their larger size and distinct chemical composition (e.g., Gurney et al., 1979; Harte and Gurney, 1981. Hops et al., 1992; Bell and Moore, 2004). A number of chemical discrimination schemes have been developed to aid in distinguishing megacrystic from peridotitic clinopyroxene and garnet, particularly for use in the classification of indicator minerals from kimberlite heavy mineral concentrates (e.g., Ramsay, 1995 and Nimis, 1998 for cpx; Schulze, 2003 and Grütter et al., 2004 for garnet). However, the discrimination is not always straightforward, as the Cr-rich megacryst compositions often overlap with those for minerals from pyroxenite, eclogite and fertile lherzolite.

Traditionally, most models of kimberlite megacryst genesis have proposed that it occurs as the result of nearly isobaric crystallization processes occurring in the deep lithosphere, where temperature is the main variable (e.g., Gurney et al., 1979), although the precise nature of the environment (e.g., a thermal aureole surrounding a magma chamber, or a system of veins or channels) and the melt-wallrock ratio remains controversial (Eggler et al., 1979; Harte and Gurney, 1981; Hops et al., 1992; Bell and Moore, 2004).

Most early studies of megacryst genesis favoured progressive fractional crystallization as the process causing chemical variations in kimberlite megacrysts (e.g., Gurney et al., 1979; Harte and Gurney, 1981). However, in many instances, the chemical and isotopic variations observed cannot be the result of such closed-system processes alone, but rather must have involved open system behaviour such as assimilation of lithospheric components, whether by bulk assimilation

of solid peridotite wallrock or by partial fusion of low-melting-temperature metasomatic vein components (e.g., Moore et al., 1992; De Bruin, 2005). Because of the pyroxene solvus and the consequent relationship between Ca# and crystallization temperature, clinopyroxene offers the ability to investigate changes in the composition of megacrysts as a function of temperature. Well-characterised megacryst suites spanning wide ranges of Ca#, such as that from the Monastery kimberlite, display clear trends with decreases in Cr# and Mg# with increasing Ca# (and presumably decreasing crystallization temperature) until minimum values of both are reached (typically near 0 for Cr#) which is followed by a rapid increase in Cr# and Mg# with further increase in Ca# (and hence decrease in temperature; e.g., Figs 1.2 and 1.3). In suites such as Monastery, it is plausible that Cr-poor and Cr-rich megacrysts are linked to a common parental magma, and that the increase in Cr# and Mg# at lower temperatures could be due to an assimilation-fractional crystallization process in which melts percolate upward through the continental lithospheric mantle, progressively decreasing in volume (due to crystallization) and progressively assimilating ambient peridotitic wallrock. Fractionation would initially control compositional variations, with a resultant drop in Mg# and Cr# as Mg and Cr are depleted in the magma, but this eventually would reverse, with Cr# and Mg# beginning to increase toward the end of the crystallisation process as melt/wallrock ratios decrease markedly and assimilated components begin to dominate the melt composition (e.g., Bell and Moore, 2004). Such a hypothesis can explain the initial decrease and subsequent increase in Mg# and Cr# with increasing Ca# values of cpx in Monastery and some other megacryst suites. However, it must be acknowledged that it is easier to plausibly relate Cr-poor and Cr-rich megacryst suites to the evolution of a single parental magma in some localities (e.g., Monastery, Jagersfontein; refs) than at others (e.g., Iron Mountain, Jericho; Eggler et al., 1979; Kopylova et al., 2009).

Despite the general consistency of the geochemical data with a magmatic origin for kimberlite megacrysts, some authors have recently suggested a metasomatic origin in which megacryst evolution occurs in the up-temperature direction, with an initially Cr-rich, ultramafic megacryst parental melt that undergoes rapid Cr-depletion due to melt-rock reaction. These studies have highlighted similarities between mineralogical compositions of megacrysts and minerals of some metasomatised peridotites from the lithospheric mantle (Kopylova et al., 2009; Pivin et al., 2009; Nimis et al., 2009; Bussweiler et al., 2016, 2018). Contrary to magmatic models that consider fractional crystallization from a magma in the lithospheric mantle, metasomatic models

consider that megacrysts would have been formed by the transformation of peridotites by liquids that are genetically associated with kimberlites. These metasomatic models consider very low liquid/rock ratios presiding at the formation of Cr-rich megacrysts (Moore and Belousova, 2005; Kopylova et al., 2009) while Cr-poor megacrysts are formed at higher liquid/rock ratios (Doyle et al., 2004; Kopylova et al., 2009).

A. TEMPERATURE CONSTRAINTS

The metasomatic model and the assimilation-fractional crystallization model are quite similar in some ways. They mainly differ in terms of the order in which processes occur. In the end-stage of the AFC model, we are dealing with small amounts of melt at low melt-wallrock ratios and this could be viewed as very similar to metasomatic scenario for megacryst generation. The metasomatic model simply has this low melt-wallrock situation (involving an Mg- and Cr-rich magma) occurring first, and over time and with increasing temperature, the metasomatised assemblage reacts with a greater and greater quantity of melt arrives and drives the composition of the system toward the generation of more typical Cr-poor megacryst magmas. This scenario seems less plausible than starting with large amounts of Cr-poor melt and letting this cool and crystallize and gradually heat and assimilate enriched metasomatic vein components from the surrounding SCLM wallrock, eventually leading to Cr-rich magmas that crystallize Cr-rich megacrysts. Also, with the metasomatic model it is difficult to reconcile (1) the larger abundance of Cr-poor relative to Cr-rich megacrysts in southern African kimberlites and (2) the more incompatible element and isotopically depleted character of the Cr-poor megacrysts, to being the end product of a long process of melt-rock reaction. None of the workers advocating the metasomatic origin have provided temperature constraints supporting the formation of Cr-rich megacrysts prior to Cr-poor megacrysts. Kopylova et al., (2009) have provided only PT estimates of Cr-rich megacrysts and these are low compared to those of Cr-poor megacrysts (Gurney et al., 1979). Temperature estimates provided by other workers for Cr-rich megacrysts are generally low, ranging from 922 to 1020 °C (Kargin et al., 2017; Bussweiller et al., 2018).

The strongest evidence in favour of the AFC model, as developed in this study, is the constraint on temperature provided from the Ca-number of pyroxene. The metasomatic models (e.g., Moore and Belousova, 2005; Kopylova et al., 2009) all ignore the constraints on how the

temperature of crystallization relates to megacryst composition. It could be argued that these models would work in a system where the lithosphere is heating up, but this scenario is likely implausible.

B. PROGRESSIVE METASOMATIC HYPOTHESIS FOR SOUTHERN AFRICAN MEGACRYSTS

This hypothesis proposes that kimberlite megacrysts form primarily by reaction of mantle peridotite with infiltrating volatile-rich kimberlitic fluids at very low fluid/rock ratios. Some authors propose this origin to explain primarily Cr-rich megacrysts (e.g., Bussweiler et al., 2016; 2018; Kopylova et al., 2009) but others propose that it can explain the origin of Cr-poor megacrysts as well (e.g., Moore and Belousova, 2005; Pivin et al., 2009). In this metasomatic scenario, as the peridotite mantle undergoes melt-rock reaction due to progressive interaction with volatile-rich kimberlite fluids, Cr-rich and Mg-rich megacrysts are formed and followed later by the formation of Cr-poor and Mg-poor megacrysts. It has been shown that the Kaapvaal lithospheric mantle is ancient, metasomatised and enriched with radiogenic Sr isotope composition (Erlank et al., 1987; Walker et al, 1989; Griffin, 2014). This could possibly explain the high Sr isotope composition and high LREE enrichment of Orapa Cr-rich cpx megacrysts. Volatile-rich kimberlitic fluids would have unradiogenic Sr isotope compositions similar to those of OIB (le Roex et al., 2003; Becker and le Roex, 2006). The megacrysts formed would have Sr isotope compositions intermediate between mantle peridotites underlying the Orapa SCLM and kimberlitic fluids. At Colossus, the lithospheric mantle is relatively depleted (Smith et al., 2009) and the cpx megacrysts display isotope compositions close to Group 1 kimberlites (le Roex et al., 2003). This is consistent with the observation that most Colossus cpx megacrysts display unradiogenic Sr isotope composition and a weak LREE enrichment. At Kalkput, the SCLM is most likely dominated by depleted peridotites and MARID rocks (Griffin et al., 2014). MARID rocks have lower Cr and Mg contents than mantle peridotites (Gregoire et al., 2002) but do have more radiogenic Sr isotopic composition and greater LREE enrichment (Kramers et al., 1983; Erlank et al., 1987; Gregoire et al., 2002). The reactions between kimberlitic fluids and depleted peridotites/MARID dominated SCLM could possibly produce Kalkput megacrysts. Therefore, the Cr-depleted, LREE enriched and radiogenic Sr composition of Kalkput cpx megacrysts could be possibly explained by a metasomatic scenario.

However, the chemical compositions of southern African megacrysts cannot be fully explained with a metasomatic model: First, it is implausible that melt-rock interaction between high-Mg# kimberlitic fluids and high-Mg# peridotite minerals could result in relatively low Mg# compositions, as possessed by many Cr-poor megacrysts. Second, how could such interaction result in Mg- and Cr-poor megacrysts with low $^{87}Sr/^{86}Sr$ ratios? Kaapvaal mantle peridotites have radiogenic Sr isotope compositions, as highlighted above, and megacysts that are formed should display chemical signatures that closely resemble to the ones display by mantle peridotites (dominant component). In addition, the tight compositional trends defined by Kalkput, Colossus, Orapa Cr-poor and as well as in many other southern African megacryst suites are most easily explained by fractional crystallization of a magma in a system with an initially high melt/rock ratio. The hypothesis of a metasomatic origin requires a totally open system in which peridotitic minerals interact with fluids and continually recrystallize and re-equilibrate with these fluids. It is difficult to envision how progressive metasomatism of initially heterogeneous lithospheric peridotite at very low melt-rock ratios would produce such systematic trends. At Orapa, some highly fractionated Cr-poor cpx megacrysts have the same Ca# but much lower and far more uniform Mg# and Cr# than the Cr-rich cpx megacrysts. This is very difficult to explain by the progressive metasomatic hypothesis. In southern Africa, many kimberlite localities have Cr-poor megacrysts that display tight and systematic compositional trends. By contrast, in many other kimberlite localities, mostly located in the Slave and Siberian cratons, Cr-poor megacrysts are absent or very minor and kimberlite megacrysts are overwhelmingly dominated by Cr-rich megacrysts exhibiting scattered compositional trends (e.g., Kostrovitsky et al., 2004; Bussweiler et al., 2018). At these localities, the progressive metasomatic hypothesis readily explains the chemical variations.

1.7.3. PETROGENESIS OF COLOSSUS (GRP. 1) CR-POOR MEGACRYSTS

Colossus cpx and garnet megacrysts both display a relatively limited range of Mg# and Cr# values that are higher than typical for Cr-poor megacryst suites (e.g., compared to Monastery or Orapa Cr-poor megacrysts). They display small to moderate ranges in LREE/HREE ratios (e.g., Fig. 7), but significant variations in Zr/Sm ratios, with the most primitive megacrysts being the most depleted in Zr and Hf relative to the middle REE similar to sputhern African Cr-poor cpx

megacrysts (e.g., Merry and le Roex, 2007). In terms of Sr isotope composition, the Colossus cpx megacrysts have a relatively low average $^{87}Sr/^{86}Sr$ value of 0.7033. This, plus their relatively low Ca#, indicative of high crystallization temperatures, all suggest that the Colossus cpx megacrysts should be grouped with the Cr-poor, rather than the Cr-rich suite of megacrysts, despite their relatively Cr-rich compositions.

Smith et al., (2009) and Pearson et al. (2019) investigated mantle xenoliths, kimberlite concentrates, and diamond inclusions from the Murowa and Sese kimberlites (538 Ma), located ≈170 km southeast of Colossus. They provided evidence that the southern Zimbabwe craton is underlain by extremely depleted lithospheric mantle of likely Mesoarchean age. It seems likely that the fact that Colossus "Cr-poor" clinopyroxene and garnet megacrysts are less depleted in Cr than typical Cr-poor megacrysts, for a given Ca# or Mg# value, could be due to interaction of Cr-poor megacryst parental magmas with such ultradepleted Cr-rich lithosphere. However, the restricted range in Mg# (in both garnet and cpx) and Ca# (in cpx) suggest that the analysed Colossus megacrysts represent only a portion of the entire fractionation sequence, which severely limits the ability to investigate the possible role of AFC or metasomatic melt-wallrock interaction processes.

1.7.4. PETROGENESIS OF ORAPA (GRP. 1) CR-POOR AND CR-RICH MEGACRYSTS

The Orapa megacrysts are instructive in that the Cr-poor suite appears to display nearly pure fractionation behaviour with little indication of assimilation or reaction with lithospheric components, whereas the Cr-rich suite shows abundant evidence for lithospheric interaction.The inference of nearly pure fractionation for the Cr-poor suite at Orapa is based on the systematic decline in Cr# and Mg# with increasing Ca# in clinopyroxene, the positive correlation of Cr_2O_3 and Mg# in the Orapa Cr-poor garnets, as well as the relatively uniform $(Nd/Yb)_N$ and Zr/Sm ratios in clinopyroxene and Ce/Yb ratios in garnet. Evidence for this is shown in Figures 1.2 and 1.3, where the Orapa Cr-poor cpx megacrysts show a single cuvilinear trend of Ca# versus both Mg# and Cr#, with the latter dropping to 0 at high Ca# values. In contrast, the Cr-rich megacrysts are chemically highly heterogeneous with much of their chemical variability not explainable by fractionation processes. The Orapa Cr-rich clinopyroxene megacrysts begin their evolution at slightly lower temperatures (max. Ca# ≈36 for Cr-rich, versus ≈30 for Cr-poor cpx) and slightly

higher Cr# and Mg# values than the Cr-poor suite, and show increaingly variable Cr# and Mg# values to both lower and much higher Cr# and Mg# values as Ca# values increase (Figs. 1.2 and 1.3).

The strongest evidence for interaction of the Orapa Cr-rich megacryst suite with lithospheric mantle wallrock is shown by highly variable but generally increasing LREE/HREE and $^{87}Sr/^{86}Sr$ ratios with increasing Ca#. This suggests a more variable, but greater overall degree of assimilation of enriched lithospheric components with decreasing crystallization temperature and (presumably) decreasing melt/wallrock ratios compared to that seen in the Cr-poor suite. Workers have provided several lines of evidence that the SCLM beneath Orapa is dominantly fertile and has experienced significant metasomatic enrichment in incompatible elments. This includes data from study of peridotite xenoliths (Stiefenhofer et al., 1997; van Achterbergh et al. 2001), garnet xenocrysts (Griffin et al., 2003) and peridotitic diamond inclusions (Stachel et al., 2004). Locally variable assimilation of such enriched lithosphere could explain the observed increasingly incompatible element-enriched, but also increasingly variable composition of the megacrysts formed during progressive crystallization. It is very unlikely that the Orapa Cr-rich megacrysts simply represent disaggregated metasomatised peridotitic minerals due to the fact that the cpx extends to lower Ca# (and hence crystallized at higher temperatures) than most peridotitic cpx, and the TiO_2 contents of garnet and cpx from the Orapa Cr-rich suite are higher than that found even in highly metasomatised peridotites from the Orapa kimberlite cluster (Stiefenhofer et al., 1997). Additionally, the TiO_2 variations with Ca# in Orapa Cr-rich cpx megacrysts is consistent with the break in slope seen in the Orapa Cr-poor and Monastery megacryst suites (Fig. 1.4), which is most easily interpreted as the result of the onset of ilmenite crystallization with decreasing temperature (Gurney et al., 1979).

1.7.5. PETROGENESIS OF THE KALKPUT (GRP. 2) CR-POOR MEGACRYSTS

Although the Kalkput Cr-poor megacrysts come from a Group 2 kimberlite, they show similarities to Cr-poor megacrysts from many Group 1 kimberlites. Most importantly, they show a systematic decrease in Cr# and Mg# with increasing Ca# that is most easily explained as being the result of simple fractional crystallization. There is no increase in Cr# or Mg# at low Ca# values and therefore, little major element evidence of interaction or assimilation with lithospheric mantle

wallrock. Unlike many Cr-poor megacryst suites, the Kalkput cpx shows a continuous increase in TiO_2 (from ≈0.15 to ≈0.7 wt.%) with decreasing Ca#, with no break in slope. This suggests that ilmenite did not begin crystallizing during the interval of crystallization sampled by the Kalkput megacrysts. Like some Cr-poor and some Cr-rich cpx megacryst suites, the Kalkput suite exhibits a marked increase in the ratio of Zr (and Hf) to the similarly incompatible middle REE, such as Sm. Zr/Sm ratios in the Kalkput suite have a clear, though non-linear, relationship to Ca#, where it increases from less than 5 to more than 50 over a range in Ca# of about 38 to 52 (Fig. 1.17). This can also be seen clearly in the primitive mantle-normalised trace element diagrams for Kalkput megacrysts. Such a fractionation of Zr/Sm would not be expected to occur from simple progressive fractionation, especially in the absence of evidence for ilmenite crystallization, and could be interpreted to result from mixing of Zr-Hf-depleted and -enriched materials, at least one of which is likely resident in the lithospheric mantle. Mantle xenoliths have Zr/Sm ratios which are highly variable, particularly in metasomatic lithologies such as MARID (mica-amphibole-rutile-ilmenite-diopside) and PIC (phlogopite-ilmenite-clinopyroxene) (Grégoire et al., 2002). The variations of some highly incompatible trace element ratios with decreasing temperatures in Kalkput cpx megacrysts provide further evidence of lithospheric assimilation. The decrease in Ce/Pb and Th/Nb ratios (Figs. 1.28b and 1.29) showed by Kalkput megacrysts with increasing Ca# (i.e., decreasing temperature) temperatures can be explained by Group II kimberlite melts (with higher Th/Nb and Ce/Pb ratios) interacting with depleted lithospheric components.

The Lace kimberlite is one of the only other Group 2 kimberlites known to contain a significant Cr-poor megacryst suite and it includes garnet as well as cpx. Lace cpx shows a similar pattern to Kalkput in terms of variations of Mg# and Cr# with Ca# and are nearly superimposed on each other on Figures 1.12 and 1.13, although Lace cpx spans a considerably narrower range of Ca# values than Kalkput cpx (37-44 versus 38-52). Garnet megacrysts from both Lace and Star kimberlites display a positive, concave upward relationship between Mg# and Cr_2O_3 content similar to most garnets from the Cr-poor megacryst suite in Group 1 kimberlites.

1.7.6. PETROGENESIS OF THE BELLSBANK (GRP. 2) CR-RICH "MEGACRYSTS"

The Bellsbank Cr-rich cpx and garnet megacrysts are unusual compared to the other suites documented here, and among kimberlite megacryst suites in general, in that they display wide variations in Cr_2O_3 and Cr# that have virtually no correlation with Ca# or Mg#. The narrow range of Ca# values (44 - 48) spanned by the Bellsbank cpx may contribute to the lack of observable trends, but they also extend to Cr# values that are considerably higher even than cpx from other Cr-rich megacryst suites (e.g., Eggler et al. 1979; Kopylova et al., 2009). Bellsbank megacrystic garnets also lack systematic compositional variations, in that they span a relatively wide range of Mg# values (69-85) but these do not correlate with other chemical indices, such as Cr_2O_3 or TiO_2. Partly, this lack of systematic chemical trends may be because of the relative rarity of megacrystic garnets at Bellsbank.

Bellsbank cpx megacrysts are notable for having the strongest enrichments in the highly compatible elements (Figs. 1.16 and 1.17), both relative to the other cpx megacrysts described in this thesis and all megacryst samples for which data are reported in the literature (e.g., Jones et al., 1987; Davies et al., 2001; Merry and le Roex, 2007). Bellsbank cpx megacrysts have similar trace element patterns to cpx from MARID xenoliths (Dawson and Smith, 1977). Like the Bellsbank megacrysts, MARID xenoliths have highly enriched LREE patterns with nearly flat slopes from La to Pr (Coussaert et al., 2003). However, cpx from MARID xenoliths, unlike the Bellsbank megacrysts, have relatively low Cr contents and Cr# values (wt.% Cr_2O_3 largely below 0.17, Cr# below 60; Grégoire et al., 2002).

There are rough negative correlations between Cr# and both incompatible element concentrations and Sr isotope ratios in Bellsbank cpx megacrysts (Fig. 1.23) that suggest mixing between a relatively incompatible element-depleted, high-Cr# component with less radiogenic $^{87}Sr/^{86}Sr$ (depleted peridotite) and a relatively enriched, low-Cr# component with more radiogenic $^{87}Sr/^{86}Sr$. MARID-type metasomatic veins appear to be a good candidate for the latter component due to the high incompatible element contents of MARID xenoliths and their elevated Sr isotope ratios (Kramers, 1979, Giuliani et al., 2015).

Are Bellsbank cpx metasomatic products of melt-rock reactions between Group 2 protokimberlite magmas and depleted peridotite/MARID metasomatic veins? Are they just the expression of an extreme assimilation process of depleted peridotite/MARID metasomatic veins

by megacryst parental magmas (with Group 2 kimberlitic affinities)? It may be that the Bellsbank cpx megacrysts are the result of assimilation or metasomatic melt/fluid-wallrock reaction occurring at such low ratios of melt/fluid to solid reactant/assimlant that the two hypotheses are essentially indistinguishable. Bellsbank cpx megacrysts are certainly unusual compared to other Cr-rich megacryst suites worldwide (e.g., Poffader, Monastery, Kimberley Granny Smith, Mbuji-Mayi, Jericho and State Line; Eggler et al., 1979; Kopylova et al., 2009; Pivin et al., 2009; Janney and Bell, 2014).

The small number of Bellsbank garnets that can be plausibly classified as megacrystic, and their lack of coherent chemical systematics, complicates the interpretation of their petrogenesis. They have a range of Cr_2O_3 contents from about 0.1 to 3.12 wt.%, similar to garnet megacrysts from the Group 2 Star and Lace kimberlites (Hill, 1989; D.R. Bell and D.J. Schulze, unpublished data). The Bellsbank garnets have significantly lower average TiO_2 values than Lace and Star garnet megacrysts, although TiO_2 contents are bimodal, with roughly half of the grains having TiO_2 values of 0.4 ± 0.1 wt.% and the other half of 0.1 ± 0.1 wt.%. The Bellsbank garnets also have unusually low concentrations of the LREE compared to those from Star or Monteleo garnet megacrysts (e.g., Nd concentrations in the Bellsbank garnets range from 0.4 to 1.1 ppm whereas for Star garnet megacrysts this range is 1.9 to 2.1 ppm, and this range appears to be typical of garnet megacrysts from Group 2 kimberlites; Perrit et al., 2015; Nowell et al., 2004). If the Bellsbank garnets crystallized from Group 2 kimberlite melts, one would expect them to display significantly higher concentrations of the LREE, and other highly incompatible elements, than this based on the measured composition of Group 2 kimberlites and reasonable partition coefficients (e.g., Becker & le Roex, 2006; Salters et al., 2002). The combination of relatively low concentrations of TiO_2 and the LREE, along with moderate Mg# values, displayed by the Bellsbank garnets is relatively similar to that seen in eclogitic and and pyroxenitic garnet from Lace (Aulbach and Viljoen 2015). Bellsbank, like Lace, has yielded a large suite of eclogite and pyroxenite xenoliths (e.g, Boctor & Boyd, 1982; Taylor & Neal et al., 1989) however the eclogitic and pyroxenitic garnets from Lace and Bellsbank generally have significantly lower Cr_2O_3 values than the Bellsbank garnets. It therefore seems plausible that the Bellsbank garnets could represent some kind of reaction product between melts of a pyroxenitic/eclogitic lithology and peridotitic wall rock, with the possible complication that some of the garnets with the lowest Cr_2O_3 and Mg# values might actually represent pyroxenitic/eclogitic garnets. Relative to nearly all of the other

garnet megacrysts in this study, the lower temperatures in Bellsbank garnets should be noted (Fig. 1.23), which supports the hypothesis that these garnets might have originated from pyroxenitic sources (possibly as pyroxenite melt-peridotitic reaction products as described above) aided by the lower melting temperature of pyroxenite relative to peridotite, and likely do not have a normal megacrystic origin.

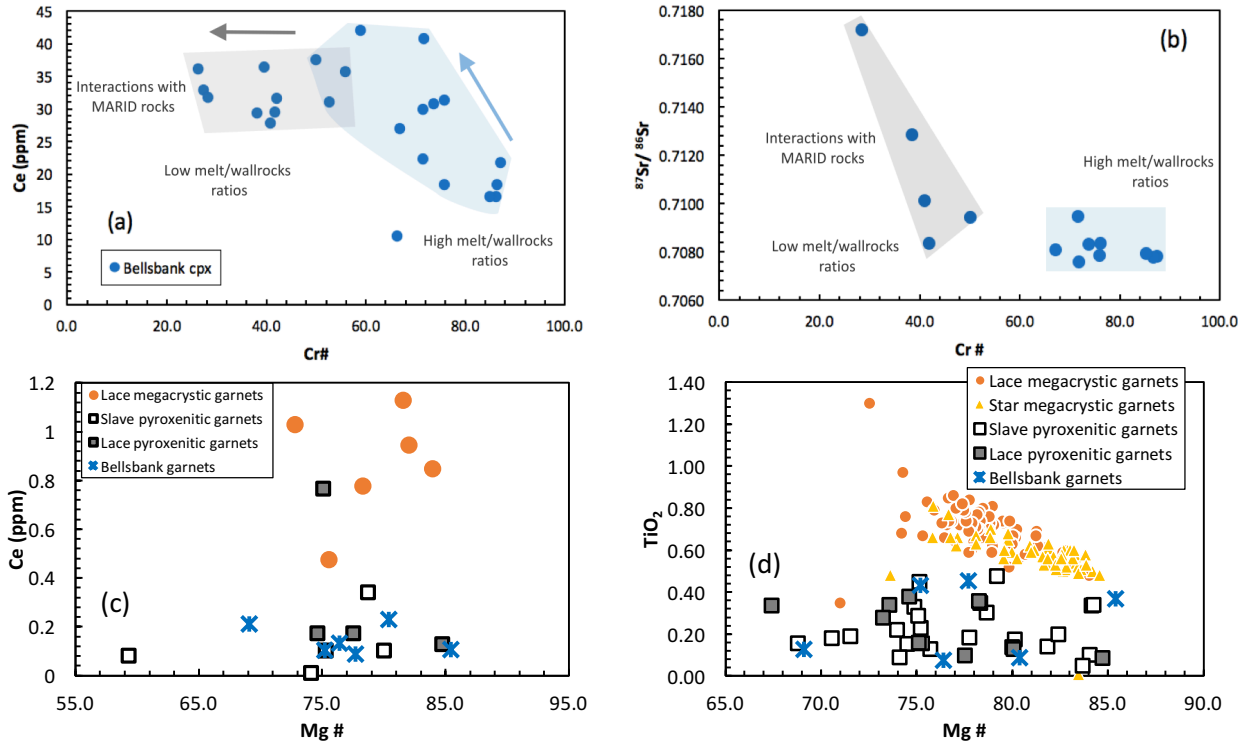

Figure 1.23: (a) Plot of Cr # versus Ce (ppm) in Bellsbank cpx megacrysts. **(b)** Plot of Cr# versus $^{87}Sr/^{86}Sr$ (measured) in Bellsbank cpx megacrysts. **(c)** Mg # versus Ce (ppm) plot of Bellsbank garnets. **(d)** Mg # versus TiO_2 plot of Bellsbank garnets. Note the higher Ce contents and $^{87}Sr/^{86}Sr$ values in the Bellsbank clinopyroxene megacrysts with lower Cr# values. Data for Lace and Star garnets are shown for comparison (UCT KRG database). Pyroxenitic garnets data from Aulbach et al., (2007) (Slave Craton) and from Aulbach and Viljoen (2015) (Kaapvaal Craton) are shown.

1.8. COMPARISON OF THE GROUP 1 AND GROUP 2 KIMBERLITE MEGACRYSTS

The compositional variations of most Group 1 and Group 2 kimberlite megacrysts appear to be consistent with their formation by similar processes of fractional crystallization of primitive, possibly sub-lithospherically derived melts combined with differing extents of assimilation of

lithospheric components (e.g., Bell and Moore, 2004). However, some differences are observable between megacryst suites from the two kimberlite types.

Differences in the major element geochemistry of Group 1 and Group 2 kimberlite megacrysts are illustrated in Figures 1.24, 1.25 and 1.26, with additional literature data from well-studied megacryst suites for each group (Monastery for Group I and Lace for Group 2). In Group 2 kimberlites, crystallization of the most primitive Cr-poor megacrysts appears to start at higher Mg# values in Group 2 kimberlite cpx megacrysts (with Mg# values below 91 for Cr-poor megacrysts from Group 1, while above 91 for Cr-poor megacrysts from Group 2 cpx megacrysts). It is noteworthy in this context that Group 1 kimberlites appear to have lower MgO contents, on average, than Group 2 kimberlite (Becker and Le Roex, 2006)

Crystallization of Cr-poor cpx megacrysts from Group 2 kimberlites appears to begin at lower temperatures compared to Group 1 kimberlites on the basis of the fact that their minimum Ca# values are higher than for cpx megacrysts from Group 1 kimberlites (with minimums of about 37 for Group 2 versus about 28 for Group 1). It is noteworthy in this regard that, on the basis of garnet xenocryst thermobarometry and geochemistry, Griffin et al., (2003) and Kobussen et al. (2008) inferred that the SCLM sampled by the main Group 2 kimberlite episode in southern Africa (≈130-110 Ma) was significantly cooler and generally less metasomatised (i.e., poorer in Ti, Zr and other incompatible elements) than that traversed later by the main pulse of Group 1 kimberlite magmatism (≈100 to 75 Ma). Such a difference in lithospheric mantle temperature could possibly explain this apparent difference in the maximum temperature of cpx megacryst crystallization.

Unlike many Group 1 kimberlite megacryst suites, there is no late increase apparent in Cr# or Mg# at high Ca# values in Group 2 cpx megacryst suites (such as Kalkput and Lace) that would be indicative of increased assimilation of peridotitic material with decreasing temperature. The absence of such an increase *in Cr# and Mg#* can potentially be explained by two hypotheses:

(1) Protokimberlitic melts with Group 2 affinities likely originate from or interact extensively with high Rb/Sr, low Sm/Nd materials such as MARID (e.g., Gregoire et al., 2002; Giuliani et al., 2015; Fitzpayne et al., 2018) rather than peridotite. MARID and similar metasomatic xenolith types tend to have lower Cr and Mg contents than garnet peridotites (Erlank et al., 1987).As mentioned above, MARID and similar metasomatic lithologies have low Cr and Mg contents compared to garnet peridotites. Therefore, assimilation of veins of such lithologies (presumably in an otherwise infertile garnet peridotite host as envisioned by

Griffin et al., 2003 and Kobussen et al., 2008), could explain the decreases in Th/Nb and Ce/Pb seen in Kalkput cpx megacrysts while the assimilation of such Mg and Cr-poor vein material during crystallization can also explain why Group 2 cpx megacrysts (e.g., Kalkput and Lace) show continuous drops in Mg# and Cr# with increasing Ca#. The overall higher Ca# values of Group 2 Cr-poor cpx megacrysts also suggests that they crystallized at a significantly lower temperature range than Cr-poor cpx megacrysts from group 1 kimberlites. Therefore, their parental magmas may have been less able to assimilate bulk peridotite (with a high melting temperature), whereas they would have been able to assimilate MARID and other metasomatic lithologies (present as veins in the lithosphere), which have relatively low melting temperatures (Sweeney et al., 1993).

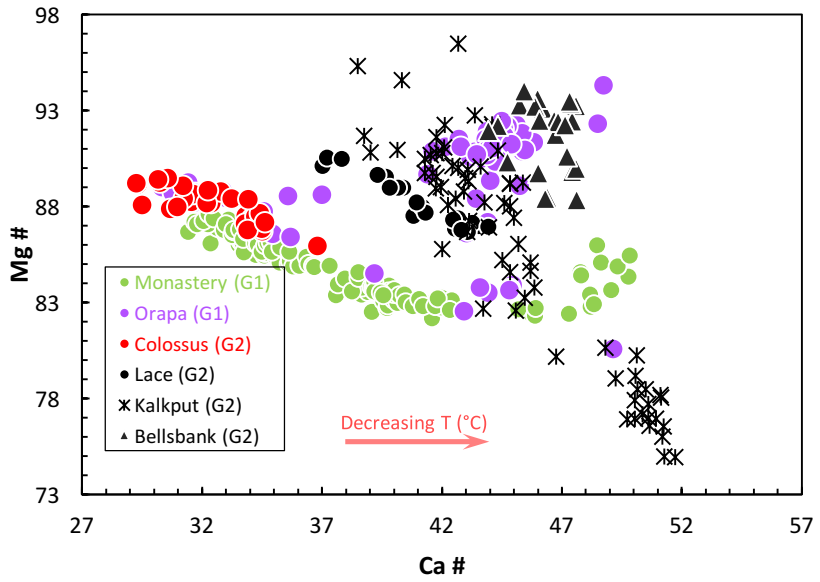

Figure 1.24: Plot of Ca # vs. Mg# for cpx megacrysts from Group 1 (coloured symbols) and Group 2 (black symbols) kimberlites. The crystallization of Group 2 kimberlite megacrysts appear to start at lower temperatures (higher Ca#) and at higher Mg# values than for megacrysts from Group 1 kimberlites. Note the two distinct trends, Mg# decreases continuously with increasingCa# in Group 2 cpx megacrysts, while, in Group 1 megacryst it initially declines with increasing Ca# and later, at higher Ca# (> 45, indicating lower temperatures) it increases again in some suites. Lace (Group 2) and Monastery (Group 1) megacryst data are shown for comparison and are from Jakob (1977), Moore (1986) and various unpublished data of D.R. Bell and D.J. Schulze. Some Kalkput data are from De Bruin (1999).

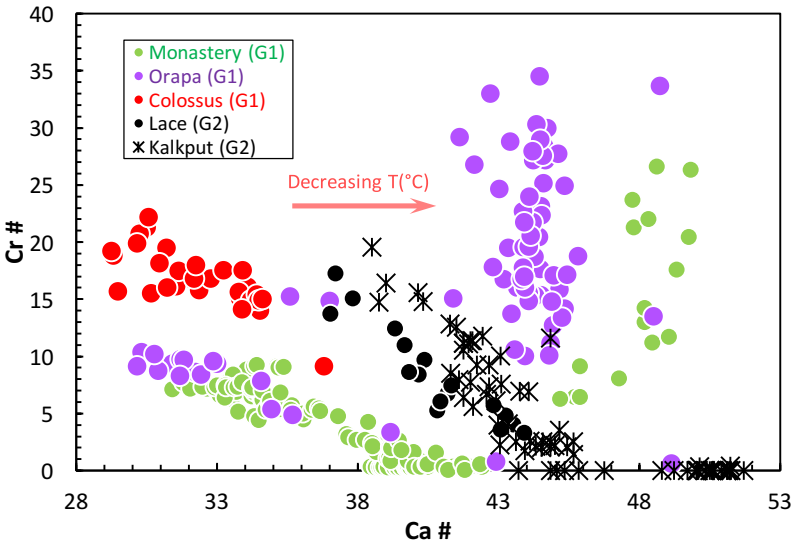

Figure 1.25: Plot of Ca# vs Cr# for Group 1 and Group 2 cpx megacrysts. Cr# continuously decreases with increasing Ca# in cpx megacrysts from Group 2 kimberlites, while it initially declines, then, above Ca# ≈ 45, Cr# dramatically rises in cpx megacrysts from Group 1 kimberlites. Data sources as in Fig 1.24. Bellsbank data do not fall within the area of the plot because of their high Cr# values.

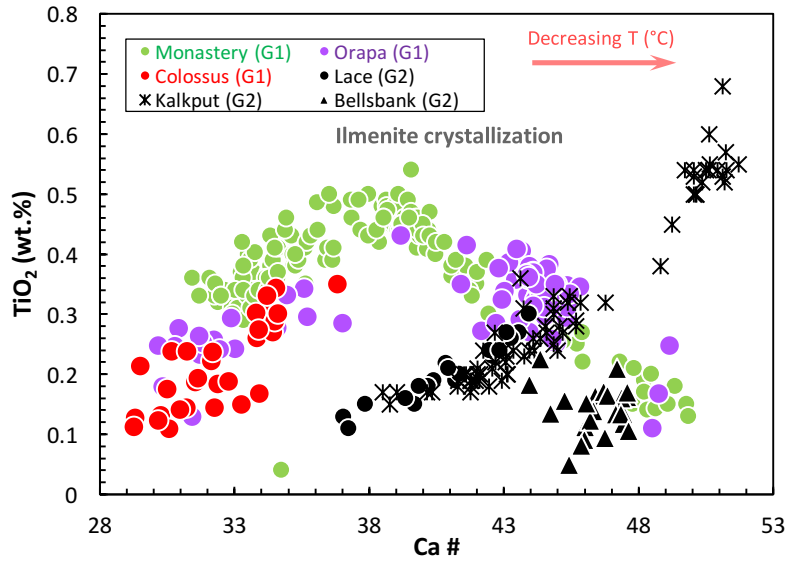

Figure 1.26: Plot of Ca# vs TiO_2 for Group 1 and Group 2 cpx megacrysts. Note that, for cpx megacrysts from Group 1 kimberlites, TiO_2 values initially increase, but then at Ca# ≈ 38, there is a break in slope and at higher Ca# values TiO_2 decreases with increasing Ca#. Data sources as in Fig 1.24.

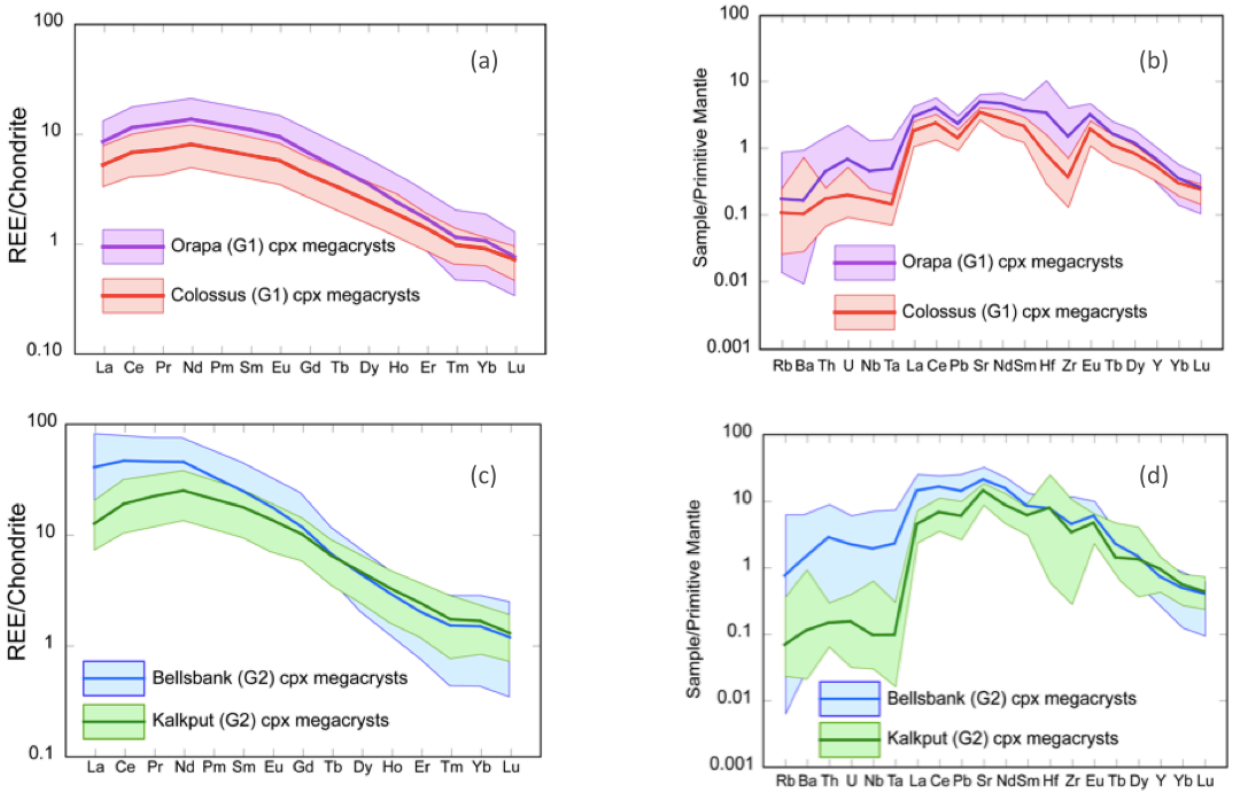

Figure 1.27: Chondrite-normalised REE and primitive mantle-normalised incompatible element plots for cpx megacrysts from Group 1 and Group 2 kimberlites from this study. (a) Chondrite-normalized REE plot of Group 1 cpx megacrysts. (b) Primitive-mantle-normalized plot of Group I cpx megacrysts. (c) Chondrite-normalized REE plot of Group 2 kimberlite cpx megacrysts. (d) Primitive-mantle-normalized plot of Group 2 kimberlite cpx megacrysts. In all figures, the range of values are shown along with the average for that group. Note the higher LREE content and more fractionated REE patterns displayed by Group 2 kimberlite megacrysts compared to Group I. Normalising values are from Sun and McDonough (1989).

Griffin et al. (2003) and Kobussen et al. (2008) suggested that Group 2 kimberlites in southern Africa sampled a relatively cool SCLM with higher proportions of depleted harzbugite and lherzolite than that sampled by later Group 1 kimberlite magmatism. Harzburgitic SCLM lacks cpx and it is likely that the amount of assimilation by megacryst magmas would be dramatically lowered compared to that possible with wall-rocks composed mainly of lherzolite therefore, the late increase in Mg# and Cr# seen in many Group 1 clinopyroxene megacryst suites would not be expected to occur in Group 2 kimberlite megacrsyts because of the lack, or much smaller extent, of assimilation of harzbugitic (rather than lherzolitic) mantle by protkimberlite melts.

The crystallization of Orapa low-Cr garnets occured at lower temperatures than the crystallization of Orapa high-Cr garnets (Fig. 1.22). It is noteworthy to mention that the Orapa low-Cr garnets have the lowest Ce/Yb ratios (Fig. 1.11), are characterized by a deflection towards higher Cr_2O_3 content at low Mg# (Fig. 1.9b) and display a trend of decreasing Ti content with decreasing Mg# (Fig. 9c). In addition, the single Colossus garnet megacryst with low Mg# also has the lowest Ce/Yb ratio of the group and lies in the midst of the trend of decreasing TiO_2 contents with decreasing Mg# . The following elements support the involvement of lithospheric assimilation in the magma parental to the low-Cr garnet megacrysts:

(1) The increase in Cr_2O_3 from values near 0 to 1% at low Mg# values, seen in the Orapa low-Cr garnets (and also in garnet megacrysts from the Frank Smith kimberlite) could indicate assimilation of Cr-rich mantle material by the megacryst parental magmas.

(2) The changing trend from an increase in TiO_2 with decreasing Mg# to a decrease in TiO_2 with further decrease in Mg# (Fig. 1.9c) is most plausibly attributable to the onset of ilmenite crystallization. As the latter has been suggested to be a late-crystallizing phase (Moore et al., 1992), the crystallization of Orapa and Colossus low-Cr garnets occurs subsequent to the crystallization of high-Cr garnets.

Therefore, the low temperatures calculated by Orapa and Colossus low-Cr garnets are consistent with the hypothesis that they crystallized after high-Cr garnets and, therefore are likely related to the Cr-rich megacryst suite. The high-Cr Orapa garnet megacrysts, which have higher calculated temperatures, appear to have crystallized earlier than the low-Cr garnets. Due to this, along with their variations in TiO_2 and Cr_2O_3 with Mg#, the high-Cr megacrysts are likely related to the Cr-poor megacryts suite.

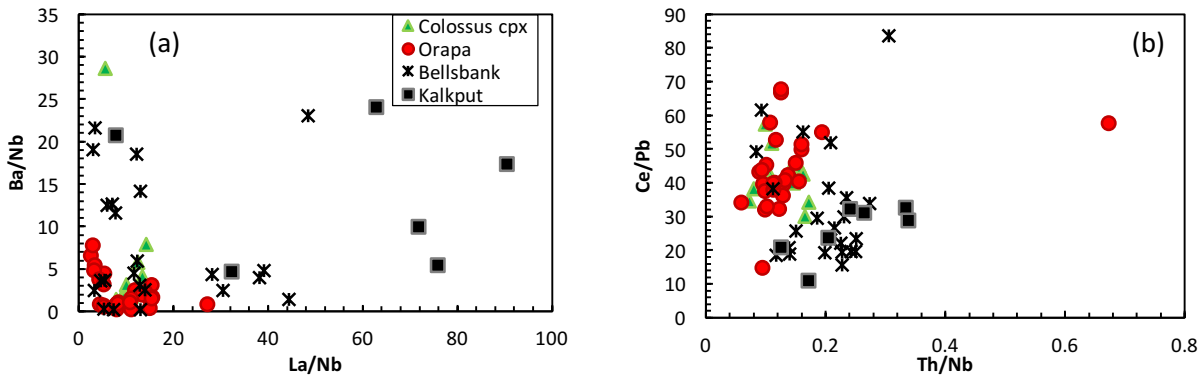

Figure 1.28: Variation of selected trace element ratios in southern African Group 1 (coloured symbols) and Group 2 (black symbols) kimberlite megacrysts investigated in this thesis. **(a)** La/Nb plotted versus Ba/Nb. **(b)** Th/Nb plotted versus Ce/Pb.

Group 2 kimberlite cpx megacrysts appear to be more enriched in LREE, LILE and, to a smaller extent, in HFSE than cpx megacrysts from Group 1 kimberlites (Fig. 1.27). $(Nd/Yb)_N$ ranges from 5.7 to 26.2 for Group 1 cpx megacrysts investigated in the present thesis, compared to a range of 13.5 to 166 for Group 2 cpx megacrysts (Fig. 1.27). It is noteworthy that Group 2 kimberlites are more LREE enriched and have, on average, higher LILE concentrations than Group I kimberlites (Becker and le Roex, 2006). Becker and le Roex (2006) found that Group I kimberlites have higher Ce/Pb ratios than Group II kimberlites, as well as lower Th/Nb, Ba/Nb and La/Nb ratios.

In this study, it is found that Group 2 kimberlite megacrysts have lower Ce/Pb ratios on average than Group 1 kimberlite megacrysts (Ce/Pb = 29.2 ± 12.2 versus 43 ± 9.99, 1SD) (Fig. 1.28) and higher Th/Nb (0.20 ± 0.06 versus 0.13 ± 0.09), Ba/Nb (8.92 ± 7.74 versus 3.14 ± 4.64) and La/Nb (24.8 ± 24.5 versus 9.65 ± 4.79) ratios on average than Group I kimberlite megacrysts (Fig. 1.28 and see Table 1.1).

Group 1 kimberlite megacrysts (in this study) have measured $^{87}Sr/^{86}Sr$ ratios ranging from 0.7025 to 0.7057, generally corresponding with the isotopic range of Group I kimberlites. Group 2 kimberlite megacrysts have measured $^{87}Sr/^{86}Sr$ ratios ranging from 0.7071 to 0.7172, overlapping with, but extending to more radiogenic values, than, Group 2 kimberlites.

Table 1.1: Trace element ratios in Southern African Group 1 and Group 2 kimberlite cpx megacrysts

		Ba/Nb		Th/Nb		La/Nb		Ce/Pb	
		avg	1SD	avg	1SD	avg	1SD	avg	1SD
Group 2	Bellsbank	7.67	7.29	0.19	0.06	15.8	14.1	32.5	16.9
	Kalkput	12	9.27	0.23	0.09	58.2	21.8	29.4	7.1
Group 1	Colossus	5.25	7.61	0.13	0.03	10.6	2.36	41.7	6.88
	Orapa Cr-rich	2.64	2.13	0.15	0.14	7.77	4.35	41.8	6.08
	Orapa Cr-poor	1.1	0.66	0.13	0.03	11.5	6.85	46.6	16.3
	Lekkerfontein	1.15	0.24	0.12	0.03	10.7	1.92	22.5	5.98
	Uintjiesberg	1.28	1.00	0.12	0.03	13.2	1.85	24.7	8.97

Lekkerfontein and Uintjiesberg megacryst data are from Merry and le Roex (2007)

In both groups, the most primitive (low-calcium, high temperature) megacrysts show a restricted range of measured Sr isotope while the more evolved megacrysts (high calcium, lower temperature), except those from Kalkput, display a higher degree of $^{87}Sr/^{86}Sr$ ratio variations (Fig. 1.8 and Fig. 1.18), likely reflecting greater incorporation of isotopically heterogeneous, but generally higher $^{87}Sr/^{86}Sr$, SCLM with increasing differentiation.

Evidence of lithospheric assimilation

All megacryst suites display changes with respect to increasing Ca# (i.e., decreasing temperature) in cpx or decreasing Mg# in garnet that cannot be simply explained by fractional crystallization and therefore require some type of assimilation or melt-rock reaction process to have occurred. Specifically, these include:

(a) increases in Zr/Sm ratios with increasing Ca# (exhibited by virtually all cpx megacryst suites for which there are data), which occurs whether or not there is evidence for ilmenite crystallization

(b) increases in Nd/Yb with increasing Ca# (exhibited by all group 1 cpx megacrysts for which there are data (e.g., Colossus, Orapa, Uintjiesberg, Lekkerfontein (this study and Merry & le Roex, 2007)

(c) Additionally, for both of Zr/Sm and Nd/Yb, their slope versus Ca# becomes greater at high Ca# values, suggesting an increase in the degree of assimilation of lithospheric components relative to crystallization.

(d) An increase in both the variability and mean value of $^{87}Sr/^{86}Sr$ ratios in clinopyroxene

megacrysts with increasing Ca# (seen in Colossus, Orapa (if Cr-poor and Cr-rich are considered together) and Bellsbank, but not Kalkput).

Observation (a) could be due to assimilation of a high Zr/Sm metasomatic lithology (such as PIC [Phlogopite-ilmenite-clinopyroxene lithology]), or possibly to progressive equilibration of a Zr-depleted melt (possilby with a carbonatitic affinity to explain the Zr-Hf depletion) with metasomatised peridotite. Observations (b), (c) and (d) could be due to assimilation of metasomatised, incompatible element enriched peridotite and/or a more explicitly metasomatic lithology such as MARID or PIC. The increasing variability of $^{87}Sr/^{86}Sr$ with increasing Ca# in several suites suggests assimilation of materials having a range of Sr concentrations and/or isotopic compositions. The lack of change in $^{87}Sr/\ ^{86}Sr$ with Ca# in the (group 2) Kalkput cpx megacryst suite does not seem to provide evidence against assimilation given (i) the fact that all of these cpx megacrysts have relatively high $^{87}Sr/^{86}Sr$ values that may not be very different from that of lithospheric materials, and (ii) there are clear variations in highly incompatible element ratios, such the drop in Ce/Pb with increasing Ca# (Fig. 1.29), that are most simply explained as the result of assimilation of lithospheric components having low Ce/Pb.

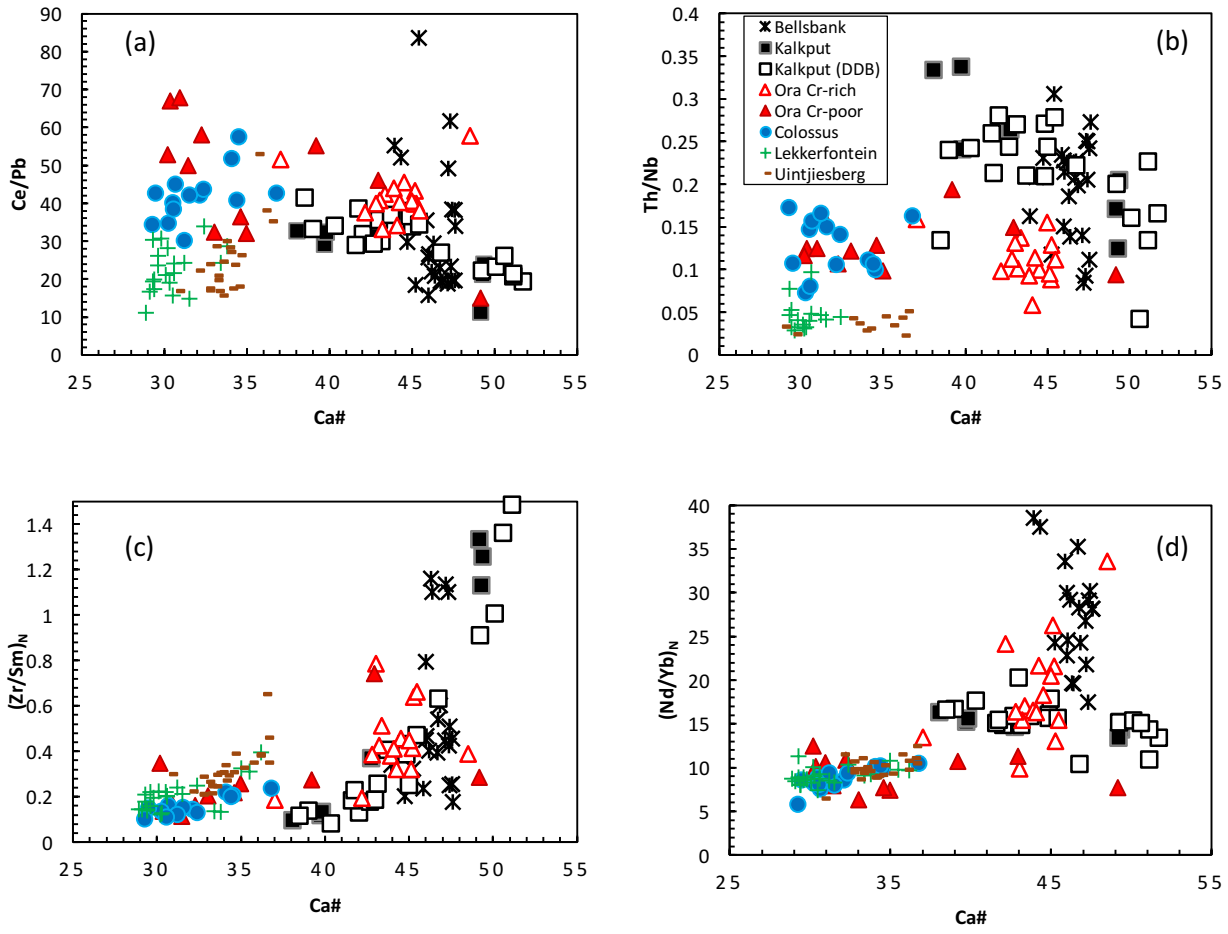

Figure 1.29: Variation of selected trace element ratios with Ca# in southern African Group 1 (coloured symbols) and Group 2 (black symbols) kimberlite clinopyroxenes megacrysts. **(a)** Ca# versus Ce/Pb plot. **(b)** Ca# versus Th/Nb plot. **(c)** Ca# versus $(Zr/Sm)_N$ plot. **(d)** Ca# versus $(Nd/Yb)_N$ plot. Some Kalkput data those marked (DDB) are unpublished data of Deon de Bruin. Lekkerfontein and Uintjiesberg data are from Merry and Le Roex, (2007). Normalizing values are from McDonough and Sun (1995).

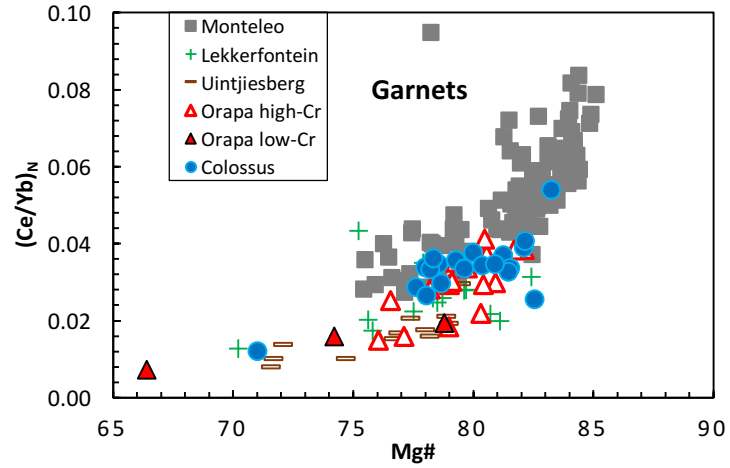

Figure 1.30: Mg# plotted versus $(Ce/Pb)_N$ in Southern African Group I kimberlite megacrysts. Lekkerfontein and Uintjiesberg data are from Merry and Le Roex (2007).

1.9. THE RELATIONSHIP BETWEEN CR-POOR AND CR-RICH MEGACRYSTS

Historically, most petrological studies have focused on the Cr-poor megacryst suite (e.g., Gurney et al., 1979; Eggler et al., 1979; Bell and Moore, 2004) but recently more attention has been devoted to the Cr-rich megacryst suite, particularly because this suite seems to be dominant in many areas outside of southern Africa (e.g., Kostrovitsky et al., 2004; Moore and Belousova, 2005; Kopylova et al., 2009; Bussweiller et al., 2016; 2018). Significant controversy remains over whether these two suites have separate origins (Eggler et al, 1979; Hunter and Taylor, 1984; Hatton, 1998) or whether the magmas parental the the Cr-rich suite are genetically related to those parental to the Cr-poor suite (Bell and Moore, 2004; Moore and Belousova, 2005).

Moore and Belousova (2005) provide evidence for a genetic relationship between Cr-poor and Cr-rich megacryst varieties, and between both and their host kimberlites. However, they, and other more recent studies (e.g., Kopylova et al., 2009) favour models in which Cr-rich megacrysts are formed earlier from primitive Mg- and Cr-rich parental magmas and Cr-poor megacrysts are formed later from more evolved, Cr- and Mg-depleted liquids in a process similar to the progressive metasomatic model discussed earlier (section 1.7.2). In contrast, Bell and Moore (2004) proposed that Cr-poor and Cr-rich megacrysts are related, but that Cr-poor megacrysts formed earlier, from deep protokimberlitic melts, and Cr-rich megacrysts may represent later crystallization products of megacryst magmas having undergone an assimilation-fractional crystallization process, where the assimilant is either lithospheric peridotite or a metasomatic vein component. These competing hypotheses will be discussed in the light of evidence provided by megacrysts from Orapa, which is the only locality studied in this thesis with extensive Cr-poor and Cr-rich megacryst suites.

1.9.1. THE EVIDENCE FOR A GENETIC RELATIONSHIP FROM ORAPA CR-RICH AND CR-POOR MEGACRYST SUITES

Among the southern African megacryst suites studied in this thesis, Cr-rich megacrysts occur at Orapa and Bellsbank. However, the megacrysts at Bellsbank do not display systematic chemical variations with respect to Mg# or Cr# and this, plus the lack of accompanying Cr-poor megacrysts and the narrow range of crystallization temperatures indicated by their small range of

Ca# values makes them atypical of southern African kimberlite megacrysts and seriously complicates interpretation of their origin.

The major and trace element geochemistry of Orapa cpx and garnet megacrysts studied in this thesis strongly support a genetic relationship between the Cr-poor and the Cr-rich suites. The relatively continuous variation in megacryst composition between Cr-poor and Cr-rich megacryst compositions seen at places like Monastery is also seen in Orapa megacryst suites (Fig. 1.2, 1.3 and 1.4). However, the Orapa and Monastery megacryst suites differ, with respect to clinopyroxene, in that the Cr-rich and Cr-poor populations overlap over a wide range of Ca# values and they show slightly different patterns. In Monastery cpx there is a trend, with increasing Ca# (i.e., decreasing temperature), of decreasing Mg# and Cr# values, then, at high Ca# values, rapidly increasing Cr# and Mg# values, making an asymmetric "U-shaped" pattern (Figs. 1.2, 1.3 and 1.4). At Orapa, in the Cr-poor suite, there is instead a relatively linear decrease in Mg# and Cr# with increasing Ca# in cpx, from moderate values (of about 89 and 10 at Ca# of ≈30, respectively) to low values (of about 80 and 0.5 at Ca# of ≈50, respectively). The drop in Mg# and Cr# can be explained simply by progressive fractional crystallization, as can the initial increase and subsequent decrease of TiO_2, of an assemblage initially containing cpx (±garnet, olivine and opx) with the later addition of ilmenite to explain the drop in TiO_2. Along this evolution path, at Ca# values of above ≈35, the Cr-rich megacrysts occur, falling at somewhat higher Mg# and Cr# values, with the upper bound of the data envelope increasing to maximum Mg# and Cr# values of 94 and 34, respectively. Unlike at Monastery, where there is only a narrow range in Mg#, Cr# or any elemental abundance or ratio at a given Ca#, there is a wide range of values spanned by the Orapa Cr-rich suite, and an even wider range if both Cr-poor and Cr-rich megacrysts are included. The pattern shown by the Orapa megacrysts is consistent with the Cr-poor suite being the product of nearly pure fractional crystallization, and the Cr-rich suite being the product of fractional crystallization combined with variable degrees of lithospheric assimilation. This view is supported by the following observations: (1) the lack of any significant or systematic change in either $^{87}Sr/^{86}Sr$ and $(Nd/Yb)_N$ ratios with respect to Ca# in the Cr-poor suite, and (2) the increase in both variability, and mean value, of $^{87}Sr/^{86}Sr$ or $(Nd/Yb)_N$ in the Cr-rich suite with increasing Ca#. Pure fractional crystallization would have either no or minimal effect on these ratios, whereas varying degrees of assimilation, or assimilation of variably metasomatised lithospheric wallrock (having relatively high $^{87}Sr/^{86}Sr$ and $(Nd/Yb)_N$ values) would result in significant increases of these ratios.

It is very difficult to envision a scenario, such as that proposed by Moore and Belousova (2005), that would first generate the (quite heterogeneous) Cr-rich megacrysts at Orapa and, from them, derive megacrysts comprising the much simpler compositional trend defined by the Cr-poor population, which have both relatively uniform and depleted compositions in terms of $^{87}Sr/^{86}Sr$ and $(Nd/Yb)_N$. Indeed, it is important to mention here that Moore and Belousova (2005) did not show, nor attempt to explain, the compositional trends of cpx megacrysts with respect to Ca#, which provides a powerful constraint on models of megacryst petrogenesis.

The evidence provided by the Orapa megacryst suite strongly supports the contention that the magma parental to the Cr-poor suite is more closely related to the initial magma parental to all of the megacrysts, and that the Cr-rich megacrysts are the product of the variably evolved Cr-poor parental magma after variable assimilation of incompatible element-, Cr- and Mg-enriched lithospheric components.

1.9.2. EVIDENCE FROM OTHER LOCALITIES WORLD-WIDE

Examination of other localities world-wide with Cr-poor and Cr-rich megacryst suites tends to support the above hypothesis. It has been shown here that the increasing value and variability of Cr# and Mg# along with $(Nd/Yb)_N$ and $^{87}Sr/^{86}Sr$ ratios with increasing Ca# observed in Cr-rich cpx megacrysts at Orapa are all likely indicative of assimilation of metasomatised lithospheric products by what were initially magmas parental to Cr-poor megacrysts. The more well-defined single trend defined by the Monastery cpx megacrysts discussed above is also consistent with an origin by fractional crystallization of an initially Cr-poor parental magma in which assimilation becomes increasingly important with decreasing temperature (although with less scatter due either to higher melt-wallrock ratios or a more homogeneous lithospheric assimilant). At several other kimberlite localities, mainly outside of southern Africa, the relationships between Cr-poor and Cr-rich megacrysts are less clear. At the Jericho (Slave craton), State Line (wyoming craton) and Mbuji-Mayi (kasai craton) localities in particular, data for Cr-poor and Cr-rich megacryst suites have been reported (Eggler et al., 1979; Kopylova et al., 2009; Pivin et al., 2009). In each case, the origins proposed strongly contrast with the progressive fractionation + assimilation model favoured here. Published datasets for these megacryst suites are

limited, with only representative analyses being included (Eggler et al., 1979; Kopylova et al., 2009; Pivin et al., 2009).

At Jericho, the crystallization of Cr-rich cpx megacrysts is marked by an increase in Cr_2O_3 content (Mg# much less) compared to the crystallization of the more evolved Cr-poor cpx megacrysts (Kopylova et al., 2009). Also, there is an increase of LREE content and trace element ratios (Nd_N/Yb_N and Zr/Sm) from Cr-poor to Cr-rich cpx megacrysts. This could possibly suggest that assimilation of metasomatised lithospheric products occurred and is evidence of a genetic link between the two megacryst population at Jericho.

In the State Line kimberlites, Cr-poor cpx megacrysts are characterized by a trend of decreasing Cr content with increasing Ca# (and therefore decreasing temperature; Eggler et al., 1979) starting at a value of about 35, followed by a dramatic increase in Cr contents at Ca# values above 42, with a significant interval where the Cr-poor and Cr-rich groups overlap, as seen at Orapa (See Fig 1.31). In addition, there is an increase of LREE content and $(Nd/Yb)_N$ from Cr-poor cpx to Cr-rich cpx megacrysts, with decreasing temperature (Eggler et al., 1979).

At Mbuji-Mayi, Cr-poor cpx megacrysts show a progressive decrease of Cr and Mg-number with increasing Ca# (Pivin et al., 2009). At higher Ca# values, there is a dramatic increase in Cr_2O_3 contents and Mg# values (Fig. 1.31). In addition, there is an increase of LREE content and (Nd_N/Yb_N) from Cr-poor to Cr-rich cpx megacryts with increasing Ca# values (i.e., with declining temperatures). Also, the increase in Cr content and Mg-number tends to coincide with a decrease in the TiO_2 contents of cpx megacrysts, likely indicating the onset of ilmenite crystallization late in the crystallization sequence.

Several studies of lithospheric composition have been conducted on the Slave, Wyoming and Kasai Cratons. For the Slave Craton underlying the Jericho kimberlite, workers have proposed: (1) a multistage metasomatic history (Heaman et al., 2006; Bussweiller et al., 2018) (2) a strongly stratified lithospheric mantle (Kopylova et al., 1999) (3) a strongly modified, metasomatised SCLM with abundant fertile lherzolites (Griffin et al., 2004; Aulbach et al., 2007). For the Wyoming Craton underlying the State Line kimberlites, it has been proposed that abundant fertile and metasomtised lherzolites are dominant in the SCLM (Griffin et al., 2004). For the Kasai Craton portion underlying the Mbuji-Mayi kimberlites, it has been proposed that it has a high proportion of fertile lherzolites and was extensively metasomatised (Batumike et al., 2009).

In southern Africa, it has been suggested that the listhophere was warmer, more metasomatised and had a high proportion of fertile lherzolites at the time of Group 1 kimberlite emplacement (Griffin et al., 2003; Kobussen et al., 2008; Griffin et al., 2014), compared to when the older Group 2 kimberlite were emplaced, and possibly copared to other cratonic lithosphere. In most cases, Group 1 kimberlite localities in southern Africa display both Cr-rich and Cr-poor megacryst suites (Monastery, Pofadder, Frank Smith, Orapa, Gibeon, Kimberley) (Gurney et al., 1979; Shee and Gurney, 1979; Boyd et al., 1984; Jones, 1987; Mitchell, 1987; Janney and Bell, 2014) . It appears that there is some correlation between Cr-rich megacryst suite occurrence and high abundance of fertile lherzolites and metasomatized materials in the SCLM.

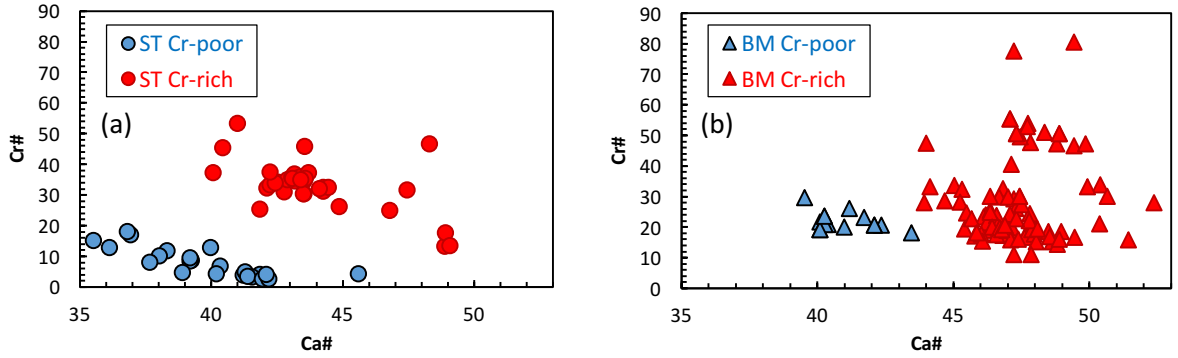

Figure 1.31: Megacryst dataset of State Line and Mbuji-Mayi localities revisited. Ca# (100*Ca/(Ca + Mg) in atomic units) versus Cr# (100*Cr/(cr +Al) in atomic units) plot. Cr-rich suites exhibit higher Cr# and appear to show a wide range of Cr variation. The appearance of Cr-rich megacrysts only at lower temperatures can be explained by the fact that the effects of lithospheric assimilation become more noticeable at low melt-wallrock ratios. Studies of the underlying SCLM at Mbuji-Mayi and State Line have revealed the abundant proportion of fertile and metasomatised lherzolites at these localities. This could explain the rise in Cr and Mg when the effect of lithospheric assimilation became much more noticeable. Data for State Line are from Eggler et al. (1979) and the UCT KRG database. Data from Mbuji-Mayi are Pivin et al. (2009) and Pivin, 2012.

1.10. ARE MEGACRYSTS GENETICALLY RELATED TO THEIR HOST KIMBERLITES?

The nature of the relationship between megacrysts and their host kimberlites has been debated for at least the past four decades. Here the evidence for and against a close genetic origin is evaluated and the possible contribution to this question of the megacryst data presented here is discussed.

1.10.1. EVIDENCE AGAINST A CLOSE GENETIC RELATIONSHIP

One line of argument against a direct genetic relationship between megacrysts and their host kimberlites is that the melts that were calculated to be in equilibrium with their host kimberlites have significantly lower REE contents, and lower enrichment in the light REE, than is measured for the host kimberlite types (e.g., Kramers et al., 1981; Hops et al., 1992; Merry and Le Roex, 2007). However, a major caveat to this argument is that most of these calculations were based on the the available mineral-melt partition coefficient data, which were determined on basaltic systems at relatively low presssures and having low dissolved volatile contents (e.g., Irving and Frey, 1984; Hauri et al., 1994). More recent data for experiments performed at higher pressures (e.g., Salters et al., 2002) and with melts containing significantly higher dissolved volatile contents (especially CO_2) that would be relevant to kimberlitic magmas (Keshav et al., 2005; Girnis et al., 2013) have yielded significantly lower mineral-melt partition coefficients. The equilibrium melts calculated from megacrysts using these partition coefficients provide a close match to kimberlite melt compositions. For example, using the new set of partition coefficients recommended by Keshav et al. (2005), Pivin et al., (2013) calculated the composition of theoretical melts in equilibrium with Mbuji-Mayi cpx megacrysts, which fall in the range of Group I kimberlite compositions. This therefore indicates that megacryst compositions could indeed be in equilibrium with kimberlitic parental melts, and shows one major objection to a near-cognate origin to be invalid.

A second line of evidence against a genetic connection based on the only study to have published Pb isotope data for kimberlite megacrysts, that of davies et al., (2001) on megacrysts from the off-craton Gibeon kimberlites of southern Namibia. They found that while the Sr and Nd isotopic composition of Gibeon kimberlites and cpx megacrysts overlapped, they did not overlap in terms of Pb isotope composition, and primarily on this basis, Davies et al. (2001) proposed that the Gibeon cpx megacrysts had no genetic relationship to the Gibeon kimberlites but rather were a feature of the regional mantle prior to kimberlite magmatism, and the kimberlites only served as a mechanism to deliver them to the surface. However, recent data presented by Janney and Bell (2014) for clinopyroxene megacrysts from Gibeon (including many of the same localities studied by Davies et al., 2001), as well as several other southern African localities found that there was

significant overlap between Gibeon kimberlites and their megacrysts, and the newer Pb isotope data, obtained using high precision and ultra-low blank methods, showed no overlap with the previous Pb isotope data of Davies et al. (2001) as well as much lower measured Pb concentrations. Because the concentrations of Pb (typically less than 1 ppm) are so much lower than for Sr and Nd (typicaly 10-100 ppm) in clinopyroxene, a likely explanation is that the Davies et al. (2001) data were affected by Pb contamination during chemical processing (performed in the 1980s), whereas the more recent data were not affected by such contamination.

1.10.2. EVIDENCE FOR A CLOSE GENETIC RELATIONSHIP

The overall similarity in Sr-Nd-Hf isotope compositions between megacrysts and their host kimberlites has long been noted (e.g., Kramers et al., 1981; Jones, 1987; Hops et al., 1992; Nowell et al., 2004). In detail, the isotopic composition of megacrysts and their host kimberlites may differ slightly, with megacrysts often having somewhat lower $^{87}Sr/^{86}Sr$ than their host. However, all published data show that the isotopic distinction between Group 1 and Group 2 kimberlites is also reflected in the Sr-Nd-Hf isotopic composition of their megacrysts. This is extremely difficult to explain if megacrysts have no genetic relationship to their host kimberlites.

Additionally, zircon megacrysts can be dated directly using the U-Pb system. Dating studies of zircon megacrysts from kimberlites show that, with very few exceptions, they have crystallized within 5 Myr of the age of the host kimberlite as determined by other means (such as Rb-Sr mica or U-Pb perovskite dating; Davis et al., 1976; Zartman and Richardson, 2005). Such similarity in age between kimberlites and their megacrysts are very hard to explain unless there is a genetic relationship between the two. Also, megacryst dating using Sr, Nd and Hf isotope isochron systematics, which also supported a close similarity in age between kimberlites and their megacrysts was presented by Kopylova et al. (2009)

1.10.3. CONTRIBUTION OF THIS STUDY TO THE CONTROVERSY: STRONG EVIDENCE FOR A CLOSE GENETIC RELATIONSHIP

It has been shown that Group I and Group II kimberlites are chemically and isotopically different (Smith, 1983). Assuming megacrysts and host kimberlite have a close genetic relationship, comparing the geochemistry of Group I kimberlite megacrysts to that of Group II kimberlite megacrysts reveal differences at least qualitatively similar to those between Group I

and Group II kimberlites. Furthermore, the major element-trace element-isotope approach, presenting data for several localities is fairly novel, and previous studies have suffered from more restricted data sets. Furthermore, megacrysts isotopic data has been provided for some localities which have published whole-rock isotopic data for their kimberlites, enabling a direct comparison (Bellsbank).

A. Comparison of Group 1 and Group 2 kimberlite megacrysts

Group 1 kimberlites are known to have radiogenic Nd ($\varepsilon_{Nd}(t)$ = 0 to +4 and unradiogenic Sr isotopic compositions ($^{87}Sr/^{86}Sr_i$ = 0.7035 to 0.7055), whereas Group 2 kimberlites have radiogenic Sr ($^{87}Sr/^{86}Sr_i$ = 0.7070 – 0.7120) and unradiogenic Nd isotopic compositions ($\varepsilon_{Nd}(t) \approx$ -5 to -12; Smith, 1983; Nowell et al., 2004; Becker and le Roex, 2006). In this study, it was shown that Group 1 kimberlite megacrysts have Sr isotope compositions falling within the range of Group I kimberlite, while Group 2 kimberlite megacrysts appeared to have a Sr isotopes falling in the range of Group 2, general pattern that others (Kramers et al., 1981; Jones, 1987; Nowell et al., 2004) have already found. This is an evidence of a close genetic relationship between megacrysts and their host kimberlites.

Group 2 kimberlite megacrysts appear to crystallize in a cool lithospheric mantle. Griffin et al., (2003) and Kobussen et al., (2008) highlighted that Group II kimberlites have sampled a cool lithospheric mantle. Group 2 kimberlite clinopyroxene megacrysts have a greater range of LREE and LILE enrichment than those from Group 1 kimberlites. Becker and le Roex (2006) found that Group 2 kimberlites have higher LREE and LILE contents than Group I kimberlites. In addition, source-sensitive trace element ratios (e.g., Ba/Nb, Th/Nb, La/Nb and Ce/Pb) demonstrate a connection between megacryts and their host kimberlites. It was shown that Group 2 kimberlite megacrysts have higher Th/Nb, Ba/Nb and La/Nb ratios than Group 1 kimberlite megacrysts, consistent with the finding of Becker and Le Roex (2006) that Group 2 kimberlites have higher Th/Nb, Ba/Nb and La/Nb ratios than Group I kimberlites.

B. Direct comparison between megacrysts and host kimberlites

Becker and le Roex (2006) provided Sr-Nd isotopic whole-rock data for the Bellsbank kimberlite. We have shown that the least evolved Bellsbank cpx megacrysts have the same range of Sr isotopic composition as their host kimberlite. Two Bellsbank kimberlite samples analyzed

display measured $^{87}Sr/^{86}Sr$ of 0.7082 (Nowell et al., 2004; Becker and Le Roex, 2006) while the least evolved Bellsbank cpx megacrysts display measured $^{87}Sr/^{86}Sr$ of 0.7081 ± 0.00055 (9 out of 14 megacryst samples analyzed from Bellsbank; Fig. 1.18 and 1.21). This is further evidence of the genetic link between megacrysts and the host kimberlite. In addition, Bellsbank megacrysts have diagnostic trace element ratios like Nb/U (30 ± 14 versus 33), Ce/Pb (32 ± 17 versus 20) and Th/Nb (0.20 ± 0.05 versus 0.25) similar to those in the Bellsbank kimberlite (Becker and le Roex, 2006).

1.11. MEGACRYST PETROGENETIC MODEL

In the AFC model developed in this thesis, relatively large amounts of sublithospheric melts is proposed to percolate upward until entering the base of the lithosphere and traveling further upward by dyking and forming networks of melt channels. As the melts travel from their injection point, they progressively crystallize and assimilate the local lithospheric mantle wallrock, both by stoping or a similar process and by diffusive exchange. The most primitive Cr-poor megacrysts crystallize first and Mg-number, Cr and Ti contents decrease with declining temperatures, as the result of fractionation. This explains why Cr-poor megacrysts are the most isotopically similar to their host kimberlites. With decreasing temperatures (increase of Ca-number), and depending on the nature and proportion of lithospheric products being assimilated by the megacryst parental magma, Cr content and Mg-number can continue to decrease or rise. A dramatic increase in Cr content and Mg-number always coincides in most cases with a rise in LREE content and Sr isotope composition. Depending on the nature of the assimilant, source-sensitive trace element ratios (Ce/Pb, Th/Nb, Ba/Nb and La/Nb) can increase or decrease. The patterns of geochemical variations observed in Cr-poor and Cr-rich megacrysts from southern African Group 1 and Group 2 kimberlites leads to the following inferences, although the small amount of data currently available means that they remain somewhat speculative: (1) It could be envisioned that in case the lithosphere has a higher proportion of depleted rocks (average composition) the evolved megacryst will likely be Cr-poor in composition and no significant increase in Sr isotope will be observed. (2) If the lithosphere has higher proportion of fertile and metasomatised rocks, the evolved megacryst will likely be Cr-rich in composition and significant Sr istope variation will be observed.

1.12. SUMMARY – Megacrysts chapter

The origin of kimberlite megacrysts, the relationship between Cr-rich and Cr-poor megacryst suites and the link between megacrysts and their host kimberlite have been the subject of controversy over the past five decades. In order to tackle these controversies, garnet and clinopyroxene megacrysts, were selected, from four Cambrian to late Cretaceous southern African kimberlites, representative of Group 1 and Group 2 kimberlites located on the Kaapvaal and the Zimbabwe cratons, for a comparative study aimed at characterizing their geochemistry and petrogenesis.

The coherent variations in major and trace elements in the Orapa, Colossus and Kalkput megacryst suites suggest that these megacrysts have formed through fractional crystallization of sublithospheric derived magmas with little interaction with the lithospheric mantle at the early stages of the fractionation. As crystallization of the megacryst magmas progressed, the effects of lithospheric assimilation became more apparent. The lowest temperature cpx and garnet megacrysts show increases in Cr# that are consistent with significant assimilation of mantle wallrock, yet they also show features, such as decreasing Ti with decreasing Mg# (garnet) or with increasing C# (cpx), that is indicative of them being derived from parent magmas having experiencd significant fractionation of minerals such as ilmenite. There are clear relationships between the compositional nature of the lithospheric mantle at the time and place of megaryst formation and the composition of the most evolved megacrysts at each locality.

The origin of the Bellsbank megacrysts remains uncertain. The cpx megacrysts may represent an extreme expression of assimilation of MARID and depleted peridotites by the megacryst parental magmas or they may represent progressive metasomatic melt-reaction products of Group 2 protokimberlitic melts interacting with MARID and depleted peridotite.

The continous compositional variations between Cr-poor and Cr-rich megacryst suites suggest that they are genetically related by differing extents of fractional crystallization and assimilation of primarily fertile lithospheric mantle rocks (e.g., fertile lherzolite, pyroxenite, MARID, PIC). For the megacryst suites studied here, the evidence seems to be the most consistent with Cr-poor megacrysts forming prior to Cr-rich, in contrast to the progressive, up-temperature metasomatic hypotheses favoured by Moore and Belousova (2005) and Kopylova et al., (2005). The magmatic/AFC model developed in this study appears to reconcile megacrysts major and trace

element variations, as well as Sr isotope composition with temperature constraints. There is some evidence suggesting a correlation between the occurrence of Cr-rich megacryst suites and the higher abundance of fertile and metasomatised lherzolite in the SCLM, at the time of megacryst formation.

Evidence in support of a close geochemical similarity and most likely with a genetic relationship between megacrysts and their host kimberlites was presented. A direct comparison of Sr isotope composition and diagnostic trace element ratios (e.g., Th/Nb, Ce/Pb and Nb/U) between megacrysts and their host kimberlite also support a genetic link. On the basis of the ranges in Ca# of clinopyroxene, the crystallization of Group 2 cpx megacrysts appears to begin at lower temperatures compared to those of Group 1 cpx megacrysts. This is consistent with the finding of workers that Group 2 kimberlite have sampled a relatively cool SCLM (Griffin et al., 2003; Kobussen et al., 2008; Griffin et al., 2014).

The overall differences seen between Group 1 and Group 2 megacrysts appear to be fairly representative of the main differences between southern African group 1 and group 2 kimberlites. Therefore, there appears to be a link between composition of the parent magma of these megacrysts and the type of kimberlite that transported the megacrysts to the surface.

CHAPTER 2: EVOLUTION OF THE SCLM BENEATH THE NORTHEASTERN KASAI CRATON: CONSTRAINTS FROM KIMBERLITE-DERIVED HEAVY MINERAL CONCENTRATES

2.1. INTRODUCTION

O'Reilly and Griffin (2006) define the subcontinental lithospheric mantle as forming "the lowermost part of the lithospheric plate complex that moves in a relatively rigid way over the hotter and rheologically weaker asthenosphere". The lithospheric mantle is made up mainly by peridotites while other lithologies such as eclogites and pyroxenites are volumetrically minor. Fragments of these mantle lithologies are brought to the surface by kimberlites and other magmas. Most of our understanding of the lithospheric mantle is based on the study of these fragments (xenoliths) during the last five decades (e.g., Danchin, 1979; Erlank et al., 1987; Finnerty and Boyd, 1987; Carlson et al., 1999; Kopylova et al., 1999; Aulbach et al., 2004; Janney et al., 2010).

Recently, not only xenoliths but xenocrysts (minerals derived from the disaggregation of xenoliths) brought to the surface by kimberlitic magmas have been used in lithospheric mantle studies (e.g. Griffin and Ryan, 1995; Griffin et al., 2003). The major and trace element compositions of garnet xenocrysts have been widely used to obtain information on the subcontinental lithospheric mantle. Griffin and coworkers have developed a technique called "chemical tomography" based on the geochemistry of garnet xenocrysts (O'Reilly and Griffin, 1996) in order to map the compositional structure and thermal state of the subcontinental lithospheric mantle. This technique allows the determination of the equilibration temperature of garnet grains using the Ni-in-garnet thermometer and P_{Cr} barometer (Ryan et al., 1996). The application of this technique to garnet xenocrysts can provide insight into the thermal structure of the lithosphere to depths of up to 250 km, as well as the characterization of the extent of depletion or metasomatism with depth in the upper mantle (Griffin et al., 1998; Griffin et al., 1999; Griffin et al., 2003; O'Reilly and Griffin, 2006).

Clinopyroxene xenocrysts may also be used in lithospheric mantle studies in a manner similar to garnet. The pressure and temperature of equilibration can be calculated using the Nimis and Taylor (2000) thermobarometer. This technique has been used, with success, in the investigation of the composition of the SCLM underlying the Zadochnaya kimberlite in Yakutia,

Russia (Nimis et al., 2009). Clinipyroxene xenocrysts have been also used to characterize the lithosphere of the Central Slave Craton (Aulbach et al., 2013).

2.1.1. CONTEXT

Despite being one of the most productive diamond mining regions, little is known about the lithospheric mantle underlying the northeastern portion of the Kasai Craton. Political unrest, lack of infrastructure, and tropical forests and climate have hampered access to this region for many years. Only one published study has focused on the composition of the SCLM underlying the northeastern portion of the Kasai Craton (Batumike et al., 2009). This study, based solely on garnet xenocrysts, provided an estimate of the thickness (approximately 210 km), and thermal structure of the lithosphere, and led to the postulation that the local lithosphere was composed of garnet lherzolite- and garnet harzbugite-dominated layers.

In an attempt to investigate the SCLM beneath this region, a field collecting trip was carried out there in June to August 2015, in order to obtain mantle materials from the Mbuji-Mayi and Tshibwe kimberlites. At Mbuji-Mayi, no fresh kimberlite or xenolith samples were found. Only heavy mineral concentrates from the M10 kimberlite (located on the westernmost section of the Mbuji-Mayi cluster. See Fig. 2.2) and the Kanshi river were recovered. The minerals present were ilmenites (90 %), garnets (9 %) and few clinopyroxenes (1%). Chemical analyses (details of paragenesis classification are provided in the following sections) showed later that all ilmenites are megacrystic, while garnets are predominantly lherzolitic (55%), some eclogitic (30%) and the rest are harzburgitic (15 %). Clinopyroxenes are mostly peridotitic (no eclogitic or megacrystic clinopyroxenes have been found). By contrast, at Tshibwe, relatively mildly altered kimberlite samples were recovered (the geochemistry of these samples are described in Chapter 3), along with additional heavy mineral concentrates. The latter were composed of ilmenites (90%), garnet (5%) and clinopyroxene (5%). Chemical analyses showed that all ilmenites are megacrystic, while garnets are predominately lherzolitic, with a minority being eclogitic and harzbugitic. The proportion of different garnet parageneses are similar to those at Mbuji-Mayi. Clinopyroxenes are mainly megacrystic (80%) and the rest are peridotitic (20%). It is noteworthy to mention the higher abundance of clinopyroxene megacrysts at Tshibwe, with some specimens measuring over 5 cm in size. The criteria used to classify the xenocrysts will be given later in the chapter when the chemical results are described.

Due to the lack of available peridotite xenoliths, the investigations documented in this chapter are based entirely on indicator minerals (xenocrysts). Peridotite xenoliths have never been reported in the Kasai region and there are no xenolith dumps at diamond mines in the region as exist at many South African mined kimberlites. The general rarity of peridotite xenoliths from DRC kimberlites can be explained by the rapid weathering of peridotites in the moist tropical climate. Nevertheless, the study of SCLM based entirely on xenocrysts present some advantages over peridotite xenoliths. Some authors have suggested that studies of xenocrysts may provide a less biased view of the nature of the lithosphere than studies based on relatively small numbers of peridotite xenoliths (O'Reilly and Griffin, 2006). The small numbers of xenolith localities compared to the larger spatial distribution of xenocryst-bearing kimberlites may also make the investigation of the latter more reprensentative of the SCLM composition (Griffin et al., 2003; O'Reilly and Griffin, 2006; Kobussen et al., 2008; Griffin et al., 2009; Kobussen et al., 2009).

2.1.2. OBJECTIVES

The Mbuji-Mayi and Tshibwe clinopyroxene and garnet xenocrysts are investigated with the objective of addressing the following question: What constraints can be placed on the composition and thermal structure of the lithospheric mantle beneath the northeastern part of the Kasai craton? In addition, geochronological work (described in chapter 3) on the Tshibwe kimberlite was carried out in order to place temporal constraints on kimberlite magmatism in the region. This information enables apparent compositional and thermal differences in between the SCLM beneath Mbuji-Mayi and Tshibwe to be better understood and provides insight into the evolution of the northeastern portion of the Kasai Craton.

Placing constraints on the interactions of (proto)kimberlitic magmas and lithospheric mantle constitutes a second objective of this chapter. The study of Mbuji-Mayi and Tshibwe megacrysts (ilmenites and clinopyroxenes) will focus on the different expressions of lithospheric assimilation into the chemical and isotopic composition of studied megacrysts.

2.2. GEOLOGICAL SETTING

The Kasai craton is located in central Africa, occupying northeastern Angola and the south-central part of the DRC. Its basement geology and geographic extent remain relatively poorly known because of abundant vegetation, cover by Phanerozoic sedimentary rocks and political turmoil over the past two decades. The combination of these factors makes geological investigations in the region challenging.

The Kasai craton is relatively well-exposed in its south-central part, in an area extending 450 km east to west by 350 km north to south, in the southwestern DRC and northeastern Lunda Norte region in Angola (Cahen et al., 1984; Fig. 2.3). Elsewhere, the Kasai craton is extensively buried beneath the Phanerozoic cover, with outcrops restricted to river valleys. Three main divisions can be distinguished between the Archean rocks of the Kasai craton: (1) The Luanyi gneisses, which predate pervasive granulite facies metamorphism and have an age of 3.8 Ga, and are assumed to be the oldest unit in this region (Delhal and Ledent, 1973); (2) rocks affected by ≈ 2.8 Ga granulite facies metamorphism (referred to as the Musefu event; Delhal et al., 1976); and (3) the Dibaya complex of granites and migmatites, a vast assemblage of NE-ENE trending migmatitic gneisses and associated calc-alkalic granitoids plutons. The Dibaya complex underlies a large part of the Kasai craton, probably extending to its northern limit and was consolidated by the Moyo-Musefu cycle of events that lasted from 2.8 Ga to 2.56 Ga (Cahen et al., 1984).

In its northeastern section, the Kasai Craton is overlain by carbonate metasediments of late Mesoproterozoic age, referred to as the Mbuji-Mayi Supergroup. Basalts dated at 948 Ma occur in the upper part of the Mbuji-Mayi Supergroup (Cahen et al., 1984; Delpomdor et al., 2015; de Wit and Linol, 2015). In its southerwestern section, the Kasai Craton is overlain by a sequence of metasediments of Paleoproterozoic age and referred to as the Luiza Supergroup. Granitoids, dated between 2.0 and 2.2 Ga, intrude these metasediments, and were covered by the Lulua Group. The latter comprises younger basaltic volcanics (with pillow lavas) dated at 1.9 Ga (Delhal, 1991; Andre 1994; de Wit and Linol, 2015).

There are three known kimberlite provinces that have intruded the Archean Kasai Craton, during the Cretaceous (Fig. 2.1). The Mbuji-Mayi and Kabinda fields are located on the northeastern section of the Kasai Craton, in the DRC, and the Lunda Norte field is located on the

southwestern section of this craton, in Angola (de Wit and Jelsma, 2015; Castillo-Oliver et al., 2016).

Mbuji-Mayi Kimberlite Field

The Mbuji-Mayi kimberlite field is located on the northeastern section of the Congo-Kasai Craton in the south-central DRC and is, itself, composed of the Mbuji-Mayi and Tshibwe kimberlite clusters in the central DRC.

Mbuji-Mayi cluster: The Mbuji Mayi cluster occurs to the south of Mbuji Mayi town (in the central of DRC) and consists of ten kimberlite pipes aligned along an E-W trend (Fig. 2.2). They intrude the Archaean basement and older sediments of the Mbuji-Mayi Supergroup (Neoproterozoic age) and arenaceous sediments of Cretaceous age (de Wit and Jelsma, 2015).

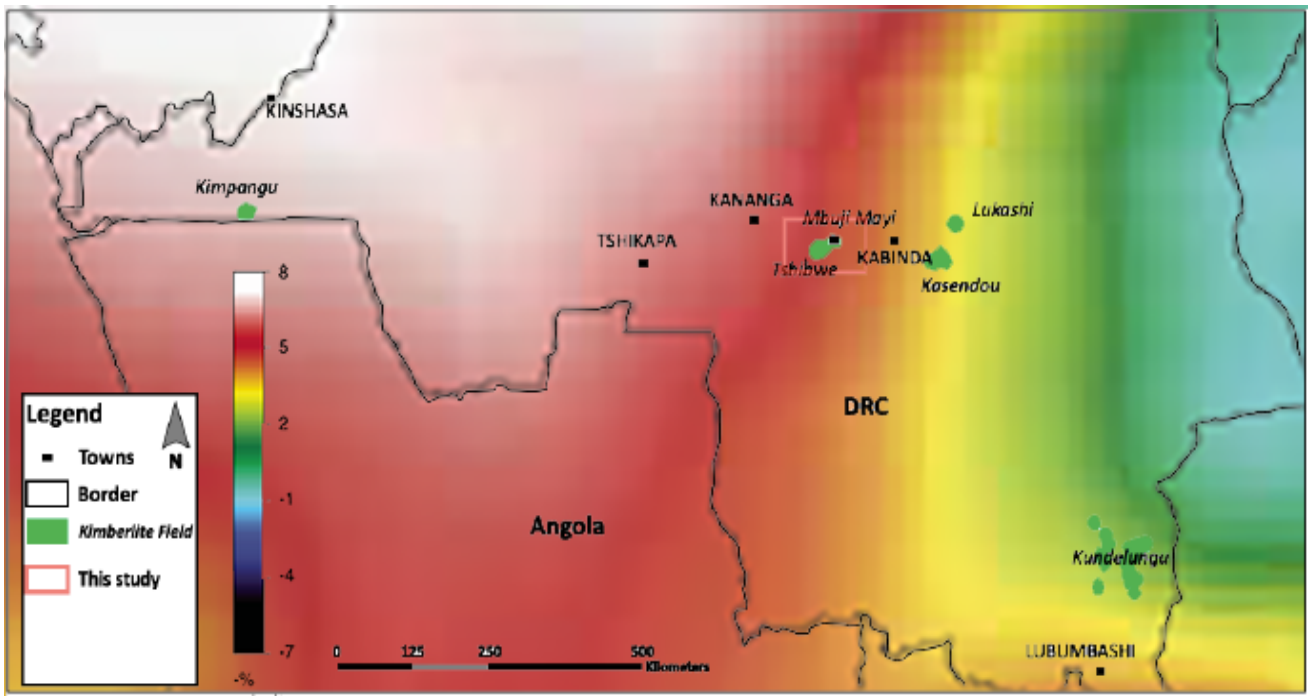

Figure 2.1: Location of the Mbuji-Mayi & Tshibwe kimberlite fields near the eastern edge of the Kasai craton (modified after de Wit and Jelsma, 2015) 150 km depth seismic shear wave velocity anomaly map is from Begg et al. (2009). Colour scale bar indicates percentage shear wave velocity anomaly.

Resedimented volcaniclastic kimberlites (green and red breccias and tuffs) and pyroclastic kimberlites are the common facies at Mbuji-Mayi (de Wit and Jelsma, 2015). Peridotitic xenoliths have not been reported, while eclogitic and crustal xenoliths are present (e.g., El Fadili &

Demaiffe, 1999). The crustal xenoliths originate from basement granite, amphibolite, granulite, dolerite and gabbro. In addition, dolomitic limestone, sandstone and shale enclaves are quite common. It is noteworthy to mention that the hypabyssal kimberlite facies has never been reported at Mbuji-Mayi (de Wit and Jelsma, 2015). Schärer et al., (1997) provided a Late Cretaceous emplacement age for the Mbuji-Mayi kimberlites (69.8 ± 0.5 Ma) on the basis of U-Pb age obtained on zircon and badelleyite. The Mbuji-Mayi kimberlites are very rich in diamonds and have produced more than 100 million carats during the past six decades (according to MIBA production data). No geochemical data for the Mbuji-Mayi kimberlites are presented in this thesis, but some data for them have been presented previously by Demaiffe & Fieremans (1981) and Weis & Demaiffe (1985).

Tshibwe cluster: As with the Mbuji-Mayi cluster, the Tshibwe kimberlite cluster is located on the northeastern section of the Kasai Craton. It is centered 30 km southwest of Mbuji-Mayi town in the DRC. It comprises six kimberlite pipes (Tshibwe, Tshambila, Tshinkasa, Kakongo, Ndaye and Tshinyama), with the Tshibwe kimberlite being the largest (Fig. 2.2).

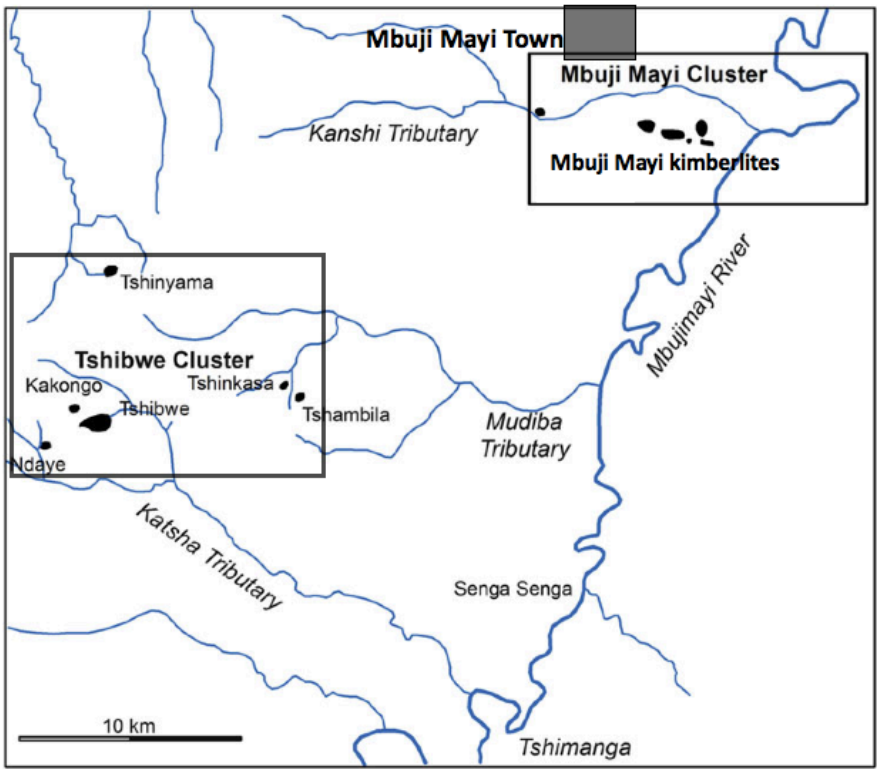

Figure 2.2: The Mbuji-Mayi and Tshibwe kimberlite clusters of the Mbuji-Mayi kimberlite field, located in the Kasai province, central DRC. Map modified after de Wit and Jelsma (2015).

The Tshibwe cluster intruded through the same sequence of crustal basement and sedimentary rocks as at Mbuji-Mayi (de Wit and Jelsma, 2015). The Tshibwe kimberlite itself is located 45 km south of Mbuji-Mayi town and the pipe has an areal extent of roughly 60 ha. Resedimented volcaniclastic kimberlite, massive pyroclastic kimberlite and transitional kimberlite types are the dominant facies at Tshibwe (de Wit and Jelsma, 2015). Peridotitic xenoliths are absent but crustal xenoliths/enclaves, from the Archean basement, are common (de Wit and Jelsma, 2015, see also Chapter 3). The Tshibwe kimberlite is very rich in diamonds and is currently mined by SACIM. There is no published emplacement age for the Tshibwe kimberlite (but see Chapter 2.7 for dating performed as part of this thesis).

Analytical techniques used were identical to those described in Chapter 1.

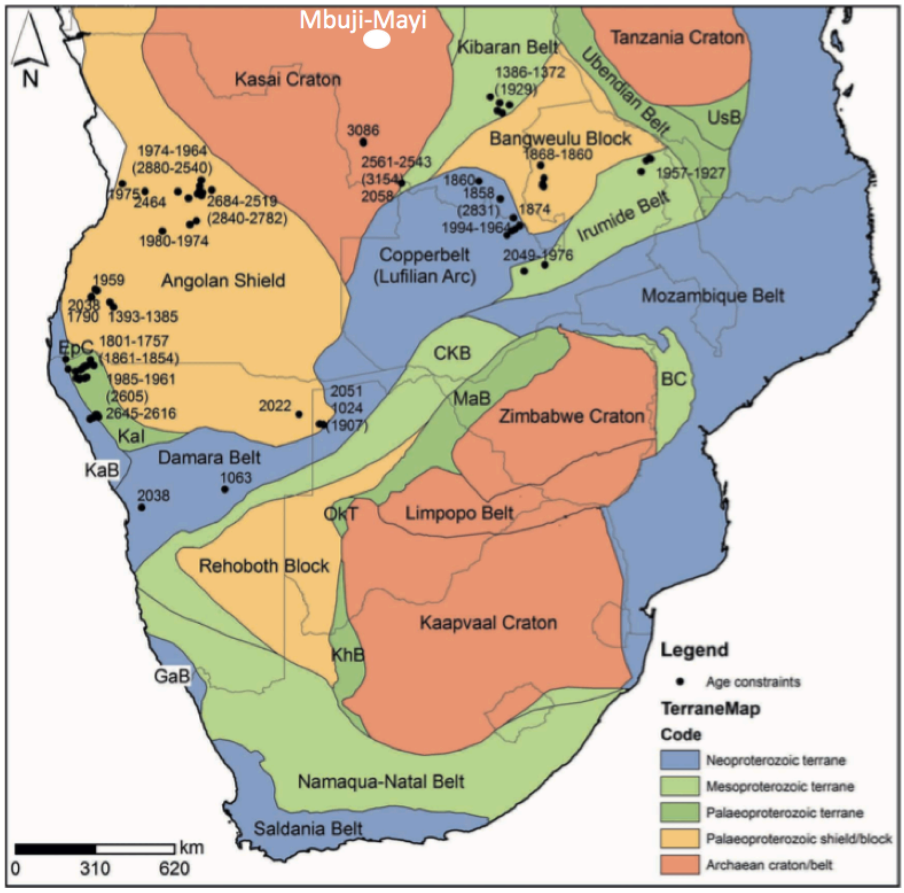

Figure 2.3: Geological map of Mccourt et al., (2013) showing the likely limit of the Kasai Craton and other major Precambrian domains of Southern Africa. The location of the Mbuji-Mayi kimberlite field is shown for reference.

2.3. PERIDOTITIC CLINOPYROXENES FROM TSHIBWE AND MBUJI-MAYI

At Tshibwe, 80 clinopyroxenes were recovered from the heavy mineral concentrates. After chemical analysis, 8 clinopyroxenes were identified as having major element compositions plotting in the garnet-lherzolite field on the Al_2O_3 vs. Cr_2O_3 clinopyroxene classification diagram of of Nimis (1998). The vast majority of clinopyroxenes (72) have major element compositions falling in or near the megacrysts field (Cr_2O_3 < 1 wt.%) of Nimis (1998) in a tight cluster (Fig. 2.4). In addition, clinopyroxenes identified as megacrystic display fractional crystallization trends (Fig 2.4b), typical of those shown by clinopyroxne megacryst suites from southern African kimberlite localities (e.g., Merry and le Roex, 2007; Bell and Moore, 204). These clinopyrexene megacrysts will be discussed later.

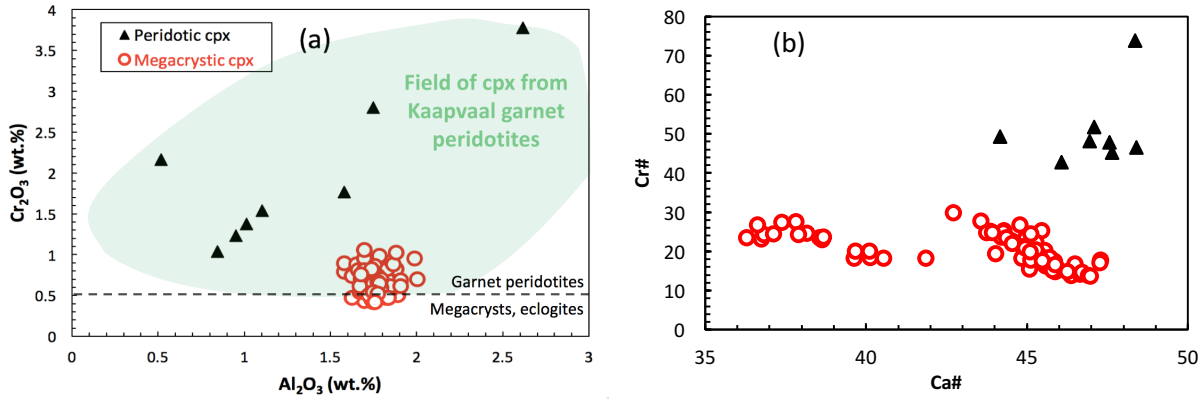

Figure 2.4: Discrimination diagrams of Tshibwe clinopyroxenes recovered from heavy mineral concentrates. **(a)** Al_2O_3 (wt.%) plotted versus Cr_2O_3 (wt.%). The fields for garnet peridotites and megacrysts & eclogites are from Nimis (1998). The Kaapvaal garnet peridotite field is from Grégoire et al., (2003) and unpublished data compilations of D.R. Bell. **(b)** Ca# plotted verus Cr# (Cr/(Cr+Al+Mg) in atomic units). Note that megacrystic cpx are clearly distinguishable from peridotitic cpx. Also note the fractional crystallization trends of decreasing Cr# with increasing Ca# in megacrystic cpx.

At Mbuji-Mayi, 22 clinopyroxenes were recovered in the course of this study. All of them plot in the garnet lherzolite field (Cr_2O_3 > 0.5 wt.%) of Nimis (1998) and so are classified as peridotitic. Megacrystic clinopyroxenes from Mbuji-Mayi were studied by Pivin et al., (2009, 2012) and they have been described as belonging to both the Cr-poor and Cr-rich megacryst suites. The large degree of compositional overlap between Cr-rich megacrystic cpx and peridotitic cpx is well known (Moore and Belousova, 2005; Pivin et al., 2009). This makes the discrimination between the two parageneses (Cr-rich megacrystic and peridotitic) using discrimination diagrams

less than straightforward. As seen in Fig. 2.5, clinopyroxene megacryst from Mbuji-Mayi are divided into two groups. Cr-poor megacrysts fall below 1 wt.% Cr_2O_3 and define a narrow range of Al_2O_3 content. In contrast, Cr-rich megacryst define a positive correlation of Al_2O_3-Cr_2O_3 contents with lower Al_2O_3 and higher Cr_2O_3 . In Fig. 2.5, Cr-poor megacrysts show a weak decrease of Cr# with Ca# while Cr-rich megacryts show a broad increase in Cr# with increasing of Ca#. By contrast, peridotitic clinopyroxenes show no correlation of Cr# with Ca#. Overall, clinopyroxene megacrysts (Cr-rich and Cr-poor suites) show a narrow range of Al_2O_3 while peridotitic clinopyroxenes have are characterized by a wider range.

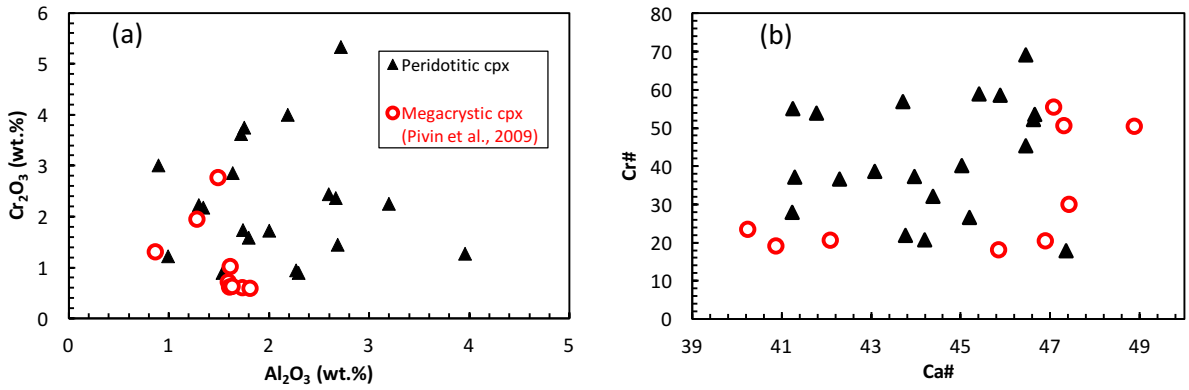

Figure 2.5: Discrimination diagrams of Mbuji-Mayi clinopyroxenes recovered from the heavy mineral concentrates. Mbuji-Mayi megacryst data are from Pivin et al. (2009) **(a)** Al_2O_3 (wt.%) plotted versus Cr_2O_3 (wt.%). **(b)** Ca# plotted versus Cr#.

2.3.1. RESULTS 1: MAJOR ELEMENT SYSTEMATICS OF PERIDOTITIC CLINOPYROXENES

Major element data on peridotitic clinopyroxenes are given in Table 17 of the Appendix. Peridotitic clinopyroxenes from Mbuji-Mayi are divided into two populations, a larger, mainly subcalcic group (termed group 1; with Ca# between 41 and 48) that shows a positive correlation of Al_2O_3 with Ca#, and a smaller calcic group (termed group 2; with Ca# between 45 and 47) that displays lower overall Al_2O_3 values and a negative correlation of Al_2O_3 with Ca# (Fig. 2.6). Both groups show moderate to strong enrichment in Cr (Cr# ranging between 17.7 and 69.1) and show a wide range of Mg# values (88.5 to 94) with a large degree of overlap, but group 2 cpx have, on average, higher Mg# and Cr# values. Both groups also show broad positive correlations of Cr#

with Mg# (Fig. 2.6). Both groups have high Na_2O contents (ranging between 1.5 to 3.6 wt %) with group 1 extending to higher Na_2O contents (Fig. 2.6).

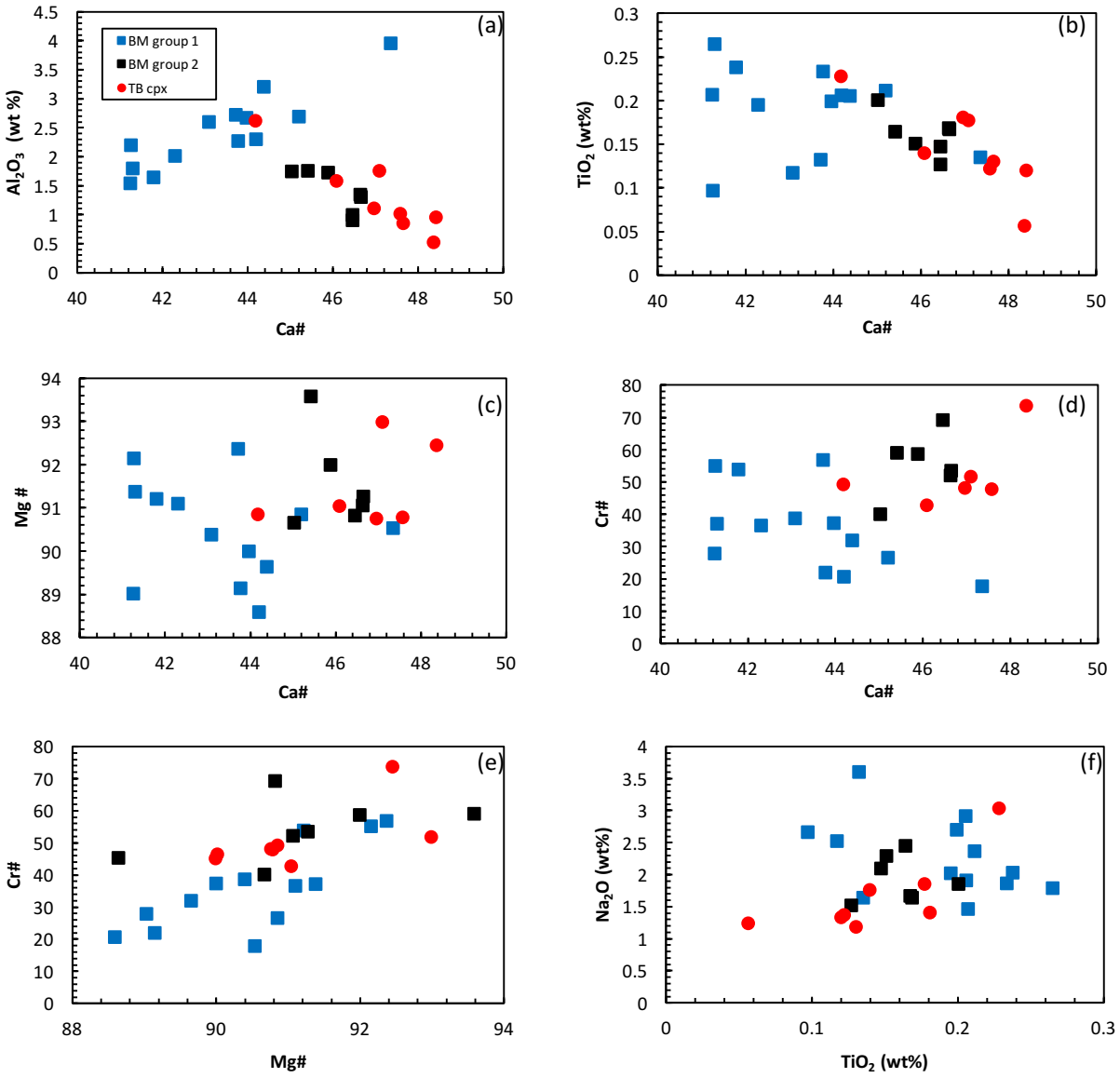

Figure 2.6. Compositional variations of peridotitic cpx from Mbuji-Mayi (BM groups 1 and 2) and Tshibwe (TB): **(a)** Ca# versus wt.% Al_2O_3; **(b)** Ca# versus wt.% TiO_2; **(c)** Ca# versus Mg#; **(d)** Ca# versus Cr#; **(e)** Mg# plotted versus Cr# ; **(f)** wt.% TiO_2 versus wt.% Na_2O. Note that the BM group 1 and 2 cpx form distinct trends or groupings in most diagrams (particularly panel a), and also note the similarity between BM group 2 and Tshibwe peridotitic cpx.

Clinopyroxenes from the Tshibwe kimberlite are similar to the group 2 clinopyroxenes from Mbuji-Mayi in terms of their major element compositions. However, the former extend to slightly higher Ca# (44 – 48) and lower Al_2O_3, TiO_2 (0.22 – 0.05 wt%) and Na_2O values (1.7 – 1.18 wt%)

than the latter, and also display stronger negative and positive correlations of TiO_2 and Na_2O versus Ca#, respectively.

2.3.2. RESULTS 2: TRACE ELEMENT AND Sr ISOTOPE SYSTEMATICS OF PERIDOTITIC CLINOPYROXENES

Trace element and Sr isotopic data are given in Tables 18 and 19 of the Appendix, respectively. Trace element patterns of Mbuji-Mayi group 1 and group 2 clinopyroxenes are similar. They show fairly uniform convex-upward and LREE-enriched patterns with group 1 cpx showing higher levels of LREE enrichment than group 2 ($(Nd/Yb)_N$ = 22.1 – 100.1 and 22.5 – 55.1 for groups 1 and 2, respectively). Both group 1 and group 2 cpx show relative depletions in Ba, Pb, Zr and Ti relative to elements of similar incompatibility, but the depletions in group 1 are stronger (Fig. 2.10). Trace element patterns of Tshibwe clinopyroxnes are very similar to Mbuji-Mayi group 2 clinopyroxenes, but with sighty less LREE-enrichement on average (Fig. 2.9) (most Tshibwe cpx have $(Nd/Yb)_N$ ratios between 30.5 and 38.7). However one Tshibwe cpx grain has an anomalously high $(Nd/Yb)_N$ value of 150.5 with a $(Sc/V)_N$ ratio of less than unity (0.87; Fig. 2.7).

Peridotitic clinopyroxenes from Mbuji-Mayi and Tshibwe span nearly identical ranges of measured $^{87}Sr/^{86}Sr$ (with ranges of 0.7031 – 0.7052 and 0.7035 – 0.7053, respectively) (Fig. 2.8), falling within the range of Group I kimberlites (including Mbuji-Mayi; Weis & Demaiffe, 1985) and the phlogopite-ilmenite-clinopyroxene (PIC) clan of metasomatic mantle xenoliths as summarised by Gregoire et al. (2002).

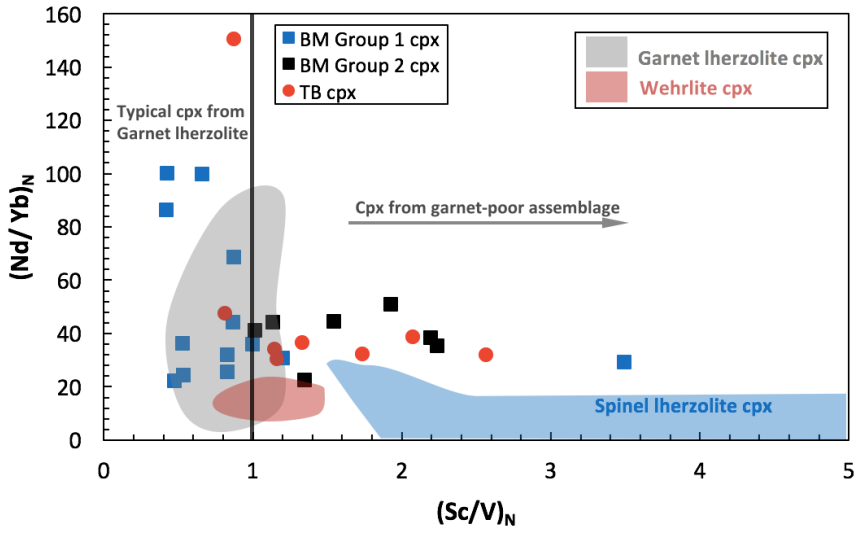

Figure 2.7: $(Sc/V)_N$ plotted versus $(Nd/Yb)_N$ in peridotitic clinopyroxenes from Mbuji-Mayi and Tshibwe. The fields of worlwide cpx from garnet lherzolites and spinel lherzolites are shown for comparison. Sources of data for fields are: Norman (1998); Gregoire et al. (2003); Aulbach et al. (2004; 2013); Gregoire et al. (2005); Rehfeldt et al. (2008). Normalizing values are from McDonough and Sun (1995). The vertical black line (at $Sc_N/V_N = 1$) divides cpx from typical garnet lherzolite to those from garnet-poor lherzolite (Nimis et al., 2009).

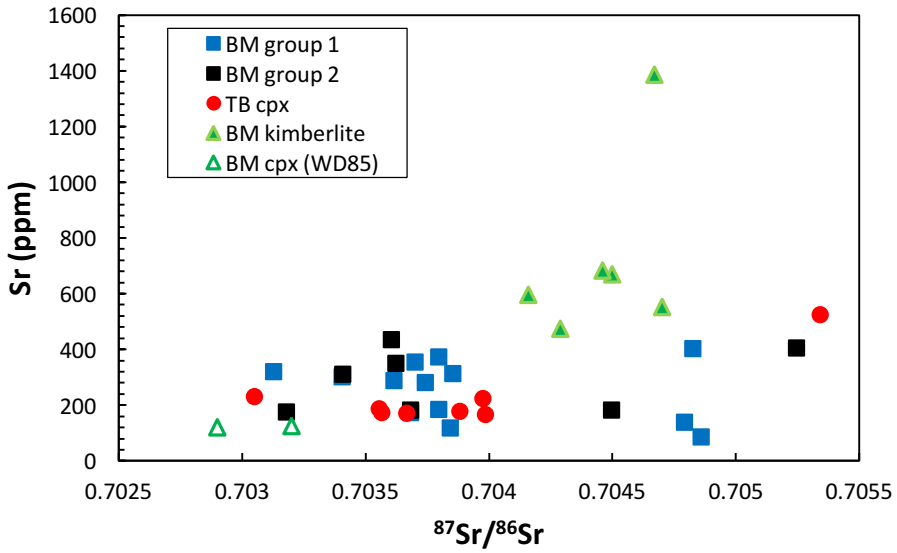

Figure 2.8: $^{87}Sr/^{86}Sr$ versus Sr (ppm) in peridotitic clinopyroxenes from Mbuji-Mayi and Tshibwe concentrates. Mbuji-Mayi kimberlite whole rock and cpx data are from Weis and Demaiffe (1985).

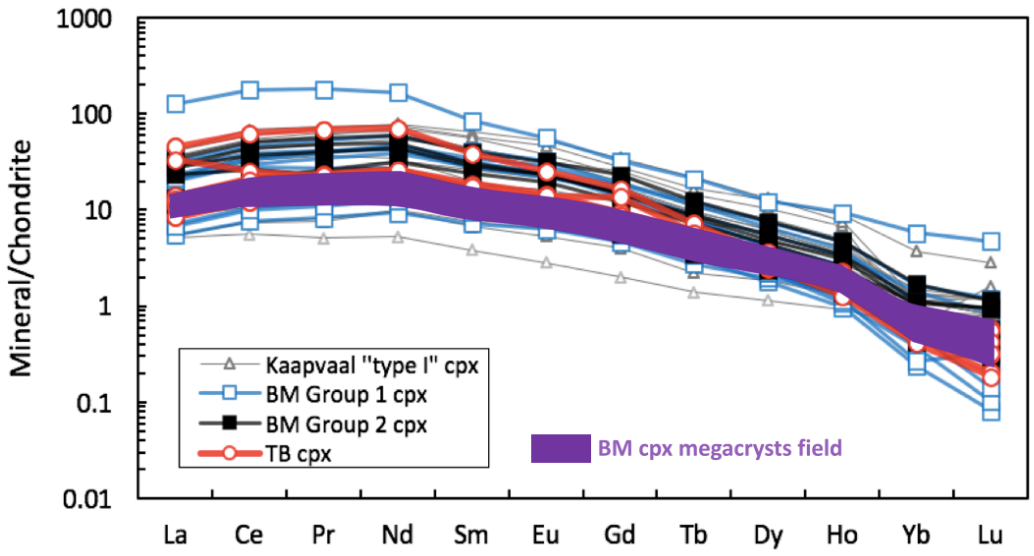

Figure 2.9: REE concentrations in Mbuji-Mayi and Tshibwe peridotitic clinopyroxenes normalized to chondrites. Note the higher degree of LREE variation at Mbuji-Mayi. "Type I" cpx from Kaapvaal metasomatised garnet-lherzolites are shown for comparison (data from Gregoire et al., 2003). Mbuji-Mayi cpx megacrysts field is from Pivin (2012). Normalizing values are from McDonough and Sun (1995).

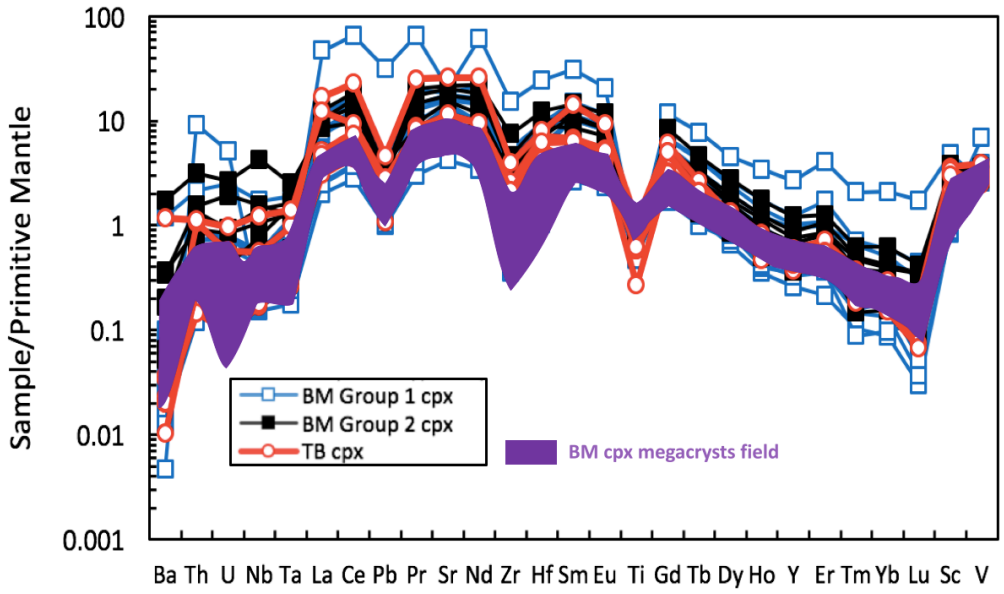

Figure 2.10: Primitive mantle-normalised incompatible element patterns for Mbuji-Mayi and Tshibwe peridotitic cpx. Note the higher degree of trace element variation at Mbuji-Mayi. Mbuji-Mayi cpx megacrysts field is from Pivin (2012). Normalizing values from McDonough and Sun (1995).

2.3.3. RESULTS 3: THERMOBAROMETRY OF PERIDOTITIC CLINOPYROXENES

The P – T equilibration conditions of peridotitic concentrate clinopyroxenes from the Mbuji-Mayi and Tshibwe kimberlites were estimated using the clinopyroxene thermobarometer of Nimis and Taylor (2000). In order to use this thermobarometer, it is required that clinopyroxene is in equilibrium with orthopyroxene and garnet. The following support this assumption at Mbuji-Mayi and Tshibwe:

- All clinopyroxenes used for these calculations have HREE depleted patterns, interpreted by several authors to be the evidence of equilibration in the presence of garnets (Nimis et al., 2009).
- Peridotitic orthopyroxene has been found in heavy mineral concentrates from Mbuji-Mayi (P.E. Janney, personal communication, 2018). Orthopyroxene megacrysts are present in many Kundelungu kimberlites (Kampata, 1993; Kampata et al., 1996; Pivin et al., 2009). It has been advocated by Pivin (2012) that the absence of orthopyroxene megacrysts in Mbuji-Mayi kimberlites (including Tshibwe) could be due to the extreme tropical conditions in the Kasai region (de Wit and Jelsma, 2015), as orthopyroxene is more susceptible to alteration than clinopyroxene and garnet. The similarity in mineralogy and geochemistry between Mbuji-Mayi and Kundelungu kimberlites support the hypothesis that orthopyroxene was present in the mineral assemblage at Mbuji-Mayi (Tshibwe) (Pivin, 2012).
- The scarcity of orthopyroxene macrocrysts in kimberlites has been explained by several authors to be a consequence of the dissolution of orthopyroxene by kimberlite magmas due to these magmas extremely low silica activities and the presence of significant H_2O(Mitchell, 2008; Russell et al., 2012; Pilbeam et al., 2013).

Temperatures and pressures calculated from the major element compositions of peridotitic clinopyroxenes using the thermobarometer of Nimis and Taylor (2000) are presented in Table 48 of the Appendix. Based on these P – T estimates, clinopyroxenes from Mbuji-Mayi and Tshibwe define a temperature profile through the northeastern Kasai craton to depths up to 220 km, a depth consistent with previous thermobarometry and geophysical studies (Batumike et al., 2009; Crosby et al., 2010). The two kimberlites sampled and entrained peridotitic clinopyroxenes from a pressure

and temperature interval spanning from 2.6 to 7.2 GPa and 967 to 1264 °C. However, the continental lithospheric mantle sampled by Tshibwe appears to have been, on average, cooler than that sampled by the Mbuji-Mayi kimberlite, as clinopyroxenes from the two kimberlites define average thermal gradients of 200°C/GPa versus 260°C/GPa, respectively (Fig. 2.11).

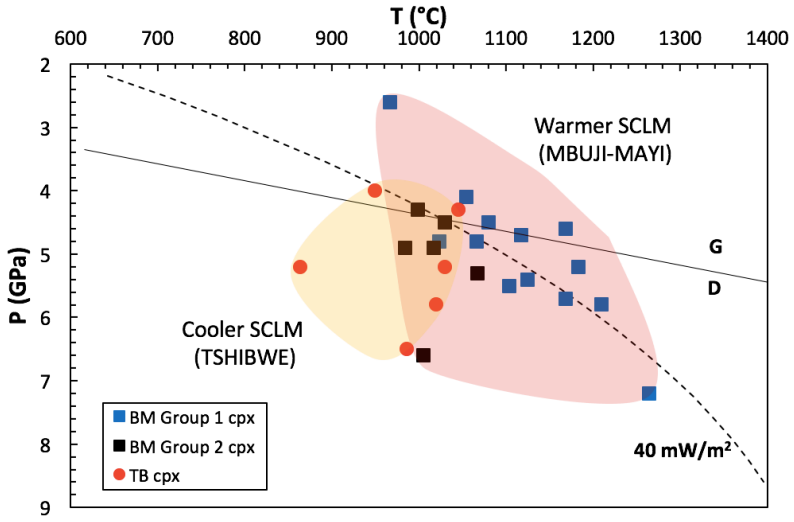

Figure 2.11: P (GPa) plotted versus T (°C) plot with values based on the Nimis and Taylor (2000) thermobarometer. The graphite-diamond phase boundary and 40 mW/m^2 geotherm are provided for reference.

2.3.4 DISCUSSION - ORIGIN OF THE PERIDOTITIC CLINOPYROXENES

Clinopyroxenes from Mbuji-Mayi and Tshibwe show typical peridotitic major element compositions, with high Mg# values and with Cr_2O_3 and Al_2O_3 concentrations that plot in the field associated with garnet-bearing lherzolites (Nimis, 1998; Fig. 2.12). The REE concentrations and patterns of Mbuji-Mayi and Tshibwe clinopyroxenes are similar to those reported for diopsides from "type 1" metasomatised garnet lherzolites from the Kaapvaal craton (Grégoire et al., 2003). Peridotitic garnets occur in abundances matching or exceeding that of clinopyroxene, in the concentrate from Mbuji Mayi and Tshibwe. It is therefore likely that garnet lherzolite is the main lithology in the mantle lithosphere of the northeastern section of the Congo-Kasai Craton beneath Mbuji-Mayi and Tshibwe.

Nearly all group 1 clinopyroxenes from Mbuji-Mayi have $(Sc/V)_N$ ratios lower than unity (0.41 – 0.99, except for one grain with a $(Sc/V)_N$ of about 3.5) , typical of clinopyroxenes from

garnet lherzolites (Glaser et al., 1999; Norman, 1998; Grégoire et al. 2003; Aulbach et al., 2004; Grégoire et al. 2005, Nimis et al., 2009). Therefore, the group 1 clinopyroxenes likely originated from garnet lherzolite. Group 2 cpx from Mbuji-Mayi strongly resembles peridotitic cpx from Tshibwe, and both have $(Sc/V)_N$ ratios greater than unity (with ranges of 1.01 – 2.19 and 1.14 – 2.56, respectively), suggesting derivation from a mantle lithology that is relatively garnet poor (Fig. 2.7).

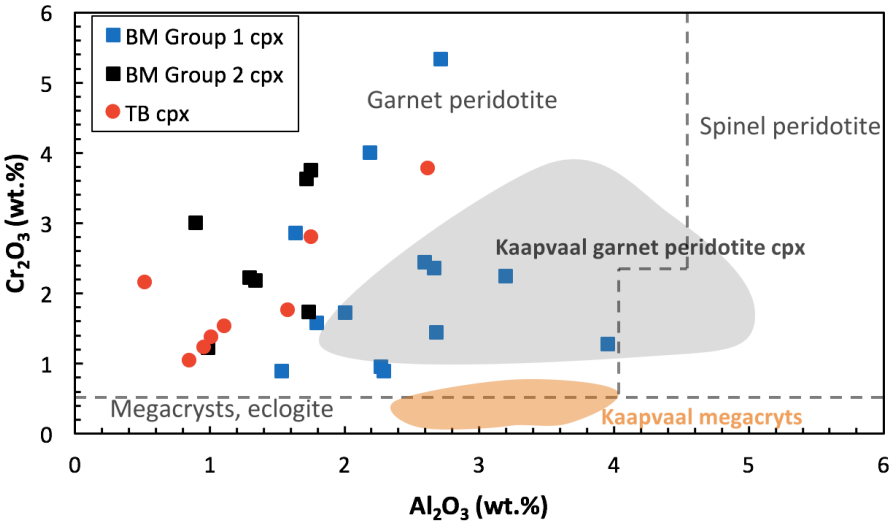

Figure 2.12: wt.% Al_2O_3 versus wt.% Cr_2O_3 in peridotitic clinopyroxenes from concentrate from Mbuji-Mayi (BM groups 1 and 2) and Tshibwe (TB). Dashed fields are from Nimis (1998). Coloured fields for cpx from Kaapvaal garnet lherzolite and Kaapvaal cpx megacrysts are shown for comparison. Source of data fields: Hops et al. (1992), Nimis et al. (1998), Grégoire et al. (2003), Merry and le Roex (2007), Aulbach et al. (2013) and this thesis.

The fairly distinct $(Sc/V)_N$ ratios and major element characteristics of the two Mbuji-Mayi cpx groups suggests that they represent two distinct lherzolite lithologies, presumably a typical garnet lherzolite lithology (Group 1) and a more garnet-poor lherzolite lithology (Group 2). The Tshibwe clinopyroxenes seem likely to belong to a garnet-poor lherzolite lithology very similar to that represented by Mbuji-Mayi Group 2 clinopyroxenes. If it can be assumed that the two kkimberlites sampled peridotitic minerals from the SCLM approximately representatively, the presence of a substantial population of peridotitic cpx at Mbuji-Mayi having low Sc/V ratios, and the lack of such a population at Tshibwe, in the concentrate minerals suggests a more lithologically diverse peridotitic SCLM beneath Mbuji-Mayi and one that is, overall, likely more garnet-rich than at Tshibwe.

A. Calculated melts in equilibrium with Mbuji-Mayi and Tshibwe clinopyroxenes.

In order to better assess the origin of the clinopyroxenes in this study, melt compositions in equilibrium with clinopyroxene were calculated by combining the trace element composition with appropriate clinopyroxene/liquid partition coefficients ($D^{Cpx/L}$). Keshav et al. (2005) experimentally determined $D^{Cpx/L}$ values for CO_2-rich kimberlite melt systems at deep mantle conditions (1430 °C and 6 GPa). However, as seen in the thermobarometry section, these conditions (temperature) significantly exceed those estimated for Mbuji-Mayi and Tshibwe clinopyroxenes.

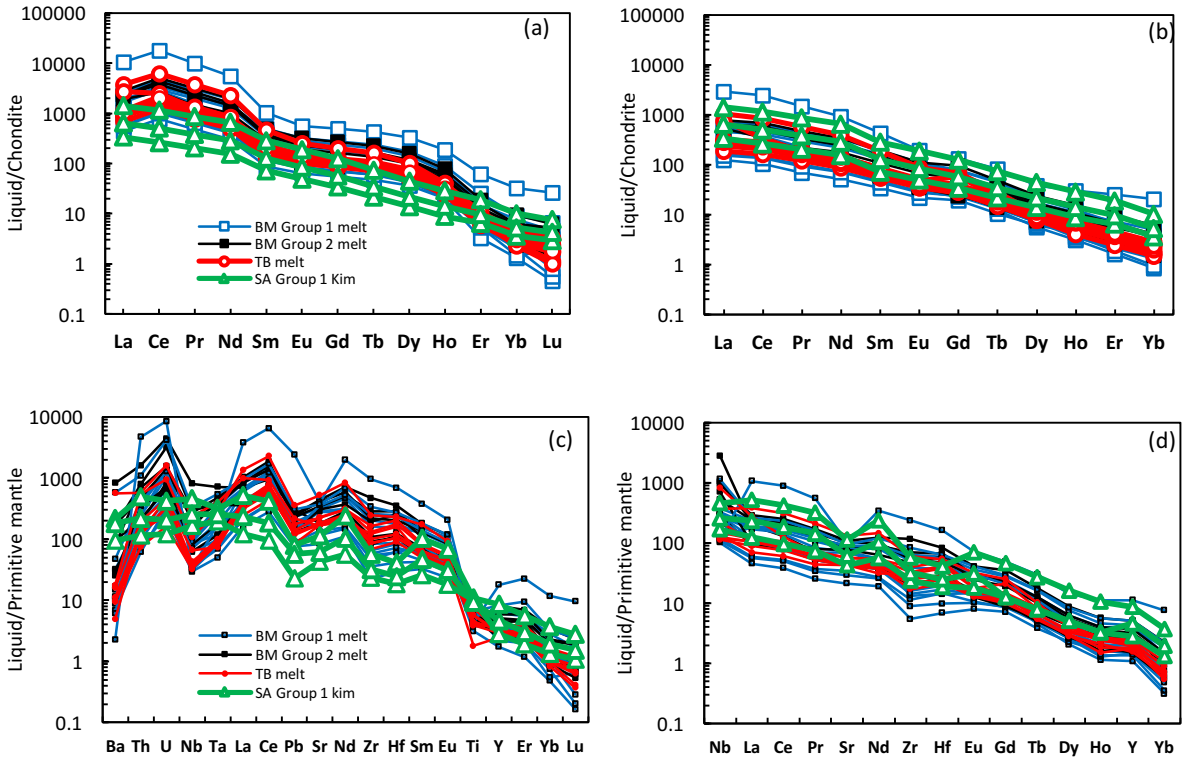

Figure 2.13: Calculated chondrite-normalised REE patterns for hypothetical melts in equilibrium with Mbuji-Mayi and Tshibwe clinopyroxene using $D^{Cpx/L}$ partition coefficients of (a) Keshav et al. (2005) and (b) Green et al. (2000); Primitive-mantle-normalized trace element patterns for the hypothetical melts in equilibrium with the Mbuji-Mayi and Tshibwe clinopyroxenes using $D^{Cpx/L}$ partition coefficients of (c) Keshav et al. (2005) and (d) Green et al. (2000). Normalizing values from McDonough & Sun (1995). South African Group 1 kimberlites are shown for comparison (data from le Roex et al., 2003).

Therefore, melts in equilibrium with clinopyroxenes have been also calculated using the $D^{Cpx/L}$ dataset of Green et al. (2000) at 1160 °C and 4 GPa, which is suitable for undersaturated basaltic

melts. It is noteworthy to mention, that unlike Keshav et al., (2005), the Green et al. (2000) experiments involved essentially volatile-free melts. The latter have been used in the modeling of liquids in equilibrium with clinopyroxenes in mantle peridotites from the Kaapvaal craton (Simon et al. 2007; Rehfeldt et al. 2008) and in DRC's megacrysts (Pivin et al., 2013).

The compositions of hypothetical melts in equilibrium with the clinopyroxenes, normalized to chondrites and primitive mantle, are shown in Figure 2.13. Hypothetical melts obtained using the Keshav et al. (2005) $D^{Cpx/L}$ values are strongly enriched in the LREE (with Ce_N values ranging from 770 to 18,000 times chondrite), as well as in Th and U, and show negative anomalies in Nb, Ta and Pb (Fig. 10c). In addition, they have chondrite-normalized REE patterns which overlap but extend to compositions significantly more LREE-enriched than group 1 kimberlite and carbonatite fields (Fig. 2.13). Incompatible element abundances for calculated melts in equilibrium with cpx using the Keshav et al. (2005) $D^{Cpx/L}$ values are so high as to be problematic for derivation even from such LREE-enriched magmas as kimberlites and carbonatites. This, plus the fact that these values were obtained in experiments at much higher temperatures than those at which the cpx equilibrated, suggest that the melt compositions calculated using the $D^{Cpx/L}$ values of Keshav et al. (2005) are not appropriate for calculating melts in equilibrium with SCLM-derived clinopyroxene. .

Hypothetical melts calculated using the dataset of Green et al. (2000) are enriched in the LREE, but also in Nb (Fig 2.13). In addition, they have chondrite-normalized REE patterns which overlap the group 1 kimberlite field (Fig 2.13). Nearly identical trace element patterns for equilibrium melts calculated for Mbuji-Mayi and Tshibwe clinopyroxenes could indicate that a similar, narrow range of metasomatic melt compositions affected the SCLM beneath both kimberlites. Therefore, clinopyroxenes from garnet lherzolites could have equilibrated with group 1 kimberlite melts during kimberlite magmatism that affected the northeastern section of the Kasai Craton during the Late Cretaceous. The similar trace element and Sr isotope systematics of Tshibwe and Mbuji-Mayi clinopyroxenes support this overprint of peridotitic cpx by kimberlite related metasomatism.

B. Metasomatism

Mbuji-Mayi peridotitic clinopyroxenes are variable in terms of light REE enrichment (e.g., $(Nd/Yb)_N = 46 \pm 24$) while at Tshibwe there is more limited variation (e.g., $(Nd/Yb)_N = 36 \pm 5.8$) with the exception of one anomalous grain (e.g., anomalously LREE enriched grain) (Fig 10b).

The apparently more extensive metasomatism at Mbuji-Mayi is also supported by the fact that peridotitic cpx from Tshibwe have slightly lower average $^{87}Sr/^{86}Sr$ values than from Mbuji Mayi. This interpretation is consistent with the strong melt-metasomatic signature inferred from the Zr-Y enriched compositions of lherzolitic garnets documented below in section 2.4.2

As described earlier, primitive mantle-normalized incompatible element patterns, both in Tshibwe and Mbuji-Mayi clinopyroxenes, are consistent with kimberlite-related metasomatism, which can explain the large degree of Sr isotopic overlap between the clinopyroxenes and whole-rock $^{87}Sr/^{86}Sr$ values for Mbuji-Mayi kimberlites (Weis & Demaiffe, 1985). Mbuji-Mayi clinopyroxenes appear to have undergone more extensive metasomatism (stronger LREE enrichment, higher overall incompatible element contents, slightly higher average $^{87}Sr/^{86}Sr$) than at Tshibwe. Moreover, the warmer average temperatures at a given pressure recorded by Mbuji-Mayi cpx relative to Tshibwe, along with their more incompatible element-enriched compositions, are consistent with more pervasive metasomatism in the SCLM beneath Mbuji-Mayi, due to pervasive melt percolation. The mantle sampled by the Mbuji-Mayi kimberlite appears to have been warmer and metasomatically more disturbed compared to the cooler and more depleted lithosphere sampled by the Tshibwe kimberlite.

2.3.5. PERIDOTITIC CLINOPYROXENES – SUMMARY

Peridotitic clinopyroxenes from Mbuji-Mayi and Tshibwe define a compositional and thermal profile through the northeast of the Kasai craton lithosphere to depth as great as 220 km. On the basis of clinopyroxene mineral chemistry, garnet lherzolite appears to be the main lithology beneath the northeastern section of the Congo-Kasai Craton. The SCLM beneath Mbuji-Mayi appears to contain both garnet-rich and garnet poor lherzolitic lithologies while the SCLM beneath Tshibwe appears to have only a garnet-poor lithological character. Clinopyroxenes from garnet lherzolites could have equilibrated with group 1 kimberlite melts during kimberlite magmatism occurring in the northeastern section of the Congo-Kasai Craton during the Late Cretaceous. Kimberlite-related metasomatism appears to have played a major role in the origin of the clinopyroxenes. The SCLM sampled by the Mbuji-Mayi kimberlites appears to have been warmer and metasomatically more disturbed, and that sampled by the Tshibwe kimberlites cooler and more depleted. For this reason, it seems likely that the Tshibwe cluster kimberlites were emplaced prior

to that at Mbuji-Mayi (70 Ma), and also prior to a major thermal and metasomatic disturbance of the SLCM. This inference is borne out by dating results presented in this chapter, section 7.

2.4. GARNETS FROM THE MBUJI-MAYI AND TSHIBWE KIMBERLITES

Garnets have been obtained from the heavy mineral concentrates from Mbuji-Mayi and Tshibwe. As mentioned earlier, at Mbuji-Mayi, heavy mineral concentrates are made of approximately 90% ilmenite, 9% garnet and 1% clinopyroxene (based on visual estimation). At Tshibwe, heavy mineral concentrates were made of approximately 90% ilmenite, 5 % garnet and 5 % clinopyroxene. Garnets were hand-picked and selected on the basis of color (three categories: red, purple and brown) for analysis. At Mbuji-Mayi, 38 orange-brown garnets, 44 red garnets and 38 purple garnets (all that were available during sampling) were selected. At Tshibwe, 44 orange-brown garnets, 44 red garnets and 26 purple garnets (again, all that were available) were selected for analysis. Garnets were further classified on the basis of wt.% Cr_2O_3 versus wt.% CaO, (Fig. 2.14). Based on the classification of Grütter et al., (2004), peridotitic and eclogitic parageneses were identified at Mbuji-Mayi and Tshibwe and are further investigated in detail in this section.

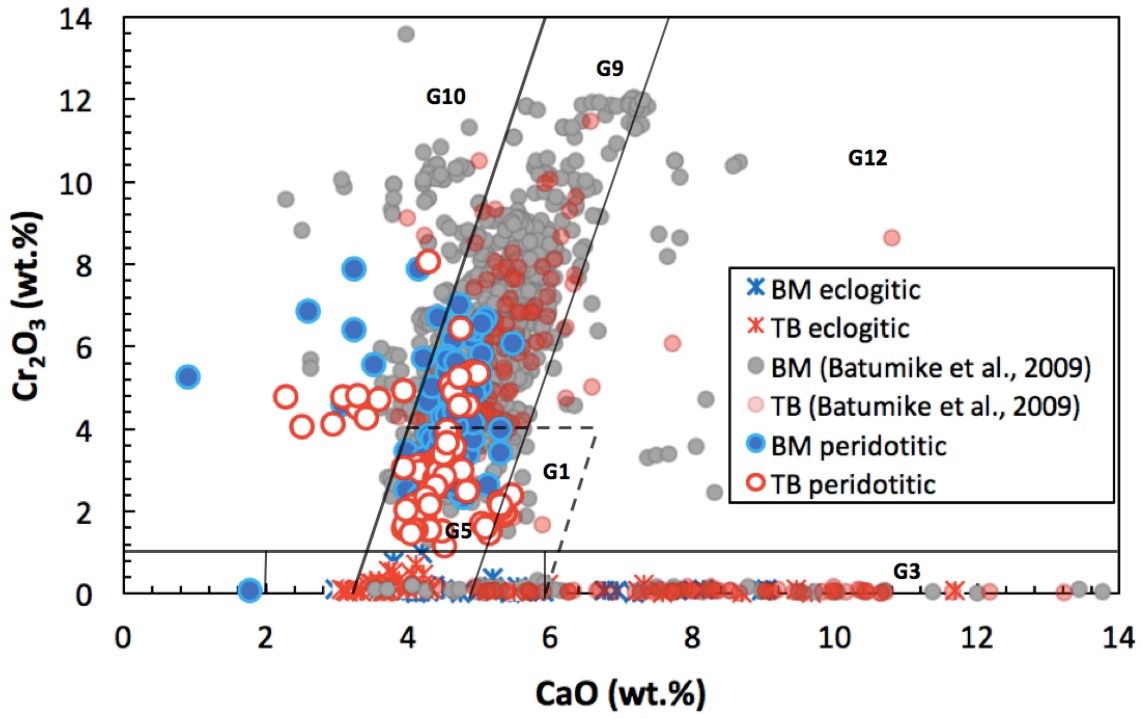

Figure 2.14: Cr_2O_3 (wt.%) versus CaO (wt.%) plot of all Mbuji-Mayi and Tshibwe garnets investigated in the present study. Two main garnet parageneses can clearly be distinguished: peridotitic and eclogitic. Concentrate garnet data of Batumike et al. (2009) from Mbuji-Mayi and Tshibwe are also shown for comparison. The fields of Grütter et al. (2004) are shown (G1: megacrystic; G3: eclogitic; G5: pyroxenitic; G9: lherzolitic; G10: harzbugitic; G12: wehrlitic).

2.4.1. ECLOGITIC GARNETS

A. Major element systematics

Major element data for eclogitic garnets from Mbuji-Mayi and Tshibwe are given in Tables 20 and 21, respectively, of the Appendix. Eclogitic garnets (orange to brown, in color) from Mbuji-Mayi and Tshibwe fall into 3 populations: a larger low-calcium group (with Ca# ranges of 10.2 – 23 and 9.8 – 17, for Mbuji-Mayi and Tshibwe, respectively), a medium-calcium group (with Ca# ranges of 25.5 – 34 and 22.9 – 33.9, for Mbuji-Mayi and Tshibwe, respectively) and a high-calcium group (with Ca# ranges of between 36.1 – 43.5 and 38.7 – 48.9 for Mbuji-Mayi and Tshibwe, respectively; Fig. 2.15).

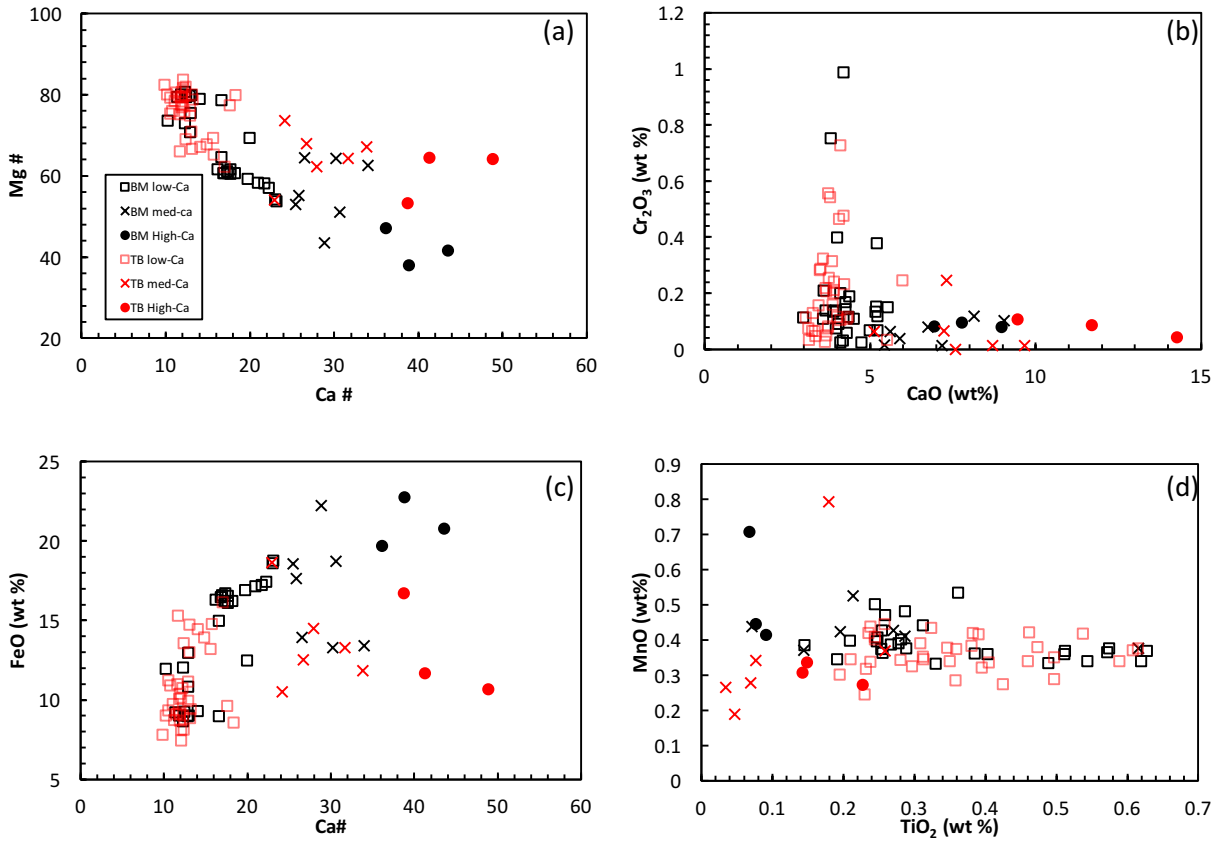

Figure 2.15: (a) Ca# (Ca/(Ca + Mg)* 100 in atomic units) versus Mg# (Mg/(Mg + Fe)* 100 in atomic units) plot of Mbuji-Mayi (BM) and Tshibwe (TB) eclogitic garnets. Note the clustering at high Mg-number and the two trends of decreasing Mg-number with increasing Ca-number. **(b)** CaO wt.% versus Cr_2O_3 wt.% plot. All the garnets fall within the field of eclogitic garnets. **(c)** FeO wt.% versus Ca# plot. Note the Fe enrichment in Mbuji-Mayi eclogitic garnets. **(d)** MnO wt.% versus TiO_2 wt.% plot.

Medium-Ca and high-Ca Tshibwe garnets have higher Mg# and lower FeO, on average, than those from Mbuji-Mayi. At both localities, high-Ca and medium-Ca garnets have lower TiO_2 contents than low-Ca garnets (i.e., below 0.3 wt.%; Fig. 2.15). There are no differences in Na_2O content between groups of eclogitic garnets at each locality.

B. Trace element systematics

Trace element data for eclogitic garnets from Mbuji-Mayi and Tshibwe are given in Tables 22 and 23, respectively, of the Appendix. All eclogitic garnets show the LREE depletions and HREE enrichments characteristic of mantle garnet. Low-Ca eclogitic garnets from Mbuji-Mayi and Tshibwe have nearly flat HREE patterns (Fig.16) and nearly identical ranges of trace element

contents. However, the Tshibwe low-Ca garnets have slightly lower HFSE and LILE concentrations than those from Mbuji-Mayi.

High-Ca garnets from Mbuji-Mayi have lower Sr, Nb, Zr contents, moderate Hf contents and higher Y contents than Tshibwe high-Ca garnets. REE concentrations normalized to chondrite of Mbuji-Mayi high-Ca garnets, show steep LREE patterns and nearly flat HREE patterns (Fig. 2.16). Medium-Ca garnets from Mbuji-Mayi have similar REE patterns to Mbuji-Mayi low-Ca garnets. However, one garnet (medium-Ca) has similarities with high-Ca garnets (low Sr, Nb, Zr; Fig. 2.16).

Medium-Ca garnets from Tshibwe display similar trace element patterns to Mbuji-Mayi medium-Ca garnets. However, they display lower HFSE and LILE concentrations. Moreover, chondrite-normalised REE concentrations show different patterns where there is a decrease from the MREE to the HREE (Fig 2.16). This observation is consistent with the generally low concentrations of Y in the Tshibwe medium-Ca (1.1 – 1.4 ppm, apart from one sample having an anomalously high value of 29 ppm) compared to Mbuji-Mayi medium-Ca garnets (16.9 – 26.8 ppm Y). Tshibwe high-Ca garnets have REE patterns intermediate between medium-Ca eclogitic garnets from Tshibwe and Mbuji-Mayi.

C. Origin of Mbuji-Mayi and Tshibwe eclogitic garnets

Eclogitic mantle nodules from the Mbuji-Mayi kimberlite have been investigated by Demaiffe et al (1999; They did not present the mineral data for these samples). They distinguished 3 groups of eclogites, out of 152 nodules studied (whole-rock samples): bimineralic eclogites, Kyanite-bearing eclogites and one diamond-bearing eclogite. Bimineralic eclogites have low TiO_2 (average of 0.15 wt.%) and Al_2O_3 contents (8 – 17 wt.%), positive Ba, Sr, Pb and Eu anomalies, and are LREE enriched ($(La/Yb)_N$ = 2 – 30), while kyanite-bearing eclogites are peraluminous (17 – 28 wt.% Al_2O_3), have high CaO contents (up to 15 wt.%) higher positive Ba, Sr, Pb and Eu anomalies and are less LREE enriched ($(La/Yb)_N$ = 2.1 – 8) than bimineralic eclogites. The whole-rock composition the diamond-bearing eclogite is distinguished by its low CaO content (5.8 %), absence of a Eu anomaly, and LREE-depletion ($(La/Yb)_N$ = 0.55). Based on the correlation of positive Ba, Sr, Pb and Eu anomalies with higher Al_2O_3 and CaO contents, they suggested that the protoliths of kyanite eclogites were plagioclase-rich rocks (cumulate gabbros, anorthosites) while the protoliths of bimineralic eclogites were probably basalts (less or unenriched in plagioclase).

Moreover, they suggested that these eclogites were variably affected by metasomatic events, indicated by sinusoidal REE patterns in garnets.

Thermobarometry data for the Mbuji-Mayi eclogite nodules were calculated by El Fadili and Demaiffe (1999). The estimated P-T intervals of kyanite and bimineralic eclogites are ≈3 GPa and 815 – 1260 °C while the single diamond-bearing eclogite sample had a calculated pressure of 5 GPa. The authors did not provide thermobarometers used or the temperature for the diamond-bearing eclogite sample.

Mbuji-Mayi and Tshibwe low-Ca garnets from this study, have high Mg#, no Eu anomaly and normal LREE-depleted REE patterns. Garnet from the Mbuji-Mayi diamond-bearing eclogite, described by Demaiffe et al, (1999), also has a normal, LREE depleted REE pattern ($(La/Yb)_N$ = 0.05), high Na_2O contents (0.18 wt.%) and no Eu anomaly. Therefore, Low-Ca garnets from Mbuji-Mayi and Tshibwe share characteristics with, and could potentially have originated from, diamond-bearing eclogites. Low-Ca garnets from Mbuji-Mayi and Tshibwe are also similar to eclogitic garnet diamond inclusions from the Jericho kimberlite in Canada, due to their high MgO contents (De Stephano et al., 2009). This feature has been interpreted as an indication of an ultramafic picritic protolith (De Stephano et al., 2009). Eclogitic garnet inclusions from Jericho diamonds also do not display Eu anomalies with normal REE patterns and lack correlations of Mg-number with Yb content, much like low-Ca eclogitic garnets from Mbuji-Mayi and Tshibwe (Fig. 2.17). Therefore, on this basis, Mbuji-Mayi and Tshibwe low-Ca eclogitic garnets could also have ultramafic picritic protoliths.

Aulbach et al., (2007) suggested that correlations of Mg# and Yb contents in eclogitic garnets were related to igneous processes in the origin of their protolith. Negative correlations (as are shown very weakly by the data in Fig. 2.17) could indicate that olivine fractionation was an important process in the origin of the eclogitic protoliths, whereas positive correlations could be the result of garnet crystallization and accumulation at high pressure.

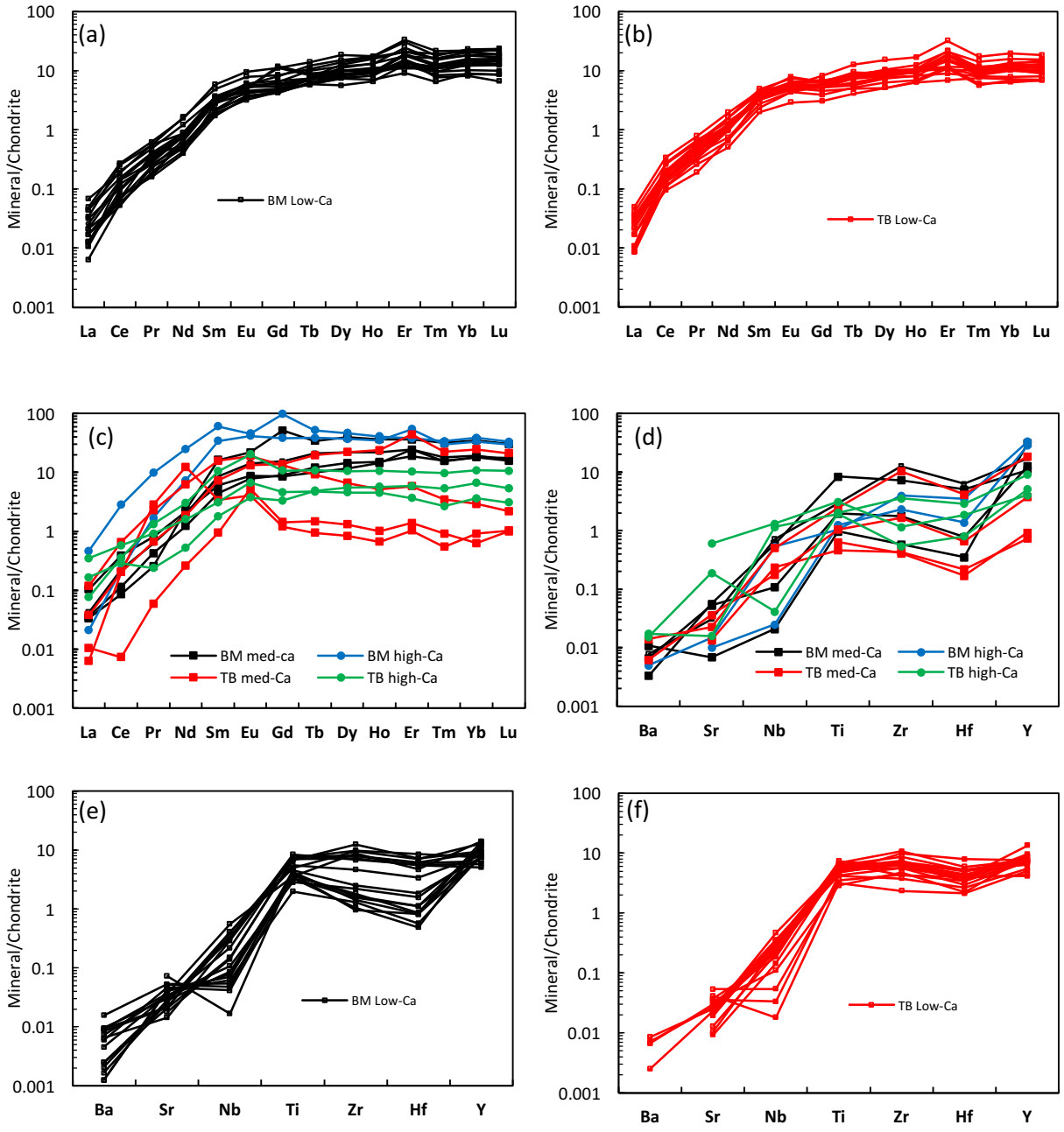

Figure 2.16: (a and b) Chondrite-normalized REE patterns of low-Ca eclogitic garnets from Mbuji-Mayi **(a)** and Tshibwe **(b)**, **(c)** Chondrite-normalized REE patterns of Mbuji-Mayi and Tshibwe medium and high-Ca garnets, **(d)** LILE and HSFE abundance patterns, normalized to chondrites, of Mbuji-Mayi and Tshibwe medium-Ca and high-Ca eclogitic garnets, Mbuji-Mayi low-Ca eclogitic garnets **(e)** and Tshibwe low-Ca eclogitic garnets **(f)**. Normalizing values from McDonough and Sun (1995). In panel (c), note the humped patterns of some Tshibwe medium-Ca garnets (with negative slopes from the MREE to HREE) and the normal patterns (with flat MREE-HREE patterns) of Mbuji-Maji medium-Ca garnets. Mbuji-Mayi high-Ca eclogitic garnets display the highest HREE contents.

Garnet inclusions in eclogitic diamonds from the Finsch and Premier kimberlites in South Africa have similar major and trace element compositions similar to some Mbuji-Mayi and Tshibwe eclogitic low-Ca garnets (e.g., low CaO, slight positive Sr anomaly and slight negative Zr and Nb anomalies, nearly flat HREE patterns with no Eu anomalies (Viljoen et al., 2010). Varying mixtures of oceanic gabbros and MORB-like basalts have been proposed as the protoliths of these eclogites. Trace element patterns having positive Sr anomalies, but lacking Eu anomalies, can be obtained by mixing gabbro and MORB at a 50:50 ratio (e.g., Viljoen et al., 2010). The lack of good correlations between Mg-number and Yb content displayed by Mbuji-Mayi and Tshibwe low-Ca garnets (Fig. 2.17), may mean that both processes could have been active at both Tshibwe and Mbuji-Mayi.

Mbuji-Mayi medium-Ca eclogitic garnets have similar REE patterns to Mbuji-Mayi low-Ca garnets and could have originated from diamond-bearing eclogites. Protoliths composed of varying mixtures of gabbro and MORB are envisaged in that case. High-Ca garnets, as well as some medium-Ca garnets, from Mbuji-Mayi are characterized by high HREE contents and low TiO_2 and Al_2O_3 contents (Fig. 2.15). These garnets are less depleted in the LREE than than the rest of the eclogitic garnets from Mbuji-Mayi. The general correspondence between the compositions of the high-Ca garnets and the whole-rock bimineralic eclogites described by Demaiffe et al., (1999) is consistent with these garnets being derived from bimineralic eclogites. . Aulbach and Viljoen (2015) found similar characteristics (low TiO_2 with ranges of 0.06 – 0.39, no Eu anomaly) in garnets from eclogites from the Lace kimberlite in South Africa. They also found that garnet in bimineralic eclogites from Lace have lower Sr and higher HREE relative to garnet in kyanite-bearing eclogites, much like the difference between the high-Ca garnets from Mbuji-Mayi. Therefore, an origin from bimineralic eclogites is favored for Mbuji-Mayi high-Ca eclogitic garnets.

Most Tshibwe medium-Ca garnets appear to have an origin distinct from their Mbuji-Mayi counterparts. This group is dominated by garnets having the lowest HREE contents (Fig. 2.17) among all eclogitic garnets investigated, with most having ‘humped’ REE patterns with negatively sloping patterns from the middle to the heavy REE, and one medium-Ca Tshibwe garnet shows a marked positive Eu anomaly (Fig. 2.16). As noted above, Mbuji-Mayi kyanite eclogitic nodules are characterised as peraluminous and high in CaO in terms of whole-rock composition, and their garnets display similar sinusoidal REE patterns (Demaiffe et al., 1999). Moreover, low HREE

contents are characteristic of kyanite-bearing eclogites. On this basis, it seems plausible that most of the medium-Ca eclogitic garnets from Tshibwe are derived from kyanite-bearing eclogites.

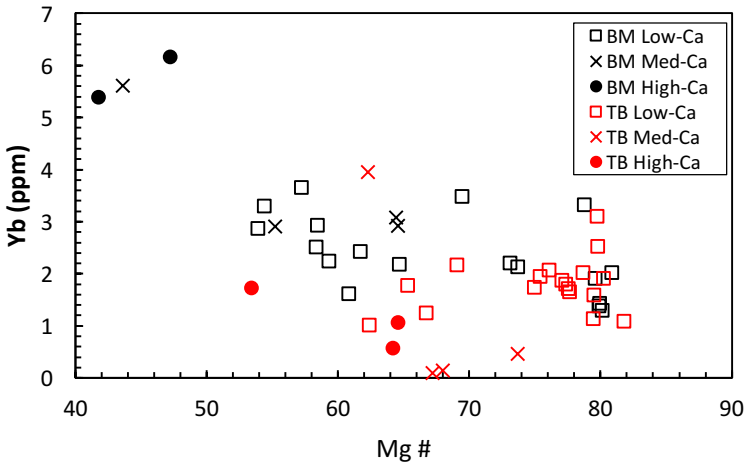

Figure 2.17: Mg# versus Yb (ppm) plot of Mbuji-Mayi and Tshibwe eclogitic garnets. There are no clear correlations in any group due the highly scattered state of the data.

Tshibwe high-Ca garnets could possibly be derived from kyanite-bearing eclogites as well because of their low HREE and high CaO contents. In addition, the similarity in REE patterns and approximately same range in TiO_2 contents of Tshibwe high-Ca and medium-Ca eclogitic garnets supports the above hypothesis.

It has been recognised that, from the major and trace element compositions of the eclogitic garnets, it is hard to identify any features that are clearly the result of metasomatic processes. (Aulbach et al, 2016). There are no significant differences in incompatible elements between Mbuji-Mayi and Tshibwe eclogitic garnets. It is therefore difficult to evaluate the extent of metasomatism at both localities using eclogitic garnets.

D. Eclogitic garnets – Summary

Eclogitic garnets derived from the heavy mineral concentrates at Mbuji-Mayi and Tshibwe appear to originate from slightly different eclogitic assemblages: diamond-bearing eclogites and bimineralic eclogites at Mbuji-Mayi and diamond-bearing eclogites and kyanite-bearing eclogites at Tshibwe. Diamond-bearing eclogites appear to be abundant within the SCLM beaneath the northeastern section of the Kasai craton and have been documented at Mbuji-Mayi (Demaiffe et al., 1999). They appear to have two distinct origins for their protoliths: ultramafic picrites and

varying mixtures of oceanic gabbro and MORB, with the latter being more closely associated with diamond-bearing eclogites. At Tshibwe, it is more likely that diamond-bearing eclogites with pricritic protoliths are dominant.

Table 2.1: Summary of the origin of eclogitic garnets from Mbuji-Mayi and Tshibwe investigated in this study

	Mbuji-Mayi		**Tshibwe**	
Eclogitic garnets	Host lithology	Protolith	Host lithology	Protoliths
Low-Ca	Diamond-bearing eclogites	Ultramafic picritic	Diamond-bearing eclogites	Ultramafic picritic
Medium-Ca	Diamond-bearing eclogites	Varying mixtures of Gabbro and MORB	Kyanite-bearing eclogites	Cumulate gabbros, anorthosites
High-Ca	Bimineralic eclogites	Basalts	Kyanite-bearing eclogites	Cumulate gabbros, anorthosites

2.4.2. PERIDOTITIC GARNETS FROM MBUJI-MAYI AND TSHIBWE

Peridotitic garnets from Mbuji-Mayi and Tshibwe include both lherzolitic (G9) and harzburgitic (G10) varieties.

A. Major element systematics

A.1. Lherzolitic (G9) garnets

Major element data for peridotitic garnets are given in Tables 24, 25, 28 and 29 of the appendix. Lherzolitic garnets occur abundantly in the heavy mineral concentrates from the Mbuji-Mayi and Tshibwe kimberlites. They display coherent trends of increasing CaO with increasing Cr_2O_3 contents and fall in the G9 (lherzolitic) and G5 (pyroxenitic) field on the CaO vs Cr_2O_3 plot of Grütter et al., (2004). Mbuji-Mayi garnets have Cr_2O_3 contents that ovelap with, but are slightly higher on average than, garnets from Tshibwe (with averages of 4.30 ± 1.27 and 3.10 ± 1.25, for Mbuji-Mayi and Tshibwe, respectively; Fig. 2.18). Lherzolitic Garnets from Mbuji-Mayi are slightly more Ca-rich, on average, than those from Tshibwe, with Ca# ranging from 12 to 16.5 (BM G9) while at Tshibwe, Ca# ranges from 11.8 to 14.9 (Tshibwe main group or TB G9; Fig.

2.18). Tshibwe garnets extend slightly to more Al-rich compositions compared to those from Mbuji-Mayi, with Al_2O_3 ranges of 18.9 – 22.9 wt.% and 18.69 – 22.29 wt.%, respectively (Fig. 2.18). There is a small difference in MnO contents between the two main groups of garnets (from Mbuji-Mayi and Tshibwe), with Mbuji-Mayi being higher and Tshibwe being lower (with average MnO contents of 0.41 ± 0.04 and 0.36 ± 0.05, for Mbuji-Mayi and Tshibwe, respectively). Another distinct feature is the lower Mg# seen in a small group of Tshibwe garnets (with a range of 77.0 – 80.9). This group is referred to as the Tshibwe low-Mg garnets (Fig. 2.18)

The Tshibwe low-Mg garnets have the bimodal TiO_2 contents, with both very high (≈0.8 wt.%) and very low TiO_2 (≈0.075 wt.%) and relatively high MnO content (≈0.05 wt.% on average). Since high TiO_2 is a crucial distinguishing characteristic of garnet megacrysts (Schulze, 2003), the Tshibwe low-Mg garnets with high TiO_2 content are likely megacrystic. The remaining Tshibwe low-Mg garnets could have a pyroxenitic origin, which could explain their low-MgO and low TiO_2 contents (Schulze, 2003; Doyle et al., 2004).

A.2. Harzburgitic garnets

Major element data for harzburgitic garnets are given in Tables 28 and 29 of the Appendix. Harzbugitic garnets from Mbuji-Mayi are richer in Cr_2O_3 content than those from Tshibwe (with averages of wt.% 6.32 ±1.13 and wt.% 4.90±1.15, respectively; Fig. 2.19). The harzbugitic garnets from Mbuji-Mayi have slightly lower Al_2O_3 contents, on average, than those from Tshibwe (with averages of 19.61 ± 0.87 at Mbuji-Mayi versus 20.67 ± 1.04 wt.% at Tshibwe; Fig. 2.19).

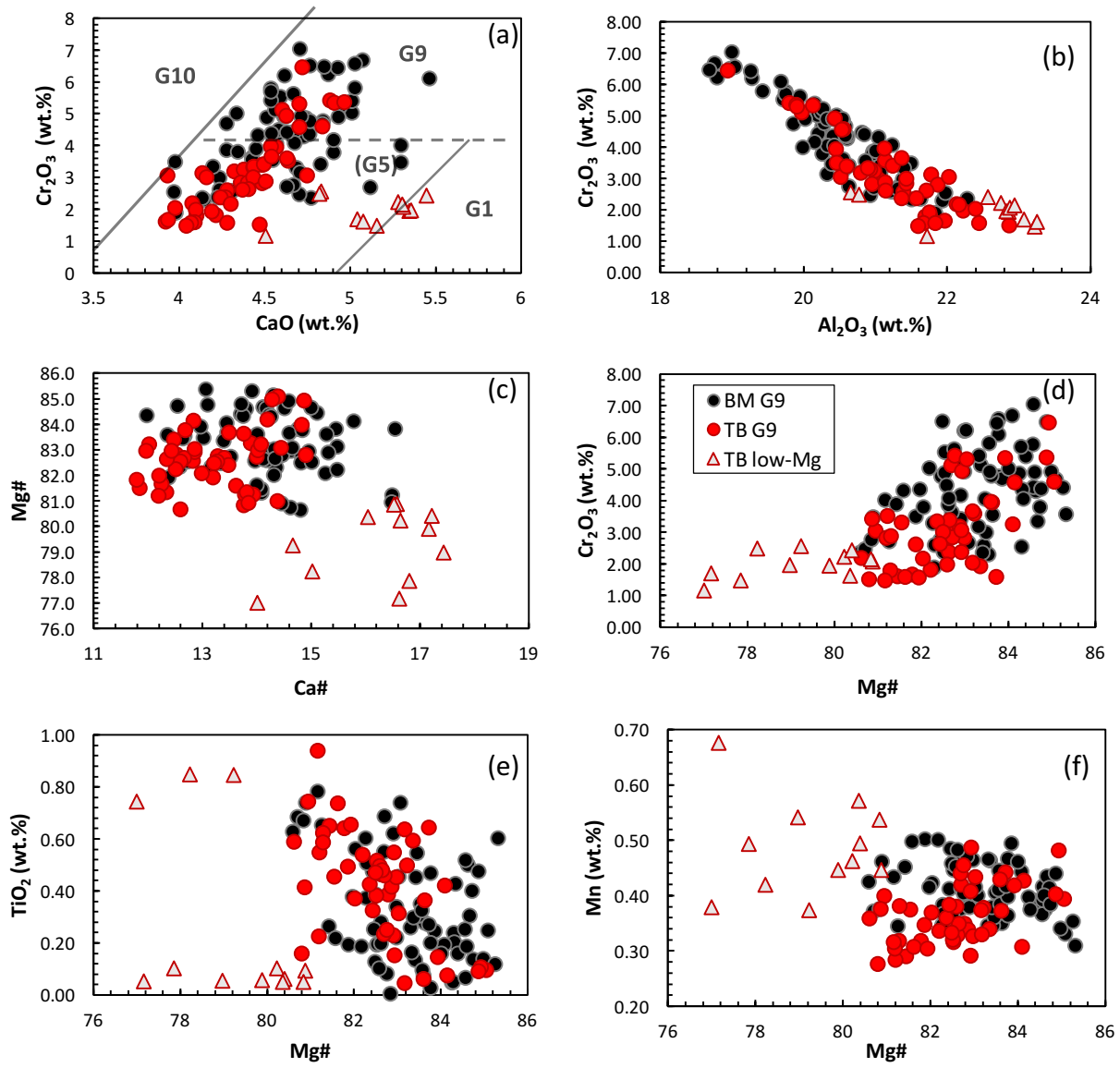

Figure 2.18: Variation of selected major element parameters in Mbuji-Mayi (BM) and Tshibwe (TB) lherzolitic (mainly G9) garnets. **(a)** CaO (wt.%) versus Cr_2O_3 (wt.%), **(b)** Al_2O_3 (wt.%) versus Cr_2O_3 (wt.%), **(c)** Ca# (Ca*100/(Ca+Mg)) versus Mg # (Mg*100/(Mg+Fe)), **(d)** Mg# versus Cr_2O_3 (wt.%), **(e)** Mg# versus TiO_2, **(f)** Mg# versus MnO (wt.%).

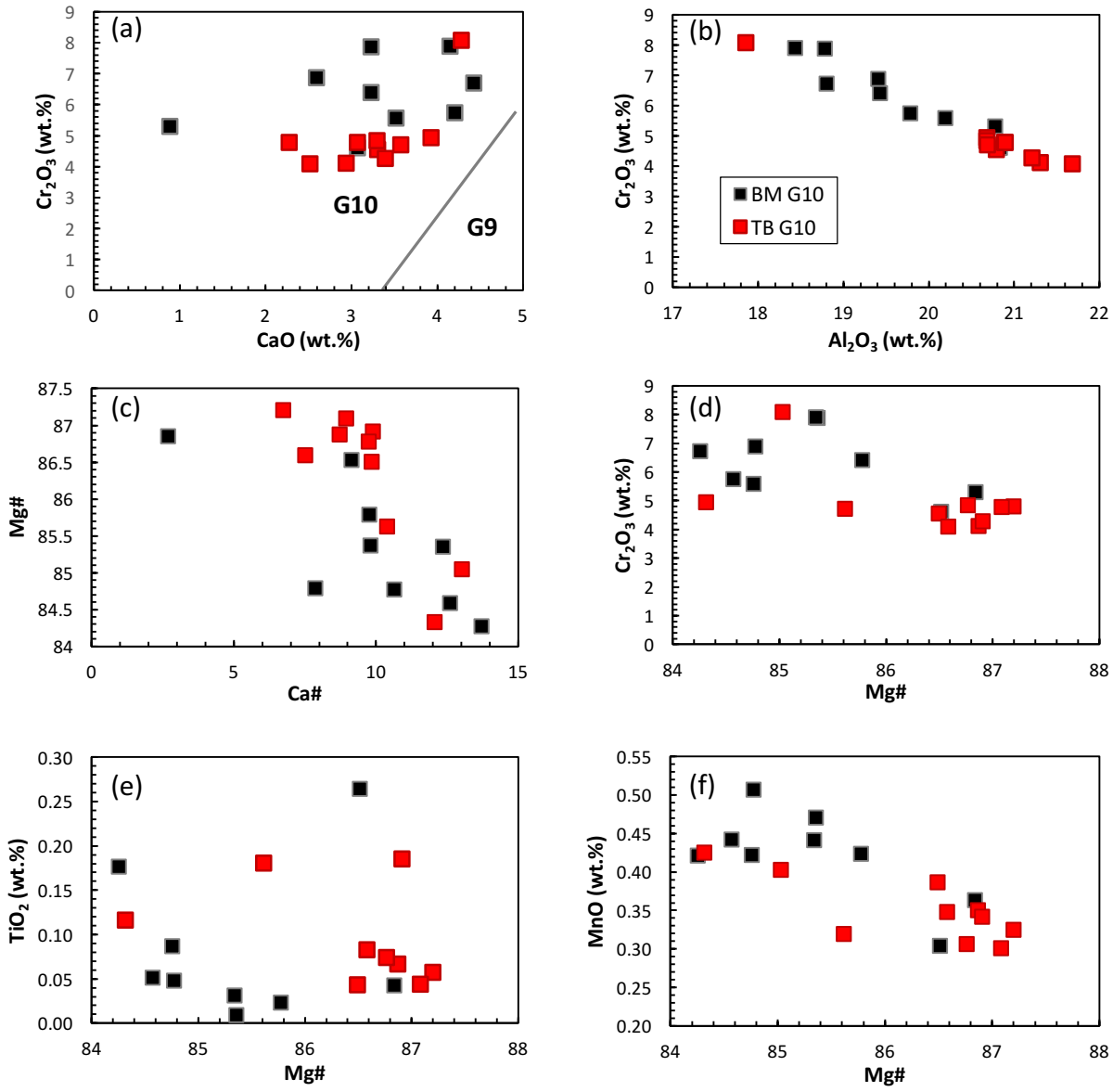

Figure 2.19: Variation of selected major element parameters in Mbuji-Mayi (BM) and Tshibwe (TB) harzburgitic garnets. **(a)** CaO (wt.%) versus Cr_2O_3 (wt.%) plot. **(b)** Al_2O_3 (wt.%) versus Cr_2O_3 (wt.%) plot. **(c)** Ca# versus Mg # plot. (d) Mg# versus Cr_2O_3 (wt.%) plot. (e) Mg# versus TiO_2 plot. (f) Mg# versus MnO (wt.%) plot.

A.3. Comparison with peridotitic garnets data from Batumike et al., (2009)

Batumike et al. (2009) provided a large major and trace element data set of peridotitic garnet compositions from Mbuji-Mayi and Tshibwe heavy mineral concentrates (these data are included in Figure 2.14, but are not shown in the other figures. Their data are similar to those presented here in terms of major element compositions, however it is notable that garnets from both Mbujo-Mayi and Tshibwe in their data set both extend to higher Cr_2O_3 values and have higher

average Cr_2O_3 than those from this study (average Cr_2O_3 contents in garnets from this study are 4.6 ± 1.2 and 3.8 ± 1.5 wt.% for Mbuji-Mayi and Tshibwe respectively, whereas those from Batumike et al. (2009) are 5.9 ± 2.1 and 3.7 ± 3.2 wt.% for Mbuji-Mayi and Tshibwe respectively). Mbuji-Mayi peridotitic garnets in both studies display a greater range of chemical variation and have higher average Cr_2O_3 contents than Tshibwe peridotitic garnets (Fig. 2.14).

B. Trace element systematics

B.1. Lherzolitic (G9) garnets

Trace element data are given in Tables 26 and 27 of the Appendix. Two groups can be distinguished based on REE patterns in chondrite-normalised diagrams: G9 garnets with normal REE patterns (62 % at Mbuji-Mayi and 82% at Tshibwe) and those "irregular" (including sinusoidal) patterns (38% at Mbuji-Mayi and 18 % at Tshibwe).

B.1.1. Lherzolitic (G9) garnets with regular REE patterns

The (G9 garnets with normal REE patterns) show strong LREE depletions and have high HREE abundances of ≈5x to ≈15x chondrite with relatively flat REE patterns from Dy to Lu. These garnets tend to have the highest Ti, Zr and Y contents. Lherzolitic garnets, with normal REE patterns, from Mbuji-Mayi and Tshibwe have similar trace element compositions. However, there are some minor differences. At Mbuji-Mayi, lherzolitic garnets show a wide variation of LREE contents ($Ce_N = 0.15 - 1.2 \times CI$ and $Ce = 0.23 - 0.90 \times CI$ at Mbuji-Mayi and Tshibwe, respectively) (Fig. 2.20). Trace element patterns for lherzolitic garnets from Tshibwe are more uniform than the ones displayed by those from Mbuji-Mayi (Fig. 2.20). Moreover, at Mbuji-Mayi, negative Ti anomalies are common in lherzolitic garnets, whereas, at Tshibwe, most lherzolitic garnets show positive Ti anomalies.

In a plot of wt.% TiO_2 versus Zr concentration (Fig. 2.22), more than half of the Mbuji-Mayi G9 garnets and more than 90% of the Tshibwe G9 garnets, having regular REE patterns, form a tight linear array clustered around a Zr/Ti ratio of 0.0075. The remaining G9 garnets all have higher Zr/Ti ratios, up to a maximum of 0.08. There is better correlation of Zr and Y contents (Fig. 2.22a) than Zr and TiO_2, with most garnets having Zr/Y ratios near 4, although there is a significant spread in Zr/Y ratios at low Zr contents. In general, garnets with regular patterns from

Mbuji-Mayi and Tshibwe are characterized by a wide range of Zr contents that correlate with Ti and Y concentrations, causing them to fall within the melt-metasomatised and depleted garnet peridotite fields of Griffin and Ryan (1995) on Figure 2.22a. Mbuji-Mayi lherzolitic garnets (with regular patterns) show a significantly greater range of Zr and Y contents compared to Tshibwe lherzolitic garnets, and nearly half of the Mbuji-Mayi red garnets fall in the melt-metasomatised field on Figure 2.22a, whereas nearly 70 % of Tshibwe lherzolitic garnets fall in the depleted peridotite field.

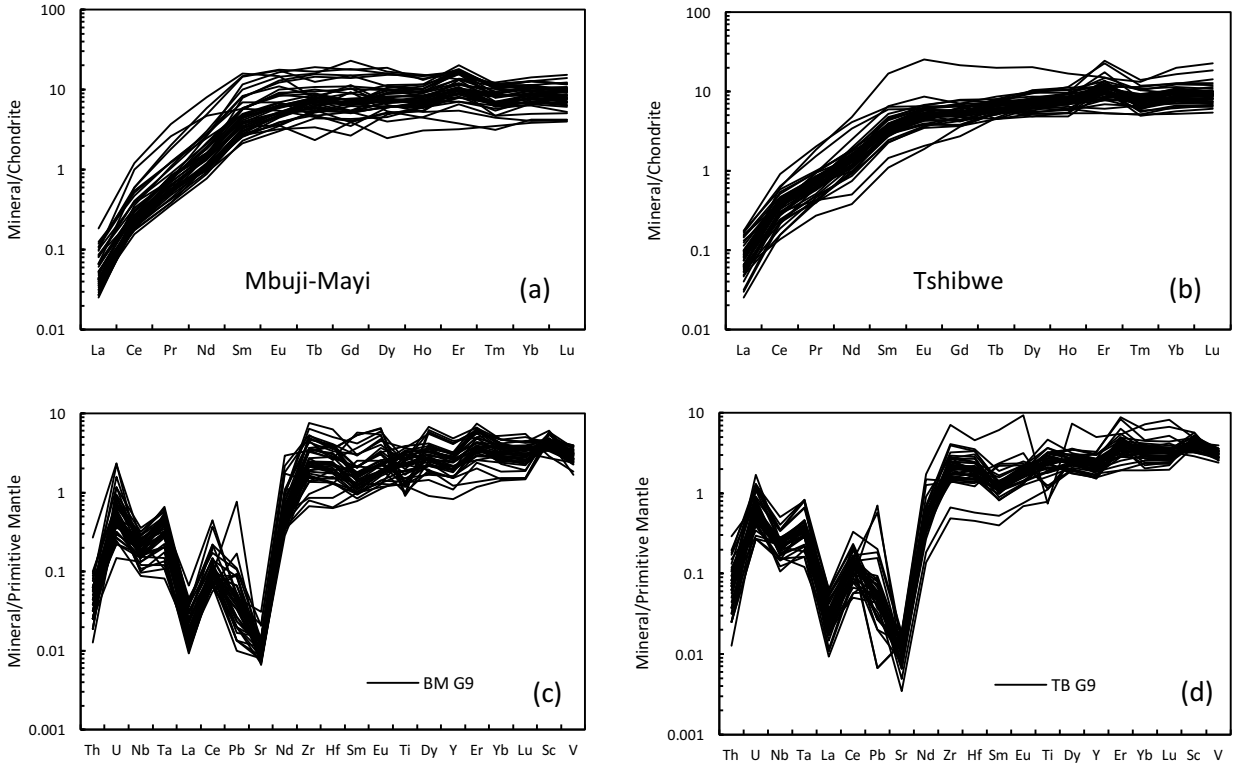

Figure 2.20: Chondrite-normalized REE patterns (a and b) and Primitive mantle-normalized incompatible element patterns (c and d) for lherzolitic garnets with regular patterns, from Mbuji-Mayi and Tshibwe, respectively. Normalizing values from McDonough and Sun (1995).

B.1.2. Lherzolitic garnets (G9) with irregular REE patterns

These lherzolitic garnets from Tshibwe and Mbuji-Mayi display REE patterns that are clearly distinct from the normal garnet REE patterns. They may display depletions in both the light and middle to heavy REE (e.g., Tb-Er)) or have sloping patterns in the middle and heavy REE that the normal patterns lack. Three types of irregular REE patterns are recognised in these garnets:

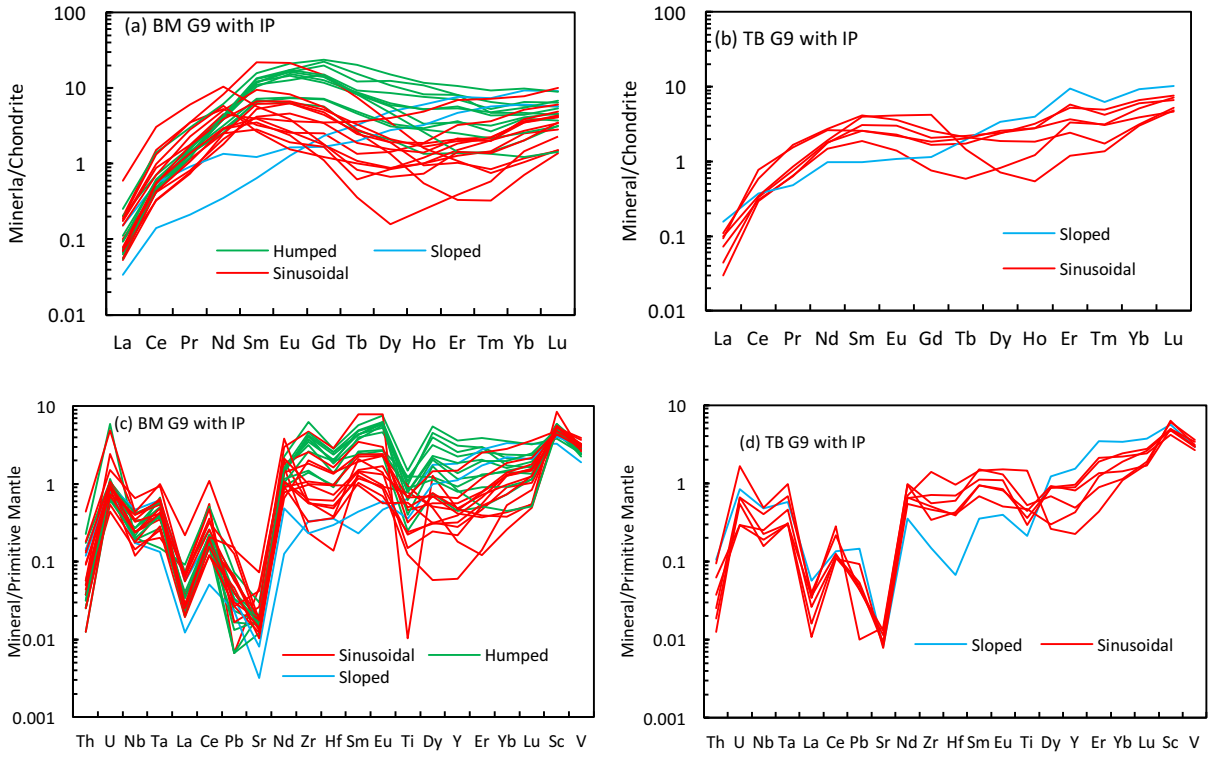

Fig. 2.21: Chondrite-normalised REE (a and b) and primitive mantle-normlaised incompatible element patterns (c and d) for lherzolitic garnets with irregular REE patterns (IP), from Mbuji-Mayi and Tshibwe, respectively. Note the different type of REE patterns: Normal, humped, sloped and "true" sinusoidal. Normalising values are from Sun and McDonough (1995).

(1) Humped REE patterns: These display enrichments in the MREE compared to both the LREE and HREE. They tend to peak at Sm or Eu, with a smooth drop to Ho or Tm followed by a nearly flat pattern from Tm to Lu. They display a high degree of HREE variation. They are dominant at Mbuji-Mayi and not observed at Tshibwe. They have higher HREE, Ti, Zr and Y contents than garnets with sinusoidal patterns but have lower abundances of these elements than garnets with normal patterns.

(2) Sloped REE patterns: garnets with these patterns have positive slope from the LREE to Ho or Er followed by flat or less steeply negatively sloping patterns in the HREE. They are the most depleted in MREE among the purple garnets. Two Mbuji-Mayi garnets and one Tshibwe purple garnet displays these patterns.

(3) Sinusoidal REE patterns: Garnets with these patterns display the traditional sinusoidal REE pattern (e.g., Hoal et al., 1994), with maxima in normalized concentration between Nd and Gd and minima between Tb and Er. The higher the degree of sinuosity (i.e., the ratio of maximum to minimum concentration), the lower the HREE content tends to be. Garnets with moderately sinusoidal patterns are characterised by positive slope in the LREE – MREE with a maximum at Sm or Eu and a minimum at Dy to Tm followed by a positive slope in the HREE. Garnets with mildly sinusoidal patterns are characterised by maxima at Sm with minima at Tb to Ho followed by a positive slope in the HREE. Garnets with strongly sinusoidal patterns are characterised by a postive slope in the LREE with maxima at Nd and a minima Dy or Ho followed by a positive slope in the HREE. Such highly sinusoidal patterns are present in some G9 garnets at Mbuji-Mayi but not observed at Tshibwe. In general, garnets with sinusoidal patterns have lower HREE, Ti, Zr and Y contents compared to garnets with the other types of REE patterns. On the Zr vs Y garnet classification diagrams of Griffin and Ryan (1995), more than 50% of Mbuji-Mayi lherzolitic garnets with sinusoidal REE patterns fall within the depleted field, as do more than 90% of those at Tshibwe (Fig. 2.22). The remaining of these garnets falling outside of this field have higher Zr and Y contents falling within the melt-metasomatised field.

B.2. Harzburgitic garnets

Trace element data of harzburgitic garnets are given in Tables 30 and 31 of the Appendix. Harzburgitic garnets from Mbuji-Mayi and Tshibwe tend to display sinusoidal REE patterns, varying from moderately to strongly sinusoidal, with four Mbuji-Mayi garnets having humped REE patterns. One garnet at Tshibwe displays a strongly sinusoidal pattern and the rest of the garnets have more uniform moderately sinusoidal patterns. At Mbuji-Mayi, harzburgitic garnets display a large degree of variation in LREE concentration (roughly three orders of magnitude) and have higher LREE contents than at Tshibwe (Fig. 2.23). They also have higher average Zr and Hf contents along with deep negative Ti anomalies compared to Tshibwe harzburgitic garnets (Fig.

2.23). Most harzburgitic garnets from Mbuji-Mayi and Tshibwe plot in the depleted field of Griffin and Ryan (1995) on the plot of Zr versus Y content (Fig. 2.22).

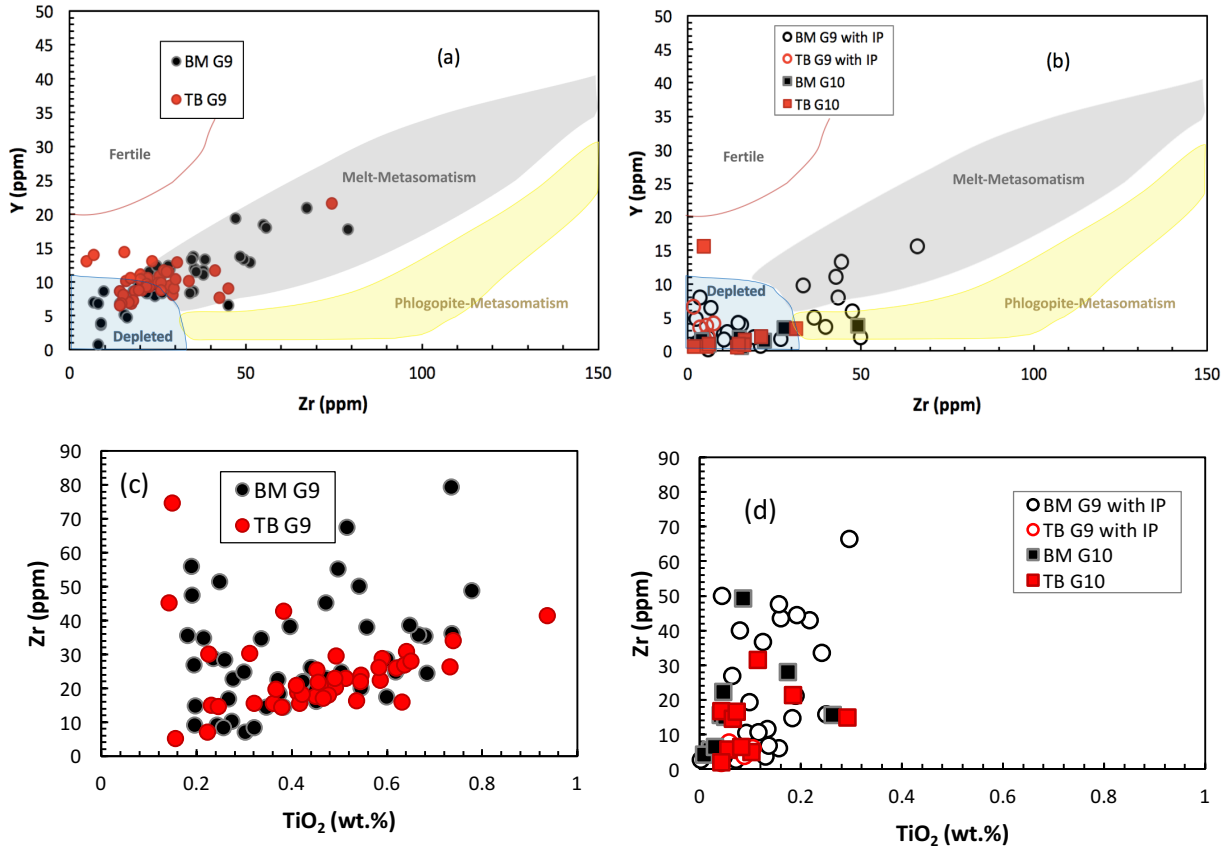

Figure 2.22: Variation of Zr, Y and TiO_2 contents in peridotitic garnets from Mbuji-Mayi and Tshibwe. **(a)** Zr(ppm) versus Y (ppm) plot for lherzolitic garnets (G9) with regular REE patterns. **(b)** Zr (ppm) versus Y (ppm) plot for harzburgitic garnets (G10), as well as lherzolitic garnets having irregular REE patterns (IP). (c) TiO_2 (wt.%) versus Zr (ppm) plot of lherzolitic (G9) garnets with regular REE patterns. (d) TiO_2 (wt.%) versus Zr (ppm) plot of harzburgitic garnets, as well as lherzolitic garnets with irregular REE patterns. The fields in (a) and (b) are from Griffin and Ryan (1995).

C. Geothermometry

Ryan et al., (1996) showed that Ni concentrations in pyrope garnets can be used to estimate the temperature (T_{Ni}) of equilibration, assuming that they are in equilibrium with olivine. This Ni-in-garnet thermometer was used to calculate temperatures of equilibration for all peridotitic garnets from Mbuji-Mayi and Tshibwe. Data are given in Tables 49 and 50 of the Appendix. The Ni-in-

garnet thermometer of Canil, (1999) gives temperatures 50°C higher than those obtained by Ryan et al., (1996) but, aside from this offset, the two thermometers provide similar results. Given the fact that Ryan et al., (1996) thermometer has been used more widely for African garnet xenocrysts (e.g., Griffin et al., 2003; Kobussen et al., (2008), including particularly the large central African garnet data set of Batumike et al., (2009), the Ryan et al., 91996) thermometer is used for garnet in this thesis.

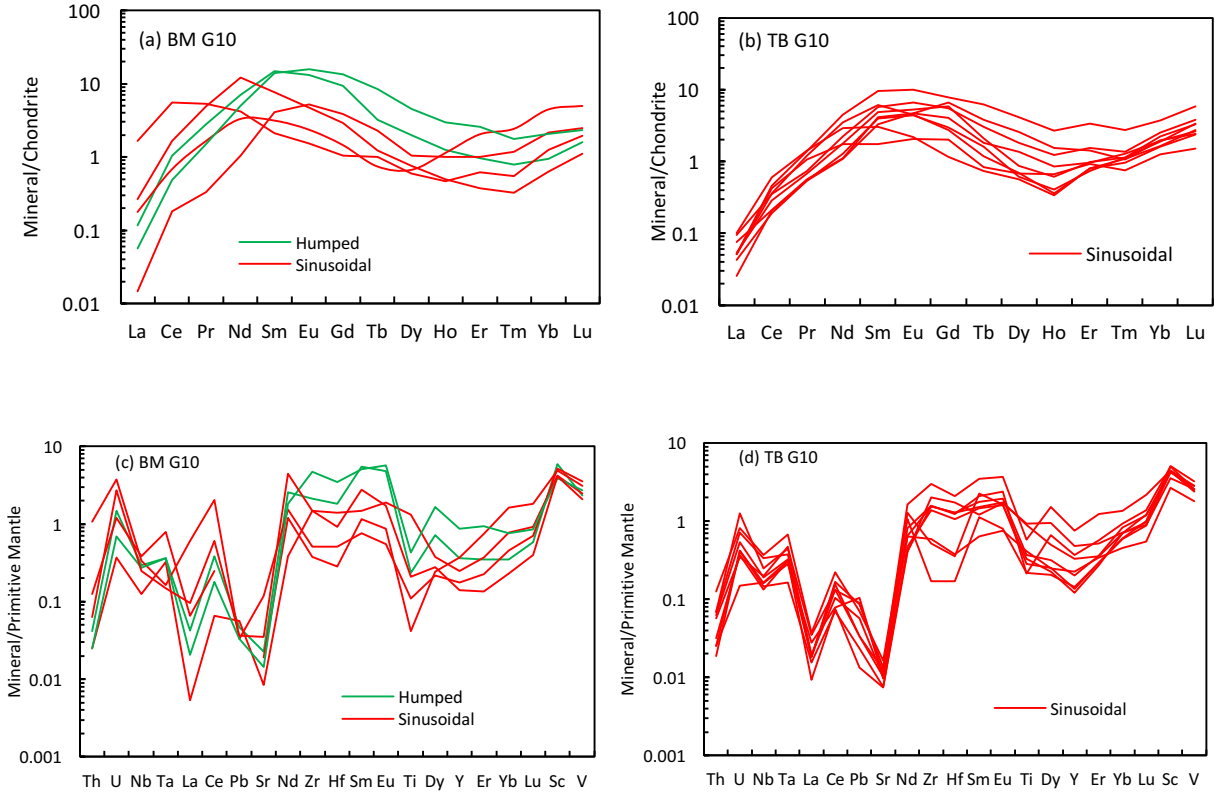

Figure 2.23: : (a, b) Chondrite-normalized REE patterns of Mbuji-Mayi and Tshibwe G10 garnets, **(c, d)** Primitive mantle-normalised trace element patterns of Mbuji-Mayi and Tshibwe G10 garnets. Normalizing values are from McDonough and Sun (1995).

C.1. Lherzolitic garnets

C.1.1. Lherzolitic garnets with regular REE patterns

Based on the Ryan et al. (1996) T_{Ni} thermometer, temperatures for lherzolitic (G9) garnets from Tshibwe are higher (but not quite, outside of 1σ uncertainties) compared to those from Mbuji-Mayi (with averages of 1207 ± 112 °C and 1085 ± 70 °C for the two localities, respectively, with the uncertainties representing 1 standard deviation). There is no correlation between temperature

(T_{Ni}) and Cr content in the garnets. The results of Batumike et al. (2009) found no differences between T_{Ni} for lherzolitic (G9) garnets from Mbuji-Mayi (1030 ± 106 °C) and Tshibwe (1023 ± 130 °C), and garnets from both localities in their study have average T_{Ni} values that are slightly cooler than (though well within uncertainties of) the mean T_{Ni} values determined here for Mbuji-Mayi and Tshibwe (Fig. 2.25).

C.1.2. Lherzolitic garnets with irregular REE patterns

Lherzolitic (G9) garnets with irregular REE patterns (IP) from Mbuji-Mayi (average T_{Ni} = 1002 ± 66 °C) display slightly lower equilibration temperatures than those from Tshibwe (average of 1085 ± 29 °C; Fig. 2.24).

C.2. Harzburgitic garnets

Mbuji-Mayi harzburgitic (G10) garnets (average of 978 ± 90 °C; Fig. 2.25) also display lower equilibration temperatures than those from Tshibwe (average T_{Ni} = 1081 ± 63 °C). In contrast, in the data set of Batumike et al. (2008), Mbuji-Mayi and Tshibwe harzburgitic garnets display effectively identical equilibration temperatures (with average of 987 ± 118 °C at Mbuji-Mayi and 953 ± 151 °C at Tshibwe; Fig. 2.25).

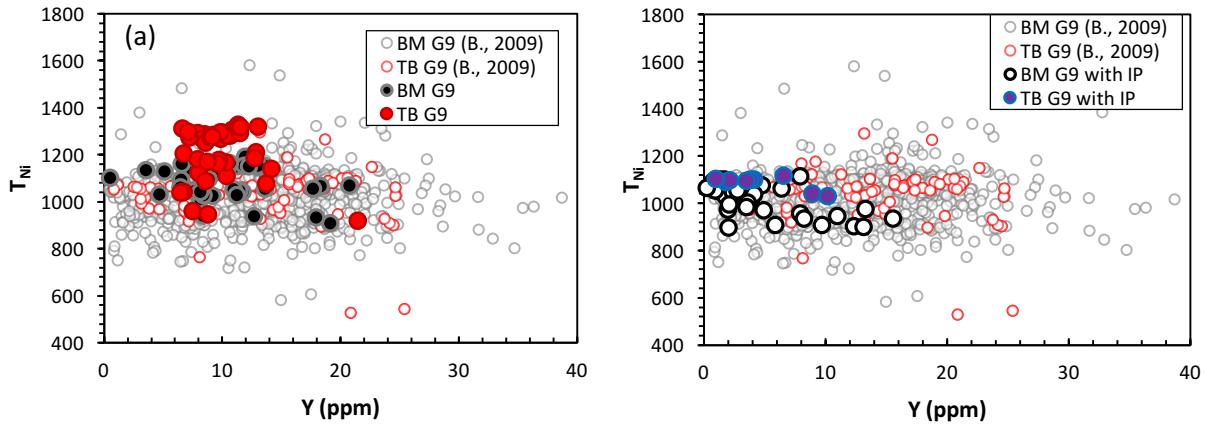

Figure 2.24: (a) Y (ppm) versus temperature (T_{Ni} in °C; Ryan et al., 1996) of Tshibwe and Mbuji-Mayi lherzolitic (G9) garnets with regular REE patterns. **(b)** Y (ppm) versus Temperature (T_{Ni} in °C) in Tshibwe and Mbuji-Mayi lherzolitic garnets with irregular REE patterns (IP). Mbuji-Mayi and Tshibwe lherzolitic garnet data from Batumike et al., (2009; abbreviated "B., 2009" in legend) are shown for comparison.

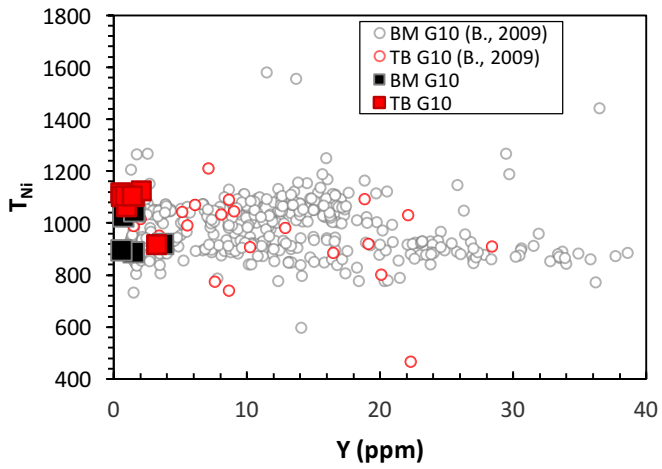

Figure 2.25: Temperature (T_{Ni} in °C) versus Y (ppm) of Tshibwe and Mbuji-Mayi harzburgitic (G10) garnets. Mbuji-Mayi and Tshibwe harzburgitic garnet data from Batumike et al., (2009) are shown for comparison.

D. DISCUSSION

D.1. Origin of G9 garnets with regular REE patterns

There is clear evidence that garnets from Mbuji-Mayi and Tshibwe falling in the G9 field are lherzolitic. Major element systematics (e.g., location in CaO-Cr_2O_3 diagram) and trace element patterns (LREE depletions and nearly flat HREE patterns) both are typical for lherzolitic garnets globally (Griffin et al, 2002; Pearson et al, 2003; Aulbach et al, 2013). A pyroxenitic or megacrystic origin is judged unlikely for garnets falling in the G5 sub-field (Fig. 2.18) because of their similarity, in TiO_2, MgO and FeO contents (and therefore also Mg#) to garnets falling in the G9 field. It has been widely recognised that, relative to peridotitic garnets, pyroxenitic and megacrystic garnets have lower TiO_2 (higher in the case of megacrystic origin) contents and lower Mg# (Kopylova et al, 1999; Grutter et al, 2004; Ziberna et al, 2013). Therefore, the fact that garnets falling in the G5/G1 fields do not display noticeably higher TiO_2 or lower Mg# values argues against a pyroxenitic or megacrystic origin. Moreover, garnets from pyroxenites and megacryst suites display a positive correlation of Mg-number and Cr_2O_3 content (Doyle et al, 2004; Bell and Moore, 2004), whereas the garnets from Mbuji Mayi and Tshibwe plotting in the G5 field don't display such correlations (Fig. 2.18d).

The positive correlations of Zr content with Ti and Y in most lherzolitic garnets (i.e., those with regular REE patterns; Figs. 2.22a &2.22c) is indicative of melt-mediated metasomatic

processes that have affected the garnet's host lithology (e.g., garnet lherzolite) in the upper mantle (e.g., Griffin and Ryan, 1995). On this basis, most of the lherzolitic garnets appear to have mainly originated from metasomatised garnet lherzolites.

D.2. Origin of G9 garnets with irregular REE patterns

These garnets from Mbuji-Mayi and Tshibwe almost entirely fall in the G9 lherzolitic field of Grütter et al. (2004). They are slightly more magnesian and calcic and are also richer in Cr_2O_3, on average, than the lherzolitic garnets with regular REE patterns. They display REE patterns ranging from humped (at Mbuji-Mayi) to strongly sinusoidal, with Zr and Y contents that mainly plot within the depleted peridotite field (Fig. 2.22b). In contrast, much larger proportion of G9 garnets with normal REE patterns (LREE-depleted REE patterns, with nearly flat HREE profiles) plot in the melt-metasomatised field on a plot of Zr vs. Y (Fig. 2.22). These differences seem to support a distinct origin: The G9 garnets with irregular REE patterns could plausibly have been mainly derived from unmetasomatised lherzolites while the G9 garnets with regular REE patterns appear to have originated mainly from melt-metasomatised lherzolites.

D.3. Origin of garnets falling in the harzburgitic field (G10)

These garnets display sinusoidal and humped REE patterns, commonly observed in harzburgitic, subcalcic garnets from cratonic regions worldwide (Shimizu and Richardson, 1987; Hoal et al., 1994; Lazarov et al., 2009). They fall mainly within the depleted field of Griffin and Ryan (1995) on the basis of Zr-Y-TiO_2 contents. An origin from mantle harzburgite is therefore suggested for these Mbuji-Mayi and Tshibwe garnets.

D.4. Perspectives from peridotitic garnet on differences in the lithospheric mantle composition at Mbuji-Mayi and Tshibwe

D.4.1. Evidence from lherzolitic garnets with regularl REE patterns

The relationship between Zr and Y in the lherzolitic garnets brings out a distinctive feature in the composition of the lithospheric mantle beneath the two localities. Aulbach et al., (2013) have suggested that Zr-Y correlations in lherzolitic garnets are the result of progressive metasomatism by originally Zr- and Y-rich melts, which become progressively depleted in these elements due to progressive re-equilibration with garnet-bearing peridotite. Mbuji-Mayi G9 garnets display a fairly strong correlation between thsese elements while the one displayed by

Tshibwe G9 garnets is much weaker, with only a single tshibwe garnet grain having Zr and Y contents above 50 and 16 ppm, respectively.

Major element systematics of lherzolitic garnets from Mbuji-Mayi and Tshibwe reveal subtle but consistent differences between the two localities. Mbuji-Mayi lherzolitic garnets have slightly higher average Cr contents, a larger degree of chemical heterogeneity (in both major and trace elements) and higher average Zr-Y-Ti contents than Tshibwe lherzolitic garnets. This is consistent with the hypothesis, suggested earlier from peridotitic clinopyroxene, of more extensive metasomatism in the upper mantle beneath Mbuji-Mayi relative to Tshibwe.

D.4.2. Evidence from lherzolitic garnets with irregular REE patterns (IP)

At Mbuji-Mayi, while the majority of these lherzolitic garnets having irregular REE patterns plot in the depleted field on the Zr vs. Y plot of Griffin and Ryan (1995), there is a significant proportion (30%) that plots in the melt-metasomatised field with higher Zr, Ti and Y contents. For Tshibwe, data with such higher Zr, Ti and Y concentrations are absent and virtually all data fall within the depleted field. Moreover, at Mbuji-Mayi, lherzolitic garnets display a larger degree of chemical variation overall (i.e., in terms of major and trace element abundances) than at Tshibwe. This would appear to support more variable and, on average, a greater extent of metasomatism in the upper mantle beneath Mbuji-Mayi than beneath Tshibwe.

D.4.3. Evidence from harzbugitic garnets

Both Tshibwe and Mbuji-Mayi harzbugitic garnets display sinusoidal REE patterns indicative of extreme melt depletion followed by metasomatism by an LREE-enriched agent. However, those from Mbuji-Mayi are distinct in displaying more varied and pronouced metasomatic characteristics, including higher $(Nd/Yb)_N$ and much lower $(Ti/Eu)_{PM}$ ratios, compared to Tshibwe harzbugitic garnets. Such characteristics are likely due to a somewhat greater extent of metasomatism of the SCLM by kimberlitic or even carbonatitic fluids (e.g., Rudnick et al., 1993) beneath Mbuji-Mayi relative to that beneath Tshibwe.

D.4.4. Additional evidence for the dominance of garnet-poor lherzolite in the SCLM beneath Tshibwe.

In the present study, more garnets were recovered at Mbuji-Mayi than Tshibwe in the heavy mineral concentrates (9% versus 5% of the total bulk concentrate collected from the two localities, respectively). The number of lherzolitic garnets, with irregular REE patterns, recovered at Mbuji-Mayi is also greater than at Tshibwe (28 versus 10 garnets). Admittedly, the limited sampling performed for this study provides only anecdotal evidence, and may be complicated by sampling bias. However, the previous work of Batumike et al., (2009), based on much more extensive concentrate sampling as part of De Beers diamond exploration efforts, supports these results. At Mbuji-Mayi, 1236 garnets were recovered, as compared to 356 garnets recovered at Tshibwe during the same exploration campaign. Additionally, at Mbuji-Mayi, 772 garnets (62.5% of the total) are lherzolitic, whereas, at Tshibwe, there are only 162 garnets classified as lherzolitic (45.5% of the total). At Mbuji-Mayi, 411 garnets are harzburgitic (33.2% of the total) while at Tshibwe only 46 were classified as harzburgitic (12.9% of the total). Taken at face value, this suggests that (1) lherzolitic garnets are somewhat more dominant over harzburgitic ones at Tshibwe compared to Mbuji-Mayi and (2) peridotitic garnets from Tshibwe are, overall, less abundant than at Mbuji-Mayi.

E. Peridotitic garnets - summary

Mbuji-Mayi and Tshibwe peridotitic garnets, recovered from heavy mineral concentrates have been investigated. With regard to the lherzolitic type, the garnets with irregular REE patterns are slightly more magnesian, calcic, and richer in Cr_2O_3, on average, those garnets with regular REE patterns. In addition, lherzolitic garnets with regular REE patterns predominantly fall within the field of melt-metasomatism of Griffin and Ryan (1995) based on the Zr-Y-TiO_2 contents. In contrast, lherzolitic garnets with irregular REE patterns predominantly fall within the depleted field. An origin from metasomatised garnet lherzolite seems most plausible for the lherzolitic garnets with regular patterns, while an origin from relatively melt-depleted garnet lherzolites appears most likely for the lherzolitic garnets with irregular patterns.

Peridotitic garnets from Mbuji-Mayi display greater ranges of chemical variation than peridotitic garnets from Tshibwe, which is consistent with the Batumike et al. (2009) data set. A more variable and greater overall extent of metasomatism in the upper mantle beneath Mbuji-Mayi

compared to Tshibwe could explain these differences. Also, the higher proportion of peridotitic garnets recovered at Mbuji-Mayi relative to Tshibwe (Batumike et al., 2009 and this study) is consistent with a garnet-poor lithological character in the SCLM beneath Tshibwe.

2.5. ILMENITES

Ilmenites are common and abundant in the heavy mineral concentrates from the Mbuji-Mayi and Tshibwe kimberlites. They are used in diamond exploration worldwide, with the aim of assessing kimberlite diamond potential (Gurney et al., 1993; Griffin and Ryan, 1995). Moore (1987) classified ilmenites by grouping them based on their major element composition. He distinguished five ilmenite parageneses: (1) ilmenites originating from the kimberlitic Cr-poor megacryst suite (i.e., discrete nodules) having MgO contents between 7 and 14 wt.% and Cr_2O_3 content less than 1 wt.%; (2) metasomatic ilmenites characterized by enrichments in both MgO (15 – 16 wt.%) and Cr_2O_3 (5 – 6 wt.%); (3) ilmenites originating from the mica-amphibole-rutile-ilmenite-diopside (MARID) xenolith suite, characterized by very low Al_2O_3 contents (less than ≈0.05 wt.%); (4) ilmenites with a peridotitic origin, characterized by higher Al_2O_3 contents (above ≈0.25 wt.%); and (5) ilmenites from diamond inclusions, characterized by high MgO contents (up to 13 wt.%) and very low Cr_2O_3 (< 0.5 wt.%) content (Moore, 1987).

More recent studies by Moore et al. (1992) and Griffin et al. (1997) described and explained the complex major and trace element variations observed in kimberlitic ilmenites. Three groups of ilmenite (including monomineralic ilmenite megacrysts and ilmenite intergrowths with silicate minerals such as subcalcic clinopyroxene, orthopyroxene, phlogopite, zircon and Fe-rich olivine) were defined for the Monastery kimberlite megacryst suite by Moore et al. (1992). Group 1 ilmenites are part of the Cr-poor megacryst suite (< 0.4 wt.% Cr_2O_3). These ilmenites are associated with garnet, clinopyroxene and orthopyroxene (i.e., the main silicate trend). Group 2 ilmenites have low MgO and high Cr_2O_3 contents (6.75 – 9.45 wt.% MgO and 0.5 – 1.2 wt.% Cr_2O_3). These are typically associated with zircon, Fe-rich olivine and phlogopite. Group 3 ilmenites have high MgO and Cr_2O_3 contents and are associated with phlogopite and calcic clinopyroxene. Based on the Cr-number and Mg-number variations in the ilmenites, Moore et al. (1992) outlined two important processes occurring within the ilmenite parental magma. Firstly, differentiation due to fractional crystallization, displayed by the group 1 ilmenites, which clearly

show a decrease in Cr# with decreasing Mg#. Secondly, assimilation of the lithospheric mantle, displayed by group 2 and group 3 ilmenites. They suggested that the incompatible behavior of Nb observed throughout the megacryst magma crystallization history is an indication of ilmenite being a minor phase in the cumulate assemblage. The beginning of ilmenite crystallization appears to occur at a fairly late stage of fractionation. They proposed four stages for the Monastery megacryst suite in which ilmenite crystallizes: (Stage 1) ilmenite + cpx +garnet+ opx followed by (Stage 2) Ilmenite + phologopite crystallization, followed by (Stage 3) ilmenite + zircon + phlogopite and lastly, (Stage 4) ilmenite + zircon + Fe-rich olivine + phlogopite. They interpreted the variations in trace element compositions of Monastery ilmenites as a likely indication of changes in the cumulate assemblages due to extended crystallization of a single batch of magma.

Griffin et al., (1997) presented trace element data for ilmenites from 20 kimberlites, located in southern Africa. They suggested that ilmenite suites from each kimberlite are the product of fractional crystallization of single batches of magma and the trace element compositions of ilmenites are affected by co-precipitation of ilmenite with other minerals (e.g., zircon, phlogopite, olivine).

Other mantle ilmenites have been described by several authors (Konzett et al., 2000; Grégoire et al., 2002; Ene, 2014). MARID ilmenites have been compared to ilmenites from metasomatised peridotites by Konzett et al., (2000). Their dataset suggests that ilmenites from metasomatised peridotites have lower major element contents except for FeO content (see table 2.2) than in ilmenites from MARID.

Ilmenites from MARID rocks have been compared to those of PIC rocks by Grégoire et al., (2002). Their dataset suggests that ilmenites from PIC rocks have higher major and trace element contents (except for FeO content) (see Table 2.1) than in ilmenites from MARID. Recently, ilmenites from five mantle lithologies (Granny Smith, MARID, Fe-rich dunites, orthopyroxenites and rutile-ilmenite nodules) have been investigated by Ene (2014). His dataset does not show any significant difference in major and trace element contents among ilmenite from the five mantle lithologies, apart from the low Al_2O_3 content of MARID ilmenites (< 0.04 wt.%) from MARID.

Table 2.2: Composition of ilmenites from metasomatised peridotites (MP), PIC rocks and MARID rocks. Kasai ilmenites from this are also shown.

	Konzett et al., (2000)			Gregoire et al., (2002)		
	MP a	MP b	MARID	PIC	MARID	Kasai ilmenites
TiO_2 (wt.%)	52		41	53-56	48-55	47 – 56
Al_2O_3				0.05 - 0.3	0-0.2	0.10 – 1.09
FeO	32		49	25-28	29-38	26 – 34
Cr_2O_3	1.5		0.7	1-2.7	0.3-2.7	1.18 – 6.15
MgO	12.7		4.7	13.75-15.5	6.4-13.2	10.17 – 14.75
Nb (ppm)	6200	3800		1060-4720	1200-1975	712 - 6637
Ta	274	287		60-970	40-185	86 – 624
Zn	103	151				118 – 382
Zr				250 - 2100	55-320	108 – 811
Ni				880 - 1800	780-975	800 – 5833

Data from Konzett et al., (2000) and Grégoire et al., (2002). Kasai ilmenites data are from this study.

In the present study, ilmenites from Mbuji-Mayi and Tshibwe are investigated. In previous sections of this chapter, the differences in the SCLM beneath Mbuji-Mayi and Tshibwe have been highlighted, based on geochemical investigations of clinopyroxene and garnet xenocrysts. The expressions of these differences in the SCLM composition are investigated with respect to the compositions of ilmenites from Mbuji-Mayi and Tshibwe ilmenites.

Analytical procedures are similar to those described in section 1.3 of chapter one. The in-house ilmenite standard ROM 264 Il-52 was analysed (see Tables 40 and 41 of the Appendix).

2.5.1. MAJOR ELEMENT SYSTEMATICS

Major element data for Mbuji-Mayi and Tshibwe ilmenites are provided in Tables 32 and 33, respectively, of the Appendix. At Mbuji-Mayi, three groups of ilmenite can be distinguished on the basis of their major element compositions. The first group, termed "Mbuji-Mayi high-Mg", has low Cr_2O_3 contents (1.4 – 2.0 wt.%), high MgO contents (13.4 – 14.7 wt.%) and is Ti- and Al-rich, as well as being Fe- and Mn-poor (Fig. 2.29). In this group, Mg# broadly increases with Cr# (Fig. 2.28). The second group, termed “Mbuji-Mayi medium-Mg” has intermediate Cr_2O_3 (2.0 – 3.9 wt.%) and MgO contents (12.0 – 13.7 wt.%) and is less enriched in TiO_2 and Al_2O_3 and more enriched in $FeO^{tot.}$ and MnO than the Mbuji-Mayi high-Mg ilmenites (Fig. 2.29). The third group, termed “Mbuji-Mayi low-Mg” is composed mainly of ilmenites with lower MgO (10.1 – 11.9

wt.%) contents and generally higher Cr_2O_3 contents (Cr_2O_3 = 3.0 – 5.0 wt.%), as well as higher MnO and $FeO^{tot.}$ and lower TiO_2 and Al_2O_3 contents than ilmenites from the medium-Mg and high-Mg groups (Figs. 2.28 and 2.29). There is broad negative correlation between Mg# and Cr# values in medium and low-Mg ilmenites from Mbuji-Mayi (Fig. 2.28).

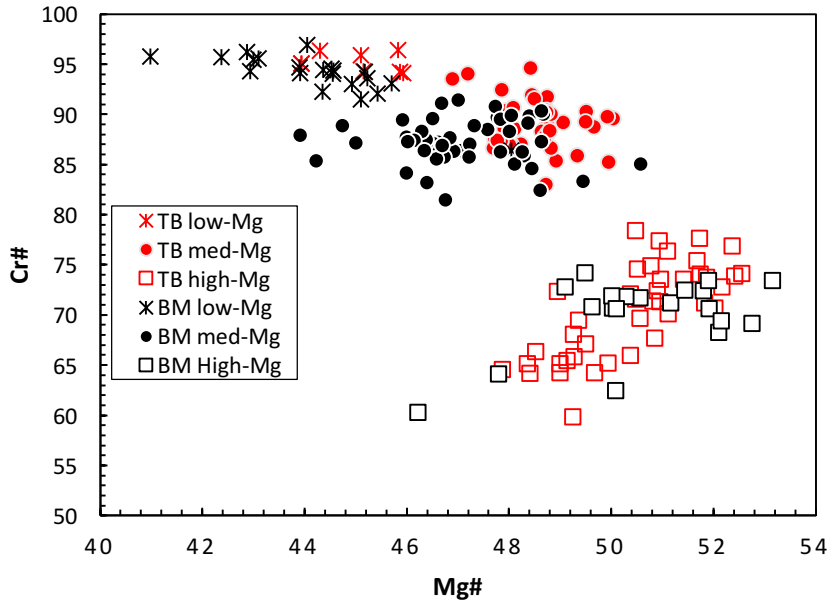

Figure 2.28: Plot of Mg# versus Cr# for Mbuji-Mayi (BM) and Tshibwe (TB) ilmenites. Note the three distinct groups of ilmenite observed at Mbuji-Mayi (BM low-Mg, BM medium-Mg and BM high-Mg) and Tshibwe (TB low-Mg, TB medium-Mg and TB high-Mg). Some Mbuji-Mayi data are from Pivin (2012).

At Tshibwe, the ilmenite population also falls into three distinct groups, roughly equivalent to those at Mbuji-Mayi. The first group, termed "Tshibwe high Mg" has the lowest Cr contents (Cr_2O_3 of 1.18 – 2.53 wt.%) and highest MgO contents (12.84 – 14.28 wt.%). In this group, Mg# broadly increases with Cr# (Fig. 2.28). Ilmenites from this group are especially Ti-rich, Al-rich, Fe-poor and Mn-poor (Fig. 2.29). The second group is composed of ilmenites with intermediate to high Cr_2O_3 (2.6 – 6.2 wt.%) and intermediate MgO (12.1 – 13.7 wt.%), and is termed the "Tshibwe med-Mg group" (Fig. 2.28). Ilmenites from this group are less enriched in Ti and Al and more enriched Fe and Mn than Tshibwe high-Mg ilmenites (Fig. 2.29). The third group is composed of ilmenites with higher Cr_2O_3 (4.1 – 4.3 wt.%) and the lowest MgO contents (10.8 – 11.7 wt.%), and are termed the “Tshibwe low-Mg” group. Cr_2O_3 contents in this group are nearly uniform (4.3±0.1 wt.%). Ilmenites from this group have the lowest Ti and Al contents and the highest Fe and Mn

contents (Fig. 2.29). There is broad negative correlation between Mg# and Cr# values in medium and low-Mg ilmenites from Tshibwe (Fig. 2.28).

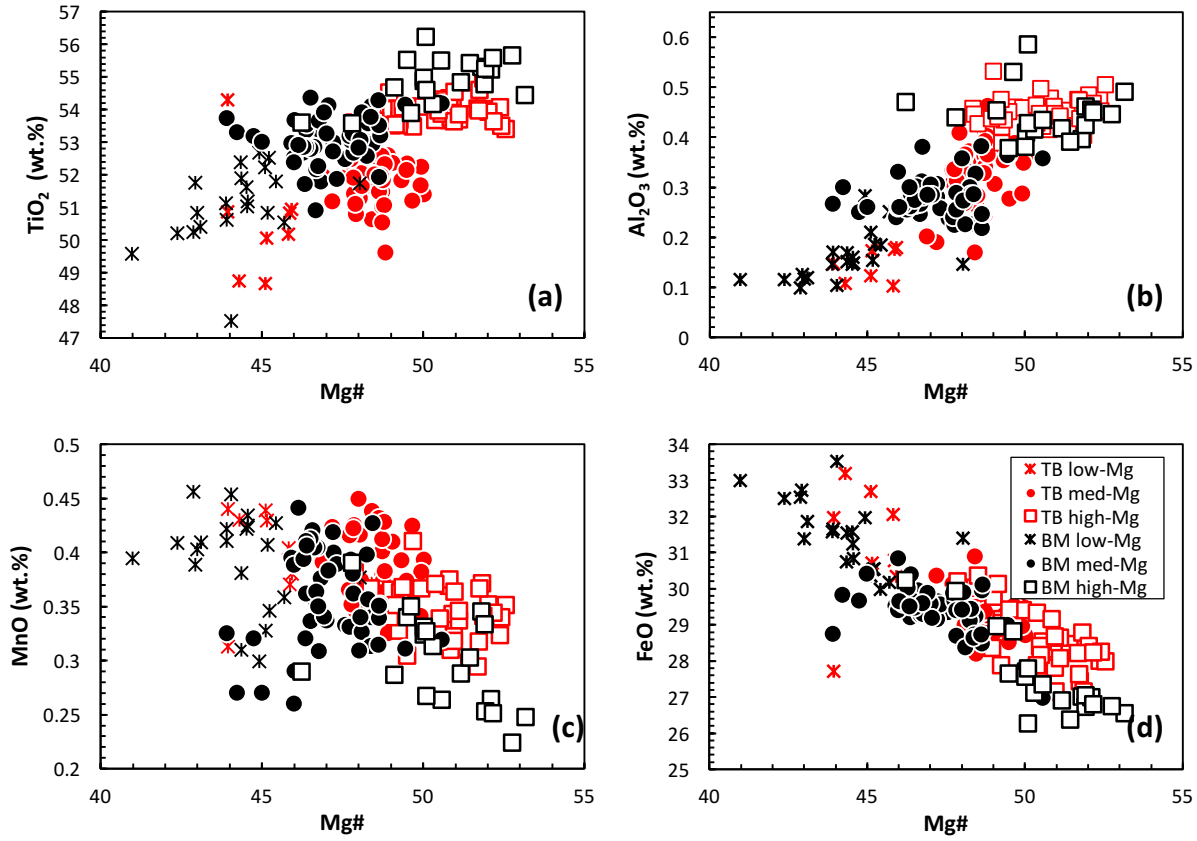

Figure 2.29: Variation diagrams of selected major elements in Mbuji-Mayi (BM) and Tshibwe (TB) ilmenites. **(a)** Mg# versus TiO_2, **(b)** Mg# versus Al_2O_3, **(c)** Mg# versus MnO, **(d)** Mg# versus FeO. Note the broad positive correlation of Mg and Ti contents. Note the well-defined negative correlation between Mg# and FeO contents. Note the broad negative correlation between Mg# and MnO contents. Some Mbuji-Mayi data are from Pivin (2012).

Comparison between Mbuji-Mayi and Tshibwe ilmenites

There are differences between the low-, medium- and high-Mg ilmenite gorups defined at Mbuji-Mayi and Tshibwe, despite remarquable similarities. In terms of relative abundances, the Mbuji-Mayi ilmenites display a more normal distribution, with the medium-Mg group being larger (54%) than the low-Mg and high-Mg groups (23 and 22%, respectively). In contrast, the Tshibwe ilmenites are more skewed toward the high-Mg group (with 8, 44 and 48% for the low-, medium- and high-Mg groups, respectively).

The high-Mg and medium-Mg ilmenite groups from Tshibwe individually span larger ranges in Cr_2O_3 contents than those from Mbuji-Mayi (i.e., in high- and medium-Mg groups, Cr_2O_3 = 1.7 ± 0.4 and 4.1 ± 0.8 wt.% for Tshibwe, versus 1.7 ± 0.4 and 4.1 ± 0.8 for Mbuji-Mayi), and the Cr_2O_3 content of the low-Mg Tshibwe group is also higher, but more uniform (4.3±0.1 wt.% for Tshibwe versus 3.8 ± 0.5 wt.% for Mbuji-Mayi; Fig. 2.28). Low- and medium-Mg ilmenites from Tshibwe tend to have higher Cr_2O_3 at a given MgO content than those from Mbuji Mayi. The slightly higher TiO_2 contents for a given MgO value in Mbuji-Mayi ilmenites should also be noted.

MnO and Al_2O_3 contents in the Mbuji-Mayi and Tshibwe ilmenites are very similar overall. MgO contents are slightly more variable in Mbuji Mayi low-Mg ilmenites than in those from Tshibwe (10.1 to 11.9 wt.% versus 10.7 to 11.7 wt.% for Mbuji-Mayi and Tshibwe, respectively).

2.5.2. TRACE ELEMENT SYSTEMATICS

Trace element concentration data are given for Mbuji-Mayi and tshibwe in Tables 34 and 35 of the appendix. Mbuji-Mayi and Tshibwe ilmenites have trace element systematics characterized by a generally broad positive relationship between Nb and Cr#, as well as a broad negative correlation between Nb and Mg# (Fig. 2.32). Also, there are tight positive correlations of Nb with Zr, Hf and Ta (Figs 2.32 and 2.33). Nb/Ta ratios remains relatively constant with the increase of Nb content while Nb/Zr shows weak trend (Fig. 2.32). There is no correlation of Mg# with Ga content. Ni show a tight positive correlation with Mg# in Mbuji-Mayi high-Mg ilmenites (Fig. 2.33) and a tight positive correlation with Cr# in Tshibwe high-Mg ilmenites (Fig. 2.40). Ni and Ga do not show any correlation with Nb content. Ni shows similar geochemical behavior to Ga (Fig. 2.33). High-Mg ilmenites display the lowest concentrations in elements such as Nb, Zr, Hf and Ta, while low-Mg ilmenites display highest concentrations in these elements.

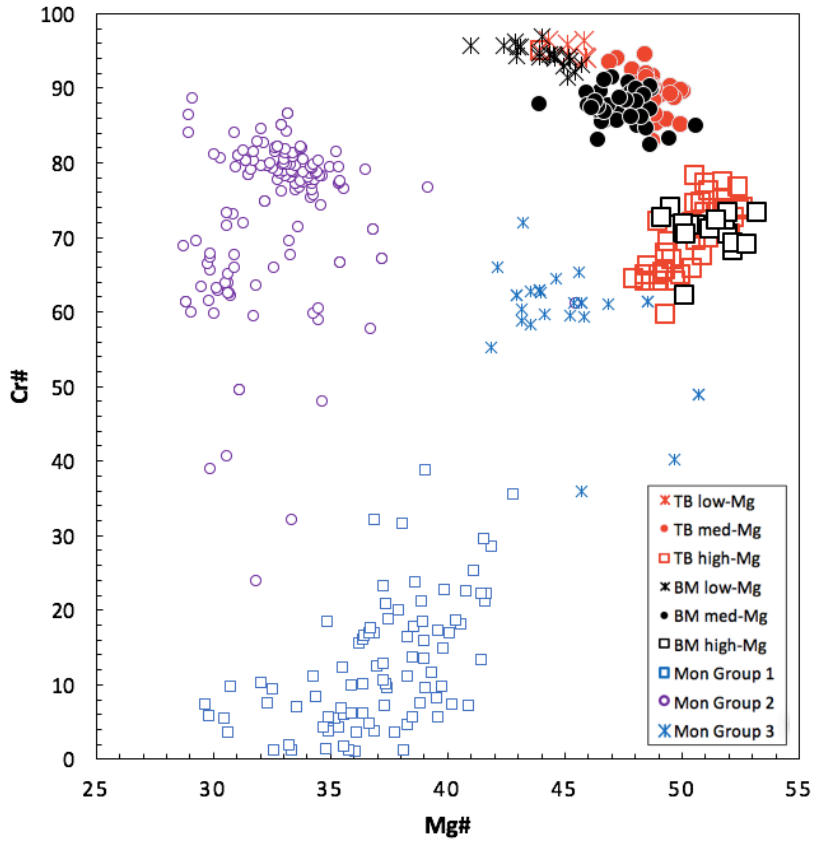

Figure 2.30: MgO (wt.%) versus Cr_2O_3 (wt.%) for Mbuji-Mayi, Tshibwe and Monastery ilmenites. Some Mbuji-Mayi data re from Pivin (2012). Monastery data are from Jakob (1977) and Moore et al., (1992).

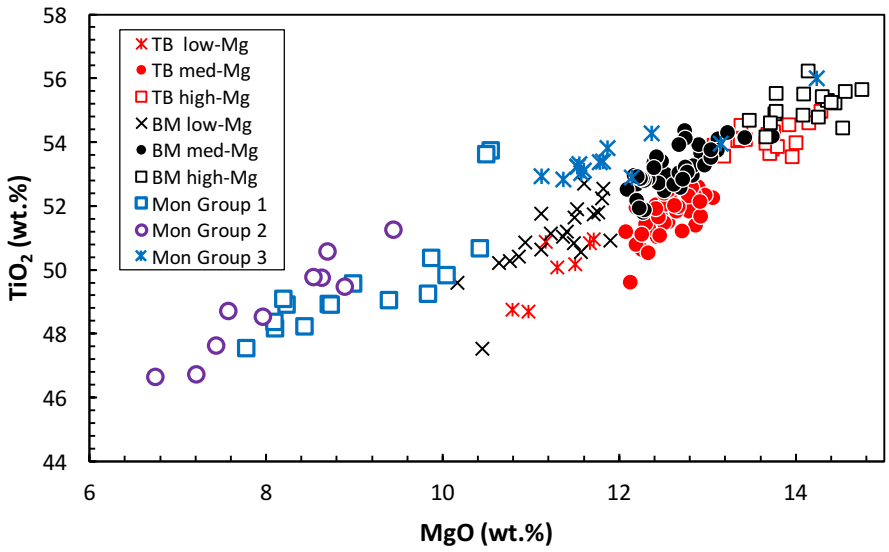

Figure 2.31: MgO (wt.%) versus TiO_2 (wt.%) plot for Mbuji-Mayi, Tshibwe and Monastery. Monastery data from Moore et al., 1992.

Comparison between Mbuji-Mayi and Tshibwe ilmenites

While both Mbuji-Mayi and Tshibwe ilmenites overall define negative correlations between Mg# and Nb, the low- and high-Mg groups from Mbuji-Mayi also define fairly strong negative correlations, whereas none of the Tshibwe ilmenite groups, individually, define significant correlations. Medium-Mg ilmenites from Tshibwe have trace element concentrations extending to higher values than those from Mbuji-Mayi. Low-Mg ilmenites from tshibwe display large ranges in Ni and Ga concentration within a fairly narrow range of Nb contents, whereas at Mbuji-Mayi, these low-Mg ilmenites display a wider range of Nb contents, extending to significantly higher values (Fig. 2.33).

Comparison with Monastery ilmenites

Monastery has the best-characterised ilmenite megacryst suite of any kimberlite, so it may represent a useful guide to help in interpreting the Mbuji-Mayi and Tshibwe ilmenite data. Overall, ilmenites from Mbuji-Mayi and Tshibwe are more Mg-rich and Cr-rich than Monastery ilmenites but have similar ranges of Al_2O_3 contents. Monastery ilmenites have higher FeO contents and lower MnO contents compared to Mbuji-Mayi and Tshibwe ilmenites.

The most noticeable difference between ilmenites from Monastery and those from Mbuji-Mayi and tshibwe is that the former have significantly lower mean contents of both Nb and Mg# than the latter two (Fig. 2.34). Additionally, Monastery ilmenites display markedly different variations of Nb with major and other trace elements than those from Mbuji-Mayi and Tshibwe which behave similarly. At Monastery, Group 1 ilmenites display a negative correlation between Nb and Mg#, whereas Group 2 and 3 ilmenites display virtually no correlation between Nb and Mg# (Fig. 2.34). In Group 2 ilmenites the lack of correlation is due to the fact that the significant variations in Nb and Mg# are uncorrelated, whereas in Group 3 it is because Nb contents are virtually uniform while Mg# is moderately variable (Fig. 2.34).

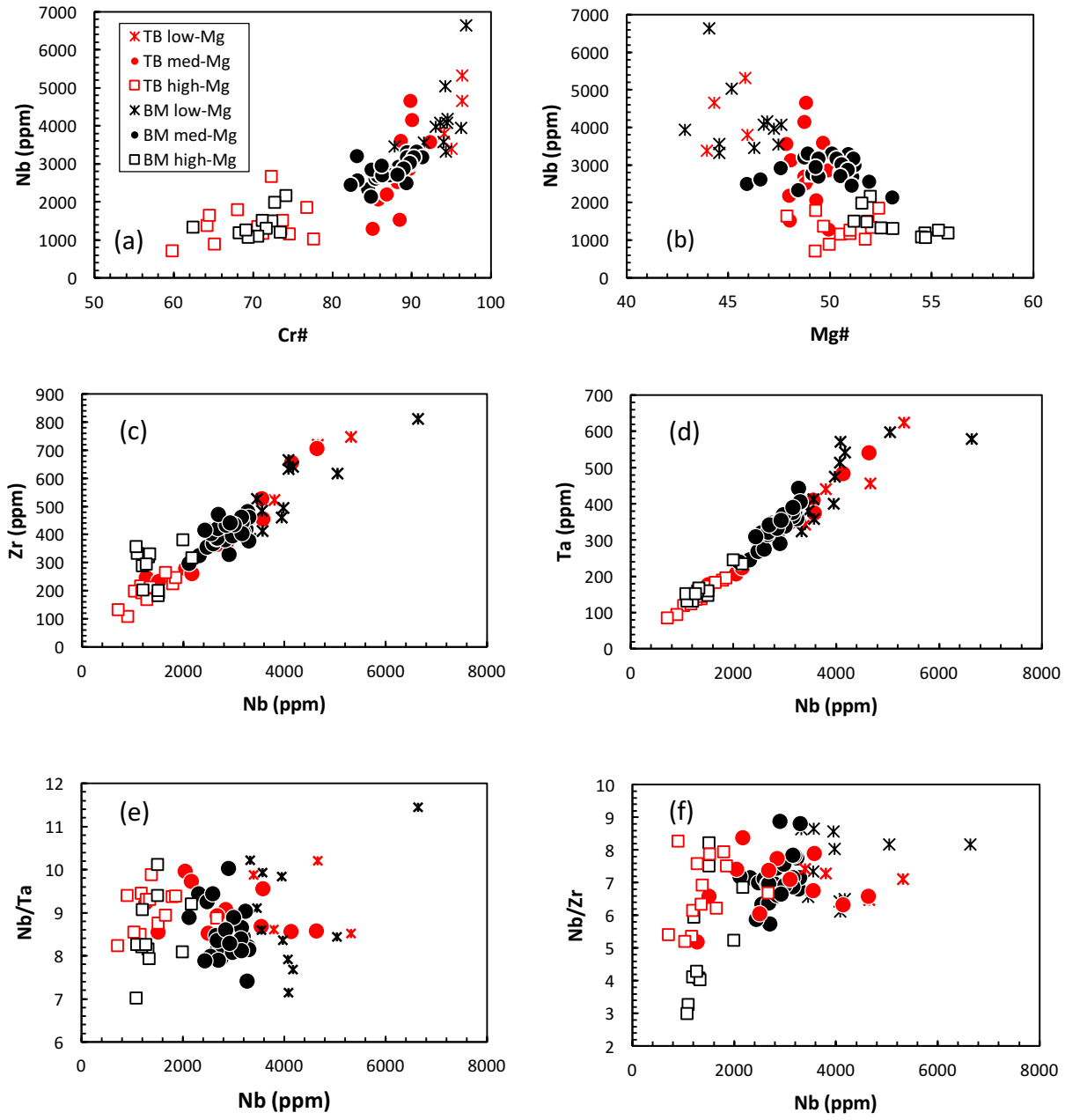

Figure 2.32: Variation of selected major and trace elements in Mbuji-Mayi and Tshibwe ilmenites. **(a)** MgO (wt.%) vs Nb (ppm). **(b)** Cr_2O_3 (wt.%) vs Nb (ppm). **(c)** MgO (wt.%) versus Zr (ppm). **(d)** Nb (ppm) versus Zr (ppm). **(e)** Nb/Ta ratio versus Nb (ppm). **(f)** Nb/Zr ratio versus Nb (ppm). Note the broad negative correlation of Nb with MgO and the broad positive correlations of Nb with Cr_2O_3, Zr and Ta. Note also the generally positive, but non-linear variation of Nb/Zr with increasing Nb content and the lack of coherent variation of Nb/Ta.

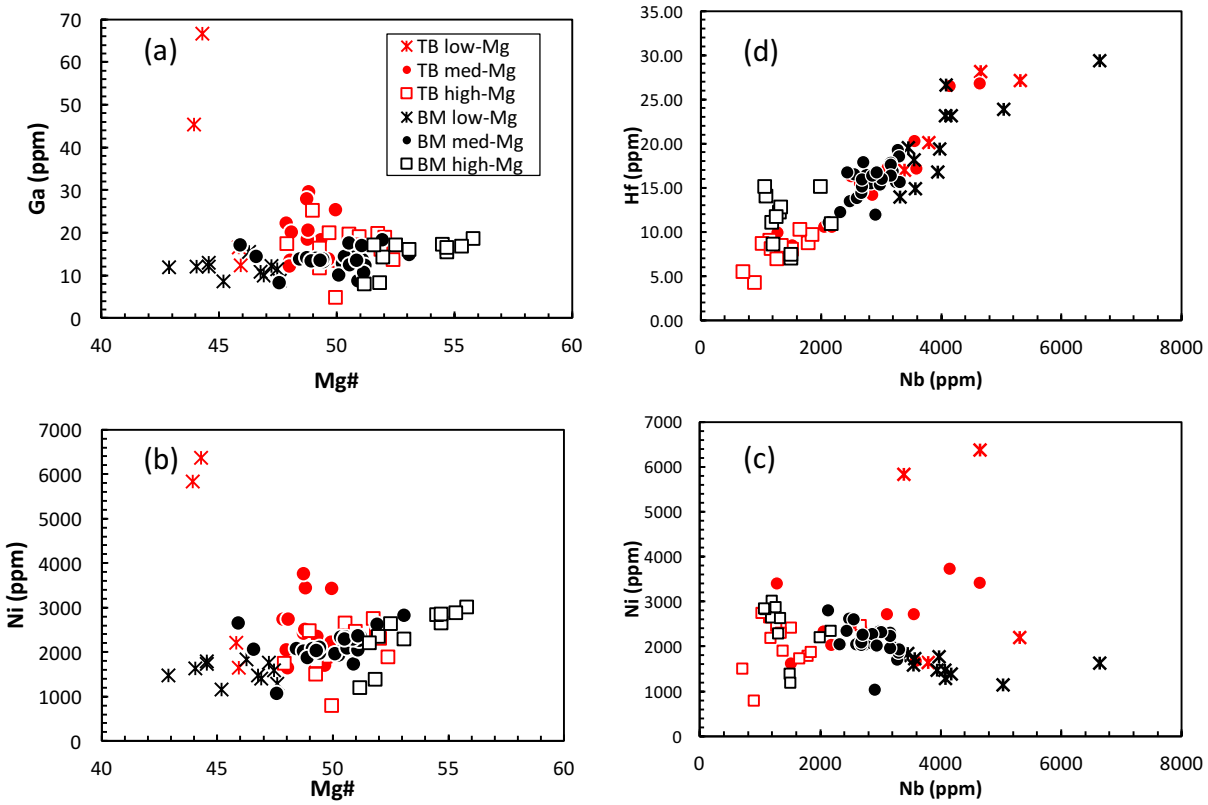

Figure 2.33: Variation of selected major and trace elements in Mbuji-Mayi and Tshibwe ilmenites. **(a)** MgO (wt.%) versus Ga (ppm). **(b)** Hf (ppm) versus Nb (ppm). **(c)** MgO (wt.%) versus Ni (ppm). **(d)** Ni (ppm) versus Nb (ppm).. Note the similar behavior of Ni and Ga with Mg content.

The changes in nature of Nb-Mg# covariations between Monastery Groups 1 and 2 was interpreted by Moore et al., (1992) as beng due to changes in the crystallizing mineral assemblage. The higher Nb and Mg# of the Group 2 Monastery megacrysts were interpreted by Moore et al., (1992) as likely crystallization products of an entirely separate batch of magma. In contrast, Nb in Mbuji-Mayi and Tshibwe ilmenites display a broad negative correlation with Mg# (Fig. 2.34) with no significant change in slope from the low- to the high-Mg ilmenite groups, and Nb contents are generally much higher (up to 6600 ppm Nb).

Similarly, the covariations of Zr and Nb differs markedly between Monastery on one hand, and Mbuji-Mayi and Tshibwe on the other. At Monastery, Zr initially sharply increases, with a Nb/Zr ratio of near unity, then decreases as Nb increases further, presumably due to onset of zircon crystallization (Fig. 2.35). In contrast, Zr and Nb in ilmenites from both Mbuji-Mayi and Tshibwe define a single tight positive correlation, with a Nb/Zr ratio of approximately 7 (Fig. 2.35).

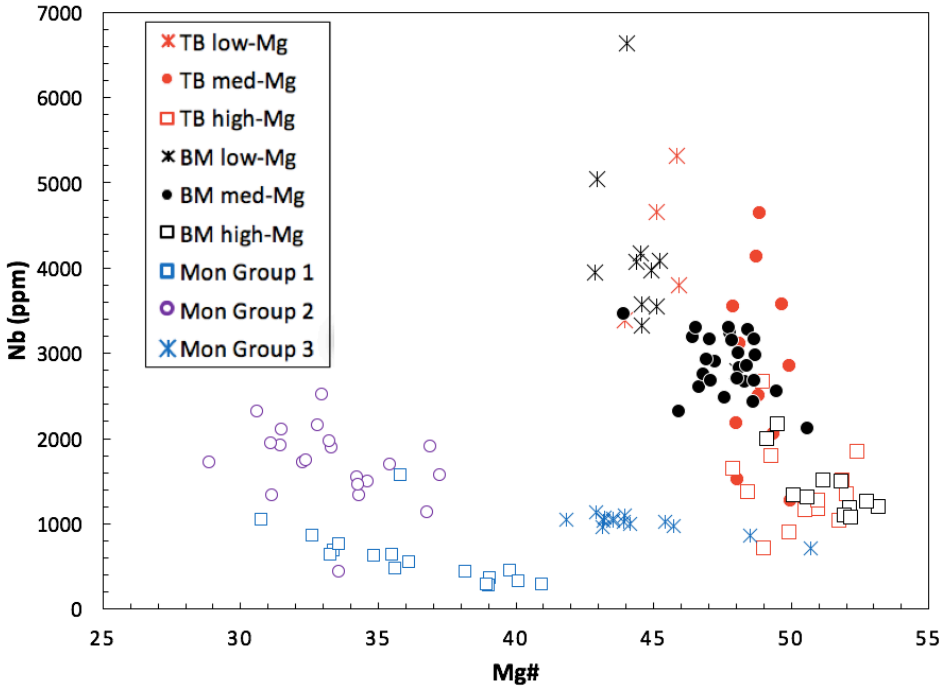

Figure 2.34: MgO (wt.%) versus Nb (ppm) plot of Mbuji-May (BM), Tshibwe(TB) and Monastery ilmenites (Mon). Monastery data from Moore et al., 1992.

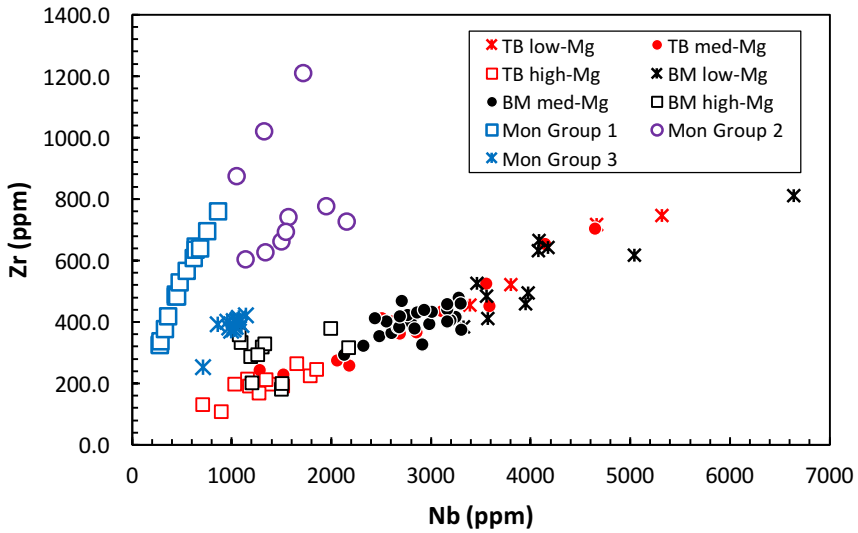

Figure 2.35: Nb (ppm) versus Zr (ppm) for of Mbuji-Mayi, Tshibwe and Monastery ilmenites. Note the different trends at Monastery and Mbuji-Mayi/Tshibwe, suggesting a difference in the mineral assemblage during ilmenite crystallization (e.g., Moore et al., 1992).

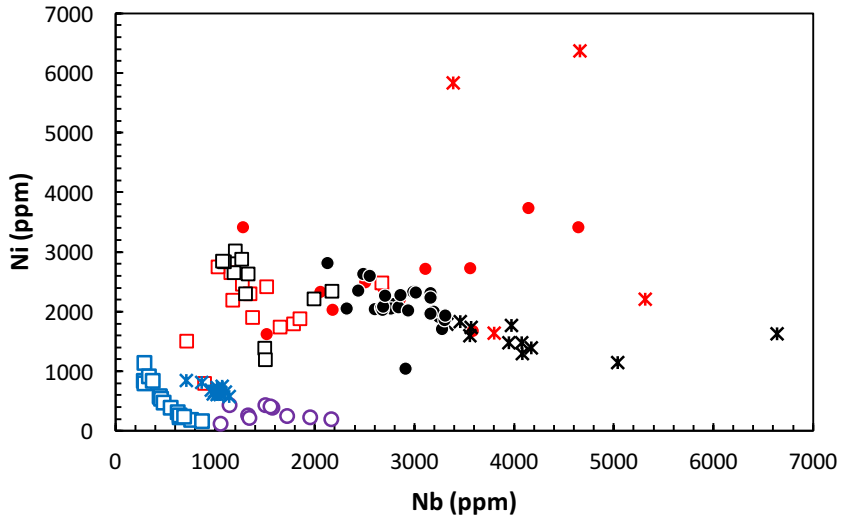

Figure 2.36: Nb (ppm) versus Ni (ppm) plot of Mbuji-Mayi (BM), Tshibwe (TB) and Monastery ilmenites (Mon). Monastery data from Moore et al., (1992).

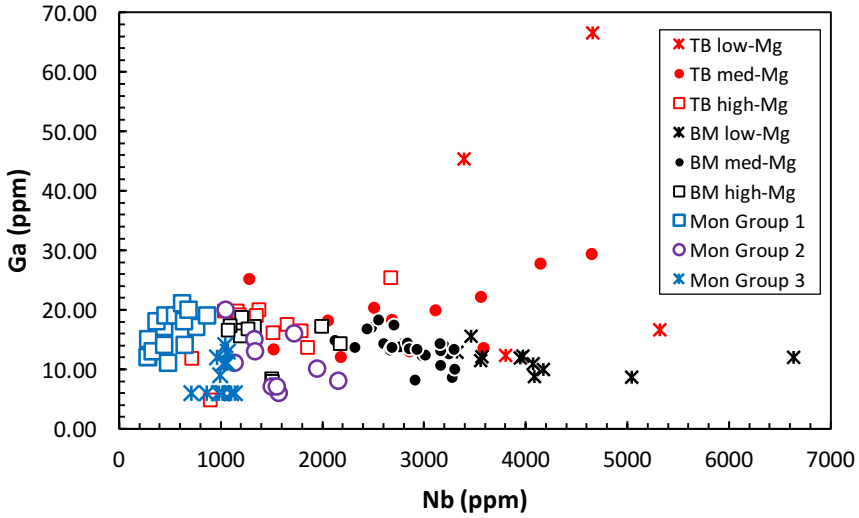

Figure 2.37: Nb (ppm) Versus Ga (ppm) plot of Mbuji-Mayi, Tshibwe and Monastery ilmenites (Mon).

The different groups of Monastery ilmenites all display decreases in Ni with increasing Nb content in Monastery Group 1 ilmenites. The Nb and Ni contents in Mbuji-Mayi and Tshibwe ilmenites are more scattered and higher than in Monastery ilmenites (Fig. 2.36).

2.5.3. DISCUSSION: ORIGIN OF MBUJI-MAYI AND TSHIBWE ILMENITES

Ilmenites from Mbuji-Mayi and Tshibwe investigated in this study have major and trace element systematics that appear to be explained by fractional crystallization and consistent with a megacrystic origin. The well-defined correlations of Mg# with Cr#, FeO, MnO, TiO_2 and Al_2O_3 contents, as well as Nb and Zr contents, displayed by Mbuji-Mayi and Tshibwe ilmenites support their likely origin by fractional crystallization of protokimberlitic magmas, undergoing extensive lithospheric assimilation.

Possible Fractional Crystallization sequence

Monastery has the best-characterised ilmenite compositions of any kimberlites. Some authors have explained that certain chemical variations (MgO – Nb, Cr_2O_3 – Nb, Nb – Zr, Nb – Ni and Nb – Ga variations) shown by Monastery ilmenites could be interpreted as possible changes in the precipitating mineral assemblage (Moore et al., 1992; Griffin et al., 1997).

At Mbuji-Mayi and Tshibwe there are not signficant changes in any of these diagnostic correlation diagrams (e.g. Fig. 2.38). It is therefore argued that Mbuji-Mayi and Tshibwe ilmenites do not likely show evidence of changes in the precipitating mineral assemblage throughout the crystallization. The increase of Nb throughout the crystallization of Mbuji-Mayi and Tshibwe ilmenites, suggested that ilmenite was a minor phase in the crystallization assemblage relative to silicate minerals (e.g., clinopyroxene, phlogopite, olivine) in which Nb is highly incompatible.

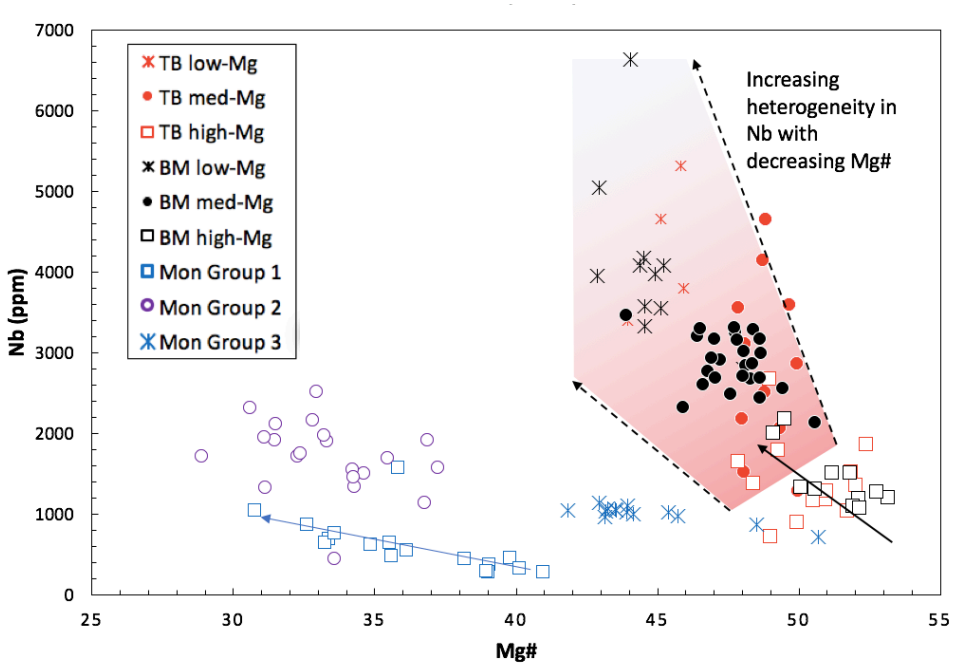

Figure 2.38: Mg# versus Nb (ppm) plot of Mbuji-Mayi and Tshibwe ilmenites. Note the tight negative correlation of Mg# with Nb in Mbuji-Mayi high-Mg ilmenites. Monastery data sources as in …

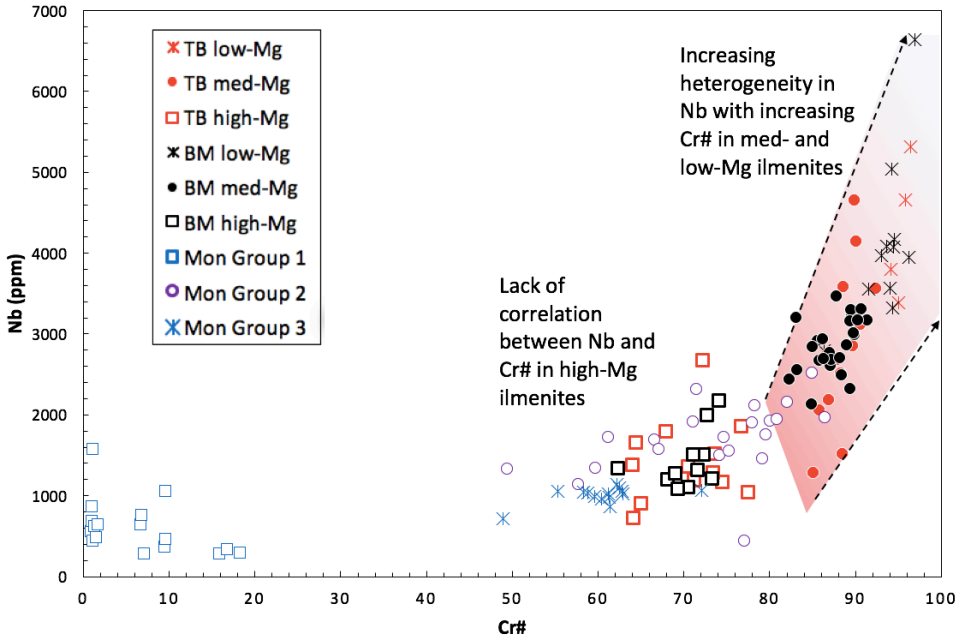

Figure 2.39: Cr# versus Nb plot of Mbuji-Mayi and Tshibwe ilmenites. Monastery data sources as in…

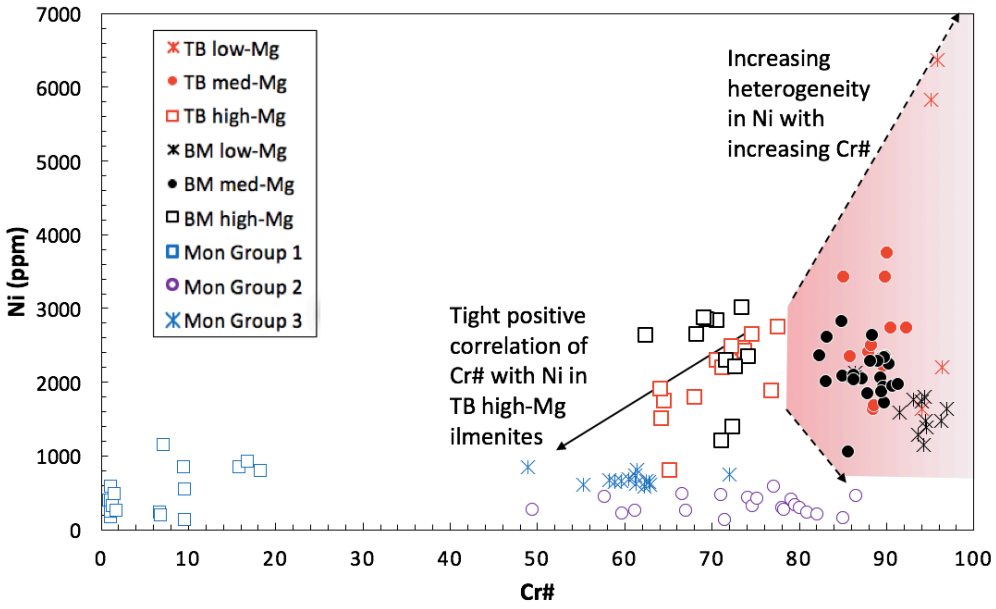

Figure 2.40: MgO (wt.%) versus TiO_2 (wt.%) plot in Mbuji-Mayi and Tshibwe ilmenites.

The tight correlation of Nb and Zr concentration data at a nearly constant slope argues against the presence of zircon as a fractionating phase during the crystallization of the ilmenites reported here from Mbuji-Mayi and Tshibwe. If zircon had crystallized, Zr content would be expected to fall or there would at least have been a significant change in the slope of the Nb-Zr trend at the start of zircon crystallization. While zircon megacrysts have been reported from Mbuji-Mayi (Schärer et al., 1997; Pivin et al., 2013), it is likely either that they did not crystallize simultaneously with the ilmenite megacrysts, or that the ilmenites reported here do not span the full range of their fractional crystallization sequence.

Griffin et al. (1997) showed that phlogopite is the only megacryst phase in which Ga is compatible. They interpreted the decrease of Ga content with increasing of Nb content as an indication of significant phlogopite crystallization. In our Mbuji-Mayi and Tshibwe dataset, there is no significant difference in the Ga range between the most primitive ilmenite megacrysts and the most evolved. Furthermore, there are no systematic changes in the Nb-Ga or MgO-Ga trends throughout the ilmenite crystallization history (Fig. 2.33 and Fig. 2.37). Phlogopite megacrysts have never been reported in the megacryst suite at Mbuji-Mayi (Mvuemba, 1980; Pivin et al., 2009; 2012).It is therefore argued that Mbuji-Mayi and Tshibwe ilmenites investigated in the present study do not show any evidence of phlogopite as a fractionating phase during the crystallization of ilmenite.

Evidence of fractional crystallization

The compositional variation of high-Mg ilmenites is consistent with nearly pure fractional crystallization. They show positive correlations of Cr# with Mg# and Ni (and a weaker positive correlation of Mg# with Ni), as well as negative correlation of Mg# with Nb (only seen clearly at Mbuji-Mayi. All of these are consistent with their compositional variations being explained by fractionation of an assemblage containing pyroxene (±garnet) and olivine in which ilmenite is a minor component. The high-Mg ilmenites closely resemble Monastery Group 1 ilmenites, and like them, show virtually no correlation of Cr# with Nb.

Evidence of significant lithospheric assimilation (+fractional crystallization)

The following observations in medium- and low-Mg ilmenites argue for lithospheric assimilation: (1) Cr# correlates negatively with Mg# and Ni (at least for Mbuji-Mayi), and (2) Cr# correlates positively with Nb, neither of which can plausibly be explained by fractional crystallization alone. These variations could possibly result from assimilation/melt-rock reaction, with fractioanal crystallization, of Cr- and Nb-rich materials.

Mbuji-Mayi and Tshibwe medium- and low-Mg ilmenites display a broad increase of Cr_2O_3 content (Fig. 2.39). As shown above, there is no evidence of cessation of silicates crystallization that could possibly explain the increase of Cr_2O_3 content. This increase can only reasonably be explained by assimilation processes.

Comparison of nature and mineralogy of assimilants at Mbuji-Mayi and Tshibwe

The differences between low- and medium-Mg ilmenites from Mbuji-Mayi and Tshibwe on the Mg# versus Ni plot (Fig. 2.33b) also suggest lithological differences in the lithospheric assimilants at the two locations. Ni, in particular is far more scattered in the ilmenites from Tshibwe, and many scatter to high Ni values. This suggests that the assimilant incorporated at Tshibwe may contain more olivine (and/or possibly Ni-rich sulphides), than at Mbuji-Mayi. This would be consistent with a more infertile SCLM-derived assimilant at Tshibwe, whereas the assimilant at Mbuji-Mayi is Ni-poor in comparison and could represent a more fertile assimilant such as fertile lherzolite.

Evidence for birfucating evolution trends: pure fractional crystallization versus assimilation+fractional crystallization

Mbuji-Mayi and Tshibwe ilmenites data appear to form two separate diverging trends, in plots of Mg# versus Cr# and Cr# versus Ni content, that converge at a common primitive composition with Mg# (≈52), high Cr# (≈80) and moderate Ni (≈2500 ppm). The trends defined by the high-Mg ilmenites are tightly defined and display positive correlations between Mg#, Cr# and Ni contents. The trends defined by the med- and low-Mg ilmenites are well less defined and/or more scattered (depending on the plot) and display increasing Cr# with decreasing Mg# as well as generally decreasing Ni with increasing Cr#. At Tshibwe, these trends are not clearly displayed and the data shows a great deal of scatter in Ni (to low and high values) that increases with increasing Cr#. At MbujiM-Mayi, both groups (i.e., high- and medium &low-Mg ilmenites) display decreasing Ni and increasing Nb with decreasing Mg#, although the decrease in Ni is steeper and the increase in Nb is shallower for a given decrease in Mg# for the high-Mg ilmenites compared to the low- and medium-Mg ilmenites. The trends displayed by the high-Mg ilmenites appear to be caused almost entirely by fractional crystallization (i.e., decrease in Mg#, Cr# and Ni and increase of Nb), whereas the trends of the low & med-Mg ilmenites is more consistent with fractional crystallization combined with very significant assimilation of (lithologically and chemically) heterogenous lithospheric mantle material (i.e., decrease in Mg# combined with variable, but generally decreasing, Ni, increase in Cr# and steep (but scattered)

The fact that the trends formed by the two ilmenite groups (high-Mg vs. low & med-Mg) converge at a fairly primitive composition strongly suggests that all ilmenites at Mbuji-Mayi and Tshibwe formed either by (1) fractionation with virtually no assimilation (high-Mg group) or (2) fractionation plus very significant lithospheric assimilation (low & med-Mg groups). There is no indication of a transition from nearly pure fractionation to fractionation + assimilation with increasing megacryst parental magma differentiation. This is unlike at Monastery, where the Group 2 ilmenites (which appear to reflect significant lithospheric assimilation) appear to have formed from magmas that had previously crystallised Group 1 ilmenites (i.e., ones formed by pure fractional crystallization). Similarly, many cpx megacryst suites from southern Africa appear to show the effects of significant lithospheric assimilation only after an initial period of apparently nearly pure fractional crystallization. It is unclear why the ilmenite evolution at Mbuji-Mayi and

Tshibwe appears to follow a different pattern than at Monastery. It is possible that in highly infertile portions of the lithosphere, that a crystallizing megacryst parental magma would not have sufficient heat to cause significant melting and assimilation of the surrounding refractory wall-rock. It is also important to point out, that all Mbuji-Mayi and Tshibwe ilmenites span a much narrower range of Mg# values than those of the Monastery suite (53-41 for Mbuji-Mayi and Tshibwe, versus 49-29 for Monastery) and so the ilmenites might record a much shorter interval of crystallization than at Monastery.

Evidences against a Metasomatic origin for Mbuji-Mayi abd Tshibwe ilmenites.

In the standard metasomatic hypothesis (e.g., Kopylova et al., 2009; Moore and Belousova, 2005) the melts from which megacrysts initially form are kimberlitic. Kimberlits are rich in both Cr and Ni (typically up to about 2000 and 1500 ppm, respectively), as well as Mg. Therefore, it is difficult to envision forming ilmenite megacrysts that are extremely Cr-rich (Cr#≈ 90+) but relatively Mg-poor (Mg# ≈40) from a kimberlite magma. If such a suitable highly enriched and moderate Mg metasomatic agent was to exist, it might be possible to explain the negative correlation between Cr# and Mg# in the low- and medium-Mg ilmenites by a process of progressively greater assimilation of olivine-rich peridotite. However, such a progression would require up-temperature evolution (the magma becoming progressively warmer and able to assimilate more and more peridotite) without significant crystallization, which would presumably crystallize an olivine-containing mineral assemblage that would remove Mg from the system. This is a major problem for the metasomatic hypothesis since a heat source to provide such an increase in temperature is unknown. This is a major problem for the metasomatic hypothesis since a heat source to provide such an increase in temperature is unknown.

Finally, at the highest temperatures and greatest degrees of peridotite assimilation, the Cr-rich to Mg-rich metasomatic ilmenite progression would terminate at the start of the high-Mg ilmenite trend, which is most plausibly explained by simple down-temperature fractionation without any significant assimilation. To have such a marked change, from high degrees of assimilation to virtually no assimilation seems implausible.

2.5.4. SUMMARY - ILMENITES

Mbuji-Mayi and Tshibwe ilmenites have been investigated geochemically. At each locality, three groups of ilmenites have been distinguished. The high-Mg ilmenites, characterized by low Cr#, high Mg# and the lowest contents of most trace elements, have been interpreted as primitive ilmenite megacrysts. The second group, the medium-Mg ilmenites, are characterized by intermediate Cr#, Mg# and trace element contents. The third group, the low-Mg ilmenites, are characterized by the highest Cr# content, low Mg# contents and higher contents of most trace elements.

A tentative petrogenetic model has been proposed to explain the chemical variations displayed by Mbuji-Mayi and Tshibwe ilmenites. The positive correlations of Cr# with Mg# and Ni content, as well as the negative correlation of Mg# with Nb content are consistent with nearly pure fractional crystallization. The compositional variations in these high-Mg ilmenites are similar to those display by Monastery Group 1 ilmenites. Medium- and low-Mg ilmenites display negative correlations between Cr#, Mg# and Ni contents, in addition to positive correlations of Cr# with Nb content. Lithospheric assimilation, of Cr- and Nb-rich materials, with fractional crystallization could possibly explain the compositional variations displayed by medium- and low-Mg ilmenites. The assimilant appear to have incorporated an infertile SCLM at Tshibwe, while at Mbuji-Mayi a more fertile SCLM appear to be a good candidate.

Temperature as well as geochemical constraints appear to argue against a metasomatic origin hypothesis for Mbuji-Mayi and Tshibwe ilmenite.

2.6. THE TSHIBWE CR-POOR CLINOPYROXENE MEGACRYST SUITE

2.6.1. MAJOR ELEMENT SYSTEMATICS

Based on the classification diagram (Al_2O_3 versus Cr_2O_3 plot) of Nimis (1998), peridotitc clinopyroxenes were distinguished from those of megacrystic origin (see section 2.3 of chapter two). Major element Data of Tshibwe clinopyroxene megacrysts are given in Table 36 of the Appendix. Two groups of clinopyroxene megacrysts can be distinguished at Tshibwe, based on their Ca#: A subcalcic group (with Ca# ranging from 36.3 to 41.9) and a calcic group (with Ca#

ranging from 42.7 to 47.3). Subcalcic clinopyroxenes are characterized by relatively low Mg# values (ranging from 87.0 to 88.9) and low TiO_2 contents (ranging from 0.12 to 0.22 wt.%). In contrast, the calcic clinopyroxenes have higher Mg# (ranging from 89.2 to 90.3; Fig. 2.41b) and higher TiO_2 content (ranging from 0.14 to 0.26 wt.%; Fig. 2.41d). Both groups have similar ranges of Cr_2O_3 content, with calcic clinopyroxenes extending to slightly lower Cr# values (13.8 to 29.8) than subcalcic ones (18.3 to 27.6). In both the subcalcic and calcic groups, Cr# shows steady decreases with increasing Ca# (and, therefore with decreasing crystallization temperature). Subcalcic and calcic clinopyroxenes have nearly identical ranges of Al_2O_3 content, as well as similar ranges of MnO and Na_2O content.

Mbuji-Mayi clinopyroxene megacrysts have been investigated by Pivin et al., (2009) and Pivin (2012). Mbuji-Mayi clinopyroxene megacrysts, like those from Tshibwe, span wide ranges in Ca# and Mg#, but these ranges are offset to significantly higher Ca# and Mg# values (Fig. 2.41). In constrast, Mbuji-Mayi megacrysts have similar to those at Tshibwe (≈12), but they extend to much higher maximumvalues (≈80 vs. 30; Fig. 2.41). In terms of TiO_2 and Al_2O_3 contents, they fall within the range of Tshibwe megacrysts, but have lower average values, although they extend to higher Na_2O contents. A major difference between the two suites is that, with increasing Ca#, the more calcic Mbuji-Mayi clinopyroxene extend to significantly higher Mg# and Cr# than calcic Tshibwe clinopyroxene megacrysts. Such increases in Mg# and Cr# with decreasing crystallization temperature is also seen in some southern African megacryst suites (e.g., Monastery and Orapa; Moore, 1986, this study) and is plausibly explained by assimilation of Cr- and Mg-rich lithospheric peridotite by late-stage megacryst parental magmas (see chapter one).

2.6.2. TRACE ELEMENT AND Sr ISOTOPE SYSTEMATICS

Trace element and Sr isotopic data for the Tshibwe clinopyroxene megacrysts are given in in Tables 37 and 38 of the Appendix. Tshibwe subcalcic and calcic clinopyroxene megacrysts are characterized by relatively uniform trace element patterns with enrichments in the LREE and MREE as well as negative Pb, Zr, Hf and Ti anomalies on primitive mantle-normalised incompatible element diagrams (Fig. 2.42). However calcic megacrysts are more enriched in incompatible elements such as the LREE, HFSE (Zr, Hf, Ta, Ti) and Sr (Fig. 2.42). Subcalcic megacrysts have $(Nd/Yb)_N$ ratios ranging from 12.3 to 23.3, whereas calcic megacrysts have

$(Nd/Yb)_N$ ratios ranging from 20.6 to 41.7. However, calcic megacrysts are more depleted in Ba than the subcalcic ones.

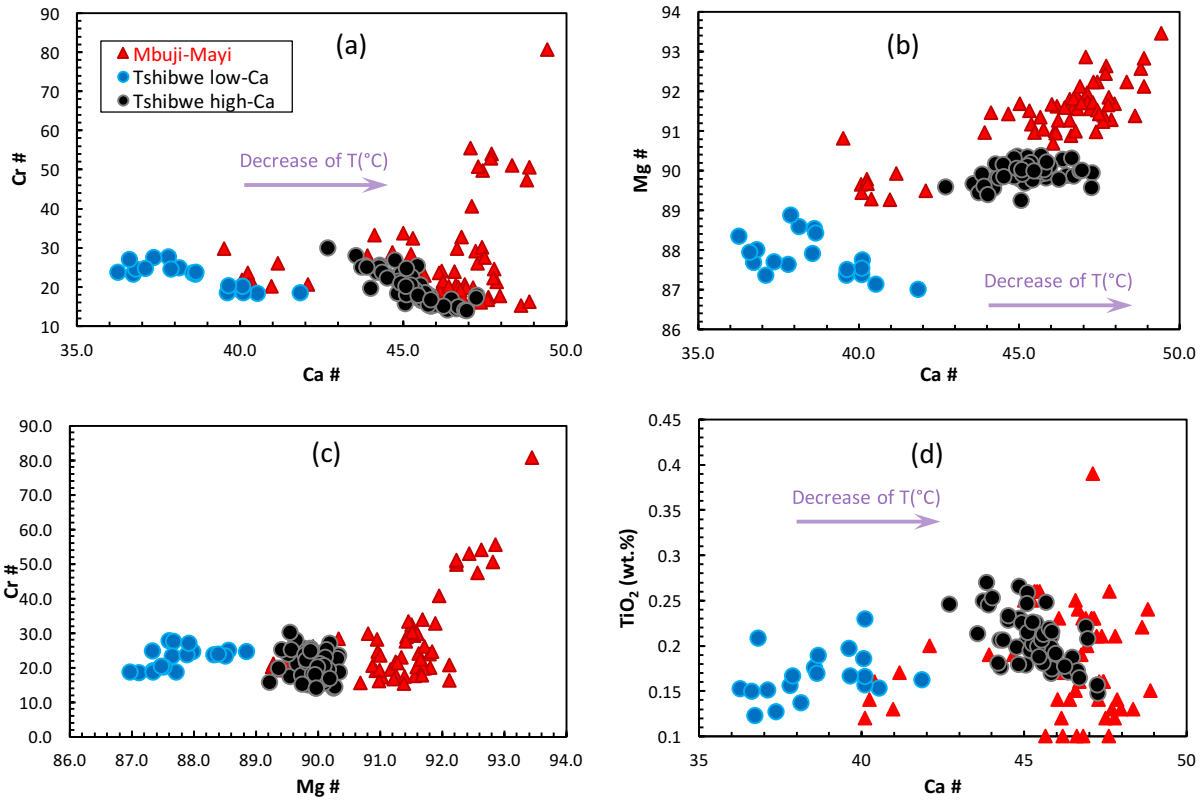

Figure 2.41: Plots of Ca# and Mg# versus selected major element contents and indices in Tshibwe clinopyroxene megacrysts. **(a)** Ca # versus Cr #. **(b)** Ca # versus Mg #, **(c)** Mg# versus Cr#, **(d)** Ca # versus TiO_2. Distinct low-Ca and high-Ca groups of Tshibwe megacrysts can be distinguished. Note the steady decrease of Cr# with increasing Ca# in low-Ca and high-Ca Tshibwe megacrysts. Cr# values decrease with increasing Ca# in each group, whereas with increasing Ca# Mg# values show a general decrease in the low-Ca cpx and little change in the high-Ca cpx megacrysts. TiO_2 content shows a general increase with Ca# in the subcalcic group and decreases with increasing Ca# in the calcic group, possibly due to co-precipitation with ilmenite. Mbuji-Mayi megacrysts data is from Pivin, (2012).

Positive correlations are observed between Ca# values and incompatible element concentrations (such as the LREE, HFSE and Sr), and negative correlations are observed with compatible elements (e.g., Ni) in Tshibwe megacrysts (Fig. 2.43). Moreover, incompatible elements tend to be positively correlated with one another, displaying strong (e.g., Hf vs Zr) to weak (e.g., Sc vs Sr) correlations (Fig. 2.43). Finally, $(Nd/Yb)_N$ and Zr/Sm ratios show systematic increases, and $(Lu/Hf)_N$ shows a systematic decrease with increasing Ca# (Fig. 2.43).

Compared to those from Tshibwe, Mbuji-Mayi clinopyroxene megacrysts (Pivin et al., 2009; Pivin, 2012) have similar LREE abundances but more variable MREE and HREE abundances (extending to both higher and lower values than Tshibwe) for the subcalcic clinopyroxenes. The Mbuji-Mayi calcic clinopyroxenes are, in most cases, more enriched in the REE overall, but particularly in the LREE, compared to those from Tshibwe. Also, there is a higher degree of LREE and MREE variation at Mbuji-Mayi than at Tshibwe, indicated by the wide range of $(Nd/Yb)_N$ ratios ranging from 9.7 to 151 for subcalcic Mbuji-Mayi megacrysts (9.7 to 21.0 if the single anomalously HREE-depleted sample is not included) and $(Nd/Yb)_N$ ratios ranging from 7.4 to 72.7 for calcic Mbuji-Mayi megacrysts.

Tshibwe clinopyroxene megacrysts have a restricted variation of $^{87}Sr/^{86}Sr$ ratios from 0.7024 to 0.7036, extending from below to within the range of published values for Group I kimberlites (e.g., Kramers et al., 1981; Smith, 1983, Becker & le Roex, 2006). Tshibwe calcic clinopyroxene megacrysts have an even more restricted span of Sr isotope values ($^{87}Sr/^{86}Sr$ = 0.7030 – 0.7036) in the upper part of this range and a weak positive correlation of Sr isotope ratios with Ca# (Fig. 2.44). It is noteworthy to mention that Weiss and Demaiffe (1985) reported Sr isotope composition for two diopside megacrysts ($^{87}Sr/^{86}Sr$ value of 0.7030 and 0.7032).

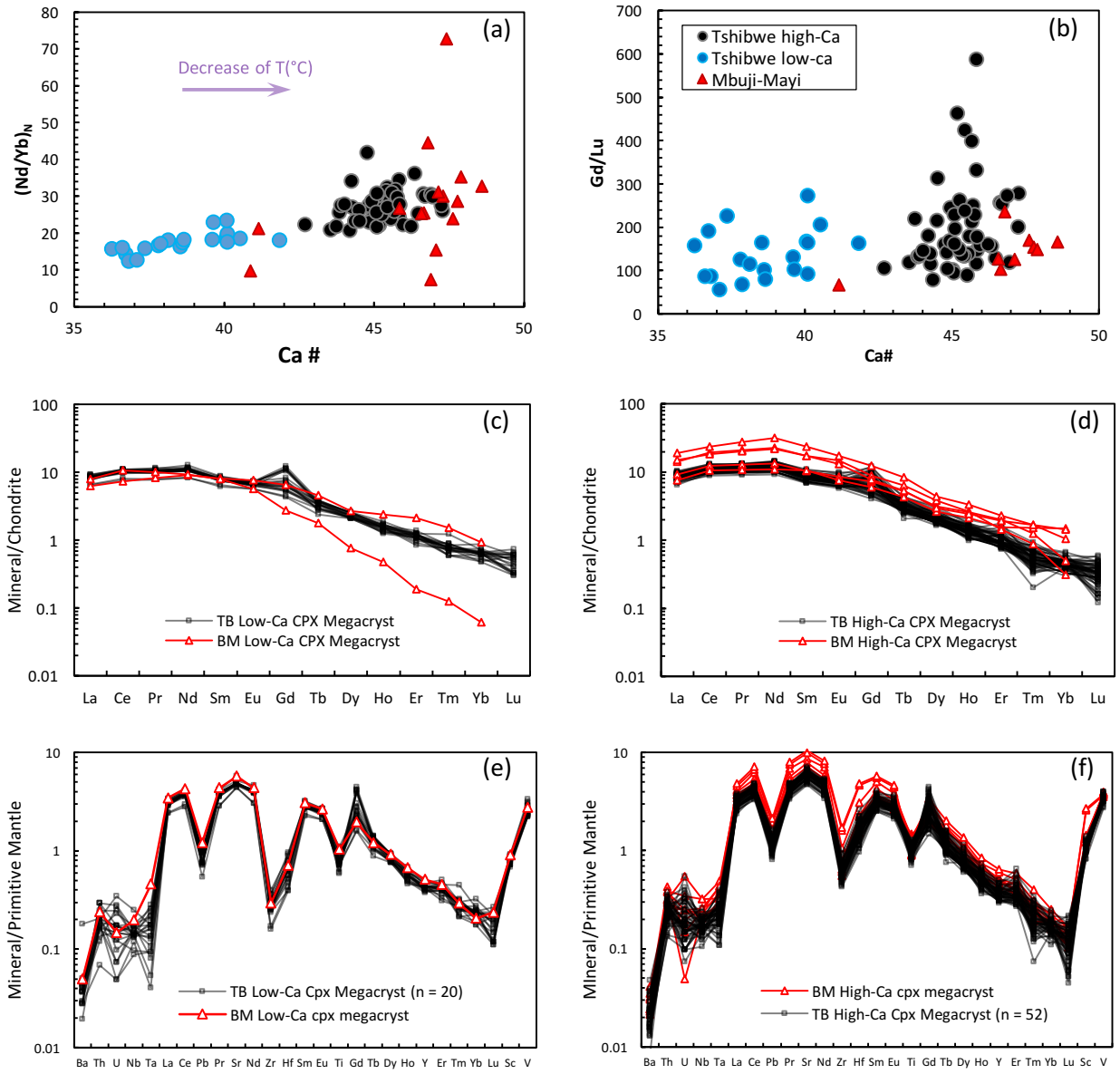

Figure 2.42: Variation of selected trace elements in Tshibwe clinopyroxene megacrysts. **(a)** Ca# versus $(Nd/Yb)_N$. **(b)** Ca# versus $(Gd/Lu)_N$. **(c)** Chondrite-normalized plot of Tshibwe and Mbuji-Mayi (representative data) Low-Ca clinopyroxene megacrysts. **(d)** Chondrite-normalized plot of Tshibwe and Mbuji-Mayi High-Ca clinopyroxene megacrysts. **(e)** Primitive mantle-normalized plot of Tshibwe low-Ca clinopyroxene megacrysts. **(f)** Primitive mantle-normalized plot of Tshibwe high-Ca clinopyroxene megacrysts. Mbuji-Mayi data are from Pivin et al., (2009) and Pivin, (2012). Normalizing values are from McDonough and Sun (1995). LREE increase with the decrease of the crystallization temperature. High-Ca megacrysts show a broad decrease of MREE with increasing Ca#. Note also the higher overall REE contents in Mbuji-Mayi megacrysts compated to Tshibwe.

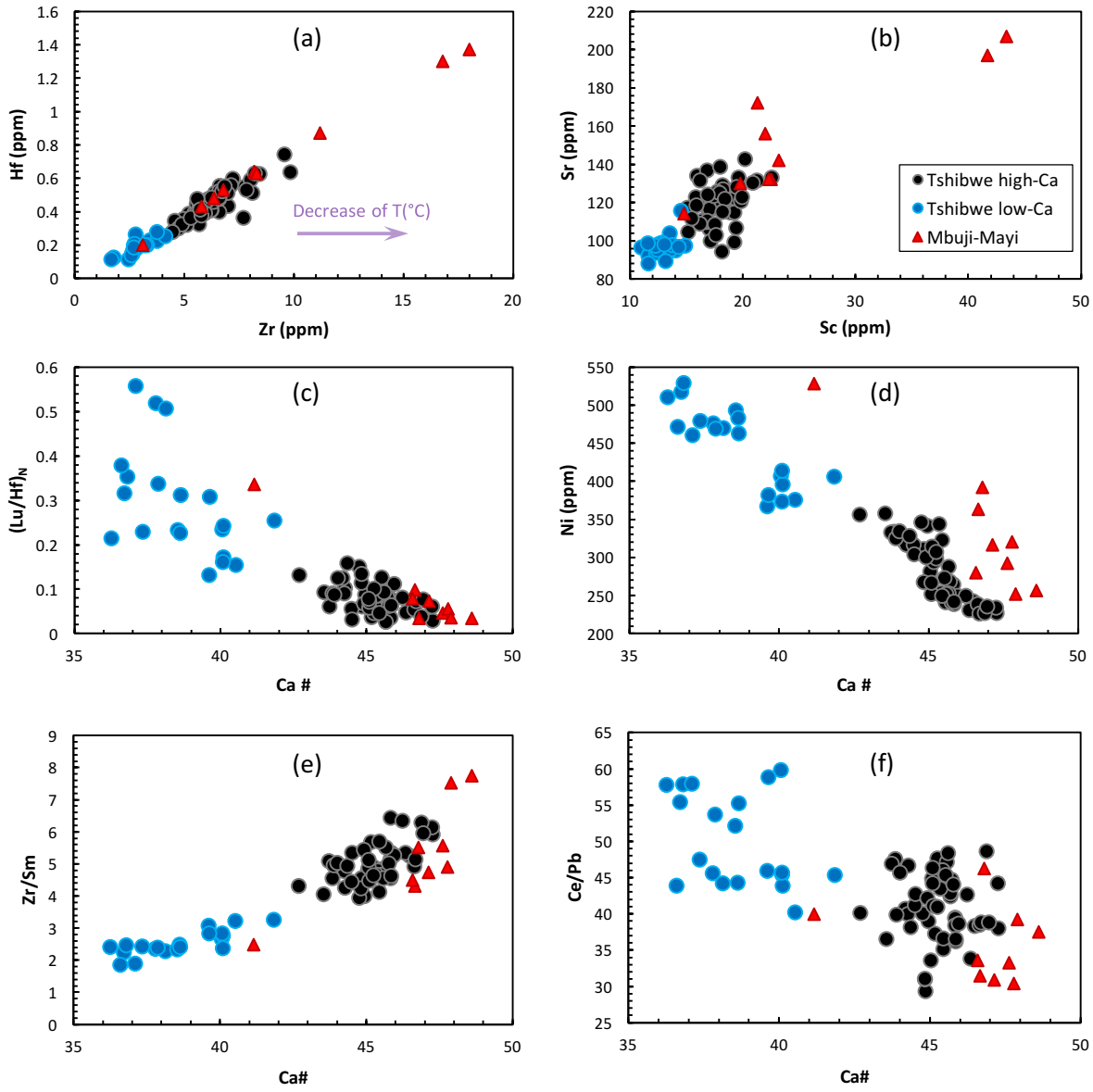

Figure 2.43: Plots of concentrations and ratios of selected trace elements in Tshibwe clinopyroxene megacrysts **(a)** Zr (ppm) versus Hf (ppm **(b)** Sc (ppm) versus Sr (ppm). **(c)** Ca# versus $(Lu/Hf)_N$. **(d)** Ca# versus Ni (ppm). (e) Ca# versus Zr/Sm. (f) Ca# versus Ce/Pb.). Note the positive correlations of Zr with Hf and Sc with Sr contents. Note also the smooth decreases in (Lu/Hf)N and Ni concentration, and increase of Zr/Sm with increasing Ca#. Finally, note the distinctly higher average Ce/Pb ratios in the low-Ca compared to the high-Ca clinopyroxene megacrysts. Data sources for Mbuji-Mayi as in Fig. 2.42.

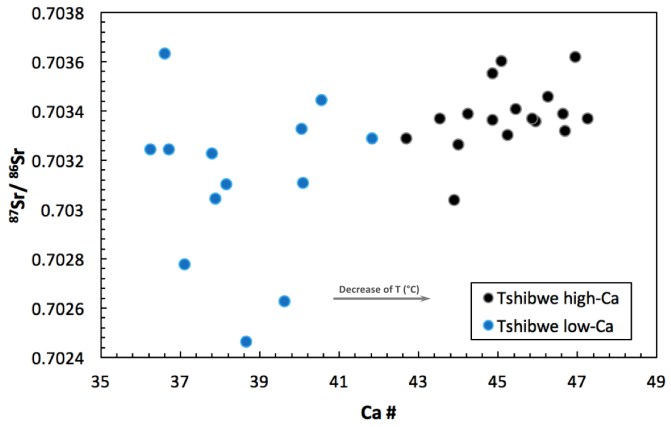

Figure 2.44: Ca# versus measured $^{87}Sr/^{86}Sr$ ratios of Tshibwe clinopyroxenes megacrysts. Note the higher values for the calcic megacrysts.

2.6.3. DISCUSSION

The subcalcic clinopyroxene megacrysts show trends of decreasing Mg# and Cr# with increasing Ca# (i.e., with decreasing crystallization temperatures), a pattern that is consistent with derivation from a magma that is undergoing compositional evolution entirely (or nearly entirely) due to fractional crystallization. (Fig. 2.41). However, there are major increases in both Cr# and Mg# values that occurs between the crystallization of the lowest temperature subcalcic and the highest temperature calcic Tshibwe clinopyroxene megacrysts (Fig. 2.41). If, as inferred in Chapter I from southern African megacrysts, both are derived from a common evolving parental magma an explanation for this would require the addition of MgO and Cr_2O_3-rich material to the magma. While it is possible that the subcalcic and calcic megacrysts at Tshibwe are not genetically related, this seems implausible given that both incompatible and compatible elements and elemental ratios (e.g., Ni, $(Nd/Yb)_N$) and Sr isotope ratios show consistent variations with Ca# in the entire Tshibwe cpx megacryst suite. Rather, the generally good correlations would seem to strongly argue for a genetic relationship between the subcalcic and calcic megacrysts at Tshibwe.

Constraints on assimilation and SCLM composition inferred from Tshibwe megacrysts.

The differences between Tshibwe subcalcic and calcic clinopyroxene megacrysts can be plausibly explained in terms of the nature of lithospheric materials assimilated at Tshibwe. Calcic

megacrysts most likely crystallized at lower melt/wallrock ratios, where the effects of lithospheric assimilation would have been most noticeable, unlike the more primitive subcalcic megacrysts, which likely formed at higher melt/wallrock ratios.

In previous sections of this Chapter, evidence has been presented that the SCLM beneath Tshibwe is both relatively depleted in incompatible elements and is dominantly characterized by garnet-poor lherzolite. The following elemental trends suggest that assimilation of lithospheric materials have occurred:

(1) The increase of Mg# and Cr# at the onset of the crystallization of calcic megacrysts;
(2) The increase of LREE/HREE at higher Ca# (low temperatures);
(3) The increase of Sr isotope composition at higher Ca# (low temperatures);
(4) The increase of Zr/REE ratios with increasing of Ca# (low temperatures);
(5) The decrease in Ce/Pb ratios at higher Ca# values (see section 1.7.3 of chapter one).

The following elements suggest that the nature of the assimilant is likely infertile and weakly metasomatised at Tshibwe relative to Mbuji-Mayi:

(1) The lack of increase of Mg# displayed by Tshibwe calcic cpx megacrysts;
(2) The decrease of some diagnostic trace element ratios like Ce/Pb with decreasing of Ca# (and therefore declining temperatures), as observed in Kalkput cpx megacrysts;
(3) The increase of incompatible element concentrations, LREE/MREE ratios and Sr isotope compositions are relatively weak (e.g., compared to what has been observed in Orapa cpx megacrysts where the increase in those elements with declining temperatures are stronger);
(4) Mbuji-Mayi calcic megacrysts display greater ranges of Cr#, Mg# and Na_2O content than Tshibwe calcic megacrysts. This is consistent with a more infertile lithosphere at Tshibwe compared to Mbuji-Mayi, inferred from peridotitic garnet and clinopyroxenes from both localities.

Tshibwe calcic megacrysts have higher Mg# than subcalcic ones, and these higher Mg# values remains relatively constant with increasing Ca#. But the Cr# values do not remain constant, instead they drop significantly with increasing Ca#. As the lithospheric mantle at Tshibwe is likely depleted (higher proportion of depleted peridotites. See evidences presented in sections 2.3, 2.4 and 2.5) the most evolved megacrysts would have Cr# and Mg# values decreasing with the

decrease of Ca# (see section 1.7.3 of chapter one). However, in this case, only Cr drops while Mg remains constant. The drop in Cr# corresponds to the onset of ilmenite crystallization. It was shown earlier in this chapter that Mbuji-Mayi and Tshibwe ilmenites are enriched in Cr (up to 6 wt.% Cr_2O_3) content. It is argued that at Tshibwe the drop in Cr content in calcic megacrysts likely explained by the onset of crystallization of Cr-rich ilmenites, is not compensated by the assimilation of lithospheric materials as the incorporated SCLM is infertile (lherzolites with low modal proportion of garnet and clinopyroxenes) relative to the one at Mbuji-Mayi.

Mbuji-Mayi calcic megacrysts display higher degree of major and trace elements variation than Tshibwe calcic megacrysts. This is consistent with the inference made from xenocryst geochemistry, that the SCLM beneath Mbuji-Mayi is largely enriched and extensively metasomatised relative to that beneath Tshibwe.

Sublithospheric sources

The Tshibwe and Mbuji-Mayi megacrysts display diagnostic trace element ratios similar to those of southern African Group 1 kimberlites and OIB. Asthenospherically derived melts such as OIB have lower Ce/Pb than the lithospheric mantle (Hoffmann et al., 1986; Becker and Le Roex, 1986). Ce/Pb ratios in Kasai megacrysts are similar to those in OIB (Hofmann et al., 1986) and southern African Group 1 kimberlites (le Roex et al., 2003). Likely, asthenospherically-derived protokimberlitic magmas with higher Ce/Pb and Th/Nb ratios underwent assimilation of depleted lithospheric materials with low Ce/Pb and high Th/Nb ratios. At Mbuji-Mayi, there are no decrease of the two trace element ratios.

Tshibwe clinopyroxene megacrysts extend to low $^{87}Sr/^{86}Sr$ values similar to depleted MORB, which are far lower than any kimberlite or mantle xenolith. This supports the evidence for their parental melts being derived from depleted asthenosphere.

2.6.4. SUMMARY-Tshibwe clinopyroxene megacrysts

Clinopyroxene megacrysts from the Tshibwe kimberlites have been analysed for major and trace element compositions, as well as Sr isotopic compositions, in order to get insight into their origin. The tight trends displayed by the Tshibwe cpx megacrysts suggest a magmatic origin for the Tshibwe clinopyroxene megacrysts via an assimilation-fractional crystallization process.

Two groups of megacrysts can be distinguished based on their major element systematics. The first group comprises low-Ca (i.e., subcalcic) megacrysts with relatively low Mg content. Megacrysts in this group are characterized by significant decreases of Mg# and Cr# values with increasing Ca#, as well as increasing TiO_2 contents. This group can be interpreted as Cr-poor megacrysts primarily derived from the fractionation of a primitive megacryst parental magma before significant lithospheric assimilation had occurred. The second group, comprises high-Ca (i.e., calcic) megacrysts with higher and relatively uniform Mg# values and a range of Cr# values similar to the low-Ca megacrysts. Megacrysts in this group are characterized by a sharp decrease of Cr# and TiO_2 contents with increasing Ca#. The continuous variation in megacryst composition between subcalcic and calcic groups suggest a genetic relationship involving progressive assimilation of lithospheric products. LREE, other incompatible elements such as the HFSE and Sr isotope ratios show general increases with increasing ca# from subcalcic to calcic Tshibwe clinopyroxene megacrysts.

The lower degree of chemical variation displayed by Tshibwe calcic megacrysts compared to Mbuji-Mayi calcic megacrysts may be explained by assimilation of a smaller amount pf, or more clinopyroxne and garnet poor, lithospheric materials. In contrast, the lithospheric materials assimilated by Mbuji-Mayi megacryst parent magmas are likely more heterogenous and enriched than at Tshibwe. This would be consistent with the inference, made from xenocrysts geochemistry, that the SCLM beneath Tshibwe was less depleted and less metasomatised compared to that one at Mbuji-Mayi at the times of kimberlite emplacements. Tshibwe clinopyroxene megacrysts display similarities in some diagnostic trace element ratios such as Ce/Pb, and radiogenic ratios, such as $^{87}Sr/^{86}Sr$, with MORB, OIB and southern African Group 1 kimberlites, suggesting a sublithospheric origin.

CHAPTER 3: EMPLACEMENT AGE OF THE TSHIBWE KIMBERLITE BY IN-SITU LAM-ICPMS U/Pb DATING OF GROUNDMASS PEROVSKITE

There are four known kimberlite fields in the Democratic Republic of Congo (DRC). The Kundelungu field (southeastern DRC) and the Kimpangu field (western DRC) are both located off-craton. In contrast, the Mbuji-Mayi field (south-central DRC) and the Kabinda field (100 km north-east of Mbuji-Mayi) are both located on the Archean Congo-Kasai craton (de Wit and Jelsma, 2015). Each of these latter kimberlite fields consist of two clusters (the Mbuji-Mayi and Tshibwe clusters in the Mbuji-Mayi field and the Lukashi and Kasendou clusters in the Kabinda field).

Unfortunately, the emplacement ages of the DRC's kimberlites are poorly known. Only the main Mbuji-Mayi kimberlite and two kimberlites from the eastern Kundelungu kimberlite cluster have been dated by radiometric techniques. The Mbuji-Mayi kimberlite was dated using the U-Pb technique on kimberlitic baddeleyite grains, as well as zircon megacrysts, indicating an emplacement age of 69.8 ± 0.5 Ma (45 analyses; Schärer et al., 1997). A lower Oligocene age of 32.3 ± 2.2 Ma was obtained from in-situ LAM-ICP-MS U-Pb dating on primary groundmass perovskites from the Kambeli and Msipashi pipes of the eastern Kundelungu kimberlite cluster (Batumike et al., 2008). The remainder of the kimberlite pipes in the DRC have no published radiometric age data.

The Tshibwe kimberlite was discovered by the MIBA corporation in 1956 and has been mined since for its diamonds (de Wit and Jelsma, 2015). It is located 53 km south-west of Mbuji-Mayi and forms a cluster with four other kimberlite pipes nearby, constituting Tshibwe cluster of the of the Mbuji-Mayi kimberlite field (also termed the Southern Group; de Wit and Jelsma, 2015). Unlike the Mbuji-Mayi cluster (Northern Group), the Tshibwe cluster has received little to no attention from the scientific community. Previous studies have focused on the Mbuji-Mayi cluster because of the ease of access and sample availability. Further, it has been assumed that the Mbuji-Mayi and Tshibwe clusters have the same emplacement ages and that the composition of the lithospheric mantle beneath the two clusters is similar, if not identical (Mvuemba, 1980; Weis and

Demaiffe, 1985; Demaiffe et al., 1991; Schärer et al., 1997; El Fadili and Demaiffe, 1999; Batumike et al., 2009; Pivin et al., 2009; Pivin et al., 2013; de Wit and Jelsma, 2015).

Recently, Castillo-Oliver et al. (2016) have investigated the emplacement age of Angolan kimberlites located in the southwestern portion of the Kasai Craton (350 km south-west from Mbuji-Mayi), by in-situ U-Pb dating of groundmass perovskite from four kimberlite localities. They obtained Early Cretaceous ages (135 - 113 Ma) for the Lunda Norte kimberlites. They suggested that the kimberlite magmatism in the southwestern section of the Congo-Kasai Craton had a main eruptive peak around 120 Ma, coinciding with Gondwana breakup and the onset of opening of the adjacent portion of the South Atlantic Ocean. From their study, and previous ones on kimberlite magmatism in regions including the Congo-Kasai Craton (Schärer et al., 1997; Jelsma et al., 2009; Eley et al., 2008; Egorov et al., 2007; Robles-Cruz et al., 2012), there is significant evidence suggesting a relationship between kimberlite magmatism in Angola and the DRC and tectonic events related to Gondwana breakup. The age data suggest that two main peaks of kimberlite magmatism occurred in the Congo-Kasai Craton region, one around 120 Ma, in the southwestern section (Lunda Norte, Angola), and a second one around 70 Ma (including Mbuji-Mayi) in the northeastern section.

New in-situ U-Pb age data on perovskite from the Tshibwe kimberlite is presented. Better constraints on the emplacement age of the Tshibwe kimberlite will provide crucial information to clarify the temporal evolution of kimberlite magmatism in the Kasai Craton and allow the patterns of this magmatism to be better compared with tectonic events affecting the African Plate.

3.1. IMPORTANCE OF IN-SITU LAM-ICPMS U/Pb DATING ON GROUNDMASS PEROVSKITE

Kimberlites are complex rocks and contain a large proportion of groundmass minerals, along with macrocrysts (of xenocrystic or phenocrystic origin) and xenoliths that have been entrained in transit from the lithospheric mantle to the Earth's surface (Mitchell, 1986). The facts that kimberlites contain a large proportion of xenolithic and xenocrystic material, and that they have assimilated significant quantities of mantle and often crustal material from the lithosphere (e.g., Micthell, 2008) makes the accurate and meaningful radiometric dating of these heterogeneous igneous rocks unusually challenging. Over the past 50 years, several approaches

have been developed to reliably date kimberlites. Approaches such as phlogopite-whole rock Rb-Sr isochron and U-Pb zircon dating are among the most widely used, but such approaches also have drawbacks. Phlogopite can have both xenocrystic and magmatic origins, and therefore emplacement ages obtained from it may not strictly represent a magmatic crystallization age (Allsopp and Barrett, 1975; Creaser et al., 2004; Sarkar et al., 2015; Phillips et al., 2017). Moreover, the Rb-Sr system is relatively easily affected by post-emplacement sample alteration, which can have a significant effect on bulk-rock Rb-Sr data (Brown et al., 1989; Kjarsgaard et al., 2009). Additionally, in many cases U-Pb dates obtained on kimberlitic zircon appear to predate the actual kimberlite emplacement age because zircon occurs as xenocrysts or megacrysts in kimberlite, and thus its age is sometimes representative of earlier magmatism that may be a precursor, or entirely unrelated, to the erupted kimberlite (Moore and Belousova, 2005; Moore et al., 2008; Batumike et al., 2008; Stanley and Flowers, 2016).

The U-Pb dating of the Ca-Ti oxide mineral perovskite, an approach initially developed in the late 1980s (Heaman, 1989), is now one of the most widely employed kimberlite dating tools (Donnelly et al., 2012; Griffin et al., 2014). Perovskite is one of the later-crystallizing phases in kimberlite magmas and it contains relatively high concentrations of Th and U but only low concentrations of Pb. It is relatively resistant to alteration, and tends to remain intact when co-existing silicate minerals have been altered (Griffin et al., 2014). Moreover, perovskite occurs in most kimberlites, where it is present as a major to minor groundmass phase (Kramers and Smith, 1983; Mitchell, 1986; Haeman, 1989, Wu et al., 2010; Tappe and Simonetti, 2012).

In situ LAM-ICPMS (Laser ablation microprobe inductively coupled plasma mass spectrometry) U-Pb analysis of perovskite has turned out to be reliable, rapid and cost-effective (Stanley and Flowers, 2016; Castillo-Oliver et al., 2016). Furthermore, this in-situ technique allows analysis of small perovskite grains because of the small laser spot size that can be used (as low as 25 μm; Batumike et al., 2008; Donnelly et al., 2012; Griffin et al., 2014; Sun et al., 2014; Castillo-Oliver et al., 2016).

3.2. SAMPLES AND METHODS

The samples investigated are from the main Tshibwe kimberlite (6°17’26.32” S and 23°21’37.44 E) and were collected during a field trip to the Mbuji-Mayi kimberlite field (DRC) in

June-July 2015. The freshest available Tshibwe kimberlite samples were selected, cut and mounted in discs of lead-free epoxy. Thirteen polished, 25 mm diameter epoxy mounts (with one block of kimberlite embedded in each) were selected for SEM characterisation on the basis of their relative lack of alteration. On the same criterion, four polished thin sections, 100 microns thick, were also selected for analysis.

All dating and geochemical characterisation of Tshibwe perovskites was performed at Macquarie University, under the supervision of Professor W.L. Griffin. Perovskites were identified and characterised by SEM analysis before proceeding with in situ U-Pb analysis.

A. SEM (Scanning electron microscope) analysis

A Zeiss EVO MA15 scanning electron microscope was used for the identification of perovskite grains and characterization of their texture, zoning patterns and the presence of alteration. The instrument used a focused beam with an accelerating voltage of 15 keV, a beam current of 20 nA and a 12 mm working distance.

B. In situ U-Pb dating using LAM-ICPMS (Laser ablation microprobe-inductively coupled plasma mass spectrometry)

The U-Pb isotopic analyses were conducted using a Photon Machines Analyte G2 Excimer laser ablation system attached to an Agilent 7700 quadrupole ICP-MS. Measurement of U and Pb isotope ratios was performed following the methods described by Batumike et al. (2008) for U–Pb dating of kimberlitic perovskite. U-Pb age determinations were performed in situ on both epoxy mounts and thin sections, using a 35-40 μm spot size. The pulse rate of the laser was set at 5 Hz, and the laser energy was set at ~5 J/cm^2.

Due to the small size of the perovskite crystals (i.e., more than 90% of grains are smaller than 80 μm), and the small number of unaltered euhedral crystals, only 12 grains were analysed (one spot per grain) for U-Pb isotope composition, from three of the epoxy mounts. The U-Pb isotope analyses of these grains were obtained in two sessions. The first consisted of 10 analyses of unknowns, bracketed by two analyses of a primary standard (Zircon Gj-1, 609 Ma) at the beginning and the end of the run. The first analysis of the primary zircon standard was followed by analysis of 3 near-concordant zircons (91500, 1065 Ma; Mud Tank, 732 Ma and Temora, 417 Ma), used as secondary standards in order to assess the accuracy and precision of the method. The

second run consisted of 2 analyses of unknowns, but with the same procedure of primary and secondary zircon standard analyses conducted before and after analysis of unknowns.

U–Pb isotope ratio data were calculated from raw signal intensities using the software program GLITTER (Griffin et al., 2008). This software permits the calculation of relevant isotopic ratios for each mass sweep of the instrument, and allows the selection of data from isotopically uniform portions of each analysis. Isotopic fractionation of the integrated ratios, due to ablation and the instrumental mass bias, is corrected by the calibration of each selected sample time-segment against the data obtained during the identical time-segments of the standard zircon (GJ) analyses.

Regression calculations were performed and an inverse-concordia plot (i.e., Tera-Wasserburg plot) was drafted using the Isoplot software package (Ludwig, 2003). The upper intercept of the regression line defined by the raw data on the inverse concordia plot is taken as the $^{207}Pb/^{206}Pb$ value of the common-Pb component of the perovskite. The lower intercept gives the crystallization age of the perovskite data population, and hence the kimberlite emplacement age. Of the twelve perovskite grains analysed, four analyses were problematic in that they indicated significant Pb loss since the time of crystallization, and these were excluded from the age calculation.

C. In situ trace-element analysis using LAM-ICPMS

Trace element measurements of perovskite grains, texturally similar to the ones dated using the U-Pb technique, were performed by LAM-ICPMS using the same Photon Machines Analyte G2 Excimer laser ablation system attached to the Agilent 7700 ICP-MS. For calibration, the NIST 610 glass was used and each analysis was corrected using the Ca values determined in the perovskite by SEM-EDS analysis as an internal standard.

Trace elements were analyzed in a run of 3 unknowns bracketed by two analyses of the standard (NIST 610) each at the beginning and the end of each run. Additionally, two analyses of the USGS BCR-2G standard were included in the run as secondary standards to monitor the accuracy of the measurements. The ablation and measurement time for each analysis was 120 s. The spot size used varied between 12 and 20 μm. The pulse rate of the laser was 5 Hz, and the laser energy was set at ~5 J/cm^2. Given the small size of the perovskite grains analysed, only one spot was measured on each grain during trace element analysis.

3.3. RESULTS

A. SEM characterisation

Perovskite grains were identified, imaged and characterised by SEM. Most of the grains are euhedral and unaltered, ranging from 25 to 90 µm in maximum dimension. Subhedral and anhedral crystals are present as well, with inclusions around edges. In addition to perovskite, zircons ranging in size from 30 to 87 µm and apatite ranging in size from 35 to 80 microns (both being anhedral and with no inclusions) were identified in the Tshibwe samples (Fig. 3.1). It is noteworthy to mention that monazite also occurs in the Tshibwe kimberlite samples. Three anhedral monazite grains (30 to 60 µm in maximum dimension) have been identified in two out of the thirteen epoxy discs examined. According to Mitchell (1986) and Mitchell and Bergman (1991) monazite does not occur in Group I kimberlites, but has only been described in Group II kimberlites (Bellsbank and Lace). However, the presence of monazite has been noted in a calcite kimberlite (Group I) in Yakutia (Siberian craton; Chakmouradian and Mitchell, 1999).

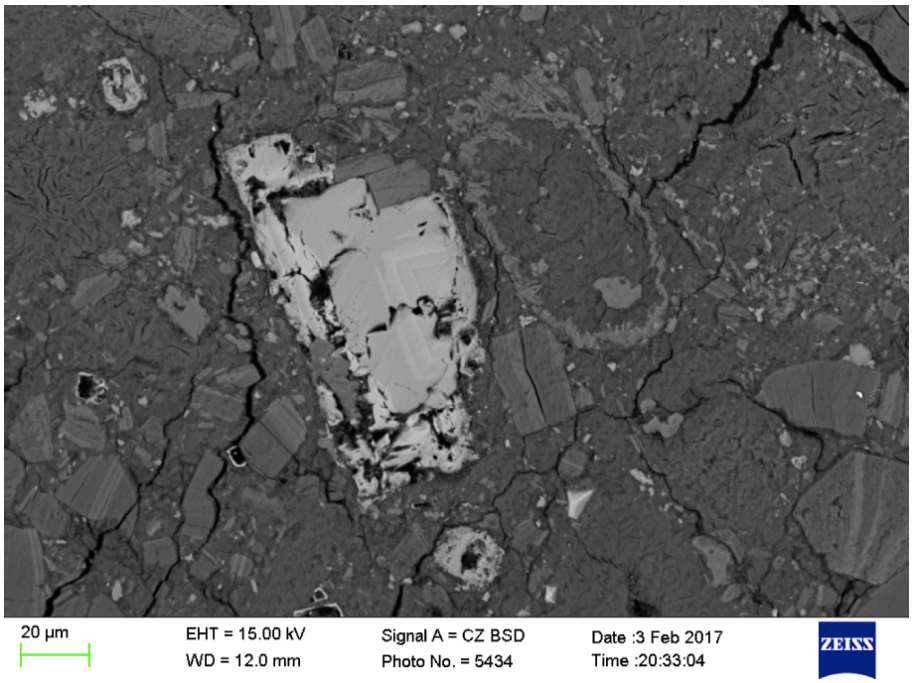

Figure 3.1: Back-scattered electron image of the Tshibwe kimberlite, showing an unusually large ≈90 µm euhedral perovskite crystal (light gray) in the groundmass. Altered rutile grains are present (small light gray with black cores) with abundant serpentine (euhedral to subhedral gray grains). Note the green scale bar. The grain shown for illustration purpose only and was not analysed for dating

B. U-Pb dating

The emplacement age of the Tshibwe kimberlite was calculated using the ISOPLOT software package (Krogh, 2003). The eight U-Pb isotopic analyses of perovskite from the Tshibwe kimberlite that had no evidence of Pb loss yield a U–Pb age of 84 ± 9.5 Ma (Fig. 3.2). The four problematic analyses (which do show evidence for post-emplacement Pb loss) are excluded from the figures and Table 3.1.

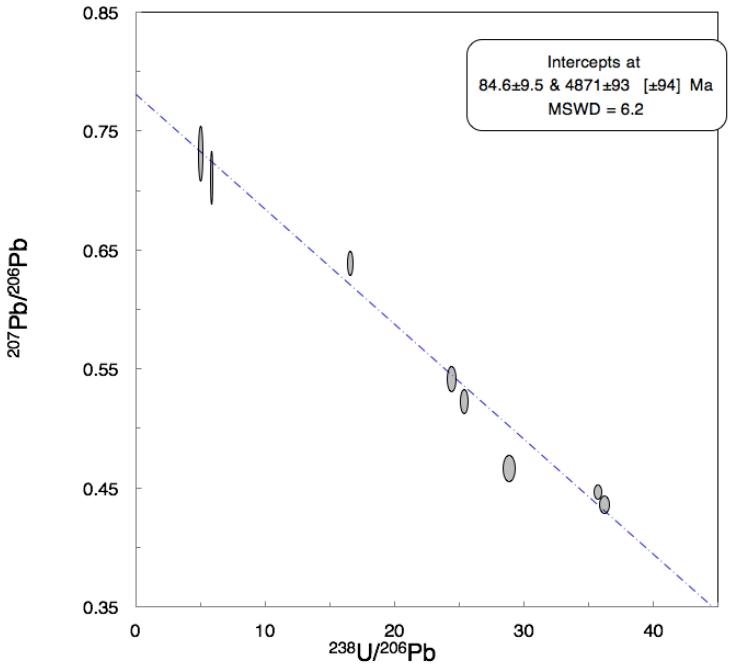

Figure 3.2: Inverse concordia plot for Tshibwe perovskite U-Pb data. The lower intercept gives the age recorded by the perovskite grains.

Table 3.1: Summary of U-Th-Pb isotopic and U-Th concentration data for perovskites from the Tshibwe kimberlite.

Analysis No.	Th (ppm)	U (ppm)	Th/U	$^{207}Pb/^{206}Pb$	± 1 sigma	$^{207}Pb/^{235}U$	± 1 sigma	$^{206}Pb/^{238}U$	± 1 sigma	$^{208}Pb/^{232}Th$	± 1 sigma
TK4-10P	6466	363	17.80	0.43377	0.00508	1.658	0.017	0.02768	0.00018	0.00629	0.00012
TK4-12P	2163	276	7.82	0.46449	0.00749	2.267	0.031	0.03467	0.00036	0.00712	0.00020
TK4-3P	3178	357	8.90	0.54071	0.00703	3.083	0.035	0.04092	0.00033	0.00854	0.00018
TK4-4P	383	26	14.63	0.73164	0.01525	19.101	0.335	0.18840	0.00281	0.02213	0.00062
TK4-5P	3338	387	8.62	0.44448	0.00391	1.731	0.013	0.02811	0.00015	0.00669	0.00008
TK4-71P	1615	94	17.27	0.71181	0.01465	16.072	0.309	0.16314	0.00192	0.01601	0.00056
TK4-7P	4035	372	10.85	0.52115	0.00690	2.849	0.034	0.03936	0.00031	0.00719	0.00015
TK4-8P	4236	212	19.96	0.63882	0.00673	5.318	0.049	0.05998	0.00040	0.00614	0.00010

C. Trace element analysis

Trace element analyses of three perovskite grains indicate that the U contents of Tshibwe kimberlite perovskite (265-317 ppm) are similar to those of perovskites from northeastern Angolan kimberlites (125-730 ppm; Castillo-Oliver et al., 2016). Moreover, similar large variations of Th contents observed in Angolan kimberlitic perovskites (100 to 5150 ppm) (Castillo-Oliver et al., 2016), are also seen in perovskites from Tshibwe (1177-5427 ppm).

The trace element patterns of the three analysed Tshibwe perovskites are relatively uniform, with deep negative K anomalies, enrichment in LREE and incompatible elements such as Th, U, Nb, Ta and depletions of Zr and Hf relative to the light REE. Virtually identical trace element patterns are observed in Lunda Norte kimberlitic perovskites (Castillo-Oliver et al., 2016; Fig. 3.3).

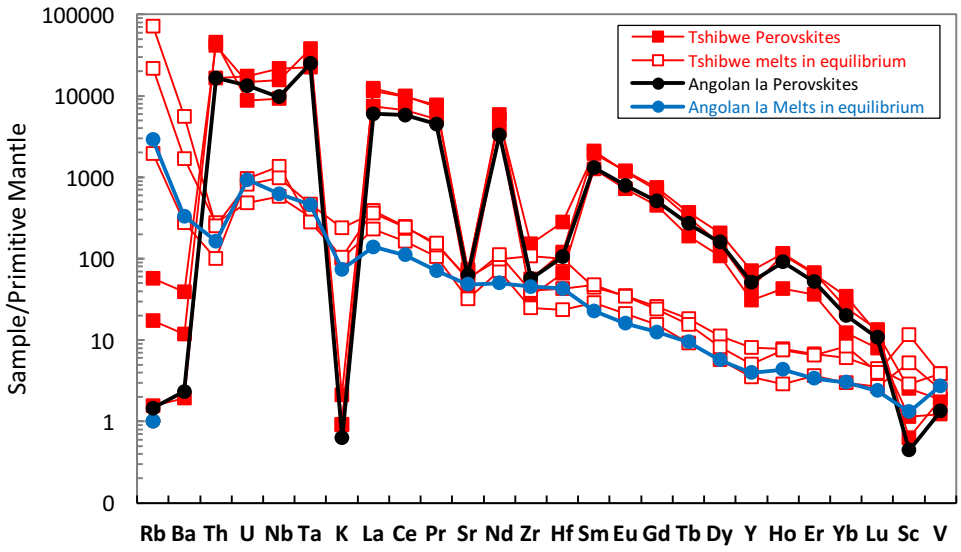

Figure 3.3: Trace element composition of Tshibwe kimberlitic perovskites normalized to primitive mantle. The melts in equilibrium with these perovskites were calculated using the partition coefficients of Chakhmouradian et al. (2013). Angolan kimberlitic perovskites (displaying the same textural characteristics as Tshibwe perovskites) and the melts in equilibrium with them are shown for comparison (Ia= average composition of primary euhedral perovskite, data from Castillo-Oliver et al., 2016). Note the overall strong similarity between the perovskites from the Tshibwe kimberlite and the average euhedral perovskite from Lunda Norte kimberlites in Angola. Primitive mantle normalizing values are from McDonough and Sun (1995).

Melts in equilibrium with Tshibwe perovskites have been calculated using the partition coefficient dataset of Chakhmouradian et al. (2013). Compared to melts in equilibrium with Lunda Norte kimberlitic perovskites, melts in equilibrium with Tshibwe perovskites appear to be

somewhat more enriched in Rb and Ba. Overall, however, the patterns displayed by Angolan and Tshibwe hypothetical melts are very similar and overlap significantly.

3.4. DISCUSSION

A. Reliability of the U-Pb age

The age of the Tshibwe kimberlite based on the 8 most precise perovskite U-Pb isotope ratio analyses is 84 ± 9.5 Ma. Although this age is somewhat less precise than other in-situ ages published recently for Cretaceous kimberlites, as indicated by the relatively high uncertainty and the relatively large MSWD value of 6.2, the altered state of the Tshibwe kimberlite groundmass, and the lack of abundant perovskite in the Tshibwe kimberlites prevented the determination of a more precise age. It is also important to point out that this first age determination for the Tshibwe kimberlite is resolvably older than the more precise age of 69.8 ± 0.5 Ma determined from U-Pb isotope analysis of zircon and badelleyite from the Mbuji-Mayi kimberlite (Schärer et al., 1997).

Table 3.2: Trace element data of perovskites from the Tshibwe kimberlite

Element (ppm)	T11-1	T11-2	T11-3	BCR-2g
Rb	10.4	0.93	34.3	50.8
Ba	77.7	12.8	258	680
Th	3621	1311	3277	5.73
U	177	353	300	1.83
Nb	6098	14204	10182	14.1
Ta	956	834.09	1388.55	0.81
K	215	222.21	512.12	17200
La	4771	8057	7422	23.4
Ce	11080	16720	16433	49.2
Pr	1324	1840	1947	6.74
Sr	799	1464	1385	341
Nd	4664	6451	7341	29.1
Zr	363	1589	591	185
Hf	18.7	79.5	33.8	4.84
Sm	515	793	856	6.38
Eu	112	185	180	2.15
Gd	246	407	379	6.34
Tb	18.6	36.7	31.4	0.93
Dy	72.0	140	102	6.01
Y	134	304	192	32.4
Ho	6.32	17.3	16.6	1.22
Er	16.0	29.3	28.4	3.31
Yb	5.43	10.9	15.1	3.61
Lu	0.54	0.90	0.81	0.48
Sc	18.6	10.2	41.1	36.1
V	100	154	154	436

The accuracy of this Late Cretaceous age is supported by the following evidence:

- This result is consistent with stratigraphic estimates of the emplacement age of this kimberlite performed in the late seventies (Fiermans, 1977). The Tshibwe kimberlite contains enclaves of sedimentary rocks (Mbuji-Mayi sandstones) that have been dated at 120 Ma (Fiermans, 1977; Fiermans and Demaiffe, 1981). Therefore, the emplacement age must be younger than 120 Ma;
- Circumstantial evidence for the Tshibwe kimberlite being older than the Mbuji-Mayi kimberlite also comes from a comparison of the geochemistry of peridotitic clinopyroxenes from the Mbuji-Mayi and Tshibwe clusters. Temperatures (Nimis and Taylor, 2000) and compositions of the clinopyroxenes from Mbuji Mayi are warmer and more incompatible element-enriched, respectively, than of those from Tshibwe, located just 30 km distant. The cooler calculated geothermal gradient and less metasomatised compositions of the Tshibwe clinopyroxenes (Nkere and Janney, 2017), are most easily explained if a regional heating and metasomatic episode occured after the emplacement of the Tshibwe kimberlite and before that of Mbuji Mayi;
- Donnelly et al. (2012) found that Pb loss can occur in highly altered perovskites and therefore could give unrealistically young ages. Problematic data can be identified by anchoring the upper intercept to the present-day terrestrial $^{207}Pb/^{206}Pb$ value. To better constrain the influence of Pb loss on the calculated age, the composition of the common-Pb component was fixed at the present-day $^{207}Pb/^{206}Pb$ terrestrial value of 0.835722 (value calculated from Stacey and Kramers, 1975). The age from the anchored regression line coincides with the one obtained without anchoring the common-Pb composition, giving the same emplacement age within error (Fig. 3.4).

Therefore, the calculated age is consistent with the available geological evidence and most likely represents the actual time of the emplacement of the Tshibwe kimberlite.

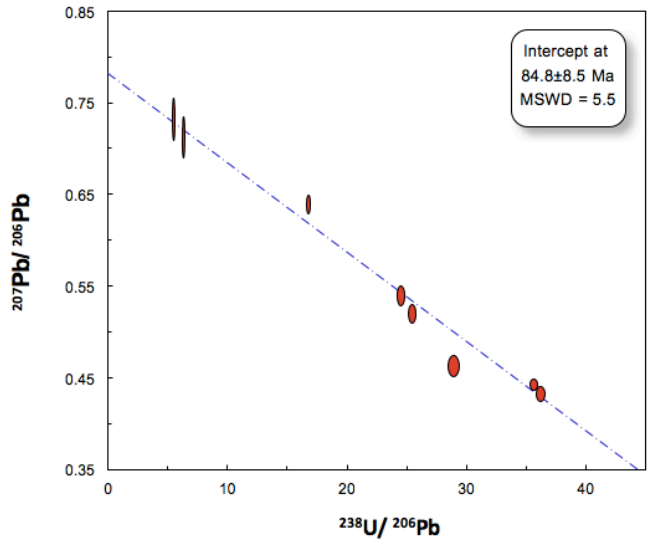

Figure 3.4: Inverse concordia plot for the Tshibwe kimberlite displaying its U-Pb age calculated using the present-day $^{207}Pb/^{206}Pb$ terrestrial value of 0.835722 (84.8 ± 8.5 Ma). This agrees within error with the age obtained without anchoring the common-Pb composition (84.6 ± 9.5 Ma). The eight Tshibwe perovskite analyses included in this age determination, therefore, do not appear to have been affected by Pb loss.

B. Tectonic implications

The onset of the South Atlantic Ocean opening was characterized by the increased rates of seafloor spreading throughout most of the Cretaceous (Torsvik et al., 2009). At around 84 Ma, a sharp decrease in Atlantic seafloor spreading rates occurred (Torsvik et al., 2009; Grannot and Dyment, 2015). This change in spreading rate likely coincided with a significant change in plate motion. The models of Jelsma et al. (2004) and Moore et al. (2008) link kimberlite magmatism to changes in plate motion directions and velocities and this, therefore, suggests a possible triggering mechanism for the generation of the Tshibwe kimberlite.

The ages reported for kimberlites on the Congo-Kasai Craton in Angola, located 100 to 250 km southwest of the Tshibwe cluster (Fig. 3.5), are Early Cretaceous (115–130 Ma), coinciding with the breakup of Gondwana and the start of opening of the South Atlantic Ocean. It has been suggested that the main eruptive age peak (120 Ma) in Angolan kimberlite magmatism correlates with the onset of seafloor spreading (Robles-Cruz et al., 2012; Castillo-Oliver et al., 2016). These kimberlites occur within the Lucapa Corridor, which is a major basement structure that trends in a NE direction through Angola. It has been suggested that this corridor is directly related to the Gondwana break-up and could represent the continuation of an oceanic fracture zone into the African continent (Marsh, 1973; De Boorder, 1982; White et al., 1995, Jelsma et al., 2009).

Kimberlite magmatism along the Lucapa Corridor could potentially reflect the propagation of stress and melt migration along such a deep fracture zone. Recently, Giuliani et al., (2017) have suggested that alkaline magmatism in southwestern Angola (and, presumably, in the whole region) could not be fully explained only by tectonic processes but rather more likely reflects the conjunction of active mantle upwelling and tectonic weak zones. Given the lack of published detailed structural mapping and geophysical characterisation of northeast Angola and the south central DRC, as well as the relatively small number of reliable ages for kimberlites and related magmas, a precise understanding of the relationship between tectonics and the emplacement kimberlites (and similar alkaline magmas) remains elusive.

The Mbuji-Mayi kimberlite field is located along the projected northeastern extension of the Lucapa Corridor into the DRC (Fig. 3.5). Some authors have speculated that the Lucapa Corridor continues further northeast into the Congo Basin (Fieremans, 1977; Egorov et al., 2007; Pettit, 2009; Pivin, 2012). However, kimberlite clusters in the Mbuji-Mayi and Kabinda field are oriented roughly east–west, while other clusters located within the Lucapa corridor are oriented northwest – southeast. This suggests the possible existence of deep-seated East – West trans-lithospheric faults or other zones of weakness, cutting across the northeastern section of the Kasai cratonic lithosphere, along which kimberlites (Mbuji-Mayi and Kabinda fields) could have been emplaced. It is interesting in this regard that recent mapping and geochronological work (Jelsma et al., 2016) has recognised the existence of a prominent shear zone, termed the Central Kasai shear zone, that extends across much of the exposed Archean Kasai craton, dividing the Neo- to Mesoarchean North Kasai terrane from the mainly Paleoarchean South Kasai terrane. In the west of the Kasai craton, the Central Kasai shear zone forms a northeastern extension of the Lucapa corridor and is oriented in the same NE-SW direction, but, in the east, it is deflected into a roughly east-west orientation before it is covered by sedimentary rocks of the Mbuji-Mayi Basin (Jelsma et al., 2016) The proposed cryptic east-west translithospheric weak zone along which the Mbuji-Mayi and Kabinda kimberlite fields were emplaced is here termed the "Kasai Corridor". Reactivation of this lithospheric discontinuity during the Late Cretaceous may have contributed to kimberlite magmatism in the area. The change in plate motion directions and velocities, likely associated with changes in South Atlantic seafloor spreading rates during the Late Cretaceous, could potentially have reactivated the Kasai Corridor and other zones of weakness. There is some geological evidence supporting the notion that the kimberlites of the Kabinda field were also

emplaced during the Late Cretaceous. These latter kimberlites intruded through conglomerates of the C4 unit of the Late Cretaceous Kwango Group (Walker et al., 2011) that display a maximum age of 79 ± 6.8 Ma based on U-Pb dating of detrital zircons (Roberts et al., 2015). Therefore, the Kabinda kimberlites ages must be younger than these conglomerates.

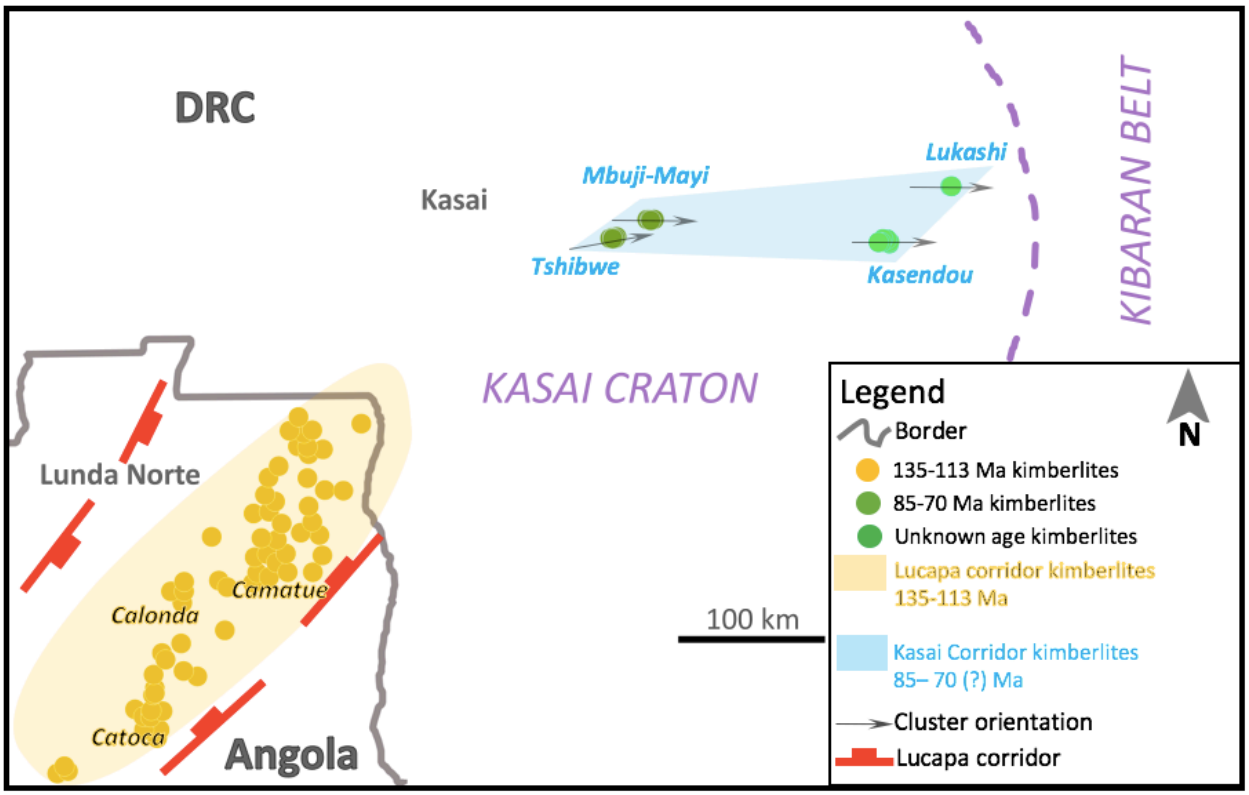

Figure 3.5: Map showing the location of kimberlite clusters on the Kasai Craton in the DRC and northeastern Angola. Note the predominant east – west orientation of kimberlite clusters that have been emplaced after 80 Ma, while kimberlite clusters contemporaneous with the onset of the opening of the South Atlantic Ocean have a northeast-southwest preferential orientation. Kimberlite pipes in the newly discovered Kabinda field (Lukashi and Kasendou clusters) have similar orientations to those of the Mbuji-Mayi kimberlite field (comprising the Mbuji Mayi and Tshibwe kimberlite clusters). Kimberlite pipe locations are from Faure (2006) and Walker (2011), Lucapa corridor boundaries are from Castillo-Oliver et al., (2016) and Kasai Craton boundary is from McCourt et al., (2013).

C. Kimberlite magmatism in the Kasai Craton

The Kasai Craton has been affected by two major episodes of kimberlite magmatism. The first pulse mainly affected the southwestern section and took place between 135 and 113 Ma (with a main eruptive peak at 120 Ma) resulting in an elongate zone of concentrated kimberlite

magmatism having a northeast-southwest orientation. Incipient continental rifting and strain accommodation have been linked to this first episode of kimberlite magmatism (Jelsma et al., 2004; 2009; Robles-Cruz et al., 2012; Castillo-Oliver et al., 2016)

The second pulse appears to have taken place in the northeastern Kasai craton in the Late Cretaceous mainly between 85 Ma and 70 Ma, although we note that the kimberlites of the (eastern) Kabinda field remain undated. Kimberlite emplacement during this episode follows an east-west primary orientation, possibly facilitated by the proposed Kasai corridor.

D. Kabinda kimberlites

The newly discovered Kabinda kimberlite field remains poorly known (De Wit and Jelsma, 2015). There are no published age data and little published geochemical investigation of mantle-derived xenocrysts. We have shown stratigraphic evidence supporting likely late cretaceous emplacement ages for Kabinda kimberlites. Walker (2011) suggested a 39 mW/m^2 local geotherm for the Kasendou cluster based on geochemical investigation of garnet xenocrysts. However, the specific thermobarometric technique used was not disclosed. The subcontinental lithospheric mantle (SCLM) sampled by the Tshibwe kimberlite appears to have been relatively cool, while further northeast, at Mbuji-Mayi the SCLM sampled appears to have been considerably warmer (Nkere and Janney, 2017). The higher geothermal gradient inferred for Kasendou (Kabinda kimberlite field) by Walker et al. (2011; 39 mW/m^2) from xenocryst thermobarometry is similar to that determined for Mbuji-Mayi (40 mW/m^2) and higher than that determined for Tshibwe (35 mW/m^2, both located in the Mbuji-Mayi kimberlite field; Nkere and Janney, 2017). Although Kasendou is located 160 km to the east of Mbuji-Mayi and Tshibwe, it has been shown in xenolith thermobarometry studies in southern Africa that lithospheric heating episodes tend to be regional in extent (on the order of several hundred kilometers; Bell et al., 2003; Kobussen et al., 2008; 2009). Therefore, it is far more plausible that the higher geothermal gradients at Mbuji-Mayi and Kasendou are the result of a single regional lithospheric heating event occurring sometime after the emplacement of the Tshibwe kimberlite and prior to the emplacement of Mbuji-Mayi, than to propose that heating of the lithosphere around Kasendou (Kabinda) occurred prior to the emplacement of the Tshibwe kimberlite but that its effects were strictly local and did not extend to the lithosphere beneath the Tshibwe cluster. This, plus the geological evidence from the age of the sedimentary rocks intruded by the Kasendou kimberlite, supports the notion that it is likely

younger than the Tshibwe kimberlite (85 Ma), and likely similar in age to the Mbuji-Mayi kimberlite (≈70 Ma). Therefore, circumstantial evidence suggests that Tshibwe is the oldest kimberlite in the "Kasai Corridor".

3.5. SUMMARY – TSHIBWE KIMBERLITE EMPLACEMENT AGE

Kimberlitic perovskites have been investigated in order to constrain the emplacement age of the Tshibwe kimberlite. Forty-four perovskites were identified in the groundmass by SEM analysis. Twelve primary euhedral perovskites were selected for in situ U-Pb isotope measurements by LAM-ICPMS, and eight yielded precise U-Pb isotope data not affected by Pb loss. In addition, three perovskite crystals were selected for in situ trace element analysis by LAM-ICPMS. The trace element composition of Tshibwe perovskites largely overlaps with those of perovskites from Angolan (Lunda Norte) kimberlites.

U-Pb isotopic analyses of eight perovskite grains from the Tshibwe kimberlite yielded an age of 84 ± 9.5 Ma, which is in agreement with stratigraphic and other circumstantial geological evidence. On this basis, the age is believed to be accurate and reliable. This Late Cretaceous age coincides with a sharp decrease of spreading rates at the southern Mid-Atlantic Ridge at about 84 Ma. This appears to have coincided with a change in the direction and velocity of African plate motion. Previous studies have proposed that such changes may provide a trigger for kimberlite magmatism.

The Kasai craton appears to have been affected by two main pulses of kimberlite magmatism, an earlier pulse at 130-113 Ma resulting in kimberlites of the NE-SW-oriented Lucapa Corridor in Angola, and a later pulse of roughly 85-70 Ma responsible for the Tshibwe, Mbuji Mayi and possibly the kimberlites of the Kabinda field in the eastern DRC, all of which are in clusters oriented roughly E-W. Although emplacement ages for the Kabinda kimberlites are lacking, a comparison of the geothermal gradients in the lithosphere beneath the Tshibwe, Mbuji-Mayi and Kasendou clusters (the latter located in the Kabinda field) indicates that the SCLM beneath Tshibwe is significantly cooler than that beneath Mbuji Mayi or Kasendou. Given that all three kimberlites are located within 200 km of each other, the simplest hypothesis is that the Tshibwe kimberlite was emplaced before a regional lithospheric heating event occurred that affected the mantle beneath Mbuji Mayi and (most likely) Kasendou. Therefore, the most

consistent interpretation is that Tshibwe is the oldest of the three and all three kimberlite clusters are likely of Late Cretaceous age. Their apparently similar age and orientation suggests that they were emplaced along an east-west oriented zone of lithospheric weakness in the northeastern Kasai craton, tentatively termed the "Kasai corridor". This corridor may be an expression of the recently described Central Kasai Shear Zone.

CHAPTER 4: GEOCHEMISTRY OF CENTRAL AFRICAN KIMBERLITES LOCATED ON AND OFF THE KASAI CRATON

4.1. INTRODUCTION

4.1.1. DEFINITION, CLASSIFICATION AND DISTRIBUTION

Kimberlites are complex rocks and this complexity is indicated by the definition of kimberlite by Skinner and Clement (1979): "*Kimberlite is a volatile-rich, potassic ultrabasic igneous rock which occurs as small volcanic pipes, dykes and sills. It has a distinctive inequigranular texture resulting from the presence of macrocrysts set in a fine grained matrix. This matrix contains as prominent primary phenocrystal and/or groundmass constituents, olivine and several of the following minerals: phlogopite, carbonate (commonly calcite), serpentine, clinopyroxene (commonly diopside), monticellite, apatite, spinels, perovskite and ilmenite. The macrocrysts are anhedral, mantle-derived, ferromagnesian minerals which include olivine, phlogopite, picroilmenite, chromian spinel, magnesian garnet, clinopyroxene (commonly chromian diopside) and orthopyroxene (commonly enstatite). Olivine is extremely abundant relative to the other macrocrysts, all of which are not necessarily present. The macrocrysts and relatively early-formed matrix minerals are commonly altered by deuteric processes, mainly serpentinization and carbonatization. Kimberlite commonly contains inclusions of upper mantle-derived ultramafic rocks. Variable quantities of crustal xenoliths and xenocrysts may also be present. Kimberlite may contain diamond but only as a very rare constituent*". Kimberlite's hybrid nature and propensity for alteration are both clearly highlighted in this definition and this causes studies of kimberlite geochemistry to be very challenging (Field et al., 2008).

Kimberlites are not only important because they are the main carriers of diamond and mantle rocks and minerals to the Earth's surface, but also because their compositions tell us about their source regions. They are known to be the magmas with the deepest origins to reach the Earth's surface. During their ascent they sample the lithospheric mantle and the crust, exhuming a wide array of mantle materials such as mantle peridotites, eclogites, megacrysts, and metasomatic and

crustal xenoliths, as well as xenocrysts derived from all of these xenolith types, along with, in many cases, diamonds. They therefore provide important insights into the composition of the lithospheric mantle and continental crust (Richardson et al., 1984; Gurney, 1990; Hops et al., 1992). Furthermore, the geochemistry of kimberlites themselves can provide useful information regarding their mantle source regions and their evolution. Additionally, it has been proposed that the distribution of kimberlites in time and space provide important information on global plate tectonic processes and deep mantle structure (Jelsma et al., 2009; Torsvik et al., 2010).

Classification

Kimberlites are classified into two groups based on petrographic, chemical and isotopic characteristics. Group I (or "archetypal") kimberlites are petrographically characterized by having olivine as the dominant (and often the only) macrocrystic mineral present, and calcite typically present as a prominent groundmass mineral. "Macrocryst" is a non-genetic term used in kimberlite petrography to indicate unusually large mineral grains (typically > 5 mm) surrounded by groundmass. In Group II kimberlites (also referred to as orangeites; Mitchell, 1995), both phlogopite and olivine are typically present as the dominant macrocryst minerals and calcite is typically not an important groudmass mineral.

In terms of composition, Group I kimberlites are potassic and calcic whereas Group II kimberlites are ultrapotassic, and peralkaline. Both kimberlite varieties are volatile-rich, but Group I kimberlites tend to be richer in CO_2 and Group II kimberlites tend to be richer in H_2O. In terms of radiogenic isotope composition, Group I kimberlites have Sr-Nd-Pb isotopic signatures overlapping with ocean island basalts (OIB) while Group II kimberlites have more highly radiogenic $^{87}Sr/^{86}Sr$ and unradiogenic $^{143}Nd/^{144}Nd$ than is found in OIB (Smith, 1983; Becker and le Roex, 2006), along with low $^{206}Pb/^{204}Pb$ combined with relatively high $^{207}Pb/^{204}Pb$ and $^{208}Pb/^{204}Pb$ (Kramers, 1977; Fraser and Hawkesworth (1992). In addition, a third minor group, termed the transitional kimberlites, has been identified to have petrographic, chemical and radiogenic isotope characteristics between those of Group I and Group II kimberlites (Skinner et al., 1994; Clark, 1994; Becker et al., 2007; Becker and le Roex, 2006). Becker and le Roex (2006) have clearly shown that Group I kimberlites have higher TiO_2, and lower SiO_2 and MgO contents

on average than Group II kimberlites. In addition, Group II kimberlites are more enriched in LILE compared to Group I kimberlites.

Distribution and emplacement of kimberlites in Central Africa

The occurrence of kimberlites is generally limited to Archean cratons and surrounding Proterozoic mobile belts. In central Africa, kimberlites have been reported in Angola, DRC and Gabon. In Gabon, several metamorphosed diamondiferous kimberlites cut across the Ntem Craton, near Miztic Town. They are believed to be the oldest kimberlites in the world, with an emplacement age estimated at 2.8 Ga. (Henning et al., 2003).

In Angola, there are more than 600 kimberlite occurrences located on and off (Faure, 2010) the Archean Kasai craton and on the Pan-African West Congo belt (Fig. 4.1). Four main kimberlite fields have been identified in Angola, which occupy a 1600 km long, northeast-southwest-oriented linear zone, termed the Lucapa corridor (Reis, 1972) which cuts across Angola and extends into the DRC (Reis, 1972). This corridor is characterized by a general northeastward younging of kimberlites, with kimberlites in the southwest yielding a 372 Ma age (Egorov et al., 2007), those in central Angola with a reported emplacement age of 252 Ma (Jelsma et al., 2013), and the northeastern kimberlites yielding ca. 120 Ma ages (Robles-Cruz et al., 2012; Castillo-Oliver et al., 2016). Other kimberlites have been reported in northwest Angola, in the west Congo Belt, but there are no published ages.

In the DRC, there are four kimberlite fields known, with a total of 66 kimberlites reported thus far (Schärer et al., 1997; Batumike et al., 2009; De Wit and Jelsma, 2015). In the west, the Kimpangu kimberlite field cuts across the West Congo belt and little is known about this field. In the central DRC, two kimberlite fields (the Mbuji-Mayi and Kabinda fields) cut across the Archean Kasai craton. These fields each have several diamondiferous kimberlites and have been emplaced during the Late Cretaceous (De Wit and Jelsma, 2015; Fig. 3.5 in chapter 3). In the southeast, the Kundelungu kimberlite fields cut across the Proterozoic Bangwelu block. The Kundelungu kimberlites are barren of diamonds, as is typical for off-craton kimberlites. These were emplaced during the Eocene-Oligocene (32 ± 2 Ma, Batumike et al., 2008).

4.1.2. BACKGROUND

Unlike the extensively studied kimberlites of southern Africa, there are few published (geochemical) data on central African kimberlites. Demaiffe and Fieremans (1981) and Weis and Demaiffe, (1985) investigated the major element composition and isotopic composition (Sr-Nd-Pb) of the Mbuji-Mayi main kimberlite and a few kimberlites of the Kundelungu cluster and suggested their derivation from depleted mantle sources. Despite the published isotope data on these kimberlites, published major and trace element data are extremely sparse. Similarly, whole rock geochemical data for Angolan kimberlites is also lacking. Therefore, central African kimberlites remain geochemically very poorly characterised and additional data are sorely needed.

4.1.3. CONTROVERSIES SURROUNDING THE ORIGIN OF KIMBERLITES

There are several controversies surrounding the origin of kimberlites.

What is the depth of kimberlite melt formation? Does it occur primarily in the convecting mantle or the lithosphere?

The lithosphere-derived kimberlite models of le Roex et al., (2003), Becker & le Roex (2006) and Gaffney et al., (2007) are very similar in that both invoke lithospheric peridotite sources for kimberlites that have been metasomatised by melts from exotic sub-lithospheric materials (plume melts for le Roex et al. and melts of subducted oceanic crust for Gaffney et al., (2007). Note that the le Roex et al., and Gafney et al., models are not mutually exclusive since the mantle sources of many ocean islands are thought to be ultimately derived from subducted oceanic crust; e.g., Hofmann, 2003). The overlap of diagnostic trace element ratios in kimberlite magmas and OIB (le Roex et al., 2003; Becker and le Roex, 2006), and the presence of trace element and isotopic signatures (particularly Nd-Hf) consistent with recycled ancient subducted oceanic crust in some kimberlite magmas (Gaffney et al., 2007), have been argued to originate from melts of deep convecting mantle sources that have metasomatised lithospheric mantle peridotites, from which the kimberlites are proposed to be derived. The evolution of kimberlite sources in these models have been proposed to occur in two ways: (1) metasomatism of the kimberlite source

region in the lithosphere prior to subsequent melting to generate kimberlite magmas (le Roex et al., 2003; Becker and le Roex, 2006) or (2) metasomatism being contemporaneous, or nearly so, to melting (Gaffney et al., 2007)

The convecting mantle-derived kimberlite **models** of Smith (1983), le Roex (1986), Haggerty (1994), Nowell et al. (2004) and Tappe et al. (2011; 2013) invoke asthenospheric or even deeper mantle sources as the main origin for Group I (and in some cases Group II) kimberlites. These are based on the general geochemical similarities in terms of trace element and radiogenic isotope ratios between kimberlites and ocean island basalts, which are widely regarded to be mainly derived from deep-seated mantle plumes. The steep arrays in Nd-Hf isotope ratio space displayed by kimberlites (Nowell et al., 2004; Paton et al., 2009; Tappe et al., 2013) are interpreted to reflect the involvement of ancient recycled basaltic crust (such as mid-ocean ridge basalt (MORB) or ocean island basalt (OIB)) that was generated, at least partly in the garnet stability field and hence has a low time-integrated Lu/Hf ratio compared to Sm/Nd, although such signatures have also been attributed to interactions between asthenospheric melts and K-rich lithospheric components (Tappe et al., 2011; Giuliani et al., 2015). The various models for derivation of kimberlites from the convecting mantle are similar in that they attribute (Group I) kimberlites to melting of the the same range of deep convecting mantle sources as those supplying ocean island basalts, with the caveat that there are some differences due to their setting (e.g., that the cratonic setting of kimberlites results in a much lower degree and deeper average depth of melting and prevents mixing with shallow asthenospheric mantle, as occurs beneath oceanic lithosphere, plus the presence of thick continental lithosphere adds a additional potential assimilant that is not present in the oceans (e.g., Tappe et al., 2011)), which may explain the presence of some of the geochemical differences observed between kimberlites and ocean island basalts.

To what extent are kimberlite melts modified by interaction with lithospheric mantle wall-rock during ascent?

The significant difference between relatively radiogenic Sr isotopic values measured in whole-rock kimberlites and the unradiogenic Sr isotope compositions found in groundmass carbonates and perovskites (Woodhead et al., 2009; Malarkey et al., 2010; Donnelly et al., 2012).

has been largely attributed to crustal contamination with some possible contribution from near-surface alteration (Donnelly et al., 2012).

However, extensive assimilation of material from lithospheric mantle wall-rocks has been postulated to significantly change kimberlite magmas compositions (Mitchell, 2008; Patterson et al., 2009; Tappe et al., 2011; Donnelly et al., 2012; Griffin et al., 2014). Several lines of evidence in support of this hypothesis have been presented: (1) the fact that Sr istope composition of whole-rock kimberlites and associated perovskites tend to be higher than convecting mantle values (Donnelly et al., 2012; Griffin et al., 2014); (2) The contrast, particularly in trace lement composition, between groundmass olivine grain cores (interpreted as xenocrysts by Pilbeam et al. 2013) and rims (interpreted as direct crystallization products from kimberlitic melts by Pilbeam et al., 2013); (3) compositional overlap between olivines found in kimberlites and those found in peridotite xenoliths (Donnelly et al., 2011; Patterson et al., 2009); (4) The fact that orthopyroxene macrocrysts tend to be virtually absent in kimberlites, whereas olivine, garnet and clinopyroxene is preferentially assimilated by kimberlite melts resulting in silica enrichment during ascent. (Mitchell, 2008; Russell et al., 2012).

However, Paton et al., (2009) provided evidence against the extensive lithospheric assimilation by kimberlitic melts based on the differences in trace element ratios and radiogenic isotope between some Indian kimberlites and their xenoliths. These authors found very little interaction between sub-lithospheric melts (i.e., kimberlitic magmas) and the lithosphere.

4.1.4. OBJECTIVES OF THIS STUDY

In light of the above, the present contribution will address the controversy of kimberlite origin and evolution by providing a new geochemical dataset for central African kimberlites. Data are presented for an Angolan kimberlite, Camatue, and the Tshibwe kimberlite in the DRC, both with no previously published geochemical data, as well for several kimberlites from the Kundelungu field, for which only a very small amount of data have been published. This new data will provide the opportunity to compare central African kimberlites with much more extensively studied southern African Group I kimberlites. Particular attention will be paid to the geochemistry of source regions, mixing relationships and evolution of mantle sources and geodynamic implications.

Further, an attempt will be made to constrain the extent of lithosphere-kimberlite interactions and how this impacted the composition of the studied kimberlites. The effects of crustal contamination, as well as alteration, will be thoroughly investigated in order to determine the likely effects of these processes on the kimberlite compositions.

4.2. GEOLOGICAL SETTING

4.2.1. THE KASAI CRATON

Please see chapter 2 for background information on the geology of the kasai craton.

CAMATUE KIMBERLITE

The Camatue kimberlite cluster is located 10 km east of the town of Lucapa in the Lunda Norte province, northeastern Angola. It comprises nine kimberlite pipes with five of them known to be diamondiferous (www.portergeo.com). However, the diamond content is rather poor compared to the Catoca kimberlite, 125 km to the southwest (www.portergeo.com). The Camatue kimberlite cluster occurs within the Lucapa corridor and was likely emplaced around 120 Ma, which is the age of the main kimberlite magmatic episode in the region (Castillo-Oliver et al., 2016). There is little published data concerning this cluster in the published literature, and no geochemical data for the Camatue kimberlite (Latitude: 8°25’40.06” S, Longitude: 20°48’37” E) have been published previously.

TSHIBWE KIMBERLITE

Please see chapter 2 for background information, location and geology of the Tshibwe kimberlite.

4.2.2. THE KUNDELUNGU PLATEAU

The Kundelungu kimberlite field is located 600 km south-east of Mbuji-Mayi, on the Kundelungu plateau, Katanga province in the southeastern DRC. The following geographical coodirnates delineate the Kundelungu plateau: North (Latitude: 8’41’56.96” S; Longitude: 28°06’38.34 E), South (Latitude: 10°54’52.10” S; Longitude: 27°52’22.34” E), West (Latitude: 10°16’12.04” S;

Longitude: 27°21’12.81” E) and East (Latitude: 10°09’18.29” S; Longitude: 28°10’04.95” E). The Kundelungu plateau is formed by rocks of the late Neoproterozoic Biano subgroup (limestones and mudstones interbedded with sandstones). The basement beneath the Kundelungu plateau has been suggested to be the extension of the Bangweulu block (Batumike et al., 2007).

THE KUNDELUNGU KIMBERLITES

The Kundelungu kimberlite field comprises two clusters: a western cluster with 17 kimberlite pipes and an eastern cluster with 16 kimberlite pipes (Fig. 4.1). Between these clusters is a wide area of Cenozoic sand cover, probably masking other kimberlite pipes (Kampata, 1993). Exposed kimberlites in the Kundelungu field are dominantly hypabyssal (de Wit and Jelsma, 2015). Batumike et al., (2008) dated the Kundelungu kimberlites (Msipashi and Kambeli pipes, eastern cluster) by in situ U-Pb dating of groundmass perovskite. They obtained an age of 32 ± 2 Ma and linked this age with the early opening of the East African Rift.

4.3. SAMPLES AND ANALYTICAL METHODS

All Camatue kimberlite samples and one Kundelungu sample were generously provided by the Royal Museum of Central Africa in Tervuren (Belgium) and the remaining Kundelungu kimberlite samples were generously provided by Prof. Daniel Demaiffe from the Université Libre de Bruxelles (Belgium). Camatue samples are core samples from a single drillhole into the Camatue pipe, and consist mainly of volcanoclastic kimberlite. The Kundelungu samples are all hypabyssal kimberlite obtained by hand sampling in the 1950's, 1960's and 1970s and were collected from surface exposures by Prof. Demaiffe and Dr. Carlos Fieremans. Tshibwe kimberlite samples were collected by the author during a field trip to the Kasai region in June 2015. Sample collection was done with a hammer and chisel at the most advanced sites of active excavation of the Tshibwe mine open pit (bottom, around 150 m below the surface). Samples of fresh (volcaniclastic) kimberlite averaging 2 kg each were collected.

Sample preparation

Kimberlite samples were split using a hydraulic splitter. Roughly 25% of each specimen was kept for thin sectioning, the other portion undergoing further splitting until obtaining fragments (1-2 cm in size) able to fit in the jaw crusher.

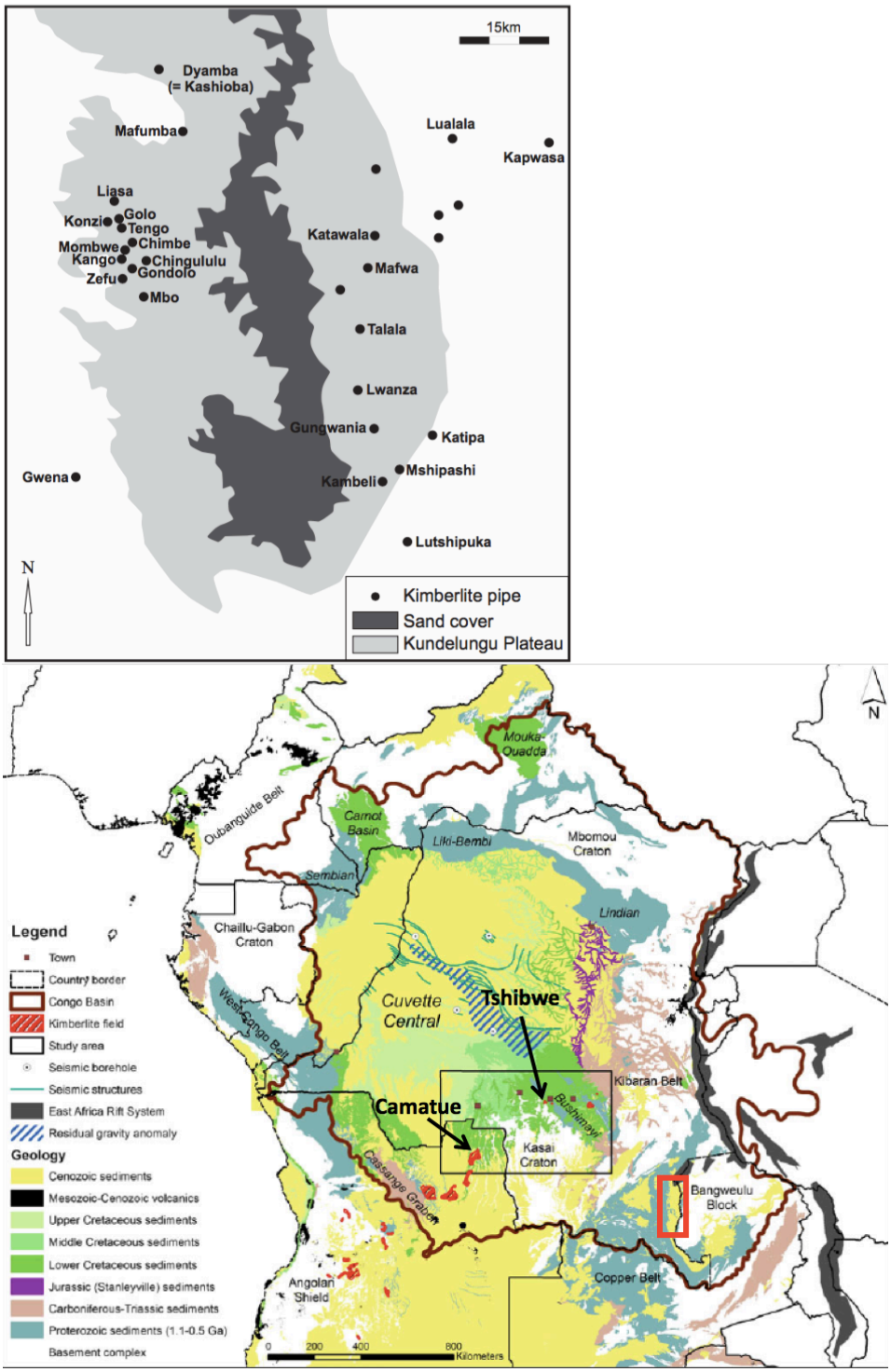

Figure 4.1: Map of the Kundelungu kimberlite field on the top, Katanga Province, southeastern DRC. The western cluster is separated from the eastern cluster by a thick layer of Cenozoic sand. (Map after Batumike et al., 2008). Samples from the Mbo, Zefu, Kashioba, Konzi and Msipashi have been analysed in this study (Kashioba = Kaloba Falls). A geological map of central Africa modified after Roberts et al., (2015) is shown (bottom) with the location of the Kundelungu plateau represented by the red square.

After crushing in a carbon steel jaw crusher, rock chips with a maximum dimension of 1 cm were obtained. These rock chips were then sieved and rock chips less than 5 mm in size were collected for sub-sampling.

The least altered fractions of kimberlite from each sample (typically more than 20 g except in a few cases with samples of the highly altered Tshibwe kimberlite, where sample sizes as small as 10 g were used) were then hand-picked under the microscope, with extremely careful attention to including only the freshest, least altered and contaminated material, in order to obtain minimally altered samples as free as possible of xenoliths. The chips were finely milled (to < 25 μm) to powders in a carbon steel disk mill and these powders were used for geochemical and radiogenic isotope ratio analysis. The disk mill was carefully cleaned before each new sample and was pre-contaminated by milling 10-20 g of intermediate grade sample (more altered than the material designiated for analysis, but still with minimal xenolithic (especially crustal) content), which was discarded.

X-ray fluorescence (XRF) major element analysis

2 g of sample powder was weighed out into crucibles, the empty weight of which was also recorded. The sample powders were dried overnight in an oven at 110 °C, and the sample + crucible weight was recorded again. This made possible the calculation of wt.% H_2O^- (i.e., adsorbed water weight) present in the kimberlite samples. The samples were then ignited in a muffle furnace for at least 4 hours at 850 °C and again the sample + crucible weights were recorded. This alllowed calculation of the weight percentage of loss on ignition (LOI).

Major element analysis by XRF was performed on fusion disks. These disks were made from 0.7 g of ignited powder, mixed with 6.0 g of Claisse flux beads (composed of a mixture of lithium tetraborate and lithium metaborate in the ratio 57:43 respectively, with 1% of a lithium-bromide releasing agent). These mixtures were then melted and homogenised in platinum crucibles in an automated Claisse M4 Fluxer. The fusion discs obtained were then stored in a dessicator prior to analysis.

Major element concentrations were measured in the fusion disks using a Panalytical Axios wavelength-dispersive XRF spectrometer using standard techniques. Calibration curves were obtained by analysis of well-characterised international rock standard reference material powders prepared as fusion disks in precisely the same manner as the unknown samples.

X-ray fluorescence (XRF) trace element analysis

Trace element analysis was performed for Sc, Cr, V, Mn, Co, Ni, Mo, Cu, Zn, Rb, Sr, Y, Zr, Nb, Ba, Pb, Th, U, Cl and F by XRF on 6 g of powder from each sample, which was made into a pressed powder pellet. Pellets were prepared using a drop of polyvinyl alcohol as a binder mixed with the powder and the pellet was made in a die using a laboratory press under 10 tons pressure. The XRF measurements were performed using the same Panalytical Axios XRF spectrometer used for the major elements. For all elements, raw intensities were corrected for background, composition-dependent mass absorption and enhancement effects (with these corrections determined either from the Rh-K Compton peak or calculated from the major element composition) and corrected for spectral overlap effects, such as Rb-K_b on Y-K_a . Similarly to the major element measurements, corrected trace element intensities were converted to elemental concentrations using calibration curves based on the analysis of international rock standards prepared in exactly the same manner as the unknowns.

ICP-MS trace element analysis

Solution ICP-MS trace element analyses were performed at the University of Cape Town on a ThermoFisher X-series 2 quadrupole ICP-MS instrument for the analysis of low abundance trace elements including the REE, Cs, Hf, Ta, Pb, Th and U, as well as several of the high-abundance trace elements also analysed by XRF. Aliquots of 0.05 g of sample powder were digested under high pressure and temperature (200°C) using steel-jacketed pressure Parr digestion vessels in order to dissolve refractory minerals (ilmenite, zircon and chromite). After digestion, the solutions were dried down and re-suspended twice in ultra-pure concentrated nitric acid to remove fluorides. The solutions were re-dissolved in ultrapure 7 M HNO3 and were then split by weight, with 15% being used for trace element analysis and the remaining 85% being set aside for elemental separation and radiogenic isotope measurement. After drying down the solution aliquots intended for trace element analysis a final time, they were diluted 10000-fold in a 5% dilute nitric acid solution spiked with 10 ppm of the internal standard elements Rh, In, Re and Bi for final dissolution and analysis by ICP-MS.

Synthetic multi-element standard solutions were used for external calibration and all sample solutions and standards were spiked with the four internal standard elements mentioned above. Each trace element analysis consisted of 3 replicates of 100 sweeps across the mass range,

with a counting time per peak of 40 ms. Data was collected using a discrete dynode detector and the dilution was sufficient that the intensities for virtually all isotopic masses measured (aside from ^{88}Sr) were collected in pulse-counting, rather than analogue mode. Total prodecural blanks were run with every batch analysed and were generally less than 100 pg except for Sr, which was slightly higher (up to 300 pg). Table 43 in appendix shows the values of the standards run during the analysis sessions.

Radiogenic isotope measurements by MC-ICP-MS

Elemental separation

Sequential Pb, Sr and Nd separations were performed using anion (Pb) and cation exchange column chromatography (Sr, Nd) in the clean laboratories of the Radiogenic Isotope Facility in the Department of Geological Sciences, UCT. All chemistry was performed in an ultraclean HEPA-filtered laminar flow hood. After drying, the samples were converted from nitrate to chloride and then to bromide form (by suspension in hydrochloric and hydrobromic acids, followed by evaporation to dryness, respectively) for Pb separation chemistry. Pb was separated from the other elements using AG1x8 anion exchange resin in a 1 M HBr medium. The non-Pb fraction of the samples were collected, dried down and converted back to chloride using concentrated hydrochloric acid. This was again dried down and the samples were re-dissolved in 1 M HCl-0.1M HF and passed through primary columns using AG50x8 cation exchange resin to collect Sr and the rare earth elements. Finally, the REE fraction was dried down and Nd was separated from this using columns filled with EiChrom™ Ln-spec resin in a medium of 0.25M HCl.

Mass spectrometry

Sr, Nd and Pb isotope analyses were performed on a Nu Instruments NuPlasma HR instrument in the Radiogenic Isotope Facility. The basic techniques used for the analysis of Sr, Nd and Pb isotope ratios by MC-ICP-MS were as described by le Roex et al. (2012).

In brief, Sr isotope ratios were analysed in a 0.2% HNO_3 solution containing approximately 200 ppb Sr using a standard quartz glass cyclonic spray chamber. Instrumental mass fractionation (mass bias) was corrected by internal normalisation, using the exponential law, and assuming a $^{86}Sr/^{88}Sr$ value of 0.1194. NIST SRM987 was used as a bracketing standard analysed before and

after every five unknowns and all measured Sr isotope data were normalised to a $^{87}Sr/^{86}Sr$ value of 0.710255 for this standard. Isobaric overlap of ^{87}Rb on ^{87}Sr was corrected by monitoring ^{85}Rb and corrected using the natural $^{85}Rb/^{87}Rb$ ratio adjusted for mass bias using the measured $^{86}Sr/^{88}Sr$ ratio. BHVO-2 was analysed as a secondary standard and had a long-term value for $^{87}Sr/^{86}Sr$ during the course of this study of 0.703490 ± 0.000036 (2 s.d.).

Nd isotope ratios were measured in 2% HNO3 solutions containing roughly 50ppb of Nd. Measurements employed a DSN-100 desolvating nebuliser. Instrumental mass fractionation (mass bias) was corrected by internal normalisation, using the exponential law, and assuming a $^{146}Nd/^{144}Nd$ value of 0.7219. The standard reference material JNdi-1 was used as reference standard (referencing all Nd isotope data done to a value of 0.512115, Tanaka et al., 2000) measured before and after every five samples. Data were corrected throughout the analyses for isobaric Sm and Ce interferences using the measured signal for ^{147}Sm and ^{140}Ce, and assuming natural Sm and Ce isotopic abundances. BHVO-2, measured as a secondary standard, had a long-term average $^{143}Nd/^{144}Nd$ ratio during the course of this study of 0.512989 ± 0.000015 (2 s.d.).

Pb isotope ratios were analysed in 2% HNO_3 solutions containing roughly 50 ppb Pb using the DSN-100 desolvating nebuliser. As Pb has only one stable, non-radiogenic isotope (^{204}Pb), mass bias normalisation was performed through spiking with roughly 5 ppb of NIST SRM 997 natural Thallium standard and measurement of the stable isotope ratio $^{205}Tl/^{203}Tl$, which was assumed to be 2.3889. This allowed an exponential mass bias correction to be applied to the Pb isotope data. NIST SRM981 was used as reference standard and all three Pb isotope ratios were normalised to the values of 36.7219, 15.4963, 16.9405 for $^{208}Pb/^{204}Pb$, $^{207}Pb/^{204}Pb$, $^{206}Pb/^{204}Pb$ respectively (Galer and Abouchami, 1998) before and after every 5 unknowns. Isobaric interferences from Hg were corrected using on peak background performed prior to every measurement. BHVO-2, measured as a secondary standard during the course of this study, had long term average values $^{208}Pb/^{204}Pb$, $^{207}Pb/^{204}Pb$ and $^{206}Pb/^{204}Pb$ values of 38.213±0.040, 15.537±0.009 and 18.628±0.025 (2 s.d.), respectively.

4.4. PETROGRAPHY

The aim of this section is to provide an overall picture of the characteristics of the central African kimberlites analyzed in this study. Their petrographic characteristics are crucial for evaluating the degree of crustal contamination, alteration, macrocryst entrainment and fractional crystallization that the kimberlites have experienced (Becker and le Roex, 2006). Constraining the involvement of these processes are necessary for understanding the petrogenesis of the kimberlites investigated. We follow the terminology of le Roex et al. (2003) who used the term macrocryst to refer to any anhedral crystal larger than 2 mm in size and phenocryst to refer to any euhedral crystal smaller than 1 mm. Crystals less than 500 microns in size are termed matrix phases or microphenocrysts. In addition, anhedral crystals less than 2 mm in size have been referred to as microcrysts by Becker and le Roex (2006).

Skinner and Clement (1977) and Clement and Skinner (1979) additionally proposed that samples with more than 10 volume % of macrocrysts are classified as macrocrystal kimberlites whereas samples with less than 10 volume % of macrocrysts are classified as aphanitic kimberlites.

The above terminology will be used in this section to characterize the petrography of Central kimberlites.

4.4.1. CAMATUE KIMBERLITE

Seven samples of drill core from the Camatue kimberlite, originating from a single hole at depths between 60 and 175.5 m subsurface, each 30 to 60 cm^3 in volume, were investigated. The samples are macrocrystal volcaniclastic or pyroclastic kimberlite breccias with clear tuffisitic (pyroclastic) textures and magmaclasts, and thus appear to represent the diatreme facies (e.g., Mitchell, 1986; Scott Smith et al., 2013).

The samples are macrocrystic, with macrocrysts composing 10 to 25 modal %. Olivine is the dominant macrocryst phase (composing 70-90% of all macrocrysts) followed by phlogopite. Only one macrocryst grain was encountered that was not a (former) olivine or phlogopite. This was a 4 mm diopside macrocryst that is also notable because it contains an inclusion of rare unaltered olivine. Olivine macrocrysts (and microcrysts) are typically 1.5 to 4 mm in maximum dimension and virtually entirely replaced by secondary minerals, mainly serpentine, chlorite and calcite. Some of the macrocrysts appear to represent the cores of juvenile lapilli, which are often

surrounded by fibrous diopside. Olivine macrocrysts (and microcrysts) may be elongated, blocky, tabular or ovoid, with the latter two morphologies being most common. Secondary calcite most often exists in the cores of the (altered) olivine macrocrysts, whereas chlorite forms rims 50 to 100 μm in width, with serpentine making up the remainder. Phlogopite macrocrysts tend to be 2 to 3 mm in size and tabular to ovoid (Fig. 4.2). Phlogopite macrocrysts tend to be unaltered, but in some cases are replaced to a small degree by chlorite-smectite.

Olivine phenocrysts and microphenocrysts (0.5 to 1 mm) are very abundant in Camatue kimberlite samples (typically composing 15-25 modal %). These grains are dominantly ovoid and display conspicuous chlorite replacement of their rims, with interiors of serpentine ± calcite (Fig. 4.3). Phlogopite phenocrysts and microphenocrysts (also typically 0.5 to 1 mm) also exist, and are usually unaltered. The phlogopite macrocrysts often contain growth zones with abundant small (<100 μm) polygonal opaque oxide grains.

The groundmass is mainly composed of interstitial serpentine and calcite, as well as replaced groundmass olivine (the latter, with prominent chlorite rims around calcite±serpentine or entirely replaced by chlorite, composing roughly 15-25 vol.% of the groundmass) and a small proportion of opaque oxides (<2 modal %), as well as fine-grained minerals.

Crustal xenoliths are relatively abundant in Camatue samples, occurring in two of the four kimbrlite thin sections, and one sample, entirely comprised by a large crustal xenolith sample was chemically analysed (RG165110). As far as can be determined, all of the crustal xenoliths are mafic and those that are not extensively altered tend to be composed of hornblende- and sometimes biotite-bearing bearing gabbronorite and websterite. Olivine, clinopyroxene, orthopyroxene, hornblende and opaque oxides in these xenoliths are most often well preserved (Fig. 4.2), whereas plagioclase tends to be more altered (often to epidote). In a few cases, hornblende is the only phase to be preserved while the rest of the xenolith is heavily altered and no other phase is identifiable (Fig. 4.2).

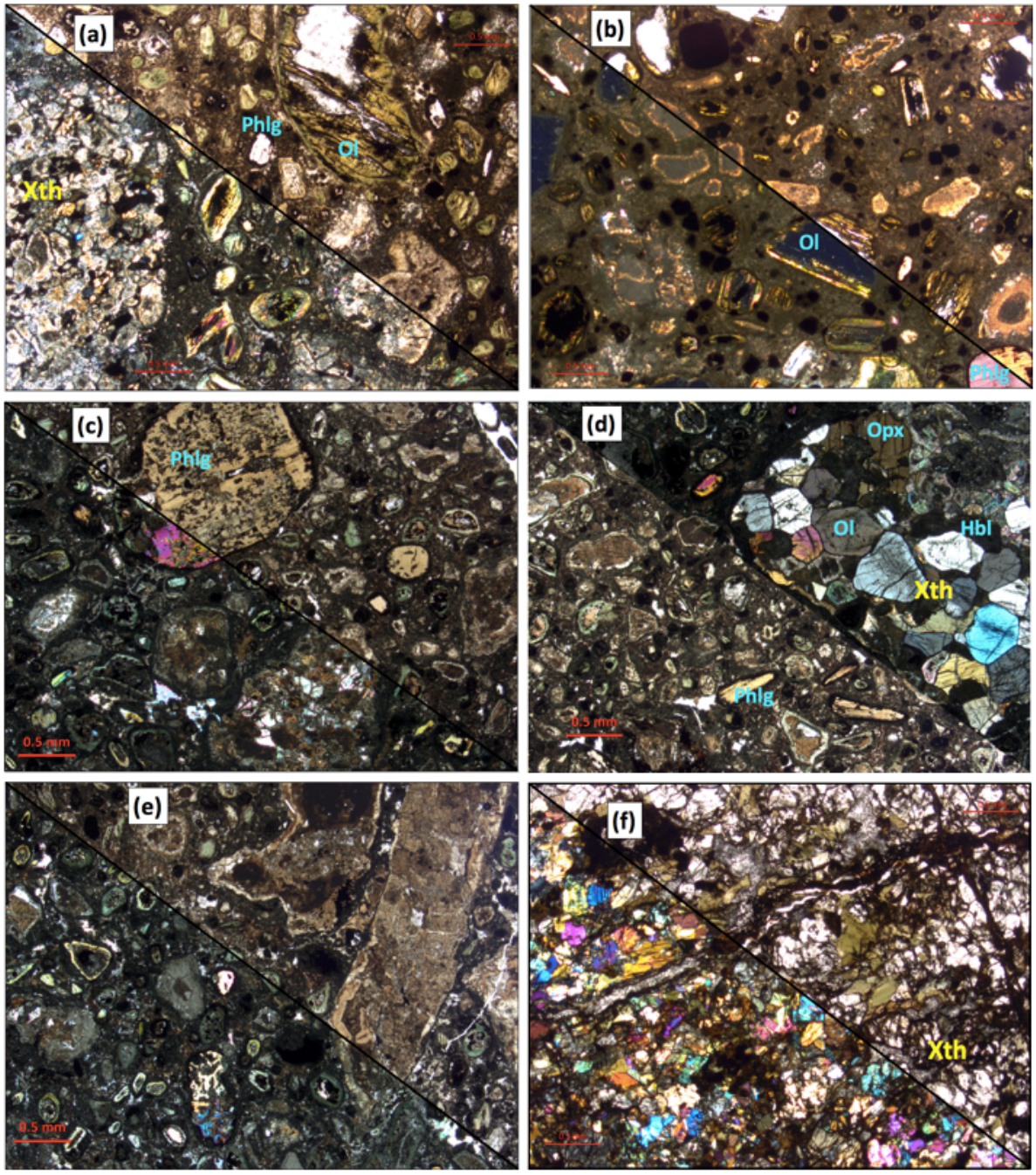

Figure 4.2: Photomicrographs of selected features of Camatue kimberlite samples and entrained crustal xenoliths. Photomicrographs are shown in plane polarised (top triangle) and cross polarised (bottom triangle) except in **(d)** where it is the opposite. Field of view is 4.5 mm. **(a)** Sample CAT 1 : abundant olivine phenocrysts and microphenocrysts. A partly altered mafic crustal xenolith can be seen with fresh hornblend while the rest is heavily altered. **(b)** Sample CAT 3: Altered olivine macrocrysts with abundant olivine microphenocrysts opaque oxides and few phlogopites. **(c)** Sample CAT 4B: macrocrystal texture with occasional phlogopite macrocrysts, abundant serpentinised and altered olivine, phlogopite microphenocrysts and opaque oxides. (d) CAT 4B: fresh hornblende

gabbronorite xenolith. **(e)** CAT 4B: macrocrystal texture, diatreme facies. **(f)** Fresh meta-gabbro xenolith with olivine, orthopyroxene, clinopyroxene, hornblende and opaque oxides. Note scale bar of 0.5 mm

These xenoliths can vary in size, from a few millimeters up to more than 25 cm in size. Crustal xenoliths were carefully excluded during sample preparation for chemical and isotopic analysis.

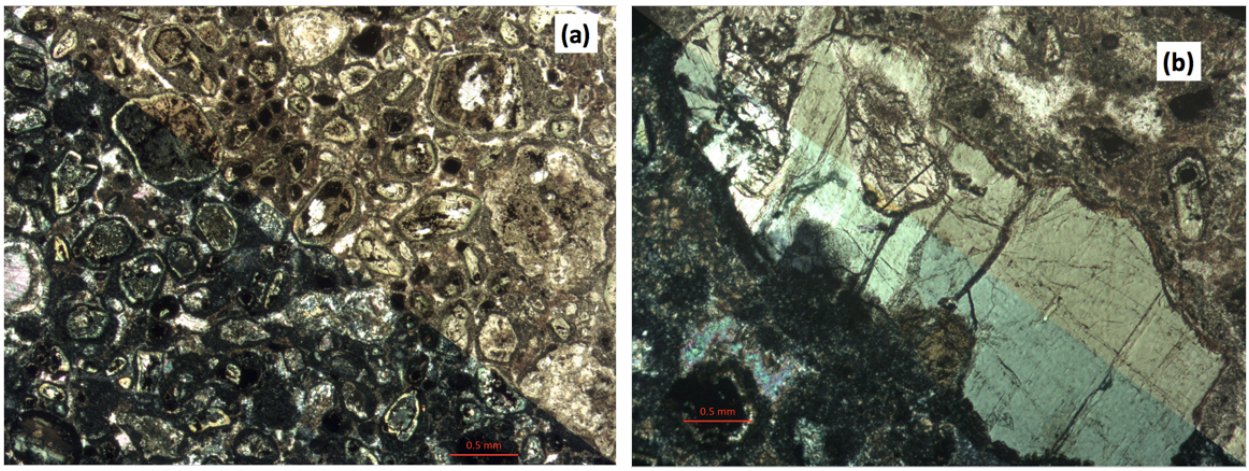

Figure 4.3: Photomicrographs of a Camatue sample showing (a) olivine phenocrysts with chlorite replacement in their rims and (b) clinopyroxene macrocryst with fresh olivine inclusion

4.4.2. TSHIBWE KIMBERLITE

Samples from the Tshibwe kimberlite display little textural variation in thin section. Tshibwe samples are more heavily serpentinised and altered than those from Camatue, and have less than 10 modal % macrocrysts, but they appear to also have a volcaniclastic (pyroclastic) texture (Scott Smith et al., 2013). Fresh olivine is not present and has been replaced by serpentine, which is the most abundant phase in the Tshibwe samples.

Textural evidence for replaced olivine macrocrysts with recognisable (euhedral to subhedral) shapes are present, but at relatively low abundance in Tshibwe samples (1-3 vol.%). However, large, sometimes spiral-shaped "books" of antigorite serpentine are fairly abundant (typically 2-5 modal%). These do not appear to represent post-emplacement replacement features, but on the basis of textural evidence they could represent syn-emplacement alteration products after olivine, such as has been documented by Porritt et al. (2012) in the Ekati kimberlites. The

size of these serpentine "books" (typically 1 to 4 mm) is similar to that expected for olivine macrocrysts, but their lack of typical olivine morphology suggests that alteration took place prior to final emplacement/deposition of the kimberlite. Rarely, (such as in sample TK-11) antigorite can be found that is undeformed and appears to be pseudomorphing ovoid olivine macrocrysts. The Tshibwe kimberlite is located within a large aquifer and a large number of pumps are required to keep the pit drained. If such an aquifer existed at the time of kimberlite eruption, the emplacement of the kimberlite into such a wet environment could potentially have resulted in alteration of olivine macrocrysts contemporaneously with emplacement that might explain the abundance of large deformed antigorite serpentines.

Garnet is the next most abundant macrocryst phase, occuring in nearly all thin sections of Tshibwe samples. Garnet macrocrysts typically constitute <1 to 2 modal %, and are 2 to 6 mm in size, although many appear to be fragmentary. Garnet microcrysts (less than 2 mm anhedral grains) are present in about half of the thin sections, but most of these are anhedral and appear to be fragmentary (often indicated by partial kelyphite rims).

Diopside clinopyroxene is the least abundant macrocryst and microcryst type present (<1 vol.%), although it is also present in most samples. Sample TK-11 contains an extraordinarily large (6 mm long) diopside macrocryst and more than half of the samples contain at least one identifiable diopside macrocryst or microcryst (Fig. 4.4). As with garnet, the diopside microcrysts are all anhedral and most appear fragmentary.

Olivines may have also been present as phenocrysts or microphenocrysts, but the alteration makes it difficult to discern them from the general (largely replaced) matrix assemblage. The groundmass of the Tshibwe kimberlite samples is dominated by serpentine (>70 vol.%), but also contains calcite (1-6 vol.%) and opaque oxides (1-3 vol.%). Fine perovskite, apatite and occasional rutile have been identified in the groundmass by electron microscopy at Macquarie University (this was done during the search for perovskite grains to date by the U-Pb technique).

As at Camatue, crustal xenoliths are common at Tshibwe, mainly seen as blocks of gabbro and gabbronorite up to 4 cm in length (Fig. 4.4). Plagioclase in these samples is extensively altered, whereas the pyroxene is relatively fresh. Unlike at Camatue, these xenoliths lack hydrous phases such as hornblende or biotite. Extreme care was taken during the picking of crushed kimberlite under the microcsope to exclude crustal xenoliths from the fractions prepared for chemical and isotopic analysis.

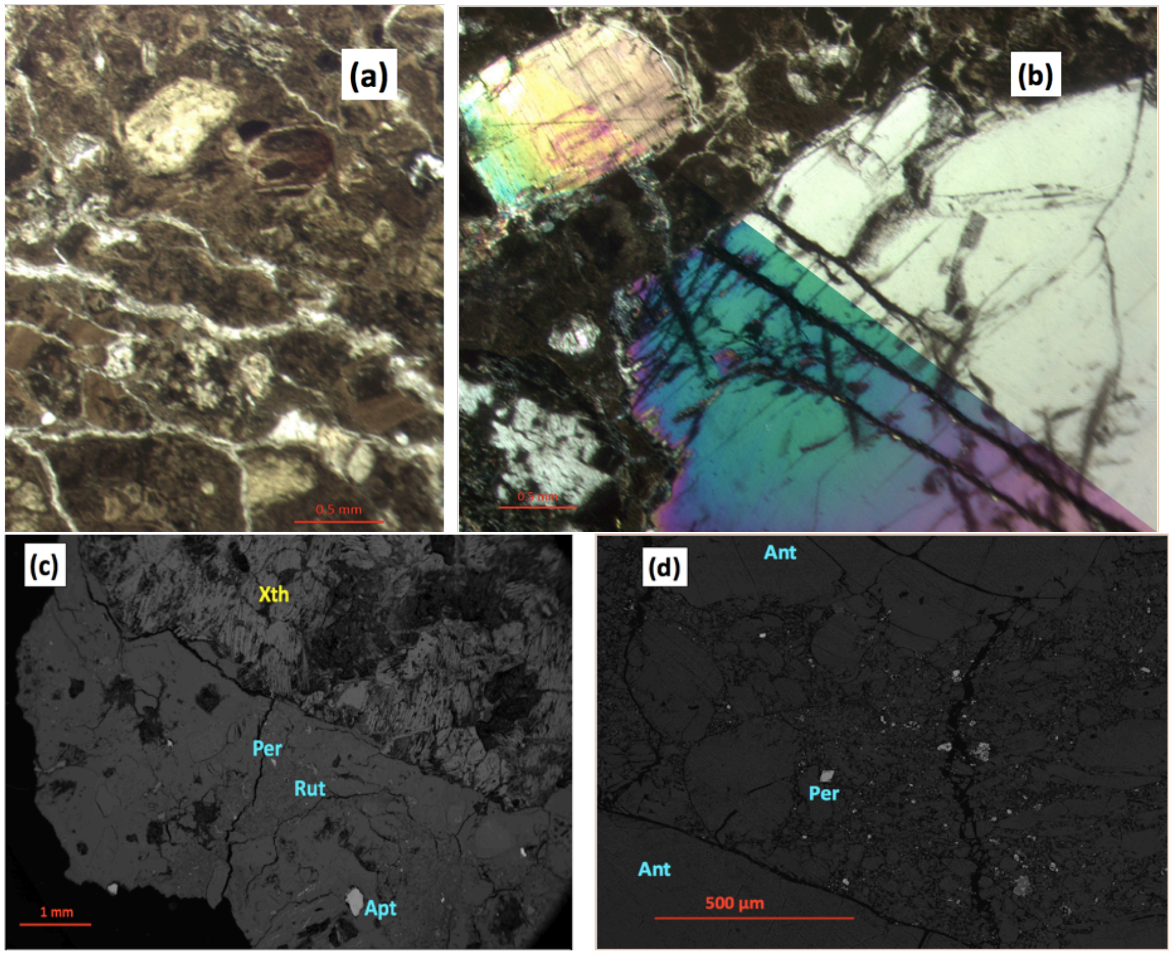

Figure 4.4: Photomicrographs of selected features of Tshibwe kimberlite samples. Photomicrographs (b) are shown in plane polarised (top triangle) and cross polarised (bottom triangle). Field of view is 4.5 mm for (b). **(a)** sample TK 2: calcite phenocryst and microphenocrysts set in a heavily serpentinised matrix. **(b)** Sample TK 11: clinopyroxene macrocryst next to Antigorite phenocryst (top left) set in a heavily altered and serpentinised matrix. **(c)** Sample TK 11: BSE image showing a massive altered crustal xenolith (gabbronorite). Perovskite grain (euhedral with no zonation, 80 µm), rutile (euhedral, zoned and altered, 30 µm) set in serpentine rich groundmass can be observed. Apatite (anhedral, 260 µm) set in serpentinised matrix is also seen. **(d)** Sample TK 8: BSE image showing serpentine phenocrysts (top left and bottom left) and microphenocrysts (centre left), serpentine rich groundmass (centre) with minerals such as perovskite, rutile, barite, ilmenite and spinel. Most of these minerals except perovskite and ilmenite are heavily altered. Small fragments of these minerals are recognizable in the groundmass.

4.4.3. KUNDELUNGU KIMBERLITES

The Kundelungu kimberlite samples investigated in this study do not contain crustal xenoliths, and all are of the hypabyssal (Coherent) facies.

Konzi

The kimberlite samples from the Konzi kimberlite (KKO-1 and KK-1) are relatively fresh. Sample KK-1 is macrocrystic, with slightly more than 10 vol.% olivine macrocrysts (these are up to 5 mm, mostly fresh aside from thin serpentine rims). Sample KKO-1 has larger, but more sparse olivine macrocrysts, and thus is strictly classified as aphanitic. However, the total modal amount of olivine in the two samples is approximately equal. Olivine macrocrysts and microcrysts are elongated, tabular or ovoid. Many macrocrysts and microcrysts display strain features such as kink bands and undulatory extinction. Olivine rims on macrocrysts are often altered and replaced by iddingsite, but the total proportion replaced is typically <15%. Microcrysts and phenocrysts (5-15 vol%) can be more altered, with up to 25% replacement.

The groundmass is composed of matrix olivine, interstitial calcite, serpentine, montecellite with variable amounts of opaque oxides (Fig. 4.5).

Msipashi

The kimberlite samples from Msipashi pipe (KM4, KM5, KM3 and KM33) are quite similar, but differ in their degree of alteration. Olivine macrocrysts, up to 8 mm in length, occupy typically 2-5 vol% and are largely (50-70 vol.%) replaced by serpentine. Olivine phenocrysts (1 mm-0.5 mm) are not abundant as in Konzi samples. When they do occur, they are nearly entirely replaced by serpentine ± calcite. Calcite microphenocrysts and groundmass grains (< 0.5 mm) are very abundant (5-15 modal %). In the least altered samples (KM33 and KM4) secondary calcite (most likely replacing olivine) is present. Garnet macrocrysts are present (<1 volume %) with ilmenite macrocrysts (up to 1 volume %). The garnet macrocrysts are often fragmentary and have partial kelyphite rims (Fig. 4.5)

The groundmass is mostly composed of serpentine, calcite, opaque oxides and perovskite, in decreasing abundance (Fig. 4.5).

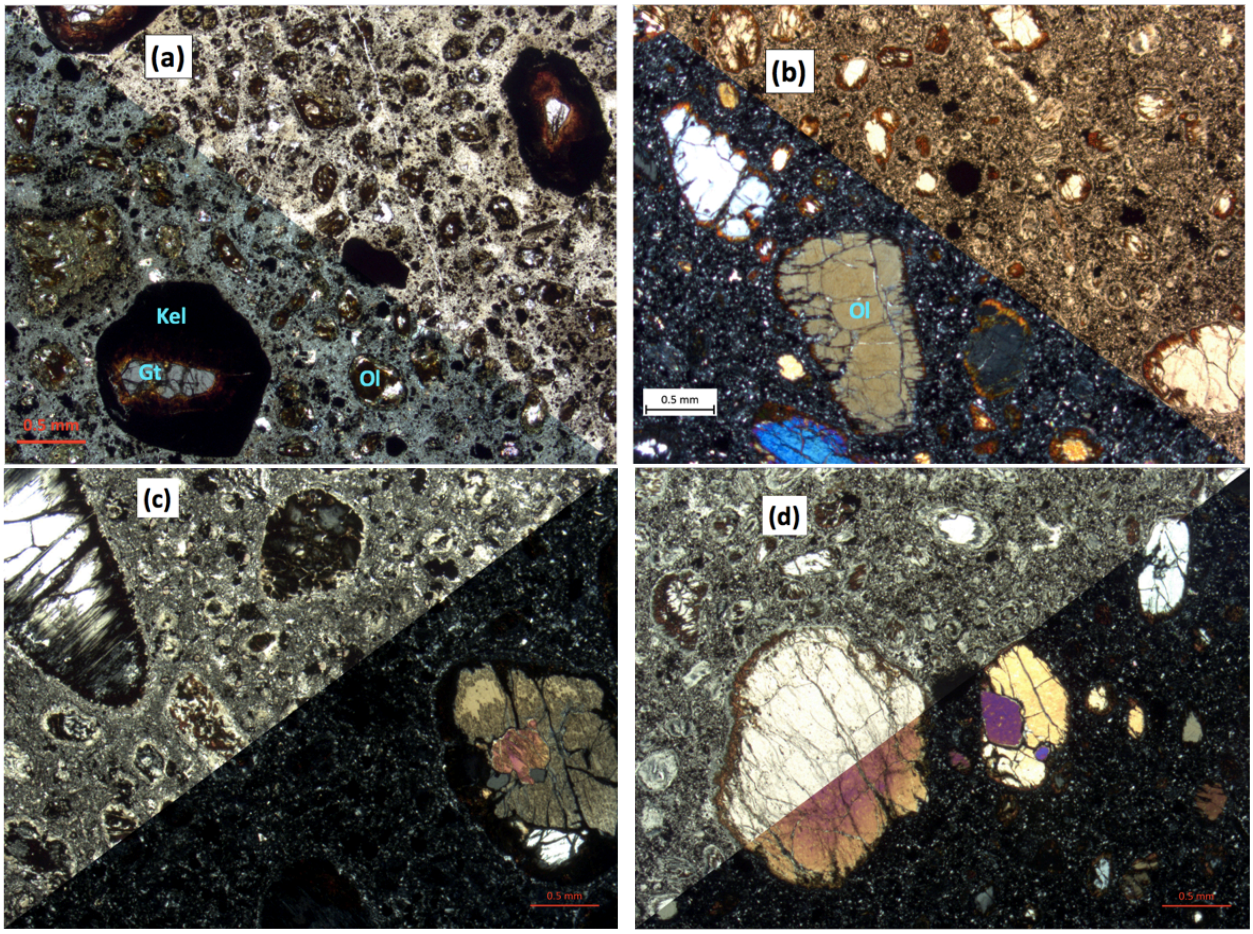

Figure 4.5: Photomicrographs of selected features of Kundelungu kimberlites. Photomicrographs are shown in plane polarised (top triangle) and cross polarised (bottom triangle) and the field of view is 4.5 mm. (a) Sample KM-33 (Msipashi): altered garnets microcrysts with kelyphite rims. Calcite and olivine microphenocrysts also occur. Note the higher abundance of interstitial calcite (small bright spots in xpl) in the groundmass. (b) Sample KKO-1 (Konzi): fresh Olivine microcrysts and microphenocrysts set in calcite-serpentine groundmass with variable amounts of opaque oxides. (c) Sample KKA-1 (Kashioba): olivine macrocryst with fresh core and olivine phenocrysts significantly replaced by serpentine. (d) Sample KZ-1 (Zefu): olivine "phemocrysts" and calcite and olivine "micrphenocrysts".

Kashioba

The kimberlite sample from Kashioba (KKA-1) is technically aphanitic, containing only 2-3% macrocrysts (mainly olivine), but abundant olivine microcrysts and phenocrysts (≈ 25 vol. % total olivine, prior to alteration). The sample also contains one exceptionally large (8 mm) clinopyroxene macrocryst with some olivine inclusions. Olivine in this sample is significantly replaced (25-100%, with the large grains being generally less replaced) by serpentine (Fig. 3.5). Serpentine is also the main groundmass constituent, along with monticellite and oxide minerals.

Zefu

The kimberlite sample from Zefu (KZ-1) contains relatively few olivine macrocrysts (up to 6 mm), composing perhaps 5-8 vol.% of the sample, and thus is classified as aphanitic. It does have abundant olivine microcrysts (typically 0.2 to 0.5 mm), now replaced by serpentine and calcite. Most are ovoid and elongate in shape, while fewer are angular. This sample is significantly more altered overall than the other Kundelungu kimberlite samples.

Garnet macrocrysts (<1 volume %) occur and have kelyphite rims. Ilmenite macrocrysts are present in lower abundance (<1 volume %). These two phases (garnet and ilmenite) occur again as microcrysts but are not abundant in Zefu samples (less than 1 volume %). The groundmass is composed of serpentine and calcite with less than 2 vol.% opaque oxides

4.5. MAJOR ELEMENT GEOCHEMISTRY

The major element geochemistry of the samples investigated from Camatue, Tshibwe and the Kundelungu kimberlites are reported in Table 4.1 and shown in Figure 4.6.

4.5.1. CAMATUE

Camatue kimberlite samples show significant variations in SiO_2 (32.3 – 40.5 wt.%), TiO_2 (1.3 to 1.9 wt.%), FeO^{tot} (8.0 – 11.5 wt.%), Na_2O (1.0 to 3.7 wt.%) and K_2O (0.1 to 0.8 wt %) with somewhat more restricted ranges of Al_2O_3 (5.1 to 6.3 wt.%), MgO (13.6 to 15.2 wt.%), CaO (11.5 to 14.1 wt.%) and P_2O_5 (0.8 to 1.1 wt.%). Their high Al_2O_3 and Na_2O values are uncharacteristic of kimberlites globally, and their MgO contents are below the range of fresh southern African Group 1 kimberlites. Therefore, it seems likely that these samples have been affected by hydrothermal alteration.

Despite the fact that the Camatue samples have Mg# values of near-primary magmas (73-77), the large modal percentage of (now replaced) olivine macrocrysts in the Camatue kimberlite samples suggests that these samples originally had significantly higher MgO contents than they do currently (with a maximum of 15.2 wt.%). The large amount of replacement of olivine by chlorite (presumably glagolevite) and chlorite-smectite would have lowered MgO and increased Al_2O_3 far more than replacement of olivine by serpentine (Giuliani et al., 2017). This likely explains why the Camatue samples fall well off of the trends of MgO versus SiO_2, TiO_2, CaO and K_2O defined

by for southern African kimberlites, which is mainly explained by variable accumulation or fractionation of olivine (e.g., le Roex et al., 2003; Becker & le Roex, 2006).

It is likely significant that the SiO_2, Al_2O_3 and MgO contents of the Camatue kimberlite samples reported here are virtually identical to those of samples of the Mbuji-Mayi kimberlite reported by Demaiffe and Fieremans (1981), described as having significant modal proportions of secondary chlorite. Additionally, samples of kimberlites from southwestern Angola (Egorov et al., 2007) share many major element similarities with the Camatue kimberlites, including relatively high Al_2O_3 and Na_2O and low MgO. The likelihood that the high SiO_2, Al_2O_3 and Na_2O (and possibly low MgO) values of the Camatue samples are due to crustal assimilation seems low, given that the only crustal xenoliths identified in these samples are mafic to ultramafic in composition. One crustal xenolith from Camatue that was sufficiently large for measurement of major and trace element composition is a plagioclase-poor gabbronorite with 47.2 wt.% SiO_2, 4.7 wt.% Al_2O_3, 16.6 wt.% MgO and 0.7 wt.% Na_2O (Table 3.1). Assimilation of such material is unable to explain the elevated Al_2O_3 and Na_2O composition of the Camatue kimberlite samples. There is also no indication from their incompatible element compositions for significant crustal assimilation (e.g., relatively high HREE and/or Pb concentrations, see section 3.6 below).

The variable and relatively high Na_2O contents of the Camatue samples seem clearly related to alteration, as Na_2O is highest in the sample with the most extensively replaced groundmass (CAT-3), which also has the lowest MgO and highest SiO_2, and lowest in the samples with less replaced groundmasses (except for groundmass olivine which is universally replaced), which have higher MgO (e.g., CAT-4A and CAT-4B).

4.5.2. TSHIBWE

Tshibwe kimberlite samples show substantial variations in MgO (20.5 – 26.7 wt.%), SiO_2 (33.9 – 39.3 wt.%), $FeO^{tot.}$ (5.1 to 7.0 wt.%) and CaO contents (3.8 to 11.2 wt.%) and much more restricted variations in TiO_2, Al_2O_3, MnO, Na_2O and K_2O. MgO and SiO_2 are only weakly correlated ($r^2 = 0.3$), but a regression through these data passes very close to the composition of mantle olivine (with ≈50 wt.% MgO and ≈40 wt.% SiO_2). MgO and FeO^{tot}. are quite strongly correlated ($r^2 = 0.9$) with a regression that also passes close to mantle olivine. Therefore, a significant amount of the variation in these oxides may have been controlled by variable olivine accumulation or fractionation. In contrast, Al_2O_3 and CaO contents show weak positive and

negative correlations, respectively, with MgO that are inconsistent with control by olivine accumulation or fractionation. The oxides TiO_2, Na_2O, K_2O and P_2O_5 show no significant correlations with MgO at all.

A strong positive correlation between wt.% CaO and loss on ignition (LOI, which is a measure of the combined CO_2 + H_2O lost during heating to 850°C; $r^2 = 0.8$) suggests that CaO variations are largely controlled by modal calcite, much of which appears to be secondary or re-crystallized on the basis of textural relations. This correlation is equally good if re-normalised, volatile-free CaO contents are plotted vs. LOI. Likely related, there is a strong negative correlation of SiO2 ($r^2 = 0.9$ or 0.7 if normalised) with LOI that likely also reflects the effect of dilution by calcite

In general, Tshibwe samples tend to have lower TiO_2, Al_2O_3, $FeO^{tot.}$, CaO, K_2O and P_2O_5 values for a given MgO content than southern African kimberlites, but higher SiO_2. Na_2O contents in Tshibswe samples are very low (from below detection to 0.04 wt.%), as they are in most southern African Group 1 kimberlites.

.

4.5.3. KUNDELUNGU

Overall, the Kundelungu kimberlite data span a wider compositional range than those from either Camatue or Tshibwe, but this is not surprising given that these samples are derived from five different kimberlites. The single sample from the Zefu kimberlite (KZ-1, western Kundelungu cluster), has, by far, the lowest MgO, SiO_2 and Fe_2O_3 contents, as well as the highest CaO content (this, plus its high loss on ignition value of 24.3 wt.%, are almost certainly related to the sample's high modal calcite content and substantial replacement of olivine by secondary calcite).

The remaining samples from the Msipashi (KM3, KM4, KM5 and KM33), Konzi (KK-1 and KKO-1), Kashioba (KKA-1) and M'Bo (KUN-1) kimberlites together show a moderate degree of major element variation that reproduces fairly well the geochemical variation of southern African Group I kimberlites, covering nearly half of the total range of major element variation of the latter. As with southern African kimberlites, these samples display a positive correlation of MgO with SiO_2 and negative correlations of MgO with TiO_2, Al_2O_3 and CaO. There are no systematic compositional differences between samples from the eastern (Msipashi) and western Kundelungu kimberlites (Kashioba, Konzi, M'Bo and Zefu). The only significant differences between the Kundelungu kimberlites and southern African Group I kimberlites in general are: a

slightly higher FeOtot. content for a given MgO value (excluding sample KZ-1), and lower average K_2O and P_2O_5 contents.

The small number of samples and localities for which whole rock data are available for central African kimberlites, plus the added uncertainties caused by variable possible extents of alteration, make it impossible to find clear, significant differences in primary kimberlite compositions either between kimberlites emplaced in on- and off-craton settings in central Africa. This is not surprising, since, even in a much broader study of entirely fresh and hypabyssal samples, Becker and le Roex (2006) found only very subtle systematic geochemical differences between on- and off-craton Group I kimberlites.

Kimberlites from Lac de Gras and the Superior craton in Canada have higher Cr_2O_3, TiO_2 contents than central African kimberlites analysed in this study. The latter display slightly lower MgO and Na_2O contents than their Canadian counterparts (Kjarsgaard et al., 2009; Tappe et al., 2017). Kimberlites from the Siberian craton display similar major element compositions to central African kimberlites analysed in this study (Kamenetsky et al., 2014; Agashev et al., 2018).

Table 4.1: XRF major element analyses of Central African kimberlites

Locality	Sample	SiO_2	TiO_2	Al_2O_3	$Fe_2O_3^{tot.}$	MnO	MgO	CaO	Na_2O	K_2O	P_2O_5	Cr_2O_3	NiO	H_2O^-	LOI	Sum	Mg#
Camatue	CAT-1	38.65	1.44	6.31	10.43	0.15	14.95	12.30	2.52	0.40	0.77	0.03	0.04	3.54	7.49	99.14	76.5
Camatue	CAT-2	32.88	1.90	5.11	12.80	0.18	14.12	13.86	1.31	0.14	1.04	0.04	0.04	4.09	11.51	99.07	71.5
Camatue	CAT-3	40.54	1.25	5.96	9.03	0.14	13.58	11.77	3.65	0.28	0.77	0.03	0.03	5.06	7.15	99.27	77.4
Camatue	CAT-4A	34.51	1.85	5.74	12.79	0.18	15.21	11.89	1.36	0.22	1.14	0.04	0.04	3.61	10.21	98.86	73.0
Camatue	CAT-4B	33.41	1.79	5.89	12.25	0.16	15.14	11.46	0.97	0.17	0.92	0.04	0.05	5.03	11.60	98.97	73.8
Camatue	CAT-5	32.33	1.66	5.83	12.33	0.21	15.01	14.14	1.13	0.83	1.05	0.04	0.04	2.22	11.74	98.59	73.5
Camatue	CATX	47.23	0.33	4.65	10.89	0.18	16.64	17.97	0.68	0.24	0.04	0.02	0.06			99.34	
Kun., Zefu	KZ-1	21.76	2.41	2.45	8.88	0.21	16.97	18.30	0.04	0.24	0.53	0.16	0.10	1.95	24.26	98.60	81.3
Kun., Kashioba	KKA-1	29.18	2.94	3.52	11.80	0.21	26.23	14.56	0.11	0.24	0.61	0.21	0.09	0.14	8.66	98.94	83.5
Kun., Konzi	KKO-1	28.62	1.84	2.01	10.35	0.17	31.87	9.34	0.08	0.59	0.37	0.24	0.12	0.16	13.04	98.90	87.5
Kun., Konzi	KK-1	29.88	2.01	2.30	10.85	0.19	32.16	10.22	0.13	0.59	0.49	0.31	0.12	0.13	9.45	99.03	87.1
Kun., Msipashi	KM33	30.17	2.71	3.21	10.59	0.19	28.31	6.70	<0.02	0.03	0.55	0.18	0.08	0.19	15.73	98.68	85.9
Kun., Msipashi	KM-3	28.71	2.76	3.21	11.01	0.19	26.74	8.52	<0.02	0.04	0.67	0.19	0.09	0.25	16.31	98.73	84.7
Kun., Msipashi	KM-4	30.96	2.72	3.21	10.53	0.19	28.61	6.02	<0.02	0.04	0.56	0.18	0.08	0.23	15.40	98.76	86.1
Kun., Msipashi	KM-5	28.58	2.76	2.91	10.68	0.19	26.83	8.49	<0.02	0.03	0.56	0.18	0.10	0.18	16.96	98.48	85.1
Kun., M'Bo	KUN-1*	32.84	1.78	2.40	10.85	0.22	35.80	5.37	<0.2	0.24	0.46	n.a.	n.a.	n.a.	10.29	100.47	88.3
Tshibwe	TK1	39.33	0.98	2.71	6.24	0.15	22.32	7.00	0.04	0.32	0.16	0.15	0.13	9.29	11.17	100.03	89.1
Tshibwe	TK2	36.86	1.10	2.47	6.42	0.16	21.92	9.01	0.02	0.31	0.14	0.15	0.13	8.67	12.60	99.98	88.6
Tshibwe	TK3	34.51	0.90	2.22	6.01	0.19	20.53	11.10	<0.02	0.26	0.13	0.16	0.13	7.56	14.31	98.05	88.6
Tshibwe	TK4	37.78	0.97	2.78	5.86	0.10	21.17	7.20	0.04	0.48	0.13	0.13	0.12	8.92	11.23	97.17	89.2
Tshibwe	TK5	37.78	1.07	2.82	7.05	0.12	24.35	5.42	0.03	0.33	0.24	0.15	0.14	7.79	11.34	98.67	88.7
Tshibwe	TK6	39.14	1.05	2.67	7.33	0.12	24.77	4.97	0.02	0.30	0.18	0.15	0.14	7.76	10.94	99.58	88.5
Tshibwe	TK7	38.04	1.22	2.68	7.59	0.12	25.37	5.03	0.04	0.36	0.31	0.16	0.14	6.86	11.01	98.97	88.4
Tshibwe	TK8	36.85	1.02	2.52	7.07	0.11	25.47	6.13	<0.02	0.34	0.16	0.14	0.14	6.35	12.39	98.79	89.1
Tshibwe	TK9	35.81	0.98	2.27	5.66	0.17	20.57	11.15	b.d.	0.23	0.13	0.12	0.12	7.69	13.79	98.74	89.2
Tshibwe	TK10	38.55	0.96	2.91	7.12	0.11	25.07	5.38	0.02	0.35	0.19	0.16	0.14	7.61	11.23	99.84	88.9
Tshibwe	TK12	39.06	1.05	2.78	6.93	0.12	24.60	5.63	0.03	0.32	0.23	0.17	0.13	7.49	11.25	99.83	89.0
Tshibwe	TK13	38.91	1.02	2.67	7.76	0.10	26.73	3.80	0.02	0.34	0.23	0.16	0.15	6.60	10.95	99.51	88.7
Tshibwe	TK15	33.94	0.79	2.07	6.32	0.21	22.31	11.27	<0.02	0.21	0.16	0.13	0.13	6.26	15.13	99.05	88.9
Tshibwe	TK16	33.86	0.89	2.38	6.89	0.18	22.80	9.95	b.d.	0.25	0.20	0.14	0.15	6.42	14.49	98.63	88.3
Tshibwe	TK17	36.20	1.05	2.51	6.38	0.15	22.49	8.68	0.02	0.33	0.15	0.17	0.13	7.20	13.14	98.74	88.9
Tshibwe	TK18	39.04	1.02	2.70	6.42	0.13	22.99	6.61	0.02	0.31	0.18	0.15	0.13	8.75	11.31	99.82	89.1
Tshibwe	TK19	36.68	0.94	2.56	6.67	0.16	23.49	7.48	0.02	0.30	0.17	0.16	0.13	7.14	12.90	98.86	88.9
Tshibwe	Tk11	37.80	0.93	2.54	7.07	0.11	25.42	5.39	0.04	0.39	0.18	0.14	0.14	7.84	10.68	98.72	89.1

All data presented are presented in weight percent. $Fe_2O_3^{tot.}$ indicates that all iron is reported as Fe_2O_3. H_2O^- is the weight percentage lost upon heating the sample to 110°C for at least 8 hours. LOI (loss on ignition) is the weight percentage lost upon heating the sample to 850°C for at least 4 hours and includes all structural water and carbon dioxide. Camatue crustal xenolith sample, CATX, included. *The data for sample Kun-1 is from Demaiffe and Fieremans (1981). Abbreviations: "b.d." means below detetection (typically below 0.01 wt.%) and n.a. means "not analysed". Mg-number (Mg#) is atomic 100*Mg/(Mg + Fe^{+2}), calculated using an Fe_2O_3/FeO ratio of 0.15

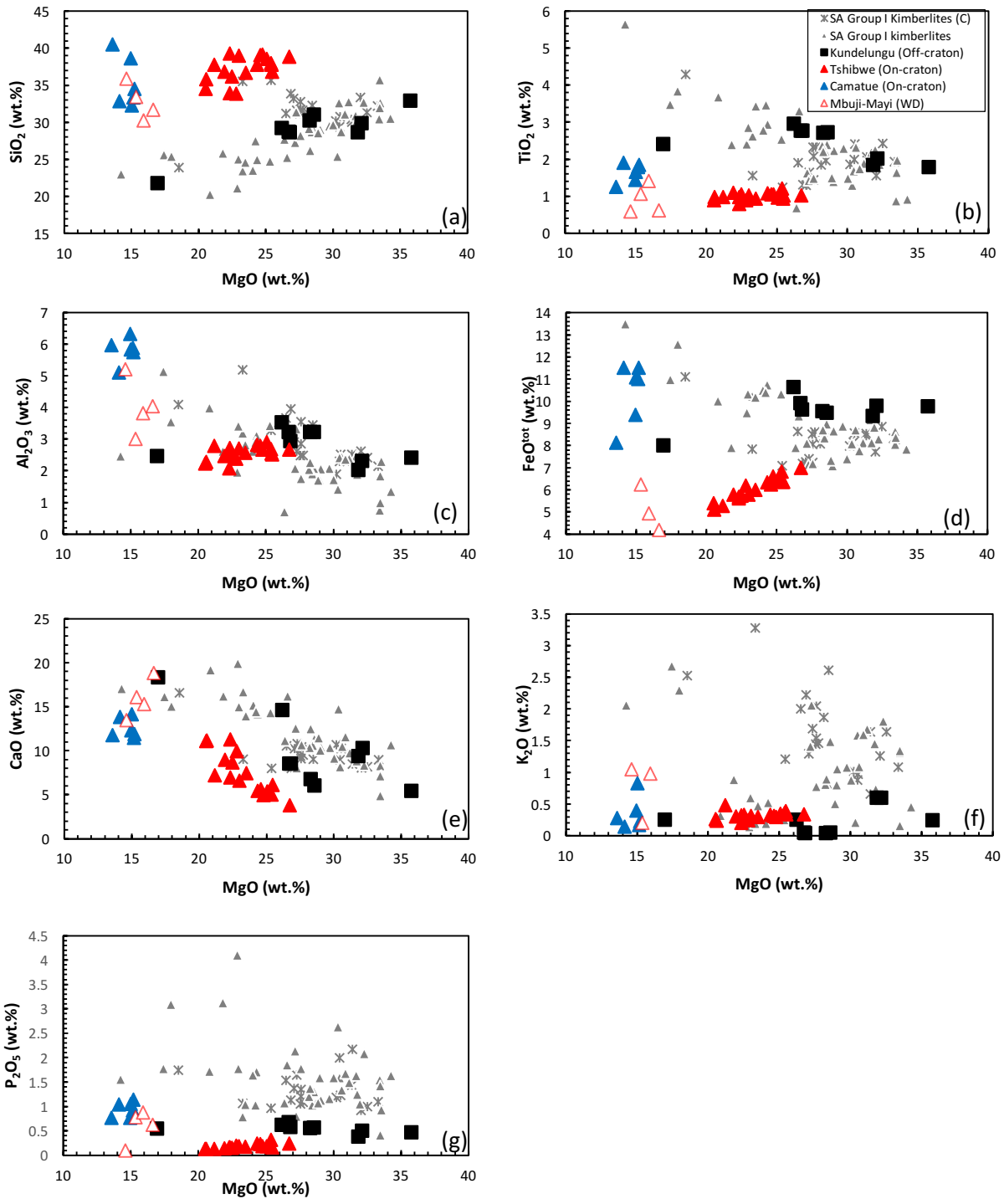

Figure 4.6: Variation of selected major oxides versus wt.% MgO for on and off-craton central African kimberlites. (a) SiO_2, (b) TiO_2, (c) Al_2O3, (d) $FeO^{tot.}$, (e) CaO, (f) K_2O, (g) P_2O_5. Values plotted are measured values (not normalised volatile free). Southern African kimberlite data are from le Roex et al., (2003) and Becker and le Roex (2006). (C in legend means crustally contaminated).

4.6. TRACE ELEMENT GEOCHEMISTRY

4.6.1. COMPATIBLE ELEMENTS

The compatible trace elements Ni and Cr display wide ranges in central African kimberlites. Both elements are weakly positively correlated with MgO in the samples as a whole. Camatue kimberlite samples have the lowest concentrations of the compatible elements Cr (254-330 ppm) and Ni (274-364 ppm), falling below the concentration range of these elements in southern African Group I kimberlites (Fig. 4.7), but close to the regression of these data projected to low MgO, Cr and Ni values. The Kundelungu kimberlites are the only single group that display significant correlations, and only if sample KZ-1 (Zefu pipe) is excluded because of its low MgO relative to its Cr and Ni contents. The Tshibwe samples fall close to, and partially overlap with the southern African Group I kimberlite data in the plots in Figure 4.7 but fall at higher average Ni and Cr contents for a given MgO content, which could indicate limited Mg loss during deuteric or post-emplacement alteration. In contrast, the Kundelungu kimberlites (again excluding KZ-1) have slighly lower average Ni, but not Cr, for a given MgO content than southern African Group I kimberlites. Because of this, the Kundelungu samples have lower Ni contents, but higher Cr, than the Tshibwe kimberlite samples (Fig. 4.7). Kimberlites from the Superior craton in Canada have higher Cr and Ni contents than central African kimberlites (Tappe et al., 2017). In addition, Kimberlites from the Siberian craton have higher Ni content than analysed central African kimberlites (Agashev et al., 2018).

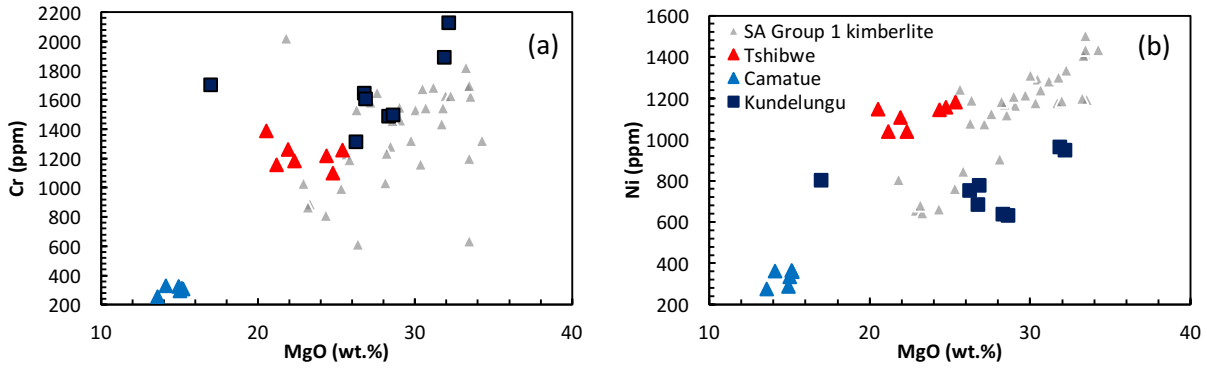

Figure 4.7: Variation of (a) Cr and (b) Ni versus MgO for central African kimberlites. Southern African kimberlites are shown for comparison (le Roex et al., 2003; Becker and le Roex, 2006) (XRF data for Cr and Ni contents).

4.6.2. INCOMPATIBLE ELEMENTS

Central African kimberlites span a wide range in incompatible element concentrations (e.g., 36- 269 ppm Zr, 156-1773 ppm Sr, 36-265 ppm La), which extend to values considerably lower than those displayed by southern African Group I kimberlites (Fig. 4.8). The lowest and least variable values are displayed by samples of the Tshibwe kimberlite, whereas the highest values are generally displayed by those from the Kundelungu kimberlites. Both the Camatue and Kundelungu sample suites tend to display positive correlations between incompatible elements (Fig. 4.8; although correlations involving Ba and Rb tend to be absent), but this is not true of the Tshibwe samples, primarily because they display very small variations in most incompatible elements, and also because variations in some elements (such as Ba) appear to be dominated by alteration processes rather than igneous petrogenesis.

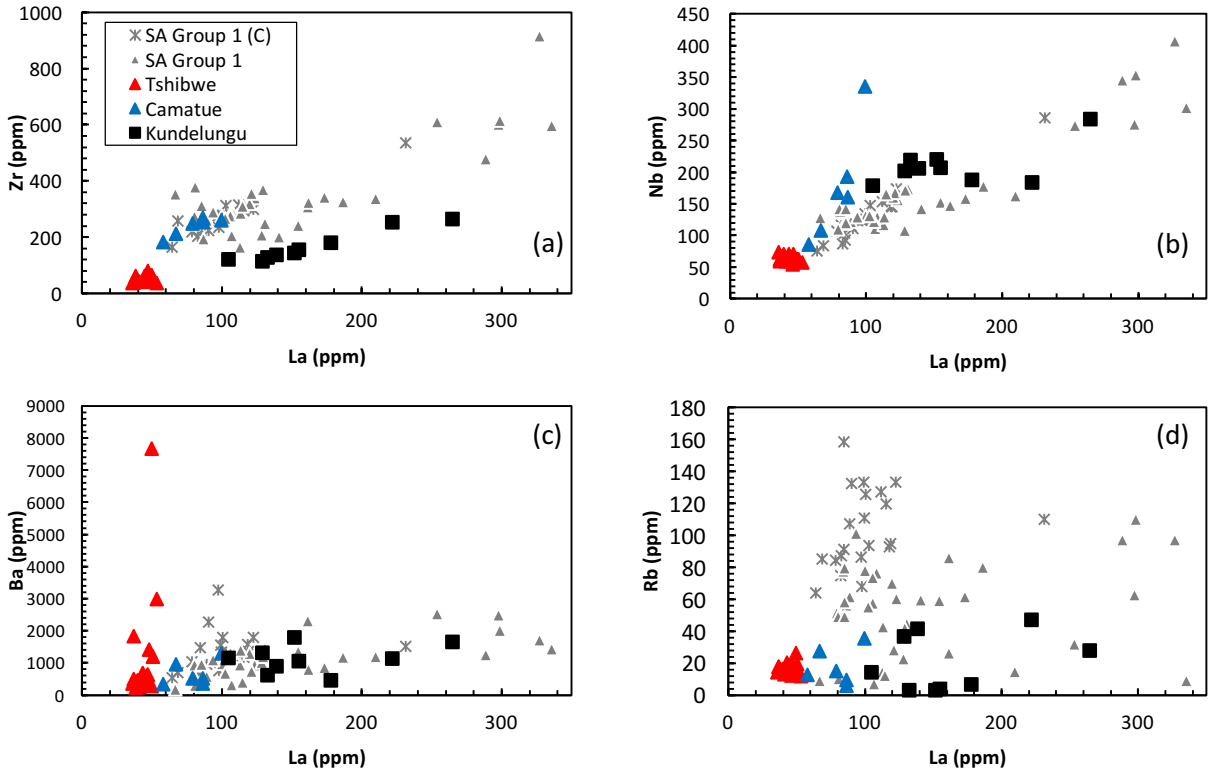

Figure 4.8: Variation of selected incompatible elements versus La for Central African kimberlites: (a) Zr, (b) Nb, (c) Ba, (d) Rb. Southern African Group I kimberlite data are from le Roex et al., (2003) and Becker and le Roex (2006).

There is limited correlation of incompatible element ratios in central African kimberlites. Nb/Zr ratios are similar in all three localities (Nb/Zr = 0.5-1.3, 0.9-2.0 and 0.7-1.8 in Camatue, Tshibwe and Kundelungu, respectively) and Ce/Pb ratios are similar in Camatue and Tshibwe (21-39 and 28-37 for Camatue and Tshibwe, respectively, excluding one anomalously Pb-rich Tshibwe sample, TK-5), although the Kundelungu samples tend to have much higher values (33-125). However, apart from TK-5 and a few anomalously Ba-rich samples of the Tshibwe kimberlite, central African samples fall within the Ba/Nb and Ce/Pb range of southern African Group I kimberlites and outside of the range of Group II kimberlites (of which most have Ce/Pb < 20 and Ba/Nb > 15; Fig. 3.9).

The three sample groups are clearly separated in terms of their $(La/Sm)_N$ ratios, with Camatue, Tshibwe and the Kundelungu kimberlites having values of 5.6 to 5.9, 6.4 to 8.0 and 9.2 to 10.5, respectively. The ratios Th/Nb and La/Nb and both correlate positively with $(La/Sm)_N$, with Camatue having the lowest and Kundelungu the highest values of these ratios (Fig. 4.9). However, unlike $(La/Sm)_N$, the three kimberlite groups have signficant overlap in La/Nb and Th/Nb ratios.

It is noteworthy to mention that kimberlites from the Superior craton in Canada and those from Siberia craton in Russia have similar incompatible trace element ratios to those displayed by southern African kimberlites (Tappe et al., 2017; Agashev et al., 2018).

4.6.3. REE PATTERNS

The central African kimberlites within each group display subparallel and nearly identical chondrite-normalised REE patterns, with enrichment in the light REE (LREE), relative to the medium and heavy REE (MREE and HREE; Fig. 4.10). The Camatue samples display very linear REE patterns, whereas the Tshibwe and Camatue samples show a slight flattening of the REE patterns in the HREE (Ho to Lu) compared to steeper slopes in the LREE and MREE.

Ce anomalies (an indication of oxidative alteration) are essentially absent in Camatue and Kundelungu kimberlite samples; they have Ce/Ce* values of between 0.91 and 1.05 (Ce/Ce* is the chondrite-normalised measured Ce concentration divided by that of the value of Ce_N logarithmically interpolated from the La and Pr concentrations). In contrast, 6 out of 18 samples of the Tshibwe kimberlite display negative Ce anomalies (i.e., Ce/Ce* < 0.9), with values as low as 0.83. None of the central African kimberlite samples display Eu anomalies.

Kundelungu kimberlite samples display greater LREE enrichment relative to HREE ($(La/Yb)_N$ = 104 to 206) than those from Tshibwe ($(La/Yb)_N$ = 59 – 98) or Camatue ($(La/Yb)_N$ = 55 – 67). However, this is controlled by both by LREE enrichment and HREE depletion, since while Kundelungu samples have the highest La concentrations (429-1083 times chondrite), samples of the Camatue kimberlite have higher La concentrations (237 – 407 times chondrite) than Tshibwe (146 – 217 times chondrite), despite having lower average $(La/Yb)_N$ values.

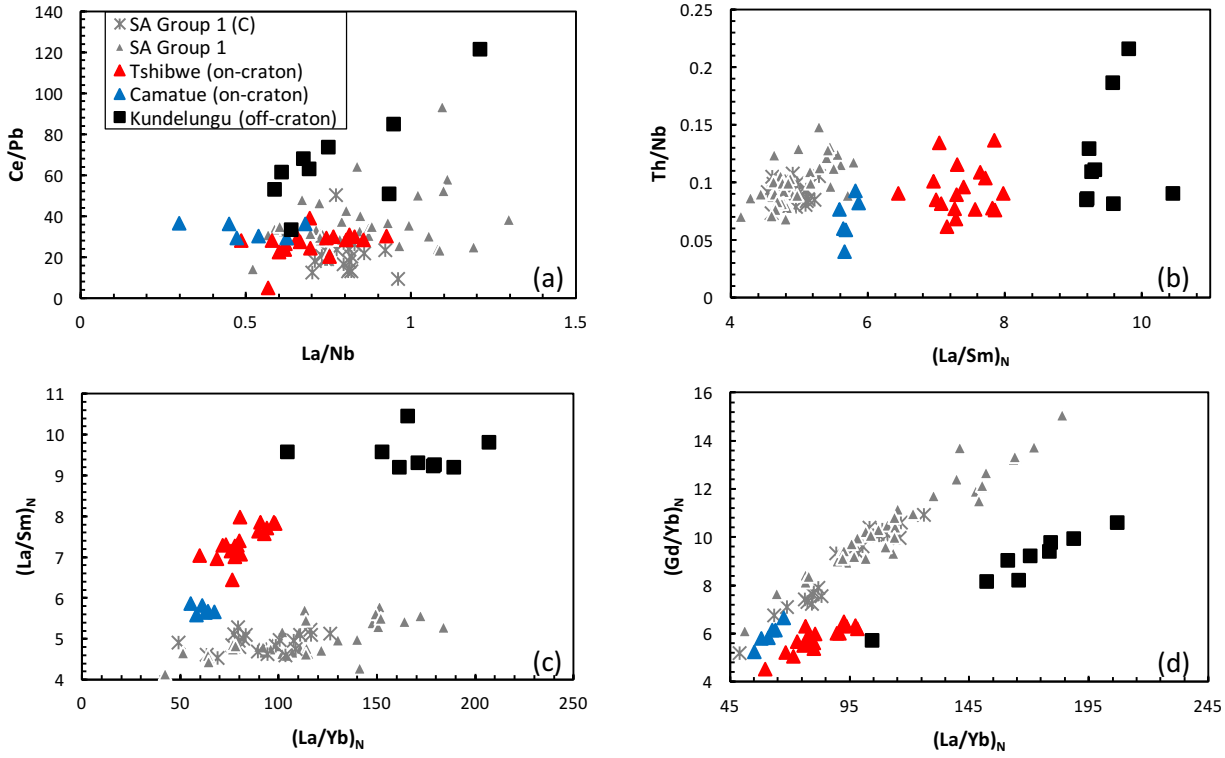

Figure 4.9: Variation of selected incompatible element ratios in Central African Kimberlites. (a) La/Nb versus Ce/Pb. (b) $(La/Sm)_N$ versus Th/Nb. (c) $(La/Yb)_N$ versus $(La/Sm)_N$. (d) $(La/Yb)_N$ versus $(Gd/Yb)_N$. Southern African Group I kimberlites data are from le Roex et al., (2003) and Becker and le Roex (2006; c = crustally contaminated).

The shape of the REE patterns of kimberlites from central Africa are noticeably different to those from southern Africa. Although the patterns of both are LREE-enriched and HREE-depleted, most southern African Group I kimberlite samples have mildly cuved, concave-downward REE patterns (le Roex et al., 2003; Becker & le Roex, 2006; Fig 4.10.). In contrast, central African kimberlites are either virtually straight (e.g., Camatue), or have a slight concave-upward curvature (Tshibwe and Kundelungu, Fig. 3.10). This causes them to fall in distinct areas on plots of $(La/Yb)_N$ versus

$(La/Sm)_N$ and versus $(Gd/Yb)_N$ (Fig. 4.9). Whether this represents a difference in source composition or mantle mineralogy/lithology is unclear.

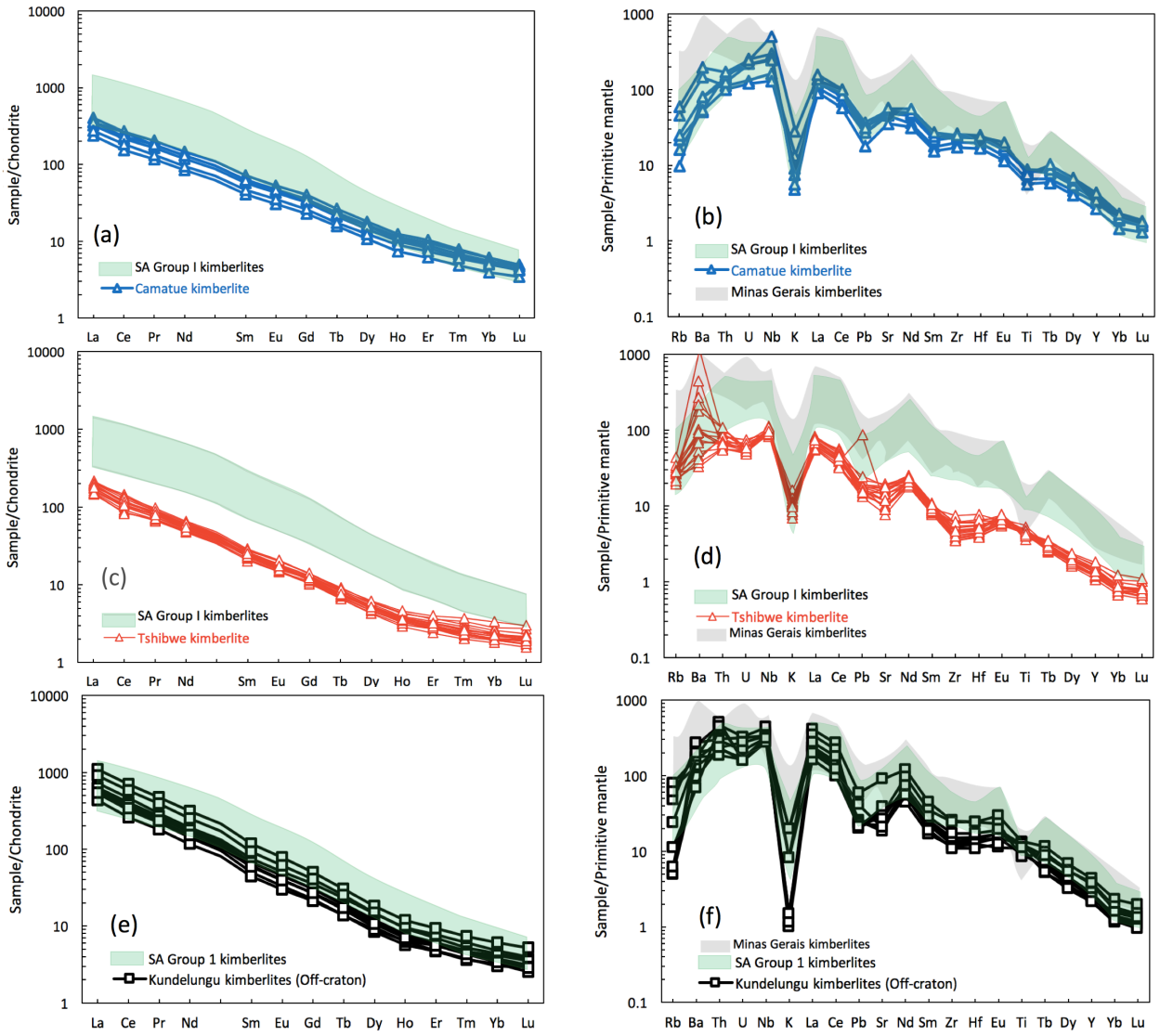

Figure 4.10: Chondrite-normalised REE and primitive mantle-normalised incompatible element patterns of central African kimberlites. Southern African Group I kimberlites and Minas Gerais kimberlites are shown for comparison (Bizzi et al., 1995; Araujo et al., 2001; le Roex et al., 2003; Becker and le Roex, 2006 and Guarino et al., 2013). Normalising values are form McDonough and Sun (1995).

4.6.4. PRIMITIVE MANTLE-NORMALISED INCOMPATIBLE ELEMENT PATTERNS

Central African kimberlite samples from each group display sub-parallel and nearly identical primitive mantle-normalised trace element patterns with variable strong negative K anomalies. In the Tshibwe samples, Ba contents are highly variable, most likely due to alteration, and patterns are characterized by weak negative Zr-Hf anomalies (Fig. 4.10). These features are somewhat distinct from those of Camatue kimberlites, which have mild positive Zr-Hf anomalies and slight negative Ti anomalies (Fig. 4.10). Kundelungu kimberlite samples are notable for having the strongest enrichments in highly incompatible elements overall, and for having the strongest relative depletions in Rb. They also display mild negative anomalies in Zr and Hf.

In general, apart from the Ba anomalies displayed by a minority of Tshibwe samples (and one sample with a positive Pb anomaly), the primitive mantle-normalised incompatible element patterns for the central African kimberlites show little evidence of alteration-related disturbance or characteristics attributable to crustal assimilation. The fact that the freshest group of samples (from Kundelungu) display the strongest negative K and Rb anomalies suggests that similar, but smaller magnitude, anomalies in these elements in the Tshibwe and Camatue kimberlites are not likely the result of alteration.

Compared to southern African Group I kimberlites, the Camatue and Tshibwe kimberlite samples are relatively poor in moderately to highly incompatible elements, and they plot either below or along the lower bound of the concentration ranges of the southern African kimberlites (Fig. 4.10). Only the Kundelungu samples have moderately to highly incompatible element concentrations that overlap with those from southern African Group 1 kimberlites. Interestingly, Cretaceous Brazilian kimberlites from the Minas Gerais region have incompatible element patterns nearly identical to those of southern African Group I kimberlites (Bizzi et al., 1995; Araujo et al., 2001; Guarino et al., 2013), with moderate to highly incompatible element abundances significantly higher than those from Camatue or Tshibwe.

It is noteworthy to mention that kimberlites from the Superior craton in Canada and those from Siberian craton in Russia have the similar trace element patterns on primitive mantle-normalized diagrams to those displayed by southern African kimberlites (Tappe et al., 2017; Agashev et al., 2018).

Table 4.2: XRF and ICPMS trace element analyses of central African kimberlites

	Tshibwe TK-1	TK-2	TK-3	TK-4	TK-5	TK-6	TK-7	TK-8	TK-9	TK-10	TK-12
XRF											
Co	83	93	127	103	98	110	115				
Cr	1179	1259	1386	1154	1218	1098	1255				
Ni	1036	1105	1146	1038	1141	1157	1178				
V	97	104	103	95	92	93	94				
Cu	19	21	21	23	22	20	22				
ICP-MS											
Sc	13.6	9.53	12.6	16.5	11.1	9.72	17.6	17.5	10.2	9.38	19.0
V	71.1	66.3	65.0	65.2	73.8	78.9	75.1	68.9	56.9	65.6	75.8
Rb	15.9	15.7	13.1	26.4	16.2	14.1	19.5	19.3	12.4	17.3	17.5
Sr	205	348	341	383	195	155	233	338	280	190	234
Y	5.33	5.91	5.68	6.98	5.14	4.99	5.74	6.43	6.30	5.01	7.20
Zr	62.4	61.6	41.0	62.7	45.0	36.8	42.8	53.5	56.8	38.5	46.5
Nb	66.0	64.2	59.2	61.9	69.7	73.6	60.9	61.9	54.3	59.6	69.9
Ba	217	302	247	7664	446	342	580	1184	611	486	669
La	38.3	44.6	41.1	49.7	39.6	35.9	46.6	50.4	46.5	36.8	43.3
Ce	58.8	76.2	64.4	93.4	63.9	55.1	71.7	87.2	75.1	54.3	68.8
Pr	6.68	7.90	7.19	8.87	7.14	6.45	8.12	8.58	7.79	6.68	7.71
Nd	23.1	26.7	24.9	30.0	24.7	22.4	27.5	28.9	26.2	23.0	26.6
Sm	3.28	3.76	3.53	4.25	3.49	3.13	3.77	4.01	3.64	3.28	3.88
Eu	0.87	0.99	0.95	1.17	0.96	0.85	1.02	1.08	1.00	0.84	1.07
Gd	2.26	2.62	2.48	3.24	2.45	2.18	2.62	2.80	2.62	2.34	2.76
Tb	0.25	0.29	0.28	0.35	0.26	0.25	0.29	0.30	0.29	0.26	0.32
Dy	1.18	1.29	1.29	1.53	1.17	1.10	1.28	1.35	1.29	1.18	1.51
Ho	0.19	0.21	0.20	0.25	0.19	0.18	0.20	0.21	0.21	0.19	0.24
Er	0.49	0.52	0.50	0.59	0.45	0.45	0.48	0.53	0.53	0.47	0.61
Tm	0.06	0.07	0.06	0.09	0.06	0.05	0.06	0.07	0.07	0.06	0.08
Yb	0.36	0.38	0.36	0.46	0.33	0.32	0.34	0.38	0.39	0.32	0.43
Lu	0.05	0.05	0.05	0.07	0.05	0.04	0.05	0.05	0.05	0.04	0.06
Hf	1.69	1.77	1.17	1.75	1.32	1.09	1.21	1.56	1.58	1.14	1.37
Ta	3.87	3.88	3.37	3.75	3.91	4.69	3.62	3.45	2.95	3.04	4.01
Pb	2.09	1.96	2.67	3.31	12.87	1.97	2.39	2.83	2.65	2.29	2.61
Th	4.53	6.19	4.57	7.15	5.69	4.55	6.33	8.45	4.93	5.07	7.07
U	1.07	1.19	1.02	1.21	1.11	1.00	1.51	1.15	1.23	1.19	1.23
Ba/Nb	3.28	4.70	4.18	124	6.40	4.65	9.52	19.1	11.2	8.16	9.57
La/Nb	0.58	0.69	0.70	0.80	0.57	0.49	0.76	0.81	0.86	0.62	0.62
Nb/U	61.5	53.8	58.0	51.3	62.8	73.5	40.3	54.1	44.3	50.2	57.1
Ce/Pb	28.1	38.8	24.1	28.2	5.0	28.0	30.0	30.8	28.3	23.7	26.4
La/Sm	11.7	11.9	11.6	11.7	11.3	11.5	12.4	12.6	12.8	11.2	11.2
Gd/Yb	6.24	6.92	6.90	7.00	7.37	6.78	7.78	7.43	6.64	7.30	6.43
(Gd/Lu)N	5.28	5.99	6.01	5.80	6.39	6.13	6.51	6.58	6.34	6.76	5.73
(La/Yb)N	71.3	79.7	77.5	72.7	80.4	75.4	93.4	90.3	79.8	77.4	68.1

All data presented are in ppm. Camatue crustal xenolith sample, CATX, included.

Table 4.2 continued

	TK-13	TK-15	TK-16	TK-17	TK-18	TK-19	TK-11	Camatue CAT-1	CAT-2	CAT-3	CAT-4A	CAT-4B
XRF												
Co							87	73	94	64	91	94
Cr							1052	325	330	254	308	312
Ni							1193	285	362	274	358	364
V							92	129	162	122	142	135
Cu							26	60	86	22	33	80
ICP-MS												
Sc	9.80	8.20	12.2	8.33	12.3	14.0		20.1	18.6	11.6	14.3	19.7
V	72.5	54.5	60.2	62.5	64.7	65.1			126	79.8	112	102
Rb	18.1	11.8	13.3	17.7	16.9	16.8	20.5	27.4	5.78	12.8	14.9	9.50
Sr	182	362	304	286	234	363	240	896	928	707	961	1037
Y	5.04	6.53	6.30	5.27	5.90	7.70	4.63	13.8	16.2	11.2	15.0	18.2
Zr	79.0	36.3	63.7	43.2	50.3	48.6	40.2	211	269	181	247	255
Nb	70.5	57.5	60.1	61.7	59.5	63.7	65.6	107	192	85.6	167	161
Ba	623	2981	274	1821	455	1415	659	950	518	340	517	352
La	46.9	53.3	49.8	37.1	44.3	48.1	43.1	66.9	86.4	58.2	79.0	86.5
Ce	73.0	86.7	81.8	53.0	67.7	76.0	66.0	116	146	97.1	137	167
Pr	8.38	9.33	8.53	6.79	7.70	8.38	7.53	12.7	17.3	11.3	15.9	17.2
Nd	28.1	31.4	28.8	23.7	26.6	29.0	25.3	44.7	61.6	39.7	56.0	61.5
Sm	3.73	4.40	4.07	3.59	3.79	4.26	3.44	7.13	9.49	6.24	8.74	9.66
Eu	0.97	1.20	1.05	0.92	1.01	1.19	0.88	2.04	2.66	1.78	2.47	2.75
Gd	2.55	3.13	2.80	2.56	2.62	3.05	2.28	5.32	6.94	4.63	6.47	7.21
Tb	0.27	0.33	0.31	0.28	0.29	0.34	0.25	0.65	0.85	0.59	0.79	0.88
Dy	1.16	1.43	1.35	1.23	1.30	1.58	1.08	3.11	3.97	2.71	3.62	4.15
Ho	0.18	0.22	0.21	0.19	0.20	0.26	0.16	0.50	0.61	0.42	0.57	0.65
Er	0.46	0.56	0.53	0.48	0.53	0.66	0.40	1.21	1.45	1.01	1.35	1.57
Tm	0.06	0.07	0.07	0.06	0.07	0.10	0.05	0.15	0.17	0.12	0.16	0.19
Yb	0.33	0.39	0.38	0.33	0.38	0.55	0.30	0.82	0.92	0.65	0.86	1.01
Lu	0.04	0.05	0.05	0.05	0.05	0.07	0.04	0.11	0.12	0.09	0.11	0.12
Hf	2.18	1.11	1.86	1.27	1.45	1.43	1.19	5.55	6.97	4.67	6.36	6.43
Ta	3.85	3.21	3.34	3.46	3.03	3.33	3.60	5.47	9.44	4.55		7.12
Pb	2.66	2.86	2.73	2.37	2.31	3.73	2.26	3.98	4.04	2.68	4.68	5.49
Th	5.38	4.43	6.54	5.58	5.32	8.55	5.11	8.86	11.4	7.96	10.1	12.4
U	1.40	1.09	1.51	1.35	1.20	1.19	1.10	2.68	5.12	2.43	4.38	4.39
Ba/Nb	8.84	51.8	4.56	29.5	7.66	22.20	10.05	8.84	2.69	3.98	3.09	2.19
La/Nb	0.67	0.93	0.83	0.60	0.74	0.75	0.66	0.62	0.45	0.68	0.47	0.54
Nb/U	50.2	52.9	39.8	45.9	49.7	53.6	59.8	40.1	37.6	35.2	38.2	36.6
Ce/Pb	27.4	30.3	30.0	22.3	29.3	20.3	29.2	29.2	36.1	36.2	29.2	30.3
La/Sm	12.6	12.1	12.2	10.3	11.7	11.3	12.5	9.40	9.10	9.32	9.04	8.95
Gd/Yb	7.81	8.01	7.43	7.77	6.89	5.57	7.65	6.46	7.57	7.17	7.57	7.14
(Gd/Lu)N	7.04	7.58	7.02	6.53	5.93	5.02	7.04	6.25	7.29	6.57	7.37	7.18
(La/Yb)N	97.0	92.2	89.4	76.2	78.6	59.4	97.8	54.9	63.7	60.8	62.4	57.9

Table 4.2 continued

	CAT-5	Kundelungu KZ-1	KKA-1	KKO-1	KK-1	KM-33	KM-3	KM-4	KM-5	KUN-1	CATX
XRF											
Co	89	142	108	113	116	109	117	105	116		94
Cr	292	1704	1313	1892	2125	1488	1644	1496	1607		183
Ni	333	801	751	961	946	639	684	632	775		329
V	143	289	249	135	159	167	227	154	185		184
Cu	64	76	65	46	60	115	126	115	117		29
ICP-MS											
Sc	16.3	18.3	37.9	44.1	25.8	20.4	19.3	36.0	24.8	21.2	66.1
V	123	176	193	103	121	128	182	105	139	172	215
Rb	35.4	14.3	28.0	47.2	41.4	2.98	2.92	6.62	3.74	36.6	3.35
Sr	1117	756	1773	611	637	415	366	532	433	408	295
Y	18.3	10.2	18.8	15.7	9.39	10.6	11.4	16.5	12.2	9.16	15.9
Zr	259	120	264	253	137	128	144	179	156	114	42.4
Nb	335	179	283	184	206	219	220	188	207	202	0.77
Ba	1279	1150	1651	1125	879	616	1779	452	1051	1316	73.6
La	99.6	105	265	222	139	133	152	178	155	129	41.6
Ce	170	166	446	366	231	216	237	296	256	205	82.2
Pr	19.6	17.4	45.7	37.6	24.4	22.3	25.9	28.3	25.7	21.2	10.5
Nd	69.8	55.2	148	119	78.7	71.5	83.7	90.4	82.4	67.0	43.7
Sm	11.0	6.83	17.9	14.1	9.41	9.01	10.2	11.6	10.4	7.69	8.11
Eu	3.07	1.72	4.49	3.52	2.30	2.28	2.64	2.94	2.59	1.90	1.82
Gd	8.22	4.81	11.70	9.54	6.12	6.24	6.96	7.99	7.03	5.35	5.45
Tb	0.99	0.51	1.14	0.94	0.61	0.65	0.70	0.86	0.72	0.51	0.62
Dy	4.55	2.29	4.56	3.75	2.43	2.71	2.94	3.65	3.04	2.11	2.89
Ho	0.70	0.36	0.67	0.53	0.36	0.39	0.43	0.54	0.44	0.32	0.50
Er	1.71	0.93	1.55	1.15	0.79	0.92	0.95	1.28	1.00	0.77	1.27
Tm	0.20	0.12	0.19	0.13	0.10	0.11	0.12	0.16	0.12	0.09	0.17
Yb	1.00	0.68	1.01	0.73	0.50	0.56	0.58	0.79	0.62	0.53	0.96
Lu	0.12	0.09	0.13	0.09	0.07	0.07	0.07	0.10	0.08	0.06	0.14
Hf	6.78	3.52	6.87	6.90	3.84	3.63	4.03	4.88	4.31	3.07	0.74
Ta	9.25	8.55	13.1		11.1	9.68	11.0	9.51	9.33	9.23	0.14
Pb	4.67	3.12	8.79	3.01	3.40	3.53	3.76	3.49	3.47	6.15	2.76
Th	13.4	14.7	36.7	39.7	17.8	18.6	24.1	35.1	23.0	18.3	1.40
U	4.93	3.32	6.57	3.16	3.44	5.59	6.45	3.40	4.33	3.21	0.46
Ba/Nb	3.82	6.43	5.82	6.12	4.27	2.82	8.09	2.41	5.08	6.52	96.1
La/Nb	0.30	0.59	0.93	1.21	0.67	0.61	0.69	0.95	0.75	0.64	54.3
Nb/U	67.8	53.9	43.2	58.2	59.8	39.1	34.1	55.2	47.8	62.9	1.67
Ce/Pb	36.5	53.1	50.7	121.6	68.0	61.3	63.1	84.8	73.7	33.3	29.7
La/Sm	9.07	15.4	14.8	15.7	14.7	14.7	14.8	15.3	14.9	16.7	5.13
Gd/Yb	8.19	7.06	11.6	13.1	12.3	11.2	12.1	10.1	11.4	10.1	5.69
(Gd/Lu)N	8.15	6.76	10.9	12.8	10.3	10.7	11.7	9.95	11.1	10.3	4.75
(La/Yb)N	67.1	188	178	206	104	178	160	152	170	165	29.5

4.7. RADIOGENIC ISOTOPE GEOCHEMISTRY

4.7.1. Sr-Nd ISOTOPE COMPOSITION

Initial $^{87}Sr/^{86}Sr$ ratios of the analysed central African kimberlite samples fall within the ranges 0.7050 – 0.7059 (Camatue), 0.7069 – 0.7075 (Tshibwe) and 0.7042 – 0.7054 (Kundelungu). The $\varepsilon_{Nd}(t)$ values of these samples vary from -1.32 to +0.05 (Camatue), -1.22 to +1.29 and (Tshibwe) and +2.37 to +2.91 (Kundelungu) (Fig. 4.11). The Kundelungu kimberlite samples therefore fall well within the Sr and Nd isotopic compositions of southern African Group I kimberlites, whereas the Camatue and Tshibwe samples fall close to, or slightly below, the lowest $\varepsilon_{Nd}(t)$ values and close to, or above. the highest $^{87}Sr/^{86}Sr_i$ values of southern African Group 1 kimberlites (Fig. 4.11).

The Mbuji-Mayi kimberlite, located only thirty kilometers northeast from Tshibwe, displays less radiogenic Sr isotope ratios (10 out of 14 samples fall within the range $^{87}Sr/^{86}Sr_{(i)}$ = 0.7040 – 0.7047; Demaiffe and Fieremans, 1981; Weis and Demaiffe, 1985) and more radiogenic Nd isotope compositions ($\varepsilon_{Nd}(t)$ = +1.4 to +5.3) than those from Camatue or Tshibwe, and they extend to more depleted compositions than any of the kimberlite data presented here (Weis and Demaiffe, 1985; Fig. 4.11).

The Tshibwe kimberlite samples have significantly more radiogenic initial $^{87}Sr/^{86}Sr$ and lower $\varepsilon_{Nd}(t)$ than samples from Mbuji Mayi (Demaiffe & Fieremans, 1981; Weis and Demaiffe, 1985). It has been long recognized that Sr isotope ratios of kimberlites may be strongly affected by post emplacement alteration by groundwater (Berg and Allsopp, 1972; Barret and Berg, 1975). Given the mobile nature of Rb and Sr in groundwater and other aqueous fluids, it is likely that the radiogenic Sr isotope composition of these samples, which from petrographic criteria are all significantly altered, have been increased by post-emplacement alteration.

It is also widely accepted that the Sm-Nd isotope system is far less prone to disturbance than the the Rb-Sr isotope system during fluid-rock interaction (Richardson, 1984; Coetzee, 2004). However, the fact that the Tshibwe and Camatue samples display lower $\varepsilon_{Nd}(t)$ values than African Group I kimberlites in general, and the Mbuji-Mayi kimberlite in particular, needs explanation. The three possibilities explaining these differences are (1) that the mantle sources of the Tshibwe and Camatue kimberlites are distinct from that of Mbuji-Mayi and have higher long-term

LREE/HREE (and Rb/Sr ratios), (2) that alteration of the Camatue and/or Tshibwe kimberlites was so extensive that it was able and decrease the $^{143}Nd/^{144}Nd$ ratios of these kimberlite samples, and/or (3) that the Camatue and Tshibwe kimberlites have experienced significant crustal assimilation during emplacement that affected their $^{143}Nd/^{144}Nd$ ratios. These will be discussed in the discussion section below.

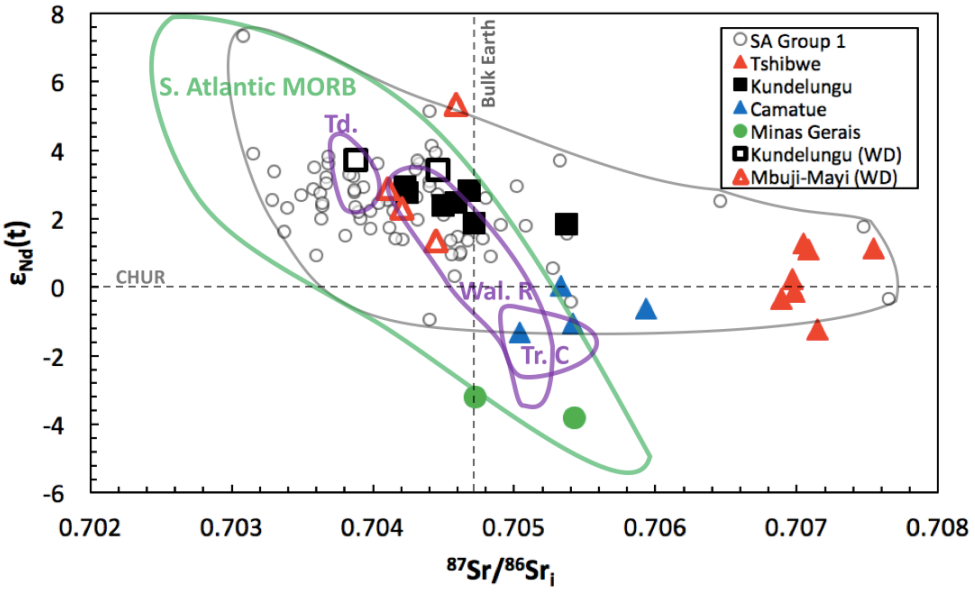

Figure 4.11: Initial $^{87}Sr/^{86}Sr$ versus $\varepsilon_{Nd}(t)$ isotope diagram for central and southern African kimberlites. Note the highly radiogenic Sr isotope ratios at Tshibwe, and the relatively unradiogenic Nd isotope ratios at Camatue, and the similarity in composition between the Kundelungu and southern African Group 1 kimberlites. Initial Sr and Nd isotope ratios are calculated assuming emplacement ages of 120 Ma for Camatue (Castillo-Oliver et al., 2016), 84 Ma for Tshibwe (based on U-Pb perovskite dating of the Tshibwe kimberlite described in this thesis, Chapter 3), 32 Ma for the Kundelungu kimberlites (Batumike et al., 2008) and 71 Ma for Mbuji-Mayi (Weis and Demaiffe, 1985). Minas Gerais kimberlites data are from Bizzi et al., (1995). Southern African Group I kimberlites are shown for comparison (Kramers et al., 1981; Smith, 1983; Davies et al., 2001; Nowell et al., 2004; Becker and le Roex, 2006; Collerson et al., 2010). Ocean island basalts are also shown, Trinidad (Td.) (Siebel, 2000), Tristan da Cunha (Tr. C) (le Roex et al., 1990), Walvis Ridge (Wal. R) (Richardson et al., 1982). South Atlantic MORB data are from Douglass et al., (1999).

On the $^{87}Sr/^{86}Sr_i$ - $\varepsilon_{Nd}(t)$ isotope diagram (Fig. 4.11), the Camatue kimberlite samples plot within or very near the field for Tristan da Cunha and the low ε_{Nd} end of the field for Walvis Ridge, and also quite closely to, but at slightly higher ε_{Nd} values than, the Cretaceous-age Minas Gerais

kimberlites of Brazil (Bizzi et al., 1995; Araujo et al., 2001; Guarino et al., 2013). The Kundelungu kimberlite samples show a weak negative correlation between Sr and Nd initial isotope ratios. They fall near the center of the field for southern African Group I kimberlites and, with the exception of sample KZ-1, in the depleted quadrant of the Sr-Nd isotope ratio diagram (Fig. 4.11).

4.7.2. Pb ISOTOPE COMPOSITION

Initial $^{206}Pb/^{204}Pb$ ratios of central African kimberlite samples fall within the following ranges: 18.02 – 18.54 for Camatue, 17.36 – 17.85 for Tshibwe and 18.19 – 19.43 for Kundelungu (Fig. 3.13). For a given $^{206}Pb/^{204}Pb_i$ ratio, $^{207}Pb/^{204}Pb_i$ and $^{208}Pb/^{204}Pb_i$ values of central African kimberlites tend to plot above the NHRL, significantly above it in the case of Camatue kimberlite samples (Figs. 4.13 and 4.14). Howevever, in the $^{208}Pb/^{204}Pb_i$ versus $^{206}Pb/^{204}Pb_i$ plot (Fig. 4.14), all but one of the Kundelungu samples plot on or very near the NHRL. Sample Kun-1 was also analysed by Weis and Demaiffe (1985), and their Pb isotope results are similar to those reported here, but differ slightly outside of analytical uncertainties ($^{206}Pb/^{204}Pb_m$ = 18.315 versus 18.353, $^{207}Pb/^{204}Pb_m$ = 15.605 versus 15.624 and $^{208}Pb/^{204}Pb_m$ = 38.256 versus 38.362 for values from Weis and Demaiffe (1985) versus those reported in Table 3.6 below). However, it is unknown whether the material analysed for this study came from the same aliquot of sample as that analysed by Weis and Demaiffe (1985), so it is impossible to determine whether these small differences reflect a sampling effect or analytical bias.

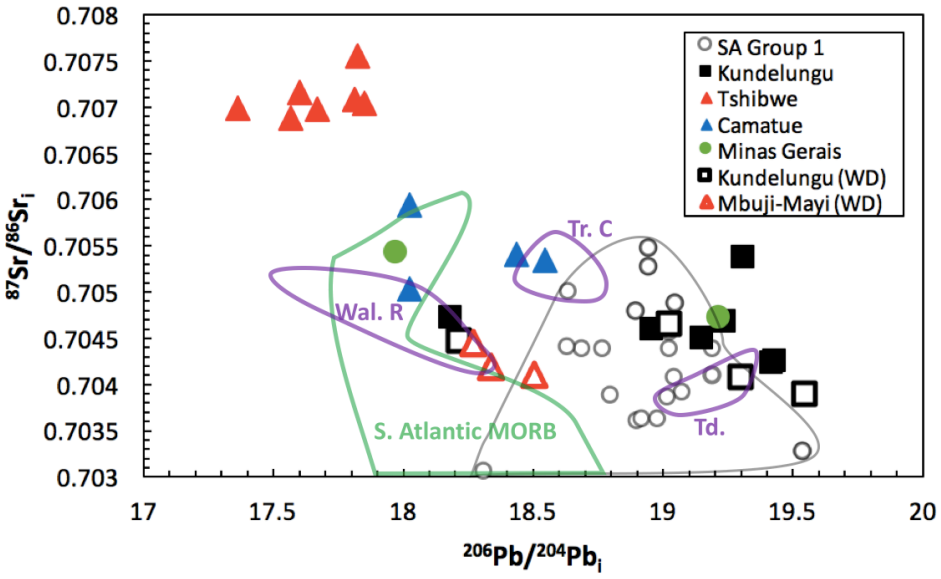

Figure 4.12: Initial $^{206}Pb/^{204}Pb$ and $^{87}Sr/^{86}Sr$ isotope diagram for central African kimberlites. Data sources as in Fig. 11.

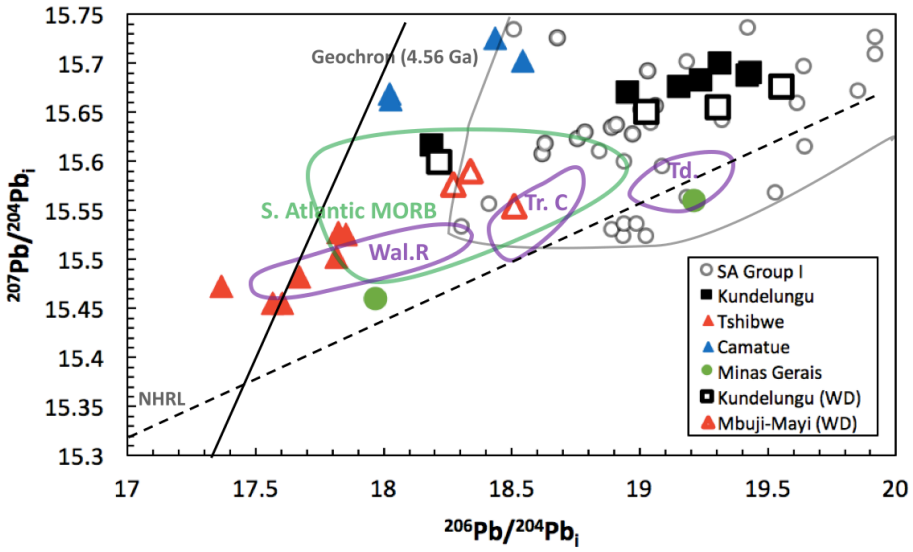

Figure 4.13: Initial $^{206}Pb/^{207}Pb$ and $^{207}Pb/^{204}Pb$ isotope correlation diagram for Central African kimberlites. Data sources as in Fig. 13. The NHRL (Northern Hemisphere Reference Line) of Hart (1984) is also shown.

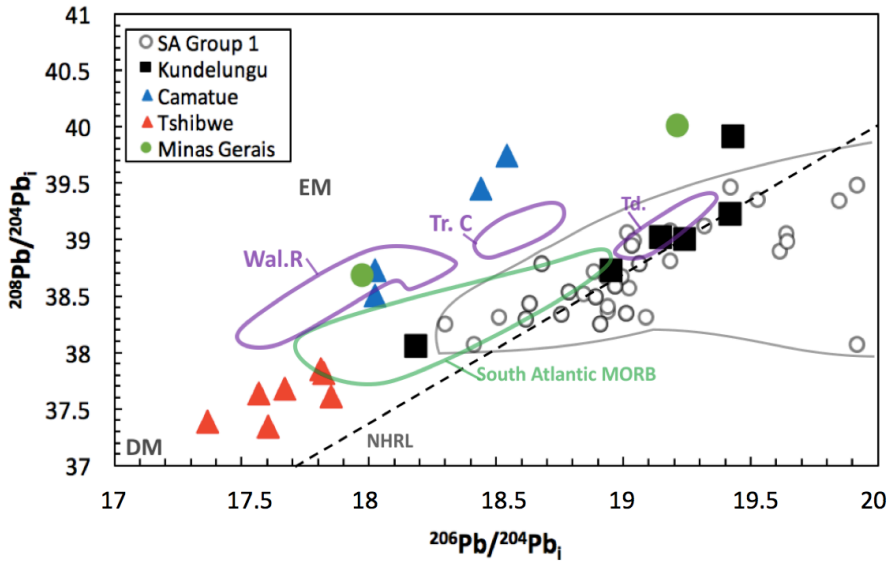

Figure 4.14: Initial $^{206}Pb/^{204}Pb$ and $^{208}Pb/^{204}Pb$ isotope correlation diagram for Central African kimberlites. Depleted-mantle and enriched-mantle OIB end-members are also shown (Stracke, 2012). Data for Mbuji-Mayi and Kundelungu from Weis and Demaiffe (1985) are not shown on this figure because Th concentrations, necessary for calculation of age-corrected $^{208}Pb/^{204}Pb_i$ values, were not determined.

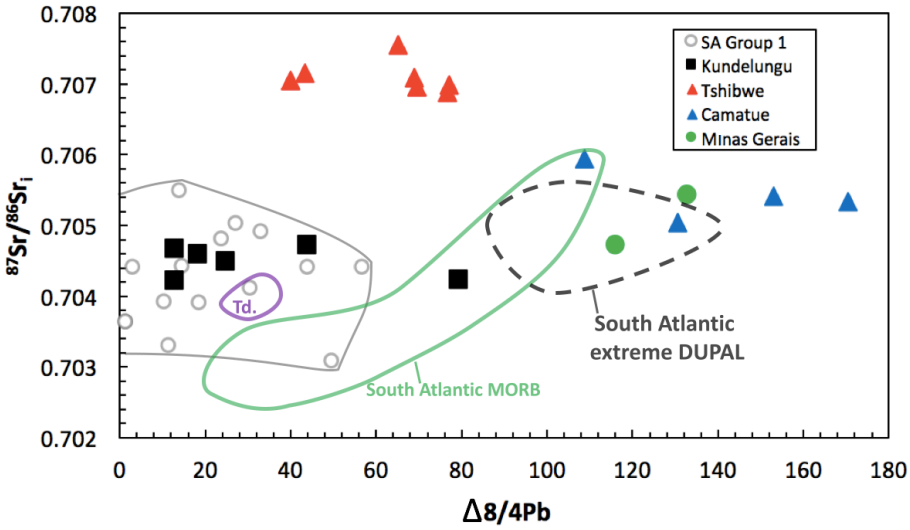

Figure 4.15: Δ8/4 Pb versus $^{87}Sr/^{86}Sr_i$ plot of central African kimberlites. South Atlantic extreme DUPAL field is shown (Class and Le Roex, 2011) (Walvis Ridge and Tristan da Cunha lavas represent this field). Δ8/4 Pb = ($^{208}Pb/^{204}Pb_{Sample} - {}^{208}Pb/^{204}Pb_{NHRL}$)×100 with $^{208}Pb/^{204}Pb_{NHRL}$ =1.209× $^{206}Pb/^{204}Pb$+15.627 (Hart, 1984). Data sources of OIB, South Atlantic MORB, southern African Goup 1 and Minas Gerais as in Fig. 11.

South Atlantic extreme DUPAL anomaly

The DUPAL anomaly (Hart, 1984) in the South Atlantic is defined by very high Δ8/4Pb (mostly above 80) and high Sr isotope composition (mostly $^{87}Sr/^{86}Sr$ above 0.7047) (Dupré and Allègre, 1983; Douglass et al., 1999; Class and le Roex, 2011). The South Atlantic extreme DUPAL field is defined by certain samples from the Walvis Ridge, Rio Grande Rise, Tristan da Cunha and from some anomalous segments of the southern Mid-Atlantic Ridge (Class and le Roex, 2011). Camatue kimberlite samples investigated in this study display isotopic compositions very similar to South Atlantic oceanic basalts with an extreme DUPAL signature (Fig. 4.15).

Table 4.3: Measured and initial Rb-Sr isotope data for central African kimberlites analysed in this study.

Kimberlite	Sample	Rb/Sr	$^{87}Rb/^{86}Sr$	$^{87}Sr/^{86}Sr$ (m)	2-sigma	Age (Ma)	$^{87}Sr/^{86}Sr$ (i)
On-Craton							
Camatue	CAT-2	0.0062	0.0180	0.705443	16	120*	0.705412
Camatue	CAT-4A	0.0155	0.0450	0.705115	9	120*	0.705038
Camatue	CAT-4B	0.0092	0.0265	0.705976	14	120*	0.705931
Camatue	CAT-5	0.0317	0.0917	0.705487	11	120*	0.705331
Tshibwe	TK-2	0.0452	0.1308	0.707204	12	84.6	0.707046
Tshibwe	TK-3	0.0386	0.1116	0.707680	13	84.6	0.707546
Tshibwe	TK-7	0.0836	0.2417	0.707273	10	84.6	0.706982
Tshibwe	TK-8	0.0571	0.1652	0.707348	11	84.6	0.707149
Tshibwe	TK-13	0.0994	0.2875	0.707234	19	84.6	0.706889
Tshibwe	TK-15	0.0324	0.0939	0.707194	12	84.6	0.707081
Tshibwe	TK-16	0.0437	0.1264	0.707124	9	84.6	0.706972
Off-Craton							
Kundelungu	KK-1	0.0650	0.1880	0.704320	10	32.3	0.704234
Kundelungu	KKA-1	0.0158	0.0457	0.704616	11	32.3	0.704595
Kundelungu	KKO-1	0.0772	0.2234	0.704346	12	32.3	0.704244
Kundelungu	KM-3	0.0080	0.0230	0.704513	12	32.3	0.704502
Kundelungu	KM-5	0.0086	0.0250	0.704696	11	32.3	0.704684
Kundelungu	KUN-1	0.0896	0.2591	0.704841	13	32.3	0.704722
Kundelungu	KZ-1	0.0189	0.0547	0.705395	9	32.3	0.705370

Initial isotope (i) ratios were calculated using kimberlite emplacement ages unless otherwise indicated (*) for which ages have been assumed. Subscript (m) indicates measured values.

Table 4.4: Measured and initial Sm-Nd isotope data for central African kimberlites analysed in this study.

Kimberlite	Sample	Sm/Nd	$^{147}Sm/^{144}Nd$	$^{143}Nd/^{144}Nd(m)$	2-sigma	Age (Ma)	$^{143}Nd/^{144}Nd$ (i)	eNd(T)
On-Craton								
Camatue	CAT-2	0.1541	0.0928	0.512494	14	120*	0.512421	-1.07
Camatue	CAT-4A	0.1561	0.0940	0.512482	12	120*	0.512409	-1.32
Camatue	CAT-4B	0.1572	0.0947	0.512519	13	120*	0.512444	-0.62
Camatue	CAT-5	0.1574	0.0948	0.512553	13	120*	0.512479	0.05
Tshibwe	TK-2	0.1407	0.0848	0.512635	25	84.6	0.512588	1.29
Tshibwe	TK-3	0.1421	0.0856	0.512627	10	84.6	0.512580	1.14
Tshibwe	TK-7	0.1373	0.0827	0.512561	10	84.6	0.512515	-0.13
Tshibwe	TK-8	0.1386	0.0835	0.512505	23	84.6	0.512459	-1.22
Tshibwe	TK-13	0.1328	0.0800	0.512549	11	84.6	0.512505	-0.33
Tshibwe	TK-15	0.1400	0.0844	0.512624	14	84.6	0.512578	1.10
Tshibwe	TK-16	0.1411	0.0850	0.512581	15	84.6	0.512534	0.25
Off-Craton								
Kundelungu	KK-1	0.1195	0.0720	0.512753	10	32.3	0.512738	2.91
Kundelungu	KKA-1	0.1210	0.0729	0.512731	14	32.3	0.512716	2.48
Kundelungu	KKO-1	0.1192	0.0718	0.512745	11	32.3	0.512729	2.75
Kundelungu	KM-3	0.1223	0.0737	0.512726	15	32.3	0.512710	2.37
Kundelungu	KM-5	0.1261	0.0760	0.512749	14	32.3	0.512733	2.82
Kundelungu	KUN-1	0.1147	0.0691	0.512698	12	32.3	0.512684	1.86
Kundelungu	KZ-1	0.1238	0.0746	0.512697	14	32.3	0.512682	1.82

Initial isotope (i) ratios were calculated using kimberlite emplacement ages unless otherwise indicated (*) for which ages have been assumed. Subscript (m) indicates measured values

Table 4.5: Measured and initial U-Th-Pb isotope data for central African kimberlites analysed in this study.

Kimberlite	Sample	Pb	Th	U	U/Pb	Th/Pb	$^{206}Pb/^{204}Pb$	$^{207}Pb/^{204}Pb$	$^{208}Pb/^{204}Pb$	$^{206}Pb/^{204}Pb_i$	$^{207}Pb/^{204}Pb_i$	$^{208}Pb/^{204}Pb_i$	Δ8/4
On-Craton													
Camatue	CAT-2	4.04	13.39	5.12	1.2683	3.3161	20.038	15.802	40.819	18.438	15.725	39.449	153
Camatue	CAT-4A	4.68	10.05	4.38	0.9346	2.1466	19.170	15.725	39.585	18.024	15.669	38.723	130
Camatue	CAT-4B	5.49	12.36	4.39	0.7994	2.2518	19.001	15.710	39.408	18.025	15.663	38.508	109
Camatue	CAT-5	4.67	14.36	4.93	1.0553	3.0728	19.873	15.767	41.018	18.542	15.702	39.749	170
Tshibwe	TK-2	1.96	6.19	1.19	0.6080	3.1538	18.363	15.550	38.477	17.853	15.526	37.610	40
Tshibwe	TK-3	2.67	4.57	1.02	0.3826	1.7124	18.141	15.542	38.293	17.822	15.527	37.825	65
Tshibwe	TK-7	2.39	6.33	1.51	0.6325	2.6503	17.888	15.496	38.113	17.364	15.471	37.393	77
Tshibwe	TK-8	2.83	8.45	1.15	0.4044	2.9838	17.937	15.471	38.152	17.602	15.455	37.341	43
Tshibwe	TK-13	2.66	5.38	1.40	0.5276	2.0223	18.005	15.476	38.185	17.567	15.455	37.635	77
Tshibwe	TK-15	2.86	4.43	1.09	0.3801	1.5487	18.129	15.517	38.276	17.813	15.502	37.852	69
Tshibwe	TK-16	2.73	6.54	1.51	0.5535	2.3962	18.130	15.504	38.340	17.668	15.482	37.685	70
Off-Craton													
Kundelungu	KK-1	3.40	17.77	3.44	1.0116	5.2233	19.756	15.703	39.802	19.421	15.687	39.233	13
Kundelungu	KKA-1	8.79	36.72	6.57	0.7474	4.1775	19.197	15.682	39.171	18.953	15.670	38.723	18
Kundelungu	KKO-1	3.01	39.66	3.16	1.0482	13.1610	19.788	15.707	41.880	19.431	15.690	40.406	79
Kundelungu	KM-3	3.76	24.09	6.45	1.7125	6.4011	19.715	15.704	39.721	19.149	15.677	39.025	25
Kundelungu	KM-5	3.47	22.98	4.33	1.2477	6.6222	19.651	15.701	39.734	19.239	15.682	39.014	13
Kundelungu	KUN-1	6.15	18.26	3.21	0.5220	2.9708	18.353	15.624	38.362	18.186	15.617	38.051	44
Kundelungu	KZ-1	3.12	14.65	3.32	1.0652	4.7011	19.661	15.717	39.426	19.310	15.701	38.917	

Initial Pb isotope ratios calculated using kimberlite emplacement ages unless otherwise indicated (*) for which ages have been assumed. Ratios with subscript m are measured values, those with subscript I are initial values.

Table 4.6: Comparison of isotope data for samples from M'Bo and Msipashi kimberlites, Kundelungu province

	W&D.			This study		
	KUN1	M1	M3	KUN1	KM-3	KM-5
$^{87}Sr/^{86}Sr_{(m)}$	0.7045	0.704	0.7046	0.70472	0.70450	0.70468
$^{143}Nd/^{144}Nd_{(m)}$	0.512778			0.512698	0.51272	0.51274
$^{206}Pb/^{204}Pb_{(m)}$	18.315	19.711	19.425	18.353	19.715	19.651
$^{207}Pb/^{204}Pb_{(m)}$	15.605	15.674	15.668	15.624	15.704	15.701
$^{208}Pb/^{204}Pb_{(m)}$	38.256	39.558	39.51	38.362	39.721	39.734

KUN-1 is from the M'bo pipe (western cluster) and M1, M3, KM-3, KM-5 samples are all from the Msipashi pipe (eastern cluster), although data were obtained on separately prepared aliquots of the same samples. W&D stands for Weis and Demaiffe (1985). M1 and KM-1 are the same sample and likewise for M3 and KM-3.

4.8. PETROGENESIS

Interpretations of chemical variations in kimberlite samples in terms of conventional igneous processes (fractionation, partial melting) cannot be done properly without the evaluation of the extent to which those samples have been affected by near-surface processes such as crustal contamination and alteration. The latter can obscure evidence of the conventional igneous processes.

4.8.1. CRUSTAL CONTAMINATION

Kimberlites are known to be able to entrain large amounts of crustally-derived material as they ascend through the continental crust (Clement and Skinner, 1985). Among the effects of crustal contamination are the decrease of MgO content and an increase in the oxides SiO_2, Al_2O_3 and Na_2O (Clement, 1982). The contamination index (CI) of Clement (1982) ((SiO_2 + Al_2O_3 + Na_2O)/(MgO + $2K_2O$)) has been widely used to assess the degree of crustal assimilation by kimberlites. However, some authors (le Roex et al., 2003; Kjarsgaard et al., 2009) have suggested that Clement's contamination index is not a robust means of distinguishing crustally contaminated from uncontaminated kimberlite samples and they have proposed alternative methodologies to do this. Among these are whether they form correlations on diagrams of wt. SiO_2 versus MgO and versus Gd/Lu ratio, and wt.% Al_2O_3 versus ppm Yb.

Variably crustally contaminated kimberlite samples would be expected to show a negative correlation between SiO_2 and MgO contents, with the most contaminated samples having higher SiO_2 and lower MgO contents (le Roex et al., 2003). However, while the Camatue samples do

have low MgO and SiO2 values outside the range of fresh southern African kimberlites, and the Tshibwe samples have MgO and SiO2 values overlapping with those of crustally contaminated southern African kimberlites (e.g., le Roex et al., 2003; Becker and le Roex, 2006), neither of the Camatue or Tshibwe sample groups display any correlation between SiO_2 and MgO contents (Fig. 3.6), whereas Kundelungu kimberlite samples show a positive correlation between the two oxides, most likely controlled by variable olivine accumulation or entrainment. Neither do the Camatue or Tshibwe sample groups show any correlations in the Al_2O_3 versus Yb crustal contamination discrimination diagram of Kjarsgaard et al. (2009; Fig. 3.16) and, due to their low HREE contents, neither the Camatue nor Tshibwe kimberlite samples overlap with crustally contaminated southern African kimberlites. They also do not display significant correlations of SiO_2 with Gd/Lu ratio, as was found by le Roex et al. (2003) to be characteristic of crustally contaminated kimberlites. Rather, Gd/Lu ratios in each of the central African kimberlite groups remain fairly constant with respect to SiO_2 content (Fig. 3.17), although there is a slight increase in average Gd/Lu ratio at the lowest SiO_2 contents and the central African kimberlite data do overlap to some extent with data for crustally contaminated southern African kimberlites.

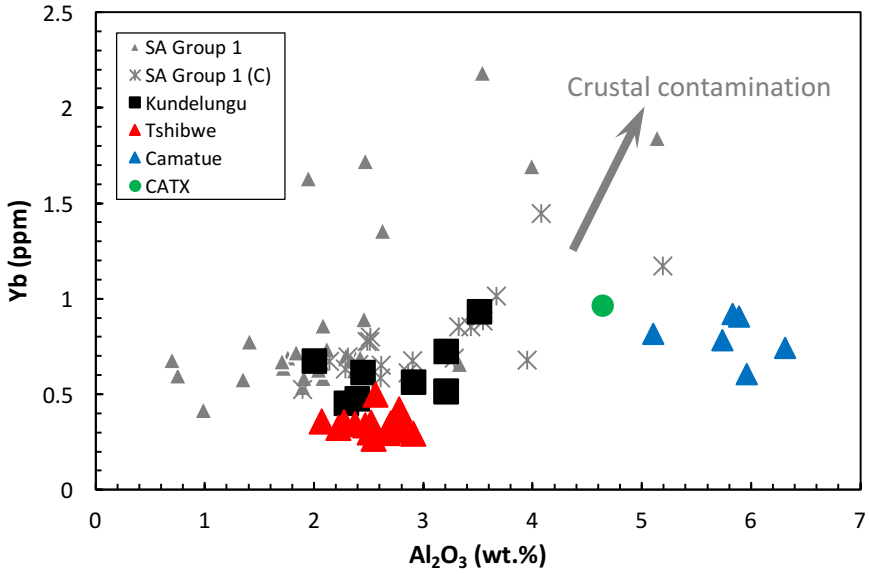

Figure 4.16: Al_2O_3 (wt.%) versus Yb (ppm), developed as a crustal contamination screening diagram by Kjarsgaard et al.,(2009), showing the central African kimberlite data. Note the absence of correlation between Al_2O_3 and Yb contents in all central African kimberlite localities. A camatue crustal xenolith (CATX) is shown for comparison.

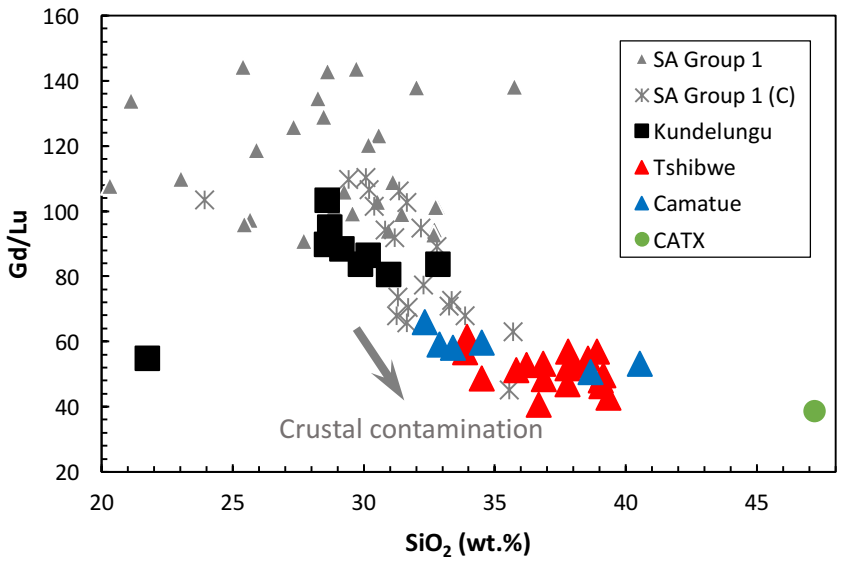

Figure 4.17: SiO_2 (wt.%) versus Gd/Lu, developed as a crustal contamination screen diagram by Le Roex et al., (2003) showing central African kimberlites. Kundelungu kimberlite samples show no clear correlation between SiO_2 content and Gd/Lu ratio. Tshibwe and Camatue samples have the same range of Gd/Lu ratio and the latter remains constant with the increase of SiO_2 content. Southern African contaminated Group 1 kimberlites show a strong negative correlation not seen in any central African kimberlite samples analysed in this study.

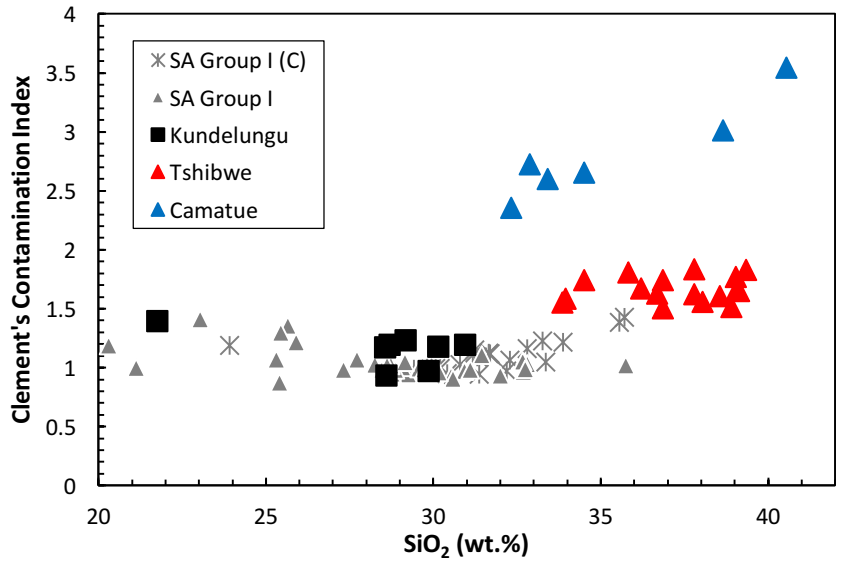

Figure 3.18: Plot of Clement's Contamination Index (CI) versus SiO_2 (wt.%) for central African kimberlites. Note the higher CI in Camatue kimberlite samples, due to their high SiO2, Al_2O_3 and Na_2O contents. Uncontaminated and crustally contaminated Southern African Group I kimberlites (C= crustally contaminated) are shown for comparison (le Roex et al., 2003). Clement's Contamination Index = (SiO_2 + Al_2O_3 + Na_2O) / (MgO + $2K_2O$) (Clement, 1982).

Curiously, the relatively fresh hypabyssal Kundelungu kimberlite samples, which show little petrographic evidence of crustal contamination and have the lowest CI values of all central African kimberlites investigated, show positive correlations of Al_2O_3 versus Yb ($r^2 = 0.3$) and negative correlation of SiO_2 versus Gd/Lu ratio ($r^2 = 0.6$; the latter excluding sample KZ-1, which is relatively altered).

Clement's contamination index is high in Camatue kimberlite samples, due to their relatively high SiO_2, Al_2O_3 and Na_2O contents (Fig. 4.18). These samples would be characterised as crustally contaminated using a CI cut-off value of 1 (Clement, 1982). However, some authors have debated the reliability of this cut-off value (le Roex et al., 2003; Coetzee, 2004; Becker and Le Roex, 2006; Kjarsgaard et al., 2009) because they found that some uncontaminated samples have high CI values (greater than 1.5). In Figure 4.18, uncontaminated and crustally contaminated southern African Group I kimberlites cannot be discriminated based on the Clement's Contamination Index alone. For example, as mentioned above, the major element compositions of the Camatue kimberlite samples are not readily explained by assimilation of crustal material similar to that occurring as crustal xenoliths in these samples, and they also do not have incompatible element characteristics that are indicative of crustal assimilation, such as positive Pb anomalies, or any noticeable Ce or Eu anomalies in the primitive-mantle normalized element patterns. Uncontaminated kimberlites with high SiO_2 contents similar to that of Camatue samples have been reported from Lac de Gras (Kjarsgaard et al., 2009) and, based on the petrographic evidence for pervasive chloritisation, it seems that elemental mobility during hydrothermal alteration or low-grade metamorphism (i.e., loss of Mg, gain of SiO_2, Al_2O_3 and Na_2O) is a more plausible explanation for the major element characteristics of the Camatue kimberlite than crustal assimilation.

At Tshibwe, in order to further constrain the likely effects of crustal assimilation on trace element content, two highly contaminated kimberlite samples, with relatively high abundances (30 vol.%) of mafic crustal xenolithic material, were chemically analysed. Tshibwe kimberlite samples have CI values of ≈5, and overall low REE abundances, with only mildly LREE-enriched patterns ($(La/Yb)_N$ = 5.8 to 8.1) and negative Ce and positive Eu anomalies (Fig. 4.19). On primitive mantle-normalised they exhibit strong Ba, Sr and Eu anomalies. It is noteworthy to mention that Tshibwe uncontaminated samples, described previously (see trace element geochemistry section)

exhibit none of these features, with the exception of some altered samples displaying elevated Ba contents.

Table 4.7: XRF major element analyses (in weight per cent) of two crustally contaminated Tshibwe samples with very high proportions of mafic xenoliths. The Clement's Contamination Index is also shown for reference

Sample	SiO_2	TiO_2	Al_2O_3	Fe_2O_3	MnO	MgO	CaO	Na_2O	K_2O	P_2O_5	SO_3	Cr_2O_3	NiO	H_2O-	LOI	Sum	Cl
TK 14 D	47.88	0.32	12.75	7.53	0.08	12.58	6.47	2.20	0.29	0.02	0.03	0.03	0.05	5.56	3.49	99.26	4.8
TK 14 F	48.54	0.28	13.58	7.16	0.07	11.66	6.59	2.46	0.30	0.02	0.02	0.03	0.05	5.30	3.21	99.28	5.3

. **Table 4.8:** XRF trace element analyses (in ppm) of two crustally contaminated Tshibwe samples with very high proportion of mafic xenoliths.

Sample	Zn (ppm)	Cu (ppm)	Ni (ppm)	Nb (ppm)	Zr (ppm)	Y (ppm)	Sr (ppm)	Rb (ppm)	Cr (ppm)	Sc (ppm)	Ba (ppm)
TK 14 D	50	77	400	4	28	8	417	6	232	20	297
TK 14 F	48	74	374	4	30	10	461	5	279	21	314

Furthermore, on a primitive-mantle-normalised diagram, these two contaminated samples have trace element patterns characterized with positive Ba, Sr and Eu anomalies (Fig. 4.19). The high magnitude positive Sr and Eu anomalies were not observed in Tshibwe uncontaminated samples described earlier. The total lack of such features strongly argues against significant crustal assimilation in the uncontaminated tshibwe kimberlite samples.

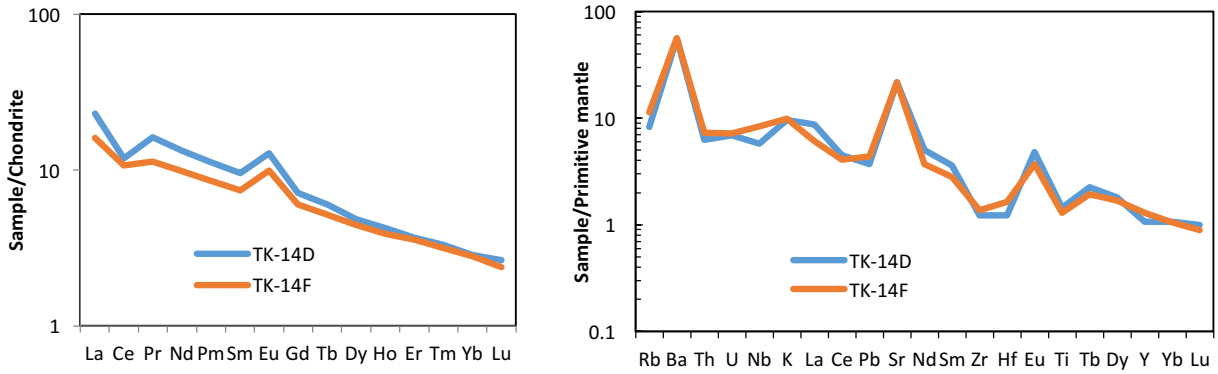

Figure 4.19: (a) Chondrite-normalised REE plot of Tshibwe crustally contaminated samples. Note the negative Ce anomalies associated with positive Eu anomalies. **(b)** Primitive-mantle-normalised plot of Tshibwe crustally contaminated samples.

4.8.2. ALTERATION

Many authors have recognized the effects of deuteric, low-temperature and hydrothermal alteration on the geochemistry of kimberlites (Berg & Allsopp, 1972; Clement, 1982; Clement and Skinner, 1985; le Roex et al., 2003; Becker and le Roex, 2006). Mobile elements (such as Rb, Ba, U, K and Pb; Fesq et al., 1975) are prone to being mobilised by the flow of deuteric fluids and groundwater. The composition of chemically altered kimberlites will not provide a true reflection of their source regions, so it is crucial to investigate whether, and to what extent, kimberlite samples investigated in this study have been affected by alteration.

CAMATUE

Petrographic analysis of the Camatue kimberlites have showed that these samples have experienced significant alteration and, possibly, low-grade metamorphism, with the sample CAT3 being the most affected. However, the Camatue kimberlite samples display little intrakimberlite geochemical variations and diagnostic trace element ratios such as Nb/U and Ce/Pb (averages of 42 ± 12 and 32 ± 3.7, respectively) are nearly identical to those in fresh southern African Group 1 kimberlites (averages of 43 ± 8 and 38 ± 14, respectively, le Roex et al., 2003).

However, the extensive replacement of olivine macro & microcrysts by chlorite, serpentine and calcite, as well as matrix replacement by secondary serpentine and other phyllosilicates, in Camatue kimberlite samples appears to be related to their low MgO, high SiO_2 and high Al_2O_3 contents. Elemental mapping has shown a pervasive widespread of Na-rich Chlorite (glagolevite) in the groundmass (see Fig. 1 in the Appendix, page 320). However, the high Na_2O requires addition from some other source, possibly hydrothermal fluids (Mitchell, 1986). In a study of hydrothermal alteration and metamorphism of the Venetia Group I kimberlite in South Africa, Stripp et al. (2006) proposed that the the Al^{3+} necessary to form secondary chlorite after olivine was derived from breakdown of plagioclase in crustal xenoliths. While this is possible in the case of Camatue (particularly given the fact that plagioclase is replaced in most Camatue crustal xenoliths), such a process must have been element-specific, since the lack of any positive Eu or Sr anomalies argues against bulk assimilation of crustally-derived plagioclase-rich xenoliths.

TSHIBWE

It is clear from their petrography that the Tshibwe kimberlite samples have been extensively affected by low-temperature alteration. Olivine is entirely replaced, mainly by serpentine and to a lesser extent by calcite, and a significant proportion of groundmass minerals are also altered to clays. The absence of opaque phases in some thin sections suggest that oxide minerals, in some cases, were also replaced largely replaced by secondary minerals. It is possible that this is related to alteration (primarily serpentinisation) and limited Mg-loss, but the strong correlation between Mg and Fe, which tend to be located in different secondary phases during alteration of silica-poor rocks (serpentine and magnetite, respectively; Frost and Beard, 2007) would seem to argue against major mobilisation of Mg in these samples

In addition to petrographic evidence, the radiogenic Sr isotope data obtained on the Tshibwe samples analysed is consistent with exchange with crustal Sr facilitated by ground water (see section 4.7.2) and, based on the observed difference with Mbuji Mayi data, the low $^{143}Nd/^{144}Nd_i$ isotope ratios of the Tshibwe kimberlite could also potentially be due to near-surface alteration processes.

The Pb isotope system does not show any clear evidence of being disturbed by alteration in the of Tshibwe samples. The relatively small ranges of U and Pb contents and U/Pb ratios of Tshibwe samples analysed for Pb isotopes are even narrower than those for the Mbuji-Mayi samples investigated by Weiss and Demaiffe (1985) and are consistent with this interpretation, as are the limited ranges in Pb isotope ratios in both the Tshibwe data presented here and the Mbuji-Mayi Pb isotope data presented previously.

As mentioned above, the very high Ba contents observed in some Tshibwe kimberlite samples likely represent the effect of near-surface chemical alteration. Coetzee (2004) suggested that individual samples displaying large variations in the mobile elements (Rb, Ba, U, K and Pb) compared to other samples from the same pipe likely indicates the effects of chemical alteration. In the Tshibwe case, Ba/Ba* values vary from 0.84 to 18.5 (Ba* is the concentration of Ba logarithmically interpolated from the concentrations of the elements of adjacent incompatibility, Rb and Th). Five out of the 18 samples analysed have conspicuous positive Ba anomalies, with Ba/Ba* values of greater than 3. If these are excluded, the mean Ba/Ba* ratio of the remaining samples is 1.6 ± 0.5 (1σ), similar to the range of fresh southern African Group 1 kimberlites (mean Ba/Ba* = 1.4 ± 0.6 (1σ)). Additionally, a single sample (TK-5) shows a large positive Pb anomaly,

whereas none of the other samples show positive Pb anomalies. This anomaly is also regarded as a feature of alteration (or, less likely, due to the lack of other chemical indicators, crustal contamination) and TK-5 is therefore excluded from the Tshibwe dataset for discussion of petrogenetic considerations.

The Tshibwe kimberlite samples are remarkable for their low concentrations of the REE and other incompatible elements compared to those of southern African kimberlites. Some of the samples do display mild negative Ce anomalies that could be indicative of oxidative alteration ($Ce/Ce^* = 0.81$ to 1.07), however other, typically highly alteration-resistant incompatible elements also have low concentrations, such as Nb. Trace element ratios, such as Nb/La and Nb/U (averages of 1.4 ± 0.2 and 53 ± 8 (1σ), respectively), show limited ranges that overlap to a large degree with the ranges displayed by fresh southern African kimberlites (1.3 ± 0.3 and 43 ± 8, respectively). This suggests that for the more immobile incompatible elements (the REE and HFSE), and even some other elements that may not be so resistant, such as U, Th and Pb (except for TK-5), Tshibwe samples may largely retain their original magmatic compositions.

KUNDELUNGU

Kundelungu kimberlite samples are mostly aphanitic and hypabyssal and show petrographic evidence for only minor alteration (e.g., partial replacement of olivine macrycrysts), with the exception of sample KZ-1. Sample KZ-1 is significantly altered and its olivine phenocrysts and microphenocrysts are extensively replaced by calcite and serpentine (see petrography). The fact that this sample has, by a small margin, the most radiogenic initial $^{87}Sr/^{86}Sr$ composition of all Kundelungu samples (0.7054 versus ≤ 0.7047) is also consistent with greater degree of alteration. However, it is important to note that, in terms of ratios of moderately and highly incompatible elements, even including such relatively alteration-sensitive elements as Rb and Ba, the composition of KZ-1 falls within the range of, or very close to, the other Kundelungu kimberlite data (e.g., Ba/Nb = 6.4 for KZ-1 versus 2.4 to 8.1 for the other Kundelungu samples). Another analysed Kundelungu sample, KUN-1, the sole sample from the M'Bo pipe, has Pb isotope data that are distinctly less radiogenic than the rest of the Kundelungu samples. However, it is still within the isotopic range of southern African Group 1 kimberlites and it does not fall significantly higher relative to the NHRL compared to the other Kundelungu data, as one would expect if it was

caused by assimilation of continental crust. The same sample was also analyzed by Weis and Demaiffe (1985) and very similar Sr-Nd-Pb radiogenic isotope data was obtained.

4.8.3. EFFECTS OF FRACTIONAL CRYSTALLIZATION

Several authors have recognized the effect of macrocrystal phases, thought to originate as xenocrysts entrained by the kimberlite magma during its ascent through the lithospheric mantle, in the bulk-rock geochemistry of the host kimberlite (Fraser and Hawkesworth, 1992; Beard et al., 2000; le Roex et al., 2003; Harris et al., 2004; Coe 2004; Becker and le Roex, 2006; Mitchell, 2008). Some authors have argued for the recognition and removal of the effect of macrocryst entrainment for each kimberlite investigated before any attempt is made to constrain the petrogenesis (le Roex et al., 2003; Becker and le Roex, 2006). These authors proposed a macrocryst correction procedure, applicable only to kimberlite samples with more than 10 volume % of olivine macrocrysts, in which the average composition of a garnet lherzolite (using the average composition from Grégoire et al., 2003) is used as a peridotite proxy.

From the procedure described above, it is not feasible to apply the macrocryst correction procedure on analysed central African kimberlites. These kimberlites are either not macrocrystic (e.g., most Kundelungu samples) or they are significantly altered such that either the quantity of olivine macrocrysts originally present is in doubt (e.g., Tshibwe), or the samples have experienced chemical alteration of their major element compositions that would make such a correction scheme unworkable (e.g., Camatue).

Effect of fractional crystallization

The role of crystal fractionation in the evolution of kimberlite magmas has been extensively debated. This fractionation may have taken place either during ascent through the SCLM or during and shortly following emplacement of kimberlites in the upper crust/subsurface (Shee, 1985; le Roex et al., 2003; Becker and le Roex, 2006). The two main phases that are believed to have fractionated from kimberlite magmas are olivine and phlogopite (Beard et al., 2000; le Roex et al., 2003; Harris et al., 2004; Coe, 2004; Becker and le Roex, 2006). Fractionation of these phases will cause major and trace element variations that should be able to be used to constrain the mineralogy of the fractionating assemblage and the and extent of crystallization.

It is important to note, however, as mentioned in section 3.5 above, that there is little clear evidence for olivine fractionation at Tshibwe and Camatue. Only the Kundelungu kimberlites show clear evidence for significant olivine control (e.g., the strong positive correlation between MgO and SiO_2 in Fig. 4.6) and even here, some of this (the large gap between the KZ-1 sample and the rest of the Kundlungu data) is likely due to post-emplacement replacement of olivine by calcite, rather than magmatic fractionation. All of the central African kimberlite samples investigated here display significant negative K anomalies in their primitive mantle-normalised incompatible element patterns, and these could potentially be the result of phlogopite fractionation. However, it has been well established that negative anomalies in K, Rb and some other elements (e.g., Zr, Hf and Ti) are characteristic of the mantle sources of many Group I kimberlites and other alkaline magmas, and also may be due to the presence of residual hydrous or Ti-bearing minerals (e.g., phlogopite, amphibole, rutile, ilmenite) in the mantle source assemblage following low-degree partial melting (e.g., Adam et al., 1993; Foley et al., 1999; le Roex et al., 2003; Becker & le Roex, 2006; Pilet et al., 2008; 2011).

4.8.4. SOURCE REGION CHARACTERISTICS

A. Approach to modelling of central African kimberlite source regions

Experimental studies have shown that kimberlitic melts are generated by low degrees of partial melting of carbonated garnet peridotite at pressures of 3 to 8 GPa (Eggler and Wendlandt, 1979; Canil and Scarfe, 1990; Dalton and Presnall, 1998). Using this information, several authors have developed approaches to model kimberlite petrogenesis by small degrees of partial melting of carbonated garnet peridotite (Tainton and McKenzie, 1994; le Roex et al., 2003; Harris et al., 2004; Coe, 2004; Chalapathi Rao et al., 2004; Becker and le Roex, 2006)

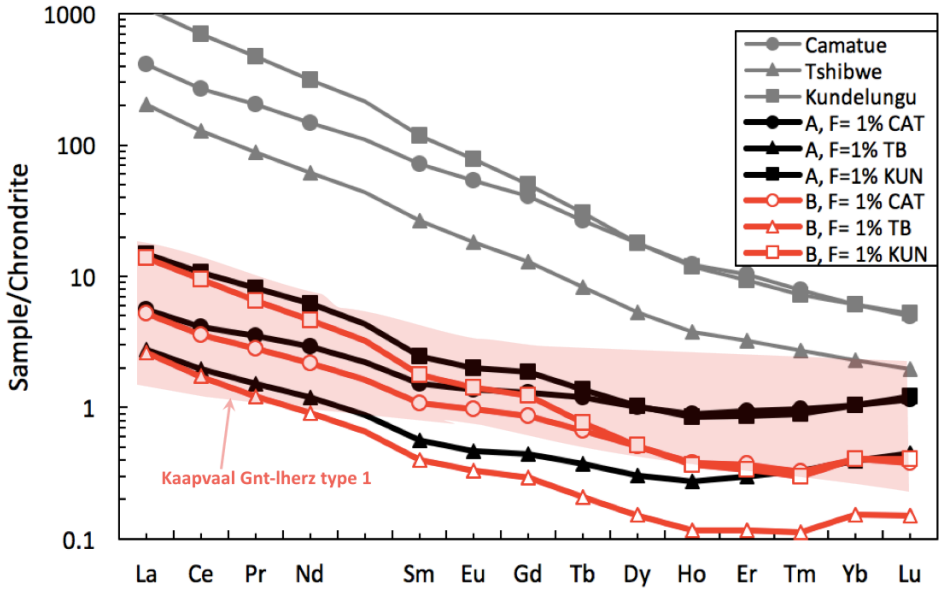

Figure 4.20: Chondrite normalized REE composition of kimberlite source regions in equilibrium with central African primitive kimberlite magmas, calculated by forward modelling and with partition coefficients from Table 3.9. The degree of melting is assumed to be 1 % and the residual source region mineralogy for the predicted kimberlite source region composition is illustrated by models A, peridotite mantle source (with 67% olivine, 26% opx, 4 % cpx and 3 % garnet and with assumed melt proportions of 0.2/0.2/0.5/0.1, respectively) and B, phlogopite bearing mantle source (with 67% olivine, 29% opx, 2% cpx, 0.5% garnet and 1.5% phlogopite with assumed melt proportions of 0.2/0.2/0.45/0.05/0.1, respectively). The pink field represents the composition of Kaapvaal type I garnet lherzolites (since type 2 garnet lherzolites have been associated with PIC and MARID rocks and therefore are not shown here) (Grégoire et al., 2003). Chondrite normalizing values are from McDonough and Sun (1995) (A= model A; B = model B; F= degree of melting; KUN= Kundelungu; TB= Tshibwe; CAT= Camatue).

Table 4.9: Partition coefficients used in the present study for modelling.

	Rb	Ba	Th	U	K	Ta	Nb	La	Ce	Pb	Pr	Sr	Nd	P
Oliv	0.001	0.001	0.001	0.001	0.001	0.001	0.001	0.001	0.001	0.001	0.001	0.001	0.001	0.001
Opx	0.001	0.001	0.001	0.001	0.001	0.001	0.001	0.001	0.001	0.001	0.001	0.001	0.001	0.001
Cpx	0.001	0.001	0.001	0.001	0.01	0.01	0.01	0.05	0.08	0.08	0.1	0.12	0.14	0.1
Gnt	0.001	0.001	0.001	0.001	0.001	0.001	0.001	0.01	0.021	0.021	0.054	0.001	0.087	0.05
Phlg	2.48	3.68	0.001	0.001	3.67	0.014	0.088	0.028	0.021	0.1		0.159	0.012	2

	Sm	Hf	Zr	Eu	Ti	Gd	Tb	Dy	Ho	Er	Tm	Yb	Lu
Oliv	0.001	0.001	0.001	0.001	0.001	0.001	0.001	0.001	0.001	0.001	0.001	0.001	0.001
Opx	0.001	0.01	0.01	0.01	0.1	0.016	0.019	0.022	0.022	0.03	0.03	0.1	0.1
Cpx	0.14	0.2	0.2	0.15	0.17	0.2	0.25	0.3	0.3	0.28	0.29	0.3	0.3
Gnt	0.13	0.1	0.1	0.2	0.1	0.3	0.6	0.9	1.4	2	3	4	6
Phlg	0.013	0.19	0.017	0.014	0.016	0.016	0.016	0.016				0.018	0.001

Compilations of Becker and le Roex, 2006 from le Roex et al., 2003 and Späth et al. (2001) and interpolated from Grégoire et al. (2003). Phlogopite Ds are from La Tourette et al. (1995) and Adam et al. (1993).

Following previous authors (le Roex et al., 2003; Becker and le Roex, 2006), melt modeling of chondrite-normalised rare earth element patterns and primitive mantle-normalised incompatible element patterns has been performed for samples from the Camatue, Tshibwe and Kundelungu kimberlites that are the most primitive and least altered (in terms of both petrographic and chemical criteria): samples CAT-5 from Camatue, TK-16 from Tshibwe and KKA-1 from Kashioba, (Kundelungu Field). The modeling here makes one key assumption: that the residual source mineralogy for these kimberlites are either anhydrous garnet lherzolite (Model A; using the average modal abundances found by Gregoire et al., 2002; 2003 in their studies of Kaapvaal peridotites), or phlogopite-bearing peridotite (model B; using average modal abundances of Grégoire et al., 2002)

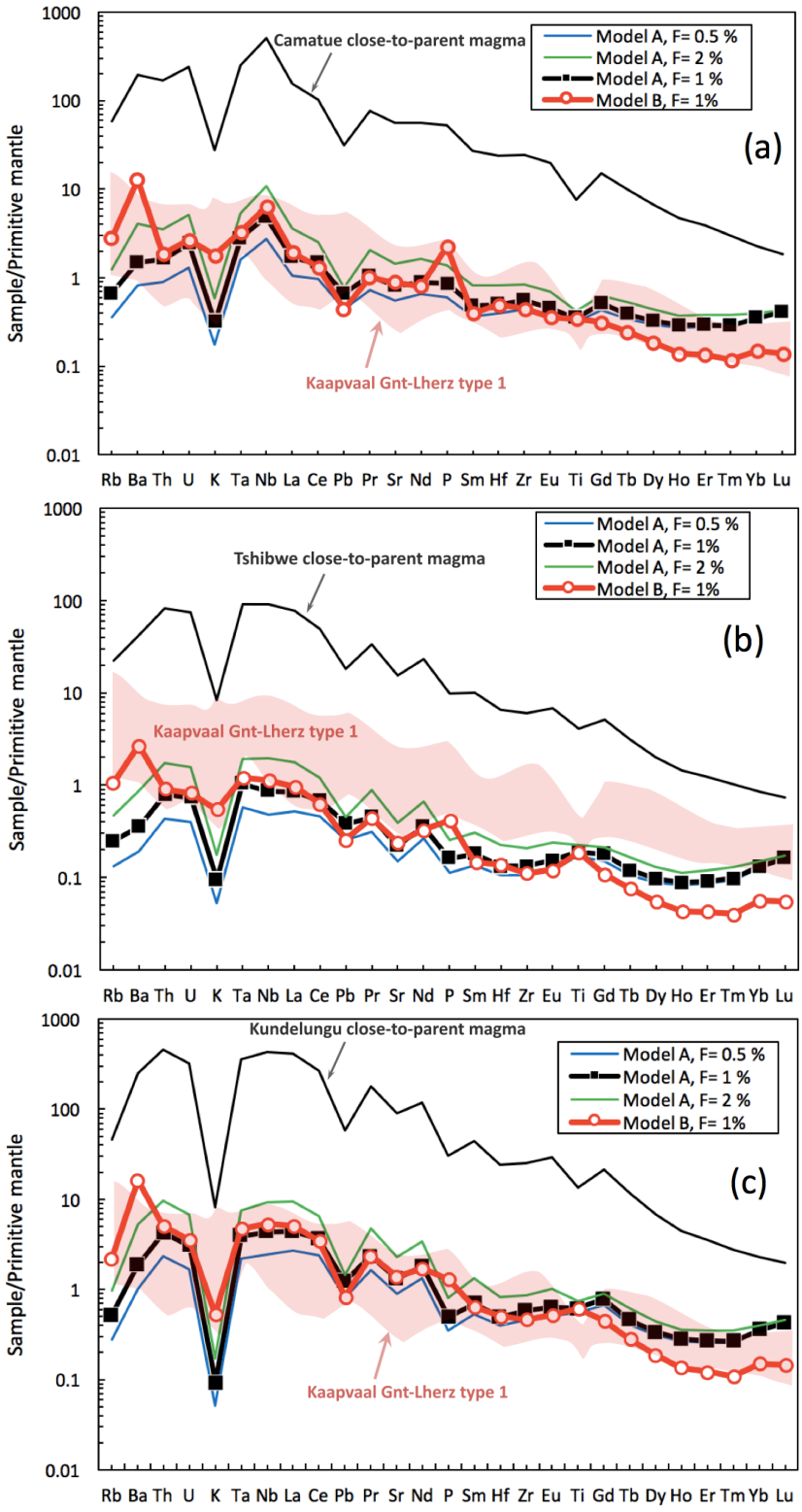

Figure 4.21: Primitive mantle-normalized patterns of the source compositions of central African kimberlites (Camatue (a), Tshibwe (b), Kundelungu (c)), calculated by forward modelling from close-to-parent kimberlite magma with F= 0.5 – 2 % and residual source region mineralogy corresponding to a garnet lherzolite (Model A) and phlogopite bearing peridotite (Model B) (see Fig. 3.20). The red shaded field represents the composition of Kaapvaal type I garnet lherzolites (Grégoire et al., 2003). Normalising values are from McDonough and Sun (1995).

Experimental work has shown that a carbonate-bearing (likely metasomatised) garnet peridotite mantle source is required to generate Group I kimberlite magmas (Ringwood et al., 1992; Brey

and Ryabchikov, 1994; Dalton and Presnall, 1998; Wyllie and Lee, 1999). However, carbonate minerals are consumed very rapidly upon melting and are extremely unlikely to remain in the residue following melting. In contrast, hydrous minerals such as phlogopite may remain in the residue after low degree melting (e.g., Adam et al., 1993) and there is abundant evidence from HREE depletion in kimberlites for the presence of residual garnet in the melting assemblage (e.g., Tainton & McKenzie, 1994; le Roex et al., 2003).

The non-modal batch melting equations of Shaw (1970) were used to calculate the mantle source compositions of the most primitive kimberlite samples from the three localities using the partition coefficients given in Table 4.9. Our results are consistent with the kimberlite trace element modelling results of previous studies (le Roex et al., 2003; Becker and le Roex, 2006), that the concentrations of most incompatible elements in the central African kimberlites are consistent with generation by 0.5 to 2% partial melting of metasomatised garnet lherzolite.

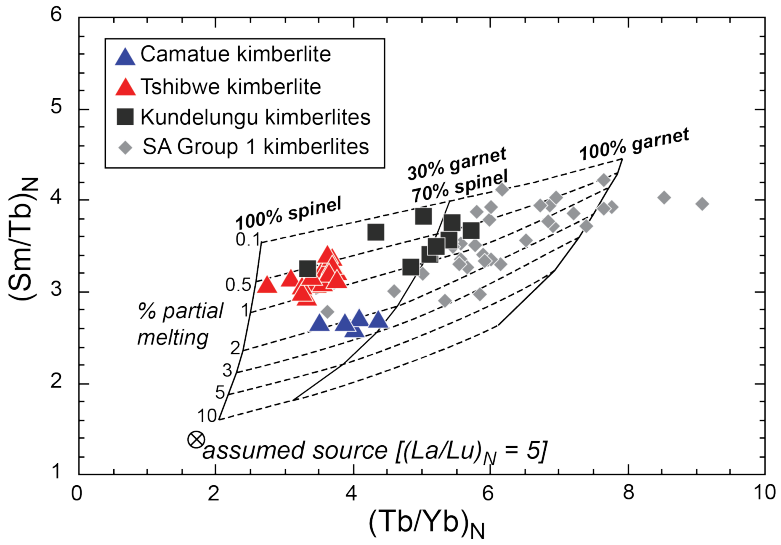

Figure 4.22: Chondrite-normalised Tb/Yb versus Sm/Tb ratios for central African kimberlite samples compared with data for South African group 1 kimberlites (data from le Roex et al., 2003 and Becker and le Roex, 2006). Melting grid shows compositions of melts of assumed source composition calculated for different degrees of partial melting (0.1 to 10%) of a peridotite mantle source having variable relative proportions of spinel and garnet. Assumed modal and melt contribution proportions of olivine/orthopyroxene/clinoproxene/(spinel + garnet) are 0.5/0.3/0.1/0.1 and 0.25/0.25/0.25/0.25, respectively. Chondrite normalising values are from Evensen et al. (1978).

B. Geochemistry of central African kimberlite source regions

The geochemistry of calculated central African kimberlite source regions is well illustrated in Figures 4.20 and 4.21. They are all characterized by enrichment in LREE relative to HREE. Assuming a degree of melting of 1% and a garnet lherzolite residual source mineralogy (model A), the source composition calculated for the Kundelungu kimberlite sample is more enriched in LREE, HREE, HFSE and LILE compared to those calculated for the Tshibwe and Camatue kimberlites. Estimated central African kimberlite source regions all have negative K anomalies on primitive mantle normalized diagrams (Fig. 4.21), although these are dramatically lessened if the mantle source contains phlogopite (model B). It is noteworthy to mention that the calculated Kundelungu source composition has the greatest negative K anomalies of all of the central African kimberlites. The calculated Kundelungu source composition displays higher LREE/MREE and LREE/HREE ratios than the calculated Tshibwe and Camatue sources. It is suggested that, for the most part, trace element differences shown by central African primitive kimberlite magmas, such as these variations in REE patterns, are likely inherited from their source regions rather than being the result of variations in degrees of melting or source mineralogy.

Becker and le Roex (2006) performed similar modeling for southern African kimberlites and their results caused them to suggest that residual accessory phases, such as phlogopite, were not necessary to explain the elemental patterns observed in their kimberlite samples. However, the extreme negative K anomalies and Rb depletions in Kundelungu suggest the presence of residual phlogopite in the Kundelungu kimberlite source. Even with a phlogopite-bearing source, the calculated source composition for Kundelungu has negative K and Rb anomalies similar to the phologopite-free source compositions calculated for the Camatue and Tshibwe kimberlites. Assuming 1% partial melting and a phlogopite bearing peridotite residual source mineralogy (model B; Fig. 4.20 and 4.21), the concentrations of K and Rb are within the range of the Kaapvaal peridotite field of Gregoire et al. (2003). However, without a phlogopite-free source (model A), the negative K and Rb anomalies are extreme, falling well below the Kaapvaal peridotite range, unlike other highly incompatible elements. This evidence strongly suggests that residual phlogopite was present in Kundelungu kimberlite sources.

The role of garnet in kimberlite partial melting can be treated more quantitatively using a plot of chondrite-normalised Tb/Yb versus Sm/Tb (Fig. 4.22), in which the degree of partial melting primarily controls Sm/Tb ratio, whereas the proportion of melting in the presence of garnet

(and the proportion of garnet in the source) mainly controls the Tb/Yb ratio. Based on the gridlines shown, the Kundelungu kimberlites appears to have formed from sources with a relatively high proportion of residual garnet than those of the other central African kimberlites, but similar to many southern African Group 1 kimberlites. The Tshibwe kimberlites, on the other hand, appear to have either formed from a more garnet-poor source, or were generated by shallower melting with in which a lower proportion of the melting occurred in the presence of garnet than for the other central African kimberlites. suggests that central African kimberlites were, on average, generated from source regions with a lower proportion of residual garnet than in southern African Group 1 kimberlites (Fig. 4.22).

C. Comparison with xenocryst geochemistry

Pivin et al. (2009) and Batumike et al. (2009) have demonstrated that peridotitic and megacrystic garnets and clinopyroxenes from Kundelungu kimberlites display compositional overlap with garnets and clinopyroxenes from Kaapvaal type 1 garnet lherzolites. In the present study, we have shown the chemical compositional similarity between Kundelungu kimberlites' source regions and Kaapvaal type 1 garnet lherzolites.

In this thesis, evidence has been presented, on the basis of the abundance of garnet xenocrysts and Sc/V ratios of clinopyroxene xenocrysts, that the SCLM beneath the Tshibwe kimberlite had higher proportion of garnet-poor lherzolites (while the SCLM beneath Tshibwe is dominantly lherzolitic, the modal proportion of garnet is low compared to Mbuji-Mayi or the Kaapvaal craton). As shown above, the composition of the Tshibwe kimberlite also suggests a relatively low modal proportion of garnet in its source region, consistent with the xenocryst evidence. It is possible that these two similar inferences could be related by extensive assimilation of garnet-poor SCLM by percolating protokimberlitic magmas beneath Tshibwe, relative to assimilation of more garnet-rich SCLM by protokimberlitic melts beneath Kundelungu. A comparison of the Camatue kimberlite source and SCLM composition is impossible due to the lack of xenolith or xenocryst geochemical data for kimberlites from Northeast Angola.

4.8.5. SOURCES AND ORIGINS OF CENTRAL AFRICAN KIMBERLITES

A. Camatue

The Camatue kimberlite samples display an extreme DUPAL anomaly. Some South American kimberlites (particularly those from the Minas Gerais region) located on and off the São Francisco craton in Brazil were investigated by Bizzi et al., (1995) (and later by Araujo et al., 2001 and Guarino et al., 2013). Based on the ≈ 120 Ma of other kimberlites in the area (Castillo-Oliver et al., 2016), Camatue was likely emplaced in the early Cretaceous, roughly contemporaneously with the Minas Gerais kimberlites (Bizzi et al., 1995). This, emplacement would have occurred during or shortly after the onset of South Atlantic rifting. The emplacement of the Lunda Norte kimberlites of Angola, including Camatue, has been linked to the opening of the South Atlantic Ocean with a main eruptive peak at 120 Ma (Jelsma et al., 2009; 2013; Robles-Cruz et al., 2012; Castillo-Oliver et al., 2016).

The Minas Gerais kimberlites display extreme-DUPAL isotopic signatures similar to the Camatue kimberlite. Bizzi et al., (1995) argued that the chemical and isotopic compositions of these kimberlites reflect mixing between two components: asthenospheric melts with low Rb/Sr, Nd/Sm and Pb/U, displaying similarities with Group I kimberlites (and OIB) and volumetrically dominant enriched subcontinental lithospheric mantle with high time-integrated Rb/Sr, Nd/Sm and Pb/U. They have proposed that these kimberlites' source regions were influenced by the Tristan da Cunha hotspot (initiated around 130 Ma). Although Tristan da Cunha lavas have lower values for trace element ratios, such as Ba/Nb, La/Nb, Nb/U and Ce/Pb than Minas Gerais kimberlites (see Table 3.10) (Le Roex et al., 1990; Bizzi et al., 1995). It was suggested, by Bizzi et al., (1995) that assimilation of enriched lithospheric mantle beneath the São Francisco craton could account for this difference.

On the basis of mineral compositions in peridotites from Somacuanza in central Angola, Camatue lithospheric mantle was suggested to be extremely depleted by Boyd and Danchin (1980). A highly depleted lithospheric mantle would likely have little to no obvious effects on the trace element ratios of rising asthenospheric melts percolating through the SCLM. Smith et al. (2009) investigated peridotite xenoliths from the Zimbabwe Craton and highlighted the extremely depleted character of the underlying lithospheric mantle. Kaapvaal metasomatised type I garnet lherzolites (Grégoire et al., 2003) have higher Ba/Nb (5 – 14 versus 0.9), Nb/U (13 – 56 versus 2)

and Ce/Pb (5 – 30 versus 0.2) than a Zimbabwe lherzolite sample investigated by Smith et al., (2009). Clearly, a depleted lithospheric mantle would likely have lower trace element ratios compared to an enriched one and therefore assimilation of its products (depleted SCLM) by asthenospheric melts would likely have little effects on trace elements ratios of rising mantle melts. It is noteworthy that Camatue kimberlite and Tristan da Cunha lavas have similar ranges in diagnostic trace element ratios, unlike Minas Gerais kimberlites which have higher ratios than in Tristan da Cunha. It is therefore suggested that assimilation of extremely depleted lithospheric products by asthenopheric melts with an extreme-DUPAL signature, similar to those seen in MORB and OIB in areas of the South Atlantic, would account for the chemical and isotopic character of the Camatue kimberlite.

Table 4.10: Ranges of selected diagnostic trace element ratios in kimberlites and mantle xenoliths from central Africa and Brazil (south America).

	Ba/Nb	Nb/U	Ce/Pb	La/Nb
Kundelungu	2.4 - 8.08	34 - 62	12 - 29	0.44 - 0.81
Tshibwe	3.27 - 11.24	39 - 73	20 - 38	0.48 - 0.85
Camatue	2.19 - 8.84	35 - 67	29 - 36	0.3 - 0.6
Minas Gerais	0.1 - 13	45 - 51	48 - 60	1.35 - 1.5
Tristan da Cunha	0.08 - 13.30	35 - 43	12 - 29	0.64 - 0.65
Goias peridotite xenoliths	7 - 21	30 - 56		0.70 - 0.95

Minas Gerais data are from Bizzi et al., 1995; Araujo et al., 2001 and Guarino et al., 2013. Goias peridotite xenoliths data are from Carlson et al., 2007.

B. Tshibwe

Tshibwe kimberlite samples have relatively unradiogenic Pb isotope ratios that are intermediate between the DMM end-member (Zindler and Hart, 1986) and South Atlantic MORB. Tshibwe samples have trace element ratios similar to OIB and MORB suggesting a sub-lithospheric origin. The observation that Mbuji-Mayi Pb isotope data are more radiogenic than Tshibwe Pb isotope data presented in this study (Fig 3.13) can possibly be explained by assimilation of different SCLM compositions. Evidence was shown in Chapter 2 for a depleted and cool SCLM beneath Tshibwe and a metasomatised, warmer SCLM beneath Mbuji-Mayi.

C. Kundelungu

Kundelungu kimberlite samples have OIB like Sr-Nd-Pb isotopic affinities. Nearly all plot in the depleted quadrant of the Sr-Nd istope correlation diagram and they fall within the isotopic ranges of southern African Group I kimberlites. Kundelungu samples have trace element ratios similar to OIB and MORB. Batumike et al., (2009) have demonstrated the strongly metasomatized character of the SCLM beneath the Kundelungu Plateau. Metasomatized SCLM are known to have more radiogenic Sr and less radiogenic Pb isotope ratios than HIMU lavas (eg., Shona, St. Helena). Kundelungu kimberlite samples are characterized by high U/Pb ratios, a well defined negative correlation between Sr and Nd isotope ratios, as well as a weak one between Sr and Pb isotope ratios. These features could possibly be interpreted as indicative of a lithospheric source contribution to the asthenospheric melts during assimilation, likely at the base of the lithosphere (Bizzi et al., 1995). Batumike et al., (2008) have linked the emplacement of Kundelungu kimberlites with the onset of the East African Rift System (EARS). It is argued that asthenospheric melts with South Atlantic OIB signatures, intermediate between HIMU and South Atlantic MORB, were formed by the start of rifting of the EARS, rose from the mantle and underwent variable assimilation of a metasomatised SCLM during ascent.

The kimberlite formation model, presented in this study, is similar to some extent to the models suggested by Tappe et al. (2011) and Griffin et al. (2014), where the final kimberlite geochemical signatures are the product of mixtures of lithospheric mantle components and asthenospherically-derived proto-kimberlitic magmas. These models invoke a homogeneous, relatively depleted convecting mantle as the source of asthenospheric proto-kimberlite melts. However, in order to explain the central African kimberlite data in this study, asthenospheric melts with distinct isotopic characteristics (comparable to moderate HIMU; e.g., Shona, St. Helena) and extreme DUPAL MORB/OIB (e.g., Tristan, "LOMU segment" MORB; e.g., Douglass et al., 1999) are required. Furthermore, Camatue samples display DUPAL type mantle source (asthenosphere-derived), undistinguishably different from the depleted mantle.

D. Location of kimberlite source regions: Subcontinental lithosphere or asthenosphere?

The origin of the DUPAL anomaly (Dupré and Allègre, 1983; Hart, 1984) has long been a subject of debate. Throughout years, models invoking a shallow origin have been advocated by several authors (Hawkesworth et al., 1986; Peate et al., 1999; Milner and le Roex, 1996; Escrig et

al., 2005; Gibson et al., 2005; Class and Le Roex, 2006; Regelous et al., 2009). Recently, Class and le Roex (2011) have provided evidence against a shallow origin for the DUPAL anomaly. They investigated xenoliths from the lower continental crust (LCC) and SCLM from the Damara Belt and Namaqua-Natal Belt of southern Africa, two Proterozoic terranes that together compose most of the lithosphere of southwestern Africa (Hartnady et al., 1985). They combined their results with previously published data for Kaapvaal craton xenoliths. They found no evidence for widespread extreme DUPAL-like isotopic signatures (i.e., high Δ8/4Pb and high Sr isotope composition) in these samples, which they assumed to be representative of the African continental lithosphere that might have detached and become incorporated into the South Atlantic upper mantle during Gondwana breakup. They took this as evidence that the strong DUPAL signatures detected in some South Atlantic OIB and MORB had a deep origin in the convecting mantle, rather than being derived from continental lithosphere adjacent to the South Atlantic. Class and le Roex (2011) argued that they might be related to the activity of three mantle plumes in the region, Tristan-Gough, Discovery and Shona.

The asthenospheric origin of the extreme DUPAL anomaly is also supported by the geochemistry of the Brazilian SCLM which appears to lack the extreme DUPAL anaomaly signatures: (1) lack of high Sr isotope composition ($^{87}Sr/^{86}Sr$ ranges from 0.7027 – 0.7046. Rivalenti et al., 2000) in mantle clinopyroxenes from peridotite xenoliths in the northeastern of Brazil (2) Most Goias peridotite xenoliths do not display high Sr isotope composition ($^{87}Sr/^{86}Sr_i$ values fall almost entirely within the range 0.7044 – 0.7048. Carlson et al., 2007) (3) Most Goias peridotite xenoliths display trace element ratios that are distinct from Tristan da Cunha lavas (see Table 4.10). This is consistent with the inference that the distinct trace element ratios displayed by the Minas Gerais kimberlites are reflective of the mixing between an enriched SCLM in incompatible elements and asthenospheric melts with extreme DUPAL signatures.

Given the above evidences, the extreme DUPAL anomaly signatures displayed by Camatue kimberlite samples and Minas Gerais kimberlites (Bizzi et al., 1995) support a deep (or sublithospheric) origin for the DUPAL signature in thse early Cretaceous kimberlites, despite their wide geographic separation. A direct causal link of Camatue and Minas Gerais kimberlites with the Tristan/Gough or other South Atlantic hotspots with DUPAL signatures is difficult to envision given that Camutue is located over 1000 km northeast of the Etendeka flood basalt province, which marks the approximate location of the Tristan hotspot in the Early Cretaceous. The Discovery and

Shona hotspots are located even further south than Tristan and there s little evidence that these hotspots existed in the early Cretaceous. Therefore, evidence from this study would appear to require a less specific origin for the extreme DUPAL anomaly than favored by Class and le Roex (2011) in which this signature may be present variably across a wide region roughly corresponding to a wide region of mantle upwelling underlain by the "African large low shear velocity province" (LLSVP; Garnero et al., 2008).

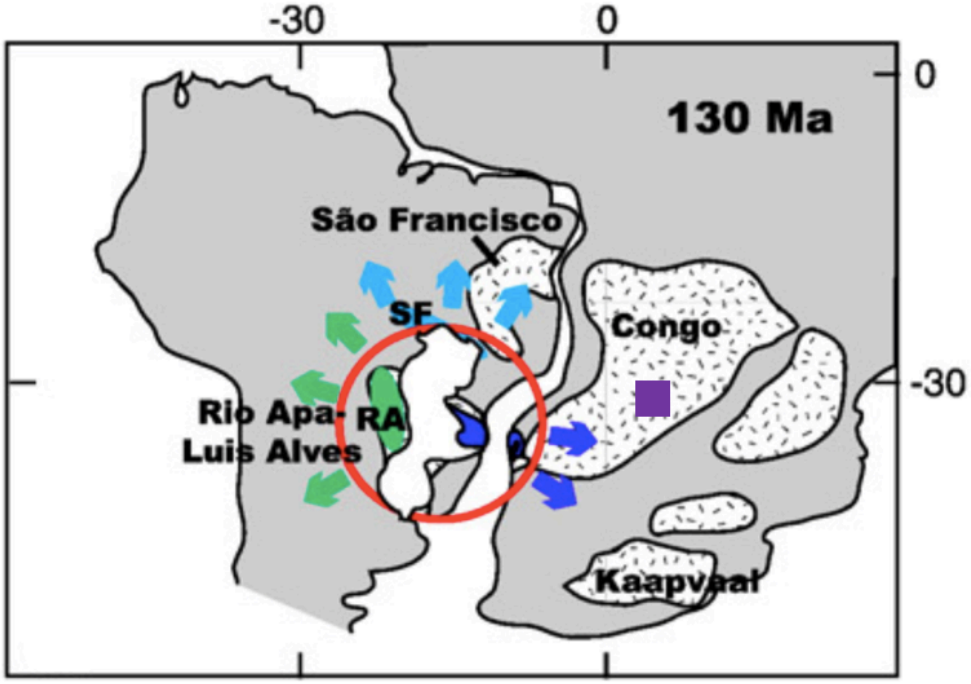

Figure 3.23: Schematic map illustrating the geodynamic constraints for lithospheric or asthenospheric origin of the South Atlantic DUPAL anomaly. The purple square represents the approximate location of the Camatue kimberlite, shortly before its emplacement (assumed to be at around 120 Ma). Map modified after Class and Le Roex (2011). The Tristan mantle plume head is represented by the red circle.

4.9. SUMMARY – KIMBERLITES CHAPTER

Central African kimberlites have been investigated in order to put geochemical and geodynamic constraints on their source regions and to contribute to several ongoing controversies in the field. On-Craton kimberlite samples include the Camatue locality located in the Lunda Norte field, northeastern Angola and, although undated, likely to be of early Cretaceous age. In addition, samples from the Tshibwe locality situated in the Mbuji-Mayi kimberlite field, central DRC and northeastern of the Kasai Craton have been studied. Off-Craton localities, situated southeast from the Kasai Craton, include Kundelungu western and eastern cluster kimberlites.

Kundelungu kimberlite samples are mostly hypabyssal aphanitic in texture, while Camatue samples are macrocryst-rich and volcaniclastic. Tshibwe samples appear to have undergone extensive ground water alteration and olivine is no longer present but replace by abundant secondary serpentine. Fresh olivine is present in most Kundelungu samples but is rare to non-existent in Camatue samples. Phlogopite is relatively abundant as phenocryst and groundmass minerals in Camatue samples but rarely occurs in Kundelungu and Tshibwe samples. Crustal xenoliths of a mafic nature are present and abundant in Camatue and Tshibwe samples and are absent in Kundelungu samples.

The major element composition of Camatue kimberlites is poorer in MgO and richer in SiO_2, Al_2O_3 and Na_2O than is typical for Group 1 kimberlites, and these charateristics are likely related to hydrothermal alteration of these kimberlites. Tshibwe kimberlites are also relatively altered, but the only major element indicators are slightly elevated SiO_2 and slightly low MgO contents compared to typical kimberlites, which is likely attributable to low temperature alteration (primarily replacement by serpentine, clays and calcite). Kundelungu samples, with one exception, appear to be quite fresh, with no detectable alteration effects on chemical composition. Trace element geochemistry of Central African kimberlites reveals the low compatible elements content (such as Cr and Ni) and La/Sm ratios of Camatue kimberlite samples. In addition, Camatue samples have higher incompatible element contents such as LREE, HFSE and LILE (except Ba) than Tshibwe samples. Despite the high LREE enrichment in Camatue samples, Tshibwe samples display higher LREE enrichment relative to HREE than in Camatue samples and also display an apparent flattening of HREE chondrite-normalised patterns. The latter display deeper negative K anomalies than in Tshibwe samples. Kundelungu kimberlites are more enriched in incompatible elements than Tshibwe and Camatue kimberlites. The enrichment in incompatible elements displayed by Kundelungu kimberlites is similar to southern African Group 1 kimberlites.

Camatue kimberlite samples show extreme DUPAL anomaly isotopic signatures ($\Delta 8/4$ Pb > 120 in most samples). Tshibwe samples fall in the array intermediate between the depleted mantle and South Atlantic MORB on a Pb-Pb isotope correlation diagram. Kundelungu kimberlite samples fall in the depleted quadrant of the Sr-Nd isotope correlation diagram. They show Sr-Nd-Pb isotopic affinity intermediate between HIMU and South Atlantic MORB.

Hypothetical source compositions of the three kimberlite groups have been calculated by quantitative modelling using the most primitive samples available, assuming low degree of melting

(0.5 – 2 %) and source mineralogies similar to moderately fertile off-craton and infertile but phlogopite-bearing garnet lherzolite. All central African kimberlite source compositions fall within or slightly below the field of Kaapvaal garnet lherzolite type I (Grégoire et al., 2003) with the Tshibwe source region having the lowest trace element content overall. However, K and Rb have the worst fits to the metasomatised peridotite source, falling below the ranges observed in Kaapvaal peridotites, and this may indicate the presence of phlogopite in the sources of these kimberlites. The trace element modelling indicates that the source regions of Kundelungu had a greater proportion of residual garnet than at Camatue and Tshibwe. Tshibwe and Kundelungu appear to have undergone a low degree of partial melting (0.5 – 1%) in their source regions while Camatue display high degree of partial melting (2 – 3%). The low MREE/HREE ratios in Tshibwe kimberlite and the evidence from calculated sources composition (low modal proportion of residual garnet) are consistent with the inference made from xenocryst geochemistry that the Tshibwe SCLM has a higher proportion of garnet-poor lherzolite.

The new central African kimberlites dataset presented in this study is not consistent with the assumption of Griffin et al., (2014) and Tappe et al., (2011) that mantle sources are homogeneous and that protokimberlitic magmas are generated from a single depleted mantle source. Asthenospheric sources like extreme-DUPAL type mantle signatures (Camatue) and depleted mantle components (Mbuji-Mayi and Kundelungu) have been identified. The similarity of Camatue and Minas Gerais kimberlites isotopic composition and emplacement age, further adds support to the hypothesis that these signatures (extreme DUPAL) have a deep origin in the convecting mantle, as this is the simplest way to explain the Early Cretaceous to recent presence of the strong DUPAL signature from southwestern Africa, across the South Atlantic, to eastern South America, over a distance of many thousands of kilometers. Evidence from this study would appear to require a greater lateral distribution for the extreme DUPAL signatures, from southwestern Africa to the far southern mid-Atlantic to Brazil, than previously recognised. The exclusive attribution of this signature, as made by Class and le Roex (2011) to the "African large low shear velocity province" (LLSVP; Garnero et al., 2008), may be premature.

CONCLUSIONS

The following conclusions have been drawn from the present study of kimberlites and related xenocrysts from southern and central Africa, highlighting its originality:

Megacryst petrogenesis:

1) The geochemistry of Colossus, Kalkput, Orapa, Tshibwe and Mbuji-Mayi (and other) southern and central African megacryst suites is generally consistent with their derivation by fractional crystallization from sublithospheric protokimberlitic magmas undergoing extensive assimilation of lithospheric peridotite;
2) The deflection towards higher Cr# and Mg# at high Ca# values (i.e., low temperatures) in clinopyroxene megacrysts from several suites (e.g., Orapa, Mbuji-Mayi) coincides with an increase in LREE/HREE ratios and Sr isotope composition. Assimilation of metasomatised SCLM by protokimberlitic magmas during fractional crystallization is proposed to explain this;
3) The absence of the above deflection and the continuous decrease of Cr# and Mg# observed at higher Ca# in some megacryst suites (e.g., Kalkput, Orapa Cr-poor, Kaalvallei suites) coincide with the lack of (or weak) increase in LREE/HREE ratios, decrease in Nb/U, Ce/Pb, Th/Nb ratios and lack of (weak) increase in Sr isotope composition. Assimilation of depleted peridotite by proto-kimberlitic magmas during fractional crystallization has been proposed to likely explain this;
4) The continuous compositional variations between Cr-poor and Cr-rich megacryst suites suggest that they are genetically related by assimilation of fertile metasomatised lithospheric rocks during fractional crystallization. The order of crystallization starts with the Cr-poor followed by Cr-rich, the latter being the most evolved, supported by the pyroxene solvus thermometry and not the reverse order proposed by Moore and Belousova (2005) and Kopylova et al., (2009). In addition, we have shown that the decrease of Ti content in Cr-rich cpx megacrysts is likely indicative of ilmenite crystallization and overwhelming evidence that ilmenite is a late crystallizing phase in kimberlite has been provided by Moore et al., (1992) and Griffin et al, (1997). There is some evidence suggesting a correlation between the occurrence of Cr-rich megacryst suites and the higher abundance of fertile and metasomatised lherzolite in the SCLM, at the time of megacryst formation;

5) The magmatic model (AFC process) developed in this study appear to reconcile megacrysts major and trace element variations, as well as Sr isotope composition with temperature constraint;
6) There is a close genetic relationship between megacrysts and host kimberlite supported by the direct comparison of Sr isotope composition (Bellsbank) as well as diagnostic trace element ratios (e.g., Th/Nb, Ce/Pb and Nb/U) (Bellsbank and Tshibwe) between megacrysts and their host kimberlite;
7) Through a new approach, the comparison of the geochemistry of Group 1 and Group 2 kimberlite megacrysts, further evidence was provided for a genetic link between megacrysts and host kimberlites. Major element, trace element, trace element ratios and Sr isotope composition similarities of Group 1 kimberlites and their megacrysts as well as of Group 2 kimberlites and their megacrysts strongly suggest a close genetic relationship.
8) The geochemistry of Group 2 kimberlite megacrysts likely suggest that Group 2 kimberlitic melts have an asthenospheric origin and not lithospheric as previously assumed by Becker & Le Roex (2006) and Giuliani et al., (2015)

Chemical and thermal state of the northeastern Kasai craton:

9) The lithospheric mantle beneath the northwestern portion of the Kasai is likely made of abundant garnet lherzolites and eclogites. Peridotitic clinopyroxene define a compositional and thermal profile to depths as great as 220 km. The SCLM beneath Tshibwe appear to have a higher proportion of garnet-poor lherzolite, depleted and cooler than the one beneath Mbuji-Mayi which appear to have been warmer, enriched and extensively metasomatised. The occurrence of different thermal and metasomatic states in mantle located in close proximity (within 35 km) suggests that the Tshibwe cluster kimberlites may have been emplaced prior to Mbuji-Mayi. The cooler thermal regime is consistent with the older age that was determined for Tshibwe in this thesis;
10) The geochemistry of peridotitic garnets, megacrystic clinopyroxenes and ilmenites from Mbuji-Mayi and Tshibwe are consistent with the inferences above;
11) U-Pb isotopic analyses of the perovskite grains from the Tshibwe kimberlite samples yielded an age of 84 ± 9.5 Ma, which is in agreement with stratigraphic and other circumstantial geological evidence. This age probably coincided with a change in the direction and velocity of African plate motion;

12) The northwestern Kasai craton appears to have been affected by a pulse of kimberlite magmatism, of roughly 85-70 Ma responsible for the Tshibwe, Mbuji Mayi and possibly the kimberlites of the Kabinda field in the DRC, all of which are in clusters oriented roughly E-W. Their apparently similar age and orientation suggests that they were emplaced along an east-west oriented zone of lithospheric weakness in the northeastern Kasai craton, tentatively termed the "Kasai corridor";

Sources and petrogenesis of central African kimberlites:

13) The composition of central African kimberlites is fairly similar to southern African kimberlites except for the lower MREE/HREE ratios, lower overall concentrations of incompatible elements and isotopic signatures ranging from depleted mantle to extreme-DUPAL displayed by central African kimberlites;
14) Trace element modelling suggest that the source regions of southern African Group 1 kimberlites had a higher proportion of residual garnet while those for central African kimberlites had lower proportion of residual garnet but residual phlogopite was likely present. In addition to the trace element modelling evidence, the low MREE/HREE ratios observed in Tshibwe kimberlite samples is consistent with the inference made from the geochemistry of peridotitic clinopyroxenes and garnets that the Tshibwe SCLM has a higher proportion of garnet-poor lherzolite;
15) The new central African kimberlites dataset presented in this study is not consistent with the assumption of Griffin et al., (2014) and Tappe et al., (2011) that mantle sources are homogeneous and that protokimberlitic magmas are generated from this single depleted mantle source. Asthenospheric sources like extreme-DUPAL type mantle signatures (Camatue) and depleted mantle components (Mbuji-Mayi and Kundelungu) have been identified.
16) The similarity of Camatue and Minas Gerais kimberlites isotopic composition and emplacement age, further adds support to the hypothesis that these signatures (extreme DUPAL) have a deep origin in the convecting mantle, as this is the simplest way to explain the Early Cretaceous to recent presence of the strong DUPAL signature from southwestern Africa, across the South Atlantic, to eastern South America, over a distance of many thousands of kilometers. Evidence from this study would appear to require a greater lateral distribution for the extreme DUPAL signatures, from southwestern Africa to the far southern mid-Atlantic to Brazil, than previously recognised. The exclusive attribution of this signature, as made by

Class and le Roex (2011) to the "African large low shear velocity province" (LLSVP; Garnero et al., 2008), may be premature.

REFERENCES

Adam, J., Green, T.H. & Sie, S.H. (1993) Proton microprobe determined partitioning of Rb, Sr, Ba, Y, Zr, Nb and Ta between experimentally produced amphiboles and silicate melts with variable F content. *Chemical Geology* **109**, 29-49.

Agashev, A.M., Nakai, S., Serov, I.V., Tolstov, A.V., Garanin, K.V., Kovalchuck, O.E., (2018) Geochemistry and origin of the Mirny fields kimberlites, Siberia. *Mineralogy and Petrology* **112**, 597 – 608.

Allsopp, H.L. & Barrett D.R. (1975) Rb-Sr age determinations on South African kimberlite pipes. *Physics and Chemistry of the Earth* **9**, 605–617.

Allsopp, H.L., Bristow, J.W. & Skinner, E.M.W. (1985) The Rb–Sr geochronology of the Colossus kimberlite pipe, Zimbabwe. *Transactions Geological Society of South Africa* **88**, 245-248

Andersen, T., Griffin, W. L. & O'Reilly, S. Y. (1987). Primary sulphide melt inclusions in mantle-derived megacrysts and pyroxenites. *Lithos* **20**, 279-294.

Andre, L. (1994) Age Rb-Sr Proterozoique inferieur du Magmatism continental du Groupe de la Lulua (Kasai, Zaire): ses implications géodynamiques. *Annales de la Société Geologique de Belgique* **116**(1), 1–12.

Anhaeusser, C.R. (1990) Precambrian crust evolution and metallogeny of Southern Africa. in Naqvi, S.M., ed., Precambrian continental crust and its economic resources: Amsterdam, Elsevier, p. 123–156.

Armstrong, R.A., Compston, W., De Wit, M.J. & Williams, I.S. (1990) The stratigraphy of the 3.5-3.2 Ga Barberton Greenstone Belt revisited: a single zircon ion microprobe study. *Earth and Planetary Science Letters* **101**, 90-106

Arndt, N.T., Guitreau, M., Boullier, A.-M., Le Roex, A., Tommasi, A., Cordier, P., Sobolev, A., (2010) Olivine, and the origin of kimberlite. *Journal of Petrology* **51**, 573–602.

Aulbach, S., Griffin, W.L., O'Reilly, S.Y. & McCandless, T.E. (2004) Genesis and evolution of the lithospheric mantle beneath the Buffalo Head Terrane, Alberta (Canada). *Lithos* **77**, 413-451.

Aulbach, S., Griffin, W.L., Pearson, N.J., O'Reilly S.Y. & Doyle, B.J. (2007) Lithosphere formation in the central Slave Craton (Canada): plume subcretion or lithosphere accretion? *Contributions to Mineralogy and Petrology* **154**, 409–427

Aulbach, S., Pearson, N.J., O'Reilly, S. & Doyle, B.J. (2007b). Origins of xenolithic eclogites and pyroxenites from the Central Slave Craton, Canada. *Journal of Petrology* **48**, 1843 – 1873.

Aulbach, S., Griffin, W.L., Pearson, N.J. & O'Reilly, S.Y. (2013) Nature and timing of metasomatism in the stratified mantle lithosphere beneath the Central Slave Craton (Canada). *Chemical Geology* **352**, 153-169.

Aulbach S. & Viljoen K.S. (2015) Eclogite xenoliths from the Lace kimberlite, Kaapvaal craton: from convecting mantle source to paleo-ocean floor and back. *Earth Planetary Science Letters* **431**, 274–286.

Aulbach, S., Gerdes, A. & Viljoen, K.S. (2016) Formation of diamondiferous kyanite-eclogite in a subduction mélange. *Geochimica et Cosmochimica Acta* **179**, 156-176

Aulbach, S., Jacob, D.E., Cartigny, P., Stern, R.A., Simonetti, S.S., Wörner, G., Viljoen, K.S. (2017) Eclogite xenoliths from Orapa: Ocean crust recycling, mantle metasomatism and Carbon cycling at the western Zimbabwe craton margin. *Geochimica et Cosmochimica Acta* **213**, 574 – 592.

Araujo, A.L.N., Carlson, R.W., Gaspar, J.C., Bizzi, L.A. (2001) Petrology of kamafugites and kimberlites from the Alto Paranaiba Alkaline Province, Minas Gerais, Brazil. *Contributions to Mineralogy and Petrology* **142**, 163-177

Barrett, D.R. & Berg, G.W. (1975) Complementary petrographic and strontium-isotope ratio studies of South African kimberlite. *Physics and Chemistry of the Earth* **9**, 619–635.

Basaltic Volcanism Study Project (1981) Basaltic Volcanism on the Terrestrial Planets. Pergamon Press, New York, 1286pp.

Batumike, J.M., O'Reilly, S.Y., Griffin, W.L. & Belousova, E.A. (2007) U–Pb and Hf-isotope analyses of zircon from the Kundelungu kimberlites, D.R. Congo: implications for crustal evolution. *Precambrian Research* **156**, 195–225.

Batumike, J.M., Griffin, W.L., Belousova, E. A., Pearson, N.J., O'Reilly, S.Y. & Shee, S.R. (2008) LAM-ICPMS U–Pb dating of kimberlitic perovskite: Eocene–Oligocene kimberlites from the Kundelungu Plateau, D.R. Congo. *Earth Planeteray Science Letters* **267**, 609–619.

Batumike, J.M., Griffin, W.L. & O'Reilly, S.Y. (2009) Lithospheric mantle structure and the diamond potential of kimberlites in southern D.R. Congo. *Lithos* **112** (S1), 166–176.

Beard, A.D., Downes, H., Hegner, E. & Sablukov, S.M. (2000) Geochemistry and mineralogy of kimberlites from the Arkhangelsk Region, NW Russia: evidence for transitional kimberlite magma types. *Lithos* **51**, 47–73.

Becker, M. & le Roex, A.P. (2006) Geochemistry of South African on- and off-craton, Group I and Group II kimberlites: petrogenesis and source region evolution. *Journal of Petrology* **47**, 673–703

Becker, M., le Roex, A.P. & Class, C. (2007) Geochemistry and petrogenesis of South African transitional kimberlites located on and off the Kaapvaal Craton. *South African Journal of Geology* **110**(4), 631-646.

Begg, G.C., Griffin, W.L., Natapov, L.M., O'Reilly, S.Y., Grand, S.P., O'Neill, C.J., Hronsky, J.M.A., Poudjom Djomani, Y., Swain, C.J., Deen, T. & Bowden, P. (2009). The lithospheric architecture of Africa: seismic tomography, mantle petrology and tectonic evolution. *Geosphere* **5**, 23-50.

Bell, D.R., Schulze, D.J., Read, G.H., Mattioli, G.S., Shimizu, N., Moore, R.O. & Gurney, J.J. (1995) Geochemistry of Cr-poor megacrysts from the Lace (Group II) kimberlite, South Africa. *Extended Abstracts Sixth International Kimberlite Conference*, Novosibirsk, Russia, 552 – 554.

Bell, D.R., Schmitz, M.D. & Janney, P.E. (2003) Mesozoic thermal evolution of the southern African mantle lithosphere. *Lithos* **71**, 273–287

Bell, D.R. & Moore, R.O., (2004) Deep chemical structure of the southern African mantle from kimberlite megacrysts. *South African Journal of Geology* **107**, 59–80.

Berg, G.W. & Allsopp, H.L. (1972). Low $^{87}Sr/^{86}Sr$ ratios in fresh South African kimberlites. *Earth and Planetary Science Letters* **16**, 27–30.

Bizzi, L.A., de Wit, M.J., Smith, C.B., McDonald, I. & Armstrong, R.A. (1995) Heterogeneous enriched mantle materials and DUPAL-type magmatism along the SW margin of the São Francisco Craton, Brazil. *Journal of Geodynamics* **20** (4), 469-491

Blenkinsop, T., Martin, A., Jelsma, H.A., & Vinyu, M.L. (1997) Zimbabwe Craton, in de Wit, M., and Ashwal, L.D., eds., Greenstone belts: London, Clarendon Press, p. 567–580.

Boctor, N. Z. & Boyd, F. R. (1982) Petrology of kimberlite from the DeBryun and Martin Mine, Bellsbank, South Africa. *American Mineralogist* **67**, 917-925.

Boyd, F.R. & Danchin, R.V. (1980) Lherzolites, eclogites and megacrysts from some kimberlites of Angola. *American Journal of Science* **280** (A), 528-549.

Boyd, F.R., Dawson, J.B. & Smith, J.V. (1984) Granny Smith diopside megacrysts from the kimberlites of the Kimberley area and Jagersfontein, South Africa. *Geochimica et Cosmochimica Acta* **48**, 381–384.

Brey, G. P. & Ryabchikov, I. D. (1994). Carbon dioxide in strongly silica undersaturated melts and origin of kimberlite magmas. *Neues Jahrbuch für Mineralogie, Monatshefte* **10**, 449–463.

Brown, R.W., Allsopp, H.L., Bristow, J.W. & Smith, C.B. (1989) Improved precision of Rb-Sr dating of kimberlitic micas: An assessment of a leaching technique. *Chemical Geology*, Isotope Geoscience Section, **79**(2), 125–136

Burgess, S.R. & Harte, B. (1998) Tracing lithosphere evolution trough the analysis of heterogeneous G9/G10 garnets in peridotites xenoliths, I: major element chemistry. In: Gurney, J.J., et al. (Ed.), Proceedings of the 7th IKC 1. Red Roof Des, Cape Town, p. 66–80.

Burgess, S.R. & Harte, B., 2004. Tracing lithosphere evolution trough the analysis of heterogeneous G9/G10 garnets in peridotites xenoliths, II: REE chemistry. *Journal of Petrology* **45**, 609–634

Bussweiler, Y., Stone, R.S., Pearson, D.G., Luth, R.W., Stachel, T., Kjarsgaard, B.A., Menzies, A., (2016) The evolution of calcite-bearing kimberlites by melt-rock reaction: evidence from polymineralic inclusions within clinopyroxene and garnet megacrysts from Lac de Gras kimberlites, Canada. *Contributions to Mineralogy and Petrology* **171**, 65

Bussweiler, Y., Pearson, D.G., Stachel, T., Kjarsgaard, B.A. (2018) Cr-rich megacrysts of clinopyroxene and garnet from Lac de Gras kimberlites, Slave Craton, Canada. Implications for the origin of clinopyroxene and garnet in cratonic lherzolites. *Mineralogy and Petrology*, 1-14

Cahen, L., Snelling, N.J., Delhal, J. & Vail, J. (1984) The geochronology and evolution of Africa. Clarendon, Oxford, 512pp

Canil D. (1999) The Ni-in-garnet geothermometer: calibration at natural abundances. *Contributions to Mineralogy and Petrology* **136**, 240-246.

Canil, D. & Scarfe, C.M. (1990) Phase relations in peridotite + CO_2 systems to 12GPa: implications for the origin of kimberlite and carbonate stability in the Earth's upper mantle. *Journal of Geophysical Research* **95**, 15805–15816.

Carlson R.W., Pearson D.G., Boyd F.R., Shirey S.B., Irvine G., Menzies A.H. & Gurney J.J. (1999) Re-Os systematics of lithospheric peridotites: implication for lithospheric formation and preservation. In Proceedings 7th International Kimberlite Conference, Gurney J.J., Gurney J.L., Pascoe M.D., Richardson S.H. (Eds), Cape Town. Goodwood S. Africa, National Book Printer, p99-108.

Carlson, R.W., Araujo, A.L.N. & Junqueira-Brod, T.C. (2007) Chemical and isotopic relationships between peridotite xenoliths and mafic-ultrapotassic rocks from Southern Brazil. *Chemical Geology* **242**, 415-434

Castillo-Oliver, M., Galí, S., Melgarejo, J.C., Griffin, W. L., Belousova, E., Pearson, Watangua, M. & O'Reilly, S.Y. (2016) Trace-element geochemistry and U–Pb dating of perovskite in kimberlites of the Lunda Norte province (NE Angola): petrogenetic and tectonic implications. *Chemical Geology* **426**, 118-134

Chaffey, D.J., Cliff, R.A. & Wilson, B.M. (1989) Characterization of the St Helena magma source. *Journal of the Geological Society London* Special Publication **42**, 257–276.

Chakhmouradian, A.R. & Mitchell, R.H. (1999) Niobian ilmenite, hydroxylapatite and Sulfatian monazite: alternative hosts for incompatible elements in calcite kimberlite from Internatsional'naya, Yakutia. *Canadian Mineralogist* **37**, 1177-1189

Chakhmouradian, A.R., Reguir, E.P., Kamenetsky, V.S., Sharygin, V.V. & Golovin, A.V. (2013) Trace-element partitioning in perovskite: implications for the geochemistry of kimberlites and other mantle-derived undersaturated rocks. *Chemical Geology* **353**, 112–131.

Chalapathi Rao, N.V., Gibson, S.A., Pyle, D.M. & Dickin, A.P. (2004) Petrogenesis of Proterozoic lamproites and kimberlites from the Cuddapah Basin and Dharwar Craton, southern India. *Journal of Petrology* **45**, 907–948.

Clark, T. C. (1994) An integrated geochemical and isotopic study of the Prieska Province kimberlites from the Republic of South Africa. Unpublished Msc. Thesis, University of the Witwatersrand, 237pp.

Class, C. & le Roex, A.P. (2006) Continental material in the shallow oceanic mantle — how does it get there? *Geology* **34**, 129–132.

Class, C. & Le Roex, A.P. (2011) South Atlantic DUPAL anomaly: Dynamic and compositional evidence against a shallow origin. *Earth and Planetary Science Letters* **305**, 92-102.

Clement, C.R. & Skinner, E.M.W. (1979) A textural –genetic classification of kimberlitic rocks. Kimberlite Symposium II, Abstracts, 18-21.

Clement, C.R. (1982) A Comparative Geological Study of Some Major Kimberlite Pipes in the Northern Cape and Orange Free State. PhD Thesis University of Cape Town, Cape Town, 431 pp

Clement, C.R. and Skinner, E.M.W. (1985) A textural-genetic classification of kimberlites. *Transactions of the Geological society of south Africa* **88**, 403-409.

Coe, N. (2004) Petrogenesis of the Swartruggens and Star Group II kimberlite dyke swarms, South Africa. M.Sc. thesis, University of Cape Town, 146 pp.

Coe, N., le Roex, A., Gurney, J., Pearson, D.G. & Nowell, G. (2008) Petrogenesis of the Swartruggens and Star Group II kimberlite dyke swarms, South Africa: constraints from whole rock geochemistry. *Contributions to Mineralogy and Petrology* **156**, 627–652.

Coetzee M. (2004), Geochemistry of selected South African Group I, Group II and Transitional kimberlites located on and off the Kaapvaal Craton. Unpublished Msc thesis, University of Cape Town.

Collerson K.D., Hapugoda S., Kamber B.S. & Williams Q. (2000) Rocks from the mantle transition zone: majorite-bearing xenoliths from Malaita, Southwest Pacific. *Science*, **288** (5469), 1215-1223

Coltorti, M., Bonadiman, C., Hinton, R.W., Siena, F. & Upton, B.G.J. (1999) Carbonatite metasomatism of the oceanic upper mantle: evidence from clinopyroxenes and glasses in ultramafic xenoliths of Grande Comore, Indian Ocean. *Journal of Petrology* **40**, 133-165

Copeland, S.R., Sponheimer, M., le Roux, P.J., Grimes, V., Lee-Thorp, J.A., de Ruiter, D.J. & Richards M.P. (2008) Strontium isotope ratios (Sr-87/Sr-86) of tooth enamel: a comparison of solution and laser ablation multicollector inductively coupled plasma mass spectrometry methods. Rapid Communication Mass Spectrometry **22**, 3187–3194

Cordier, C., Sauzeat, L., Arndt, N.T., Boullier, A.-M.M., Batanova, V.G.V., Barou, F., (2015) Metasomatism of the lithospheric mantle immediately precedes kimberlite eruption: new evidence from olivine composition and microstructures. *Journal of* Petrology **56**, 1775–1796.

Coussaert, N. (2005) Evaluation du degré d'équilibre dans les péridotites mantéliques du Lesotho. PhD Thesis, ULB, Université de la Rochelle, 321 pp.

Coussaert, N., Grégoire, M., Mercier, J.C., Bell, D., Demaiffe, D., le Roex, A.P. & Andre, L. (2003) The origin of clinopyroxene in cratonic mantle. 8th IKC, FLA0383, 1-5.

Creaser, R.A., Grütter, H., Carlson, J., Crawford, B. (2004) Macrocrystal phlogopite Rb-Sr dates for the Ekati property kimberlites, Slave Province, Canada: evidence for multiple intrusive episodes in the Paleocene and Eocene. *Lithos* **76**, 399-414

Dasgupta, R., Hirschmann, M.M., McDonough, W.F., Spiegelman, M., Withers, A.C. (2009) Trace element partitioning between garnet lherzolite and carbonatite at 6.6 and 8.6 GPa with applications to the geochemistry of the mantle and of mantle-derived melts. *Chemical Geology* **262**, 57–77.

Dalton, J. A. & Presnall, C. (1998) The continuum of primary carbonatitic–kimberlitic melt compositions in equilibrium with lherzolite: data from the system $CaO–MgO–Al_2O_3–SiO_2–CO_2$ at 6 GPa. *Journal of Petrology* **39**, 1953–1964.

Danchin, R.V. (1979) Mineral and bulk chemistry of garnet lherzolite and garnet harzburgite xenoliths from the Premier Mine, South Africa. In: Boyd, F. R. & Meyer, H. O. A. (eds) The Mantle Sample: Inclusions in Kimberlites and Other Volcanics. Washington, DC: American Geophysical Union, p. 104-126.

Davies, G.R., Spriggs, A.J. & Nixon, P.H. (2001) A non-cognate origin for the Gibeon kimberlite megacryst suite, Namibia: Implications for the origin of Namibian kimberlites. *Journal of Petrology* **42**, 159–172

Davis, G.L., Krogh, T.E., & Erlank, A.J. (1976) The ages of zircon from kimberlites from South Africa: *Carnegie Institution of Washington Yearbook* **75**, 821–824.

Davis, G. L. (1977) The ages and uranium contents of zircons from kimberlites and associated rocks. *Carnegie Institution of Washington Yearbook* **76**, 631–635.

Dawson, J.B. (1980) Kimberlites and Their Xenoliths. Springer Verlag, New York. 252 pp.

Dawson, J.B. & Smith, J.V. (1977) The MARID (mica-amphibole-rutile-ilmenite-diopside) suite of xenoliths in kimberlite. *Geochimica et Cosmochimica Acta* **41**, 309-323.

De Boorder, H. (1982) Deep-reaching fracture zones in the crystalline basement surrounding the West Congo System and their control of mineralization in Angola and Gabon. *Geoexploration* **20**, 259-273.

de Bruin, D. (2005) Multiple compositional megacryst groups from the Uintjiesberg and Witberg kimberlites, South Africa. *South African Journal of Geology* **108**, 233–246.

Delhal, J. & Ledent, D. (1973) Résultats de quelques mésures d'âges radiométriques par la méthode Rb/Sr dans les pegmatites de la Haute Luanyi, région du Kasai (Zaïre). Rapport Annuel, Musée Royal de l'Afrique Centrale, Tervuren, Belgique, Département de Géologie et Minéralogie, p. 102–103.

Delhal, J., Ledent, D. & Torquato, J.R. (1976) Nouvelles données géochronologiques rélatives au complexe gabbronoritique et charnockitique du bouclier du Kasai et à son prolongement en Angola. *Annales Societé Géologique de Belgique* **99**, 211–226.

Delhal, J. (1991) Situation géochronologique 1990 du Precambrian du Sud-Kasai et de l'Ouest-Shaba. Rapport annuel du Musée Royal de l'Afrique centrale, Tervuren (Belgique), Département de Géologie et de Minéralogie, p. 119–125

Delpomdor, F., Blanpied, C., Virgone, A. & Préat A. (2015) Sedimentology and Sequence Stratigraphy of the 4 Late Precambrian Carbonates of the Mbuji-Mayi Supergroup in the Sankuru-Mbuji-Mayi-Lomami-Lovoy Basin (Democratic Republic of the Congo). In: de Wit, M., Guillocheau, F., de Wit, M. (eds) Geology and Resource Potential of the Congo Basin. Regional Geology Reviews. Springer, Berlin, Heidelberg p. 59-76.

Demaiffe D. & Fieremans M. (1981) Strontium isotopic geochemistry of the Mbuji-Mayi and Kundelungu kimberlites (Zaire, Central Africa). *Chemical Geology* **31**, 311-323.

Demaiffe, D., Fieremans, M. & Fieremans, C. (1991) The kimberlites of Central Africa: a review. In: Kampunzu, A., Lubala, T. (Eds.), Magmatism in Extensional Structural Setting: the Phanerozoic African Plate. Springer-Verlag, p. 537–559.

Demaiffe, D., El fadili, S. & Andre, L. (1999) Geochemical and isotopic (Sr, Nd) study of eclogite nodules from the Mbuji-Mayi kimberlite, kasai, Congo. Nature of the protoliths and evidence of for mantle metasomatism. In: Gurney JJ, Gurney JL, Pascoe MD, Richardson SH (eds) Proceedings of the 7th international kimberlite conference, National Book Printer, Cape Town. Goodwood, South Africa, p 190 - 192

de Stefano, A., Kopylova, M.G., Cartigny, P. & Afanasiev, V. (2009) Diamonds and eclogites of the Jericho kimberlite (Northern Canada). *Contributions to Mineralogy and Petrology* **158**, 295-315

de Wit, M.J., Roering, C., Hart, R.J., Armstrong, R.A., de Ronde, C.E.J., Green, R.W.E., Tredoux, M., Peberdy, E. & Hart, R.A. (1992) Formation of an Archean continent. *Nature* **357**, 553–562.

de Wit, M.J. (1998) On Archean granites, greenstones, cratons and tectonics: Does the evidence demand a verdict? *Precambrian Research* **91**, 181–224

de Wit, M.C.J. & Jelsma, H.A. (2015) A Review of the Kimberlites of the Democratic Republic of Congo. In: de Wit, M., Guillocheau, F., de Wit M. (eds) Geology and Resource Potential of the Congo Basin. Regional Geology Reviews. Springer, Berlin, Heidelberg p. 361-369.

de Wit, M.J. & Linol, B. (2015) Precambrian Basement of the Congo Basin and Flanking Terranes. In: De Wit, M., Guillocheau F, de Wit, M. (eds) The geology and resource potential of the Congo Basin. Springer, Heidelberg p. 19-37.

Dirks, P.H.G.M. & Jelsma, H.A. (2002) Crust-mantle decoupling and the growth of the Archaean Zimbabwe craton. *Journal of African Earth Sciences* **34**, 157–166

Donnelly, C.L., Griffin, W.L., O'Reilly, S.Y., Pearson, N.J. & Shee, S.R. (2011) The kimberlites and related rocks of the Kuruman Kimberlite Province, Kaapvaal Craton, South Africa. *Contributions to Mineralogy and Petrology* **161**, 351-371.

Donnelly, C.L., Griffin, W.L., Yang, J.-H., O'Reilly, S.Y., Li, Q.-L., Pearson, N.J. & Li, X.-H. (2012) In situ U-Pb dating and Sr-Nd isotopic analysis of perovskite: constraints on the age and petrogenesis of the Kuruman Kimberlite Province, Kaapvaal Craton, South Africa. *Journal of Petrology* **53**, 2497–2522.

Douglass, J., Schilling, J.-G. & Fontignie, D. (1999) Plume–ridge interactions of the discovery and Shona mantle plumes with the southern Mid-Atlantic Ridge (40°–55°S). *Journal of Geophysical Research* **104**, 2941–2962

Doyle, P.M., Bell, D.R. & le Roex, A.P. (2004) Fine-grained pyroxenites from the Gansfontein

kimberlite, South Africa: Evidence for megacryst magma - mantle interaction. *South African Journal of Geology* **107**, 285-300.

Dupré, B. & Allègre, C.J. (1983) Pb–Sr isotope variation in Indian Ocean basalts and mixing phenomena. *Nature* **303**, 142–146.

Edgar, A.D. & Charbonneau, H.E. (1993) Melting experiments on a SiO2-poor, CaO-rich aphanitic kimberlite from 5–10 GPa and their bearing on sources of kimberlite magmas. *American Mineralogist* **78**, 132–142.

Eggins, S. M., Woodhead, J. D., Kinsley, L.P.J., Mortimer, G. E., Sylvester, P. J., McCulloch, M. T., Hergt, J. M. & Handler, M. R. (1997) A simple method for the precise determination of forty trace elements in geological samples by ICPMS using enriched isotope internal standardisation. *Chemical Geology* **134**, 311–326.

Eggler, D.H. & Wendlandt, R.F. (1979) Experimental studies on the relationship between kimberlite magmas and partial melting of peridotite. In: Boyd, F. R. & Meyer, H. O. A. (eds) Kimberlites, Diatremes and Diamonds; their Geology, Petrology and Geochemistry. Washington, DC: American Geophysical Union, p. 330–338.

Eggler, D.H., Mc Callum, M.E. & Smith, C.B. (1979) Megacryst assemblage in kimberlite from Northern Colorado and Southern Wyoming: petrology, geothermometry – barometry and a real distribution. *Proceedings of the 2nd IKC* **2**, 213–226

Eglington, B.M. (2006) Evolution of the Namaqua-Natal Belt, southern Africa—A geochronological and isotope geochemical review. *Journal of African Earth Sciences* **46**, 93–111

Egorov, K.N., Roman, E.F., Podvysotsky, V.T., Sablukov, S.M., Garanin, V.K. & D'yakonov, D.B. (2007) New data on kimberlite magmatism in southwestern Angola. *Russian Geology and Geophysics* **48**, 323–336.

Eley, R., Grütter, H., Louw, A., Tunguno, C. & Twidale, J. (2008) Exploration geology of the Luxinga kimberlite cluster (Angola) with evidence supporting the presence of kimberlite lava. 9th International Kimberlite Conference, Extended Abstract, p. 1–3

El Fadili S. & Demaiffe D. (1999) Petrology of eclogite and granulite nodules from Mbuji- Mayi kimberlites (Kasai, Congo): Significance of kyanite-omphacite intergrowths. In Proceedings 7th International Kimberlite Conference, Gurney J.J., Gurney J.L., Pascoe M.D., Richardson S.H. (Eds), Cape Town. Goodwood S. Africa, National Book Printer, p. 205-213.

Ene, V.V. (2014) Major and trace element geochemistry of ilmenite suites from the Kimberley diamond mines, South Africa. Unpublished Msc Thesis, University of Toronto.

Erlank, A.J., Waters, F.G., Hawkesworth, C.J., Haggerty, S.E., Allsopp, H.L., Rickard, R.S. & Menzies, M.A. (1987) Evidence for mantle metasomatism in peridotite nodules from the Kim- berley pipes, South Africa. In: Menzies, M.A., Hawkesworth, C.J. (Eds.), Mantle Metasomatism. Academic Press, London, p. 221 – 311.

Escrig, S., Schiano, P., Schilling, J.G. & Allègre, C.J. (2005) Rhenium–osmium isotope systematics in MORB from the Southern Mid-Atlantic Ridge (40 degrees–50 degrees S). *Earth Planetary Science Letters* **235**, 528–548.

Evensen, N.M., Hamilton, P.J. & O'Nions, R.K. (1978) Rare-earth abundances in chondritic meteorites. *Geochimica et Cosmochimica Acta* **42** (8), 1199–1212.

Faure, S. (2006) World kimberlites database, Version 2006- 2: Consortium de Recherche en Exploration Minérale CONSOREM, (www.consorem.ca), Université du Québec à Montréal.

Fesq, H.W., Kable, E.D.J. & Gurney, J.J. (1975) Aspects of the geochemistry of kimberlites from the Premier Mine, and other selected South African occurences with particular reference to the rare earth elements. *Physics and chemistry of the Earth* **9**, 686-707.

Field, M., Stiefenhofer, J., Robey, J. & Kurszlaukis, S. (2008) Kimberlite-hosted diamond deposits of southern Africa: a review. *Ore Geology Reviews* **34**, 33–75

Fieremans, C. (1977) Mode of occurrence and tectonic control of the kimberlite bodies in East Kasai (Zaire). 2nd International Kimberlite Conference, Santa Fe (abstract).

Finnerty, A.A. & Boyd, F.R. (1987) Thermobarometry for garnet peridotite xenoliths: A basis for mantle

stratigraphy, *in* Nixon, P.H., ed., Mantle xenoliths: Chichester, UK, Wiley, p. 381–402.
Fitzpayne, A., Giuliani, A., Hergt, J., Philips, D., Janney, P. (2018) New geochemical constraints on the origins of MARID and PIC rocks: Implications for mantle metasomatism and mantle –derived potassic magmatism. *Lithos* **318**, 478 – 493.
Foley, S.F., Petibon, C.M., Jenner, G.A. & Kjarsgaard, B.A. (2001) High U/Th partitioning by clinopyroxene from alkali silicate and carbonatite metasomatism: an origin for Th/U disequilibrium in mantle melts? *Terra Nova* **13**, 104–109.
Fraser, K.J. & Hawkesworth, C.J. (1992) The petrogenesis of group 2 ultrapotassic kimberlite from Finsch mine, South Africa. *Lithos* **28**, 327–345
Frost, B.R. & Beard, J.S. (2007) On silica activity and serpentinization. *Journal of Petrology* **48**, 1351–1368
Gaffney, A.M., Blichert-Toft, J., Nelson, B.K., Bizzarro, M., Rosing, M. & Albarede, F. (2007) Constraints on source-forming processes of West Greenland kimberlites inferred from Hf-Nd isotope systematics. *Geochimica et Cosmochimica Acta* **71**, 2820–2836.
Galer S.J.G. & Abouchami, W. (1998) Practical application of lead triple spiking for correction of instrumental mass discrimination. *Mineralogical Magazine* **62**A, 491–492.
Garnero, E. J. & McNamara, A. K. (2008) Structure and dynamics of Earth's lower mantle. *Science* **320**, 626–628.
Gibson, S.A., Thompson, R.N., Day, J.A., Humphris, S.E. & Dickin, A.P. (2005) Melt generation processes associated with the Tristan mantle plume: constraints on the origin of EM-1. *Earth and Planetary Science Letters* **237**, 744–767.
Giuliani, A., Phillips, D., Woodhead, J.D., Kamenetsky, V.S., Fiorentini, M.L., Maas, R., Soltys, A. & Armstrong, R.A. (2015) Did diamond-bearing orangeites originate from MARID- veined peridotites in the lithospheric mantle? *Nature Communications* **6**, 6837.
Giuliani, A., Campeny, M., Kamenetsky, VS., Afonso, JC., Maas, R., Melgarejo, JC., Kohn, BP., Matchan, EL., Mangas, J., Goncalves, AO. & Manuel, J. (2017) Southwestern Africa on the burner: Pleistocene carbonatite volcanism linked to deep mantle upwelling in Angola. *Geology* **45** (11), 971-974.
Glaser, S.M., Foley, S.F. & Günther, D. (1999) Trace element compositions of minerals in garnet and spinel peridotite xenoliths from the Vitim volcanic field, Transbaikalia, eastern Siberia. *Lithos* **48**, 263–285.
Gore, D.E., James, T.G. Zengeni, et al. (2009) Crustal structure of the Zimbabwe Craton and the Limpopo Belt of southern Africa: new constraints from seismic data and implications for its evolution. *South African Journal of Geology* **112**, 213-228
Granot R. & Dyment J. (2015) The Cretaceous opening of the South Atlantic Ocean. *Earth Planetary Sciences Letters* **414**, 156-163
Grégoire, M., Bell, D.R. & le Roex, A.P. (2002) Trace element geochemistry of phlogopite-rich mafic mantle xenoliths: their classification and their relationship to phlogopite-bearing peridotites and kimberlites revisited. *Contributions to Mineralogy and Petrology* **142**, 603-625.
Green, T., Blundy, J., Adam, J. & Yaxley, G. (2000) SIMS determination of trace element partition coefficients between garnet, clinopyroxene and hydrous basaltic liquids at 2–7.5 Gpa and 1080–1200 °C. *Lithos* **53**, 165-187
Grégoire, M., Bell, D.R. & Le Roex, A.P. (2003) Garnet lherzolites from the Kaapvaal craton (South Africa): trace element evidence for a metasomatic history. *Journal of Petrology* **44**, 629–657.
Grégoire, M., Tinguely, C., Bell, D.R. & le Roex, A.P. (2005) Spinel lherzolite xenoliths from the Premier kimberlite (Kaapvaal craton, South Africa): Nature and evolution of the shallow upper mantle beneath the Bushveld complex. *Lithos* **84**, 185-205.
Griffin, W.L., Smith, D., Boyd, F.R., Cousens, D.R., Ryan, C.G., Sie, S.H. & Suter, G.F. (1989) Trace element zoning in garnets from sheared mantle xenoliths. *Geochimica et Cosmochimica Acta* **53**, 561–567
Griffin, W.L. & Ryan, C.G. (1995) Trace elements in indicator minerals: Area selection and target

evaluation in diamond exploration. *Journal of Geochemical Exploration* **53**, 311–337
Griffin, W.L., Moore, R.O., Ryan, C.G., Gurney, J.J. & Win, T.T. (1997) Geochemistry of magnesian ilmenite megacrysts from southern African kimberlites. *Russian Geology and Geophysics* **38**, 421–443
Griffin, W.L., O'Reilly, S.Y., Ryan, C.G., Gaul, O. & Ionov, D. (1998) Secular variation in the composition of subcontinental lithospheric mantle. In: Braun, J., Dooley, J.C., Goleby, B.R., van der Hilst, R.D., Klootwijk, C.T. (Eds.), Structure and Evolution of the Australian Continent, Geodynamics, vol. 26. American Geopyhysical Union, Washington, DC, pp. 1–26.
Griffin, W.L., Fisher, N.I., Friedman, J., Ryan, C.G. & O'Reilly, S.Y. (1999) Cr-pyrope garnets in the lithospheric mantle. I. Compositional systematics and relations to tectonic settings. *Journal of Petrology* **40**, 679–704
Griffin, W.L., Fisher, N.I., Friedman, J., O'Reilly, S.Y. & Ryan, C.G. (2002) Cr-pyrope garnets in the lithospheric mantle: II. Compositional populations and their distribution in time and space. *Geochemistry, Geophysics and Geosystems* **3** (1073), 12 – 47.
Griffin, W. L., O'Reilly, S. Y., Natapov L. M. & Ryan C. G. (2003) The evolution of lithospheric mantle beneath the Kalahari Craton and its margins. *Lithos* **71**, 215–241
Griffin, W.L., O'Reilly S.Y., Doyle, B.J., Pearson N.J., Coopersmith, H., Kivi, K., Malkovets, V. & Pokhilenko, N. (2004) Lithosphere mapping beneath the North American plate. *Lithos* **77**, 873-922.
Griffin, W.L., Powell, W.J., Pearson, N., O'Reilly, S.Y., (2008) GLITTER: data reduction software for laser ablation ICP-MS. In: Sylvester, P. (Ed.), Laser Ablation–ICP–MS in the Earth Sciences. Mineralogical Association of Canada Short Course Series, p. 204–207.
Griffin, W.L., O'Reilly S.Y. Afonso J.C., Begg G.C. (2009) The composition and evolution of lithospheric mantle: a re-evaluation and its tectonic implications. *Journal of Petrology* **50**, 1185-1204.
Griffin, W.L., Batumike, J.M., Greau, Y., Pearson, N.J., Shee, S.R. & O'Reilly, S.Y. (2014) Emplacement ages and sources of kimberlites and related rocks in southern Africa: U– Pb ages and Sr–Nd isotopes of groundmass perovskite. *Contributions to Mineralogy and Petrology* **168**, 1032
Grütter, H., Gurney, J.J., Menzies, A.H. & Winter, F. (2004) An updated classification scheme for mantle-derived garnet, for use by diamond explorers. *Lithos* **77**, 841–857.
Gurney, J.J., Jakob, W.R.O. & Dawson, J.B. (1979) Megacrysts from the Monastery kimberlite pipe South Africa. In Proceedings of the 2nd International Kimberlite Conference, Boyd F.R. and Meyer H.O.A. (Eds), AGU, 227-243.
Gurney, J. J. (1990) The diamondiferous roots of our wandering continent. *South African Journal of Geology* **93**, 424-437.
Gurney, J.J., Helmstaedt, H. & Moore, R.O. (1993) A review of the use and application of mantle mineral geochemistry in diamond exploration. *Pure and Applied Chemistry* **65**, 2423–2442.
Gurney, J.J. & Zweistra, P. (1995) The interpretation of the major element compositions of mantle minerals in diamond exploration. *Journal of Geochemical Exploration* **53**, 293–310
Guarino, V., Wu, F-Y., Lustrino, M., Melluso, L., Brotzu, P., Gomes, C. dB., Ruberti, E., Tassinari, C. C. G. & Svisero, D. P. (2013) U-Pb ages, Sr–Nd- isotope geochemistry, and petrogenesis of kimberlites, kamafugites and phlogopite-picrites of the Alto Paranaíba Igne-ous Province, Brazil. *Chemical Geology* **353**, 65–82
Haggerty, S. E. (1994) Superkimberlites: a geodynamic diamond window to the Earth's core. *Earth and Planetary Science Letters* **122**, 57–69.
Harris, C., le Roux, P., Cochrane, R., Martin, L., Duncan, A.R., Marsh, J.S., le Roex, A.P. & Class, C. (2015) The oxygen isotope composition of Karoo and Etendeka picrites: High δ18O mantle or crustal contamination? *Contributions to Mineralogy and Petrology* **170**, 1-24
Harris, M., le Roex, A.P. & Class, C. (2004) Geochemistry of the Uintjiesberg kimberlite, South Africa: petrogenesis of an off-craton, group I, kimberlite. *Lithos* **74**, 149–165.

Hart, S. R. (1984) A large scale isotope anomaly in the southern hemisphere mantle. *Nature* **309**, 753–757.
Hartnady, C.J.H. & le Roex, A.P. (1985) Southern Ocean hotspot tracks and the Cenozoic absolute motion of the African, Antarctic and South American plates. *Earth and Planetary Science Letters* **75**, 245–257.
Harte, B. & Gurney, J.J. (1981) The mode of formation of chromium-poor megacryst suites from kimberlites. *Journal of Geology* **89**, 749–753.
Harte, B. (1983) Mantle peridotite and processes – the kimberlite sample. In: Hawkesworth, C.J., Norry, M.J. (eds) Continental basalts and mantle xenoliths. Shiva Publishing, England, p. 46–91
Hatton, C.J. (1998) The kimberlite-megacryst link at Monastery mine. *Extended abstracts 7th international kimberlite conference*, Cape Town p. 314–316
Hauri, E. H., Wagner, T. P. & Grove, T. L. (1994). Experimental and natural partitioning of Th, U, Pb and other trace elements between garnet, clinopyroxene and basaltic melts. *Chemical Geology* **117**, 149-166.
Hawkesworth, C. J., Mantovani, M. S. M., Taylor, P. N. & Palacz, Z. (1986) Evidence from Parana of south Brazil for a continental contribution to Dupal basalts. *Nature* **322**, 356–359.
Heaman, L.M. (1989) The nature of the subcontinental mantle from Sr, Nd and Pb isotopic studies on kimberlitic perovskite. *Earth Planetary Sciences Letters* **92**, 323–334.
Heaman, L. M., Creaser, R. A. & Cookenboo, H. O. (2006) Multi-stage modification of the northern Slave mantle lithosphere: Evidence from zircon- and diamond-bearing eclogite xenoliths entrained in Jericho kimberlite, Canada. *Journal of Petrology* 47, 821-858
Henning, A., Kiviets, G., Kurzlaukis, S., Barton, E. & Mayaga-Mikolo, F. (2003) Early Proterozoic metamorphosed kimberlites from Gabon. In: Long Abstract, 8th International Kimberlite conference, Victoria, Canada.
Hildebrand, P.H., 1993. The diamond potential of Zimbabwe: historical, geotectonic and kimberlite heavy mineral considerations. B.Sc. (Hons.) Thesis, University of Cape Town, South Africa (unpublished), 65 pp plus appendices.
Hill, S.J. (1989) A study of the diamonds and xenoliths from the Star kimberlite, Orange Free State, South Africa, MSc Thesis, University of Cape Town.
Hoal, K.E.O., Hoal, B.G., Erlank, A.J. & Shimizu N. (1994) Metasomatism of the mantle lithosphere recorded by rare earth elements in garnets. *Earth and Planetary Science Letters* **126**, 303-313.
Hops, J.J., Gurney, J.J. & Harte, B. (1992) The Jagersfontein Cr-poor megacryst suite – towards a model for megacryst paragenesis. *Journal of Volcanology and Geothermal Research* **50**, 143–160
Horstwood, M.S.A., Nesbitt, R.W., Noble, S.R. and Wilson, J.F. (1999). U-Pb zircon for an extensive early Archaean craton in Zimbabwe: a reassessment of the timing of craton formation, stabilisation and growth. Geology, 27, 707–710.
Howarth G.H. (2018) Olivine megacryst chemistry, monastery kimberlite: constraints on the mineralogy of the HIMU mantle reservoir in southern Africa. *Lithos* **314 – 315**, 658 – 668.
Howarth, G.H., Taylor, L.A., (2016) Multi-stage kimberlite evolution tracked in zoned olivine from the Benfontein sill, South Africa. *Lithos* **262**, 384–397
Hunter, R.H. & Taylor, L.A. (1984) Magma-mixing in the low velocity zone: kimberlitic megacrysts from Fayette County, Pennsylvania. *American Mineralogist* **69**, 16–29.
Ionov, D.A., Chanefo, I. & Bodinier, J.-L. (2005) Origin of Fe-rich lherzolites and wehrlites from Tok, SE Siberia by reactive melt percolation in refractory mantle peridotites. *Contributions to Mineralogy and Petrology* **150**, 335–353.
Ionov, D.A., Chazot, G., Chauvel, C., Merlet, C., Bodinier, J.-L. (2006) Trace element distribution in peridotite xenoliths from Tok, SE Siberian craton: a record of pervasive, multi-stage metasomatism in shallow refractory mantle. *Geochimica et Cosmochimica Acta* **70**, 1231–1260.
Irving, A. J. & Frey, F. A. (1984) Trace element abundances in megacrysts and their host basalts: constraints on partition coefficients and megacryst genesis. *Geochimica et Cosmochimica Acta* **47**, 1201–1221.

Jakob, W.R.O. (1977) Geochemical aspects of the megacryst suite from the Monastery kimberlite pipe. MSc thesis, (unpublished), University Cape Town, pp. 81

Janney, P.E., le Roex, A.P. & Carlson, R.L. (2005) Hafnium isotope and trace element constraints on the nature of mantle heterogeneity beneath the Central Southwest Indian Ridge. *Journal of Petrology* **46**, 2427-2464

Janney, P.E., Shirey, S.B., Carlson, R.W., Pearson, D.G., Bell, D.R., le Roex, A.P., Ishikawa, A., Nixon, P.H. & Boyd, F.R. (2010) Age, composition and thermal characteristics of South African off-craton mantle lithosphere: Evidence for a multi-stage history. *Journal of Petrology* **51**, 1849–1890.

Janney, P.E. & Bell, D.R. (2014) Constraints on lithospheric assimilation by sublithospheric melts in the generation of southern African kimberlite megacrysts: a comparison of on- and off-craton megacryst suites. Conference paper, IMA

Janney, P.E. & Bell, D.R. (2017) Hidden reservoirs in the continental lithosphere? Evidence from Hf-Sr-Nd-Pb isotopes in southern African kimberlite megacrysts. 11th International Kimberlite Conference Extended Abstract No. 11IKC-4630

Jelsma, H.A., Vinyu, M.L., Valbracht, P.J., Davies, G.R., Wijbrans, J.R. & Verdurmen, E.A.T. (1996) Constraints on Archaean crustal evolution of the Zimbabwe craton: a U–Pb zircon, Sm–Nd and Pb–Pb whole-rock isotope study. *Contributions to Mineralogy and Petrology* **124**, 55–70

Jelsma, H.A., de Wit, M.J., Thiart, C., Dirks, P.H.G.M., Viola, G., Basson, I.J. & Anckar, E. (2004) Preferential distribution along transcontinental corridors of kimberlites and related rocks of Southern Africa. *South African Journal of Geology* **107**, 301-324

Jelsma, H., Barnett, W., Richards, S. & Lister, G. (2009) Tectonic setting of kimberlites. *Lithos*, **112**S, 55-165

Jelsma, H., Krishnan, U., Perritt, S., Preston, R., Winter, F., Lemotlo, L., van der Linde, G., Armstrong, R., Phillips, D., Joy, S., Costa, J., Facatino, M., Posser, A., Kumar, M., Wallace, C., Chinn, I. & Henning, A. (2013) Kimberlites from central Angola: a case study of exploration findings. In: Proceedings of the 10th International Kimberlite Conference.

Jelsma, H.A., Perritt, S.H., Joy, S. & Armstrong, R.A. (2016) Basement architecture of the central African Kasai craton revealed using high precision SHRIMP II U-Pb zircon geochronology. 35th International Geological Congress, Cape Town, abstract No 1835

Jones, R.A. (1987) Strontium and Neodymium isotope and rare earth element evidence for the genesis of megacrysts in kimberlites of southern Africa. In: Nixon PH (ed) Mantle Xenoliths. Wiley, NewYork, p 711–724

Kable, E.J.D., Fesq, H.W. & Gurney, J.J. (1975) The significance of the inter-element relationships of some minor and trace elements in South African kimberlites. *Physics and Chemistry of the Earth* **9**, 709-734.

Kamenetsky, V.S., Golovin, A.V., Maas, R., Giuliani, A., Kamenetsky, M.B. & Weiss Y. (2014) Towards a new model for kimberlite petrogenesis: evidence from unaltered kimberlites and mantle minerals. *Earth-Science Reviews* **139**, 145–167

Kamenetsky, V.S. & Yaxley, G.M. (2015) Carbonate-silicate liquid immiscibility in the mantle propels kimberlite magma ascent. *Geochimica et Cosmochimica Acta* **158**, 48–56.

Kampata, M.D. (1993) Minéralogie et géochimie des kimberlites du Haut Plateau de Kundelungu (Shaba, Zaïre). unpublished Doctorate Thesis, Catholic University of Louvain, Belgium, 248 pp.

Kampata M.D., Demaiffe D., Hertogen J., Moreau J., Nixon P.H. 1996. Composition chimique et isotopique des mégacristaux et des diamants des kimberlites du Kundelungu (Zaïre). *Annales de la Societe Géologique de Belgique* **119**, 55-70.

Kargin AV, Sazonova LV, Nosova AA, et al (2017) Cr-rich clinopyroxene megacrysts from the Grib kimberlite, Arkhangelsk province, Russia: Relation to clinopyroxene– phlogopite xenoliths and evidence for mantle metasomatism by kimberlite melts. *Lithos* **292 – 293**, 34 – 48.

Keshav, S., Corgne, A., Gudfinnsson, G.H., Bizimis, M., McDonough, W.F. & Fei, Y. (2005) Kimberlite petrogenesis: insights from clinopyroxene-melt partitioning experiments at 6 GPa in the CaO-MgO-Al_2O_3-SiO_2-CO_2 system. *Geochimica et Cosmochimica Acta* **69**, 2829–2845

Kjarsgaard, B.A., Pearson, D.G., Tappe, S., Nowell, G.M. & Dowall, D.P. (2009) Geochemistry of hypabyssal kimberlites from Lac de Gras, Canada: comparisons to a global database and applications to the parent magma problem. *Lithos* **112**, 236–248.

Kobussen, A. F., Griffin, W. L., O'Reilly, S. Y. & Shee, S. R. (2008). Ghosts of lithospheres past: imaging an evolving lithospheric mantle in southern Africa. *Geology* **36**, 515-518.

Kobussen A.F., Griffin W.L. & O'Reilly S.Y. (2009) Cretaceous thermo-chemical modification of the Kaapvaal cratonic lithosphere, South Africa. *Lithos* **112**S, 886-895.

Konzett, J., Armstrong, R.A. & Gunther, D. (2000) Modal metasomatism in the Kaapvaal craton lithosphere: constraints on timing and genesis from U–Pb zircon dating of metasomatised peridotites and MARID-type xenoliths. *Contributions to Mineralogy and Petrology* **139**, 704–719

Kopylova, M.G., Russell, J.K. & Cookenboo, H. (1999) Petrology of peridotite and pyroxenite xenoliths from the Jericho kimberlite: implications for the thermal state of the mantle beneath the Slave Craton, Northern Canada. *Journal of Petrology* **40**, 79–104

Kopylova, M.G., Matveev, S. & Raudsepp, M. (2007) Searching for parental kimberlite melt. *Geochimica et Cosmochimica Acta* **71**, 3616–3629.

Kopylova, M.G., Nowell, G.M., Pearson, D.G. & Markovic, G. (2009) Crystallization of megacrysts from proto- kimberlitic fluids: Geochemical evidence from high-Cr megacrysts in the Jericho kimberlite. Proceedings of the 9th International Kimberlite Conference. *Lithos* **112S**, 284–295.

Kramers, J.D. (1979) Pb, U, Sr, K and Rb in inclusions bearing diamonds and mantle derived xenoliths from R.S.A. *Earth and Planetary Science Letters* **42**, 58-70.

Kramers, J.D., Smith, C.B., Lock, N.P., Harmon, R.S. & Boyd, F.R. (1981) Can kimberlite be generated from ordinary mantle? *Nature* **291**, 53–56

Kramers, J.D. & Smith, C. B. (1983) A feasibility study of U−Pb and Pb−Pb dating of kimberlites using groundmass mineral fractions and whole-rock samples. *Chemical Geology* **41**, 23–38.

Kröner, A., & Tegtmeyer, A., 1994, Gneiss-greenstone relationships in the Archean Gneiss Complex of south-west- ern Swaziland, southern Africa and implications for early crustal evolution. *Precambrian Research* **67**, 109 – 139

La Tourette, T., Hervig, R.L. & Holloway, J.R. (1995) Trace element partitioning between amphibole, phlogopite and basanite melt. *Earth and Planetary Science Letters* **135**, 13-30.

Lazarov, M., Brey, G.B. & Weyer, S. (2009) Time steps of depletion and enrichment in the Kaapvaal craton as recorded by subcalcic garnets from Finsch (SA). *Earth Planetary Sciences Letters* **27**, 1-10

Le Maitre, R.W. (Ed.) Streckheisen, A., Zanettin, B., Le Bas, M.J., Bonin, B., Bateman, P., Bellieni, G., Dudek, A., Etremova, S., Keller, J., Lameyer, J., Sabine, P.A., Schmid, R., Sørensen, H., Wooley, A.R. (2002). Igneous Rocks: A classification and glossary of terms. Recommendations of the International Union of the Geological Sciences Subcomission on the Systematics of the igneous rocks, Cambridge University Press, Cambridge, 236pp.

le Roex, A.P., Cliff, R.A. & Adair, B.J.I. (1990) Tristan da Cunha, South Atlantic: geochemistry and petrogenesis of a basanite–phonolite lava series. *Journal of Petrology* **31**, 779–812.

le Roex, A.P., Bell, D.R. & Davis, P. (2003) Petrogenesis of group I kimberlites from Kimberley, South Africa: evidence from bulk-rock geochemistry. *Journal of Petrology* **44**, 2261–2286.

le Roux, P. J., le Roex, A. P., Schilling, J. G., Shimizu, N., Perkins, W. W. & Pearce, N. J. G. (2002). Mantle heterogeneity beneath the southern Mid-Atlantic Ridge: trace element evidence for contamination of ambient asthenospheric mantle. *Earth and PlanetaryScience Letters* **203**, 479–498

Ludwig, K.R. (2003) Isoplot/Ex version 4.0: a geochemical toolkit for Microsoft Excel. *Berkeley Geochronological Center* Special Publication **4**, 1–70.

Marsh, J. (1973) Relationships between transform directions and alkaline igneous rock lineaments in Africa and South America. *Earth and Planetary Science Letters* **18**, 317–323.

McCourt, S., Armstrong, R.A., Jelsma, H. & Mapeo, R.B.M. (2013) New U−Pb SHRIMP ages from the Lubango region, SW Angola: insights into the Palaeoproterozoic evolution of the Angolan Shield, southern Congo Craton, Africa. *Journal of the Geological Society* **170**, 353 – 363.

McDonough, W.F. & Sun, S.-s. (1995) The composition of the Earth. *Chemical Geology* **120**, 223–253.

Merry M. & le Roex A.P. (2007) Megacryst suites from the Lekkerfontein and Uintjiesberg kimberlites, southern Africa: evidence for a non-cognate origin. *South African Journal of Geology* **110**, 597-610

Meyer, H.O.A and McCallister, R.H. (1984) Two pyroxene megacrysts from South African kimberlites. *Develop Petrol* **11B**, 133-144.

Milner, S.C. & le Roex, A.P. (1996) Isotope characteristics of the Okenyenya igneous complex, northwestern Namibia; constraints on the composition of the early Tristan Plume and the origin of the EM 1 mantle component. *Earth Planetary Science Letters* **141**, 277–291.

Mitchell, R.H. (1986) Kimberlites: Mineralogy, Geochemistry and Petrology. Plenum Press, New York. 442 pp.

Mitchell, R.H. (1987) Megacrysts in kimberlites from the Gibeon field, Namibia. *Neues Jahrbuch Mineral Abh* 157, 267–283

Mitchell, R.H. (1995) Kimberlites, Orangeites, and Related Rocks. Plenum Press, New York. 409 pp.

Mitchell, R.H. & Bergman, S.C. (1991) Petrology of lamproites. Plenum Press, New York. 447 pp.

Mitchell, R. H. (2004). Experimental studies at 5–12 GPa of the Ondermatjie hypabyssal kimberlite. *Lithos* **76**, 551–564.

Mitchell, R.H. (2008) Petrology of hypabyssal kimberlites: relevance to primary magma compositions. *Journal of Volcanology and Geothermal Research* **174**, 1–8.

Mitchell, R.H. (2013) Paragenesis and oxygen isotopic studies of serpentine in kimberlite. In: Pearson DG et al (eds) Proceedings of the 10th kimberlite conference, vol 1, special issue of J Geol Soc India, p 1–12

Moore, R.O. (1986). A study of the kimberlites, diamonds and associated rocks and minerlas from the Monastery Mine, South Africa. Unpublished PhD thesis, University of Cape Town, South Africa, 354pp.

Moore, A.E. (1987) A model for the origin of ilmenite in kimberlite and diamond: Implications for the genesis of the discrete nodule (megacryst) suite. *Contributions to Mineralogy and Petrology* **95**, 245–253.

Moore, A.E. & Lock, N.P. (2001) The origin of mantle-derived megacrysts and sheared peridotites – evidence from kimberlites in the northern Lesotho – Orange Free State (South Africa) and Botswana pipe clusters. *South African Journal of Geology* **104**, 23–38.

Moore, A.E. (2012) The case for a cognate, polybaric origin for kimberlitic olivines. *Lithos* **128-131**, 1–10.

Moore, A. & Belousova, E. (2005) Crystallization of Cr-poor and Cr-rich megacryst suites from the host kimberlite magma: implications for mantle structure and the generation of kimberlite magmas. *Contributions to Mineralogy and Petrology* **149**, 462–481.

Moore, A., Blenkinsop, T. & Cotterill, F. (2008) Controls on post-Gondwana alkaline volcanism in Southern Africa. *Earth and Planetary Science Letters* **268**, 151-164

Moore, A.E. & Costin, G. (2016) Kimberlitic olivines derived from the Cr-poor and Cr-rich megacryst suites. *Lithos* **258**, 215-227.

Moore, R.O., Griffin, W. L., Gurney, J. J., Ryan, C. G., Cousens, D. R., Sie, S. H. & Suter, G. F. (1992) Trace element geochemistry of ilmenite megacrysts from the monastery kimberlite, South Africa, *Lithos* **29**, 1

Mvuemba, N.F. (1980) Minéralogie des mégacristaux, des xénolites éclogitiques et granulitiques et des inclusions minérales dans les diamants provenant de la kimberlite du Kasaï Oriental (Zaïre).

Departement de Minéralogie et Géologie, Université Catholique de Louvain. Unpublished PhD Thesis.

Navon, O. & Stolper, E. (1987) Geochemical consequences of melt percolation: the upper mantle as a chromatographic column. *Journal of Geology* **95**, 285–307.

Neal, C. R., Taylor, L. A., Davidson, J. P., Holden, P., Halliday, A. N., Nixon, P. H., Paces, J. B., Clayton, R. N. & Mayeda, T. K. (1990) Eclogites with oceanic crustal and mantle signatures from the Bellsbank kimberlite, South Africa. 2. Sr, Nd, and O isotope geochemistry. *Earth Planetary Sciences Letters* **99**, 362–379.

Nimis, P. (1998) Evaluation of diamond potential from the composition of peridotitic chromian diopside. *European Journal of Mineralogy* **10**, 505 – 519

Nimis, P. & Taylor, W.R. (2000) Single clinopyroxene thermobarometry for garnet peridotites. Part I. Calibration and testing of a Cr-in-Cpx barometer and an enstatite-in-Cpx thermometer. *Contributions of Mineralogy and Petrology* **139**, 541–554.

Nimis, P., Zanetti, A., Dencker, I. & Sobolev, N.V. (2009) Major and trace element composition of chromian diopsides from the Zagadochnaya kimberlite (Yakutia, Russia): Metasomatic processes, thermobarometry and diamond potential. *Lithos* **112**, 397 – 412.

Nixon, P.H., Boyd, F.R. (1973b) The discrete nodule (megacryst) association in kimberlites from Northern Lesotho. In: Nixon, P.H. (Ed.), Lesotho Kimberlites. Lesotho National Development Corporation, Maseru, p. 67–76.

Nkere, J.B. & Janney, P.E. (2017) Geochemistry of peridotitic clinopyroxene from the diamondiferous Mbuji-Mayi and Tshibwe kimberlites (DRC): Insight into the compositional and thermal State of the SCLM beneath the northeastern Kasai Craton. 11th International Kimberlite Conference Extended Abstract No. 11IKC-4570, Gaborone.

Norman, M.D. (1998) Melting and metasomatism in the continental lithosphere: laser ablation ICPMS analysis of minerals in spinel lherzolites from Eastern Australia. *Contributions to Mineralogy and Petrology* **130**, 240 – 255.

Nowell, G.M., Pearson, D.G., Bell, D.R., Carlson, R.W., Smith, C.B., Kempton, P.D. & Noble, S.R. (2004) Hf isotope systematics of kimberlites and their megacrysts: new constraints on their source regions. *Journal of Petrology* **45**, 1583–1612

Oberthür, T., Davis, D.W., Blenkinsop, T.G. & Höhndorf, A. (2002) Precise U-Pb mineral ages, Rb-Sr and Sm-Nd systematics for the Great Dike, Zimbabwe: constraints on late Archean events in the Zimbabwe craton and Limpopo belt. *Precambrian Research* **113**, 293-305

O'Reilly, S.Y. & Griffin, W.L. (1996) 4D lithosphere mapping: Methodology and examples. *Tectonophysics* **262**, 3–18

O'Reilly, S.Y. & Griffin, W.L. (2006) Imaging global chemical and thermal heterogeneity in the subcontinental lithospheric mantle with garnets and xenoliths: Geophysical implications. *Tectonophysics* **416**, 289–309

Paton, C., Hergt, J.M., Woodhead, J.D., Phillips, D. & Shee, S.R. (2009) Identifying the asthenospheric component of kimberlite magmas from the Dharwar Craton, India. *Lithos* **112**S, 296–310.

Patterson, M., Francis, D. & McCandless, T. (2009) Kimberlites: magmas or mixtures? *Lithos* **112**S, 191–200.

Pearson, D.G., Canil, D., Shirey, S.B. & Carlson, R.W. (2003) Mantle samples included in volcanic rocks: xenoliths and diamonds, Treatise on Geochemistry. Vol. 2. The Mantle and Core, Amsterdam Elsevier (p. 171 – 276)

Peate, D.W., Hawkesworth, C.J., Mantovani, M.S.M., Rogers, N.W. & Turner, S.P. (1999) Petrogenesis and stratigraphy of the High-Ti/Y Urubici magma type in the Paraná Flood Basalt Province and implications for the nature of the 'Dupal'-type mantle in the South Atlantic Region. *Journal of Petrology* **40**, 451–473.

Perritt, S., Preston, R., Viljoen, F., Van der linde, G., (2015) Morphology, micro-structure and chemistry of a deformed garnet megacryst suite from Monteleo kimberlite, Free state province, South Africa. *South African Journal of Geology* **118**, 439-454

Pettit, W. (2009) Geophysical signatures of some recently discovered large (>40 ha) kimberlites pipes on the Alto Cuilo concession in northeastern Angola. In: Stephen F et al (eds) Proceedings 9 IKC, *Lithos* **122**S, Special Issue, 106–115

Phillips, D., Kiviets, G.B., Barton, E.S., Smith, C.B., Viljoen, K.S. & Fourie, L.F., (1999) 40Ar/39Ar dating of kimberlites and related rocks. Problems and solutions. In: Gurney, J.J., Gurney, J.L., Pasco, M.D., Richardson, S.H. (Eds.), *Proceedings of the VIIth International kimberlite Conference* **2**, p. 677–688.

Phillips, D., Zhong, D., Matchan, E.R., et al. (2017) A comparison of Geochronology Methods Applied to Kimberlites and Related Rocks from the Karelian Craton, Finland. Conference paper, 11th IKC Extended abstract 11IKC-4480.

Pilbeam, L.H., Nielsen, T.F.D. & Waight, T.E. (2013) Digestion fractional crystallization (DFC): an important process in the genesis of kimberlites. Evidence from olivine in the Majuagaa kimberlite, Southern West Greenland. *Journal of Petrology* **54**, 1399–1425

Pin, C., Gannoun, A. & Dupont, A. (2014) Rapid, simultaneous separation of Sr, Pb, and Nd by extraction chromatography prior to isotope ratios determination by TIMS and MC-ICP-MS. *Journal of Analytical Atomic Spectrometry* **29**, 1858-1870

Pivin, M., Féménias, O. & Demaiffe, D. (2009) Metasomatic mantle origin for Mbuji-Mayi and Kundelungu garnet and clinopyroxene megacrysts (Democratic Republic of Congo). *Lithos* **112S**, 951–960

Pivin, M. (2012) La suite complexe des mégacristaux des kimberlites de Mbuji-Mayi en République Democratique du Congo: témoins du métasomatisme dans le manteau lithosphérique sous-continental archéen du craton du Congo-Kasaı¨ (Thèse de Doctorat). Université Libre de Bruxelles, Bruxelles, Belgique (475 pp)

Pivin, M., Debaille, V., Mattielli, N. & Demaiffe D. (2013) Nd–Hf Isotope Systematics of Megacrysts from the Mbuji-Mayi Kimberlites, D. R. Congo: Evidence for a Metasomatic Origin Related to Kimberlite Interaction with the Cratonic Lithospheric Mantle. PROC 10 IKC, vol 1, J GEOL SOC INDIA, Spec Vol, p 123-136

Porritt, L.A., Cas, R.A.F., Schaefer, B. & Mcknight, S.W. (2012) Textural analysis of strongly altered kimberlite: examples from the ekati diamond mine, NWT, Canada. *Canadian Mineralogist* **50**, 625–641

Price, S.E., Russell, J.K. & Kopylova, M.G. (2000) Primitive magma from the Jericho Pipe, N.W.T., Canada: constraints on primary kimberlite melt chemistry. *Journal of Petrology* **41**, 789–808.

Ramsay, R.R. (1995) Geochemistry of diamond indicator minerals. Unpublished PhD Thesis, University of Western Australia, Perth.

Rehfeldt, T., Foley, S.F., Jacob, D.E., Carlson, R.W. & Lowry, D. (2008) Contrasting types of metasomatism in dunite, wehrlite and websterite xenoliths from Kimberley, South Africa. *Geochimica et Cosmochimica Acta* **72**, 5722-5756.

Regelous, M., Niu, Y.L., Abouchami, W. & Castillo, P.R. (2009) Shallow origin for South Atlantic Dupal Anomaly from lower continental crust: geochemical evidence from the Mid-Atlantic Ridge at 26 degrees S. *Lithos* **112**, 57–72.

Reis, B. (1972) Preliminary note on the distribution and tectonic controls on kimberlites in Angola. 24th International Geological Congress, Montreal, Section 4, p. 276–281.

Richardson, S.H., Erlank, A.J., Duncan, A.R. & Reid, D.L. (1982) Correlated Nd, Sr and Pb isotope variation in Walvis Ridge basalts and implications for the evolution of their mantle source. *Earth and Planetary Science Letters* **59**, 327–342.

Richardson, S.H. (1984) Sr, Nd and O isotope variation in an extensive Karro dolerite sheet, southern Namibia. In: Erlank, A. J. (ed) Petrogenesis of the volcanic rocks of the Karro province. Special Publication of the Geological Society of South Africa, Johannesburg, 13, p. 289-293.

Richardson, S.H., Gurney, J.J., Erlank, A.J. & Harris, J.W. (1984) Origin of diamonds in old enriched mantle. *Nature* **310**, 198-202.

Ringwood, A.E., Kesson S.E., Hibberson, W. & Ware, N. (1992) Origin of kimberlites and related magmas. *Earth and Planetary Science Letters* **113**, 521–538.

Rivalenti, G., Mazzucchelli, M., Girardi, V.A.V., Vannucci, R., Barbieri, M.A., Zanetti, A. & Goldstein, S.L. (2000) Composition and processes of the mantle lithosphere in northeastern Brazil and Fernando de Noronha: evidence from mantle xenoliths. *Contributions to Mineralogy and Petrology* **138**, 308-325

Rivalenti, G., Zanetti, A., Girardi, V.A.V., Mazzucchelli, M., Tassinari, C.G.C., Bertotto, G.W. (2007) The effect of the Fernando de Noronha plume on the mantle lithosphere in north-eastern Brazil. *Lithos* **94**, 111–131.

Roberts, E., Jelsma, H.A. & Hegna, T. (2015) Mesozoic Sedimentary Cover Sequences of the 9 Congo Basin in the Kasai Region, Democratic Republic of Congo. In: de Wit M., Guillocheau F., de Wit M. (eds) Geology and Resource Potential of the Congo Basin. Regional Geology Reviews. Springer, Berlin, Heidelberg

Robles-Cruz, S.E., Escayola, M., Jackson, S., Galí, S., Pervov, V., Watangua, M., Gonçalves, A. & Melgarejo, J.C. (2012) U–Pb SHRIMP geochronology of zircon from the Catoca kimberlite, Angola: implications for diamond exploration. *Chemical Geology* **310-311**, 137–147.

Rogers, N.W., Hawkesworth, C.J. & Palacz, Z.A. (1992) Phlogopite in the generation of olivine-melilitites from Namaqualand, South Africa, and its implications for element fractionation processes in the upper mantle. *Lithos* **28**, 347–365.

Roy P., Balaram V., Kumar A.P., Satyanarayanan M., Gnaneshwar Rao T. (2007) New REE and trace element data on two kimberlitic reference materials by ICP-MS, *Geostandards and Geoanalytical Research* **31**, 261-273

Rudnick, R.L., McDonough, W.F.& Chappell, B.W. (1993) Carbonatite metasomatism in the northern Tanzanian mantle: petrographic and geochemical characteristics. *Earth and Planetary Science Letters* **114**, 463–475.

Russell, J.K., Porritt, L.A., Lavallee, Y. & Dingwell, D.B. (2012) Kimberlite ascent by assimilation-fuelled buoyancy. *Nature* **481**, 352–356.

Ryan, C.G, Griffin, W.L. & Pearson, N.J. (1996) Garnet geotherms: pressure-temperature data from Cr-pyrope garnet xenocrysts in volcanic rocks. *Journal of Geophysical Research* **101**, 5611 – 5626.

Salters, V. J. M., Longhi, J. E. & Bizimis, M. (2002) Near mantle solidus trace element partitioning at pressures up to 3·4 GPa. *Geochemistry, Geophysics, Geosystems* **3**, 1-23

Sarkar, C., Heaman, L.M., Pearson, D.G. (2015) Duration and periodicity of kimberlite volcanic activity in the Lac de Gras kimberlite field, Canada and some recommendations for kimberlite geochronology. *Lithos* **218–219**, 155-166

Schärer, U., Corfu, F. & Demaiffe, D. (1997) U–Pb and Lu–Hf isotopes in baddeleyite and zircon megacrysts from Mbuji-Mayi kimberlite: constraints on the subcontinental mantle. *Chemical Geology* **143**, 1–16.

Schulze, D.J. (1984) Cr-poor megacrysts in the Hamilton Branch kimberlite, Kentucky. In: Kornprobst J (ed) Proceedings 3rd international kimberlite conference **2**, Elsevier, Amsterdam, p.97–108

Schulze, D.J. (1987) Megacrysts from alkalic volcanic rocks. In: Nixon PH (ed) Mantle Xenoliths, Wiley, New York, p. 433–451

Schulze, D.J. (2003) A classification scheme for mantle-derived garnets in kimberlite: a tool for investigating the mantle and exploring for diamonds. *Lithos* **71**, 195–213.

Scott Smith B.H., Nowicki, T.E., Russell, J.K., et al., (2013) Kimberlite terminology and classification. D. G. Pearson et al. (eds.), Proceedings of 10th International Kimberlite Conference, Volume 2, Special Issue of the Journal of the Geological Society of India

Shaw, D.M. (1970) Trace element fractionation during anatexis. *Geochimica et Cosmochimica Acta* **34**, 237-243.

Shee, S.R. (1978) The mineral chemistry of xenoliths from the Orapa kimberlite pipe, Botswana. MSc

thesis, University of Cape Town
Shee, S.R. & Gurney, J.J. (1979) The mineralogy of xenoliths from Orapa, Botswana. In: Boyd, F.R., Meyer, H.O.A. (Eds.), Proceedings of the 2nd International Kimberlite Conference **2,** Sante Fe AGU, p. 37–49.
Shee, S.R. (1985) The petrogenesis of the Wesselton Mine Kimberlite, Kimberley, Cape Province, R.S.A. Ph.D. thesis, University of Cape Town.
Shimizu, N. & Richardson, S.H. (1987) Trace element abundance patterns of garnet inclusions in peridotite suite diamonds. *Geochimica et Cosmochimica Acta* **51**, 755-758
Simon, N.S.C., Carlson, R.W., Pearson, D.G., Davies, G.R. (2007) The origin and evolution of the Kaapvaal cratonic lithospheric mantle. *Journal of Petrology* **48**, 589-625.
Skinner, E.M.W. & Clement, C.R. (1977) Mineralogical classification of South African kimberlites. IInd International Kimberlite Conference, abstracts, unpaginated.
Skinner E.W.M. & Clement C.R. (1979) Mineralogical classification of Southern African kimberlites. In Proceedings of the 2nd International Kimberlite Conference, Boyd F.R. and Meyer H.O.A. (Eds), AGU, 129-139.
Skinner, E.M.W., Smith, C.B., Viljoen, K.S. & Clark, T.C. (1994) The petrography, tectonic setting and emplacement ages of kimberlites in the south western border region of the Kaapvaal Craton, Prieska area, South Africa. In: Meyer, H. O. A. and Leornados, O. H. (Eds) Kimberlites, Related rocks and Mantle Xenoliths, CPRM, Brazil, 80-97.
Smith, C.B. (1983) Pb, Sr and Nd isotopic evidence for sources of southern African kimberlites. *Nature* **304**, 51–54
Smith, C. B., Allsopp, H. L., Kramers, J. D., Hutchinson, G. & Roddick, J. C. (1985). Emplacement ages of Jurassic–Cretaceous South African kimberlites by the Rb–Sr method on phlogopite and whole-rock samples. *Transactions of the Geological Society of South Africa* **88**, 249–266.
Smith, C.B., Allsopp, H.L., Gravie, O.G., Kramers, J.D., Jackson, P.F.S. & Clement, C.R. (1989) Note on the U–Pb perovskite method for dating kimberlites: examples from the Wesselton and De Beers mines, South Africa, and Somerset Island, Canada. *Chemical Geology* **79**, 137–145.
Smith, C.B., Clark, T.C., Barton, E.A. & Bristow, J.W. (1994) Emplacement ages of kimberlite occurrences in the Prieska region, southwest border of the Kaapvaal Craton, South Africa. *Chemical Geology* (Isotope Geoscience) **113**, 149-169
Smith, C.B., Pearson, D.G., Bulanova, G.P., Beard, A.D., Carlson, R.W., Wittig, N., Sims, K., (...), & Muchemwa, E. (2009) Extremely depleted lithospheric mantle and diamonds beneath the southern Zimbabwe Craton. *Lithos* **112**, 1120-1132.
Sodoudi, F., Yuan, X.H., Kind, R., Lebedev, S., Adam, J.M.C., Kastle, E. & Tilmann, F., (2013) Seismic evidence for stratification in composition and anisotropic fabric within the thick lithosphere of Kalahari Craton. *Geochemistry, Geophysics, Geosystems* **14**, 5393-5412
Späth, A., le Roex, A.P. & Opiyo-Akech, N. (2001) Plume–lithosphere interaction and the origin of continental rift-related alkaline volcanism—the Chyulu Hills Volcanic Province, southern Kenya. *Journal of Petrology* **42**, 765–787.
Stachel, T., Viljoen, K.S., McDade, P. & Harris, J.W. (2004) Diamondiferous lithospheric roots along the western margin of the Kalahari Craton—the peridotitic inclusion suite in diamonds from Orapa and Jwaneng. *Contributions to Mineralogy and Petrology* **147**, 32 – 47
Stacey, J.S. & Kramers, J.D. (1975) Approximation of terrestrial lead isotope evolution by a two-stage model. *Earth Planetary Sciences Letters* **26**, 207–221.
Stanley, J.R. & Flowers R.M. (2016) Dating kimberlite emplacement with zircon and perovskite (U-Th)/He geochronology. *Geochemistry, Geophysics, Geosystems* **17**(11), 4517–4533.
Stiefenhofer, J. (1993) The petrography, mineral chemistry and isotope geochemistry of a mantle xenolith suite from the Lhethlakane DK1 and DK2 kimberlite pipes, Botswana. PhD thesis, Rhodes University

Stiefenhofer, J., Viljoen, K. S. & Marsh, J. S. (1997) Petrology and geochemistry of peridotite xenoliths from the Letlhakane kimberlites, Botswana. *Contributions to Mineralogy and Petrology* **127**, 147–158.

Stracke, A. (2012) Earth's heterogeneous mantle: A product of convection-driven interaction between crust and mantle. *Chemical Geology* **330–331**, 274– 299.

Stripp, G.R., Field, M., Schumacher, J.C. & Sparks, R.S.J. (2006) Post emplacement serpentinization and related hydrothermal metamorphism in a kimberlite from Venetia, South Africa. *Journal of Metamorphic geology* **24**, 515–534

Sun, J., Liu, C.-Z., Tappe, S., Kostrovitsky, S.I., Wu, F.-Y., Yakovlev, D., Yang, Y.-H. & Yang, J.-H. (2014) Repeated kimberlite magmatism beneath Yakutia and its relationship to Siberian flood volcanism: insights from in situ U–Pb and Sr–Nd perovskite isotope analysis. *Earth Planetary Sciences Letters* **404**, 283–295.

Sun, S.-s. & McDonough, W. F. (1989) Chemical and isotopic systematics of oceanic basalts: implications for mantle composition and processes. In: Saunders, A. D. & Norry, M. J. (eds) Magmatism in the Ocean Basins. Geological Society, London, Special Publications 42, 313–345.

Sweeney, R.J., Thompson, A.B. & Ulmer, P. (1993) Phase relations of a natural MARID composition and implications for MARID genesis, lithospheric melting and mantle metsomatism. *Contributions to Mineralogy and Petrology* **115** (2), 225-241

Tainton, K.M. and McKenzie, D. (1994). The generation of kimberlites, lamproites, and their source rocks. *Journal of Petrology* **35**, 787–817.

Tanaka T, et al. (2000) JNdi-1: a neodymium isotopic reference in consistency with LaJolla neodymium. *Chemical Geology* **168**, 279–281

Tappe, S., Pearson, D.G., Nowell, G., Nielsen, T., Milstead, P. & Muehlenbachs, K. (2011) A fresh isotopic look at Greenland kimberlites: cratonic mantle lithosphere imprint on deep source signal. *Earth and Planetary Science Letters* **305**, 235–248.

Tappe, S. & Simonetti A. (2012) Combined U-Pb geochronology and Sr-Nd isotope analysis of the Ice River perovskite standard, with implications for kimberlite and alkaline rock petrogenesis. *Chemical Geology* **304 – 305**, 10–17.

Tappe S., Pearson, D.G., Kjarsgaard, B.A., Nowell, G. & Dowall., D. (2013) Mantle transition zone input to kimberlite magmatism near a subduction zone: origin of anomalous Nd-Hf isotope systematics at Lac de Gras, Canada. *Earth and Planetary Science Letters* **371–372**, 235–251.

Tappe, S., Kjarsgaard, B.A., Kurszlaukis, S., Nowell, G.M. & Phillips, D. (2014) Petrology and Nd-Hf isotope geochemistry of the neoproterozoic Amon Kimberlite Sills, Baffin Island (Canada): evidence for deep mantle magmatic activity linked to supercontinent cycles. *Journal of Petrology* **55**, 2003–2042.

Tappe, S., Brand, N.B., Stracke, A., Van Ancken, D., et al., (2017) Plates or plumes in the origin of kimberlites: U/Pb perovskite and Sr-Nd-Hf-Os-C-O isotope constraints from the Superior craton (Canada*). Chemical Geology* **455**, 53 – 83.

Tappe, S., Smart, K., Torsvik, T., Massuyeau, M. & de Witt, M. (2018) Geodynamics of kimberlites on a cooling Earth: clues to plate tectonic evolution and deep volatile cycles. *Earth Planetary and Science Letters* **484**, 1–14.

Taylor, L.A. & Neal, C.R. (1989) Eclogites with oceanic crustal and mantle signatures from the Bellsbank kimberlite, South Africa: Part I. Mineralogy, petrography and whole rock chemistry. *Journal of Geology* **97**, 551–567.

Tollo, R.P. (1982) Petrography and mineral chemistry of ultramafic and related inclusions from the Orapa A/K-1 kimberlite pipe, Botswana. PhD thesis, University of Massachusetts.

Torsvik, T.H., Rousse, S., Labails, C. & Smethurst, M.A. (2009) A new scheme for the opening of the South Atlantic Ocean and the dissection of an Aptian salt basin. *Geophysical Journal International* **177**, 1315-1333

van Achterbergh E., Griffin, W.L. & Stiefenhofer, J. (2001) Metasomatism in mantle xenoliths from the Letlhakane kimberlites: estimation of element fluxes. *Contributions to Mineralogy and Petrology* **141**, 397-414.

Van Reenen, D.D., Roering, C., Ashwal, L.D. & De Wit, M.J. (1992) Regional geological settings of the Limpopo belt. *Precambrian Research* **55** (1-4), 1-5

Viljoen, K.S, Smith, C.B. & Sharp, Z.D. (1996) Stable and radiogenic isotope study of eclogite xenoliths from the Orapa kimberlite, Botswana. *Chemical Geology* **131**, 235-255.

Viljoen, F., Dobbe, R., Harris, H. & Smit, B. (2010) Trace element chemistry of mineral inclusions in eclogitic diamonds from the Premier (Cullinan) and Finsch kimberlites, South Africa: Implications for the evolution of their mantle source. *Lithos* **118**, 156-168

Walker PWE (2011) Competent person's report on a portfolio of diamond exploration properties in Botswana and the Democratic Republic of Congo for Botswana diamonds Plc. and Finncap Ltd. VP3 Geoservices (Pty.) Ltd., 90 pp

Wass, S.Y. & Rogers, N.W. (1980) Mantle metasomatism—precursor to continental alkaline volcanism. *Geochimica et Cosmochimica Acta* **44**, 1811–1823.

Weis, D. & Demaiffe, D. (1985) A depleted mantle source for kimberlites from Zaire: Nd, Sr and Pb isotopic evidence. *Earth and Planetary Science Letters* **73**, 269–277.

White, S.H., de Boorder, H. & Smith C.B. (1995) Structural controls of kimberlite and lamproite emplacement. Journal of Geochemical Exploration 53 (1–3), 245-264.

Wilson, J.F., Nesbitt, R.W. & Fanning, C.M. (1995) Zircon geochronology of Archaean felsic sequences in the Zimbabwe craton: a revision of greenstone stratigraphy and a model for crustal growth. In: Coward, M.P. & Ries, A.C. (eds) Early Precambrian Processes. Geological Society, London, Special Publications, 95, 109–126.

Wu, F.-Y., Yang, Y.-H., Mitchell, R. H., Li, Q.-L., Yang J.-H. & Zhang, Y.-B. (2010) In situ U–Pb age determination and Nd isotopic analysis of perovskites from kimberlites in southern Africa and Somerset Island, Canada. Lithos 115(1–4), 205–222

Wyllie, P. J. & Lee, W.-J. (1999). Kimberlites, carbonatites, peridotites and silicate–carbonate liquid immiscibility explained in parts of the system CaO-(Na_2O+K_2O)-$(MgO+FeO)$-$(SiO_2+Al_2O_3)$-CO_2. In: Gurney, J. J., Gurney, J. L., Pascoe, M. D. & Richardson, S. H. (eds) Proceedings of the VIIth International Kimberlite Conference. Cape Town, Red Roof Design, p. 923–932.

Zartman, R.E. & Richardson, S.H. (2005) Evidence from kimberlitic zircon for a decreasing mantle Th/U since the Archean. *Chemical Geology* **220**, 263–283.

Ziberna, L., Nimis, P., Zanetti, A. Marzoli A. & Sobolev, N. (2013) Metasomatic processes in the central Siberian cratonic mantle: evidence from garnet xenocrysts from the Zagadochnaya kimberlite. *Journal of Petrology* **54** (11), 2379-2409.

APPENDIX

A. SOUTHERN AFRICAN MEGACRYSTS

A.1. Major element geochemistry

A.1.1. Clinopyroxene

All major elements are expressed in Wt.% while trace elements data are in ppm

Table 1: Major element composition of Colossus clinopyroxene megacrysts

Colossus	SiO_2	TiO_2	Al_2O_3	Cr_2O_3	FeO	MnO	MgO	CaO	Na_2O	K_2O	Total	Ca#	Mg#	Cr#
cpx1	54.45	0.22	2.52	0.75	4.97	0.14	21.16	13.97	1.59	0.04	99.8	32.2	88.3	16.6
cpx2	54.54	0.18	2.55	0.71	5.07	0.15	21.11	14.09	1.50	0.02	99.9	32.4	88.1	15.7
cpx3	54.59	0.17	2.56	1.03	4.60	0.15	21.85	13.37	1.55	0.02	99.9	30.5	89.4	21.2
cpx4	54.59	0.24	2.70	0.74	5.27	0.15	21.33	13.15	1.62	0.03	99.8	30.7	87.8	15.5
cpx5	54.76	0.19	2.55	0.73	5.06	0.17	21.22	13.63	1.59	0.03	99.9	31.6	88.2	16.1
cpx6	55.02	0.13	2.64	1.03	4.67	0.11	21.64	13.09	1.67	0.03	100.0	30.3	89.2	20.7
cpx7	54.14	0.26	2.27	0.60	5.3	0.14	20.79	14.81	1.48	0.04	99.8	33.9	87.5	15.0
cpx8	54.59	0.19	2.48	0.78	4.95	0.15	21.56	13.91	1.50	0.04	100.1	31.7	88.6	17.4
cpx9	54.71	0.30	2.32	0.66	5.33	0.16	20.64	14.88	1.38	0.03	100.4	34.1	87.3	16.0
cpx10	54.66	0.30	2.35	0.65	5.41	0.16	20.48	14.56	1.45	0.04	100.1	33.8	87.1	15.6
cpx11	53.79	0.34	2.36	0.57	5.55	0.16	20.24	14.88	1.49	0.03	99.4	34.6	86.7	13.9
cpx12	54.49	0.19	2.36	0.71	4.81	0.13	21.27	14.46	1.33	0.04	99.8	32.8	88.7	16.7
cpx13	54.54	0.24	2.61	0.74	5.05	0.19	21.54	13.64	1.64	0.02	100.2	31.3	88.4	16.0
cpx14	54.45	0.33	2.37	0.62	5.23	0.20	20.41	14.79	1.49	0.03	99.9	34.2	87.4	14.9
cpx15	54.38	0.24	2.49	0.75	5.04	0.20	21.03	13.91	1.51	0.03	99.6	32.2	88.1	16.8
cpx16	54.97	0.13	2.75	0.95	4.77	0.19	21.84	12.63	1.69	0.03	99.9	29.3	89.1	18.8
cpx17	54.85	0.21	2.47	0.68	5.36	0.10	22.11	12.89	1.39	0.03	100.1	29.5	88.0	15.7
cpx18	54.22	0.27	2.30	0.62	5.18	0.11	20.56	15.04	1.41	0.03	99.7	34.4	87.6	15.3
cpx19	54.84	0.11	2.77	0.98	4.79	0.11	22.11	12.75	1.69	0.03	100.2	29.3	89.2	19.2
cpx20	55.31	0.14	2.60	0.94	4.62	0.14	21.04	13.31	1.61	0.03	99.7	31.2	89.0	19.5
cpx21	55.29	0.11	2.58	1.09	4.50	0.14	21.38	13.12	1.54	0.03	99.8	30.6	89.4	22.1
cpx22	54.86	0.35	2.37	0.35	5.63	0.15	19.27	15.64	1.46	0.03	100.1	36.8	85.9	9.1
cpx23	54.79	0.29	2.33	0.61	5.40	0.14	19.96	14.64	1.40	0.04	99.6	34.5	86.8	14.9
cpx24	54.76	0.27	2.40	0.59	5.46	0.14	20.05	14.33	1.42	0.03	99.4	33.9	86.7	14.1
cpx25	55.08	0.12	2.65	0.98	4.57	0.14	21.61	13.00	1.55	0.03	99.7	30.2	89.4	19.8
cpx26	55.10	0.15	2.39	0.75	4.89	0.13	20.81	14.45	1.37	0.03	100.1	33.3	88.4	17.5
cpx27	55.02	0.30	2.30	0.60	5.31	0.13	20.17	14.88	1.36	0.03	100.1	34.6	87.1	15.0
cpx28	55.35	0.14	2.68	0.88	5.08	0.15	20.79	13	1.61	0.03	99.7	31.0	87.9	18.1
cpx29	55.43	0.14	2.51	0.82	4.69	0.14	20.86	13.84	1.47	0.02	99.9	32.3	88.8	17.9
cpx30	55.34	0.17	2.24	0.71	4.83	0.13	20.54	14.69	1.26	0.03	99.9	33.9	88.4	17.5

Table 2: Major element composition of Orapa clinopyroxene megacrsysts

Orapa														
Cr-poor	SiO_2	TiO_2	Al_2O_3	Cr_2O_3	FeO	MnO	MgO	CaO	Na_2O	K_2O	Total	Ca#	Mg#	Cr#
cpx1	55.43	0.13	3.30	0.50	4.45	0.13	20.64	13.19	2.00	0.03	99.80	31.5	89.2	9.3
cpx18	55.44	0.33	3.25	0.27	5.26	0.17	18.99	14.22	2.13	0.03	100.08	35.0	86.5	5.3
cpx19	55.19	0.26	2.87	0.40	4.85	0.13	20.84	13.81	1.79	0.03	100.16	32.3	88.4	8.6
cpx38	54.07	0.32	2.81	0.03	6.20	0.20	16.39	17.17	2.31	0.02	99.51	42.9	82.5	0.7
cpx45	54.33	0.43	2.68	0.14	5.94	0.19	18.14	16.28	2.04	0.03	100.20	39.2	84.5	3.3
cpx43	54.20	0.30	2.71	0.20	5.42	0.17	19.29	14.92	1.84	0.03	99.09	35.7	86.4	4.8
cpx46	54.95	0.28	3.38	0.42	4.81	0.14	19.22	14.16	2.19	0.04	99.58	34.6	87.7	7.8
cpx48	53.75	0.25	3.37	0.03	6.24	0.15	14.50	19.53	2.36	0.06	100.23	49.2	80.5	0.6
cpx49	54.77	0.23	2.67	0.43	4.85	0.16	21.30	13.78	1.71	0.03	99.95	31.7	88.7	9.7
cpx56	54.57	0.24	3.29	0.50	4.74	0.13	20.29	13.94	2.21	0.03	99.93	33.0	88.4	9.3
cpx68	55.81	0.25	2.60	0.41	4.79	0.14	20.46	13.31	1.73	0.03	99.54	31.8	88.4	9.6
cpx70	55.99	0.18	2.75	0.47	4.67	0.16	21.13	12.82	1.72	0.03	99.91	30.4	89.0	10.3
cpx71	55.91	0.24	2.44	0.33	4.84	0.14	20.56	13.76	1.55	0.04	99.81	32.5	88.3	8.4
cpx74	55.61	0.28	2.69	0.38	4.91	0.18	20.97	13.08	1.67	0.03	99.79	30.9	88.4	8.7
cpx75	56.18	0.25	2.65	0.44	4.77	0.15	20.93	12.97	1.70	0.04	100.06	30.8	88.7	10.1
cpx77	55.78	0.29	2.39	0.37	4.58	0.16	20.35	13.88	1.58	0.05	99.43	32.9	88.8	9.5
cpx78	55.58	0.25	2.80	0.42	4.62	0.15	21.58	12.99	1.69	0.03	100.09	30.2	89.3	9.1
cpx79	56.02	0.26	2.66	0.36	4.94	0.15	20.64	13.35	1.73	0.03	100.12	31.7	88.2	8.2
Cr-rich														
cpx2	54.78	0.37	2.22	0.80	3.22	0.14	17.89	19.08	1.62	0.03	100.15	43.4	90.8	19.5
cpx3	55.05	0.33	2.21	0.62	2.97	0.11	17.42	20.00	1.52	0.03	100.26	45.2	91.3	15.8
cpx4	54.61	0.29	2.19	1.08	2.86	0.10	17.23	19.89	1.65	0.04	99.93	45.3	91.5	24.9
cpx5	54.74	0.36	2.73	0.99	4.34	0.13	16.52	18.01	2.29	0.02	100.13	43.9	87.1	19.5
cpx6	54.70	0.36	2.26	1.01	3.01	0.11	17.39	19.43	1.81	0.03	100.11	44.5	91.2	23.1
cpx7	54.84	0.35	2.31	0.57	3.10	0.13	17.28	19.98	1.66	0.03	100.23	45.4	90.9	14.1
cpx8	54.71	0.35	2.12	1.66	2.81	0.10	17.24	19.23	1.85	0.03	100.09	44.5	91.6	34.4
cpx9	54.65	0.25	2.75	0.59	5.40	0.14	15.76	17.93	2.29	0.02	99.79	45.0	83.9	12.6
cpx10	54.71	0.35	2.16	0.74	2.90	0.12	17.07	20.12	1.58	0.03	99.76	45.8	91.3	18.7
cpx11	54.72	0.34	2.39	1.41	2.85	0.12	17.07	19.17	1.93	0.03	100.04	44.7	91.4	28.3
cpx12	54.80	0.36	2.20	0.70	2.93	0.11	17.57	19.61	1.54	0.03	99.85	44.5	91.5	17.6
cpx13	54.74	0.38	2.26	0.61	3.08	0.13	17.67	19.75	1.65	0.02	100.27	44.5	91.1	15.3
cpx14	54.98	0.38	2.30	1.27	2.73	0.10	17.14	19.28	1.90	0.03	100.11	44.7	91.8	27.1
cpx15	54.35	0.32	2.32	0.53	3.73	0.13	17.02	19.61	1.80	0.01	99.83	45.3	89.0	13.4
cpx16	54.77	0.33	2.21	1.26	2.62	0.10	17.37	19.90	1.74	0.03	100.31	45.1	92.2	27.7
cpx17	54.83	0.32	2.10	0.80	2.95	0.10	17.78	19.81	1.57	0.03	100.30	44.5	91.5	20.4

Table 2 continued

Orapa Cr-rich	SiO_2	TiO_2	Al_2O_3	Cr_2O_3	FeO	MnO	MgO	CaO	Na_2O	K_2O	Total	Ca#	Mg#	Cr#
cpx20	55.15	0.40	2.31	0.66	3.28	0.12	17.52	18.93	1.74	0.03	100.15	43.7	90.5	16.0
cpx21	54.33	0.11	1.97	0.46	2.53	0.12	16.96	22.26	1.28	0.02	100.04	48.5	92.3	13.5
cpx22	54.67	0.36	2.33	0.80	3.24	0.11	17.58	19.48	1.72	0.03	100.31	44.3	90.6	18.7
cpx23	54.13	0.34	2.23	0.60	3.00	0.17	17.90	19.84	1.52	0.03	99.75	44.3	91.4	15.3
cpx24	54.40	0.27	2.77	0.46	5.73	0.20	16.26	17.76	2.28	0.03	100.15	44.0	83.5	10.0
cpx25	54.01	0.37	2.22	0.61	3.05	0.14	17.98	19.74	1.63	0.03	99.76	44.1	91.3	15.5
cpx26	54.80	0.35	2.38	0.62	3.68	0.15	17.24	18.90	1.78	0.03	99.93	44.1	89.3	14.9
cpx27	54.61	0.30	2.17	0.93	2.80	0.15	17.57	19.65	1.64	0.04	99.85	44.5	91.8	22.3
cpx28	54.65	0.33	2.25	0.93	2.98	0.14	17.69	19.54	1.74	0.03	100.28	44.2	91.4	21.7
cpx29	54.90	0.35	2.23	0.68	3.01	0.15	17.44	19.86	1.58	0.03	100.22	45.0	91.2	17.0
cpx30	54.64	0.27	1.89	1.03	3.22	0.15	18.44	18.72	1.54	0.04	99.93	42.2	91.1	26.7
cpx31	54.54	0.35	2.31	0.60	3.16	0.15	17.63	19.37	1.66	0.04	99.79	44.1	90.9	14.8
cpx32	54.40	0.38	2.25	0.64	3.03	0.14	17.76	19.40	1.64	0.03	99.67	44.0	91.3	16.0
cpx33	54.22	0.25	2.70	0.50	5.56	0.18	15.99	18.12	2.28	0.03	99.82	44.9	83.7	11.1
cpx34	54.92	0.33	2.29	1.00	2.78	0.16	17.58	19.15	1.76	0.02	99.97	43.9	91.9	22.6
cpx35	54.39	0.31	2.07	1.02	2.76	0.15	17.27	19.96	1.61	0.03	99.56	45.4	91.8	24.9
cpx36	54.63	0.37	2.12	0.77	3.00	0.15	17.75	19.50	1.53	0.03	99.83	44.1	91.3	19.6
cpx37	54.10	0.29	2.74	0.48	5.68	0.20	16.40	17.66	2.30	0.01	99.86	43.6	83.7	10.5
cpx39	54.43	0.26	2.77	0.46	5.56	0.18	15.90	17.98	2.29	0.01	99.83	44.8	83.6	10.0
cpx40	54.48	0.33	2.26	1.25	3.27	0.14	17.09	18.88	1.94	0.02	99.64	44.3	90.3	27.1
cpx41	54.18	0.32	2.21	0.85	2.99	0.13	17.69	19.49	1.66	0.02	99.54	44.2	91.3	20.5
cpx42	54.59	0.37	2.26	0.73	3.23	0.16	17.58	19.14	1.66	0.02	99.72	43.9	90.7	17.7
cpx44	54.35	0.35	2.36	0.62	3.73	0.17	18.13	17.84	1.73	0.02	99.30	41.4	89.6	15.0
cpx47	54.98	0.31	2.12	1.35	2.65	0.12	17.37	19.59	1.75	0.03	100.26	44.8	92.1	29.9
cpx50	54.23	0.28	1.91	1.40	3.03	0.13	18.24	18.94	1.67	0.04	99.87	42.7	91.5	32.9
cpx51	54.56	0.36	2.42	1.46	3.96	0.16	16.87	18.04	2.22	0.03	100.07	43.4	88.4	28.8
cpx52	54.17	0.34	2.16	1.39	2.80	0.13	17.62	19.57	1.88	0.04	100.08	44.4	91.8	30.3
cpx53	53.84	0.33	2.13	1.21	2.74	0.12	17.65	19.77	1.73	0.04	99.56	44.6	92.0	27.5
cpx54	54.47	0.37	2.24	1.12	2.84	0.13	17.47	19.59	1.77	0.04	100.03	44.6	91.6	25.1
cpx55	54.22	0.34	2.54	1.23	4.65	0.16	16.79	17.66	2.32	0.03	99.94	43.0	86.6	24.6
cpx57	54.31	0.37	2.26	1.06	2.88	0.10	17.74	19.49	1.77	0.02	100.00	44.1	91.6	24.0
cpx58	54.54	0.41	2.06	1.26	3.30	0.10	18.37	18.25	1.74	0.02	100.05	41.6	90.8	29.1
cpx59	55.09	0.36	2.38	0.98	3.04	0.10	17.68	19.29	1.86	0.03	100.81	43.9	91.2	21.7
cpx60	54.33	0.33	2.35	0.72	3.07	0.09	17.26	20.04	1.77	0.02	99.97	45.5	90.9	17.1
cpx61	54.18	0.17	1.19	0.90	1.87	0.09	17.33	22.96	1.12	0.00	99.79	48.8	94.3	33.6
cpx62	54.29	0.31	2.13	1.29	2.60	0.08	17.70	19.76	1.72	0.02	99.90	44.5	92.4	28.9
cpx63	54.22	0.35	2.16	1.25	2.91	0.08	17.63	19.46	1.72	0.02	99.80	44.2	91.5	27.9

Table 2 continued

Cr-rich	SiO_2	TiO_2	Al_2O_3	Cr_2O_3	FeO	MnO	MgO	CaO	Na_2O	K_2O	Total	Ca#	Mg#	Cr#
cpx64	54.37	0.39	2.27	0.68	3.35	0.10	17.96	19.02	1.72	0.01	99.87	43.2	90.5	16.7
cpx65	54.65	0.37	2.32	0.69	2.98	0.08	17.97	19.55	1.64	0.02	100.26	43.9	91.5	16.7
cpx66	54.45	0.36	2.27	0.69	3.17	0.10	17.81	19.43	1.62	0.02	99.92	43.9	90.9	16.9
cpx67	55.54	0.34	2.31	0.62	4.52	0.12	19.51	15.03	1.65	0.04	99.67	35.6	88.5	15.2
cpx69	55.43	0.38	2.21	0.71	3.08	0.13	17.65	18.40	1.66	0.03	99.68	42.8	91.1	17.8
cpx72	55.16	0.31	2.09	0.98	3.04	0.13	17.28	18.98	1.65	0.03	99.65	44.1	91.0	23.9
cpx73	54.94	0.28	2.12	0.55	4.50	0.12	19.59	16.03	1.49	0.03	99.65	37.0	88.6	14.8
cpx76	55.41	0.35	2.28	0.59	2.92	0.14	17.00	19.30	1.60	0.04	99.60	44.9	91.2	14.8
cpx80	55.25	0.41	2.27	0.54	3.23	0.14	17.59	18.84	1.62	0.02	99.89	43.5	90.7	13.7

Table 3: Major element composition of Kalkput clinopyroxene megacrysts

Kalkput	SiO_2	TiO_2	Al_2O_3	Cr_2O_3	FeO	MnO	MgO	CaO	Na_2O	K_2O	Total	Ca#	Mg#	Cr#
cpx1	54.17	0.48	2.33	0.00	10.93	0.17	11.97	16.27	3.28	0.05	99.6	49.4	66.1	0.1
cpx2	54.46	0.41	2.25	0.00	10.86	0.16	12.23	16.50	3.14	0.05	100.1	49.2	66.7	0.0
cpx3	55.21	0.13	2.25	0.62	3.97	0.11	19.69	16.85	1.20	0.06	100.1	38.1	89.8	15.5
cpx4	54.81	0.15	2.14	0.41	4.54	0.15	18.81	17.28	1.34	0.05	99.7	39.8	88.1	11.4
cpx5	54.58	0.14	1.96	0.42	4.60	0.16	18.92	17.45	1.28	0.05	99.6	39.8	88.0	12.5
cpx6	54.01	0.46	2.65	0.05	10.44	0.19	12.12	16.42	3.39	0.07	99.8	49.3	67.4	1.3
cpx7	54.48	0.24	2.13	0.09	6.81	0.18	16.56	17.23	1.85	0.03	99.6	42.8	81.3	2.7

Table 4: Major element composition of Bellsbank clinopyroxene megacrysts

Bellsbank	SiO_2	TiO_2	Al_2O_3	Cr_2O_3	FeO	MnO	MgO	CaO	Na_2O	K_2O	Total	Ca#	Mg#	Cr#
cpx1	55.25	0.16	1.47	1.52	3.76	0.14	16.18	19.49	2.11	0.01	100.1	46.4	88.5	41.0
Cpx2	55.14	0.11	0.68	2.58	3.37	0.09	16.53	19.61	1.92	0.03	100.1	46.0	89.7	71.7
Cpx3	55.05	0.14	1.23	2.06	3.74	0.14	16.00	19.22	2.11	0.01	99.7	46.3	88.4	52.9
Cpx5	55.17	0.23	2.40	2.64	2.46	0.13	16.28	18.05	2.61	0.03	100.0	44.3	92.2	42.4
Cpx6	55.18	0.16	1.00	2.98	2.18	0.11	16.99	19.53	1.90	0.03	100.0	45.2	93.3	66.6
Cpx9	55.30	0.12	0.56	1.70	2.34	0.10	17.71	21.17	1.31	0.02	100.3	46.2	93.1	67.1
Cpx10	55.59	0.09	0.39	1.48	2.18	0.09	17.91	21.23	1.07	0.03	100.1	46.0	93.6	71.9
Cpx11	55.70	0.08	0.39	1.63	2.33	0.08	17.93	21.15	1.04	0.03	100.4	45.9	93.2	73.8
Cpx12	55.42	0.09	0.21	2.12	2.76	0.11	17.20	21.01	1.26	0.02	100.2	46.7	91.7	87.3
Cpx14	55.46	0.05	2.76	1.48	1.88	0.10	16.58	19.21	2.12	0.02	99.7	45.4	94.0	26.5
Cpx15	54.86	0.18	2.40	2.36	2.57	0.11	16.41	17.91	2.51	0.02	99.3	43.9	91.9	39.8
Cpx16	55.28	0.13	2.18	1.24	3.21	0.10	16.82	18.96	1.84	0.02	99.8	44.7	90.3	27.6
cpx21	55.01	0.16	0.30	1.44	2.27	0.09	17.53	22.14	1.00	0.02	100.0	47.6	93.2	76.1
cpx22	55.25	0.17	0.90	1.94	2.45	0.10	16.89	20.60	1.61	0.01	99.9	46.7	92.5	59.2
cpx23	54.98	0.13	0.19	1.78	2.54	0.12	17.40	21.85	1.06	0.03	100.1	47.4	92.4	86.6
cpx24	55.16	0.16	0.34	1.59	2.20	0.07	17.41	21.81	1.15	0.02	99.9	47.4	93.4	75.9

Table 4 continued

Bellsbank	SiO_2	TiO_2	Al_2O_3	Cr_2O_3	FeO	MnO	MgO	CaO	Na_2O	K_2O	Total	Ca#	Mg#	Cr#
cpx26	54.99	0.12	0.92	1.75	3.31	0.12	16.34	20.52	1.65	0.01	99.7	47.4	89.8	56.2
cpx27	54.64	0.16	0.23	2.15	2.53	0.13	17.30	21.23	1.33	0.02	99.7	46.8	92.4	86.3
cpx28	55.21	0.15	0.45	1.70	2.55	0.11	17.61	20.93	1.24	0.02	100.0	46.1	92.5	71.7
cpx29	54.93	0.13	0.19	1.66	2.62	0.10	17.45	21.67	1.12	0.02	99.9	47.1	92.2	85.3
cpx30	57.63	0.17	1.51	1.40	3.01	0.07	15.12	19.11	1.82	0.02	99.9	47.6	90.0	38.4
cpx31	55.12	0.13	1.14	1.22	2.11	0.10	16.94	21.19	1.44	0.01	99.4	47.3	93.5	41.8
cpx32	54.80	0.21	0.96	1.44	3.04	0.12	16.49	20.53	1.64	0.01	99.3	47.2	90.6	50.1
cpx33	55.63	0.11	1.69	1.00	3.70	0.09	15.72	19.89	1.51	0.01	99.4	47.6	88.3	28.4

A.1.2. Garnets

Table 5: Major element composition of Colossus garnets

Colossus	SiO_2	TiO_2	Al_2O_3	Cr_2O_3	FeO	MnO	MgO	CaO	Na_2O	Total	Ca#	Mg#
gt1	42.12	0.79	21.21	2.16	9.16	0.26	19.84	4.48	0.06	100.1	14.0	79.4
gt2	41.96	0.896	21.28	1.95	9.505	0.262	19.58	4.7025	0.080	100.2	14.7	78.6
gt3	42.30	0.56	21.08	2.89	7.68	0.24	21.10	4.30	0.06	100.2	12.8	83.0
gt4	42.1	0.71	21.29	2.26	9.03	0.26	19.83	4.47	0.08	100.0	13.9	79.6
gt5	42.29	0.50	21.75	2.27	8.30	0.23	20.20	4.44	0.06	100.0	13.6	81.3
gt6	42.22	0.81	21.35	1.99	9.39	0.25	19.4	4.53	0.08	100.0	14.4	78.6
gt7	41.84	0.96	21.53	1.82	9.73	0.28	19.50	4.61	0.08	100.3	14.5	78.1
gt8	42.03	1.00	21.44	1.73	9.84	0.29	19.16	4.78	0.08	100.3	15.2	77.6
gt9	42.11	0.56	21.62	2.29	8.33	0.24	20.68	4.39	0.06	100.3	13.2	81.6
gt10	41.92	0.74	20.92	2.74	8.28	0.25	20.43	4.65	0.08	100.0	14.1	81.5
gt11	42.09	0.50	21.35	2.67	8.11	0.26	20.78	4.55	0.05	100.4	13.6	82.0
gt12	41.61	0.77	21.46	2.19	9.07	0.27	20.37	4.48	0.09	100.3	13.6	80.0
gt13	41.76	0.97	20.99	1.91	9.56	0.27	19.54	4.82	0.09	99.9	15.0	78.5
gt14	41.64	0.81	21.22	2.31	9.16	0.28	19.81	4.65	0.09	100.0	14.4	79.4
gt15	41.7	0.91	21.35	2.2	9.16	0.27	19.99	4.78	0.07	100.4	14.7	79.5
gt16	41.47	0.88	21.22	2.18	9.54	0.28	19.75	4.75	0.08	100.1	14.7	78.7
gt17	41.50	0.80	21.53	2.10	9.05	0.24	20.36	4.39	0.08	100.0	13.4	80.0
gt18	41.35	0.95	21.08	2.45	9.29	0.27	19.96	4.84	0.10	100.3	14.8	79.3
gt19	41.54	0.91	21.34	2.14	9.27	0.25	19.86	4.53	0.07	99.9	14.1	79.2
gt20	41.86	0.62	21.47	2.29	8.36	0.25	21.17	4.29	0.10	100.4	12.7	81.9
gt21	41.54	0.88	21.34	1.99	9.3	0.29	20.03	4.54	0.09	100.0	14.0	79.3
gt22	41.37	1.08	21.20	1.99	9.75	0.30	19.40	4.95	0.08	100.1	15.5	78.0
gt23	41.55	0.59	21.33	2.57	8.15	0.31	21.16	4.37	0.07	100.1	12.9	82.2
gt24	41.51	0.78	21.21	2.43	9.15	0.32	19.83	4.58	0.09	99.9	14.2	79.4
gt25	41.39	0.68	21.51	2.03	9.06	0.31	20.82	4.46	0.09	100.3	13.3	80.4

Table 5 continued

Colossus	SiO_2	TiO_2	Al_2O_3	Cr_2O_3	FeO	MnO	MgO	CaO	Na_2O	Total	Ca#	Mg#
gt26	41.38	0.84	21.25	2.03	9.35	0.31	20.24	4.61	0.07	100.1	14.1	79.4
gt27	41.30	0.85	21.36	2.06	9.25	0.31	20.29	4.61	0.09	100.1	14.0	79.6
gt28	40.98	1.01	21.18	1.94	9.84	0.33	19.84	4.86	0.10	100.1	15.0	78.2
gt29	41.07	0.99	21.43	1.60	10.02	0.31	20.01	4.62	0.09	100.1	14.2	78.1
gt30	41.91	0.51	21.48	2.47	8.07	0.29	20.82	4.51	0.08	100.1	13.5	82.1
gt31	41.01	0.79	22.27	0.12	12.98	0.44	17.86	4.46	0.08	100.0	15.2	71.0
gt32	40.98	1.11	20.88	2.18	9.68	0.33	19.67	5.13	0.09	100.0	15.8	78.4
gt33	41.21	0.89	21.43	1.78	9.86	0.33	19.67	4.66	0.11	99.9	14.5	78.0
gt34	41.57	0.84	21.21	2.20	8.98	0.30	20.15	4.54	0.08	99.9	13.9	80.0
gt35	41.78	0.79	21.36	2.22	8.91	0.30	20.35	4.47	0.09	100.3	13.6	80.3
gt36	41.60	0.84	21.34	2.10	9.08	0.31	19.93	4.52	0.07	99.8	14.0	79.6
gt37	41.96	0.54	21.26	2.84	7.58	0.28	21.18	4.27	0.07	100.0	12.6	83.3
gt38	41.90	0.57	21.31	2.80	7.95	0.31	20.55	4.50	0.08	100.0	13.6	82.2
gt39	41.24	1.05	20.81	2.21	9.71	0.33	19.65	4.96	0.08	100.0	15.4	78.3
gt40	41.62	0.74	21.52	2.07	8.88	0.32	20.33	4.42	0.08	100.0	13.5	80.3
gt41	41.42	0.81	21.22	2.22	8.62	0.31	20.50	4.69	0.07	99.8	14.1	80.9
gt42	41.89	0.43	21.62	2.48	7.95	0.28	21.13	4.25	0.07	100.1	12.6	82.6
gt43	41.76	0.60	21.41	2.48	8.06	0.30	20.68	4.55	0.07	99.9	13.7	82.0
gt44	41.66	0.74	21.38	2.27	8.77	0.31	20.45	4.43	0.08	100.1	13.5	80.6

Table 6: Major element composition of Orapa garnets

Orapa high-Cr	SiO_2	TiO_2	Al_2O_3	Cr_2O_3	FeO	MnO	MgO	CaO	Na_2O	Total	Ca#	Mg#
gt1	41.00	1.00	20.51	2.33	9.61	0.30	20.55	4.61	0.11	100.0	13.9	79.2
gt2	41.57	1.00	21.22	1.86	9.55	0.32	20.16	4.55	0.11	100.3	14.0	79.0
gt3	41.30	1.13	21.12	1.44	9.90	0.29	19.90	4.49	0.10	99.7	13.9	78.2
gt4	41.44	0.92	21.10	2.44	8.73	0.31	20.30	4.66	0.10	100.0	14.2	80.6
gt5	41.56	0.99	21.46	1.48	9.47	0.29	20.29	4.41	0.11	100.1	13.5	79.2
gt6	41.28	1.16	21.26	1.55	10.49	0.35	19.23	4.66	0.09	100.1	14.8	76.6
gt7	41.56	0.91	21.09	2.43	8.71	0.33	20.49	4.65	0.09	100.3	14.0	80.7
gt8	41.85	0.96	21.70	1.15	9.25	0.27	20.42	4.26	0.10	100.0	13.0	79.7
gt9	41.44	0.97	21.99	1.16	10.49	0.36	18.69	4.64	0.09	99.8	15.1	76.0
gt10	41.35	0.98	20.78	3.01	8.89	0.39	19.65	4.98	0.10	100.1	15.4	79.7
gt11	41.53	0.98	20.94	2.21	8.89	0.31	20.57	4.55	0.10	100.1	13.7	80.5
gt12	41.71	0.93	21.92	1.09	8.93	0.25	20.58	4.33	0.09	99.8	13.1	80.4
gt15	41.57	0.89	21.98	1.09	8.89	0.25	20.86	4.29	0.10	99.9	12.9	80.7
gt16	41.23	0.95	21.76	1.25	10.57	0.37	19.23	4.63	0.10	100.1	14.7	76.4
gt18	41.15	1.08	21.52	1.71	10.31	0.36	19.09	4.61	0.12	99.9	14.8	76.7
gt20	41.44	1.04	21.16	1.74	9.86	0.35	19.84	4.54	0.11	100.1	14.1	78.2

Table 6 continued

Orapa high-Cr	SiO_2	TiO_2	Al_2O_3	Cr_2O_3	FeO	MnO	MgO	CaO	Na_2O	Total	Ca#	Mg#
gt21	41.76	1.12	21.1	2.23	9.32	0.33	19.76	4.66	0.08	100.3	14.5	79.1
gt22	41.43	0.96	21.9	1.22	10.46	0.39	18.94	4.57	0.09	99.9	14.8	76.3
gt23	41.27	1.11	20.7	1.98	9.47	0.30	20.12	4.55	0.10	99.6	14.0	79.1
gt24	41.11	1.09	21.0	1.56	10.12	0.34	20.06	4.47	0.10	99.9	13.8	77.9
gt25	41.21	0.88	21.0	2.33	9.31	0.41	19.62	4.75	0.09	99.6	14.8	79.0
gt26	41.19	1.04	21.7	1.19	10.35	0.40	19.55	4.61	0.10	100.1	14.5	77.1
gt27	41.30	1.08	20.9	1.98	9.80	0.29	20.10	4.57	0.12	100.2	14.0	78.5
gt28	41.16	0.95	21.8	1.16	10.47	0.37	19.52	4.56	0.08	100.0	14.4	76.9
gt30	41.86	0.91	21.7	1.04	9.13	0.27	20.89	4.25	0.11	100.1	12.7	80.3
gt31	41.92	0.93	21.7	1.04	9.12	0.29	20.52	4.25	0.08	99.9	12.9	80.0
gt32	41.26	1.05	21.1	2.03	9.43	0.36	20.04	4.51	0.13	99.9	13.9	79.1
gt33	41.33	1.08	21.1	1.82	9.64	0.32	20.01	4.54	0.08	99.9	14.0	78.7
gt34	41.58	1.00	21.0	2.08	9.29	0.31	20.30	4.50	0.11	100.1	13.7	79.6
gt36	41.42	1.05	21.3	1.63	10.00	0.35	19.66	4.54	0.10	100.1	14.2	77.8
gt38	41.55	1.04	21.3	1.64	9.71	0.31	20.03	4.48	0.09	100.2	13.9	78.6
gt39	41.54	1.01	21.4	1.56	9.38	0.31	20.32	4.47	0.07	100.0	13.7	79.4
gt40	41.42	1.05	21.1	1.70	9.21	0.33	20.19	4.49	0.08	99.6	13.8	79.6
gt41	41.40	1.05	21.6	1.56	10.18	0.38	19.39	4.56	0.07	100.1	14.4	77.2
gt42	41.51	1.04	21.1	1.98	8.71	0.32	20.71	4.52	0.08	100.0	13.6	80.9
gt45	41.60	1.12	21.3	1.59	9.42	0.38	20.11	4.64	0.08	100.2	14.2	79.2
gt46	41.51	0.88	21.5	2.03	8.77	0.38	20.12	4.75	0.08	100.1	14.5	80.3
gt47	41.67	1.13	21.1	1.75	9.24	0.33	20.25	4.61	0.10	100.2	14.1	79.6
gt49	41.65	1.11	21.2	1.86	9.03	0.35	20.39	4.57	0.10	100.3	13.9	80.1
gt50	41.68	1.08	20.9	2.12	8.69	0.33	20.41	4.63	0.08	99.9	14.0	80.7
gt51	41.48	0.84	21.6	2.06	8.77	0.38	20.11	4.71	0.11	100.1	14.4	80.3
gt52	41.57	1.15	21.0	1.98	9.03	0.35	20.34	4.69	0.09	100.2	14.2	80.1
gt53	41.48	1.12	20.8	2.35	8.52	0.35	20.72	4.65	0.10	100.1	13.9	81.3
gt56	41.48	1.17	21.1	1.71	9.49	0.29	19.75	4.67	0.11	99.8	14.5	78.8
gt57	41.47	1.10	21.5	1.52	9.84	0.35	19.51	4.65	0.10	100.0	14.6	77.9
gt58	41.96	0.85	21.8	1.11	8.30	0.26	21.39	4.29	0.08	100.0	12.6	82.1
gt59	41.32	1.10	21.3	1.60	9.64	0.35	19.81	4.54	0.11	99.8	14.1	78.5
gt60	41.64	1.15	21.5	1.50	9.41	0.34	20.08	4.50	0.10	100.2	13.9	79.2
gt61	41.66	1.10	21.1	1.90	9.09	0.31	20.33	4.58	0.10	100.2	13.9	79.9
gt62	41.96	0.97	21.8	1.07	8.35	0.27	21.37	4.27	0.08	100.1	12.5	82.0
gt63	41.59	1.06	21.5	1.54	8.79	0.28	20.91	4.42	0.11	100.1	13.2	80.9
gt64	41.65	1.10	21.1	1.91	9.11	0.27	20.40	4.58	0.09	100.2	13.9	80.0
gt65	41.40	1.07	21.7	1.11	10.12	0.35	19.48	4.49	0.10	99.8	14.2	77.4
gt67	41.67	1.06	21.0	1.73	8.83	0.32	20.61	4.45	0.09	99.7	13.4	80.6

Table 6 continued

Orapa high-Cr	SiO_2	TiO_2	Al_2O_3	Cr_2O_3	FeO	MnO	MgO	CaO	Na_2O	Total	Ca#	Mg#
gt68	41.10	1.07	21.3	1.41	10.09	0.41	19.75	4.60	0.12	99.8	14.3	77.7
gt69	41.52	1.14	21.1	1.68	9.60	0.35	19.98	4.60	0.11	100.1	14.2	78.8
gt70	41.74	1.16	20.9	1.86	9.15	0.34	20.56	4.61	0.11	100.4	13.9	80.0
gt71	41.83	1.11	20.7	1.97	8.92	0.34	20.64	4.60	0.08	100.2	13.8	80.5
gt73	41.91	0.95	21.5	1.13	8.89	0.31	20.76	4.29	0.11	99.8	12.9	80.6
gt74	42.46	0.95	21.5	1.10	8.61	0.29	20.62	4.33	0.12	99.9	13.1	81.0
gt75	42.12	1.09	20.9	1.97	9.05	0.36	20.01	4.68	0.13	100.3	14.4	79.8
gt77	41.42	1.10	21.3	1.56	9.47	0.31	20.46	4.56	0.10	100.2	13.8	79.4
gt78	41.14	1.05	21.0	2.09	8.94	0.37	20.56	4.71	0.09	100.0	14.1	80.4
gt79	41.49	1.07	20.7	2.19	8.74	0.29	21.08	4.62	0.12	100.3	13.6	81.1
gt80	41.56	1.06	21.3	1.52	9.95	0.36	19.77	4.65	0.11	100.3	14.5	78.0
gt81	40.93	1.14	21.7	1.12	10.04	0.37	20.12	4.66	0.10	100.2	14.3	78.1
gt82	41.44	1.15	20.9	1.67	9.42	0.36	20.56	4.61	0.09	100.2	13.9	79.5
gt83	41.97	0.92	21.6	1.11	8.62	0.26	21.08	4.30	0.09	99.9	12.8	81.3
gt84	42.19	1.13	21.0	1.77	9.46	0.31	19.90	4.68	0.09	100.5	14.4	78.9
gt85	42.00	0.98	21.4	1.64	8.92	0.29	20.52	4.38	0.10	100.3	13.3	80.4
gt87	42.21	1.02	21.3	1.40	8.56	0.28	21.14	4.33	0.09	100.3	12.8	81.5
gt88	41.89	1.02	20.7	2.79	8.34	0.31	20.88	4.70	0.07	100.7	13.9	81.7
gt89	41.46	1.04	21.1	1.75	9.92	0.34	19.57	4.43	0.10	99.7	14.0	77.9
gt91	41.60	1.10	20.9	1.83	9.92	0.33	19.83	4.42	0.10	100.0	13.8	78.1
gt92	41.66	0.95	20.7	2.41	9.02	0.34	20.09	4.40	0.10	99.7	13.6	79.9
gt94	42.03	0.90	21.7	1.19	8.96	0.29	20.67	4.06	0.09	99.9	12.4	80.4
gt95	42.09	1.01	21.5	1.13	8.52	0.29	20.53	4.11	0.11	99.3	12.6	81.1
gt96	41.47	1.10	21.0	1.67	10.10	0.35	19.74	4.36	0.12	99.9	13.7	77.7
gt97	41.83	0.98	21.3	1.60	9.39	0.35	20.59	4.26	0.11	100.5	12.9	79.6
gt98	41.53	1.02	21.1	1.63	10.02	0.35	19.82	4.25	0.10	99.8	13.3	77.9
gt100	41.51	1.19	20.8	1.84	9.91	0.35	20.06	4.44	0.12	100.3	13.7	78.3
gt101	41.45	1.08	21.6	1.05	10.89	0.41	19.19	4.34	0.10	100.1	14.0	75.8
gt102	41.38	0.85	20.2	3.60	8.60	0.40	19.80	4.86	0.10	99.8	15.0	80.4
gt103	41.63	1.08	21.0	1.84	9.79	0.32	20.16	4.30	0.11	100.3	13.3	78.6
gt104	41.28	0.72	20.0	4.59	8.49	0.42	19.40	5.20	0.09	100.2	16.2	80.3
gt105	41.67	1.05	21.1	1.87	9.63	0.34	20.09	4.42	0.10	100.2	13.6	78.8
Orapa low-Cr												
gt54	41.38	1.19	21.87	0.38	11.65	0.39	18.80	4.41	0.12	100.2	14.4	74.2
gt76	41.14	0.56	22.49	0.08	14.25	0.49	17.23	4.06	0.09	100.4	14.5	68.3
gt44	40.65	0.54	21.81	1.00	14.36	0.61	15.92	4.99	0.05	99.9	18.4	66.4
gt106	41.07	0.58	22.58	0.05	14.68	0.48	17.34	3.65	0.10	100.5	13.1	67.8
gt13	41.56	0.78	22.28	1.22	9.07	0.37	18.89	5.52	0.12	99.8	17.3	78.8
gt55	40.47	0.64	21.63	1.04	14.33	0.62	15.79	5.34	0.07	99.9	19.6	66.3
gt14	41.37	0.91	21.74	2.02	8.32	0.39	18.80	6.40	0.14	100.1	19.6	80.1

Table 7: Major element composition of Bellsbank garnets

Bellsbank	SiO_2	TiO_2	Al_2O_3	Cr_2O_3	FeO	MnO	MgO	CaO	Na_2O	Total	Ca#	Mg#
gt1	40.90	0.13	22.13	2.27	13.26	0.57	16.65	4.43	0.04	100.4	16.0	69.1
gt2	41.69	0.08	23.51	0.81	10.45	0.44	18.97	4.16	0.03	100.1	13.6	76.4
gt4	41.90	0.46	23.50	0.10	10.02	0.26	19.60	3.96	0.10	99.9	12.7	77.7
gt9	41.59	0.43	23.07	0.48	11.04	0.42	18.80	4.16	0.07	100.1	13.7	75.2
gt10	41.77	0.09	22.48	3.06	8.58	0.43	19.75	4.41	0.05	100.6	13.8	80.4
gt12	41.85	0.37	22.10	3.12	6.58	0.29	21.66	4.32	0.09	100.4	12.5	85.4

A.2. Trace element geochemistry

A.2.1. Clinopyroxene

Table 8: Trace element composition (in ppm) of Colossus cpx megacrysts

Colossus	cpx1	cpx2	cpx3	cpx4	cpx5	cpx6	cpx9	cpx11	cpx17	cpx18	cpx19	cpx20	cpx21	cpx22
Sc	16.12	14.77	15.01	14.78	15.25	14.43	16.68	15.64	12.47	16.01	13.16	14.65	13.41	17.72
V	163	155	152	157	166	143	191	185	133	187	129	153	141	229
Ni	581	579	572	571	579	601	496	477	602	470	581	579	595	376
Rb	0.027	0.126	0.017	0.038	0.024	0.163	0.026	0.042	0.053	0.083	0.045	0.159	0.028	0.096
Sr	75.27	71.64	66.94	62.02	73.17	66.04	76.33	74.71	66.98	79.21	57.66	66.01	58.35	88.57
Y	2.45	2.14	1.80	2.41	2.42	1.92	3.06	3.02	2.48	2.86	1.87	1.79	1.50	3.17
Zr	3.66	2.73	2.50	3.48	3.51	2.48	7.34	6.63	3.55	6.04	1.50	2.30	1.56	8.17
Nb	0.11	0.09	0.10	0.12	0.12	0.18	0.15	0.14	0.15	0.16	0.06	0.07	0.08	0.14
Ba	0.47	0.52	0.24	0.27	0.29	5.25	0.26	0.21	0.20	0.27	0.25	0.55	0.24	47.73
La	1.26	1.13	0.97	1.12	1.18	1.02	1.64	1.50	1.17	1.52	0.80	0.99	0.76	1.79
Ce	4.16	3.80	3.46	3.75	3.93	3.28	5.71	5.47	3.96	5.32	2.44	3.22	2.61	5.90
Pr	0.67	0.60	0.53	0.61	0.63	0.50	0.91	0.86	0.64	0.86	0.38	0.50	0.42	0.99
Nd	3.76	3.24	2.90	3.26	3.48	2.76	5.02	4.85	3.54	4.64	2.18	2.78	2.22	5.31
Sm	1.00	0.83	0.71	0.86	0.90	0.72	1.30	1.26	0.93	1.18	0.59	0.74	0.56	1.36
Eu	0.34	0.29	0.26	0.30	0.32	0.25	0.43	0.40	0.32	0.39	0.22	0.25	0.19	0.45
Gd	0.91	0.75	0.67	0.77	0.82	0.64	1.16	1.09	0.83	1.03	0.55	0.64	0.51	1.16
Tb	0.13	0.10	0.09	0.11	0.12	0.09	0.15	0.16	0.12	0.14	0.08	0.10	0.07	0.17
Dy	0.61	0.52	0.45	0.58	0.64	0.46	0.82	0.80	0.62	0.73	0.43	0.47	0.37	0.85
Ho	0.11	0.10	0.08	0.09	0.10	0.08	0.13	0.12	0.10	0.12	0.07	0.06	0.06	0.15
Er	0.24	0.20	0.17	0.22	0.23	0.17	0.29	0.29	0.22	0.27	0.17	0.17	0.13	0.28
Tm	0.03	0.03	0.02	0.03	0.03	0.02	0.03	0.03	0.02	0.02	0.02	0.02	0.02	0.03
Yb	0.16	0.12	0.12	0.15	0.15	0.12	0.18	0.18	0.15	0.16	0.13	0.11	0.10	0.18
Lu	0.02	0.02	0.01	0.02	0.01	0.01	0.02	0.02	0.02	0.02	0.02	0.02	0.01	0.02
Hf	0.23	0.14	0.15	0.21	0.23	0.12	0.45	0.43	0.19	0.38	0.09	0.13	0.11	0.51
Ta	0.005	0.007	0.003	0.005	0.006	0.008	0.006	0.006	0.007	0.006	0.003	0.003	0.005	0.009
Pb	0.10	0.09	0.09	0.08	0.09	0.10	0.11	0.10	0.09	0.13	0.07	0.11	0.07	0.14
Th	0.011	0.013	0.014	0.018	0.018	0.013	0.016	0.014	0.016	0.017	0.010	0.012	0.006	0.022
U	0.003	0.005	0.003	0.003	0.003	0.007	0.004	0.002	0.003	0.002	0.003	0.011	0.003	0.064

Table 9: Trace element composition (in ppm) of Orapa cpx megacrysts

Orapa Cr-rich	cpx2	cpx3	cpx6	cpx15	cpx16	cpx21	cpx29	cpx30	cpx34	cpx55	cpx57	cpx60	cpx63
Sc	20.84	20.95	23.17	27.47	21.34	70.42	19.28	17.83	18.95	28.88	21.90	26.38	20.14
V	320	302	311	324	275	264	281	278	286	305	319	322	287
Ni	337	278	287	260	341	265	281	423	354	315	352	280	345
Rb	0.572	0.241	0.066	0.194	0.326	0.038	0.144	0.149	0.029	0.074	0.124	0.025	0.040
Sr	108.70	112.45	115.87	106.77	139.15	488.82	101.75	91.87	125.32	94.07	108.25	104.73	119.60
Y	2.89	2.08	2.76	3.57	2.08	6.85	1.93	1.46	2.45	4.24	2.62	2.89	2.01
Zr	22.35	16.96	21.31	31.70	14.66	59.79	17.22	6.07	17.30	39.61	17.34	27.68	12.56
Nb	0.95	0.60	0.21	0.37	0.87	1.33	0.62	0.37	0.49	0.24	0.25	0.36	0.37
Ba	6.31	3.30	0.23	1.64	6.75	1.19	3.06	1.41	0.42	0.07	0.13	0.21	1.18
La	2.30	1.95	1.74	1.91	2.51	35.90	1.96	1.55	2.12	1.88	1.83	1.81	1.90
Ce	7.79	7.12	6.82	7.20	8.19	79.89	6.44	5.40	7.57	7.27	6.86	6.33	6.88
Pr	1.10	1.18	1.20	1.26	1.34	8.88	1.07	0.91	1.27	1.28	1.16	1.06	1.15
Nd	6.52	6.25	6.74	6.90	7.31	35.71	5.74	4.88	7.16	7.04	6.28	6.08	6.22
Sm	1.69	1.59	1.81	1.92	1.78	5.95	1.49	1.22	1.76	1.95	1.63	1.62	1.52
Eu	0.54	0.53	0.61	0.66	0.56	1.63	0.50	0.37	0.57	0.66	0.52	0.52	0.47
Gd	1.30	1.18	1.46	1.59	1.23	3.66	1.13	0.84	1.33	1.77	1.30	1.34	1.13
Tb	0.17	0.14	0.19	0.21	0.15	0.44	0.15	0.10	0.16	0.24	0.17	0.17	0.13
Dy	0.80	0.66	0.87	1.09	0.66	2.06	0.64	0.47	0.74	1.23	0.82	0.86	0.59
Ho	0.12	0.09	0.12	0.14	0.08	0.32	0.09	0.07	0.11	0.19	0.12	0.12	0.08
Er	0.25	0.18	0.23	0.31	0.17	0.62	0.17	0.14	0.20	0.41	0.23	0.24	0.16
Tm	0.03	0.01	0.02	0.03	0.02	0.07	0.01	0.01	0.02	0.05	0.02	0.02	0.02
Yb	0.13	0.10	0.13	0.19	0.10	0.37	0.10	0.07	0.15	0.25	0.14	0.14	0.10
Lu	0.01	0.01	0.01	0.02	0.01	0.04	0.01	0.01	0.02	0.02	0.01	0.02	0.01
Hf	1.06	1.03	1.41	2.09	0.83	2.11	1.03	0.40	0.92	2.73	1.24	1.60	0.83
Ta	0.051	0.034	0.017	0.023	0.057	0.077	0.035	0.021	0.028	0.021	0.020	0.019	0.027
Pb	0.18	0.16	0.15	0.18	0.21	1.38	0.16	0.14	0.17	0.18	0.20	0.17	0.17
Th	0.130	0.053	0.021	0.047	0.082	0.893	0.097	0.037	0.045	0.031	0.015	0.040	0.042
U	0.048	0.020	0.005	0.008	0.038	0.112	0.034	0.010	0.031	0.017	0.010	0.012	0.011

Table 9 continued

	cpx64	cpx69	cpx73	Cr-poor	Cpx1	cpx18	cpx19	cpx45	cpx46	cpx48	cpx56	cpx70	cpx74	cpx78
Sc	21.78	18.31	15.55		10.24	14.81	11.34	20.49	14.10	38.96	14.10	11.13	12.25	17.94
V	313	283	225		116	201	148	303	179	470	160	135	153	232
Ni	327	304	414		612	501	594	284	512	226	546	641	615	442
Rb	0.052	0.130	0.014		0.034	0.027	0.009	0.072	0.039	0.080	0.089	0.013	0.072	0.063
Sr	99.77	88.28	93.45		82.33	80.89	83.93	112.03	84.73	35.81	86.50	84.14	80.91	95.90
Y	3.13	2.08	2.57		2.44	3.99	3.20	4.56	3.57	1.06	3.98	3.16	3.57	3.00
Zr	19.64	13.81	6.13		2.56	9.19	5.64	14.93	7.92	2.56	7.26	4.69	6.08	13.51
Nb	0.21	0.17	0.14		0.14	0.14	0.14	0.20	0.12	0.20	0.13	0.15	0.14	0.18
Ba	0.19	0.16	0.21		0.43	0.35	0.23	0.09	0.28	0.15	0.26	0.26	0.22	0.20
La	1.62	1.37	1.52		2.10	1.60	2.01	2.99	1.69	1.05	1.73	2.33	2.11	1.96
Ce	6.06	5.57	5.46		6.23	5.55	6.65	9.76	5.74	2.53	5.69	7.27	6.90	6.66
Pr	1.07	0.96	0.91		0.82	0.94	1.03	1.55	0.94	0.32	0.95	1.10	1.09	1.08
Nd	6.17	5.13	5.10		3.87	5.12	5.52	8.24	5.13	1.42	5.00	5.54	5.73	5.88
Sm	1.79	1.38	1.28		0.87	1.39	1.36	2.10	1.41	0.35	1.37	1.33	1.45	1.50
Eu	0.55	0.45	0.43		0.29	0.49	0.44	0.69	0.47	0.14	0.48	0.43	0.46	0.51
Gd	1.45	1.07	1.12		0.75	1.33	1.14	1.78	1.29	0.34	1.28	1.17	1.26	1.25
Tb	0.20	0.14	0.14		0.10	0.19	0.17	0.26	0.17	0.05	0.17	0.16	0.18	0.16
Dy	0.93	0.63	0.70		0.57	0.99	0.86	1.29	0.93	0.29	1.02	0.81	0.90	0.83
Ho	0.12	0.09	0.10		0.10	0.18	0.14	0.18	0.16	0.04	0.16	0.13	0.14	0.13
Er	0.27	0.18	0.20		0.23	0.38	0.28	0.42	0.34	0.11	0.35	0.26	0.31	0.28
Tm	0.03	0.01	0.02		0.02	0.04	0.03	0.05	0.03	0.01	0.04	0.04	0.04	0.03
Yb	0.14	0.11	0.13		0.17	0.24	0.18	0.27	0.23	0.06	0.28	0.19	0.19	0.17
Lu	0.02	0.01	0.02		0.02	0.03	0.02	0.03	0.03	0.01	0.03	0.02	0.02	0.02
Hf	1.24	0.95	0.37		0.16	0.52	0.30	1.04	0.51	0.13	0.50	0.25	0.32	0.78
Ta	0.016	0.014	0.010		0.004	0.007	0.004	0.013	0.007	0.023	0.010	0.008	0.007	0.010
Pb	0.18	0.14	0.11		0.12	0.17	0.11	0.18	0.16	0.17	0.18	0.11	0.10	0.13
Th	0.021	0.019	0.022		0.022	0.013	0.015	0.039	0.016	0.019	0.016	0.019	0.017	0.021
U	0.007	0.007	0.005		0.016	0.013	0.006	0.012	0.006	0.005	0.006	0.005	0.006	0.004

Table 10. Trace element composition of Kalkput cpx megacrysts

	Kalkput	cpx1	cpx2	cpx3	cpx4	cpx5	cpx6	cpx7
Sc		74.9	76.7	14.2	19.0	20.6	69.6	43.0
V		731	630	159	200	211	657	457
Ni		8.58	9.46	394	276	238	10.5	72.8
Rb		0.226	0.423	0.015	0.019	0.032	0.023	0.035
Sr		349	311	185	213	226	355	248
Y		4.45	3.92	1.95	2.62	2.74	4.15	4.02
Zr		99.9	92.1	3.38	5.38	6.27	85.0	26.2
Nb		0.12	0.39	0.03	0.02	0.03	0.04	0.05
Ba		6.23	1.83	0.58	0.52	0.51	0.44	0.27
La		3.94	3.04	1.74	1.94	2.09	3.35	2.44
Ce		14.5	12.2	6.27	7.43	8.14	12.7	9.97
Pr		2.50	2.13	1.08	1.34	1.42	2.27	1.87
Nd		14.3	12.2	6.24	7.71	8.11	12.9	11.3
Sm		3.08	2.67	1.37	1.75	1.84	2.91	2.74
Eu		0.87	0.78	0.39	0.50	0.53	0.81	0.78
Tb		0.27	0.26	0.12	0.15	0.16	0.26	0.25
Gd		2.64	2.31	1.21	1.73	1.75	2.82	2.54
Dy		1.36	1.17	0.59	0.74	0.73	1.30	1.19
Ho		0.22	0.20	0.09	0.12	0.12	0.19	0.18
Er		0.49	0.41	0.19	0.26	0.28	0.47	0.42
Tm		0.06	0.04	0.02	0.02	0.02	0.04	0.04
Yb		0.35	0.32	0.13	0.18	0.18	0.30	0.27
Lu		0.05	0.04	0.02	0.02	0.02	0.04	0.03
Hf		5.88	5.47	0.20	0.30	0.36	5.06	1.61
Ta		0.012	0.005	0.002	0.002	0.002	0.006	0.006
Pb		0.61	1.09	0.19	0.26	0.25	0.61	0.32
Th		0.025	0.067	0.009	0.007	0.007	0.006	0.013
U		0.004	0.067	0.004	0.002	0.002	0.003	0.003

Table 11: Trace element composition (in ppm) of Bellsbank cpx megacrysts

Bellsbank	cpx1	cpx2	cpx3	cpx5	cpx6	cpx9	cpx10	cpx11	cpx12	cpx14	cpx15	cpx16
Sc	70.3	68.4	68.2	42.8	53.3	66.9	62.5	46.5	81.1	47.8	35.2	39.1
V	231	194	223	299	210	270	246	260	373	193	254	322
Ni	284	289	289	281	345	288	311	395	274	310	268	338
Rb	0.945	0.528	0.936	0.094	0.043	0.797	3.924	0.154	0.147	0.358	0.542	0.317
Sr	486	402	577	394	209	441	442	396	428	490	359	288
Y	3.70	2.95	3.53	3.91	2.25	3.57	4.17	3.53	2.82	2.55	3.52	2.18
Zr	91.5	61.1	98.2	42.3	18.4	37.6	52.5	25.8	44.9	44.9	31.9	13.3
Nb	4.30	1.09	2.73	0.80	1.09	0.68	4.97	0.22	0.20	2.05	1.12	0.92
Ba	17.36	20.81	34.55	2.88	3.35	14.77	22.52	0.54	0.80	8.86	13.99	5.42
La	12.64	7.65	12.76	10.26	3.77	7.96	16.21	8.46	5.71	12.31	13.86	11.20
Ce	27.50	22.14	30.75	31.45	10.45	26.79	40.58	30.69	21.51	35.97	36.19	32.57
Pr	3.69	3.31	4.00	4.73	1.68	4.26	5.73	4.87	3.67	5.59	4.53	4.32
Nd	17.15	16.35	18.68	23.16	9.25	21.17	26.18	23.71	18.00	26.29	20.96	19.58
Sm	3.21	2.97	3.27	4.15	2.19	3.63	4.51	4.22	3.22	3.74	3.62	2.56
Eu	0.96	0.82	0.92	1.15	0.65	1.01	1.19	1.10	0.85	0.97	0.99	0.58
Tb	0.22	0.21	0.22	0.29	0.16	0.23	0.29	0.28	0.22	0.22	0.27	0.15
Gd	1.93	2.36	2.54	2.60	1.37	2.16	2.84	2.74	2.02	2.10	2.69	1.60
Dy	1.04	0.97	1.04	1.22	0.68	1.09	1.41	1.20	1.01	0.89	1.13	0.64
Ho	0.16	0.15	0.16	0.19	0.10	0.17	0.20	0.19	0.15	0.12	0.17	0.09
Er	0.34	0.32	0.36	0.34	0.20	0.34	0.40	0.34	0.30	0.21	0.33	0.21
Tm	0.05	0.05	0.05	0.03	0.02	0.05	0.05	0.05	0.03	0.02	0.03	0.02
Yb	0.31	0.25	0.33	0.22	0.13	0.25	0.30	0.25	0.22	0.16	0.19	0.14
Lu	0.04	0.03	0.05	0.02	0.01	0.04	0.03	0.03	0.02	0.02	0.02	0.01
Hf	2.39	2.95	2.87	1.87	1.24	1.80	3.11	2.06	3.48	1.46	1.63	0.53
Ta	0.299	0.065	0.248	0.078	0.047	0.035	0.178	0.005	0.010	0.170	0.086	0.059
Pb	1.32	1.41	1.05	0.61	0.57	1.22	1.58	0.86	1.11	0.43	0.66	1.09
Th	0.594	0.248	0.506	0.166	0.129	0.154	0.746	0.052	0.046	0.627	0.182	0.212
U	0.094	0.051	0.095	0.028	0.027	0.029	0.111	0.042	0.010	0.114	0.036	0.095

Table 11 continued

Bellsbank	cpx21	cpx22	cpx23	cpx24	cpx26	cpx27	cpx28	cpx29	cpx30	cpx31	cpx32	cpx33
Sc	54.4	69.8	71.1	51.5	66.9	72.2	76.9	71.1	59.6	35.8	68.9	30.7
V	238	202	345	292	225	273	292	234	230	135	229	234
Ni	292	315	269	263	315	272	284	260	316	267	241	355
Rb	0.204	1.344	0.004	0.494	0.012	0.018	0.090	0.025	0.066	0.038	0.016	0.121
Sr	313	517	377	437	492	338	420	342	485	616	671	515
Y	2.35	4.40	2.25	3.20	3.54	2.46	4.38	2.48	3.62	5.30	4.50	1.25
Zr	16.7	58.6	36.0	38.8	33.8	39.9	51.3	31.2	53.4	113.2	128.4	19.8
Nb	0.40	3.14	0.09	0.71	0.96	0.10	0.25	0.09	1.35	2.14	1.64	1.20
Ba	7.37	44.36	0.35	16.36	0.20	0.26	1.22	0.23	1.90	0.37	0.42	13.93
La	5.17	17.12	4.59	9.22	13.27	4.04	7.72	4.13	9.89	11.30	12.65	9.58
Ce	18.17	41.85	18.12	31.13	35.52	16.32	29.71	16.41	29.24	29.42	37.38	31.52
Pr	2.90	6.15	3.04	4.66	5.25	2.68	4.85	2.78	4.31	3.95	5.17	5.17
Nd	14.25	30.04	15.11	22.00	26.63	13.84	24.36	14.49	22.58	19.09	24.45	28.50
Sm	2.54	5.77	2.73	3.54	5.25	2.56	4.26	2.70	4.53	3.97	4.37	4.34
Eu	0.70	1.64	0.73	0.95	1.40	0.67	1.11	0.70	1.26	1.27	1.23	0.87
Tb	0.18	0.37	0.17	0.24	0.32	0.19	0.29	0.19	0.29	0.34	0.28	0.12
Gd	1.81	4.12	1.96	3.23	3.47	3.05	5.04	3.18	5.28	5.26	5.09	2.74
Dy	0.83	1.60	0.83	1.11	1.32	0.83	1.44	0.83	1.16	1.59	1.33	0.44
Ho	0.12	0.21	0.12	0.16	0.19	0.13	0.23	0.12	0.17	0.22	0.21	0.06
Er	0.26	0.42	0.27	0.34	0.34	0.26	0.47	0.26	0.36	0.48	0.41	0.11
Tm	0.03	0.05	0.03	0.04	0.04	0.03	0.06	0.03	0.05	0.06	0.05	0.01
Yb	0.18	0.30	0.17	0.26	0.22	0.20	0.35	0.19	0.28	0.38	0.39	0.06
Lu	0.03	0.03	0.02	0.03	0.03	0.02	0.05	0.02	0.03	0.05	0.05	0.01
Hf	1.24	3.11	3.38	2.13	1.85	3.24	3.40	2.49	1.92	3.44	3.35	1.12
Ta	0.025	0.188	0.007	0.043	0.079	0.005	0.018	0.004	0.146	0.186	0.181	0.046
Pb	0.93	1.82	0.93	1.33	0.92	0.85	1.12	0.87	0.76	0.48	0.76	0.93
Th	0.096	0.651	0.024	0.178	0.196	0.021	0.054	0.013	0.151	0.197	0.137	0.328
U	0.010	0.125	0.004	0.038	0.032	0.004	0.010	0.003	0.031	0.040	0.023	0.056

A.2.2. Garnets

Table 12: Trace element composition of Colossus garnet megacrysts

Colossus	gt1	gt2	gt5	gt8	gt9	gt10	gt12	gt16	gt18	gt22
Sc	80.2	79.5	88.8	92.8	81.1	83.3	88.0	99.4	89.8	103.9
V	246	288	229	307	225	247	238	284	279	326
Ni	117	98	119	91	119	116	117	104	113	100
Rb	0.80				0.33	0.08	0.03	0.07	0.04	0.27
Sr	1.25	0.38	0.43	0.40	0.40	0.48	0.52	0.57	0.53	0.59
Y	23.1	21.2	15.9	25.8	15.6	19.6	21.9	29.5	27.8	30.6
Zr	55.7	61.3	30.8	77.8	30.9	47.9	51.5	78.8	72.3	95.1
Nb	0.26	0.18	0.16	0.21	0.19	0.18	0.20	0.19	0.20	0.23
Ba	16.25	0.02	0.01	0.02	0.02	0.02	0.06	0.07	0.01	0.56
La	0.16	0.03	0.04	0.04	0.03	0.04	0.04	0.06	0.05	0.06
Ce	0.52	0.39	0.32	0.38	0.31	0.32	0.42	0.45	0.49	0.54
Pr	0.17	0.13	0.09	0.14	0.10	0.10	0.11	0.15	0.15	0.17
Nd	1.38	1.28	1.00	1.36	0.92	1.11	1.27	1.51	1.62	1.81
Sm	1.23	0.96	0.74	1.21	0.71	0.92	0.95	1.24	1.28	1.40
Eu	0.59	0.52	0.37	0.64	0.35	0.53	0.50	0.65	0.65	0.77
Tb	0.49	0.47	0.32	0.55	0.33	0.42	0.45	0.59	0.55	0.64
Gd	2.30	2.16	1.44	2.41	1.37	1.90	1.98	2.48	2.43	2.90
Dy	3.93	3.77	2.60	4.32	2.53	3.49	3.53	4.88	4.46	5.20
Ho	0.93	0.92	0.61	0.99	0.65	0.76	0.89	1.10	1.03	1.17
Er	2.85	2.53	1.90	3.08	1.86	2.35	2.61	3.54	3.17	3.53
Tm	0.45	0.36	0.32	0.47	0.31	0.36	0.38	0.50	0.49	0.54
Yb	3.36	2.89	2.26	3.47	2.40	2.56	2.92	3.91	3.57	4.14
Lu	0.51	0.42	0.34	0.49	0.35	0.41	0.41	0.52	0.49	0.56
Hf	1.54	1.68	0.84	2.10	0.77	1.32	1.41	2.05	1.84	2.29
Ta	0.016	0.013	0.010	0.017	0.013	0.012	0.011	0.013	0.012	0.022
Pb	0.023	0.004	0.014	0.022	0.012	0.013	0.014	0.032	0.016	0.007
Th	0.022	0.004	0.008	0.005	0.006	0.007	0.016	0.012	0.010	0.012
U	0.016	0.019	0.007	0.013	0.009	0.010	0.024	0.018	0.017	0.017

Table 12 continued

Colossus	gt25	gt27	gt28	gt29	gt30	gt31	gt32	gt38	gt41	gt42
Sc	81.2	82.0	83.4	85.5	81.7	120.1	97.2	101.9	96.7	95.5
V	242	268	312	286	222	342	341	246	286	223
Ni	112	117	97	105	114	19	100	122	106	136
Rb	0.07	0.97	0.46	0.11	0.06	0.33	0.10	0.08	0.14	0.16
Sr	0.44	1.20	0.58	0.43	0.38	0.41	0.46	0.48	0.52	0.45
Y	21.0	24.8	24.9	29.2	13.6	30.7	30.5	17.6	22.5	18.9
Zr	47.6	61.1	73.9	79.6	25.4	150.3	97.1	36.6	69.3	24.5
Nb	0.14	0.17	0.18	0.16	0.15	0.15	0.22	0.18	0.20	0.10
Ba	0.02	3.58	0.48	0.04	0.00	0.47	0.02	0.05		0.02
La	0.03	0.05	0.05	0.03	0.04	0.02	0.05	0.04	0.04	0.04
Ce	0.38	0.41	0.42	0.40	0.32	0.20	0.52	0.36	0.41	0.25
Pr	0.11	0.12	0.14	0.15	0.09	0.07	0.15	0.10	0.13	0.07
Nd	1.22	1.29	1.44	1.45	0.84	0.95	1.83	0.99	1.30	0.83
Sm	0.95	1.09	1.15	1.22	0.64	0.97	1.51	0.80	1.06	0.63
Eu	0.49	0.57	0.61	0.62	0.35	0.52	0.79	0.39	0.55	0.38
Tb	0.42	0.51	0.56	0.59	0.29	0.60	0.65	0.39	0.51	0.37
Gd	1.92	2.23	2.35	2.55	1.33	2.31	3.19	1.57	2.20	1.54
Dy	3.40	4.16	4.19	4.92	2.31	5.07	5.15	2.79	3.69	2.88
Ho	0.82	0.98	0.98	1.16	0.55	1.29	1.22	0.68	0.90	0.69
Er	2.47	2.97	2.95	3.56	1.76	3.90	3.55	2.00	2.75	2.29
Tm	0.38	0.46	0.42	0.56	0.28	0.58	0.48	0.29	0.37	0.32
Yb	2.88	3.18	3.31	3.94	2.11	4.43	3.78	2.29	3.09	2.52
Lu	0.44	0.49	0.48	0.65	0.29	0.64	0.54	0.34	0.40	0.39
Hf	1.31	1.52	1.94	1.94	0.69	3.49	2.63	0.82	1.73	0.60
Ta	0.008	0.011	0.017	0.013	0.009	0.019	0.021	0.013	0.018	0.010
Pb	0.015	0.021	0.007	0.014	0.009	0.018	0.008	0.018	0.016	0.024
Th	0.007	0.013	0.011	0.006	0.008	0.010	0.008	0.009	0.005	0.003
U	0.015	0.015	0.012	0.012	0.013	0.019	0.025	0.016	0.010	0.007

Table 13: Trace element composition of Orapa garnet megacrysts

Orapa high-Cr	gt2	gt4	gt5	gt6	gt8	gt9	gt11	gt20	gt23	gt25
Sc	59.4	85.8	66.4	70.3	65.2	81.0	73.8	76.8	61.7	76.1
V	254	293	277	322	256	288	277	286	247	292
Ni	98.0	99.8	109.9	75.0	123.7	54.6	112.1	93.7	93.6	58.6
Rb	0.154	0.029	0.076	0.024	0.069	0.057	0.016	0.070	0.030	0.067
Sr	0.39	0.44	0.45	0.38	0.54	0.26	0.50	0.419	0.39	0.18
Y	17.0	17.6	19.2	20.8	20.3	19.9	19.4	21.3	18.6	16.1
Zr	47.4	56.2	55.1	60.0	57.4	63.4	59.3	62.7	51.3	62.5
Nb	0.12	0.19	0.19	0.15	0.18	0.13	0.18	0.130	0.15	0.12
Ba	0.018	0.014				0.019	0.020	< b.d.	0.017	
La	0.026	0.040	0.037	0.020	0.031	0.013	0.038	0.047	0.023	0.010
Ce	0.27	0.32	0.34	0.28	0.34	0.15	0.37	0.292	0.29	0.15
Pr	0.09	0.10	0.10	0.08	0.12	0.06	0.12	0.106	0.10	0.06
Nd	0.98	1.10	1.07	0.98	1.08	0.70	1.19	1.054	0.98	0.62
Sm	0.80	0.93	0.91	0.90	0.96	0.71	0.96	0.925	0.92	0.68
Eu	0.43	0.48	0.47	0.50	0.51	0.41	0.53	0.503	0.49	0.38
Tb	0.39	0.38	0.45	0.45	0.41	0.40	0.40	0.476	0.42	0.36
Gd	1.75	1.74	1.89	1.91	1.94	1.68	1.82	2.022	1.86	1.47
Dy	3.16	2.85	3.23	3.47	3.29	3.11	3.38	3.433	3.42	2.86
Ho	0.70	0.66	0.74	0.82	0.78	0.78	0.73	0.779	0.75	0.63
Er	2.15	1.98	2.24	2.57	2.31	2.32	2.19	2.469	2.34	1.92
Tm	0.32	0.27	0.35	0.40	0.35	0.32	0.28	0.376	0.32	0.28
Yb	2.44	2.21	2.49	2.89	2.62	2.63	2.34	2.682	2.46	2.15
Lu	0.33	0.31	0.35	0.40	0.38	0.36	0.34	0.381	0.34	0.31
Hf	1.35	1.38	1.33	1.60	1.44	1.48	1.42	1.604	1.36	1.60
Ta	0.011	0.010	0.017	0.014	0.012	0.010	0.018	0.009	0.012	0.010
Pb	0.006	0.018	0.005	0.005	0.007	0.009	0.007	0.016	0.004	0.006
Th	0.007	0.006	0.010	0.004	0.007	0.003	0.007	0.006	0.005	0.002
U	0.016	0.016	0.011	0.011	0.011	0.009	0.013	0.017	0.014	0.011

Table 13 continued

Orapa	gt26	gt58	gt63	gt88	gt102	gt104	**low-Cr**	gt54	gt44	gt13
Sc	85.3	58.3	65.2	75.6	79.5	86.3		56.7	124.2	65.4
V	301	229	259	273	338	256		224	196	290
Ni	54.0	126.1	112.1	105.9	69.5	57.0		53.0	23.4	50.3
Rb	0.071	0.017	0.014	0.043	0.015	0.072		0.058	0.028	0.064
Sr	0.28	0.47	0.45	0.53	0.22	0.31		0.25	0.17	0.64
Y	22.1	17.0	20.6	18.3	11.7	18.0		19.9	48.7	27.2
Zr	76.2	47.0	54.1	55.5	48.2	56.6		59.2	191.9	140.0
Nb	0.10	0.17	0.15	0.16	0.17	0.18		0.10	0.14	0.15
Ba				0.021	0.024					42.4
La	0.006	0.031	0.028	0.041	0.012	0.020		0.015	0.021	0.054
Ce	0.18	0.31	0.30	0.33	0.18	0.20		0.20	0.22	0.23
Pr	0.07	0.11	0.09	0.12	0.06	0.09		0.06	0.08	0.06
Nd	0.80	1.03	1.02	1.11	0.71	1.06		0.78	1.14	0.90
Sm	0.82	0.81	0.91	0.91	0.67	0.90		0.73	1.35	1.14
Eu	0.47	0.41	0.49	0.51	0.34	0.53		0.42	0.82	0.67
Tb	0.51	0.37	0.45	0.43	0.26	0.46		0.41	0.96	0.59
Gd	1.88	1.60	1.85	1.91	1.29	1.83		1.64	3.37	2.57
Dy	3.74	2.78	3.34	3.20	2.13	3.11		3.57	8.26	4.82
Ho	0.86	0.65	0.83	0.70	0.46	0.68		0.86	2.17	1.08
Er	2.58	1.97	2.40	2.02	1.47	2.01		2.70	6.51	3.12
Tm	0.38	0.29	0.35	0.32	0.22	0.31		0.42	0.98	0.41
Yb	3.01	2.10	2.61	2.23	1.57	2.33		3.19	7.98	3.08
Lu	0.42	0.31	0.36	0.32	0.23	0.32		0.44	1.07	0.38
Hf	1.98	1.19	1.38	1.34	1.17	1.26		1.60	4.20	3.07
Ta	0.014	0.011	0.012	0.016	0.022	0.021		0.010	0.020	0.007
Pb	0.006	0.012	0.006	0.014	0.024	0.028		0.004	0.008	0.011
Th	0.006	0.010	0.006	0.010	0.007	0.005		0.005	0.004	0.014
U	0.009	0.007	0.013	0.014	0.011	0.018		0.012	0.018	0.018

Table 14: Trace element composition of Bellsbank garnets

Bellsbank	gt1	gt2	gt4	gt9	gt10	gt12
Sc	82.1	73.5	31.2	62.6	65.8	66.2
V	114	148	143	198	119	207
Ni	20.2	26.2	52.2	44.7	18.5	38.4
Rb	0.024	0.052	0.014	0.028		0.028
Sr	0.21	0.14	0.15	0.11	0.12	0.16
Y	14.09	8.59	9.66	16.70	8.19	15.47
Zr	24.18	15.84	10.07	31.88	4.50	27.81
Nb	0.07	0.08	0.02	0.12	0.13	0.01
Ba	0.020		0.016	0.016	0.014	0.050
La	0.021	0.008	0.009	0.008	0.013	0.016
Ce	0.21	0.13	0.09	0.10	0.23	0.11
Pr	0.08	0.06	0.03	0.03	0.08	0.04
Nd	1.11	0.72	0.35	0.44	0.66	0.65
Sm	1.13	0.64	0.34	0.45	0.17	0.64
Eu	0.61	0.30	0.27	0.26	0.11	0.34
Tb	0.36	0.19	0.23	0.27	0.14	0.35
Gd	1.98	1.04	0.91	1.07	0.52	1.50
Dy	2.86	1.54	1.71	2.46	1.17	2.87
Ho	0.61	0.41	0.43	0.70	0.34	0.68
Er	2.38	1.46	1.61	3.13	1.44	3.14
Tm	0.31	0.18	0.18	0.41	0.19	0.33
Yb	2.11	1.48	1.29	3.49	1.55	2.51
Lu	0.33	0.23	0.18	0.55	0.23	0.38
Hf	0.26	0.20	0.19	0.65	0.06	0.54
Ta	0.010	0.006	0.003	0.014	0.003	0.002
Pb	0.010	0.005	0.004	0.019	0.007	0.022
Th	0.020	0.005	0.003	0.008	0.010	0.015
U	0.049	0.032	0.006	0.008	0.036	0.005

A.3. Sr isotope composition (clinopyroxene)

Table 15: Measured Sr isotope composition of Colossus and Orapa cpx megacrysts

Colossus	$^{87}Sr/^{86}Sr$	**Orapa Cr-rich**	$^{87}Sr/^{86}Sr$
cpx1	0.7032	cpx2	0.7037
Cpx2	0.7029	cpx3	0.7030
cpx3	0.7028	cpx15	0.7032
cpx4	0.7031	cpx16	0.7036
cpx5	0.7034	cpx21	0.7057
cpx11	0.7030	cpx34	0.7051
cpx17	0.7030	cpx55	0.7026
cpx18	0.7030	cpx57	0.7029
cpx19	0.7030	cpx69	0.7049
cpx21	0.7027	cpx73	0.7028
cpx22	0.7042	cpx80	0.7030
cpx23	0.7033		
		Orapa Cr-poor	
		cpx1	0.7042
		cpx18	0.7031
		cpx19	0.7032
		cpx38	0.7030
		cpx45	0.7030
		cpx46	0.7029
		cpx48	0.7025
		cpx56	0.7029
		cpx70	0.7030
		cpx74	0.7031
		cpx78	0.7029

Table 16: Measured Sr isotope composition of Kalkput and Bellsbank cpx megacrysts

Kalkput	$^{87}Sr/^{86}Sr$	**Bellsbank**	$^{87}Sr/^{86}Sr$
cpx 1	0.7076	cpx1	0.7101
cpx 2	0.7074	Cpx2	0.7095
cpx 3	0.7073	Cpx9	0.7081
cpx4	0.7076	Cpx11	0.7083
cpx 5	0.7073	Cpx12	0.7078
cpx 6	0.7071	cpx21	0.7084
cpx 7	0.7076	cpx23	0.7078
		cpx24	0.7078
		cpx28	0.7076
		cpx29	0.7079
		cpx30	0.7129
		cpx31	0.7084
		cpx32	0.7094
		cpx33	0.7172

A.2. KASAI XENOCRYSTS

A.2.1. Peridotitic clinopyroxenes

Table 17: Major element composition of Mbuji-Mayi and Tshibwe peridotitic cpx

BM Group 1	SiO_2	TiO_2	Al_2O_3	Cr_2O_3	FeO	MnO	MgO	CaO	Na_2O	K_2O	Total	Ca#	Mg#	Cr#
BM-CPX1-g1	54.69	0.21	2.69	1.44	2.88	0.13	16.06	18.44	2.36	0.03	98.91	45.2	90.9	26.5
BM-CPX1-g3	55.21	0.10	2.19	4.00	2.53	0.11	16.67	16.30	2.67	0.06	99.82	41.3	92.1	55.1
BM-CPX1-g4	54.88	0.12	2.60	2.44	3.08	0.12	16.27	17.14	2.52	0.03	99.19	43.1	90.4	38.7
BM-CPX1-g6	54.77	0.21	1.54	0.89	4.05	0.14	18.45	18.03	1.46	0.03	99.55	41.2	89.0	27.9
BM-CPX1-g7	54.80	0.21	2.30	0.89	3.90	0.12	16.98	18.72	1.91	0.04	99.85	44.2	88.6	20.6
BM-CPX1-g8	55.14	0.20	2.67	2.36	3.18	0.11	16.03	17.51	2.70	0.02	99.89	44.0	90.0	37.3
BM-CPX1-g10	54.86	0.24	1.64	2.86	3.00	0.12	17.46	17.45	2.03	0.05	99.69	41.8	91.2	53.9
BM-CPX1-g11	55.22	0.20	2.01	1.73	3.07	0.14	17.64	18.00	2.02	0.05	100.05	42.3	91.1	36.6
BM-CPX1-g13	55.15	0.27	1.80	1.58	3.09	0.15	18.37	17.99	1.79	0.04	100.20	41.3	91.4	37.1
BM-CPX1-g19	55.56	0.13	2.72	5.34	2.14	0.13	14.51	15.69	3.60	0.01	99.80	43.7	92.4	56.9
BM-CPX1-g20	54.68	0.23	2.27	0.95	3.70	0.12	17.05	18.48	1.87	0.05	99.40	43.8	89.1	21.9
BM-CPX1-g21	53.64	0.14	3.96	1.27	3.00	0.11	16.09	20.14	1.64	0.01	99.98	47.4	90.5	17.8
BM-CPX1-g22	55.47	0.21	3.20	2.25	3.10	0.10	15.07	16.74	2.92	0.01	99.04	44.4	89.6	32.0
BM Group 2														
BM-CPX1-g2	54.71	0.15	0.90	3.01	2.89	0.12	16.05	19.39	2.09	0.01	99.31	46.5	90.8	69.2
BM-CPX1-g5	54.69	0.20	1.74	1.74	3.09	0.11	16.82	19.18	1.85	0.03	99.44	45.0	90.7	40.1
BM-CPX1-g9	55.12	0.13	0.99	1.22	3.86	0.11	16.90	20.41	1.52	0.02	100.28	46.5	88.6	45.3
BM-CPX1-g12	55.10	0.16	1.75	3.75	1.93	0.12	15.80	18.30	2.45	0.01	99.37	45.4	93.6	59.0
BM-CPX1-g14	54.48	0.15	1.72	3.63	2.46	0.12	15.87	18.73	2.29	0.02	99.45	45.9	92.0	58.6
BM-CPX1-g17	54.80	0.17	1.30	2.23	2.84	0.11	16.67	20.30	1.67	0.02	100.09	46.7	91.3	53.4
BM-CPX1-g18	55.06	0.17	1.34	2.18	2.89	0.11	16.53	20.11	1.64	0.02	100.04	46.6	91.1	52.1
TB														
TB-CPX2-g1	55.12	0.12	1.01	1.38	3.02	0.07	16.70	21.10	1.37	0.01	99.91	47.6	90.8	47.8
TB-CPX2-g3	55.30	0.12	0.96	1.23	3.26	0.11	16.47	21.51	1.33	0.02	100.29	48.4	90.0	46.4
TB-CPX2-g33	54.93	0.14	1.58	1.76	2.91	0.09	16.60	19.76	1.76	0.02	99.54	46.1	91.0	42.7
TB-CPX2-g39	54.53	0.06	0.52	2.16	2.43	0.05	16.69	21.77	1.24	0.01	99.45	48.4	92.4	73.7
TB-CPX2-g40	54.71	0.23	2.62	3.78	2.73	0.11	15.19	16.73	3.04	0.01	99.13	44.2	90.8	49.2
TB-CPX2-g42	54.59	0.18	1.75	2.80	2.18	0.07	16.18	20.05	1.85	0.02	99.66	47.1	93.0	51.7
TB-CPX1-g14	55.25	0.18	1.11	1.53	3.05	0.13	16.81	20.72	1.41	0.03	100.21	47.0	90.8	48.1
TB-CPX1-g21	55.21	0.13	0.85	1.04	3.34	0.12	16.86	21.36	1.18	0.01	100.10	47.7	90.0	45.2

Table 18: Trace element composition of Mbuji-Mayi (BM) and Tshibwe (TB) peridotitic cpx

	Group 1								
	BM-cpx1-g1	BM-cpx1-g3	BM-cpx1-g4	BM-cpx1-g6	BM-cpx1-g7	BM-cpx1-g8	BM-cpx1-g10	BM-cpx1-g11	BM-cpx1-g13
Sc	38.27	14.73	18.85	13.43	24.72	22.10	14.65	14.26	16.34
V	302	212	204	268	282	241	263	318	291
Ni	249	353	332	334	293	312	390	413	432
Rb	< b.d.	0.016	0.016	0.041	0.015	0.068	0.009	0.024	0.068
Sr	317	279	311	84	183	299	137	286	115
Y	4.02	1.12	2.66	1.55	2.11	4.43	1.52	1.40	1.97
Zr	34.2	14.0	26.7	3.70	11.0	43.0	7.83	9.06	6.09
Nb	0.37	0.29	0.27	0.10	0.22	0.32	0.12	0.12	0.11
Ba	0.21	0.23	0.15	0.16	0.44	0.65	0.12	0.14	0.10
La	6.63	3.42	4.81	1.30	2.89	5.45	1.69	5.22	1.61
Ce	23.7	12.4	18.4	4.70	10.4	21.4	6.44	17.0	6.18
Pr	3.80	2.05	3.22	0.77	1.76	3.76	1.11	2.54	1.03
Nd	19.7	10.9	18.0	4.27	9.23	21.2	6.08	12.2	5.76
Sm	4.16	2.28	4.14	1.07	2.12	5.13	1.48	2.58	1.40
Eu	1.26	0.66	1.24	0.35	0.66	1.62	0.48	0.64	0.45
Tb	0.32	0.12	0.27	0.10	0.17	0.41	0.12	0.13	0.13
Gd	3.14	1.54	3.01	0.93	1.50	3.63	1.12	1.19	1.15
Dy	1.34	0.44	1.07	0.49	0.74	1.61	0.55	0.58	0.55
Ho	0.19	0.05	0.14	0.08	0.09	0.21	0.06	0.06	0.07
Er	0.43	0.09	0.28	0.19	0.23	0.48	0.16	0.16	0.22
Tm	0.04	0.01	0.02	0.01	0.02	0.02	0.01	0.01	0.02
Yb	0.22	0.04	0.09	0.07	0.10	0.17	0.06	0.04	0.08
Lu	0.02	0.00	0.01	0.01	0.01	0.01	0.00	0.01	0.01
Hf	1.74	0.86	1.56	0.29	0.83	2.47	0.61	0.60	0.42
Ta	0.045	0.016	0.025	0.007	0.013	0.041	0.009	0.014	0.010
Pb	0.45	0.29	0.31	0.15	0.25	0.28	0.18	0.37	0.16
Th	0.058	0.039	0.038	0.012	0.033	0.067	0.019	0.015	0.010
U	0.017	0.016	0.013	0.003	0.008	0.017	0.006	0.005	0.004

Table 18 continued

					Group 2				
	BM-cpx1-g19	BM-cpx1-g20	BM-cpx1-g21	BM-cpx1-g22	BM-cpx1-g2	BM-cpx1-g5	BM-cpx1-g9	BM-cpx1-g12	BM-cpx1-g14
Sc	24.88	23.56	78.48	31.96	53.67	33.43	61.18	54.69	46.09
V	562	270	213	303	227	235	264	269	282
Ni	265	303	278	303	272	396	233	275	286
Rb	0.010	0.036	0.009	0.376	0.193	1.500	0.163	0.041	0.012
Sr	353	171	401	370	433	179	348	403	308
Y	2.35	2.05	11.55	5.26	5.24	2.71	3.77	3.26	2.93
Zr	41.3	9.77	161	57.0	78.8	18.1	47.9	36.8	32.4
Nb	0.31	0.24	0.11	1.13	0.94	2.78	1.03	0.52	0.21
Ba	0.08	0.16	0.03	7.92	1.11	11.4	2.23	0.35	0.42
La	5.12	2.99	30.3	7.52	8.20	5.56	6.65	6.72	3.13
Ce	20.5	9.99	110	28.6	31.0	16.1	22.8	26.6	12.9
Pr	3.66	1.57	16.7	4.88	5.17	2.14	3.71	4.41	2.40
Nd	20.4	8.37	76.9	26.9	27.5	11.0	19.9	22.9	14.4
Sm	4.66	1.91	12.6	6.05	5.88	2.35	4.28	4.55	3.53
Eu	1.36	0.63	3.18	1.81	1.80	0.72	1.30	1.30	1.09
Tb	0.29	0.15	0.76	0.43	0.45	0.18	0.32	0.30	0.26
Gd	2.68	1.28	6.38	3.73	4.58	1.66	2.93	2.92	2.49
Dy	1.04	0.72	3.04	1.79	1.86	0.91	1.33	1.18	1.09
Ho	0.11	0.10	0.51	0.26	0.26	0.13	0.18	0.17	0.14
Er	0.27	0.28	1.79	0.75	0.55	0.38	0.47	0.38	0.36
Tm	0.01	0.02	0.14	0.05	0.04	0.03	0.03	0.03	0.02
Yb	0.08	0.12	0.93	0.26	0.27	0.17	0.18	0.16	0.11
Lu	0.00	0.01	0.12	0.03	0.03	0.02	0.02	0.01	0.01
Hf	2.31	0.72	6.88	2.69	3.49	1.22	2.81	2.02	2.50
Ta	0.033	0.021	0.023	0.070	0.061	0.093	0.047	0.057	0.015
Pb	0.28	0.33	4.73	0.60	0.50	0.60	0.44	0.47	0.26
Th	0.056	0.029	0.725	0.170	0.108	0.250	0.122	0.053	0.028
U	0.016	0.006	0.104	0.051	0.019	0.054	0.039	0.009	0.010

Table 18 continued

	BMcpx1-g17	BMcpx1-g18	**Tshibwe** TB-cpx1-g14	TB-cpx1-g21	TB-cpx2-g1	TB-cpx2-g3	TB-cpx2-g33	TB-cpx2-g39	TB-cpx2-g40	TB-cpx2-g42
Sc	30.90	32.55	34.4	49.0	32.8	58.3	27.8	54.6	23.3	20.9
V	289	271	244	224	271	318	226	201	253	244
Ni	281	280	248	274	226	223	282	303	302	322
Rb	0.215	0.205	0.013	0.026	0.039	0.011	0.024	0.017	< b.d.	0.376
Sr	172	179	176	228	169	220	185	170	522	164
Y	1.54	1.67	1.98	2.28	1.86	2.54	2.10	1.59	2.12	1.82
Zr	13.8	15.3	17.0	22.4	14.5	27.3	14.8	20.6	41.2	11.6
Nb	0.70	0.28	0.12	0.12	0.11	0.15	0.23	0.13	0.37	0.81
Ba	2.39	1.31	0.13	0.07	0.13	0.15	0.22	0.13	0.24	7.73
La	2.81	2.63	2.92	3.05	2.52	3.30	2.96	1.98	10.9	7.91
Ce	9.85	9.72	10.3	12.3	9.34	13.0	11.0	7.45	38.3	15.5
Pr	1.59	1.69	1.79	2.12	1.60	2.23	1.86	1.33	6.38	2.02
Nd	8.38	8.60	9.42	11.9	8.30	11.9	9.89	7.09	32.5	8.94
Sm	1.76	1.81	2.06	2.58	1.89	2.77	2.13	1.66	5.73	1.63
Eu	0.56	0.58	0.65	0.79	0.57	0.83	0.68	0.57	1.42	0.58
Tb	0.15	0.13	0.17	0.21	0.14	0.22	0.17	0.15	0.26	0.14
Gd	1.13	1.24	1.71	2.73	1.30	1.89	1.76	1.60	3.30	1.38
Dy	0.58	0.63	0.71	0.90	0.65	0.90	0.75	0.60	0.83	0.62
Ho	0.09	0.07	0.12	0.12	0.08	0.13	0.11	0.10	0.11	0.07
Er	0.20	0.22	0.20	0.21	0.26	0.31	0.24	0.17	0.19	0.20
Tm	0.02	0.01	0.02	0.01	0.02	0.03	0.02	0.01	0.02	0.02
Yb	0.07	0.07	0.09	0.11	0.09	0.13	0.11	0.08	0.08	0.07
Lu	0.01	0.01	0.01	0.01	0.01	0.01	0.01	0.01	0.01	0.00
Hf	1.13	1.04	1.19	1.75	1.05	2.03	1.03	1.60	2.29	0.90
Ta	0.048	0.022	0.012	0.011	0.011	0.013	0.010	0.013	0.036	0.052
Pb	0.32	0.26	0.23	0.27	0.26	0.34	0.24	0.16	0.69	0.42
Th	0.073	0.033	0.019	0.021	0.012	0.021	0.031	0.019	0.084	0.089
U	0.017	0.008	0.004	0.003	0.002	0.006	0.006	0.004	0.012	0.020

Table 19: Measured Sr isotope composition of Mbuji-Mayi (BM) and Tshibwe (TB) peridotitic cpx

Mbuji-Mayi	$^{87}Sr/^{86}Sr$	Tshibwe	$^{87}Sr/^{86}Sr$
Group 1			
BM-CPX1-g1	0.7031	TB-CPX2-g1	0.7037
BM-CPX1-g3	0.7037	TB-CPX2-g3	0.7040
BM-CPX1-g4	0.7039	TB-CPX2-g33	0.7036
BM-CPX1-g6	0.7049	TB-CPX2-g39	0.7036
BM-CPX1-g7	0.7038	TB-CPX2-g40	0.7053
BM-CPX1-g8	0.7034	TB-CPX2-g42	0.7040
BM-CPX1-g10	0.7048	TB-CPX1-g14	0.7039
BM-CPX1-g11	0.7036	TB-CPX1-g21	0.7031
BM-CPX1-g13	0.7038		
BM-CPX1-g19	0.7037		
BM-CPX1-g20	0.7037		
BM-CPX1-g21	0.7048		
BM-CPX1-g22	0.7038		
Group 2			
BM-CPX1-g2	0.7036		
BM-CPX1-g5	0.7037		
BM-CPX1-g9	0.7036		
BM-CPX1-g12	0.7052		
BM-CPX1-g14	0.7034		
BM-CPX1-g17	0.7032		
BM-CPX1-g18	0.7045		

A.2.2. Eclogitic garnets

Table 20: Major element composition of Mbuji-Mayi eclogitic garnets

BM Low-Ca	SiO_2	TiO_2	Al_2O_3	Cr_2O_3	FeO	MnO	MgO	CaO	Na_2O	Total	Ca#	Mg#
BM-GAR2-gt3	42.15	0.49	23.36	0.21	9.20	0.33	20.11	3.59	0.09	99.5	11.4	79.6
BM-GAR2-gt4	41.63	0.57	23.15	0.11	12.05	0.37	18.37	3.58	0.11	99.9	12.3	73.1
BM-GAR2-gt7	39.96	0.14	23.50	0.11	16.12	0.39	14.57	4.36	0.09	99.2	17.7	61.7
BM-GAR2-gt8	40.82	0.31	23.17	0.09	16.45	0.44	14.33	4.04	0.13	99.8	16.8	60.8
BM-GAR2-gt9	41.45	0.40	23.54	0.11	11.96	0.36	18.82	2.98	0.10	99.7	10.2	73.7
BM-GAR2-gt10	40.26	0.21	23.26	0.02	16.93	0.40	13.83	4.73	0.11	99.7	19.7	59.3
BM-GAR2-gt11	41.39	0.62	22.58	0.99	9.00	0.34	20.11	4.19	0.09	99.3	13.0	79.9
BM-GAR2-gt12	39.74	0.29	23.01	0.13	18.79	0.48	12.32	5.16	0.14	100.1	23.1	53.9
BM-GAR2-gt13	40.22	0.24	22.89	0.15	18.61	0.50	12.44	5.18	0.12	100.4	23.0	54.4
BM-GAR2-gt14	41.57	0.36	23.38	0.38	8.99	0.53	18.73	5.19	0.10	99.2	16.6	78.8
BM-GAR2-gt15	41.95	0.51	23.17	0.40	8.64	0.36	20.47	3.99	0.08	99.6	12.3	80.8
BM-GAR2-gt16	41.08	0.26	23.32	0.15	12.47	0.47	15.91	5.53	0.08	99.3	20.0	69.4
BM-GAR2-gt17	41.70	0.54	22.65	0.75	9.00	0.34	20.33	3.81	0.07	99.2	11.9	80.1
BM-GAR2-gt18	40.82	0.33	23.12	0.14	14.96	0.33	15.37	4.25	0.15	99.5	16.6	64.7
BM-GAR2-gt19	41.67	0.51	23.30	0.20	8.99	0.37	20.01	4.10	0.07	99.2	12.8	79.9
BM-GAR2-gt20	40.29	0.25	23.11	0.07	17.17	0.40	13.53	4.99	0.11	99.9	20.9	58.4
BM-GAR2-gt22	40.70	0.27	23.06	0.07	17.43	0.39	13.07	5.21	0.11	100.3	22.3	57.2
BM-GAR2-gt23	39.37	0.29	23.13	0.12	17.22	0.38	13.52	5.21	0.14	99.4	21.7	58.3
BM-GAR2-gt25	41.16	0.25	23.45	0.14	12.98	0.41	17.66	3.65	0.10	99.8	12.9	70.8
BM-GAR2-gt26	40.51	0.28	23.09	0.02	16.61	0.40	14.44	4.10	0.13	99.6	16.9	60.8
BM-GAR2-gt27	40.70	0.26	23.18	0.06	16.56	0.36	14.31	4.28	0.10	99.8	17.7	60.6
BM-GAR2-gt28	40.68	0.19	23.34	0.14	16.32	0.35	14.72	3.96	0.12	99.8	16.2	61.6
BM-GAR2-gt30	40.64	0.25	23.21	0.17	16.71	0.43	14.55	4.26	0.07	100.3	17.4	60.8
BM-GAR2-gt32	40.70	0.25	23.27	0.03	16.24	0.38	14.36	4.17	0.10	99.5	17.3	61.2
BM-GAR2-gt33	41.20	0.57	23.41	0.13	10.82	0.38	18.83	3.89	0.05	99.3	12.9	75.6
BM-GAR2-gt34	41.21	0.38	23.77	0.07	9.24	0.36	20.09	3.96	0.09	99.2	12.4	79.5
BM-GAR2-gt36	40.62	0.28	23.00	0.19	16.22	0.39	14.10	4.37	0.12	99.3	18.2	60.8
BM-GAR2-gt38	41.41	0.63	23.41	0.11	9.31	0.37	19.77	4.50	0.11	99.6	14.1	79.1
BM Med-ca												
BM-GAR2-gt2	39.79	0.07	22.80	0.01	22.22	0.44	9.63	5.44	0.03	100.4	28.8	43.6
BM-GAR2-gt5	40.36	0.14	23.34	0.04	17.62	0.37	12.18	5.90	0.12	100.1	25.8	55.2
BM-GAR2-gt6	40.81	0.21	23.34	0.12	13.27	0.53	13.50	8.15	0.09	100.0	30.2	64.4
BM-GAR2-gt24	39.64	0.62	22.71	0.01	13.94	0.38	14.26	7.17	0.19	98.9	26.5	64.6
BM-GAR2-gt29	40.03	0.20	23.01	0.08	18.72	0.42	10.97	6.75	0.10	100.3	30.6	51.1
BM-GAR2-gt31	40.30	0.27	23.38	0.10	13.42	0.43	12.62	9.05	0.08	99.6	34.0	62.6
BM-GAR2-gt37	40.28	0.29	22.90	0.06	18.56	0.41	11.79	5.61	0.13	100.0	25.5	53.1
BM High-Ca												
BM-GAR2-gt1	39.56	0.08	22.81	0.09	19.68	0.45	9.88	7.78	0.03	100.3	36.1	47.2
BM-GAR2-gt21	38.98	0.09	22.55	0.08	20.78	0.41	8.35	8.97	0.06	100.3	43.5	41.7
BM-GAR2-gt35	38.96	0.07	22.66	0.08	22.74	0.71	7.84	6.94	0.00	100.0	38.9	38.1

Table 21: Major element composition of Tshibwe eclogitic garnets

TB Low-Ca	SiO_2	TiO_2	Al_2O_3	Cr_2O_3	FeO	MnO	MgO	CaO	Na_2O	Total	Ca#	Mg#
TB-GAR2-gt1	42.29	0.46	23.73	0.20	9.00	0.42	19.92	3.89	0.11	100.0	12.3	79.8
TB-GAR2-gt2	41.81	0.35	23.68	0.05	10.38	0.38	19.58	3.67	0.07	100.0	11.9	77.1
TB-GAR2-gt3	42.26	0.31	23.61	0.16	11.15	0.35	18.73	3.86	0.08	100.5	12.9	75.0
TB-GAR2-gt4	42.16	0.38	23.49	0.21	9.93	0.42	19.03	3.91	0.07	99.6	12.9	77.3
TB-GAR2-gt7	42.06	0.50	23.77	0.07	9.02	0.29	20.56	3.25	0.13	99.6	10.2	80.2
TB-GAR2-gt8	42.01	0.54	23.37	0.29	9.74	0.42	20.16	3.50	0.12	100.1	11.1	78.7
TB-GAR2-gt9	42.22	0.50	23.42	0.24	8.12	0.35	20.46	3.90	0.05	99.2	12.0	81.8
TB-GAR2-gt10	41.99	0.46	23.52	0.22	10.05	0.34	19.58	3.66	0.10	99.9	11.8	77.6
TB-GAR2-gt11	42.06	0.43	24.04	0.03	9.08	0.27	20.03	3.64	0.12	99.7	11.5	79.7
TB-GAR2-gt13	40.86	0.23	23.24	0.11	16.16	0.32	15.04	4.29	0.09	100.3	17.0	62.4
TB-GAR2-gt14	41.14	0.21	23.76	0.05	13.57	0.35	17.00	3.34	0.09	99.5	12.4	69.1
TB-GAR2-gt15	41.80	0.39	23.41	0.56	9.20	0.42	19.99	3.73	0.08	99.6	11.8	79.5
TB-GAR2-gt16	41.50	0.36	23.66	0.13	10.89	0.37	19.46	3.27	0.10	99.7	10.8	76.1
TB-GAR2-gt18	41.04	0.26	23.08	0.46	14.77	0.44	15.60	4.05	0.13	99.8	15.7	65.3
TB-GAR2-gt19	42.22	0.40	23.94	0.06	9.36	0.34	20.30	3.32	0.08	100.0	10.5	79.4
TB-GAR2-gt20	41.62	0.36	23.44	0.26	10.14	0.29	19.67	3.74	0.07	99.6	12.0	77.6
TB-GAR2-gt21	41.03	0.31	23.29	0.28	14.75	0.39	16.58	3.48	0.05	100.1	13.1	66.7
TB-GAR2-gt22	41.36	0.40	23.72	0.03	11.21	0.32	19.28	3.15	0.10	99.6	10.5	75.4
TB-GAR2-gt23	42.69	0.47	23.88	0.07	7.79	0.38	20.59	3.13	0.12	99.1	9.8	82.5
TB-GAR2-gt24	41.71	0.28	23.69	0.21	10.74	0.34	18.96	3.68	0.05	99.6	12.2	75.9
TB-GAR2-gt25	41.11	0.23	23.94	0.03	9.61	0.24	18.52	5.50	0.07	99.2	17.6	77.5
TB-GAR2-gt27	40.75	0.30	23.58	0.08	13.01	0.32	17.87	3.73	0.10	99.7	13.0	71.0
TB-GAR2-gt28	40.67	0.24	23.52	0.11	13.22	0.40	16.82	4.33	0.10	99.4	15.6	69.4
TB-GAR2-gt29	41.48	0.19	23.67	0.24	8.56	0.30	19.15	5.98	0.03	99.6	18.3	79.9
TB-GAR2-gt30	42.00	0.32	23.83	0.32	8.72	0.43	20.36	3.58	0.06	99.6	11.2	80.6
TB-GAR2-gt31	41.74	0.61	22.96	0.23	8.86	0.38	20.09	4.22	0.07	99.2	13.1	80.2
TB-GAR2-gt35	41.67	0.59	22.88	0.73	7.45	0.34	21.51	4.11	0.07	99.3	12.1	83.7
TB-GAR2-gt36	40.36	0.24	23.11	0.54	14.45	0.34	16.63	3.80	0.10	99.6	14.1	67.2
TB-GAR2-gt37	40.55	0.24	23.54	0.11	15.28	0.41	16.69	3.06	0.10	100.0	11.6	66.0
TB-GAR2-gt38	41.63	0.24	23.65	0.12	13.92	0.42	16.47	4.00	0.07	100.5	14.8	67.8
TB-GAR2-gt39	41.78	0.35	23.65	0.07	9.08	0.34	19.66	3.71	0.08	98.7	11.9	79.4
TB-GAR2-gt40	41.56	0.31	23.57	0.16	10.98	0.35	18.82	3.44	0.10	99.3	11.6	75.3
TB-GAR2-gt42	41.33	0.24	23.86	0.31	8.69	0.44	20.52	3.85	0.07	99.3	11.9	80.8
TB-GAR2-gt43	41.90	0.61	23.33	0.11	8.14	0.37	20.86	4.09	0.07	99.5	12.3	82.0
TB-GAR2-gt44	41.50	0.38	23.38	0.48	9.42	0.38	19.82	4.20	0.04	99.6	13.2	78.9
TB Med-Ca												
TB-GAR2-gt5	41.50	0.08	23.83	0.25	10.51	0.34	16.49	7.32	0.02	100.3	24.2	73.7
TB-GAR2-gt6	40.98	0.05	23.99	0.01	11.82	0.19	13.58	9.68	0.02	100.3	33.9	67.2
TB-GAR2-gt12	40.26	0.18	23.31	0.06	14.50	0.79	13.43	7.24	0.13	99.9	27.9	62.3
TB-GAR2-gt17	41.06	0.03	24.01	0.00	12.53	0.26	14.92	7.57	0.02	100.4	26.7	68.0
TB-GAR2-gt26	40.15	0.07	23.69	0.01	13.29	0.28	13.48	8.70	0.01	99.7	31.7	64.4
TB-GAR2-gt34	39.50	0.26	23.08	0.06	18.65	0.37	12.35	5.12	0.10	99.5	22.9	54.1
TB High-Ca												
TB-GAR2-gt32	39.92	0.15	23.35	0.11	16.72	0.34	10.75	9.46	0.07	100.8	38.7	53.4
TB-GAR2-gt33	40.25	0.14	23.20	0.09	11.68	0.31	11.95	11.70	0.08	99.4	41.3	64.6
TB-GAR2-gt41	40.15	0.23	23.32	0.04	10.66	0.27	10.73	14.27	0.10	99.8	48.9	64.2

Table 22: Trace element composition of Mbuji-Mayi eclogitic garnets

	BM Low-Ca											
	BM-GAR2-g3	BM-GAR2-g4	BM-GAR2-g7	BM-GAR2-g8	BM-GAR2-g9	BM-GAR2-g10	BM-GAR2-g11	BM-GAR2-g12	BM-GAR2-g13	BM-GAR2-g14	BM-GAR2-g15	BM-GAR2-g16
Sc	27.8	25.9	33.8	37.8	28.3	31.8	41.3	36.3	38.4	81.8	54.0	59.7
V	134.0	104.5	70.77	110.8	77.68	67.12	248.0	102.7	104.2	181.9	259.4	106.9
Ni	50.7	55.2	18.5	47.8	45.7	11.9	71.6	21.1	20.6	29.2	52.3	11.0
Rb	0.042	0.020	0.077	0.052	0.005	0.051	0.007	0.040	0.026	< b.d.	0.021	0.006
Sr	0.15	0.22	0.30	0.53	0.16	0.25	0.19	0.21	0.25	0.19	0.15	0.27
Y	14.9	14.3	12.9	12.1	12.9	14.4	9.1	16.9	20.5	20.5	10.2	22.1
Zr	47.8	30.7	4.96	5.38	17.8	8.48	26.0	3.68	3.98	36.1	30.0	33.4
Nb	0.036	0.053	0.015	0.004	0.084	0.026	0.076	0.021	0.019	0.098	0.096	0.133
Ba	0.006	0.023	0.003	< b.d.	0.022	0.018	0.006	0.005	0.011	0.004	0.021	0.022
La	0.003	0.011	0.003	0.008	0.006	0.003	0.016	0.002	0.004	0.008	0.011	0.012
Ce	0.060	0.094	0.057	0.063	0.086	0.048	0.115	0.036	0.032	0.156	0.124	0.165
Pr	0.03	0.04	0.03	0.03	0.03	0.01	0.05	0.02	0.02	0.05	0.04	0.06
Nd	0.36	0.40	0.41	0.36	0.35	0.18	0.40	0.20	0.22	0.75	0.55	0.72
Sm	0.43	0.48	0.52	0.48	0.42	0.40	0.47	0.25	0.28	0.72	0.50	0.86
Eu	0.28	0.29	0.32	0.34	0.23	0.31	0.25	0.20	0.18	0.44	0.26	0.53
Tb	0.32	0.30	0.26	0.27	0.25	0.26	0.21	0.27	0.28	0.39	0.21	0.50
Gd	2.33	2.20	1.16	1.33	0.97	1.20	0.90	0.90	0.86	1.66	0.99	2.19
Dy	2.47	2.44	2.11	2.20	2.06	2.39	1.81	2.72	3.09	3.37	1.85	4.53
Ho	0.57	0.60	0.54	0.50	0.55	0.55	0.39	0.72	0.87	0.91	0.44	0.95
Er	1.72	1.91	2.15	1.89	2.09	2.19	1.45	2.79	3.30	3.36	2.43	5.32
Tm	0.27	0.28	0.29	0.24	0.28	0.28	0.16	0.40	0.40	0.47	0.24	0.53
Yb	1.92	2.22	2.44	1.62	2.14	2.24	1.44	2.88	3.31	3.33	2.03	3.49
Lu	0.30	0.32	0.39	0.24	0.31	0.36	0.21	0.41	0.46	0.46	0.31	0.54
Hf	0.73	0.64	0.06	0.08	0.35	0.16	0.58	0.08	0.05	0.73	0.62	0.48
Ta	0.006	0.004	< b.d.	< b.d.	0.009	0.004	0.003	0.002	0.001	0.011	0.007	0.014
Pb	0.003	< b.d.	0.011	0.010	0.005	0.006	0.003	0.004	0.004	< b.d.	0.022	0.011
Th	0.002	0.002	0.002	0.002	0.003	< d.l.	0.006	< b.d.	< b.d.	0.004	0.007	0.003
U	0.002	0.002	0.002	0.002	0.004	0.003	0.004	0.002	< b.d.	0.007	0.009	0.011

Table 22 continued

							BM Med-Ca				**BM High-Ca**	
	BM-GAR2-g17	BM-GAR2-g18	BM-GAR2-g19	BM-GAR2-g20	BM-GAR2-g22	BM-GAR2-g23	BM-GAR2-g2	BM-GAR2-g5	BM-GAR2-g6	BM-GAR2-g24	BM-GAR2-g1	BM-GAR2-g21
Sc	36.3	31.2	49.3	35.7	40.7	35.0	33.8	32.0	57.0	42.8	30.8	38.1
V	182.9	108.6	248.7	107.1	113.0	94.10	269	69.5	78.2	163	199	125
Ni	64.7	36.5	42.4	28.9	28.3	23.9	1.10	14.2	17.1	30.2	1.10	3.64
Rb	< b.d.	0.013	0.040	0.042	0.037	< b.d.	< b.d.	< b.d.	0.020	< b.d.	0.072	< d.l.
Sr	0.10	0.38	0.13	0.34	0.39	0.31	0.05	0.38	0.22	0.41	0.11	0.07
Y	11.8	12.1	7.9	18.6	22.0	11.9	48.9	19.7	26.8	17.0	52.1	44.9
Zr	37.4	9.52	27.7	5.95	6.92	6.27	2.23	6.74	48.2	27.8	15.1	8.87
Nb	0.070	0.012	0.034	0.010	0.013	0.017	0.005	0.026	0.172	0.141	< d.l.	0.006
Ba	0.016	< d.l.	< b.d.	0.015	0.038	0.003	0.026	0.016	0.019	0.008	0.012	< d.l.
La	0.003	0.005	0.005	0.003	< b.d.	0.004	0.008	0.009	0.010	0.025	0.110	0.005
Ce	0.086	0.034	0.075	0.040	0.045	0.043	0.053	0.070	0.138	0.239	1.73	0.138
Pr	0.04	0.02	0.02	0.02	0.02	0.04	0.02	0.04	0.06	0.08	0.91	0.16
Nd	0.35	0.25	0.25	0.30	0.32	0.24	1.06	0.56	0.90	0.98	11.3	3.34
Sm	0.42	0.31	0.31	0.42	0.54	0.32	2.40	0.66	1.27	0.90	8.92	5.07
Eu	0.30	0.20	0.21	0.28	0.33	0.25	1.23	0.45	0.80	0.49	2.56	2.33
Tb	0.26	0.23	0.21	0.36	0.44	0.25	1.24	0.43	0.75	0.36	1.87	1.40
Gd	1.07	0.83	0.86	1.27	1.58	0.88	10.2	1.76	3.05	1.70	19.5	7.55
Dy	2.05	1.95	1.38	2.88	3.69	1.94	9.65	3.53	5.36	2.87	11.4	9.04
Ho	0.49	0.50	0.36	0.70	0.93	0.52	1.98	0.82	1.19	0.79	2.22	1.90
Er	2.39	2.83	2.01	3.91	4.82	3.03	5.77	3.01	3.94	3.90	6.06	8.69
Tm	0.19	0.29	0.21	0.37	0.44	0.31	0.78	0.39	0.45	0.38	0.84	0.74
Yb	1.31	2.19	1.39	2.93	3.66	2.52	5.62	2.92	3.09	2.93	6.17	5.40
Lu	0.16	0.35	0.21	0.46	0.58	0.38	0.74	0.39	0.41	0.44	0.82	0.73
Hf	0.87	0.19	0.57	0.12	0.09	0.11	0.04	0.08	0.65	0.52	0.36	0.14
Ta	0.004	0.001	0.002	< d.l.	0.002	0.001	< d.l.	< d.l.	0.008	0.024	< d.l.	0.001
Pb	0.098	0.012	0.011	0.006	0.004	0.015	0.005	0.003	0.007	0.010	0.005	0.001
Th	0.003	< b.d.	< b.d.	0.001	0.002	< b.d.	0.012	< d.l.	< d.l.	0.002	0.008	0.002
U	0.006	0.001	0.002	0.001	0.002	0.003	0.002	0.002	0.007	0.008	0.006	0.003

Table 23: Trace element composition of Tshibwe eclogitic garnets

	TB Low-Ca											
	TB-GAR2-g1	TB-GAR2-g2	TB-GAR2-g3	TB-GAR2-g4	TB-GAR2-g7	TB-GAR2-g8	TB-GAR2-g9	TB-GAR2-g10	TB-GAR2-g11	TB-GAR2-g13	TB-GAR2-g14	TB-GAR2-g15
Sc	46.0	37.2	32.1	48.0	26.9	36.6	40.1	44.6	40.7	37.8	31.3	38.0
V	255	134	103	158	114	153	200	155	241	128	86.8	161
Ni	27.8	34.6	44.6	40.9	32.2	23.1	60.7	48.9	24.8	59.3	35.9	43.8
Rb	0.059	0.036	0.019	0.040	0.026	0.069	0.013	0.043	0.057	0.019	0.031	0.052
Sr	0.09	0.19	0.17	0.16	0.21	0.27	0.08	0.14	0.07	0.30	0.24	0.15
Y	15.1	11.2	11.5	11.7	11.8	12.8	6.48	10.1	21.1	8.01	13.8	10.5
Zr	26.4	26.4	21.4	27.4	40.7	23.3	16.3	32.8	28.4	8.97	18.3	25.0
Nb	0.050	0.053	0.072	0.064	0.069	0.045	0.067	0.079	0.035	0.004	0.027	0.078
Ba	< b.d.	0.021	< b.d.	< b.d.	< b.d.	< b.d.	< b.d.	< b.d.	< b.d.	< b.d.	< b.d.	< b.d.
La	0.002	0.007	0.008	0.003	0.005	0.006	0.002	0.003	0.009	0.004	0.004	0.005
Ce	0.089	0.120	0.122	0.097	0.095	0.111	0.067	0.108	0.078	0.057	0.082	0.099
Pr	0.04	0.05	0.05	0.03	0.04	0.04	0.02	0.05	0.03	0.02	0.05	0.03
Nd	0.34	0.56	0.55	0.49	0.46	0.46	0.23	0.53	0.29	0.31	0.73	0.46
Sm	0.41	0.56	0.47	0.49	0.64	0.53	0.29	0.55	0.50	0.35	0.72	0.50
Eu	0.24	0.32	0.29	0.31	0.44	0.34	0.16	0.32	0.32	0.25	0.41	0.28
Tb	0.29	0.27	0.30	0.28	0.34	0.31	0.15	0.26	0.45	0.19	0.31	0.23
Gd	1.06	1.08	1.06	1.16	1.28	1.30	0.60	1.02	1.61	0.77	1.35	1.03
Dy	2.54	2.11	2.12	2.09	2.18	2.42	1.25	1.95	3.73	1.54	2.42	1.93
Ho	0.67	0.49	0.53	0.51	0.50	0.55	0.35	0.51	0.91	0.37	0.57	0.44
Er	3.33	2.47	2.47	2.29	2.99	2.99	1.73	2.57	5.06	1.85	3.41	2.44
Tm	0.35	0.22	0.25	0.25	0.26	0.28	0.14	0.21	0.42	0.15	0.27	0.21
Yb	2.54	1.88	1.75	1.81	1.92	2.03	1.09	1.66	3.11	1.02	2.17	1.59
Lu	0.38	0.28	0.24	0.28	0.27	0.30	0.17	0.22	0.45	0.17	0.35	0.23
Hf	0.39	0.52	0.30	0.54	0.61	0.39	0.41	0.53	0.40	0.22	0.23	0.45
Ta	0.001	0.007	0.005	0.003	0.008	0.002	0.005	0.002	0.002	< b.d.	0.001	0.010
Pb	0.003	0.003	0.009	0.007	0.013	0.011	0.007	0.007	0.003	0.004	0.002	0.003
Th	0.001	0.005	< b.d.	0.001	0.003	0.006	0.002	< b.d.	0.014	< b.d.	< b.d.	0.002
U	0.009	0.005	0.005	0.006	0.007	0.004	< b.d.	0.005	0.019	0.001	0.003	0.003

Table 23 continued

							TB Med-Ca				TB High-Ca		
	TB-GAR2-g16	TB-GAR2-g18	TB-GAR2-g19	TB-GAR2-g20	TB-GAR2-g21	TB-GAR2-g22	TB-GAR2-g5	TB-GAR2-g6	TB-GAR2-g12	TB-GAR2-g17	TB-GAR2-g32	TB-GAR2-g33	TB-GAR2-g41
Sc	34.0	48.3	18.9	31.4	41.5	25.9	46.5	9.04	66.9	5.61	49.5	86.3	56.5
V	107	117	115	190	132	95.7	112	28.7	78.0	12.5	100	189	117
Ni	23.8	59.9	51.2	40.7	62.4	37.4	13.7	83.8	7.03	25.1	23.9	34.3	40
Rb	< b.d.	0.026	0.024	0.040	0.029	0.065	< b.d.	0.020	0.060	0.027	< b.d.	0.150	0.130
Sr	0.20	0.39	0.17	0.17	0.26	0.22	0.26	< b.d.	0.16	0.10	1.37	0.11	4.37
Y	11.3	11.6	6.88	11.9	8.60	13.9	5.86	1.45	29.2	1.15	14.2	8.03	6.35
Zr	24.7	16.7	21.4	37.9	14.4	27.0	6.31	1.56	39.5	1.65	13.4	2.09	4.42
Nb	0.086	0.013	0.112	0.077	0.008	0.056	0.043	< b.d.	0.121	< b.d.	0.010	0.275	0.314
Ba	0.017	< b.d.	0.006	< b.d.	< b.d.	0.016	0.015	< b.d.	0.034	< b.d.	0.037	0.042	< b.d.
La	0.012	0.010	0.002	0.002	0.007	0.008	0.028	0.003	0.009	0.002	0.018	0.039	0.082
Ce	0.205	0.158	0.165	0.066	0.086	0.096	0.402	0.005	0.126	0.125	0.218	0.178	0.353
Pr	0.07	0.06	0.06	0.03	0.03	0.04	0.21	0.01	0.06	0.26	0.12	0.02	0.08
Nd	0.89	0.73	0.62	0.44	0.50	0.51	2.86	0.12	0.85	5.64	1.37	0.24	0.73
Sm	0.66	0.63	0.48	0.57	0.47	0.50	2.33	0.14	1.09	0.50	1.55	0.26	0.46
Eu	0.32	0.35	0.29	0.36	0.26	0.33	1.06	0.30	0.74	0.23	1.13	0.21	0.38
Tb	0.21	0.26	0.18	0.28	0.20	0.27	0.33	0.05	0.71	0.03	0.39	0.18	0.17
Gd	1.09	1.26	0.91	1.36	1.02	1.33	2.64	0.29	2.76	0.24	2.12	0.66	0.92
Dy	1.94	2.22	1.24	2.09	1.78	2.29	1.63	0.32	5.44	0.21	2.59	1.35	1.12
Ho	0.52	0.53	0.35	0.56	0.45	0.58	0.28	0.06	1.30	0.04	0.58	0.31	0.25
Er	2.85	1.71	1.08	1.65	1.41	1.84	0.93	0.22	7.01	0.17	1.64	0.94	0.59
Tm	0.23	0.21	0.19	0.25	0.20	0.28	0.09	0.02	0.55	0.01	0.24	0.13	0.07
Yb	2.08	1.78	1.14	1.72	1.25	1.95	0.47	0.10	3.96	0.15	1.74	1.07	0.58
Lu	0.36	0.28	0.17	0.25	0.20	0.32	0.05	0.02	0.52	0.03	0.26	0.13	0.08
Hf	0.35	0.36	0.40	0.81	0.27	0.44	0.07	0.02	0.43	0.02	0.29	0.08	0.19
Ta	0.005	0.002	0.016	0.003	< b.d.	0.007	0.002	< b.d.	0.017	< b.d.	< b.d.	0.005	0.007
Pb	0.008	0.009	0.011	0.006	0.002	0.003	0.002	0.008	0.003	0.004	0.004	0.001	0.002
Th	< b.d.	< b.d.	0.002	< b.d.	< b.d.	< b.d.	0.003	< b.d.	0.002	< b.d.	< b.d.	0.015	0.094
U	0.011	0.002	0.007	0.003	0.002	0.005	0.018	< b.d.	0.009	0.011	0.006	0.006	0.007

A.2.3. Peridotitic garnets

(1) G9 GARNETS with regular

Table 24: Major element composition of Mbuji-Mayi G9 garnets with regular REE patterns.

BM G9	SiO_2	TiO_2	Al_2O_3	Cr_2O_3	FeO	MnO	MgO	CaO	Na_2O	Total	Ca#	Mg#
BM-GAR1-gt1	42.39	0.35	21.94	2.28	7.41	0.35	21.12	4.15	0.07	100.1	12.4	83.5
BM-GAR1-gt2	41.98	0.28	21.09	3.53	7.32	0.35	21.00	4.55	0.06	100.1	13.5	83.6
BM-GAR1-gt3	42.34	0.47	21.33	2.73	7.79	0.41	20.52	4.40	0.04	100.0	13.3	82.4
BM-GAR1-gt4	42.53	0.45	21.24	2.56	7.31	0.34	20.68	4.32	0.04	99.5	13.0	83.4
BM-GAR1-gt5	42.02	0.19	21.50	3.47	7.97	0.50	20.21	3.98	0.07	99.9	12.4	81.9
BM-GAR1-gt6	41.98	0.47	19.86	4.74	6.93	0.36	20.09	4.85	0.04	99.3	14.8	83.8
BM-GAR1-gt7	42.00	0.62	20.64	3.40	7.42	0.38	20.22	4.83	0.06	99.6	14.6	82.9
BM-GAR1-gt8	42.03	0.24	20.27	4.66	6.49	0.33	20.81	4.84	0.03	99.7	14.3	85.1
BM-GAR1-gt10	42.15	0.30	21.39	2.97	7.38	0.40	20.97	4.24	0.06	99.9	12.7	83.5
BM-GAR1-gt11	42.00	0.55	20.56	3.60	7.58	0.37	20.35	4.43	0.07	99.5	13.5	82.7
BM-GAR1-gt12	42.23	0.26	21.07	3.16	7.26	0.34	20.36	4.39	0.04	99.1	13.4	83.3
BM-GAR1-gt13	42.07	0.60	20.57	3.28	7.70	0.35	20.07	4.69	0.04	99.4	14.4	82.3
BM-GAR1-gt14	42.05	0.63	21.51	2.33	8.46	0.42	19.72	4.78	0.06	99.9	14.8	80.6
BM-GAR1-gt15	42.42	0.24	21.99	2.52	6.95	0.38	20.96	3.98	0.06	99.5	12.0	84.3
BM-GAR1-gt16	41.39	0.37	21.84	1.88	7.62	0.38	19.87	3.99	0.09	97.4	12.6	82.3
BM-GAR1-gt17	41.93	0.50	20.61	4.27	6.68	0.37	20.65	4.73	0.05	99.8	14.1	84.6
BM-GAR1-gt18	41.96	0.52	20.21	4.42	6.60	0.42	20.33	4.68	0.06	99.2	14.2	84.6
BM-GAR1-gt19	41.71	0.68	20.34	3.13	7.23	0.41	19.42	4.71	0.06	97.7	14.8	82.7
BM-GAR1-gt20	42.17	0.68	20.94	2.45	8.40	0.37	19.73	4.71	0.07	99.5	14.6	80.7
BM-GAR1-gt22	42.20	0.28	20.98	3.85	7.49	0.46	19.99	4.28	0.07	99.6	13.3	82.6
BM-GAR1-gt23	41.86	0.25	20.29	4.75	7.41	0.48	19.57	4.74	0.07	99.4	14.8	82.5
BM-GAR1-gt24	42.17	0.67	20.64	2.74	8.37	0.37	19.83	4.67	0.08	99.5	14.5	80.9
BM-GAR1-gt26	42.22	0.20	20.42	4.34	6.83	0.38	20.62	4.77	0.03	99.8	14.2	84.3
BM-GAR1-gt27	42.43	0.30	21.40	3.32	6.77	0.43	21.01	4.20	0.08	99.9	12.6	84.7
BM-GAR1-gt28	41.90	0.65	20.98	2.69	8.33	0.34	20.29	4.64	0.08	99.9	14.1	81.3
BM-GAR1-gt30	42.08	0.56	20.27	3.77	7.62	0.42	19.56	4.91	0.05	99.2	15.3	82.1
BM-GAR1-gt31	42.31	0.43	20.34	4.04	6.80	0.39	20.56	4.55	0.05	99.5	13.7	84.4
BM-GAR1-gt33	42.24	0.54	20.43	4.04	7.18	0.36	20.35	4.57	0.09	99.8	13.9	83.5
BM-GAR1-gt34	41.78	0.18	20.20	5.01	7.59	0.50	19.66	5.02	0.06	100.0	15.5	82.2
BM-GAR1-gt36	42.28	0.40	20.97	3.78	6.64	0.41	20.69	4.35	0.08	99.6	13.1	84.7
BM-GAR1-gt37	41.95	0.19	20.47	4.86	7.52	0.44	19.96	4.52	0.05	99.9	14.0	82.5
BM-GAR1-gt38	42.17	0.51	21.22	2.59	7.69	0.37	20.09	4.24	0.06	98.9	13.2	82.3
BM-GAR1-gt39	41.92	0.44	20.16	4.15	7.36	0.38	20.03	4.91	0.06	99.4	15.0	82.9
BM-GAR1-gt40	41.81	0.37	20.62	4.34	7.71	0.41	19.68	4.58	0.04	99.6	14.3	82.0
BM-GAR1-gt41	42.26	0.60	20.87	3.55	6.48	0.31	21.16	4.43	0.04	99.7	13.1	85.3
BM-GAR1-gt43	42.30	0.38	21.64	2.35	7.86	0.36	20.82	4.23	0.07	100.0	12.7	82.5
BM-GAR1-gt44	41.86	0.34	20.03	4.90	7.33	0.40	20.08	4.62	0.05	99.6	14.2	83.0
BM-GAR1-gt25	41.98	0.78	20.00	3.99	7.96	0.43	19.26	5.30	0.12	99.8	16.5	81.2
BM-GAR1-gt32	42.24	0.74	21.32	2.66	7.28	0.40	20.07	5.12	0.09	99.9	15.5	83.1
BM-GAR1-gt42	41.70	0.74	20.40	3.45	8.11	0.46	19.29	5.30	0.06	99.5	16.5	80.9
BM-GAR1-gt9	41.42	0.45	18.80	6.21	7.42	0.41	20.39	4.88	0.03	100.0	14.7	83.0
BM-GAR1-gt21	41.98	0.32	19.43	5.79	7.01	0.41	20.02	5.03	0.04	100.0	15.3	83.6
BM-GAR1-gt29	41.78	0.27	19.27	6.42	7.03	0.42	20.31	4.93	0.05	100.5	14.9	83.7
BM-GAR1-gt35	41.85	0.47	18.69	6.46	6.47	0.44	20.39	4.85	0.08	99.7	14.6	84.9

Table 25: Major element composition of Tshibwe G9 garnets with regular patterns. Low-Mg garnets are also shown

TB G9	SiO_2	TiO_2	Al_2O_3	Cr_2O_3	FeO	MnO	MgO	CaO	Na_2O	Total	Ca#	Mg#
TB-GAR1-gt1	41.92	0.38	21.78	3.12	7.69	0.35	20.77	4.14	0.07	100.2	12.5	82.8
TB-GAR1-gt2	42.45	0.51	21.40	2.57	7.88	0.31	20.91	4.29	0.09	100.4	12.8	82.5
TB-GAR1-gt3	42.36	0.41	20.80	3.16	7.74	0.34	21.04	4.33	0.10	100.3	12.9	82.9
TB-GAR1-gt4	42.18	0.36	20.46	3.93	7.34	0.37	21.05	4.57	0.06	100.3	13.5	83.6
TB-GAR1-gt6	42.87	0.46	21.38	2.36	7.92	0.33	21.17	4.28	0.08	100.8	12.7	82.6
TB-GAR1-gt9	42.44	0.65	21.83	1.60	8.51	0.29	20.97	3.93	0.08	100.3	11.9	81.5
TB-GAR1-gt10	41.92	0.59	22.14	2.17	8.70	0.36	20.31	4.08	0.07	100.3	12.6	80.6
TB-GAR1-gt12	42.49	0.38	21.05	2.99	7.83	0.32	20.75	4.17	0.07	100.0	12.6	82.5
TB-GAR1-gt13	41.96	0.55	20.46	3.50	8.48	0.28	20.58	4.64	0.04	100.5	13.9	81.2
TB-GAR1-gt14	41.92	0.54	21.77	1.80	8.16	0.33	21.18	4.22	0.09	100.0	12.5	82.2
TB-GAR1-gt15	41.80	0.62	21.71	1.78	8.58	0.32	20.94	4.11	0.08	99.9	12.3	81.3
TB-GAR1-gt16	42.53	0.59	21.76	1.91	7.51	0.34	21.11	4.20	0.06	100.0	12.5	83.4
TB-GAR1-gt17	42.20	0.42	21.00	3.23	7.19	0.31	21.35	4.38	0.08	100.1	12.8	84.1
TB-GAR1-gt18	42.17	0.74	20.52	3.03	8.51	0.40	20.29	4.75	0.05	100.5	14.4	81.0
TB-GAR1-gt19	42.37	0.16	22.87	1.50	8.52	0.27	20.13	4.48	0.02	100.3	13.8	80.8
TB-GAR1-gt20	41.97	0.49	21.14	3.58	7.40	0.38	20.62	4.64	0.05	100.2	13.9	83.2
TB-GAR1-gt21	42.19	0.64	22.46	1.56	7.33	0.44	21.17	4.29	0.06	100.1	12.7	83.7
TB-GAR1-gt22	41.77	0.49	22.23	1.96	7.84	0.38	20.90	4.10	0.08	99.7	12.4	82.6
TB-GAR1-gt23	41.76	0.45	20.96	2.81	7.76	0.33	21.24	4.37	0.06	99.7	12.9	83.0
TB-GAR1-gt24	42.11	0.45	20.93	3.29	8.14	0.37	20.20	4.44	0.04	100.0	13.6	81.6
TB-GAR1-gt25	41.75	0.64	21.97	1.65	8.39	0.32	21.15	3.94	0.11	99.9	11.8	81.8
TB-GAR1-gt26	42.25	0.73	21.68	1.57	8.44	0.31	21.05	4.10	0.07	100.2	12.3	81.6
TB-GAR1-gt28	42.54	0.65	21.85	1.56	8.26	0.30	21.04	4.08	0.09	100.4	12.2	81.9
TB-GAR1-gt30	41.92	0.46	21.44	2.82	7.69	0.42	20.65	4.41	0.08	99.9	13.3	82.7
TB-GAR1-gt31	41.78	0.22	21.88	2.80	8.32	0.30	20.17	4.49	0.03	100.0	13.8	81.2
TB-GAR1-gt32	42.09	0.94	21.60	1.46	8.64	0.31	20.91	4.05	0.08	100.1	12.2	81.2
TB-GAR1-gt33	42.27	0.48	20.60	3.37	7.78	0.35	20.82	4.49	0.08	100.2	13.4	82.7
TB-GAR1-gt34	42.57	0.42	20.90	3.32	7.80	0.36	20.46	4.44	0.05	100.3	13.5	82.4
TB-GAR1-gt35	42.49	0.63	22.40	2.03	7.53	0.33	20.91	3.98	0.14	100.4	12.0	83.2
TB-GAR1-gt36	42.01	0.47	21.44	2.99	7.86	0.33	20.80	4.44	0.07	100.4	13.3	82.5
TB-GAR1-gt37	42.34	0.32	21.72	2.61	7.89	0.38	20.79	4.41	0.03	100.5	13.2	82.4
TB-GAR1-gt38	42.25	0.58	21.14	2.86	8.28	0.38	20.20	4.51	0.10	100.3	13.8	81.3
TB-GAR1-gt40	42.00	0.41	21.25	3.40	8.47	0.37	20.10	4.50	0.05	100.5	13.9	80.9
TB-GAR1-gt41	42.39	0.49	21.15	2.60	8.15	0.35	20.66	4.38	0.05	100.2	13.2	81.9
TB-GAR1-gt42	41.65	0.55	21.58	2.35	7.87	0.29	21.45	4.25	0.06	100.0	12.4	82.9
TB-GAR1-gt43	42.14	0.37	22.17	2.16	8.08	0.37	20.70	4.31	0.05	100.3	13.0	82.0
TB-GAR1-gt44	42.20	0.23	22.04	3.04	7.62	0.41	20.78	3.94	0.07	100.3	12.0	82.9
TB-GAR1-gt8	42.04	0.23	19.98	5.11	7.57	0.44	20.30	4.61	0.06	100.3	14.0	82.7
TB-GAR1-gt29	41.71	0.15	20.44	4.91	7.47	0.49	20.38	4.63	0.04	100.2	14.0	82.9
TB-GAR1-gt39	41.27	0.25	19.81	5.39	7.43	0.45	20.03	4.89	0.06	99.6	14.9	82.8
TB low-Mg												
TB-GAR1-gt5	41.52	0.74	21.72	1.17	10.58	0.38	19.87	4.51	0.07	100.5	14.0	77.0
TB-GAR1-gt11	41.38	0.85	20.65	2.56	9.43	0.37	20.20	4.83	0.08	100.3	14.7	79.2
TB-GAR1-gt27	41.57	0.85	20.77	2.49	9.72	0.42	19.59	4.82	0.07	100.3	15.0	78.2

Table 26: Trace element composition of Mbuji-Mayi G9 garnets with regular REE patterns

	BM G9											
	BM-GAR1-g1	BM-GAR1-g2	BM-GAR1-g3	BM-GAR1-g4	BM-GAR1-g5	BM-GAR1-g6	BM-GAR1-g7	BM-GAR1-g8	BM-GAR1-g10	BM-GAR1-g11	BM-GAR1-g12	BM-GAR1-g13
Sc	56.7	62.3	59.2	60.6	74.7	72.6	60.4	72.7	58.5	54.1	64.1	63.9
V	185	216	199	207	138	278	222	223	189	197	208	251
Ni	68.9	72.6	70.1	72.0	32.6	65.0	60.1	67.2	67.5	69.0	71.9	77.5
Rb	0.067	0.024	0.006	0.037	0.037	0.083	0.024	0.050	0.080	0.029	0.033	0.107
Sr	0.14	0.16	0.16	0.16	0.26	0.19	0.15	0.17	0.15	0.17	0.13	0.18
Y	8.49	8.35	11.3	10.3	19.2	9.33	8.90	3.57	6.94	10.5	6.63	12.0
Zr	14.3	10.1	22.8	19.1	47.2	19.8	24.7	9.04	6.99	19.9	8.32	28.5
Nb	0.064	0.146	0.097	0.103	0.209	0.124	0.110	0.156	0.101	0.133	0.112	0.067
Ba	< b.d.	0.022	< b.d.	0.011	0.013	0.024	< b.d.	0.026	< b.d.	< b.d.	0.040	0.026
La	0.008	0.020	0.010	0.007	0.010	0.011	0.010	0.016	0.007	0.011	0.010	0.007
Ce	0.115	0.155	0.111	0.119	0.221	0.141	0.129	0.154	0.127	0.109	0.136	0.151
Pr	0.04	0.05	0.05	0.04	0.10	0.06	0.05	0.05	0.04	0.04	0.05	0.05
Nd	0.49	0.51	0.49	0.46	1.37	0.61	0.50	0.69	0.43	0.40	0.45	0.52
Sm	0.41	0.39	0.46	0.38	1.48	0.59	0.48	0.51	0.31	0.41	0.40	0.56
Eu	0.20	0.22	0.26	0.25	0.82	0.29	0.27	0.20	0.17	0.27	0.18	0.34
Tb	0.19	0.19	0.26	0.23	0.58	0.27	0.24	0.09	0.16	0.27	0.12	0.29
Gd	1.33	1.24	1.55	1.40	4.56	1.80	1.40	0.79	0.85	1.09	0.53	1.36
Dy	1.47	1.52	2.02	1.76	4.13	1.89	1.68	0.61	1.12	2.03	1.20	2.22
Ho	0.37	0.32	0.47	0.44	0.83	0.39	0.40	0.17	0.33	0.45	0.33	0.52
Er	1.41	1.26	1.67	1.59	2.14	1.12	1.29	0.51	1.13	1.89	1.30	2.14
Tm	0.20	0.17	0.22	0.22	0.27	0.14	0.16	0.09	0.16	0.20	0.14	0.24
Yb	1.43	1.23	1.70	1.63	1.70	1.05	1.29	0.62	1.28	1.60	1.19	1.73
Lu	0.25	0.21	0.25	0.26	0.26	0.15	0.18	0.10	0.17	0.25	0.19	0.23
Hf	0.38	0.36	0.64	0.49	0.72	0.63	0.64	0.24	0.18	0.58	0.18	0.79
Ta	0.004	0.013	0.010	0.012	0.023	0.014	0.011	0.012	0.006	0.015	0.008	0.007
Pb	0.003	0.116	0.002	0.005	0.004	0.005	0.002	0.006	0.008	0.003	0.008	0.010
Th	0.004	0.007	0.002	0.002	0.003	0.005	0.004	0.003	0.000	0.005	0.002	0.005
U	0.012	0.007	0.007	0.009	0.010	0.009	0.005	0.010	0.005	0.010	0.011	0.010

Table 26 continued

	BM G9											
	BM-GAR1-g14	BM-GAR1-g15	BM-GAR1-g16	BM-GAR1-g17	BM-GAR1-g18	BM-GAR1-g19	BM-GAR1-g20	BM-GAR1-g22	BM-GAR1-g23	BM-GAR1-g24	BM-GAR1-g26	BM-GAR1-g27
Sc	43.9	46.3	56.3	63.1	69.9	63.8	75.3	87.1	90.1	69.3	75.4	67.4
V	194	150	204	214	217	275	321	222	237	313	322	254
Ni	48.7	51.2	54.9	55.3	55.6	68.1	70.3	46.7	36.4	70.5	58.1	51.8
Rb	0.007	0.015	0.029	0.079	< b.d.	0.033	0.023	0.036	0.089	0.023	0.066	0.034
Sr	0.19	0.16	0.22	0.25	0.24	0.17	0.17	0.26	0.41	0.21	0.27	0.24
Y	9.24	11.7	8.16	18.4	20.8	8.33	13.6	8.22	12.7	11.9	6.55	7.73
Zr	26.1	28.6	22.4	55.0	67.4	24.4	35.2	22.6	51.4	35.6	14.6	24.6
Nb	0.058	0.124	0.108	0.072	0.079	0.102	0.097	0.111	0.208	0.174	0.088	0.125
Ba	0.167	0.051	< b.d.	0.022	0.012	0.008	0.021	0.001	0.038	0.043	0.005	< b.d.
La	0.011	0.008	0.008	0.006	0.009	0.013	0.011	0.021	0.026	0.016	0.023	0.028
Ce	0.107	0.150	0.166	0.134	0.147	0.125	0.153	0.202	0.364	0.188	0.619	0.332
Pr	0.04	0.05	0.06	0.05	0.07	0.05	0.05	0.07	0.17	0.07	0.24	0.11
Nd	0.50	0.68	0.64	0.66	1.19	0.47	0.55	0.89	2.23	0.70	2.15	1.13
Sm	0.48	0.64	0.52	1.18	1.70	0.44	0.56	0.87	2.15	0.61	0.86	0.72
Eu	0.29	0.36	0.29	0.73	0.92	0.26	0.28	0.47	0.98	0.35	0.31	0.35
Tb	0.21	0.26	0.20	0.56	0.69	0.22	0.26	0.32	0.45	0.29	0.16	0.24
Gd	1.03	1.29	1.02	3.00	3.54	1.09	1.34	1.44	2.99	1.34	0.80	1.06
Dy	1.75	1.93	1.49	3.94	4.58	1.69	2.59	1.89	2.71	2.25	1.28	1.47
Ho	0.41	0.49	0.34	0.80	0.73	0.44	0.63	0.35	0.56	0.55	0.30	0.37
Er	1.43	2.19	1.46	2.64	2.89	1.53	2.48	1.68	2.47	2.80	1.67	1.70
Tm	0.21	0.30	0.17	0.20	0.27	0.16	0.28	0.15	0.19	0.25	0.17	0.17
Yb	1.36	2.30	1.33	1.54	1.69	1.13	2.05	1.01	1.47	1.84	1.22	1.26
Lu	0.21	0.37	0.20	0.21	0.20	0.15	0.29	0.13	0.19	0.24	0.16	0.19
Hf	0.54	0.51	0.50	1.16	1.42	0.68	1.08	0.54	1.00	1.09	0.54	0.65
Ta	0.003	0.011	0.011	0.005	0.005	0.012	0.011	0.016	0.022	0.015	0.008	0.012
Pb	0.026	0.008	0.002	< b.d.	0.010	0.007	0.013	0.003	0.017	0.004	0.008	< b.d.
Th	0.003	0.002	0.002	0.002	0.002	0.003	0.005	0.007	0.002	0.005	0.022	0.005
U	0.005	0.006	0.011	0.009	0.009	0.007	0.005	0.024	0.019	0.013	0.047	0.032

Table 26 continued

	BM G9											
	BM-GAR1-g28	BM-GAR1-g30	BM-GAR1-g31	BM-GAR1-g33	BM-GAR1-g34	BM-GAR1-g36	BM-GAR1-g37	BM-GAR1-g38	BM-GAR1-g39	BM-GAR1-g40	BM-GAR1-g41	BM-GAR1-g43
Sc	71.9	74.3	66.8	63.5	77.5	78.7	98.4	66.4	65.7	70.4	67.1	60.3
V	317	265	254	254	266	222	216	236	285	251	255	238
Ni	69.6	52.3	69.2	70.3	36.7	53.2	35.9	69.9	72.7	49.4	59.9	68.5
Rb	0.042	0.016	0.023	0.089	0.010	0.022	0.045	0.005	0.001	0.016	0.073	0.027
Sr	0.21	0.23	0.19	0.20	0.62	0.30	0.43	0.14	0.17	0.22	0.14	0.18
Y	13.2	11.5	8.19	13.1	8.39	11.0	18.0	12.3	10.7	8.48	6.57	8.37
Zr	38.6	37.9	21.9	49.9	35.4	38.2	55.8	24.6	26.0	18.2	17.3	14.4
Nb	0.121	0.112	0.106	0.109	0.170	0.165	0.233	0.163	0.150	0.162	0.087	0.103
Ba	0.031	0.012	0.003	0.017	0.008	0.018	0.001	0.014	0.009	0.010	0.014	0.004
La	0.012	0.012	0.007	0.010	0.044	0.015	0.016	0.010	0.013	0.013	0.009	0.009
Ce	0.186	0.187	0.166	0.144	0.741	0.184	0.366	0.114	0.159	0.167	0.095	0.152
Pr	0.08	0.07	0.08	0.06	0.35	0.07	0.19	0.06	0.06	0.07	0.03	0.05
Nd	0.70	0.83	0.74	0.72	3.65	0.84	2.69	0.44	0.62	0.66	0.35	0.53
Sm	0.67	0.73	0.70	0.84	2.33	0.84	2.17	0.44	0.51	0.55	0.34	0.38
Eu	0.34	0.39	0.33	0.56	0.83	0.51	1.01	0.27	0.30	0.28	0.20	0.22
Tb	0.28	0.31	0.27	0.39	0.28	0.34	0.60	0.29	0.25	0.22	0.20	0.17
Gd	1.33	1.44	1.27	2.18	2.27	2.04	3.56	1.27	1.28	1.01	0.78	0.69
Dy	2.42	2.37	1.78	2.52	1.67	2.40	3.87	2.21	1.76	1.52	1.24	1.47
Ho	0.60	0.56	0.38	0.49	0.39	0.45	0.75	0.52	0.42	0.34	0.29	0.39
Er	2.84	2.72	1.59	1.83	1.38	1.74	2.60	1.91	1.55	1.46	1.58	2.11
Tm	0.27	0.26	0.20	0.25	0.16	0.16	0.29	0.22	0.21	0.16	0.12	0.17
Yb	2.05	1.84	1.36	1.53	1.10	1.41	2.04	1.76	1.39	1.26	1.07	1.39
Lu	0.28	0.30	0.23	0.22	0.17	0.25	0.29	0.23	0.24	0.17	0.17	0.21
Hf	1.11	0.86	0.61	1.10	0.75	0.82	1.01	0.51	0.68	0.43	0.38	0.45
Ta	0.017	0.021	0.018	0.011	0.016	0.016	0.021	0.019	0.018	0.004	0.008	0.008
Pb	0.004	0.008	0.006	0.003	0.007	0.003	0.006	0.014	0.002	0.004	0.014	0.007
Th	0.003	0.005	0.002	0.003	0.006	0.008	0.002	0.002	0.001	0.004	0.002	0.004
U	0.009	0.013	0.010	0.008	0.046	0.015	0.024	0.017	0.010	0.014	0.003	0.006

Table 26 continued

	BM-GAR1-g44	BM-GAR1-g25	BM-GAR1-g32	BM-GAR1-g42	BM-GAR1-g9	BM-GAR1-g21	BM-GAR1-g29	BM-GAR1-g35
Sc	87.3	68.8	57.7	68.4	78.6	86.2	95.1	87.7
V	262	285	259	312	245	255	300	290
Ni	51.4	53.5	53.5	49.2	66.2	61.5	49.8	54.4
Rb	0.102	0.031	0.048	0.025	0.057	0.040	0.036	0.103
Sr	0.24	0.25	0.28	0.15	0.23	0.17	0.28	0.29
Y	8.20	13.7	17.7	11.3	5.19	0.59	4.72	6.50
Zr	34.4	48.6	79.3	36.0	15.9	8.24	16.7	45.1
Nb	0.136	0.196	0.142	0.122	0.139	0.119	0.188	0.183
Ba	< b.d.	0.018	0.022	0.017	0.029	0.004	0.015	0.021
La	0.024	0.019	0.020	0.009	0.016	0.009	0.030	0.026
Ce	0.237	0.244	0.250	0.159	0.187	0.160	0.290	0.316
Pr	0.07	0.08	0.10	0.06	0.08	0.06	0.12	0.11
Nd	1.00	0.96	1.21	0.67	0.73	0.65	1.29	1.29
Sm	0.87	0.85	1.20	0.66	0.70	0.51	1.02	1.23
Eu	0.48	0.49	0.69	0.35	0.39	0.16	0.39	0.61
Tb	0.28	0.36	0.53	0.28	0.21	0.03	0.17	0.30
Gd	1.52	1.77	2.77	1.25	1.86	0.30	1.05	2.07
Dy	1.83	2.83	3.73	2.17	1.31	0.10	0.98	1.59
Ho	0.37	0.64	0.82	0.51	0.24	0.03	0.25	0.29
Er	1.70	3.24	2.69	2.69	0.60	0.19	1.05	0.87
Tm	0.15	0.29	0.28	0.22	0.08	0.02	0.12	0.11
Yb	1.13	2.06	1.84	1.71	0.67	0.40	0.81	0.65
Lu	0.19	0.34	0.23	0.24	0.10	0.09	0.13	0.10
Hf	0.76	1.13	1.78	0.89	0.42	0.20	0.36	0.94
Ta	0.017	0.019	0.019	0.012	0.011	0.010	0.017	0.025
Pb	0.013	0.007	0.007	0.008	0.006	0.014	0.016	< b.d.
Th	0.004	0.008	0.003	0.005	0.005	0.001	0.002	0.005
U	0.011	0.015	0.019	0.015	0.010	0.007	0.017	0.015

Table 27: Trace element composition of Tshibwe G9 garnets with regular REE patterns.

	TB G9											
	TB-GAR1-g1	TB-GAR1-g2	TB-GAR1-g3	TB-GAR1-g4	TB-GAR1-g6	TB-GAR1-g9	TB-GAR1-g10	TB-GAR1-g12	TB-GAR1-g13	TB-GAR1-g14	TB-GAR1-g15	TB-GAR1-g16
Sc	63.1	51.8	71.6	72.9	65.6	52.3	46.5	64.5	79.1	63.0	56.1	59.0
V	255	230	248	284	256	225	196	236	294	251	228	261
Ni	39.4	95.5	96.9	98.2	101	106	62.9	93.2	104	98.7	96.0	96.5
Rb	0.085	0.024	0.007	0.112	0.003	< b.d.	0.008	< b.d.	0.032	0.038	0.031	0.037
Sr	0.19	0.21	0.27	0.27	0.28	0.26	0.15	0.22	0.39	0.19	0.28	0.29
Y	7.51	9.47	8.56	7.97	10.9	11.4	10.4	8.35	13.0	9.99	10.7	9.28
Zr	42.6	22.8	18.5	15.3	20.5	28.0	22.2	14.4	23.7	16.2	25.8	28.7
Nb	0.112	0.161	0.221	0.230	0.229	0.127	0.081	0.144	0.170	0.232	0.153	0.140
Ba	< b.d.	< b.d.	0.013	0.012	< b.d.	< b.d.	< b.d.	< b.d.	< b.d.	0.017	< b.d.	< b.d.
La	0.016	0.019	0.027	0.041	0.023	0.011	0.006	0.023	0.021	0.014	0.037	0.020
Ce	0.222	0.255	0.267	0.356	0.230	0.184	0.096	0.238	0.331	0.165	0.234	0.214
Pr	0.07	0.07	0.07	0.09	0.06	0.05	0.04	0.05	0.09	0.06	0.07	0.06
Nd	0.88	0.65	0.61	0.80	0.65	0.55	0.34	0.53	0.84	0.50	0.59	0.54
Sm	0.77	0.49	0.48	0.51	0.50	0.43	0.33	0.44	0.64	0.44	0.49	0.53
Eu	0.38	0.24	0.25	0.26	0.28	0.26	0.20	0.22	0.34	0.26	0.26	0.29
Tb	0.26	0.22	0.19	0.22	0.22	0.28	0.21	0.16	0.31	0.22	0.25	0.19
Gd	1.54	1.07	1.11	1.06	1.24	1.25	0.94	0.94	1.41	1.06	1.12	1.14
Dy	1.68	1.68	1.53	1.49	1.91	1.81	1.69	1.53	2.41	1.75	1.83	1.58
Ho	0.33	0.38	0.32	0.35	0.40	0.47	0.39	0.39	0.57	0.43	0.45	0.40
Er	0.85	1.24	1.11	0.97	1.39	1.33	1.27	1.48	2.16	1.60	1.77	1.54
Tm	0.13	0.19	0.16	0.17	0.21	0.22	0.19	0.16	0.26	0.20	0.22	0.19
Yb	0.84	1.37	1.29	1.12	1.63	1.63	1.37	1.39	1.96	1.53	1.63	1.65
Lu	0.13	0.21	0.20	0.18	0.21	0.28	0.22	0.21	0.30	0.25	0.25	0.25
Hf	1.00	0.54	0.54	0.39	0.55	0.69	0.52	0.47	0.60	0.50	0.68	0.85
Ta	0.012	0.013	0.024	0.025	0.031	0.014	0.006	0.011	0.012	0.030	0.011	0.017
Pb	0.008	0.009	0.007	0.004	0.012	0.014	0.014	0.024	0.007	0.011	0.001	0.007
Th	0.023	0.006	0.014	0.016	0.015	0.002	0.001	0.005	0.009	0.009	0.002	0.007
U	0.015	0.013	0.017	0.023	0.027	0.009	0.009	0.011	0.011	0.019	0.006	0.013

Table 27 continued

	TB G9											
	TB-GAR1-g17	TB-GAR1-g18	TB-GAR1-g19	TB-GAR1-g20	TB-GAR1-g21	TB-GAR1-g22	TB-GAR1-g23	TB-GAR1-g24	TB-GAR1-g25	TB-GAR1-g26	TB-GAR1-g28	TB-GAR1-g30
Sc	70.8	68.4	78.5	70.0	60.7	63.1	75.0	84.4	56.8	53.3	55.6	81.2
V	267	321	230	274	231	225	267	249	211	231	226	279
Ni	94.1	92.9	81.8	65.4	76.9	73.4	95.9	75.1	98.4	99.0	104	72.1
Rb	0.005	0.028	0.049	0.062	0.012	0.055	0.032	0.065	0.035	0.090	0.030	< b.d.
Sr	0.27	0.28	0.07	0.16	0.13	0.13	0.32	0.21	0.25	0.24	0.29	0.21
Y	7.23	9.91	12.9	8.01	12.7	10.3	10.4	9.72	11.5	9.85	11.4	9.61
Zr	15.5	34.0	5.1	29.5	30.7	20.1	17.4	25.1	26.8	26.2	27.9	21.7
Nb	0.162	0.157	0.071	0.096	0.110	0.097	0.176	0.159	0.140	0.147	0.142	0.131
Ba	0.019	< b.d.	0.020	< b.d.	< b.d.	0.016	< b.d.	0.020	0.002	0.018	< b.d.	0.015
La	0.019	0.036	0.014	0.007	0.015	0.008	0.024	0.016	0.031	0.015	0.021	0.013
Ce	0.256	0.312	0.084	0.131	0.134	0.145	0.281	0.213	0.202	0.244	0.233	0.171
Pr	0.08	0.09	0.03	0.06	0.04	0.05	0.08	0.08	0.06	0.06	0.09	0.05
Nd	0.69	0.84	0.17	0.66	0.45	0.40	0.71	0.63	0.59	0.63	0.65	0.61
Sm	0.59	0.56	0.16	0.67	0.41	0.36	0.46	0.51	0.47	0.48	0.47	0.44
Eu	0.30	0.34	0.11	0.34	0.26	0.21	0.27	0.31	0.29	0.30	0.29	0.27
Tb	0.20	0.26	0.19	0.21	0.28	0.18	0.23	0.24	0.24	0.21	0.27	0.24
Gd	0.98	1.31	0.71	1.36	1.06	0.84	0.98	1.10	1.03	1.11	1.00	0.97
Dy	1.36	1.94	2.06	1.79	2.36	1.77	1.86	1.85	2.05	1.79	1.99	1.77
Ho	0.32	0.44	0.52	0.40	0.53	0.47	0.45	0.43	0.50	0.41	0.46	0.43
Er	1.25	1.63	2.34	1.31	1.98	1.75	1.58	1.47	1.81	1.71	1.75	1.49
Tm	0.15	0.19	0.33	0.18	0.27	0.20	0.19	0.18	0.21	0.18	0.23	0.19
Yb	1.19	1.48	3.19	1.39	1.85	1.71	1.56	1.43	1.78	1.53	1.71	1.39
Lu	0.18	0.23	0.56	0.23	0.27	0.25	0.22	0.23	0.25	0.22	0.22	0.24
Hf	0.42	0.95	0.13	0.69	0.80	0.61	0.58	0.59	0.56	0.67	0.76	0.62
Ta	0.016	0.017	0.007	0.008	0.009	0.015	0.014	0.014	0.011	0.012	0.007	0.014
Pb	0.001	< d.l.	0.007	0.005	0.007	0.009	0.028	0.009	0.009	0.004	0.008	0.006
Th	0.006	0.005	0.009	0.002	0.006	0.006	0.008	0.005	0.006	0.003	0.010	0.003
U	0.026	0.010	0.012	0.006	0.017	0.008	0.014	0.006	0.012	0.015	0.009	0.012

Table 27 continued

	TB G9											
	TB-GAR1-g31	TB-GAR1-g32	TB-GAR1-g33	TB-GAR1-g34	TB-GAR1-g35	TB-GAR1-g36	TB-GAR1-g37	TB-GAR1-g38	TB-GAR1-g40	TB-GAR1-g41	TB-GAR1-g42	TB-GAR1-g43
Sc	92.6	54.4	65.3	69.1	56.8	72.5	71.4	68.8	72.9	67.8	62.3	60.6
V	206	230	287	280	279	253	267	239	210	294	276	265
Ni	57.4	104	102	99.6	68.3	80.8	75.6	89.7	59.1	94.5	95.1	73.7
Rb	0.046	0.058	< b.d.	0.040	0.027	0.004	0.057	< b.d.	0.031	0.070	0.030	0.021
Sr	0.10	0.22	0.27	0.27	0.16	0.16	0.14	0.28	0.15	0.27	0.31	0.16
Y	13.7	11.6	6.68	7.16	14.2	6.78	7.95	8.61	8.62	9.03	9.21	8.78
Zr	7.0	41.4	17.9	18.1	15.9	16.9	15.5	25.9	20.7	22.8	21.8	19.7
Nb	0.101	0.137	0.152	0.181	0.148	0.116	0.333	0.156	0.106	0.184	0.129	0.120
Ba	< b.d.	< b.d.	0.003	< b.d.	< b.d.	< b.d.	< b.d.	0.018	< b.d.	0.043	< b.d.	0.018
La	0.012	0.018	0.018	0.034	0.015	0.010	0.015	0.030	0.013	0.016	0.022	0.020
Ce	0.096	0.222	0.266	0.284	0.148	0.177	0.188	0.258	0.114	0.246	0.240	0.146
Pr	0.04	0.05	0.08	0.08	0.04	0.07	0.04	0.07	0.04	0.06	0.07	0.04
Nd	0.23	0.65	0.66	0.75	0.52	0.45	0.42	0.68	0.43	0.74	0.62	0.49
Sm	0.21	0.56	0.49	0.44	0.40	0.45	0.34	0.55	0.45	0.57	0.52	0.43
Eu	0.12	0.33	0.28	0.24	0.28	0.22	0.20	0.30	0.25	0.31	0.32	0.21
Tb	0.17	0.29	0.21	0.21	0.28	0.16	0.19	0.22	0.18	0.22	0.23	0.20
Gd	0.54	1.17	0.83	0.89	1.08	0.73	0.73	1.01	0.85	0.97	1.00	0.76
Dy	1.68	2.11	1.20	1.28	2.32	1.19	1.40	1.56	1.54	1.63	1.68	1.48
Ho	0.52	0.47	0.27	0.29	0.62	0.30	0.38	0.38	0.40	0.38	0.40	0.39
Er	3.88	2.79	1.53	1.70	3.65	1.98	2.03	2.14	2.19	1.95	2.00	1.89
Tm	0.35	0.20	0.14	0.14	0.29	0.16	0.16	0.17	0.15	0.20	0.15	0.18
Yb	2.67	1.61	0.99	1.06	2.03	1.19	1.24	1.31	1.36	1.53	1.47	1.38
Lu	0.46	0.23	0.16	0.17	0.35	0.17	0.19	0.20	0.24	0.24	0.22	0.22
Hf	0.16	0.94	0.49	0.48	0.41	0.43	0.43	0.53	0.44	0.61	0.53	0.46
Ta	0.006	0.013	0.015	0.017	0.011	0.011	0.029	0.013	0.005	0.015	0.013	0.008
Pb	0.009	0.007	0.003	0.010	0.005	0.003	0.011	0.013	0.008	0.086	0.004	0.106
Th	0.005	0.007	0.006	0.012	0.002	0.005	0.011	0.007	0.003	0.006	0.004	0.003
U	0.009	0.007	0.015	0.009	0.014	0.016	0.026	0.010	0.006	0.011	0.010	0.013

Table 27 continued

					TB low-Mg		
	TB-GAR1-g44	TB-GAR1-g8	TB-GAR1-g29	TB-GAR1-g39	TB-GAR1-g5	TB-GAR1-g11	TB-GAR1-g27
Sc	77.3	84.7	91.6	81.9	60.6	64.5	74.8
V	252	273	216	293	309	331	346
Ni	37.6	51.5	34.1	51.0	73.2	74.3	64.8
Rb	< b.d.	0.039	< b.d.	0.011	0.042	0.054	0.054
Sr	0.26	0.36	0.38	0.32	0.20	0.27	0.20
Y	8.83	6.76	21.5	6.50	13.6	10.6	10.5
Zr	29.9	14.9	74.6	14.5	39.4	37.9	36.8
Nb	0.124	0.267	0.159	0.172	0.093	0.156	0.138
Ba	< b.d.	0.008	< b.d.	< b.d.	< b.d.	< b.d.	< b.d.
La	0.013	0.041	0.018	0.039	0.012	0.023	0.021
Ce	0.201	0.553	0.376	0.392	0.183	0.266	0.211
Pr	0.09	0.19	0.17	0.14	0.05	0.07	0.07
Nd	1.14	1.86	2.17	1.56	0.68	0.81	0.69
Sm	0.96	0.94	2.49	0.88	0.67	0.71	0.58
Eu	0.49	0.37	1.42	0.34	0.38	0.35	0.34
Tb	0.26	0.16	0.72	0.20	0.29	0.25	0.27
Gd	1.40	1.31	4.27	1.06	1.55	1.29	1.08
Dy	1.73	1.29	4.95	1.32	2.52	2.54	1.91
Ho	0.37	0.29	0.92	0.33	0.57	0.61	0.52
Er	1.72	0.85	2.40	1.66	1.82	1.82	1.59
Tm	0.16	0.13	0.26	0.12	0.28	0.20	0.20
Yb	1.30	1.04	1.52	0.90	2.04	1.53	1.59
Lu	0.20	0.16	0.23	0.15	0.31	0.23	0.20
Hf	0.47	0.34	1.28	0.38	1.01	0.98	1.01
Ta	0.011	0.031	0.014	0.017	0.008	0.011	0.007
Pb	0.009	0.031	0.006	0.008	0.006	0.011	0.005
Th	0.004	0.008	0.003	0.007	0.003	0.004	0.007
U	0.017	0.023	0.022	0.035	0.007	0.017	0.016

(2) G9 GARNETS with irregular REE patterns and G10 garnets.

Table 28: Major element composition of Mbuji-Mayi G9 garnets with irregular patterns. G10 garnets are shown

BM G9 with IP	SiO_2	TiO_2	Al_2O_3	Cr_2O_3	FeO	MnO	MgO	CaO	Na_2O	Total	Ca#	Mg#
BM-GAR3-gt2	41.07	0.16	20.16	5.39	6.66	0.38	20.23	5.02	0.03	99.1	15.1	84.4
BM-GAR3-gt3	41.56	0.26	21.01	3.87	7.93	0.45	19.51	4.46	0.08	99.1	14.1	81.4
BM-GAR3-gt4	40.85	0.22	19.28	6.19	7.24	0.46	19.83	4.62	0.07	98.7	14.3	83.0
BM-GAR3-gt5	40.63	0.24	20.59	4.67	7.07	0.49	20.62	4.28	0.08	98.7	13.0	83.9
BM-GAR3-gt6	40.55	0.19	19.73	5.51	7.52	0.46	19.96	4.60	0.04	98.5	14.2	82.6
BM-GAR3-gt7	41.71	0.22	21.05	4.31	7.92	0.50	19.69	4.47	0.05	99.9	14.0	81.6
BM-GAR3-gt8	42.25	0.13	22.29	2.33	7.28	0.38	20.55	4.14	0.02	99.4	12.6	83.4
BM-GAR3-gt9	41.05	0.25	19.76	5.76	6.62	0.36	20.35	4.54	0.06	98.7	13.8	84.6
BM-GAR3-gt11	41.44	0.30	20.25	5.10	7.17	0.46	20.18	4.57	0.05	99.5	14.0	83.4
BM-GAR3-gt12	40.76	0.16	19.89	5.40	7.17	0.46	20.12	4.54	0.02	98.5	14.0	83.3
BM-GAR3-gt13	40.94	0.13	18.98	6.49	7.33	0.46	19.38	4.77	0.06	98.5	15.0	82.5
BM-GAR3-gt16	41.60	0.05	20.56	4.84	6.81	0.40	20.47	4.75	0.04	99.5	14.3	84.3
BM-GAR3-gt17	41.61	0.00	20.27	5.21	7.24	0.47	19.63	4.95	0.03	99.4	15.3	82.9
BM-GAR3-gt18	41.66	0.19	18.77	6.67	6.55	0.44	19.44	5.08	0.05	98.8	15.8	84.1
BM-GAR3-gt19	41.64	0.07	20.52	4.76	7.00	0.38	20.04	4.77	0.03	99.2	14.6	83.6
BM-GAR3-gt20	41.18	0.05	19.76	5.68	6.79	0.37	20.44	4.54	0.03	98.8	13.8	84.3
BM-GAR3-gt23	41.70	0.06	19.01	7.02	6.47	0.39	19.93	4.71	0.04	99.3	14.5	84.6
BM-GAR3-gt24	41.98	0.18	20.33	4.88	6.50	0.40	20.07	4.94	0.05	99.3	15.0	84.6
BM-GAR3-gt25	41.74	0.09	20.41	4.90	7.13	0.44	20.38	4.63	0.06	99.8	14.0	83.6
BM-GAR3-gt26	41.17	0.20	19.05	6.56	6.81	0.47	19.75	5.03	0.07	99.1	15.5	83.8
BM-GAR3-gt27	41.19	0.08	19.96	5.61	7.35	0.40	19.82	4.67	0.04	99.1	14.5	82.8
BM-GAR3-gt28	41.44	0.10	20.82	4.46	7.52	0.45	20.03	4.59	0.07	99.5	14.1	82.6
BM-GAR3-gt29	41.82	0.13	20.59	4.35	6.58	0.38	20.52	4.55	0.06	99.0	13.7	84.8
BM-GAR3-gt30	41.69	0.16	20.46	5.00	6.80	0.46	20.06	4.34	0.05	99.0	13.5	84.0
BM-GAR3-gt31	42.16	0.14	20.55	4.90	6.37	0.34	20.23	4.72	0.06	99.4	14.3	85.0
BM-GAR3-gt33	41.56	0.20	21.24	4.06	7.52	0.48	20.08	4.68	0.05	99.8	14.3	82.6
BM-GAR3-gt34	41.37	0.03	19.69	6.08	6.83	0.40	19.79	5.47	0.06	99.7	16.6	83.8
BM-GAR3-gt38	41.94	0.12	20.85	4.40	6.34	0.35	20.59	4.64	0.01	99.2	13.9	85.3
BM G10												
BM-GAR3-gt1	41.44	0.05	19.41	6.86	6.98	0.51	21.81	2.60	0.08	99.7	7.9	84.8
BM-GAR3-gt14	41.47	0.02	19.44	6.39	6.32	0.42	21.38	3.23	0.05	98.7	9.8	85.8
BM-GAR3-gt15	41.38	0.01	18.79	7.87	6.51	0.47	21.29	3.23	0.05	99.6	9.8	85.4
BM-GAR3-gt10	40.73	0.05	19.79	5.73	6.80	0.44	20.91	4.21	0.03	98.7	12.6	84.6
BM-GAR3-gt35	41.99	0.26	20.84	4.59	6.07	0.30	21.87	3.07	0.04	99.0	9.2	86.5
BM-GAR3-gt36	41.57	0.09	20.20	5.57	6.79	0.42	21.19	3.52	0.04	99.4	10.7	84.8
BM-GAR3-gt21	41.47	0.18	18.81	6.70	6.65	0.42	19.98	4.43	0.06	98.7	13.7	84.3
BM-GAR3-gt32	41.16	0.03	18.44	7.88	6.46	0.44	21.10	4.15	0.04	99.7	12.4	85.3
BM-GAR3-gt22	41.99	0.04	20.79	5.29	6.23	0.36	23.06	0.89	0.08	98.7	2.7	86.8

Table 29: Major element composition of Tshibwe G9 garnets with irregular patterns and G10 garnets. Low-Mg garnets data is also shown.

TB G9 with IP	SiO_2	TiO_2	Al_2O_3	Cr_2O_3	FeO	MnO	MgO	CaO	Na_2O	Total	Ca#	Mg#
TB-GAR3-gt3	42.16	0.06	21.13	3.95	7.13	0.43	20.42	4.54	0.03	99.8	13.8	83.6
TB-GAR3-gt5	42.46	0.04	21.37	3.64	7.17	0.37	19.91	4.55	0.03	99.5	14.1	83.2
TB-GAR3-gt8	41.61	0.09	20.56	4.58	6.47	0.39	20.67	4.84	0.03	99.2	14.4	85.1
TB-GAR3-gt9	42.22	0.07	20.54	4.56	6.85	0.43	20.41	4.71	0.01	99.8	14.2	84.2
TB-GAR3-gt10	41.80	0.14	20.13	5.32	6.90	0.42	20.24	4.91	0.04	99.9	14.8	83.9
TB-GAR3-gt12	41.73	0.11	18.95	6.44	6.43	0.48	20.35	4.73	0.04	99.2	14.3	84.9
TB-GAR3-gt16	41.97	0.09	19.91	5.34	6.48	0.40	20.43	4.97	0.03	99.6	14.9	84.9
TB-GAR3-gt20	41.80	0.31	19.91	5.29	7.28	0.43	20.00	4.71	0.04	99.8	14.5	83.0
TB G10												
TB-GAR3-gt2	42.21	0.12	20.69	4.93	6.81	0.42	20.54	3.93	0.03	99.7	12.1	84.3
TB-GAR3-gt6	42.93	0.04	20.80	4.54	6.03	0.39	21.68	3.31	0.04	99.7	9.9	86.5
TB-GAR3-gt11	43.14	0.07	21.31	4.10	5.94	0.35	22.06	2.94	0.03	99.9	8.7	86.9
TB-GAR3-gt13	42.56	0.06	20.89	4.78	5.91	0.32	22.58	2.28	0.03	99.4	6.8	87.2
TB-GAR3-gt15	43.03	0.04	20.90	4.77	5.91	0.30	22.37	3.07	0.04	100.4	9.0	87.1
TB-GAR3-gt18	42.75	0.08	21.69	4.08	6.15	0.35	22.26	2.52	0.03	99.9	7.5	86.6
TB-GAR3-gt19	42.58	0.18	21.21	4.26	5.95	0.34	22.18	3.40	0.03	100.1	9.9	86.9
TB-GAR3-gt22	42.44	0.07	20.69	4.83	5.96	0.31	21.94	3.30	0.03	99.6	9.8	86.8
TB-GAR1-gt7	41.76	0.18	20.69	4.70	6.61	0.32	22.09	3.58	0.04	100.0	10.4	85.6
TB-GAR3-gt21	41.83	0.29	17.86	8.06	6.44	0.40	20.52	4.28	0.04	99.7	13.0	85.0
TB low-Mg												
TB-GAR3-gt1	41.99	0.10	22.75	2.22	8.35	0.46	19.00	5.28	0.04	100.2	16.6	80.2
TB-GAR3-gt4	42.05	0.06	22.86	1.94	8.31	0.45	18.53	5.35	0.02	99.5	17.2	79.9
TB-GAR3-gt7	42.10	0.10	23.22	1.47	9.30	0.49	18.34	5.16	0.02	100.2	16.8	77.8
TB-GAR3-gt14	42.28	0.06	22.82	1.96	8.65	0.54	18.22	5.36	0.01	99.9	17.4	79.0
TB-GAR3-gt17	42.04	0.06	22.57	2.42	8.17	0.49	18.81	5.45	0.02	100.0	17.2	80.4
TB-GAR3-gt23	41.87	0.05	23.07	1.69	9.58	0.68	18.16	5.04	0.02	100.1	16.6	77.2
TB-GAR3-gt24	42.12	0.09	22.87	2.08	8.09	0.45	19.19	5.31	0.04	100.2	16.6	80.9
TB-GAR3-gt25	41.87	0.05	23.26	1.62	8.31	0.57	19.08	5.08	0.02	99.8	16.0	80.4
TB-GAR3-gt26	42.03	0.05	22.94	2.14	8.14	0.54	19.26	5.31	0.03	100.4	16.5	80.8

Table 30: Trace element composition of Mbuji-Mayi G9 garnets with irregular patterns and G10 garnets.

	BM G9 with IP										
	BM-GAR3-g2	BM-GAR3-g3	BM-GAR3-g4	BM-GAR3-g5	BM-GAR3-g6	BM-GAR3-g7	BM-GAR3-g8	BM-GAR3-g9	BM-GAR3-g11	BM-GAR3-g12	BM-GAR3-g13
Sc	68.1	62.4	82.7	72.5	95.2	64.8	53.8	74.4	61.7	74.8	97.0
V	240	168	184	196	204	161	155	230	202	238	262
Ni	41.0	31.6	37.1	32.4	41.5	31.3	63.3	48.5	35.9	38.8	40.5
Rb	0.052	0.072	0.042	0.067	0.056	0.131	0.095	0.069	0.036	0.122	0.046
Sr	0.93	0.22	0.35	0.33	0.30	0.26	0.06	0.42	0.59	0.31	0.38
Y	1.98	12.4	11.0	9.76	13.3	13.2	7.94	3.96	15.6	7.96	4.97
Zr	5.93	28.3	42.8	33.4	44.4	34.7	3.51	15.6	66.3	43.4	36.5
Nb	0.115	0.118	0.178	0.127	0.177	0.148	0.116	0.141	0.133	0.222	0.276
Ba	< b.d.	< b.d.	0.015	< b.d.	0.021	0.025	< b.d.	0.034	0.019	0.013	0.018
La	0.047	0.016	0.013	0.018	0.017	0.016	0.008	0.016	0.060	0.022	0.048
Ce	0.929	0.307	0.343	0.303	0.256	0.270	0.086	0.339	0.861	0.290	0.432
Pr	0.32	0.13	0.12	0.12	0.12	0.10	0.02	0.13	0.28	0.15	0.15
Nd	2.41	1.50	1.81	1.94	1.76	1.53	0.16	1.45	2.83	1.77	1.96
Sm	0.48	1.16	1.75	1.63	1.75	1.52	0.10	1.07	2.34	1.54	1.79
Eu	0.14	0.56	0.98	0.71	0.92	0.81	0.07	0.42	1.18	0.87	0.81
Tb	0.05	0.37	0.56	0.34	0.44	0.38	0.12	0.18	0.72	0.32	0.30
Gd	0.50	2.58	4.47	3.00	3.94	3.29	0.46	1.43	4.74	2.54	2.34
Dy	0.35	2.24	2.67	2.13	3.06	2.62	1.19	0.82	3.70	1.55	1.39
Ho	0.10	0.49	0.45	0.41	0.59	0.57	0.33	0.16	0.64	0.28	0.18
Er	0.34	1.65	1.30	1.13	1.30	1.72	1.22	0.58	1.71	0.91	0.56
Tm	0.06	0.18	0.16	0.13	0.12	0.23	0.18	0.07	0.23	0.11	0.08
Yb	0.57	1.51	0.93	1.06	0.76	1.73	1.48	0.63	1.58	0.71	0.66
Lu	0.10	0.25	0.14	0.16	0.11	0.26	0.22	0.09	0.22	0.13	0.11
Hf	0.15	0.35	0.67	0.39	0.74	0.38	0.10	0.26	0.80	0.52	0.58
Ta	0.008	0.012	0.023	0.010	0.019	0.012	0.005	0.025	0.006	0.014	0.021
Pb	0.001	0.006	0.002	0.004	< b.d.	0.029	0.004	0.001	0.011	0.003	0.006
Th	0.011	0.006	0.002	0.003	0.002	0.002	0.012	0.003	0.018	0.002	0.014
U	0.021	0.019	0.013	0.024	0.013	0.009	0.017	0.013	0.121	0.018	0.022

Table 30 continued

	BM-GAR3-g17	BM-GAR3-g16	BM-GAR3-g18	BM-GAR3-g19	BM-GAR3-g20	BM-GAR3-g23	BM-GAR3-g24	BM-GAR3-g25	BM-GAR3-g26	BM-GAR3-g27	BM-GAR3-g28
Sc	70.2	136.7	84.6	66.2	91.2	83.7	76.4	78.0	70.2	77.5	80.6
V	265	214	302	248	264	252	262	227	262	236	225
Ni	52.8	31.0	59.5	56.7	61.1	49.4	50.6	52.1	45.3	42.6	44.0
Rb	0.056	0.058	0.045	0.072	0.031	0.108	0.038	0.096	0.112	0.053	0.142
Sr	0.29	0.52	0.25	0.16	0.27	0.38	0.44	0.27	0.33	0.36	0.36
Y	1.21	2.07	0.78	4.77	1.39	1.79	4.14	2.44	3.64	3.54	2.07
Zr	2.48	49.9	21.0	2.45	3.42	26.8	14.5	10.3	8.92	39.8	19.1
Nb	0.430	0.266	0.095	0.310	0.160	0.226	0.155	0.158	0.242	0.273	0.078
Ba	< b.d.	0.002	0.015	< b.d.	< b.d.	0.008	0.018	0.023	0.003	0.010	0.016
La	0.041	0.044	0.013	0.036	0.024	0.036	0.063	0.023	0.052	0.022	0.017
Ce	0.541	0.803	0.205	0.336	0.270	0.438	0.611	0.259	0.608	0.376	0.329
Pr	0.17	0.32	0.07	0.09	0.11	0.21	0.21	0.08	0.18	0.15	0.16
Nd	2.04	3.74	0.82	0.61	1.15	2.33	1.71	0.97	1.59	1.91	1.75
Sm	0.59	3.22	0.79	0.18	0.42	1.41	0.64	0.61	0.72	1.96	0.98
Eu	0.15	1.21	0.36	0.09	0.11	0.47	0.24	0.26	0.26	0.92	0.37
Tb	0.04	0.27	0.09	0.07	0.02	0.10	0.12	0.07	0.12	0.30	0.12
Gd	0.36	2.96	0.88	0.33	0.33	1.12	0.77	0.68	0.75	2.77	1.04
Dy	0.22	0.85	0.33	0.68	0.21	0.47	0.75	0.38	0.73	1.15	0.52
Ho	0.05	0.09	0.03	0.18	0.06	0.05	0.15	0.08	0.16	0.14	0.09
Er	0.21	0.17	0.05	0.75	0.24	0.16	0.55	0.35	0.50	0.23	0.32
Tm	0.04	0.02	0.01	0.14	0.05	0.02	0.07	0.05	0.07	0.03	0.05
Yb	0.40	0.17	0.11	0.98	0.56	0.19	0.61	0.62	0.53	0.20	0.44
Lu	0.07	0.04	0.03	0.14	0.11	0.04	0.09	0.12	0.08	0.04	0.09
Hf	0.04	0.81	0.40	0.08	0.10	0.46	0.25	0.21	0.21	0.55	0.38
Ta	0.035	0.020	0.010	0.023	0.013	0.024	0.017	0.016	0.022	0.022	0.011
Pb	0.019	0.003	0.004	0.005	0.009	0.009	0.020	0.010	0.001	0.005	0.005
Th	0.015	0.005	0.003	0.010	0.005	0.011	0.006	0.004	0.024	0.003	0.004
U	0.031	0.049	0.009	0.020	0.021	0.022	0.017	0.019	0.073	0.020	0.019

Table 30 continued

							BM G10					
	BM-GAR3-g29	BM-GAR3-g30	BM-GAR3-g31	BM-GAR3-g33	BM-GAR3-g34	BM-GAR3-g38	BM-GAR3-g1	BM-GAR3-g14	BM-GAR3-g15	BM-GAR3-g35	BM-GAR3-g36	BM-GAR3-g22
Sc	79.8	82.8	78.2	66.7	85.0	70.5	95.4	83.3	78.8	68.6	63.4	66.2
V	271	199	256	216	324	242	192	287	253	201	224	171
Ni	53.4	32.4	54.6	35.8	55.2	60.8	30.0	48.8	51.9	61.7	33.8	31.0
Rb	0.067	< b.d.	0.019	0.078	0.005	0.083	0.030	0.005	0.079	0.064	0.065	0.073
Sr	0.21	0.31	0.35	0.49	0.27	0.83	0.45	2.35	0.38	0.17	0.28	0.70
Y	2.81	5.87	6.40	8.28	0.26	1.71	1.55	0.76	1.58	1.06	3.73	0.60
Zr	11.3	47.5	6.62	26.7	5.92	10.4	22.1	5.39	3.93	15.5	49.2	15.5
Nb	0.117	0.132	0.267	0.140	0.155	0.216	0.195	0.220	0.255	0.083	0.181	0.163
Ba	0.009	0.015	0.027	< b.d.	< b.d.	< b.d.	< b.d.	0.019	< b.d.	< b.d.	0.037	0.003
La	0.017	0.013	0.019	0.016	0.013	0.042	0.028	0.395	0.043	0.004	0.014	0.063
Ce	0.199	0.276	0.345	0.428	0.263	0.604	0.640	3.401	0.416	0.111	0.300	1.015
Pr	0.07	0.11	0.13	0.24	0.10	0.26	0.26	0.49	0.15	0.03	0.14	0.46
Nd	1.14	2.00	1.35	2.67	1.32	2.65	3.21	1.90	1.51	0.48	2.28	5.58
Sm	0.92	2.01	0.59	1.84	0.52	0.39	2.22	0.31	0.46	0.60	2.07	1.13
Eu	0.36	0.97	0.20	0.71	0.13	0.09	0.74	0.09	0.13	0.29	0.88	0.27
Tb	0.09	0.31	0.13	0.27	0.01	0.04	0.12	0.04	0.03	0.08	0.31	0.04
Gd	0.94	2.93	0.70	2.12	0.22	0.25	1.85	0.21	0.29	0.77	2.66	0.58
Dy	0.47	1.45	0.98	1.58	0.04	0.21	0.49	0.15	0.17	0.25	1.12	0.19
Ho	0.10	0.29	0.27	0.35	0.01	0.07	0.07	0.03	0.06	0.06	0.16	0.03
Er	0.52	0.87	1.10	1.25	0.06	0.30	0.15	0.10	0.33	0.16	0.41	0.06
Tm	0.09	0.12	0.18	0.15	0.01	0.05	0.02	0.01	0.06	0.03	0.04	0.01
Yb	0.83	0.88	1.26	1.35	0.23	0.58	0.15	0.20	0.72	0.34	0.33	0.10
Lu	0.15	0.17	0.25	0.21	0.06	0.10	0.04	0.05	0.12	0.06	0.06	0.03
Hf	0.28	0.73	0.17	0.46	0.14	0.27	0.51	0.14	0.08	0.39	0.98	0.26
Ta	0.016	0.015	0.023	0.016	0.018	0.016	0.014	0.006	0.029	0.012	0.014	0.006
Pb	0.007	0.006	0.023	0.012	0.006	0.004	0.007	0.005	< b.d.	0.009	0.005	0.006
Th	0.002	0.001	0.008	0.002	0.001	0.007	0.003	0.086	0.010	0.002	0.002	0.005
U	0.011	0.014	0.015	0.016	0.015	0.020	0.030	0.076	0.025	0.008	0.014	0.055

Table 31: Trace element composition of Tshibwe G9 garnets with irregular patterns and G10 garnets. Some Mbuji-Mayi G10 garnets are also shown. In addition low-Mg garnets from Tshibwe are also presented.

				TB G9 with IP							
	BM-GAR3-g10	BM-GAR3-g21	BM-GAR3-g32	TB-GAR3-g3	TB-GAR3-g5	TB-GAR3-g8	TB-GAR3-g9	TB-GAR3-g10	TB-GAR3-g12	TB-GAR3-g16	TB-GAR3-g20
Sc	72.9	81.5	90.9	67.4	91.6	76.8	79.6	77.9	98.7	80.2	81.7
V	237	262	260	219	241	239	245	264	297	279	236
Ni	50.3	47.9	53.0	61.3	63.8	59.1	61.3	51.4	60.4	60.1	49.5
Rb	0.070	0.048	0.177	0.024	0.019	0.103	0.106	0.094	0.151	0.063	0.066
Sr	0.24	0.31	1.46	0.18	0.16	0.16	0.18	0.23	0.26	0.29	0.40
Y	1.96	3.41	0.94	4.12	6.56	1.83	3.80	8.93	2.11	3.50	10.2
Zr	14.9	27.8	6.22	7.46	1.56	4.82	5.35	45.1	5.90	3.56	30.1
Nb	0.159	0.218	0.287	0.166	0.317	0.147	0.103	0.146	0.268	0.319	0.114
Ba	0.017	0.003	0.189	< b.d.	0.041	0.034	< b.d.	0.021	0.027	0.011	0.004
La	0.015	0.027	0.142	0.017	0.037	0.007	0.011	0.023	0.026	0.022	0.017
Ce	0.260	0.366	1.855	0.187	0.226	0.181	0.204	0.265	0.361	0.475	0.405
Pr	0.13	0.12	0.56	0.06	0.05	0.06	0.07	0.10	0.16	0.14	0.13
Nd	1.18	1.29	4.76	0.80	0.45	0.68	0.83	1.20	1.24	1.20	1.70
Sm	1.03	0.97	0.84	0.45	0.14	0.28	0.38	0.94	0.61	0.38	1.18
Eu	0.36	0.41	0.22	0.17	0.06	0.08	0.13	0.51	0.20	0.12	0.49
Tb	0.10	0.17	0.03	0.08	0.07	0.02	0.06	0.29	0.08	0.07	0.35
Gd	1.14	1.40	0.36	0.41	0.23	0.15	0.33	1.60	0.51	0.37	2.92
Dy	0.51	0.77	0.16	0.60	0.83	0.20	0.59	2.09	0.47	0.63	2.19
Ho	0.07	0.15	0.04	0.15	0.22	0.07	0.18	0.45	0.10	0.15	0.47
Er	0.22	0.40	0.23	0.93	1.53	0.53	0.83	1.32	0.39	0.59	1.43
Tm	0.04	0.05	0.03	0.10	0.15	0.08	0.12	0.13	0.04	0.08	0.18
Yb	0.32	0.41	0.33	0.98	1.49	0.83	1.07	0.83	0.50	0.63	1.22
Lu	0.08	0.08	0.09	0.16	0.25	0.18	0.19	0.15	0.13	0.11	0.18
Hf	0.27	0.56	0.11	0.20	0.02	0.11	0.11	1.02	0.17	0.12	0.80
Ta	0.015	0.014	0.037	0.017	0.022	0.011	0.012	0.016	0.026	0.036	0.018
Pb	0.001	0.010	0.022	0.008	0.022	0.014	0.008	0.014	0.007	0.002	0.005
Th	0.003	0.004	0.035	0.005	0.009	0.002	0.002	0.001	0.001	0.008	0.011
U	0.022	0.016	0.101	0.006	0.017	0.014	0.011	0.006	0.014	0.034	0.034

Table 31 continued

	TB G10									
	TB-GAR3-g2	TB-GAR3-g6	TB-GAR3-g11	TB-GAR3-g13	TB-GAR3-g15	TB-GAR3-g18	TB-GAR3-g19	TB-GAR3-g22	TB-GAR1-g7	TB-GAR3-g21
Sc	72.4	80.3	69.3	81.7	72.1	43.1	57.4	69.9	68.4	102
V	194	212	205	262	232	147	210	199	231	252
Ni	33.8	61.4	63.9	61.4	61.4	54.9	65.3	61.9	61.6	61.6
Rb	0.094	0.031	0.129	0.095	0.090	0.076	< b.d.	0.132	0.034	0.084
Sr	0.26	0.22	0.15	0.20	0.33	0.25	0.15	0.20	0.19	0.23
Y	3.24	1.58	0.52	0.58	0.62	0.96	2.07	0.86	1.40	0.96
Zr	31.4	16.5	14.3	5.39	1.80	6.14	21.3	16.3	16.1	14.7
Nb	0.088	0.164	0.097	0.126	0.244	0.222	0.108	0.131	0.107	0.125
Ba	0.018	0.017	< b.d.	0.003	0.013	0.020	0.005	0.006	0.021	< b.d.
La	0.012	0.023	0.010	0.012	0.024	0.012	0.006	0.013	0.018	0.024
Ce	0.282	0.218	0.118	0.222	0.371	0.260	0.127	0.174	0.130	0.212
Pr	0.13	0.07	0.05	0.11	0.13	0.10	0.05	0.06	0.05	0.08
Nd	2.04	1.02	0.58	1.61	1.33	0.79	0.50	0.81	0.51	0.88
Sm	1.41	0.84	0.59	0.91	0.45	0.26	0.49	0.71	0.61	0.59
Eu	0.57	0.37	0.25	0.25	0.12	0.12	0.26	0.30	0.26	0.23
Tb	0.22	0.11	0.06	0.04	0.03	0.03	0.14	0.08	0.07	0.05
Gd	1.56	1.10	0.59	0.54	0.23	0.40	1.33	1.16	0.81	0.84
Dy	1.02	0.45	0.15	0.17	0.14	0.17	0.64	0.21	0.34	0.18
Ho	0.15	0.07	0.02	0.02	0.02	0.04	0.08	0.03	0.05	0.03
Er	0.54	0.25	0.12	0.13	0.13	0.15	0.23	0.16	0.15	0.19
Tm	0.07	0.03	0.03	0.03	0.02	0.02	0.03	0.03	0.03	0.03
Yb	0.60	0.41	0.31	0.27	0.26	0.20	0.32	0.36	0.31	0.48
Lu	0.15	0.09	0.08	0.07	0.06	0.04	0.06	0.08	0.06	0.12
Hf	0.60	0.35	0.30	0.10	0.05	0.11	0.49	0.36	0.36	0.27
Ta	0.012	0.017	0.006	0.012	0.025	0.014	0.012	0.018	0.011	0.011
Pb	0.013	0.014	0.004	0.005	0.011	0.005	0.002	0.009	0.016	0.007
Th	0.003	0.006	0.002	0.005	0.010	0.006	0.002	0.005	0.002	0.003
U	0.008	0.026	0.008	0.011	0.017	0.015	0.003	0.007	0.009	0.006

Table 31 continued

	TB low-Mg								
	TB-GAR3-g1	TB-GAR3-g4	TB-GAR3-g7	TB-GAR3-g14	TB-GAR3-g17	TB-GAR3-g23	TB-GAR3-g24	TB-GAR3-g25	TB-GAR3-g26
Sc	67.1	108	57.8	122	128	71.9	98.1	135	86.6
V	82.4	103	67.6	118	88.9	84.0	94.4	64.5	112
Ni	9.26	11.7	9.71	6.68	12.5	5.98	9.84	8.83	8.33
Rb	0.116	0.137	0.031	0.096	0.060	0.053	0.058	0.008	0.049
Sr	0.03	0.79	0.11	0.17	0.05	0.14	0.07	0.12	0.12
Y	15.6	23.1	8.95	21.3	31.0	12.8	22.6	42.6	16.5
Zr	4.67	20.8	4.43	14.8	11.2	5.56	10.4	19.8	4.25
Nb	< b.d.	0.005	0.002	0.003	0.008	0.002	0.017	0.002	0.001
Ba	< b.d.	1.089	0.357	0.012	< b.d.	0.038	0.018	0.005	0.020
La	0.010	0.009	0.010	0.003	0.027	0.006	0.081	0.024	0.009
Ce	0.068	0.283	0.193	0.148	0.165	0.179	0.158	0.276	0.125
Pr	0.00	0.19	0.11	0.12	0.02	0.11	0.04	0.17	0.09
Nd	0.08	2.96	1.26	2.18	0.17	1.91	0.51	2.60	1.72
Sm	0.19	2.88	0.70	2.10	0.32	1.64	0.42	2.49	0.97
Eu	0.16	1.25	0.34	1.01	0.27	0.76	0.30	1.29	0.44
Tb	0.24	0.62	0.21	0.59	0.49	0.38	0.40	0.87	0.36
Gd	0.82	3.84	1.15	3.27	2.60	3.81	2.23	6.91	2.30
Dy	2.30	4.29	1.86	4.36	4.44	2.41	3.50	6.83	2.74
Ho	0.71	1.03	0.39	0.96	1.14	0.56	0.95	1.75	0.69
Er	3.85	4.14	1.45	3.53	4.16	1.77	3.76	6.68	2.86
Tm	0.45	0.42	0.11	0.44	0.63	0.21	0.50	0.89	0.39
Yb	3.52	3.12	0.79	3.41	5.22	1.73	4.07	6.63	3.38
Lu	0.61	0.52	0.10	0.52	0.76	0.23	0.63	0.97	0.50
Hf	0.13	0.21	0.07	0.12	0.23	0.14	0.22	0.24	0.10
Ta	0.001	0.003	0.001	0.001	< b.d.	< b.d.	0.001	< b.d.	0.001
Pb	0.011	0.067	0.011	0.002	0.010	0.004	0.014	0.008	0.003
Th	0.002	0.008	0.003	< b.d.	0.007	0.002	0.021	0.003	< b.d.
U	0.004	0.005	0.001	< b.d.	0.051	< b.d.	0.034	0.009	0.003

A.2.4. ILMENITE MEGACRYSTS

Table 32: Major element composition of Mbuji-Mayi ilmenites (including those from Lukelenge concentrates)

BM Low-Mg	TiO_2	Al_2O_3	Cr_2O_3	FeO	MnO	MgO	NiO	Total	Mg#	Cr#
BM-ILM1-g2	51.20	0.15	3.70	30.85	0.42	11.41	0.07	97.8	44.6	94.3
BM-ILM1-g4	50.64	0.17	4.07	31.66	0.42	11.12	0.09	98.2	43.9	94.1
BM-ILM1-g6	51.04	0.16	3.78	31.24	0.43	11.37	0.12	98.1	44.6	94.0
BM-ILM1-g7	51.14	0.15	3.89	31.58	0.41	11.23	0.08	98.5	43.9	94.7
BM-ILM1-g8	50.41	0.12	3.83	31.87	0.41	10.87	0.09	97.6	43.1	95.5
BM-ILM1-g9	50.85	0.12	3.70	31.39	0.40	10.94	0.13	97.5	43.0	95.5
BM-ILM1-g12	50.27	0.10	3.77	32.55	0.46	10.77	0.07	98.0	42.9	96.2
BM-ILM1-g17	47.53	0.10	4.87	33.53	0.45	10.45	0.10	97.0	44.0	96.9
BM-ILM1-g21	50.22	0.12	3.86	32.51	0.41	10.64	0.09	97.8	42.4	95.7
BM-ILM1-g22	49.60	0.12	3.91	32.99	0.39	10.17	0.15	97.3	41.0	95.8
BM-ILM1-g29	51.80	0.19	3.21	29.99	0.43	11.77	0.10	97.5	45.4	92.1
BM-ILM1-g41	50.55	0.25	5.05	30.19	0.36	11.57	0.13	98.1	45.7	93.1
BM-ILM1-g43	50.84	0.15	3.78	30.53	0.41	11.49	0.16	97.4	45.2	94.3
LUK_G1	51.64	0.15	3.79	31.59	0.42	11.50		99.1	44.5	94.5
LUK_G4	52.24	0.21	3.38	30.35	0.33	11.81		98.3	45.1	91.5
LUK_G8	51.89	0.15	3.84	31.54	0.38	11.52		99.2	44.4	94.4
LUK_G13	51.74	0.15	3.18	31.41	0.38	11.71		98.6	48.0	86.4
LUK_G16	52.54	0.19	3.70	30.55	0.35	11.82		99.2	45.2	93.6
LUK_G26	52.69	0.28	3.05	31.97	0.30	11.60		99.8	44.9	93.0
LUK_G32	51.76	0.13	3.09	32.73	0.39	11.12		99.2	42.9	94.3
BM med-Mg										
BM-ILM1-g1	52.99	0.28	2.79	29.65	0.40	12.53	0.12	98.7	47.2	87.0
BM-ILM1-g5	53.39	0.31	2.77	29.52	0.40	12.49	0.20	99.1	46.7	85.7
BM-ILM1-g10	52.95	0.33	2.67	29.23	0.43	12.83	0.16	98.6	48.5	84.6
BM-ILM1-g11	52.96	0.24	3.01	29.53	0.39	12.17	0.13	98.4	45.9	89.4
BM-ILM1-g13	52.47	0.24	2.70	29.34	0.33	12.51	0.14	97.7	47.6	88.4
BM-ILM1-g14	50.91	0.25	3.73	29.84	0.35	11.90	0.12	97.1	46.7	91.0
BM-ILM1-g16	52.71	0.31	2.73	29.14	0.42	12.45	0.15	97.9	47.2	85.7
BM-ILM1-g18	52.77	0.30	2.65	29.66	0.42	12.30	0.16	98.2	46.6	85.5
BM-ILM1-g19	52.85	0.27	2.70	29.95	0.40	12.33	0.13	98.6	46.6	87.1
BM-ILM1-g20	52.68	0.25	2.71	29.67	0.39	12.20	0.15	98.1	46.3	87.7
BM-ILM1-g25	52.57	0.30	2.78	29.11	0.40	12.70	0.16	98.0	48.3	86.2
BM-ILM1-g26	52.78	0.26	2.64	29.49	0.41	12.29	0.18	98.0	46.5	87.0
BM-ILM1-g28	53.36	0.27	2.72	29.20	0.36	12.40	0.16	98.5	46.4	87.0
BM-ILM1-g30	52.67	0.29	2.68	28.69	0.36	12.62	0.15	97.5	47.8	86.2
BM-ILM1-g31	51.80	1.09	2.63	29.63	0.38	12.28	0.16	98.0	46.9	87.6
BM-ILM1-g32	52.52	0.26	2.74	29.40	0.39	12.09	0.14	97.5	46.0	87.7
BM-ILM1-g33	52.17	0.27	2.63	29.27	0.36	12.20	0.14	97.0	46.7	86.9
BM-ILM1-g35	52.86	0.26	2.71	29.71	0.41	12.27	0.14	98.4	46.4	87.4
BM-ILM1-g38	52.84	0.27	3.05	30.01	0.39	12.25	0.18	99.0	46.3	88.2
BM-ILM1-g42	52.90	0.26	2.71	29.58	0.44	12.21	0.15	98.2	46.2	87.3
BM-ILM1-g44	51.87	0.26	3.03	29.55	0.39	12.29	0.13	97.5	47.3	88.8
LUK_G3	53.03	0.22	2.90	29.66	0.39	12.68		98.8	47.8	89.7
LUK_G5	54.17	0.36	3.01	26.96	0.32	13.74		98.6	50.6	85.0

Table 32 continued

	TiO_2	Al_2O_3	Cr_2O_3	FeO	MnO	MgO	NiO	Total	Mg#	Cr#
LUK_G7	53.57	0.29	2.57	29.43	0.36	12.96		99.2	48.3	85.8
LUK_G9	54.09	0.23	2.95	28.72	0.34	13.12		99.4	48.4	89.8
LUK_G10	53.52	0.29	2.10	30.39	0.41	12.43		99.2	46.4	83.1
LUK_G11	53.65	0.28	2.65	29.30	0.31	12.92		99.1	46.8	87.0
LUK_G12	54.36	0.27	2.73	29.47	0.34	12.75		99.9	46.5	89.5
LUK_G14	53.18	0.24	3.04	29.87	0.33	12.40		99.1	47.7	90.7
LUK_G15	53.91	0.23	3.28	28.37	0.33	12.90		99.0	48.1	85.0
LUK_G17	53.25	0.30	2.57	29.57	0.34	12.84		98.9	47.0	91.4
LUK_G18	51.92	0.22	3.43	29.95	0.34	12.23		98.1	48.6	87.2
LUK_G19	53.27	0.26	2.60	29.39	0.38	12.97		98.9	47.8	89.5
LUK_G24	53.20	0.25	3.11	30.11	0.35	12.75		99.8	48.7	89.9
LUK_G25	53.73	0.27	3.54	28.74	0.33	13.11		99.7	43.9	87.9
LUK_G30	53.51	0.25	3.41	28.48	0.35	13.04		99.0	48.6	90.3
LUK_G31	54.14	0.36	2.69	28.99	0.31	13.42		100.0	49.5	83.2
LUK_G33	54.11	0.28	2.68	29.19	0.38	12.75		99.4	47.1	86.3
LUK_G36	53.06	0.27	3.60	29.90	0.34	12.78		99.9	48.1	89.8
LUK_G37	53.76	0.29	3.46	28.64	0.31	13.04		99.5	48.4	89.1
LUK_G38	52.83	0.36	4.00	29.41	0.31	12.72		99.6	48.0	88.2
LUK_G39	54.28	0.38	2.66	28.72	0.31	13.23		99.6	48.6	82.4
LUK_G40	53.91	0.28	2.66	29.88	0.34	12.68		99.7	46.9	86.3
BM High-Mg										
BM-ILM1-g3	54.88	0.41	1.47	27.71	0.32	13.77	0.21	98.8	50.0	70.6
BM-ILM1-g15	54.17	0.42	1.58	27.11	0.31	13.66	0.18	97.4	50.3	71.8
BM-ILM1-g23	55.31	0.40	1.55	27.02	0.35	14.36	0.17	99.1	51.8	72.3
BM-ILM1-g27	54.85	0.42	1.54	26.91	0.29	14.08	0.20	98.3	51.2	71.1
BM-ILM1-g34	54.97	0.38	1.45	27.56	0.33	13.78	0.20	98.7	50.0	71.8
BM-ILM1-g36	54.78	0.46	1.90	26.74	0.33	14.26	0.14	98.6	51.9	73.4
BM-ILM1-g39	54.60	0.43	1.53	27.79	0.33	13.72	0.18	98.6	50.1	70.6
BM-ILM1-g40	55.42	0.39	1.53	26.37	0.30	14.30	0.17	98.5	51.5	72.4
LUK_G2	55.50	0.44	1.64	27.34	0.26	14.09		99.3	50.6	71.7
LUK_G6	55.22	0.46	1.46	26.99	0.26	14.45		98.9	52.1	68.2
LUK_G20	54.44	0.49	2.02	26.55	0.25	14.53		98.3	53.2	73.4
LUK_G21	55.25	0.42	1.52	27.04	0.25	14.40		98.9	51.9	70.6
LUK_G22	55.59	0.45	1.52	26.80	0.25	14.56		99.2	52.2	69.3
LUK_G23	56.22	0.59	1.45	26.27	0.27	14.14		98.9	50.1	62.4
LUK_G28	55.53	0.38	1.62	27.65	0.34	13.78		99.3	49.5	74.1
LUK_G29	55.65	0.45	1.49	26.74	0.22	14.75		99.3	52.8	69.1
LUK_G34	54.67	0.45	1.80	28.95	0.29	13.47		99.7	49.1	72.7

Table 33: Major element composition of Tshibwe ilmenite megacrysts

TB Low-Mg	TiO_2	Al_2O_3	Cr_2O_3	FeO	MnO	MgO	NiO	Total	Mg#	Cr#
TB-ILM1-g6	48.69	0.12	4.25	32.70	0.44	10.97	0.03	97.2	45.1	95.9
TB-ILM1-g7	48.75	0.11	4.30	33.19	0.43	10.79	0.04	97.6	44.3	96.4
TB-ILM1-g36	50.95	0.18	4.26	30.35	0.38	11.71	0.08	97.9	45.9	94.1
TB-ILM2-g12	50.07	0.17	4.30	30.71	0.43	11.30	0.11	97.1	45.2	94.3
TB-ILM2-g16	50.84	0.18	4.27	30.79	0.37	11.67	0.07	98.2	45.9	94.2
TB-ILM2-g23	50.87	0.15	4.24	31.97	0.44	11.17	0.09	98.9	43.9	95.0
TB-ILM1-g23	54.31	0.78	1.37	27.72	0.31	13.88	0.10	98.5	43.9	95.0
TB-ILM2-g38	50.18	0.10	4.10	32.06	0.40	11.50	0.12	98.5	45.8	96.4
TB med-Mg										
TB-ILM1-g1	52.59	0.37	3.17	30.10	0.33	12.90	0.14	99.6	48.9	85.3
TB-ILM1-g2	51.83	0.35	3.19	29.25	0.39	12.80	0.13	97.9	49.3	85.8
TB-ILM1-g5	51.39	0.36	4.62	28.70	0.39	12.87	0.12	98.4	50.0	89.5
TB-ILM1-g8	52.25	0.35	2.98	29.48	0.38	13.07	0.18	98.7	50.0	85.2
TB-ILM1-g9	51.19	0.19	4.41	30.35	0.42	12.08	0.12	98.8	47.2	94.0
TB-ILM1-g10	52.33	0.28	3.81	28.96	0.36	12.98	0.17	98.9	49.5	90.2
TB-ILM1-g12	51.46	0.24	4.02	29.69	0.40	12.55	0.10	98.5	48.8	91.7
TB-ILM1-g15	51.48	0.41	4.88	29.44	0.40	12.56	0.19	99.4	48.8	88.9
TB-ILM1-g21	51.68	0.29	3.74	28.96	0.34	12.93	0.17	98.1	49.9	89.7
TB-ILM1-g24	52.36	0.31	3.75	28.76	0.41	12.85	0.17	98.6	49.1	89.1
TB-ILM1-g25	51.64	0.37	3.70	30.01	0.36	12.48	0.15	98.7	48.3	87.0
TB-ILM1-g30	50.63	0.17	4.37	30.89	0.44	12.26	0.14	98.9	48.4	94.6
TB-ILM1-g35	51.02	0.33	4.62	29.58	0.41	12.44	0.17	98.6	48.7	90.4
TB-ILM1-g40	52.30	0.34	3.37	29.87	0.42	12.57	0.18	99.0	48.1	86.9
TB-ILM1-g41	51.29	0.33	3.78	29.62	0.35	12.34	0.14	97.8	48.1	88.5
TB-ILM1-g42	49.61	0.46	6.15	29.23	0.35	12.13	0.19	98.1	48.8	89.9
TB-ILM1-g43	51.42	0.23	4.23	29.45	0.42	12.31	0.15	98.2	47.9	92.4
TB-ILM2-g1	51.47	0.35	3.90	29.33	0.43	12.52	0.21	98.2	48.6	88.2
TB-ILM2-g3	50.78	0.41	5.66	28.61	0.34	12.19	0.17	98.2	47.9	90.3
TB-ILM2-g5	51.11	0.33	3.78	29.59	0.37	12.26	0.13	97.6	47.9	88.5
TB-ILM2-g6	52.57	0.26	4.45	28.19	0.37	12.76	0.18	98.8	48.5	91.9
TB-ILM2-g7	52.59	0.33	3.28	29.69	0.45	12.62	0.17	99.1	48.0	86.9
TB-ILM2-g9	51.20	0.39	4.52	29.51	0.42	12.72	0.16	98.9	49.7	88.7
TB-ILM2-g10	52.03	0.31	3.21	30.12	0.42	12.42	0.14	98.6	47.7	87.5
TB-ILM2-g13	52.57	0.36	2.62	28.86	0.38	12.83	0.15	97.8	48.7	82.9
TB-ILM2-g14	52.04	0.27	3.84	28.99	0.37	12.53	0.22	98.3	48.1	90.6
TB-ILM2-g17	52.39	0.33	3.23	29.51	0.37	12.52	0.18	98.5	47.7	86.6
TB-ILM2-g20	51.83	0.34	3.71	29.40	0.37	12.65	0.17	98.5	48.8	88.0
TB-ILM2-g22	52.31	0.37	3.51	29.68	0.38	12.79	0.16	99.2	48.8	86.6
TB-ILM2-g24	51.65	0.37	4.18	29.63	0.36	12.45	0.16	98.8	48.1	88.5
TB-ILM2-g25	51.96	0.33	3.48	30.12	0.36	12.68	0.19	99.1	48.7	87.7
TB-ILM2-g31	51.07	0.40	4.52	29.26	0.43	12.46	0.17	98.3	48.8	88.3
TB-ILM2-g32	51.91	0.31	3.20	29.63	0.42	12.42	0.14	98.0	47.9	87.3
TB-ILM2-g35	52.14	0.36	4.48	28.51	0.37	12.92	0.21	99.0	49.5	89.2
TB-ILM2-g37	51.96	0.20	4.27	29.73	0.39	12.20	0.17	98.9	46.9	93.5
TB-ILM2-g39	52.01	0.28	4.54	29.24	0.37	12.63	0.15	99.2	48.5	91.5
TB-ILM2-g41	50.53	0.39	5.33	29.36	0.36	12.33	0.20	98.5	48.8	90.1
TB-ILM2-g42	52.48	0.34	3.45	29.70	0.35	12.56	0.18	99.1	47.8	87.3

Table 33 continued

TB High-Mg	TiO_2	Al_2O_3	Cr_2O_3	FeO	MnO	MgO	NiO	Total	Mg#	Cr#
TB-ILM1-g3	53.67	0.41	1.84	28.11	0.37	13.65	0.15	98.2	50.8	74.8
TB-ILM1-g4	53.49	0.46	1.23	29.00	0.41	13.30	0.07	97.9	49.7	64.2
TB-ILM1-g11	54.10	0.46	1.27	29.40	0.37	13.53	0.12	99.2	49.9	65.1
TB-ILM1-g13	54.08	0.48	2.36	28.00	0.32	14.20	0.20	99.6	52.4	76.8
TB-ILM1-g14	54.01	0.44	1.21	29.84	0.36	13.26	0.11	99.2	49.0	65.1
TB-ILM1-g16	54.34	0.45	1.87	28.47	0.30	14.02	0.18	99.6	51.4	73.5
TB-ILM1-g17	54.01	0.46	1.69	28.79	0.37	14.02	0.17	99.5	51.8	71.1
TB-ILM1-g18	54.34	0.48	1.77	28.49	0.37	13.83	0.15	99.4	50.8	71.3
TB-ILM1-g19	53.40	0.50	2.15	27.99	0.35	14.06	0.14	98.6	52.6	74.1
TB-ILM1-g20	53.94	0.48	1.73	28.42	0.35	14.06	0.13	99.1	52.0	70.6
TB-ILM1-g22	53.67	0.46	1.33	29.34	0.32	13.56	0.13	98.8	50.4	65.9
TB-ILM1-g26	53.51	0.45	1.90	28.26	0.34	14.06	0.19	98.7	52.4	73.8
TB-ILM1-g27	53.53	0.53	1.18	29.77	0.37	13.21	0.11	98.7	49.0	64.2
TB-ILM1-g28	53.77	0.44	1.36	29.16	0.31	13.71	0.14	98.9	50.9	67.6
TB-ILM1-g31	54.04	0.47	2.16	28.21	0.29	14.01	0.17	99.4	51.7	75.3
TB-ILM1-g32	53.65	0.47	1.86	28.23	0.34	14.03	0.18	98.7	52.2	72.8
TB-ILM1-g33	53.44	0.46	1.27	29.91	0.37	12.95	0.12	98.5	48.4	65.1
TB-ILM1-g34	53.89	0.46	1.80	28.32	0.34	13.75	0.14	98.7	50.9	72.4
TB-ILM1-g37	53.88	0.42	1.44	28.54	0.32	13.66	0.10	98.4	50.6	69.6
TB-ILM1-g38	53.70	0.44	1.53	28.64	0.34	13.76	0.14	98.5	51.1	70.1
TB-ILM1-g39	53.69	0.42	1.20	29.16	0.36	13.25	0.15	98.2	49.3	65.8
TB-ILM1-g44	53.60	0.44	1.19	30.20	0.39	12.85	0.12	98.8	47.9	64.5
TB-ILM2-g2	54.08	0.44	1.65	28.41	0.33	13.69	0.15	98.7	50.5	71.5
TB-ILM2-g4	53.91	0.45	1.19	30.03	0.35	13.08	0.14	99.1	48.4	64.1
TB-ILM2-g8	54.60	0.44	1.85	27.44	0.37	14.15	0.16	99.0	51.7	74.0
TB-ILM2-g11	53.78	0.46	2.34	27.80	0.32	13.74	0.18	98.6	51.0	77.3
TB-ILM2-g15	53.65	0.43	1.60	28.68	0.32	13.71	0.14	98.5	51.0	71.2
TB-ILM2-g18	54.04	0.39	1.23	29.05	0.35	13.34	0.12	98.5	49.3	68.0
TB-ILM2-g19	53.98	0.47	2.44	27.64	0.32	14.00	0.18	99.0	51.7	77.6
TB-ILM2-g21	54.32	0.50	2.17	28.16	0.34	13.75	0.16	99.4	50.5	74.5
TB-ILM2-g26	54.09	0.45	1.37	29.43	0.30	13.43	0.15	99.2	49.5	67.0
TB-ILM2-g27	53.53	0.47	2.53	27.87	0.33	13.96	0.21	98.9	49.3	59.8
TB-ILM2-g28	54.08	0.43	1.47	28.92	0.37	13.37	0.17	98.8	49.4	69.4
TB-ILM2-g29	53.97	0.45	2.41	27.37	0.32	13.66	0.21	98.4	50.5	78.4
TB-ILM2-g30	54.24	0.43	1.64	27.88	0.37	13.69	0.14	98.4	50.4	72.0
TB-ILM2-g33	54.54	0.45	1.85	27.15	0.36	13.93	0.18	98.4	51.0	73.5
TB-ILM2-g34	54.96	0.40	1.69	27.16	0.34	14.29	0.15	99.0	51.9	73.7
TB-ILM2-g36	53.66	0.43	1.25	30.36	0.35	13.05	0.08	99.2	48.5	66.3
TB-ILM2-g40	54.53	0.44	1.70	28.35	0.34	13.38	0.19	98.9	49.0	72.3
TB-ILM2-g43	53.55	0.44	1.24	30.12	0.35	13.19	0.13	99.0	49.2	65.4
TB-ILM2-g44	53.87	0.44	2.12	28.08	0.35	13.80	0.21	98.9	51.1	76.3

Table 34: Trace element composition of Mbuji-Mayi ilmenites (including those from Lukelenge concentrates)

BM Low-Mg	Sc	V	Co	Ni	Cu	Zn	Ga	Y	Zr	Nb	Hf	Ta	Nb/Ta	Nb/Zr
BM_ILM1_gr2	37.3	2623	292	1795	50.6	334	12.9	0.052	385	3324	13.9	325	10.2	8.64
BM_ILM1_gr6	43.9	2636	284	1734	43.5	275	12.1	0.046	412	3569	14.9	359	9.93	8.66
BM_ILM1_gr12	47.8	2782	280	1475	39.8	280	11.8	0.091	460	3947	16.7	401	9.83	8.57
BM_ILM1_gr17	72.0	3826	282	1632	38.3	275	12.0	0.060	811	6637	29.3	580	11.4	8.18
LUK_G1	57.5	2600	246	1393		171	9.93		642	4173	23.1	543	7.69	6.51
LUK_G4	46.9	2607	263	1591		192	11.4	0.065	484	3555	18.1	414	8.59	7.35
LUK_G8	56.0	2638	250	1473		177	10.9	0.064	633	4074	23.1	515	7.91	6.43
LUK_G13	61.3	2447	244	1291		158	8.78	0.074	665	4081	26.6	571	7.14	6.13
LUK_G16	46.3	2702	279	1765		196	12.2	0.080	494	3974	19.4	475	8.36	8.04
LUK_G26	50.2	3115	269	1836		182	15.5	0.076	526	3458	19.5	380	9.10	6.58
LUK_G32	59.6	2662	259	1149		150	8.67	0.054	617	5043	23.8	598	8.43	8.17
BM med-Mg														
BM_ILM1_gr10	38.4	2286	261	2056	44.7	296	13.7	0.055	324	2316	12.3	246	9.43	7.15
BM_ILM1_gr11	34.1	2642	323	2632	58.2	260	17.0	0.058	354	2481	13.5	268	9.25	7.00
BM_ILM1_gr13	34.5	1968	196	1050	28.0	264	8.13	0.058	328	2907	12.0	290	10.0	8.87
BM_ILM1_gr18	38.3	2475	286	2051	49.2	289	14.3	0.056	365	2600	13.9	276	9.43	7.12
LUK_G3	41.3	2541	276	1921		195	12.6	0.056	418	3242	15.7	359	9.03	7.75
LUK_G5	29.3	2267	293	2816		197	14.8	0.083	295	2122	11.1	239	8.89	7.19
LUK_G7	37.5	2451	274	2066		193	13.2	0.066	384	2666	14.4	315	8.47	6.95
LUK_G9	51.2	1994	265	1711		163	8.58	0.053	480	3274	19.3	442	7.41	6.81
LUK_G10	37.7	2633	307	2004		122	14.0	0.112	408	3192	16.9	378	8.44	7.82
LUK_G11	38.2	2467	287	2130		151	14.3	0.065	401	2792	16.1	348	8.01	6.96
LUK_G12	40.2	2432	276	2062		178	13.8	0.085	424	2759	16.5	347	7.95	6.51
LUK_G14	45.5	2434	262	1864		167	13.3	0.073	461	3296	18.5	402	8.20	7.16
LUK_G15	42.6	2081	293	1942		178	10.0	0.065	375	3303	15.7	406	8.13	8.80
LUK_G17	38.7	2557	290	2081		197	14.4	0.070	380	2834	15.5	344	8.24	7.45
LUK_G18	42.5	2556	263	1968		175	13.1	0.074	442	3161	17.9	365	8.65	7.15
LUK_G19	36.8	2411	277	2038		190	13.6	0.076	385	2678	15.1	329	8.14	6.95
LUK_G24	44.0	2650	283	2318		181	14.3	0.094	459	3156	17.6	376	8.39	6.88
LUK_G25	46.0	2279	290	2334		176	12.3	0.061	394	2981	15.4	369	8.08	7.57
LUK_G30	45.5	2171	285	2244		168	10.6	0.066	403	3161	16.4	390	8.11	7.85
LUK_G31	35.5	2416	306	2605		120	18.2	0.069	402	2550	16.5	320	7.98	6.34
LUK_G33	40.2	2426	279	2092		170	13.7	0.077	421	2682	16.0	321	8.35	6.38
LUK_G36	44.1	2448	276	2323		178	12.4	0.062	434	3007	16.1	338	8.89	6.93
LUK_G37	44.5	2451	270	2281		183	13.4	0.078	432	2855	16.4	332	8.60	6.61
LUK_G38	42.5	2503	265	2276		175	17.5	0.071	471	2702	17.9	342	7.89	5.74
LUK_G39	36.8	2327	274	2353		181	16.8	0.054	414	2435	16.8	309	7.87	5.88
LUK_G40	42.3	2450	271	2022		189	13.3	0.072	440	2930	16.8	354	8.29	6.66

Table 34 continued

BM High-Mg	Sc	V	Co	Ni	Cu	Zn	Ga	Y	Zr	Nb	Hf	Ta	Nb/Ta	Nb/Zr
BM_ILM1_gr23	28.4	1405	169	1389	29.5	233	8.35	0.059	182	1499	7.00	148	10.1	8.24
BM_ILM1_gr27	27.0	1436	163	1199	26.5	225	7.96	0.059	200	1505	7.41	160	9.40	7.52
LUK_G2	27.4	2190	281	2297		183	16.1	0.105	320	1308	12.2	160	8.16	4.09
LUK_G6	26.7	2121	299	2650		181	15.6	0.086	288	1189	11.0	145	8.22	4.13
LUK_G20	26.8	2645	338	3018		118	18.7	0.076	202	1202	8.60	133	9.07	5.96
LUK_G21	28.0	2187	313	2838		133	17.3	0.114	333	1093	14.0	132	8.26	3.28
LUK_G22	30.0	2111	294	2851		143	16.6	0.126	357	1072	15.1	153	7.02	3.00
LUK_G23	27.7	2204	314	2637		178	17.2	0.105	330	1332	12.8	168	7.93	4.04
LUK_G28	27.9	2230	303	2343		185	14.3	0.100	316	2170	10.9	236	9.20	6.87
LUK_G29	25.7	2125	305	2875		179	16.8	0.092	294	1264	11.7	153	8.26	4.30
LUK_G34	41.8	2318	274	2210		164	17.2	0.073	380	1992	15.2	246	8.09	5.24

Table 35: Trace element composition of Tshibwe ilmenites

	Sc	V	Co	Ni	Cu	Zn	Ga	Y	Zr	Nb	Hf	Ta	Nb/Ta	Nb/Zr
TB Low-Mg														
TB_ILM1_gr36	47.9	2576	267	1643	34.2	262	12.3	0.066	522	3800	20.1	442	8.61	7.28
TB_ILM2_gr23	34.9	5887	775	5833	227	239	45.3	0.058	456	3392	17.0	343	9.88	7.44
TB_ILM2_gr38	71.1	2936	271	2204	48.9	190	16.6	0.053	747	5316	27.1	624	8.52	7.12
TB_ILM1_gr7	32.4	8722	1056	6367	272	317	66.6	0.042	719	4660	28.2	457	10.2	6.48
TB med-Mg														
TB_ILM1_gr2	28.3	2344	284	2338	54.5	382	18.2	0.032	277	2052	10.6	206	9.96	7.41
TB_ILM1_gr8	34.8	3389	375	3415	115	259	25.2	0.075	246	1275	10.0	138	9.23	5.19
TB_ILM1_gr21	35.0	2283	281	2209	42.7	246	13.1	0.047	369	2851	14.2	314	9.07	7.74
TB_ILM1_gr41	43.2	1576	169	1627	24.4	264	13.4	0.060	230	1515	8.47	177	8.55	6.58
TB_ILM1_gr42	38.7	4206	446	3423	62.6	240	29.4	0.058	706	4644	26.8	542	8.57	6.58
TB_ILM1_gr43	44.2	3238	347	2730	50.6	256	22.2	0.077	526	3553	20.3	410	8.67	6.76
TB_ILM2_gr7	37.4	1867	248	2038	46.4	270	12.1	0.046	260	2177	10.6	224	9.72	8.38
TB_ILM2_gr9	41.0	2684	286	1682	46.2	302	13.6	0.042	454	3580	17.2	375	9.54	7.89
TB_ILM2_gr14	35.6	2957	333	2726	56.2	212	19.9	0.034	437	3109	17.3	349	8.91	7.11
TB_ILM2_gr20	34.1	2602	287	2403	50.2	224	18.3	0.056	364	2681	14.6	300	8.93	7.37
TB_ILM2_gr31	47.4	2773	284	2493	44.9	213	20.4	0.048	414	2504	16.3	294	8.51	6.05
TB_ILM2_gr41	37.5	3973	441	3740	66.8	205	27.8	0.052	654	4141	26.5	484	8.56	6.33

Table 35 continued

TB High-Mg	Sc	V	Co	Ni	Cu	Zn	Ga	Y	Zr	Nb	Hf	Ta	Nb/Ta	Nb/Zr
TB_ILM2_gr4	24.3	2447	300	1902	81.4	293	20.0	0.064	198	1375	7.93	139	9.88	6.94
TB_ILM2_gr21	30.7	2763	308	2652	87.8	212	19.8	0.050	216	1158	9.02	136	8.49	5.37
TB_ILM2_gr19	28.6	2812	308	2745	93.9	199	19.8	0.051	198	1030	8.69	121	8.54	5.21
TB_ILM2_gr18	29.7	2325	303	1798	76.2	213	16.4	0.054	225	1790	8.78	191	9.38	7.96
TB_ILM2_gr15	24.4	2566	300	2196	88.3	277	19.2	0.055	191	1179	8.10	125	9.45	6.16
TB_ILM2_gr33	28.0	2253	298	2458	85.4	255	17.1	0.048	168	1274	6.92	137	9.31	7.59
TB_ILM2_gr34	29.2	2407	316	2421	85.6	213	16.2	0.060	192	1514	8.00	173	8.76	7.89
TB_ILM2_gr40	32.5	3463	418	2481	90.3	223	25.3	0.045	399	2670	16.0	301	8.88	6.70
TB_ILM1_gr11	33.0	754	96	800.1	16.8	357	4.81	0.072	108	896	4.29	95.3	9.40	8.29
TB_ILM1_gr13	26.1	1887	224	1882	39.6	300	13.6	0.058	246	1851	9.67	197	9.39	7.53
TB_ILM1_gr20	30.3	2559	302	2301	83.6	268	19.0	0.075	212	1347	8.49	145	9.30	6.35
TB_ILM1_gr27	33.5	1639	185	1507	50.5	233	11.8	0.056	131	712	5.50	86.4	8.23	5.42
TB_ILM1_gr44	37.2	2404	284	1741	62.9	252	17.5	0.078	265	1650	10.3	185	8.94	6.23

A.2.5. TSHIBWE CLINOPYROXENE MEGACRYSTS

Table 36: Major element composition of Tshibwe cpx megacrysts

TB High-Ca	SiO2	TiO_2	Al_2O_3	Cr_2O_3	FeO	MnO	MgO	CaO	Na_2O	K_2O	Total	Ca#	Mg#	Cr#
TB-CPX2-g2	55.53	0.26	1.75	0.77	3.42	0.09	17.46	19.78	1.52	0.03	100.6	44.9	90.1	22.7
TB-CPX2-g4	55.12	0.19	1.65	0.50	3.43	0.07	17.04	20.61	1.25	0.02	99.9	46.5	89.9	16.7
TB-CPX2-g5	55.59	0.17	1.70	0.50	3.44	0.08	17.42	20.53	1.21	0.01	100.7	45.8	90.0	16.6
TB-CPX2-g6	55.31	0.17	1.69	0.44	3.44	0.09	17.42	20.54	1.24	0.02	100.4	45.9	90.0	14.9
TB-CPX2-g7	55.33	0.18	1.70	0.63	3.55	0.07	17.45	19.91	1.44	0.02	100.3	45.1	89.8	19.8
TB-CPX2-g8	55.22	0.15	1.81	0.58	3.34	0.04	16.74	20.91	1.34	0.02	100.1	47.3	89.9	17.8
TB-CPX2-g9	54.86	0.18	1.57	0.80	3.61	0.13	17.81	19.71	1.42	0.02	100.1	44.3	89.8	25.4
TB-CPX2-g10	55.35	0.21	1.57	0.90	3.67	0.10	17.84	19.18	1.43	0.02	100.3	43.6	89.6	27.8
TB-CPX2-g11	55.26	0.20	1.88	0.52	3.72	0.08	17.30	19.76	1.47	0.02	100.2	45.1	89.2	15.5
TB-CPX2-g12	55.32	0.17	1.75	0.42	3.33	0.06	17.32	20.85	1.23	0.03	100.5	46.4	90.3	13.9
TB-CPX2-g13	55.30	0.23	1.84	0.83	3.29	0.10	17.27	19.64	1.45	0.03	100.0	45.0	90.3	23.3
TB-CPX2-g14	55.30	0.21	1.73	0.55	3.51	0.08	17.32	20.41	1.26	0.03	100.4	45.8	89.8	17.5
TB-CPX2-g15	55.07	0.21	1.69	0.85	3.44	0.12	17.16	19.91	1.45	0.03	99.9	45.5	89.9	25.3
TB-CPX2-g17	55.09	0.21	1.79	0.60	3.45	0.06	17.19	20.13	1.41	0.03	99.9	45.7	89.9	18.4
TB-CPX2-g18	55.18	0.17	1.74	0.43	3.31	0.07	17.27	21.02	1.27	0.01	100.5	46.7	90.3	14.2
TB-CPX2-g19	55.18	0.20	1.65	0.90	3.39	0.08	17.50	19.75	1.35	0.03	100.0	44.8	90.2	26.7
TB-CPX2-g20	54.97	0.16	1.85	0.57	3.49	0.08	16.78	20.93	1.41	0.02	100.2	47.3	89.6	17.1
TB-CPX2-g21	55.13	0.19	1.82	0.71	3.54	0.09	17.22	19.77	1.46	0.02	99.9	45.2	89.7	20.8
TB-CPX2-g27	54.89	0.20	1.75	0.58	3.42	0.07	17.33	20.32	1.29	0.02	99.9	45.7	90.0	18.1
TB-CPX2-g28	54.86	0.20	1.74	0.47	3.49	0.06	17.45	20.57	1.25	0.02	100.1	45.8	89.9	15.3
TB-CPX2-g29	55.18	0.19	1.77	0.48	3.39	0.07	17.33	20.53	1.26	0.02	100.2	46.0	90.1	15.3
TB-CPX2-g30	55.40	0.16	1.84	0.47	3.42	0.07	16.98	20.72	1.33	0.02	100.4	46.7	89.8	14.7
TB-CPX2-g32	54.78	0.18	1.62	0.75	3.69	0.10	17.71	19.53	1.43	0.02	99.8	44.2	89.5	23.6
TB-CPX2-g34	55.06	0.20	1.67	0.72	3.32	0.08	17.37	20.00	1.33	0.03	99.8	45.3	90.3	22.4
TB-CPX2-g35	54.45	0.18	1.62	0.47	3.44	0.09	17.57	20.49	1.23	0.02	99.5	45.6	90.1	16.3
TB-CPX2-g36	54.86	0.20	1.82	0.58	3.56	0.10	17.47	20.24	1.36	0.03	100.2	45.4	89.7	17.6
TB-CPX2-g37	54.78	0.21	1.75	0.87	3.46	0.08	17.77	19.65	1.36	0.02	99.9	44.3	90.1	24.9
TB-CPX2-g38	55.00	0.21	1.75	0.66	3.42	0.06	17.42	20.28	1.32	0.04	100.2	45.5	90.1	20.3
TB-CPX2-g41	54.75	0.23	1.79	0.72	3.52	0.07	17.42	19.72	1.37	0.03	99.6	44.9	89.8	21.2
TB-CPX2-g44	54.57	0.18	1.66	0.55	3.43	0.09	17.89	20.25	1.23	0.02	99.9	44.8	90.3	18.2
TB-CPX1-g2	55.49	0.27	1.85	0.93	3.51	0.14	17.50	19.04	1.53	0.03	100.3	43.9	89.9	25.2
TB-CPX1-g4	55.30	0.23	1.71	0.75	3.43	0.12	17.55	19.60	1.29	0.03	100.0	44.5	90.1	22.7
TB-CPX1-g5	55.43	0.25	1.66	0.82	3.70	0.15	17.57	19.02	1.41	0.03	100.0	43.8	89.4	24.8
TB-CPX1-g7	55.34	0.24	1.66	0.82	3.67	0.15	17.69	19.28	1.47	0.03	100.3	43.9	89.6	24.9
TB-CPX1-g9	55.15	0.25	1.91	0.69	3.67	0.15	17.30	18.94	1.55	0.03	99.6	44.0	89.4	19.5
TB-CPX1-g12	55.27	0.25	1.84	0.62	3.28	0.15	17.21	20.15	1.35	0.04	100.2	45.7	90.3	18.4
TB-CPX1-g16	55.81	0.21	1.72	0.79	3.51	0.13	17.33	19.24	1.39	0.03	100.2	44.4	89.8	23.5
TB-CPX1-g18	55.24	0.22	2.00	0.71	3.30	0.14	17.00	19.65	1.53	0.03	99.8	45.4	90.2	19.1
TB-CPX1-g19	55.72	0.23	1.77	0.74	3.51	0.14	17.38	19.43	1.38	0.03	100.3	44.5	89.8	22.0

Table 36 continued

	SiO2	TiO_2	Al_2O_3	Cr_2O_3	FeO	MnO	MgO	CaO	Na_2O	K_2O	Total	Ca#	Mg#	Cr#
TB-CPX1-g20	55.48	0.22	1.79	0.70	3.39	0.14	17.20	19.54	1.40	0.03	99.9	44.9	90.0	20.9
TB-CPX1-g22	55.09	0.21	1.72	0.51	3.46	0.12	17.38	20.29	1.24	0.03	100.0	45.6	90.0	16.5
TB-CPX1-g23	55.13	0.21	1.91	0.62	3.50	0.14	17.53	20.05	1.42	0.03	100.5	45.1	89.9	17.8
TB-CPX1-g24	55.46	0.22	1.76	0.42	3.35	0.12	16.84	20.70	1.34	0.02	100.2	46.9	90.0	13.9
TB-CPX1-g25	55.53	0.26	1.74	0.84	3.47	0.14	17.28	19.78	1.35	0.04	100.4	45.1	89.9	24.5
TB-CPX1-g27	55.45	0.22	1.81	0.48	3.40	0.12	17.15	20.16	1.31	0.02	100.1	45.8	90.0	15.2
TB-CPX1-g28	55.62	0.18	1.83	0.48	3.44	0.14	16.90	20.24	1.33	0.03	100.2	46.3	89.8	14.8
TB-CPX1-g29	55.60	0.23	1.77	0.67	3.38	0.12	17.25	19.86	1.39	0.04	100.3	45.3	90.1	20.3
TB-CPX1-g30	55.30	0.25	1.78	0.66	3.43	0.14	17.31	19.79	1.39	0.03	100.1	45.1	90.0	20.0
TB-CPX1-g31	55.31	0.24	1.69	1.07	3.67	0.12	17.68	18.35	1.49	0.04	99.7	42.7	89.6	29.8
TB-CPX1-g33	55.49	0.19	1.74	0.56	3.44	0.14	17.31	20.09	1.36	0.03	100.3	45.5	90.0	17.6
TB-CPX1-g35	55.37	0.21	1.77	0.53	3.36	0.10	17.32	20.43	1.27	0.03	100.4	45.9	90.2	16.6
TB-CPX1-g36	55.30	0.21	1.76	0.42	3.37	0.14	16.99	20.95	1.30	0.03	100.5	47.0	90.0	13.8
TB low-Ca														
TB-CPX2-g16	55.26	0.18	1.73	0.64	4.78	0.10	18.73	17.44	1.44	0.03	100.3	40.1	87.5	20.0
TB-CPX2-g22	54.93	0.15	1.74	0.58	4.88	0.13	18.53	17.59	1.31	0.03	99.9	40.6	87.1	18.3
TB-CPX2-g23	55.37	0.16	1.69	0.96	4.85	0.11	19.23	16.28	1.37	0.04	100.0	37.8	87.6	27.6
TB-CPX2-g24	55.35	0.13	1.78	1.00	4.88	0.13	19.48	16.18	1.46	0.03	100.4	37.4	87.7	27.4
TB-CPX2-g25	54.74	0.16	1.75	0.60	4.86	0.10	18.82	17.55	1.41	0.04	100.0	40.1	87.4	18.8
TB-CPX2-g26	54.87	0.16	1.76	0.59	4.83	0.09	18.11	18.15	1.44	0.02	100.0	41.9	87.0	18.3
TB-CPX2-g31	55.26	0.12	1.87	0.84	4.92	0.09	19.59	15.84	1.48	0.03	100.0	36.7	87.7	23.2
TB-CPX2-g43	54.87	0.14	1.67	0.82	4.53	0.12	19.68	16.90	1.31	0.03	100.0	38.2	88.6	24.7
TB-CPX1-g1	55.69	0.15	1.83	0.84	4.65	0.14	19.73	15.64	1.43	0.04	100.1	36.3	88.3	23.5
TB-CPX1-g3	55.76	0.21	1.86	0.89	4.74	0.19	19.47	15.80	1.43	0.04	100.4	36.8	88.0	24.4
TB-CPX1-g6	55.43	0.23	1.68	0.57	4.66	0.16	18.67	17.42	1.42	0.04	100.3	40.1	87.7	18.4
TB-CPX1-g8	55.31	0.17	1.66	0.62	4.63	0.16	18.21	16.98	1.27	0.04	99.0	40.1	87.5	20.0
TB-CPX1-g10	55.42	0.18	1.71	0.78	4.64	0.18	18.89	16.50	1.36	0.04	99.7	38.6	87.9	23.5
TB-CPX1-g11	55.66	0.17	1.69	0.81	4.35	0.17	19.47	16.54	1.32	0.04	100.2	37.9	88.9	24.4
TB-CPX1-g13	55.35	0.17	1.73	0.77	4.41	0.17	19.08	16.73	1.33	0.04	99.8	38.6	88.5	23.0
TB-CPX1-g15	55.43	0.20	1.79	0.60	4.81	0.17	18.64	17.03	1.36	0.03	100.1	39.6	87.3	18.4
TB-CPX1-g17	55.71	0.15	1.98	0.96	4.90	0.14	18.97	15.59	1.62	0.03	100.0	37.1	87.3	24.5
TB-CPX1-g26	55.76	0.17	1.75	0.66	4.73	0.18	18.56	16.98	1.45	0.04	100.2	39.7	87.5	20.1
TB-CPX1-g32	55.72	0.19	1.67	0.77	4.48	0.17	19.17	16.82	1.31	0.04	100.3	38.7	88.4	23.6
TB-CPX1-g34	55.70	0.15	1.88	1.03	4.77	0.20	19.50	15.69	1.65	0.03	100.6	36.6	87.9	26.8

Table 37: Trace element composition of Tshibwe cpx megacrysts

	TB high-Ca											
	TB-cpx2-g2	TB-cpx2-g4	TB-cpx2-g5	TB-cpx2-g6	TB-cpx2-g7	TB-cpx2-g8	TB-cpx2-g9	TB-cpx2-g10	TB-cpx2-g11	TB-cpx2-g12	TB-cpx2-g13	TB-cpx2-g14
Sc	17.3	18.1	18.2	18.2	16.0	21.3	15.2	13.4	18.2	19.7	17.1	18.9
V	298	295	297	294	316	287	324	328	323	302	257	270
Ni	304	242	251	238	311	226	324	356	280	230	340	263
Rb	0.032	0.003	< b.d.	0.009	0.037	< b.d.	0.018	0.008	< b.d.	< b.d.	0.007	< b.d.
Sr	116	121	93.8	129	134	131	104	98.5	121	130	106	114
Y	1.48	1.67	1.44	1.98	1.64	1.57	1.71	1.43	1.99	1.58	1.64	1.40
Zr	5.79	6.57	5.24	7.83	6.44	8.45	4.99	4.61	7.82	7.25	5.48	5.69
Nb	0.13	0.10	0.11	0.09	0.12	0.11	0.08	0.07	0.11	0.11	0.13	0.13
Ba	0.11	0.10	0.13	0.06	0.15	0.09	0.15	0.22	0.15	0.19	0.10	0.16
La	2.01	1.80	1.69	1.94	2.20	1.98	1.76	1.64	2.13	2.16	1.53	2.28
Ce	6.89	6.39	5.47	6.90	7.44	6.90	5.96	5.63	7.55	7.25	6.05	7.19
Pr	1.08	1.04	0.84	1.10	1.20	1.13	0.93	0.92	1.20	1.12	1.05	1.19
Nd	5.59	5.28	4.22	5.88	6.23	6.04	4.94	4.45	6.44	6.03	5.88	5.90
Sm	1.28	1.26	1.02	1.47	1.42	1.43	1.18	1.14	1.63	1.36	1.38	1.26
Eu	0.42	0.40	0.32	0.48	0.44	0.45	0.37	0.38	0.54	0.44	0.40	0.37
Tb	0.10	0.13	0.10	0.15	0.11	0.13	0.11	0.09	0.16	0.12	0.13	0.10
Gd	0.91	0.95	0.81	1.17	1.06	1.11	0.97	0.89	1.13	1.01	1.95	1.82
Dy	0.50	0.48	0.42	0.68	0.51	0.57	0.44	0.45	0.64	0.54	0.55	0.49
Ho	0.05	0.08	0.07	0.08	0.07	0.09	0.07	0.06	0.11	0.08	0.08	0.07
Er	0.20	0.21	0.17	0.29	0.25	0.18	0.22	0.19	0.25	0.20	0.15	0.14
Tm	0.008	0.010	0.014	0.013	0.016	0.016	0.013	0.013	0.023	0.009	0.010	0.014
Yb	0.073	0.074	0.063	0.076	0.075	0.082	0.065	0.075	0.085	0.059	0.087	0.061
Lu	0.006	0.008	0.007	0.008	0.011	0.004	0.009	0.008	0.012	0.007	0.008	0.006
Hf	0.42	0.48	0.39	0.54	0.51	0.62	0.35	0.34	0.55	0.59	0.39	0.32
Ta	0.008	0.008	0.008	0.010	0.010	0.007	0.007	0.008	0.007	0.008	0.014	0.011
Pb	0.24	0.17	0.14	0.19	0.22	0.18	0.13	0.15	0.17	0.22	0.16	0.18
Th	0.024	0.018	0.018	0.023	0.017	0.012	0.018	0.016	0.024	0.027	0.011	0.021
U	0.003	0.004	0.002	0.003	0.007	0.005	0.004	0.002	0.003	0.003	0.002	0.007

Table 37 continued

	TB high-Ca											
	TB-cpx2-g15	TB-cpx2-g17	TB-cpx2-g18	TB-cpx2-g19	TB-cpx2-g20	TB-cpx2-g21	TB-cpx2-g27	TB-cpx2-g28	TB-cpx2-g29	TB-cpx2-g30	TB-cpx2-g32	TB-cpx2-g34
Sc	15.2	16.1	19.7	15.9	22.6	16.9	18.3	19.5	19.3	20.9	16.3	16.4
V	267	279	263	281	263	274	290	273	284	301	228	251
Ni	321	287	237	345	233	293	267	241	249	225	318	298
Rb	0.031	0.009	0.015	0.010	0.008	< b.d.	< b.d.	0.046	0.046	0.028	< b.d.	0.012
Sr	117	121	133	123	133	136	126	107	98.9	130	109	110
Y	1.35	1.30	1.31	1.36	1.86	1.98	1.48	1.44	1.26	1.52	1.74	1.57
Zr	5.13	6.19	6.63	4.75	9.59	8.07	5.99	7.02	5.58	7.17	5.66	5.85
Nb	0.12	0.09	0.11	0.13	0.13	0.13	0.17	0.10	0.14	0.13	0.11	0.11
Ba	0.24	0.10	0.10	0.21	0.14	0.11	0.11	0.16	0.08	0.10	0.13	0.12
La	2.25	2.30	2.30	2.21	2.24	2.17	2.20	1.82	1.88	2.42	1.66	1.93
Ce	7.36	7.59	7.97	7.31	7.63	7.46	7.64	6.32	5.92	8.07	6.04	6.27
Pr	1.08	1.10	1.17	1.10	1.18	1.19	1.17	1.00	0.87	1.22	0.97	0.97
Nd	6.06	5.68	6.28	5.74	6.48	6.48	5.89	5.09	4.61	6.27	4.96	5.07
Sm	1.25	1.28	1.35	1.21	1.56	1.42	1.26	1.09	1.06	1.40	1.16	1.20
Eu	0.38	0.38	0.42	0.40	0.50	0.53	0.41	0.40	0.36	0.45	0.39	0.41
Tb	0.11	0.09	0.12	0.11	0.11	0.15	0.10	0.08	0.09	0.12	0.11	0.11
Gd	1.69	1.70	1.80	1.68	2.09	2.31	2.25	2.05	1.82	2.41	2.16	1.18
Dy	0.50	0.45	0.43	0.46	0.68	0.77	0.47	0.51	0.41	0.50	0.55	0.52
Ho	0.08	0.06	0.06	0.07	0.09	0.10	0.07	0.09	0.07	0.08	0.07	0.07
Er	0.12	0.14	0.15	0.12	0.17	0.20	0.12	0.14	0.14	0.13	0.15	0.15
Tm	0.013	0.010	0.013	0.011	0.021	0.019	0.005	0.017	0.015	0.017	0.021	0.018
Yb	0.066	0.069	0.073	0.049	0.084	0.104	0.066	0.074	0.073	0.074	0.085	0.068
Lu	0.004	0.008	0.007	0.011	0.011	0.005	0.009	0.004	0.012	0.010	0.012	0.005
Hf	0.32	0.42	0.55	0.30	0.74	0.59	0.46	0.43	0.44	0.56	0.41	0.43
Ta	0.009	0.010	0.006	0.014	0.009	0.009	0.005	0.008	0.009	0.009	0.007	0.009
Pb	0.21	0.18	0.21	0.18	0.17	0.20	0.17	0.17	0.15	0.21	0.15	0.13
Th	0.020	0.017	0.021	0.014	0.021	0.023	0.024	0.019	0.014	0.025	0.014	0.023
U	0.004	0.003	0.004	0.004	0.003	0.008	0.004	0.005	0.004	0.004	0.004	0.005

Table 37 continued

	TB high-Ca											
	TB-cpx2-g35	TB-cpx2-g36	TB-cpx2-g37	TB-cpx2-g38	TB-cpx2-g41	TB-cpx2-g44	TB-cpx1-g2	TB-cpx1-g4	TB-cpx1-g5	TB-cpx1-g7	TB-cpx1-g9	TB-cpx1-g12
Sc	19.3	19.4	17.0	18.0	16.3	18.3	17.1	17.0	16.8	16.9	17.5	19.9
V	256	281	275	277	264	262	280	269	295	313	305	275
Ni	240	252	316	272	310	267	333	315	332	324	333	252
Rb	0.005	0.057	0.037	0.046	0.002	0.013	< b.d.	0.022	< b.d.	0.022	0.021	0.016
Sr	114	122	116	119	131	115	116	124	110	110	123	120
Y	1.60	1.48	1.51	1.33	1.73	1.62	1.64	1.60	1.97	1.79	1.79	1.51
Zr	6.62	6.27	6.23	5.58	6.61	5.72	6.13	5.66	6.34	6.07	7.73	7.01
Nb	0.08	0.10	0.11	0.10	0.15	0.10	0.14	0.12	0.10	0.10	0.12	0.12
Ba	0.17	0.21	0.17	0.13	0.16	0.15	0.19	0.19	0.15	0.10	0.13	0.24
La	1.78	2.33	2.10	2.14	2.05	1.87	2.24	1.95	1.78	1.78	2.25	2.31
Ce	6.61	7.58	7.01	6.98	7.57	6.36	7.57	6.70	6.30	6.14	7.82	7.36
Pr	1.07	1.21	1.20	1.05	1.22	0.99	1.12	1.04	1.01	0.97	1.23	1.16
Nd	5.34	6.04	5.83	5.30	6.18	6.02	6.00	5.54	5.39	5.24	6.67	5.85
Sm	1.37	1.31	1.31	1.20	1.46	1.36	1.35	1.28	1.25	1.23	1.54	1.27
Eu	0.42	0.44	0.44	0.38	0.46	0.42	0.44	0.42	0.40	0.41	0.48	0.41
Tb	0.15	0.13	0.09	0.09	0.14	0.12	0.10	0.11	0.12	0.12	0.14	0.12
Gd	1.17	1.26	1.17	1.02	1.45	1.75	1.32	1.29	1.42	1.27	1.53	1.19
Dy	0.57	0.51	0.49	0.49	0.61	0.56	0.53	0.52	0.58	0.56	0.61	0.51
Ho	0.07	0.08	0.09	0.07	0.09	0.07	0.08	0.07	0.09	0.09	0.09	0.08
Er	0.19	0.14	0.14	0.14	0.18	0.14	0.15	0.15	0.17	0.16	0.14	0.15
Tm	0.009	0.014	0.009	0.017	0.018	0.013	0.012	0.011	0.014	0.019	0.011	0.016
Yb	0.079	0.068	0.061	0.065	0.096	0.077	0.083	0.075	0.088	0.068	0.085	0.080
Lu	0.009	0.010	0.009	0.012	0.014	0.013	0.010	0.006	0.007	0.010	0.011	0.003
Hf	0.39	0.41	0.40	0.39	0.52	0.39	0.47	0.46	0.46	0.46	0.36	0.51
Ta	0.007	0.009	0.008	0.013	0.010	0.004	0.010	0.005	0.004	0.005	0.015	0.010
Pb	0.14	0.17	0.18	0.15	0.25	0.21	0.16	0.16	0.13	0.15	0.17	0.17
Th	0.017	0.015	0.023	0.023	0.023	0.024	0.021	0.022	0.016	0.011	0.027	0.020
U	0.004	0.011	0.006	0.002	0.007	0.004	0.003	0.003	0.004	0.003	0.009	0.003

Table 37 continued

	TB high-Ca											
	TB-cpx1-g16	TB-cpx1-g18	TB-cpx1-g19	TB-cpx1-g20	TB-cpx1-g22	TB-cpx1-g23	TB-cpx1-g24	TB-cpx1-g25	TB-cpx1-g27	TB-cpx1-g28	TB-cpx1-g29	TB-cpx1-g30
Sc	16.3	17.8	17.6	18.1	17.2	18.0	19.5	16.0	18.5	20.3	15.6	17.0
V	283	269	280	278	262	242	263	262	270	260	273	269
Ni	327	343	303	299	251	251	226	313	240	248	306	266
Rb	0.021	0.024	0.054	0.006	0.018	0.039	< b.d.	0.056	0.041	0.039	0.020	0.060
Sr	108	125	108	138	99.4	125	128	118	122	142	111	124
Y	1.60	1.70	1.54	1.96	1.32	1.49	1.48	1.66	1.61	2.17	1.37	1.66
Zr	5.98	6.61	6.28	8.13	4.93	6.63	8.24	5.62	6.76	9.87	5.33	6.86
Nb	0.12	0.14	0.10	0.11	0.12	0.12	0.11	0.12	0.13	0.09	0.13	0.12
Ba	0.11	0.13	0.09	0.13	0.17	0.12	0.16	0.15	0.15	0.13	0.26	0.16
La	1.75	1.82	1.90	2.06	1.87	2.46	1.97	1.97	2.35	2.18	2.12	2.14
Ce	6.15	6.58	6.14	7.15	5.86	8.03	6.72	6.48	7.62	7.37	6.62	7.06
Pr	1.00	1.12	0.98	1.18	0.92	1.21	1.06	1.03	1.21	1.22	1.02	1.11
Nd	5.25	6.13	5.23	6.21	4.68	6.32	5.63	5.55	6.04	6.60	5.11	5.87
Sm	1.21	1.42	1.18	1.50	1.09	1.36	1.31	1.26	1.35	1.56	1.15	1.34
Eu	0.40	0.46	0.38	0.47	0.34	0.44	0.42	0.42	0.42	0.56	0.35	0.42
Tb	0.12	0.13	0.10	0.15	0.09	0.12	0.10	0.11	0.13	0.16	0.10	0.11
Gd	1.13	1.29	1.10	1.34	1.24	1.48	1.50	1.56	1.71	1.92	1.27	1.61
Dy	0.58	0.61	0.50	0.61	0.45	0.51	0.50	0.58	0.52	0.71	0.44	0.50
Ho	0.10	0.08	0.06	0.09	0.06	0.07	0.08	0.07	0.07	0.09	0.07	0.07
Er	0.18	0.19	0.15	0.18	0.13	0.15	0.14	0.15	0.16	0.22	0.12	0.16
Tm	0.017	0.014	0.014	0.020	0.012	0.010	0.015	0.018	0.015	0.020	0.012	0.013
Yb	0.080	0.084	0.080	0.077	0.053	0.073	0.065	0.091	0.072	0.107	0.073	0.081
Lu	0.015	0.010	0.004	0.008	0.007	0.007	0.006	0.008	0.008	0.012	0.009	0.010
Hf	0.39	0.47	0.48	0.51	0.32	0.48	0.63	0.47	0.52	0.63	0.36	0.55
Ta	0.007	0.010	0.010	0.008	0.005	0.010	0.009	0.011	0.012	0.012	0.010	0.008
Pb	0.16	0.15	0.14	0.17	0.12	0.18	0.14	0.16	0.17	0.17	0.16	0.15
Th	0.018	0.018	0.022	0.021	0.017	0.030	0.021	0.021	0.028	0.021	0.025	0.015
U	0.003	0.008	0.004	0.004	0.005	0.003	0.002	0.002	0.005	0.006	0.002	0.007

Table 37 continued

					TB low-Ca							
	TB-cpx1-g31	TB-cpx1-g33	TB-cpx1-g35	TB-cpx1-g36	TB-cpx2-g16	TB-cpx2-g22	TB-cpx2-g23	TB-cpx2-g24	TB-cpx2-g25	TB-cpx2-g26	TB-cpx2-g31	TB-cpx2-g43
Sc	13.2	17.7	18.2	20.0	13.6	14.1	12.9	13.5	13.7	14.6	11.1	11.8
V	222	272	280	258	221	239	185	190	234	261	183	182
Ni	355	249	241	234	405	374	475	478	372	405	516	469
Rb	0.018	0.009	0.046	< b.d.	0.055	< b.d.	0.034	0.044	0.020	0.021	0.041	0.055
Sr	94.8	103	115	123	103	94.5	98.8	94.3	95.3	115	96.1	93.2
Y	1.44	1.33	1.49	1.47	1.95	1.94	1.86	2.02	1.79	2.18	2.08	1.68
Zr	4.49	5.81	5.76	7.87	3.47	3.77	2.68	2.84	3.22	4.15	2.71	2.48
Nb	0.12	0.14	0.12	0.12	0.09	0.12	0.16	0.11	0.10	0.08	0.09	0.10
Ba	0.24	0.31	0.23	0.10	0.28	0.19	1.19	0.20	0.24	0.13	0.25	0.30
La	1.83	1.78	2.02	1.91	2.15	2.07	2.19	2.07	1.99	1.83	1.86	1.91
Ce	5.99	6.11	6.79	6.41	6.86	6.58	6.84	6.50	6.48	6.63	6.28	5.93
Pr	0.92	0.97	1.09	1.04	1.06	0.98	0.98	1.02	1.01	1.07	0.96	0.91
Nd	4.63	4.64	5.19	5.48	5.79	5.27	5.08	5.18	5.04	5.35	4.89	5.14
Sm	1.05	1.02	1.25	1.33	1.31	1.18	1.15	1.17	1.17	1.28	1.22	1.09
Eu	0.35	0.34	0.38	0.42	0.41	0.41	0.40	0.40	0.36	0.42	0.41	0.38
Tb	0.10	0.09	0.09	0.12	0.13	0.14	0.12	0.13	0.12	0.14	0.14	0.10
Gd	0.89	0.95	1.06	1.12	2.08	1.64	2.24	2.25	2.17	2.43	2.28	1.53
Dy	0.44	0.46	0.46	0.56	0.61	0.61	0.56	0.63	0.51	0.63	0.63	0.54
Ho	0.06	0.07	0.08	0.07	0.10	0.08	0.07	0.09	0.08	0.09	0.10	0.08
Er	0.15	0.14	0.14	0.15	0.17	0.15	0.19	0.20	0.14	0.19	0.20	0.17
Tm	0.011	0.012	0.011	0.018	0.019	0.018	0.019	0.031	0.019	0.017	0.019	0.020
Yb	0.073	0.061	0.066	0.065	0.111	0.101	0.108	0.116	0.091	0.105	0.121	0.101
Lu	0.009	0.004	0.006	0.010	0.013	0.008	0.018	0.010	0.008	0.015	0.012	0.014
Hf	0.27	0.37	0.41	0.53	0.23	0.22	0.15	0.18	0.20	0.25	0.16	0.11
Ta	0.011	0.008	0.009	0.010	0.009	0.010	0.007	0.005	0.004	0.002	0.006	0.005
Pb	0.15	0.17	0.19	0.17	0.12	0.16	0.15	0.14	0.14	0.15	0.11	0.13
Th	0.018	0.022	0.022	0.021	0.015	0.024	0.017	0.013	0.024	0.015	0.010	0.018
U	0.006	0.004	0.007	0.003	0.004	0.004	0.007	0.005	0.006	0.001	0.006	0.002

Table 37 continued

	TB low-Ca											
	TB-cpx1-g1	TB-cpx1-g3	TB-cpx1-g6	TB-cpx1-g8	TB-cpx1-g10	TB-cpx1-g11	TB-cpx1-g13	TB-cpx1-g15	TB-cpx1-g17	TB-cpx1-g26	TB-cpx1-g32	TB-cpx1-g34
Sc	11.7	12.4	15.0	13.8	12.6	12.5	12.3	14.4	13.2	13.1	11.6	11.7
V	188	193	273	249	218	197	192	237	198	224	202	188
Ni	509	528	395	413	493	468	482	366	460	381	462	470
Rb	0.030	0.011	0.024	0.017	0.041	0.003	0.033	0.019	0.019	0.020	0.082	0.030
Sr	92.0	93.3	97.1	97.4	98.0	95.0	97.0	96.4	88.9	97.6	98.3	87.9
Y	1.88	2.04	1.89	1.77	1.76	1.66	1.73	1.86	1.79	1.86	1.74	1.62
Zr	2.67	2.86	2.81	3.33	2.60	2.73	2.76	3.77	1.80	3.25	2.72	1.69
Nb	0.09	0.10	0.11	0.11	0.09	0.12	0.09	0.10	0.06	0.09	0.09	0.06
Ba	0.32	0.24	0.19	0.27	0.33	0.28	0.28	0.18	0.19	0.25	0.30	0.24
La	1.97	2.07	1.99	2.05	1.92	1.94	2.01	2.02	1.56	2.17	1.94	1.58
Ce	6.23	6.18	6.49	6.63	6.29	6.06	6.29	6.51	4.72	6.55	6.23	4.93
Pr	0.91	0.98	0.98	0.98	0.93	0.96	0.96	1.00	0.72	0.99	0.90	0.73
Nd	4.82	4.98	5.15	5.08	4.89	4.83	4.85	5.13	3.82	5.07	4.91	3.82
Sm	1.11	1.17	1.19	1.18	1.12	1.15	1.12	1.23	0.96	1.15	1.14	0.91
Eu	0.39	0.39	0.38	0.37	0.37	0.36	0.35	0.39	0.32	0.37	0.38	0.32
Tb	0.12	0.14	0.10	0.14	0.12	0.12	0.11	0.12	0.11	0.13	0.11	0.09
Gd	1.26	1.29	1.37	1.23	1.23	1.04	1.11	1.11	0.89	1.47	1.06	0.87
Dy	0.58	0.62	0.59	0.55	0.53	0.53	0.52	0.58	0.51	0.58	0.52	0.51
Ho	0.09	0.09	0.09	0.09	0.08	0.09	0.08	0.08	0.07	0.07	0.08	0.07
Er	0.19	0.22	0.18	0.19	0.18	0.19	0.17	0.21	0.19	0.18	0.16	0.18
Tm	0.018	0.021	0.022	0.019	0.017	0.022	0.020	0.015	0.020	0.015	0.022	0.015
Yb	0.109	0.143	0.104	0.077	0.106	0.100	0.099	0.100	0.107	0.079	0.096	0.085
Lu	0.008	0.015	0.015	0.008	0.008	0.016	0.011	0.009	0.016	0.015	0.014	0.010
Hf	0.16	0.18	0.26	0.20	0.14	0.19	0.20	0.27	0.12	0.20	0.18	0.11
Ta	0.002	0.008	0.003	0.007	0.006	0.008	0.005	0.011	0.004	0.007	0.007	0.004
Pb	0.11	0.11	0.15	0.15	0.12	0.11	0.14	0.14	0.08	0.11	0.11	0.11
Th	0.019	0.017	0.014	0.014	0.016	0.011	0.013	0.016	0.006	0.024	0.020	0.013
U	0.003	0.004	0.002	0.003	0.003	0.003	0.003	0.004	0.001	0.002	0.005	0.003

Table 38: Measured Sr isotope composition of Tshibwe cpx megacrysts

TB High-Ca	$^{87}Sr/^{86}Sr$	TB Low-Ca	$^{87}Sr/^{86}Sr$
TB-CPX2-g2	0.7036	TB-CPX2-g16	0.7033
TB-CPX2-g8	0.7034	TB-CPX2-g22	0.7034
TB-CPX2-g10	0.7034	TB-CPX2-g23	0.7032
TB-CPX2-g18	0.7034	TB-CPX2-g26	0.7033
TB-CPX2-g29	0.7034	TB-CPX2-g31	0.7032
TB-CPX2-g30	0.7033	TB-CPX2-g43	0.7031
TB-CPX2-g34	0.7033	TB-CPX1-g1	0.7032
TB-CPX2-g37	0.7034	TB-CPX1-g6	0.7031
TB-CPX2-g41	0.7034	TB-CPX1-g11	0.7030
TB-CPX1-g7	0.7030	TB-CPX1-g17	0.7028
TB-CPX1-g9	0.7033	TB-CPX1-g26	0.7026
TB-CPX1-g25	0.7036	TB-CPX1-g32	0.7025
TB-CPX1-g28	0.7035	TB-CPX1-g34	0.7036
TB-CPX1-g31	0.7033		
TB-CPX1-g33	0.7034		
TB-CPX1-g35	0.7034		
TB-CPX1-g36	0.7036		

See chapter 1.3 for details of analysis.

Table 39: Average major elements values for mineral standards analysed by electron microprobe analysis

	SiO_2	TiO_2	Al_2O_3	Cr_2O_3	FeO	MnO	MgO	CaO	Na_2O	K_2O	Total
(a) In house garnet											
Average	41.73	0.07	23.61	1.02	7.86	0.40	20.36	4.56	0.03	n.a.	99.64
Relative std. Dev	0.39	0.02	0.25	0.07	0.31	0.05	0.35	0.14	0.02	n.a.	0.41
Accepted values	41.79	0.08	23.49	1.09	7.90	0.40	20.33	4.62	0.03	n.a.	99.91
(b) In house clinopyroxene											
Average	54.28	0.24	2.95	0.78	1.65	0.07	16.72	21.53	1.52	0.01	99.75
Relative std. Dev.	0.33	0.03	0.10	0.03	0.20	0.03	0.18	0.58	0.08	0.01	0.46
Accepted values	54.32	0.26	3.00	0.77	1.74	0.07	16.70	21.38	1.63	0.07	99.83

Averages represent the means of 32 analyses of garnet and 22 analyses of clinopyroxene standards, analysed as unknowns during the electron microprobe analysis sessions. Relative standard deviations represent the 1σ standard deviation of these replicate data for each oxide expressed as a percentage of the average value obtained. The abbreviation "n.a." stands for "not analysed".

Table 40: Average major elements values for ilmenite standard analysed by electron microprobe analysis

	TiO_2	Al_2O_3	Cr_2O_3	FeO	MnO	MgO	NiO	Total
In house ilmenite								
average	46.08	0.03	0.03	46.43	4.58	0.34	0.03	97.47
Relative Std. Dev	0.53	0.01	0.02	0.56	0.09	0.03	0.02	0.50
Accepted values	46.13	0.03	0.04	45.85	4.55	0.33	0.04	97.51

Average represent the means of 16 analyses of ilmenite standard, analysed as unknowns during the eletron licroprobe analysis sessions. Relative standard deviations represent the 1σ standard deviation of these replicate data for each oxide expressed as a percentage of the average value obtained.

Table 41: Trace element values for Monastery IL-52 ilmenite megacryst analysed in this study.

	IL-52 laser average	**1SD**	**IL-52 solution**
SC	30.5	1.62	29.4
V	1898	18.2	1884
Co	264	12.01	267
Ni	1521	32.8	1531
Cu	49.0	7.67	43.16
Zn	348	41.9	323.3
Ga	26.1	0.74	27.3
Y	0.29	0.04	0.3
Zr	437	21.1	422
Nb	389	10.6	383
Ba	0.03	0.01	0.025
Hf	14.6	0.64	14.4
Ta	34.3	1.30	33.9

Average represent the means of 17 analyses of IL-52 ilmenite standard, analysed as unknown during the LA-ICPMS analysis sessions. 1SD represents 1σ standard deviation of these replicate data for each element expressed as percentage of the value obtained. Trace elment results obtained by solution ICP-MS (4 aliquots) following high-T, high-P bomb digestion (high and low-concentration elements run at different dilution factors).

Table 42: Trace element values for *JJG 1424* garnet and clinopyroxene analysed in this study

	JJG1424 garnet laser average	1SD	JJG1424 garnet solution	1SD	JJG1424 cpx laser ablation average	1SD	JJG1424 cpx solution	1 SD
Sc	55.6	5.86	50.9	5.71	27.9	1.43	28.1	1.08
V	149	22.9	155	10.8	552	35.5	531	14.2
Cr	8977	2210	7921	249	5534	332	5480	137
Ni	14.1	1.05	14.1	4.98	224	5.31	222	7.08
Rb	0.049	0.024	0.032	0.154	0.035	0.041	0.082	0.032
Sr	0.07	0.06	0.33	1.23	300	19.6	290	4.17
Y	12.5	1.70	12.4	0.58	2.13	0.13	2.26	0.08
Zr	16.8	2.95	16.8	0.28	39.7	3.19	41.2	3.97
Nb	0.02	0.08	0.04	0.02	0.05	0.13	0.28	0.02
Ba	0.13	0.26	0.90	6.39	1.19	3.25	3.2	0.8
La	0.01	0.01	0.07	0.03	22.1	1.59	22.3	0.10
Ce	0.17	0.02	0.18	0.08	61.2	3.63	61.9	0.53
Pr	0.06	0.01	0.06	0.01	7.13	0.40	7.70	0.11
Nd	0.65	0.07	0.52	0.01	27.6	1.41	27.3	0.75
Sm	0.60	0.06	0.66	0.13	3.79	0.16	3.82	0.09
Eu	0.37	0.04	0.43	0.12	1.05	0.04	1.02	0.02
Gd	1.62	0.44	1.50	0.32	2.72	0.75	2.66	0.48
Tb	0.34	0.05	0.34	0.08	0.22	0.02	0.24	0.01
Dy	2.49	0.26	2.41	0.40	0.85	0.05	0.91	0.03
Ho	0.57	0.06	0.57	0.10	0.10	0.01	0.11	0.00
Er	2.28	0.49	1.75	0.22	0.19	0.03	0.18	0.01
Tm	0.25	0.03	0.25	0.06	0.01	0.00	0.02	0.00
Yb	1.85	0.20	1.75	0.28	0.08	0.01	0.09	0.00
Lu	0.26	0.03	0.24	0.07	0.01	0.00	0.01	0.00
Hf	0.24	0.06	0.21	0.02	1.98	0.19	2.31	0.14
Ta	0.001	0.001	0.010	0.005	0.004	0.011	0.019	0.001
Pb	0.02	0.02	0.02	0.01	0.31	0.12	0.31	0.01
Th	0.01	0.00	0.01	0.00	1.27	0.11	1.49	0.03
U	0.007	0.003	0.007	0.001	0.070	0.012	0.116	0.003

The average values shown are means of 23 *JJG1224* garnet and 12 *JJG1224* clinopyroxene standard analyses obtained during LA-ICPMS analysis in the course of this PhD project. 1SD represents the 1σ standard deviation of these replicate data for each element expressed as a percentage of the average value obtained. Solution values were obtained by analysis of three aliquots of *JJG1424* garnet carefully picked, washed, minimally leached and dissolved using 4:1 concentrated HF:HNO3 and analysed in solution mode. Values in highlighted yellow fields do not represent averages, but rather represent the lowest values obtained of the three because of apparent issues with contamination from mineral inclusions. These values should be treated with caution.

Table 43. Trace element concentrations for rock standards measured as unknowns by ICP-MS

	Accepted V5-40-56	This study V5-40-56G	% RSD (2s)	Accepted AGV-1	This study AGV-1	% RSD (2s)	Accepted SARM-39	This study SARM-39	%RSD (2s)
Li	no data	4.19	4.5	10.7	10.2	2.7	no data	6.82	5.9
Sc	37.6	37	6.5	12.6	11.6	2.5	13.7	11.9	5.5
V	250	257	5	126	118	3.4	115.5	116	3.8
Cr	249	235	3.3	9	8.53	3.7	1274.2	1213	4.0
Co	44	34.1	2.8	15.3	14.5	3.3	69	62.1	4.2
Ni	98	95.2	3	16	14.2	10.1	936.8	977	5.5
Cu	46	53.5	3.6	58	60.5	13.9	59.4	71.0	3.0
Zn	90	104	6.5	87	92.9	3.7	69.5	64.8	5.9
Rb	2.98	2.97	3.6	68.3	67.1	5.4	50.8	50.5	2.4
Sr	203	197	3.5	655	661	3.8	1451.4	1432	3.3
Y	37.9	37.6	3.5	21	23.7	3.2	16.4	15.4	4.9
Zr	175	172	5.4	240	236	3.5	243.2	248	4.5
Nb	8.46	8.22	5.1	14.9	14.6	1.9	109.2	113	2.5
Cs	0.035	0.04	11.1	1.3	1.21	2.1	no data	3.25	4.7
Ba	29.9	29.9	5.9	1223	1205	3.2	1683.3	1439	2.3
La	8.02	7.84	3	38.5	38.3	2.1	89.2	91.0	1.9
Ce	22.5	21.6	2.1	68.5	68.3	2.4	182.9	180	2.8
Pr	3.42	3.27	3.4	8.45	8.3	2.7	21.5	21.8	1.9
Nd	16.7	16.5	3	31.6	31.4	2.1	82.2	82.9	2.2
Sm	4.98	4.93	4.3	5.82	5.7	3.1	12.2	12.6	7.1
Eu	1.75	1.77	5.8	1.565	1.56	3.3	3.14	3.05	7.9
Gd	6.14	6.29	3.2	4.73	4.66	3.3	8.58	8.56	7.1
Tb	1.06	1.1	4.2	0.664	0.652	3.5	0.99	1.03	5.7
Dy	6.81	6.85	3.3	3.54	3.51	4.5	4.23	4.51	5.5
Ho	1.41	1.41	5.8	0.69	0.685	3.3	0.62	0.682	4.2
Er	3.99	4.06	2.4	1.856	1.83	2.4	1.52	1.52	4.5
Tm	0.6	0.608	3.4	0.28	0.28	5.2	0.18	0.178	4.0
Yb	3.71	3.71	2.4	1.644	1.61	5.1	0.98	1.05	3.7
Lu	0.56	0.584	3.3	0.248	0.249	4.4	0.13	0.141	4.5
Hf	4.08	4.04	4.3	5.0	4.95	2.9	5.02	5.05	5.9
Ta	0.5	0.559	8.2	0.882	0.864	8.7	7.3	7.43	4.1
Pb	0.92	0.948	6.6	37.27	36.9	4.7	9.98	17.9	2.1
Th	0.47	0.48	7.1	6.53	6.35	4.6	9.75	9.94	6.5
U	0.19	0.186	7.2	1.885	1.86	3.0	2.52	2.57	6.3

Sources for standard data are: V5-40-56G (MORB glass in-house standard), Janney et al. (2005) with additional data for V, Cr, Co, Ni, Cu and Zn from Le Roux et al. (2002); AGV-1 (USGS Guano Valley Andesite), Eggins et al. (1997); SARM-39 kimberlite values from compilation of Roy et al. (2007). %RSD is the relative standard deviation (2*standard deviation/mean, expressed as a percentage) for analysis of each of the rock standards, measured with each analysis batch during the course of this study.

Table 44: Major element composition of Kalkput clinopyroxene megacrysts from unpublished data of Deon de Bruin (DDB)

Kalkput (DDB)	SiO_2	TiO_2	Al_2O_3	Cr_2O_3	FeO	MnO	MgO	CaO	Na_2O	Ca#	Cr#	Mg#
KPC-40	53.59	0.17	2.54	0.92	3.84	0.09	19.40	16.89	1.34	38.5	19.55	95.31
KPC-18	55.18	0.17	2.15	0.63	4.05	0.10	19.44	17.30	1.23	39.02	16.43	90.81
KPC-26	54.01	0.17	2.01	0.52	4.33	0.16	19.11	17.97	1.19	40.34	14.79	94.56
KPC-10	55.16	0.20	1.78	0.38	4.89	0.15	18.51	18.28	1.33	41.52	12.53	90.67
KPC-16	55.20	0.20	2.17	0.28	4.92	0.13	18.18	18.01	1.48	41.6	7.97	89.74
KPC-28	55.23	0.19	1.87	0.19	5.21	0.15	18.14	18.08	1.41	41.75	6.38	88.95
KPC-29	54.91	0.17	1.82	0.34	4.79	0.14	18.44	18.39	1.34	41.76	11.14	91.59
KPC-27	55.14	0.19	1.77	0.33	5.11	0.14	18.27	18.36	1.26	41.95	11.12	89
KPC-41	55.36	0.21	1.92	0.24	5.43	0.17	17.72	17.86	1.40	42.02	7.74	85.76
KPC-7	55.01	0.20	1.83	0.35	4.97	0.15	18.29	18.44	1.35	42.02	11.37	90.78
KPC-49	53.96	0.20	1.92	0.17	5.33	0.16	17.92	18.13	1.44	42.11	5.61	92.24
KPC-38	55.28	0.24	1.71	0.26	5.15	0.16	18.00	18.31	1.35	42.24	9.26	88.08
KPC-36	55.30	0.21	1.69	0.18	4.91	0.15	17.99	18.55	1.32	42.57	6.67	88.42
KPC-48/2	53.10	0.27	1.44	0.17	6.40	0.17	17.89	18.52	1.46	42.67	7.34	96.46
KPC-1	54.82	0.22	1.71	0.26	5.33	0.13	17.96	18.60	1.34	42.68	9.26	90.01
KPC-21	55.06	0.19	1.95	0.19	5.11	0.12	17.85	18.67	1.32	42.92	6.14	88.78
KPC-15	54.50	0.24	2.11	0.13	5.96	0.15	17.33	18.17	1.60	42.98	3.97	89.47
KPC-37	54.94	0.22	2.06	0.07	5.79	0.17	17.30	18.20	1.47	43.06	2.23	86.67
KPC-20	54.83	0.23	1.68	0.28	5.31	0.14	17.71	18.64	1.43	43.08	10.06	89.92
KPC-11	54.91	0.20	1.75	0.12	5.57	0.15	17.31	18.27	1.49	43.14	4.4	87.25
KPC-24	53.84	0.24	1.74	0.11	5.30	0.16	17.63	18.77	1.40	43.36	4.07	92.74
KPC-34	53.68	0.36	2.08	0.08	6.10	0.15	16.54	17.80	1.90	43.62	2.52	90.06
KPC-32	54.93	0.31	1.62	0.00	8.26	0.20	16.19	17.49	1.82	43.72	0	82.68
KPC-48/1	53.46	0.26	1.45	0.16	6.61	0.18	17.17	18.83	1.44	44.09	6.89	92.28
KPC-50	53.82	0.24	1.75	0.07	5.36	0.14	17.32	19.03	1.41	44.13	2.61	92.15
KPC-45	53.71	0.26	2.14	0.07	5.97	0.17	16.64	18.44	1.73	44.34	2.15	90.9
KPC-35	54.43	0.28	1.60	0.05	6.86	0.19	16.37	18.28	1.61	44.53	2.05	85.19
KPC-14	54.40	0.33	2.13	0.00	6.91	0.16	15.78	17.85	1.95	44.85	0	84.56
KPC-39	53.34	0.31	1.57	0.06	7.08	0.20	16.22	18.35	1.71	44.85	2.5	89.2
KPC-13	54.81	0.24	1.77	0.06	5.73	0.15	16.74	19.05	1.52	45	2.22	87.4
KPC-33	54.91	0.28	0.95	0.00	7.38	0.20	16.38	18.69	1.38	45.07	0	82.58
KPC-47	53.20	0.32	2.02	0.00	7.39	0.16	15.77	18.21	1.92	45.36	0	89.24
KPC-43	54.92	0.33	1.89	0.06	7.45	0.16	15.68	18.16	1.93	45.44	2.09	83.23
KPC-6	54.69	0.32	2.37	0.00	7.03	0.16	15.44	18.18	2.02	45.85	0	83.76
KPC-25	54.23	0.32	2.83	0.00	8.76	0.21	13.94	17.03	2.61	46.76	0	80.17
KPC-4/1	54.24	0.45	2.03	0.00	9.66	0.18	13.24	17.86	2.66	49.23	0	79.04
KPC-5	54.17	0.54	2.22	0.00	10.62	0.18	12.37	17.01	3.15	49.71	0	76.9
KPC-4/2	54.09	0.50	2.36	0.00	10.46	0.19	12.16	16.94	3.32	50.04	0	77.88
KPC-3	54.26	0.53	2.45	0.00	10.56	0.20	11.97	16.68	3.46	50.05	0	76.93

Table 44 continued

Kalkput (DDB)	SiO_2	TiO_2	Al_2O_3	Cr_2O_3	FeO	MnO	MgO	CaO	Na_2O	Ca#	Cr#	Mg#
KPC-23	54.13	0.54	2.84	0.00	10.38	0.17	11.88	16.56	3.68	50.06	0	79.15
KPC-12	53.85	0.50	2.53	0.00	9.98	0.16	12.32	17.21	3.29	50.11	0	80.24
KPC-9	54.23	0.52	2.39	0.00	10.58	0.17	12.06	17.01	3.34	50.35	0	77.17
KPC-8	54.23	0.54	2.35	0.00	10.42	0.15	12.15	17.24	3.34	50.5	0	78.47
KPC-17	54.17	0.54	2.34	0.00	10.45	0.17	11.93	16.99	3.44	50.59	0	77.71
KPC-46	54.15	0.60	2.74	0.00	10.28	0.18	11.73	16.72	3.56	50.61	0	76.95
KPC-31	54.32	0.55	2.41	0.00	10.13	0.16	12.19	17.40	3.15	50.65	0	76.56
KPC-22	54.40	0.54	2.63	0.00	10.35	0.18	11.88	17.14	3.42	50.92	0	76.92
KPC-44	53.70	0.53	2.26	0.00	10.85	0.18	11.66	16.96	3.49	51.12	0	78.17
KPC-30	53.58	0.68	2.75	0.00	12.01	0.17	10.92	15.89	4.14	51.13	0	78.02
KPC-19	53.70	0.52	2.19	0.00	12.41	0.21	11.10	16.20	3.81	51.2	0	75.98
KPC-42	54.37	0.54	2.37	0.00	11.18	0.18	11.51	16.84	3.53	51.26	0	74.97
KPC-2	53.65	0.55	2.27	0.00	12.57	0.19	10.79	16.08	3.92	51.72	0	74.92
JJG4008-12	55.63	0.149	2.28	0.587	3.96	0.131	19.54	17.20	1.37	38.76	14.73	91.66
JJG4008-14	55.38	0.173	2.44	0.670	3.81	0.106	18.93	17.66	1.38	40.15	15.56	90.93
JJG4008-4	55.60	0.177	1.90	0.416	4.27	0.125	18.72	18.31	1.30	41.29	12.81	90.46
JJG4008-6	55.66	0.187	1.87	0.259	4.78	0.151	18.55	18.15	1.38	41.3	8.52	89.74
JJG4008-20	55.43	0.190	1.82	0.319	4.75	0.162	18.33	18.29	1.46	41.77	10.52	90.78
JJG4008-5	55.33	0.181	1.79	0.335	4.61	0.137	18.35	18.31	1.32	41.77	11.16	89.54
JJG4008-19	55.32	0.186	1.81	0.347	4.59	0.137	18.37	18.57	1.37	42.09	11.38	91.07
JJG4008-3	55.36	0.181	1.75	0.347	4.40	0.135	18.23	18.70	1.31	42.45	11.76	90.11
JJG4008-8	55.02	0.200	1.93	0.236	4.82	0.140	17.76	18.71	1.38	43.1	7.58	89.3
JJG4008-9	55.45	0.226	1.64	0.183	5.28	0.149	17.43	18.86	1.50	43.76	6.95	88.19
JJG4008-10	55.64	0.239	2.22	0.058	5.74	0.159	16.90	18.43	1.79	43.95	1.72	86.9
JJG4008-17	55.00	0.272	1.77	0.068	5.87	0.168	16.71	18.70	1.74	44.59	2.52	88.16
JJG4008-7	55.42	0.299	1.22	0.239	5.47	0.146	17.19	19.44	1.53	44.85	11.61	89.18
JJG4008-16	54.94	0.252	1.74	0.055	5.89	0.173	16.64	18.82	1.70	44.85	2.07	88
JJG4008-15	55.07	0.266	1.78	0.097	6.34	0.176	16.33	18.72	1.74	45.18	3.53	86.04
JJG4008-11	55.15	0.282	1.66	0.064	6.67	0.186	16.11	18.84	1.71	45.68	2.52	84.62
JJG4008-18	54.98	0.293	2.03	0.044	6.83	0.172	15.75	18.42	1.99	45.68	1.43	85.08
JJG4008-1	55.07	0.384	2.35	0.000	7.86	0.176	13.86	18.38	2.55	48.81	0	80.64
JJG4008-13	54.73	0.501	2.88	0.015	9.36	0.159	12.20	17.07	3.48	50.15	0.35	78.45
JJG4008-2	54.81	0.566	2.31	0.014	11.38	0.174	11.30	16.51	3.96	51.23	0.4	76.53

Table 45: Temperature and pressure estimates data of clinopyroxene megacrysts from Orapa using the Nimis and Taylor (2000) thermobarometer.

Ora Cr-poor	P (Ga)	T(°C)	**Ora Cr-rich**	P (Ga)	T (°C)	**Ora Cr-rich**	P (Ga)	T (°C)
ORAcpx1	5.2	1375	ORAcpx2	4.9	1124	ORAcpx35	4.5	1024
ORAcpx18	5.4	1317	ORAcpx3	4.5	1057	ORAcpx36	4.8	1098
ORAcpx19	5.5	1368	ORAcpx4	4.4	1028	ORAcpx39	8.5	1139
ORAcpx45	8.8	1302	ORAcpx5	5.3	1091	ORAcpx40	5.0	1073
ORAcpx43	5.9	1318	ORAcpx6	4.8	1054	ORAcpx41	4.7	1065
ORAcpx46	5.2	1313	ORAcpx7	4.5	1026	ORAcpx42	4.9	1104
ORAcpx48	1.8	779	ORAcpx8	4.6	1063	ORAcpx44	5.4	1192
ORAcpx49	5.7	1379	ORAcpx9	6.8	1110	ORAcpx47	4.6	1058
ORAcpx56	5.5	1330	ORAcpx10	4.5	1016	ORAcpx50	5.1	1126
ORAcpx68	6.1	1400	ORAcpx11	4.5	1049	ORAcpx51	5.3	1101
ORAcpx70	5.7	1412	ORAcpx12	4.6	1086	ORAcpx52	4.7	1016
ORAcpx71	6.0	1399	ORAcpx13	4.7	1058	ORAcpx53	4.5	1010
ORAcpx74	5.7	1399	ORAcpx14	4.7	1054	ORAcpx54	4.6	1038
ORAcpx75	5.9	1410	ORAcpx15	5.0	1026	ORAcpx55	5.9	1114
ORAcpx77	6.2	1398	ORAcpx16	4.4	1020	ORAcpx57	4.6	1050
ORAcpx78	5.6	1404	ORAcpx17	4.8	1072	ORAcpx58	5.3	1174
ORAcpx79	6.0	1396	ORAcpx20	5.2	1124	ORAcpx59	4.8	1076
			ORAcpx21	3.0	741	ORAcpx60	4.4	981
			ORAcpx22	4.6	1065	ORAcpx61	3.7	623
			ORAcpx23	4.4	1055	ORAcpx62	4.5	1032
			ORAcpx24	9.0	1173	ORAcpx63	4.6	1057
			ORAcpx25	4.7	1046	ORAcpx64	5.1	1109
			ORAcpx26	5.1	1106	ORAcpx65	4.6	1079
			ORAcpx27	4.7	1062	ORAcpx66	4.7	1085
			ORAcpx28	4.7	1061	ORAcpx67	6.1	1352
			ORAcpx29	4.6	1057	ORAcpx69	5.4	1183
			ORAcpx30	5.4	1176	ORAcpx72	5.1	1130
			ORAcpx31	4.8	1082	ORAcpx73	6.0	1327
			ORAcpx32	4.8	1082	ORAcpx76	4.8	1107
			ORAcpx34	4.8	1098	ORAcpx80	5.1	1149

Table 46: Temperature and pressure estimates data of clinopyroxene megacrysts from southern African kimberlites obtained with the Nimis and Taylor (2000) thermobarometer.

Colossus	P (Ga)	T (°C)	**Kalkput (DDB)**	P (Ga)	T (°C)
COLcpx1	5.4	1372	KPC-40	4.7	1282
COLcpx2	5.2	1372	KPC-18	5.1	1284
COLcpx3	5.2	1396	KPC-26	5.1	1244
COLcpx4	5.3	1383	KPC-10	6.2	1213
COLcpx5	5.5	1383	KPC-16	5.6	1209
COLcpx6	5.3	1400	KPC-28	6.9	1208
COLcpx7	5.7	1352	KPC-29	6.1	1205
COLcpx8	5.4	1382	KPC-27	6.0	1212
COLcpx9	5.3	1351	KPC-41	6.3	1213
COLcpx10	5.4	1355	KPC-7	6.1	1199
COLcpx11	5.4	1333	KPC-49	6.7	1184
COLcpx12	5.2	1375	KPC-38	7.4	1199
COLcpx13	5.4	1378	KPC-36	7.8	1192
COLcpx14	5.4	1346	KPC-1	7.1	1181
COLcpx15	5.3	1374	KPC-21	5.6	1184
COLcpx16	5.3	1407	KPC-15	7.1	1161
COLcpx17	5.3	1407	KPC-37	6.0	1178
COLcpx18	5.4	1345	JJG4008-12	5.2	1283
COLcpx19	5.3	1404	JJG4008-14	4.8	1257
COLcpx20	5.3	1397	JJG4008-4	5.7	1227
COLcpx21	5.2	1407	JJG4008-6	6.5	1221
COLcpx22	5.4	1313	JJG4008-20	7.4	1201
COLcpx23	5.4	1353	JJG4008-5	6.2	1213
COLcpx24	5.3	1360	JJG4008-19	6.3	1197
COLcpx25	5.2	1407	JJG4008-3	6.3	1194
COLcpx26	5.2	1376	JJG4008-8	5.9	1174
COLcpx27	5.3	1353	**Kalkput**		
COLcpx28	5.3	1396	KTPcpx3	5.0	1313
COLcpx29	5.3	1391	KPTcpx4	5.4	1273
COLcpx30	5.3	1378	KPTcpx5	5.6	1274
			Bellsbank		
			BBCpx5	4.7	1037
			BBCpx6	5.4	1046
			BBCpx11	7.8	1121
			BBCpx14	4.1	1021
			BBCpx15	5.0	1091
			BBCpx16	5.0	1101
			BB_cpx22	7.6	1022
			BB_cpx31	7.5	973
			BB_cpx33	5.4	1068

Table 47: Temperature estimates of garnet megacrsts from southern Africa obtained with the thermometer of Ryan et al., (1996)

Ora High-Cr	T (°C)	**Colossus**	T (°C)	**Bellsbank**	T (°C)
Oragt2	1291	Colgt2	1290	BB gt1	794
Oragt4	1299	Colgt5	1384	BB gt2	852
Oragt5	1346	Colgt8	1256	BB gt4	1045
Oragt6	1176	Colgt9	1388	BB gt9	996
Oragt8	1406	Colgt10	1373	BB gt10	774
Oragt9	1060	Colgt12	1379	BB gt12	952
Oragt11	1355	Colgt16	1319		
Oragt20	1271	Colgt18	1362		
Oragt23	1270	Colgt22	1300		
Oragt25	1085	Colgt25	1357		
Oragt26	1056	Colgt27	1375		
Oragt58	1417	Colgt28	1288		
Oragt63	1355	Colgt29	1324		
Oragt88	1328	Colgt30	1366		
Oragt102	1147	Colgt31	776		
Oragt104	1075	Colgt32	1301		
Ora Low-Cr		Colgt37	1459		
Oragt54	1050	Colgt38	1400		
Oragt44	826	Colgt41	1330		
Oragt13	1033	Colgt42	1460		

Table 48: Temperature and pressure estimates of peridotitic clinopyroxenes from Mbuji-Mayi (BM) and Tshibwe (TB) kimberlites obtained with the thermobarometer of Nimis and Taylor (2000)

Tshibwe	T (°C)	P (kb)
TB-CPX2-g1	986	65
TB-CPX2-g33	1030	52
TB-CPX2-g39	864	52
TB-CPX2-g40	1045	43
TB-CPX2-g42	949	40
TB-CPX1-g14	1020	58
BM Group 1		
BM-CPX1-g1	1168	46
BM-CPX1-g3	1117	47
BM-CPX1-g4	1264	72
BM-CPX1-g6	1104	55
BM-CPX1-g7	1066	48
BM-CPX1-g8	1183	52
BM-CPX1-g10	1168	57
BM-CPX1-g11	1209	58
BM-CPX1-g13	1054	41
BM-CPX1-g19	1125	54
BM-CPX1-g20	967	26
BM-CPX1-g21	1080	45
BM-CPX1-g22	1023	48
BM Group 2		
BM-CPX1-g2	1005	66
BM-CPX1-g5	1067	53
BM-CPX1-g9	1030	45
BM-CPX1-g12	999	43
BM-CPX1-g14	984	49
BM-CPX1-g17	1017	49

Table 49: Temperature estimates data of peridotitic garnets from Mbuji-Mayi (BM) obtained with the thermometer of Ryan et al., (1996)

BM G9	T (°C)	**BM G9 with IP**	T (°C)
BM-GAR1-g1	1143	BM-GAR3-g2	971
BM-GAR1-g2	1163	BM-GAR3-g3	899
BM-GAR1-g3	1150	BM-GAR3-g4	942
BM-GAR1-g4	1160	BM-GAR3-g5	905
BM-GAR1-g5	907	BM-GAR3-g6	974
BM-GAR1-g6	1122	BM-GAR3-g7	896
BM-GAR1-g7	1093	BM-GAR3-g8	1112
BM-GAR1-g8	1134	BM-GAR3-g9	1022
BM-GAR1-g10	1136		
BM-GAR1-g11	1144	BM-GAR3-g11	933
BM-GAR1-g12	1160	BM-GAR3-g12	954
BM-GAR1-g13	1189	BM-GAR3-g13	967
BM-GAR1-g14	1023	BM-GAR3-g17	894
BM-GAR1-g15	1039	BM-GAR3-g16	1049
BM-GAR1-g16	1062	BM-GAR3-g18	1090
BM-GAR1-g17	1064	BM-GAR3-g19	1073
BM-GAR1-g18	1066	BM-GAR3-g20	1099
BM-GAR1-g19	1139		
BM-GAR1-g20	1151	BM-GAR3-g23	1027
BM-GAR1-g22	1010	BM-GAR3-g24	1035
BM-GAR1-g23	937	BM-GAR3-g25	1045
BM-GAR1-g24	1152	BM-GAR3-g26	1000
BM-GAR1-g26	1081	BM-GAR3-g27	982
BM-GAR1-g27	1043	BM-GAR3-g28	992
BM-GAR1-g28	1147	BM-GAR3-g29	1053
BM-GAR1-g30	1046	BM-GAR3-g30	905
BM-GAR1-g31	1145	BM-GAR3-g31	1060
BM-GAR1-g33	1151		
BM-GAR1-g34	939	BM-GAR3-g33	932
BM-GAR1-g36	1052	BM-GAR3-g34	1064
BM-GAR1-g37	933	BM-GAR3-g38	1098
BM-GAR1-g38	1149	**BM G10**	
BM-GAR1-g39	1164	BM-GAR3-g1	886
BM-GAR1-g40	1027	BM-GAR3-g14	1024
BM-GAR1-g41	1092	BM-GAR3-g15	1044
BM-GAR1-g43	1141	BM-GAR3-g35	1103
BM-GAR1-g44	1041	BM-GAR3-g36	917
		BM-GAR3-g22	894
BM-GAR1-g9	1128	BM-GAR3-g10	1034
BM-GAR1-g21	1101	BM-GAR3-g21	1018
BM-GAR1-g29	1030	BM-GAR3-g32	1051
BM-GAR1-g35	1059		
BM-GAR1-g25	1053		
BM-GAR1-g32	1053		
BM-GAR1-g42	1026		

Table 50: Temperature estimates data of peridotitic garnets from Tshibwe (TB) obtained with the thermometer of Ryan et al., (1996)

TB G9	T (°C)
TB-GAR1-g1	959
TB-GAR1-g2	1279
TB-GAR1-g3	1286
TB-GAR1-g4	1292
TB-GAR1-g6	1305
TB-GAR1-g9	1327
TB-GAR1-g10	1110
TB-GAR1-g12	1268
TB-GAR1-g13	1320
TB-GAR1-g14	1294
TB-GAR1-g15	1281
TB-GAR1-g16	1284
TB-GAR1-g17	1272
TB-GAR1-g18	1267
TB-GAR1-g19	1211
TB-GAR1-g20	1124
TB-GAR1-g21	1186
TB-GAR1-g22	1168
TB-GAR1-g23	1281
TB-GAR1-g24	1177
TB-GAR1-g25	1293
TB-GAR1-g26	1296
TB-GAR1-g28	1320
TB-GAR1-g30	1161
TB-GAR1-g31	1078
TB-GAR1-g32	1318
TB-GAR1-g33	1311
TB-GAR1-g34	1298
TB-GAR1-g35	1140
TB-GAR1-g36	1206
TB-GAR1-g37	1180
TB-GAR1-g38	1251
TB-GAR1-g40	1088
TB-GAR1-g41	1274
TB-GAR1-g42	1277
TB-GAR1-g43	1169
TB-GAR1-g44	946
TB-GAR1-g8	1041
TB-GAR1-g29	919
TB-GAR1-g39	1038

TB G9 with IP	T (°C)
TB-GAR3-gt3	1100
TB-GAR3-gt5	1115
TB-GAR3-gt8	1087
TB-GAR3-gt9	1100
TB-GAR3-gt10	1041
TB-GAR3-gt12	1095
TB-GAR3-gt16	1093
TB-GAR3-gt20	1028
TB G10	
TB-GAR3-gt2	916
TB-GAR3-gt6	1101
TB-GAR3-gt11	1115
TB-GAR3-gt13	1101
TB-GAR3-gt15	1101
TB-GAR3-gt18	1062
TB-GAR3-gt19	1124
TB-GAR3-gt22	1104
TB-GAR1-gt7	1102
TB-GAR3-gt21	1102

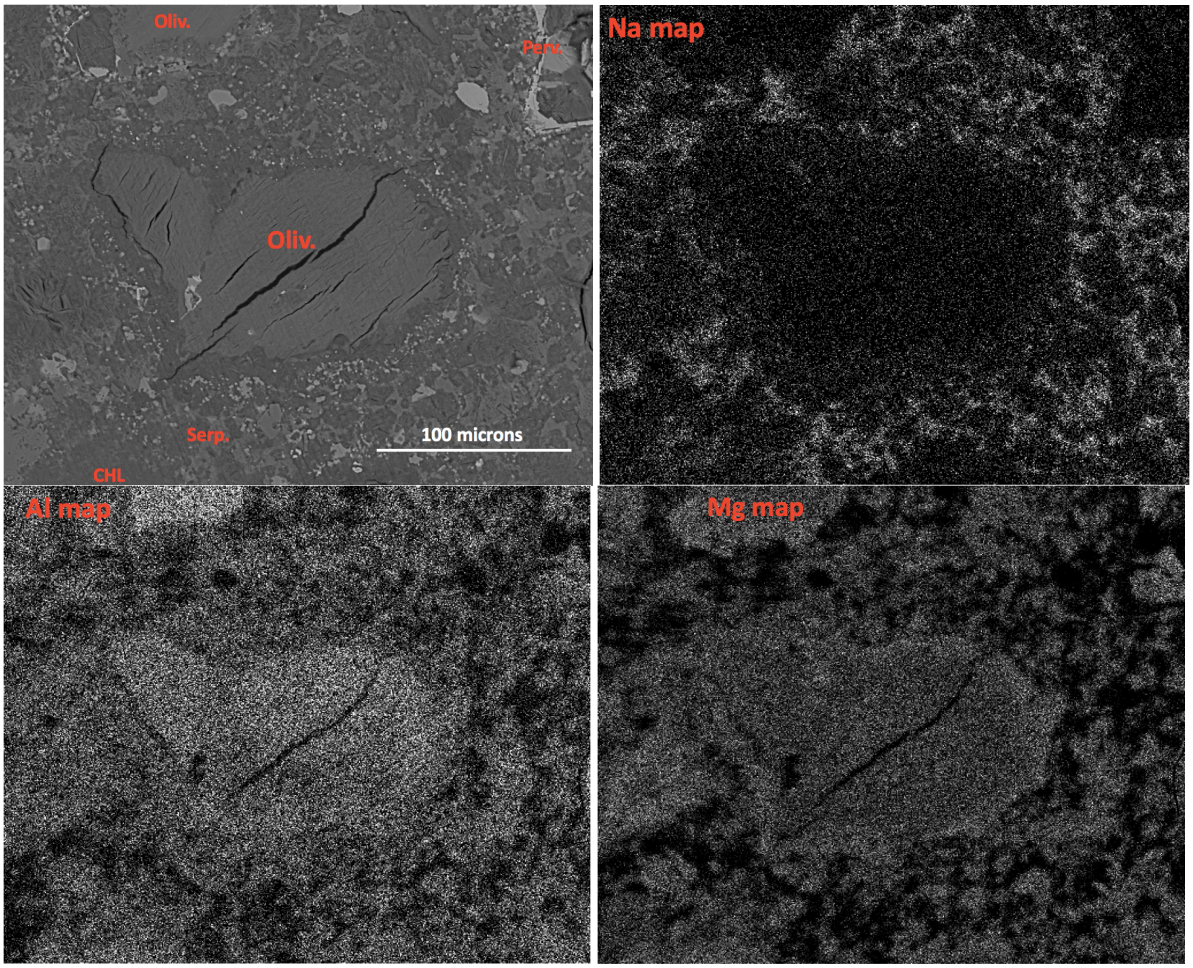

Figure 1: Camatue sample RG165675. The Na elemental map showing chlorite (glagolevite) as the main Na phase in the groundmass. CHL (chlorite), Oliv. (Olivine), Serp. (serpentine).